Local Estimation of the Earth's Core Magnetic Field

Hammer, Magnus Danel

Publication date:
2018

Document Version
Publisher's PDF, also known as Version of record

Local Estimation of the Earth's Core Magnetic Field

PhD thesis presented by

Magnus Danel Hammer

for the degree of Doctor of Philosophy to

DTU Space - National Space Institute
Technical University of Denmark

September 2018

Supervisors

Prof. Christopher Charles Finlay
Geomagnetism, DTU Space
Technical University of Denmark
Denmark

Prof. Nils Olsen
Geomagnetism, DTU Space
Technical University of Denmark
Denmark

Location

DTU Space
National Space Institute
Technical University of Denmark
Kongens Lyngby, Denmark

Ph.D. thesis

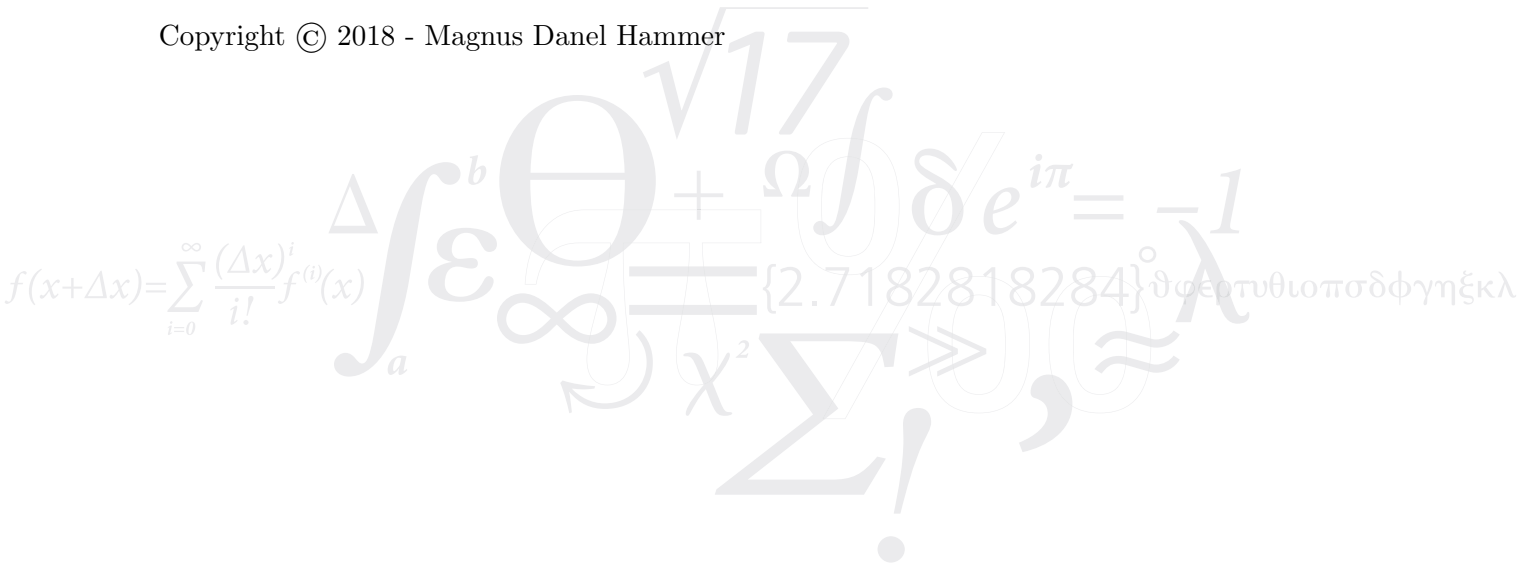

Preface

This Phd thesis entitled *Local Estimation of the Earth's Core Magnetic Field* is the outcome of a three-year PhD program at the Division of Geomagnetism, at the Technical University of Denmark.

The project supervisors were:

- Prof. Christopher Charles Finlay at DTU Space, Technical University of Denmark
- Prof. Nils Olsen at DTU Space, Technical University of Denmark

The project was funded by the Technical University of Denmark and The Danish Council for Independent Research - Natural Sciences, Grant DFF-4002-00366.

In connection with this thesis, work carried out has been included in two scientific articles enclosed in Appendix A:

- Magnus Danel Hammer and Christopher Charles Finlay, 2019. Local Averages of the Core-mantle Boundary Magnetic Field from Satellite Observations. *Geophysical Journal International*, 216, 1901-1918
- Olivier Barrois, Magnus Danel Hammer, Christopher Charles Finlay, Yannick Martin and Nicolas Gillet, 2018. Assimilation of ground and satellite magnetic measurements: inference of core surface magnetic and velocity field changes. *Geophysical Journal International*, 215(1), 695-712

Abstract

The geomagnetic field is generated in the Earth's outer core by fluid motions in a process known as the geodynamo. During the past 18 years satellite magnetic measurements have provided new insights into the spatial structure of the field and its time variations. Among these observations are the decay of the dipole field, the signature of a high latitude jet, pulse-like features in the second time derivative of the field at the core-mantle boundary (CMB) and rapid field changes called geomagnetic jerks. Theories into the origin and dynamics of these phenomena may begin to converge as numerical dynamo simulations reach more Earth like conditions and magnetic field measurements are made continuously spanning longer time intervals. In order to gain further geophysical insights into the geodynamo processes, there is a need for robust estimation of the core field and its evolution and to quantify the uncertainty and resolution of these estimates. In this thesis two local techniques for estimating the core-generated magnetic field are described and implemented using satellite data from the *Swarm* and CHAMP satellite missions.

The first technique is the Virtual Observatory (VO) method, in which time series of the field and field gradients at pre-specified locations at satellite altitude, are calculated via a local procedure, such that short-period variations of the core signal can be investigated. These VO time series resembles the time series from ground observatories which have higher temporal resolution. We show that using a refined VO setup together with an improved data selection and handling scheme, the VO time series exhibit strong correlation in all three field components with time series of nearby ground observatories. Using the VO time series, signs of field changes over South America around 2016 and in the Pacific region in 2017 may be the first indications of a new geomagnetic jerk taking place. We find that field models built using both vector and gradient VO data show evidence for secular acceleration activity in the Pacific region.

In order to construct reliable estimates of the field tracking its evolution at the CMB, appraisal is crucial. Appraisal consists of spatial resolution and variance estimation. The second technique used builds on a modified Backus-Gilbert inversion approach called Subtractive Optimally Localized Averages (SOLA). Using the SOLA method, localized averages of the field and its first time derivative are estimated at the CMB, determined via spatial averaging kernels, accounting for both internal and external field sources. We incorporate information from data error covariance matrices which include along-track serial error correlation. We show an example of a global collection of SOLA estimates for the radial main field (MF), with widths of the averaging kernel varying between $\sim 18^\circ$ and $\sim 54^\circ$ depending on latitude, with a standard deviation of $\sim 10\mu$T. We present global collections of SOLA estimates for the radial secular variation (SV) at the CMB, based on 2yr data windows, with averaging kernel widths of $\sim 42^\circ$, $\sim 33^\circ$ and $\sim 30^\circ$ at the equator, with corresponding standard deviations of $\sim 0.25\mu$T/yr, $\sim 2.5\mu$T/yr and $\sim 5\mu$T/yr. We find that the morphology of the MF and SV maps agree well with results from spherical harmonic (SH) based field models, however our method involves only averaging in time and space and not spectral truncation or temporal regularization. We compute the local accumulated secular acceleration (SA) by subtracting the SV SOLA estimates, based on 2yr data windows, from epochs 2 years apart, which have averaging kernel widths of $\sim 42^\circ$ at the equator and standard deviation of ~ 0.2T/yr^2. Comparison of the SOLA based SA and SH field models show good agreement, however we have direct control over the chosen time window length and spatial averaging kernel. Investigating the time evolution of the SA along the geographical equator and pushing towards higher temporal resolution, we

compute 1 year SV differences, based on 1yr data windows. We are able to track coherent structures of the SA and their evolution in time-longitude plots. In particular, we find a distinctive SA "cross-over" event having adjacent and strong oppositely signed SA features, at longitude 25°W in mid 2007. The SOLA technique proves to be well suited for high resolution local studies of the rapidly evolving SA, while at the same time providing the necessary means of appraisal.

Dansk Resumé

Jordens magnetfelt genereres dybt inde i vores planet, hvor bevægelser af flydende metal i den ydre kerne inducerer elektriske strømme i en proces kendt som geodynamoen. Satellitmålinger af jordens magnetfelt er ideelle til at studere denne proces. I denne afhandling udvikles og anvendes to metoder til at undersøge magnetfeltet, og der gøres brug af data indsamlet af *Swarm*- og CHAMP-satellitmissionerne.

Den første metode er kendt som Virtual Observatory (VO) metoden, der genererer tidsserier af feltet og feltgradienter i forudbestemte positioner i satellithøjde. VO-tidsserierne ligner tidserier fra jordbaserede observatorier, men er ikke begrænset af den uregelmæssige geografiske fordeling af jordstationer. I afhandlingen foreslår vi et forbedret dataudvælgelses- og håndteringsprogram, der valideres ved sammenligninger med jordobservatorier. Ved hjælp af VO-tidserierne finder vi tegn på ændringer i feltaccelerationen over Sydamerika i 2016 og over Stillehavsområdet i 2017. Kuglefunktionsmodeller bygget ved brug af VO-tidserier af feltet og feltgradienter viser også tegn på feltacceleration i Stillehavsområdet. Dette har tidligere været anset for at være et område med svag geomagnetisk aktivitet.

Den anden metode indebærer bestemmelse af lokale estimater beregnet som middelværdier af magnetfeltet 2891km under jordens overflade ved kerne-kappe grænsen i yderkanten af geodynamoen. Metoden kaldes Subtractive Optimally Localized Averages (SOLA), og er en videreudvikling af Backus-Gilbert metoden indenfor seismologi og helioseismologi. Denne metode muliggøre en omhyggelig kvalitetsvurdering af feltetestimaterne og deres tidsafledte. I afhandlingen beskrives de teoretiske rammer og den numeriske implementering af metoden i detaljer. Vi præsenterer anvendelser af metoden til estimering af det radiale felt, dets første tidsafledte (feltændringen, SV) og dens anden tidsafledte (feltaccelerationen, SA). Ved hjælp af SOLA metoden viser vi, at det er muligt at kortlægge tidsudviklingen af sammenhængende strukturer i SA. Specielt identificerer vi en markant SA "crossover"hændelse ved længdegrad 25°W i midten af 2007. SOLA metoden har vist sig at være velegnet til lokale studier med høj opløsning af feltaccelerationen, samtidig med at den tilvejebringer den nødvendige kvalitetsvurdering.

Acknowledgements

On a hot sunny day in May 2011 I was lost, completely lost. I was driving a minivan heading to the 46th Nordic Geomagnetic Workshop in Brorfelde, but somehow I missed a turn and found myself outside of the map that I had brought with me. Unfortunately, it was not only myself, I had lost, but also the small group of scientists that I was driving to the workshop. Luckily, a young scientist came to my aid, and with his smart-phone guided us through the countryside and back on track towards Brorfelde. Now, some seven years later, that same man has guided me through whatever detours and obstacles that I have encountered during the course of this three year PhD program at DTU. Thank you Chris, for giving me the opportunity to work with this topic in geomagnetism, and for introducing me to all the lovely people working in the geomagnetic community. Your strong commitment, fountain of ideas and enthusiasm has carried over and truly made this an enjoyable project to be part of. Thanks for supervising me and for always keeping up the good mood and high spirits in spite of my many detours and accompanying despair.

I would like thank Nils Olsen for always giving me useful advices with clarity and new ways of understanding and looking at theoretical and computational aspects, and always with a kind smile. Thank you Nils, for providing me with advice and recommendations on data selection and for providing Matlab codes used in the thesis.

I would like to thank both former and current colleagues at the Division of Geomagnetism. In particular Nynne Lauritsen, Cecille Aakjær, Livia Kother, Maria Gleerup, Clemens Kloss, Arne Døssing, Poul Erik Olsen, Lars Pedersen and Anna Willer for many delightful and useful discussions in a nice and relaxing working environment. I would like to thank Stavros Kotsiaros for many useful discussions regarding SIVW and field gradients and for providing me with a Matlab script for computing field gradients design matrices. I would like to thank Lars Tøffner-Clausen for many helpful discussions regarding satellite data, geomagnetic field models, rotation matrices and for giving me computer assistance. Also, I would like to thank Aslak Stubsgaard for helpful discussions regarding computational considerations that improved my code.

During the last three years, I have had the chance of meeting and collaborating with inspiring people from the geomagnetic community. I would like to thank all these people, and in particular, it has been a great pleasure to get to know and work with João Domingos, Kathy Whaler, Nicolas Gillet and Olivier Barrois.

I would like to thank The Danish Council for Independent Research, Natural Sciences (FNU) funding this Ph.D. project. The financial support is gratefully acknowledged.

Finally I would like to give special thanks to my family, my wife Marie and our kids Ida and Carl for all your love, patience and support during the last three years.

Magnus Danel Hammer
September 2018

Acrynoms

ADM	Axial Dipole Moment
ASM	Absolute Scalar Magnetometer
AT	Along-Track
BVP	Boundary Value Problem
C^3FM	Continuous Covariant Constrained endpoints Field Model
CHAMP	CHAllenging Mini-Satellite Payload
CHAOS	Geomagnetic Field Model
CI	Comprehensive Inversion
CIY4	*Swarm* CI Field Model
CM	Comprehensive Model
CM4	CM Field Model
CMB	Core Mantle Boundary
CRF	Common Reference Frame
CT	Cross-Track
DBC	Dirichlet Boundary Condition
DGRF	Definitive Magnetic Reference Field
ECEF	Earth-Centered-Earth-Fixed
EEJ	Equatorial Electroject
ESD	Equivalent Source Dipole
ESA	European Space Agency
EQ	Equal Area
FAC	Field Aligned Current
FGM	Fluxgate Vector Magnetometer
FWHM	Full Width at Half Mean
GO	Ground Observatory
GRIMM	GFZ Reference Internal Magnetic Model
GSM	Geocentric Solar Magnetospheric Coordinate System
gufm1	Geomagnetic Field model from 1590 A.D. to 1990 A.D.
HMW	Hourly Mean Values
IAGA	International Association of Geomagnetism and Aeronomy
IGRF	International Geomagnetic Reference Field
IHFAC	Interhemispheric Field-Aligned Current
IMF	Interplanetary Magnetic Field
IMO	INTERMAGNET Magnetic Observatory
IRLS	Iteratively Re-weighted Least-Squares
LSC-1	Lithospheric Field Model
LEO	Low Earth Orbiting
LT	Local Time
LSQR	Least Squares Quadratic Regularization
MEF	Merging Electric Field
MEME	Model of the Earth's Magnetic Environment
MF	Main Field
MF7	Crustal Field Model
MHD	Magnetohydrodynamics
MOLA	Multiplicative Optimally Localized Averages
NBC	Neumann Boundary Condition

Continues on next page

NBVP	Neumann Boundary Value Problem
NEC	Norht-East-Center Coordinate System
NGDC-720	Crustal Field Model
NWU	North West Up
OLA	Optimally Localized Averages
OMNI	Solar wind magnetic field and plasma data at Earth's Bow Shock Nose
PCA	Principal Component Analysis
PEJ	Polar Electroject
POMME	Potsdam Magnetic Model of the Earth
QD	Quasi Dipole
QG	Quasi-Geostrophic
RC	Ring Current index
RMS	Root-Mean-Square
SA	Secular Acceleration
SAC-C	Scientific Applications Satellite - C
SCARF	Satellite Constellation Application and Research Facility
SEU	South-East-Up Coordinate System
SH	Spherical Harmonic
SHA	Spherical Harmonic Analysis
SIFM	Swarm Initial Field Model
SIVW	Selective Infinite-Variance Weightning
SM	Solar Magnetospheric
SOLA	Subtractive Optimally Localized Averages
Sq	Solar Quiet
STR	Star Tracker
SV	Secular Variation
SWA	*Swarm* satellite *Alpha*
SWB	*Swarm* satellite *Bravo*
SWC	*Swarm* satellite *Charlie*
TL	Time-Longitude
UT	Universal Time
VFM	Vector Field Magnetometer
VO	Virtual Observatory
WDC	World Data Center for Geomagnetism

Symbols and notation

Symbol	*Name*
α	Regularization parameter
β	Polynomila coefficients
$\hat{\beta}$	Least squares solution
Γ^p_{kq}	Christoffel symbol
γ	Angular distance or variogram
γ^m_n	Gauss coefficient in complex notation
Δd	Magnetic data differences
Δd^{AT}	Along-track magnetic data differences
Δd^{EW}	East-west magnetic data differences
ΔG	Data kernels associated with data differences
$\delta(\mathbf{r}-\mathbf{r}')$	Dirac delta function
$\delta(\Omega-\Omega')$	Dirac delta function angular part
$\delta\mathbf{B}$	Residual magnetic field vector
$\delta\mathbf{B}_{VO}$	VO residual magnetic field vector
δX	Residual magnetic field in northward direction
δY	Residual magnetic field in eastward direction
δZ	Residual magnetic field in downward direction
δt	Time lag
ϵ	Residuals between data and model or external part of RC index
ζ_n	Angle of degree correlation
ν	Coefficients of VO magnetic potential
μ	Lagrange multiplier
Θ	Objective function
ι	Internal part of RC index
κ	Width parameter of Fisher function
λ	SOLA trade-off parameter
ρ	Source function or correlation coefficient
ρ_n	Degree correlation
ρ_r	Correlation coefficient of radial component
ρ_θ	Correlation coefficient of meridional component
ρ_ϕ	Correlation coefficient of azimuthal component
$\widehat{\sigma}$	SOLA error estimate
σ	Electrical conductivity or standard deviation
Σd	Magnetic data sums
Σd^{AT}	Along-track magnetic data sums
Σd^{EW}	East-west magnetic data sums
ΣG	Data kernels associated with data sums
σ_w	Huber weighted data uncertainies
Ψ	Angular distance or scalar function
ψ	Magnetic scalar potential
ψ^{int}	Internal magnetic scalar potential
ψ^{ext}	External magnetic scalar potential
ψ_C	Magnetic potential of core-generated field
ψ_M	Magnetic potential of magnetospheric field

Continues on next page

$\nabla\mathbf{B}$	3×3 magnetic gradient field tensor
$\nabla\mathbf{B}_{VO}$	VO 3×3 magnetic gradient field tensor
τ	Target time or correlation time
Φ	Scalar function
ϖ	IMF clock angle
η	Magnetic diffusivity

$\mathbf{A}$	Magnetic vector potential
A	Area of spherical surface
a	Radius of source surface S_1 or mean Earth radius (also r_a)
$\mathbf{B}$	Magnetic vector field
$\widehat{B_r}$	SOLA radial magnetic field estimate
$\tilde{B}_L$	Truncated SH expansion of radial magnetic field
$\mathbf{B}_C$	Outer core-generated magnetic field
$\mathbf{B}_M$	Large-scale magentospheric field
$\dot{B}_r$	First time derivative of radial magnetic field
B_r	Magnetic field component in radial direction
B_θ	Magnetic field component in meridional (southward) direction
B_ϕ	Magnetic field component in zonal/azimuthal (eastward) direction
$\mathbf{B}_t$	Magnitude of IMF field
$\mathbf{B}_x$	IMF field component in sun-ward direction (GSM frame)
$\mathbf{B}_y$	IMF field component in dusk-ward direction (GSM frame)
$\mathbf{B}_z$	IMF field component in northward direction (GSM frame)
$\mathbf{B}^{crust}$	Crustal magnetic vector field
$\mathbf{B}^e_{pol}$	External poloidal magnetic field
$\mathbf{B}^i_{pol}$	Internal poloidal magnetic field
$\mathbf{B}^e_{tor}$	External toroidal magnetic field
$\mathbf{B}^i_{tor}$	Internal toroidal magnetic field
$\mathbf{B}^{iono}$	Ionospheric magnetic vector field
$\mathbf{B}^{mag}$	Magnetospheric magnetic vector field
$\mathbf{B}^{MF}$	Main magnetic vector field
$\mathbf{B}^{MF}_{VO}$	VO main field magnetic vector field
$\mathbf{B}_{VO}$	VO magnetic vector field
$\mathbf{B}^{satellite}$	Satellite magnetic vector field measurements
$\mathbf{B}^{sh}_{pol}$	Poloidal magnetic field in a shell
$\mathbf{B}^{sh}_{tor}$	Toroidal magnetic field in a shell
b	Radius of source surface S_2
c_w	Huber turning constant
d_{VO}	VO search radius
$\mathbf{E}$	Electric vector field
$\underline{\underline{\mathbf{E}}}$	Data error covariance matrix
E_m	Merging electric field
$F_{10.7}$	Solar flux index at wavelength 10.7cm
f	Frequency
$\underline{\underline{G}}$	Design matrix
$\underline{\underline{G}}^\dagger$	Generalized inverse
G^*	General notation of data kernels for vector data or data sums and differences

Continues on next page

G_C	Exterior data kernels
G_M	Interior data kernels
g_n^m	Internal Gauss coefficients
H	Heaviside function or temporal kernel function
$\underline{\underline{H}}$	Temporal kernel Matrix
h_n^m	Internal Gauss coefficients
h_{VO}	Altitude of VO above r_a
$\underline{\underline{I}}$	Identity matrix
$\mathcal{J}$	Weight function
$\mathbf{J}$	Electrical current density
$\mathbf{J}_b$	Electrical current density of bounded currents
$\mathbf{J}_d$	Electrical current density of displacement currents
$\mathbf{J}_f$	Electrical current density of free currents
$\mathbf{J}^e$	Electrical currents external to the ionosphere
$\mathbf{J}^i$	Electrical currents internal to the Earth's surface
$\mathbf{J}^e_{tor}$	Toroidal electrical currents external to the ionosphere
$\mathbf{J}^i_{tor}$	Toroidal electrical currents internal to the Earth's surface
$\mathbf{J}^{sh}_{tor}$	Toroidal electrical currents within the ionosphere
$\mathcal{K}$	Averaging kernel
$\mathcal{K}_C$	Averaging kernel for core source
$\mathcal{K}_M$	Averaging kernel for magnetospheric source
k	Field component index r, θ, ϕ
Kp	Planetary geomagnetic activity index
$\underline{\underline{\mathbf{L}}}$	Regularization matrix
l_p	Lebedev quadrature weights
$M(n,m)$	Sensitivity matrix
M_l	B-spline basis functions
N_C	Exterior Neumann Green's function
N_M	Interior Neumann Green's function
N_{lm}	Surface spherical harmonic pre-factor
N_{VO}	Number of VO's
$\hat{\mathbf{n}}$	Normal vector
P	Poloidal scalar potential
P^{ext}	External poloidal scalar potential
P^{int}	Internal poloidal scalar potential
P_l^m	Associated Legendre functions of degree l and order m
P_l	Legendre polynomials of degree l
q	SOLA weighting coefficients
q_c	Electrical charge
q_n^m	External Gauss coefficients
$\mathbb{R}$	Real numbers
$\underline{\underline{R}}$	Resolution matrix
R^e	External power spectrum
R^i	Internal power spectrum
R^t	Toroidal power spectrum
$\underline{\underline{\mathbf{R}}}_y$	Rotation matrix about the y axes
$\underline{\underline{\mathbf{R}}}_z$	Rotation matrix about the z axes
$\underline{\underline{R}}^{SEU}_{ECEF}$	Rotation matrix from the ECEF to the SEU frame

Continues on next page

$\underline{\underline{R}}_{SEU}^{ECEF}$	Rotation matrix from the SEU to the ECEF frame
RC	Ring Current index
$\mathbf{r}_0$	SOLA target position vector
$\mathbf{r}_p$	Lebedev position vector
r_a	Mean Earth radius, 6371.2km
r_c	Mean CMB radius, 3480km
r_m	Mean magnetosphere radius, $4r_a$
S_1	NBVP source surface 1
S_2	NBVP source surface 2
S_C	CMB source surface
S_M	Magnetosphere source surface
$\mathbf{SA}_{VO}$	VO secular acceleration
$\mathbf{SV}_{VO}$	VO secular variation
s_n^m	External Gauss coefficients
$\mathcal{T}$	Target kernel
$\mathcal{T}_C$	Target kernel for core source
$\mathcal{T}_M$	Target kernel for magnetospheric source
t	Time
t_0	SOLA target time
t_{ref}	Taylor series expansion reference time
$t_n^{m,c}$	Toroidal expansion coefficients
$t_n^{m,s}$	Toroidal expansion coefficients
$\mathbf{u}$	Velocity vector field
V	Volume or magnetic potential
v	Solar wind velocity
$\underline{\underline{\mathbf{W}}}$	Lebedev matrix
W_L	Averaging window function
w	Huber weights
X	Magnetic field component in meridional (northward) direction
Y	Magnetic field component in zonal/azimuthal (eastward)
Y_{lm}	Surface spherical harmonics
$Y_{n,c}^m$	Normalized (surface) spherical harmonics
$Y_{n,s}^m$	Normalized (surface) spherical harmonics
Z	Magnetic field component in vertical downward direction

Physical Constants

Symbol	*Quantity*	*Value*	*SI units*
ϵ_0	permittivity of vacuum	$1/(\mu_0 c^2) = 8.854187817 \times 10^{-12}$	F/m
μ_0	permeability of vacuum	$4\pi = 12.566370614 \times 10^{-7}$	H/m
c	speed of light	2.99792458×10^8	m/s

Contents

Chapter 1

Introduction

The Earth's magnetic field at any given time and position is the sum of the magnetic field contributions from a wide range of sources, all of which vary in both space and time. Deciphering this signal in an effort to uncover and investigate the underlying sources and their underlying processes is a major challenge in geomagnetism. The study of the geomagnetic field continuously evolves as more magnetic field measurements are acquired and new analysis technologies are developed, such that better understanding and new insights into the geophysical mechanisms can be established. One major piece of this puzzle is the core-generated magnetic field, originating in the dynamics of the electrical conducting liquid outer core of the Earth. The core field is generated by a dynamo that is essentially fuelled by the cooling of the Earth. Improved knowledge of the core field and how it evolves in time may lead to new insights into the inner workings of the dynamo and to what causes the observed temporal field changes. Perhaps most importantly, a better understanding of the core dynamics holds the prospects of being able to estimate how the field will evolve in the near future.

For the past 18 years magnetic field measurements from low Earth orbiting satellites have provided new information on small-scale field features exhibiting short time scale variations (Olsen and Mandea, 2008; Lesur et al., 2008; Finlay et al., 2016b). Studies of the first and second time derivative of the main field (MF), termed secular variations (SV) and secular acceleration (SA), respectively, have shown that rapid subdecadal changes are taking place. Such changes may be probed down to a period of perhaps 1 year, limited by mantle filtering (Mandea et al., 2010; Chulliat et al., 2015). Lately, spatial differences of multiple satellite magnetic field observations have been used in order to enhance the recovery of small-scale field features. Compared to using vector data, differences of magnetic field measurements are less sensitive towards unmodelled large-scale external field contamination (Kotsiaros et al., 2015; Olsen et al., 2015; Finlay et al., 2016b). Geomagnetic field models built using *Swarm* measurements have shown that the radial SV can be determined up to spherical harmonic (SH) degree 11 from 1 year of measurements (Olsen et al., 2015, 2016). However, time-dependent geomagnetic field models based on spherical harmonics and B-splines are forced to imposed model regularization in a non-uniform manner that typically influences higher SH degrees more strongly (Constable and Parker, 1988; Olsen et al., 2009). This complicates the interpretation of the truncated SV and SA signals plotted in global maps, especially in light of the SV and SA power spectra being blue (i.e. the power increases with SH degree), and because the instantaneous SA may be

formally undefined (Bouligand et al., 2016).

A number of striking observations have been made concerning the morphology and time evolution of the field. For example, during the last 180 years the dipole field has decayed in strength by ∼9%, and studies have linked this decay to either expulsion of toroidal magnetic field due to fluid upwelling, or the combined effect of asymmetries in the magnetic field and the motions of a planetary-scale gyre in the southern hemisphere (Gubbins, 1987; Olson and Amit, 2006; Finlay et al., 2016a). On shorter time scales, using 3 year data time windows, pulsating features in the radial SA at the CMB focused along the geographical equator have been reported and interpreted as waves propagating at the core surface, and possibly in a stably stratified layer at the top of the core (Chulliat and Maus, 2014; Chulliat et al., 2015). On the other hand, dynamo simulations have suggested that the SA should be expected to exhibit pulse like behaviour with distinctive equatorial localization (Aubert, 2018). Geomagnetic jerks have been associated with a change in polarity of SA pulses (i.e. in between consecutive pulses of opposite sign), and to sign changes in the non-zonal azimuthal core flow acceleration. Very recently, dynamo simulations have been used to link geomagnetic jerks with the sudden buoyancy release from within the core, and the associated triggering of hydromagnetic waves (Aubert and Finlay, 2018). However, many observational details of the SA signal at short length and time scales remain unclear.

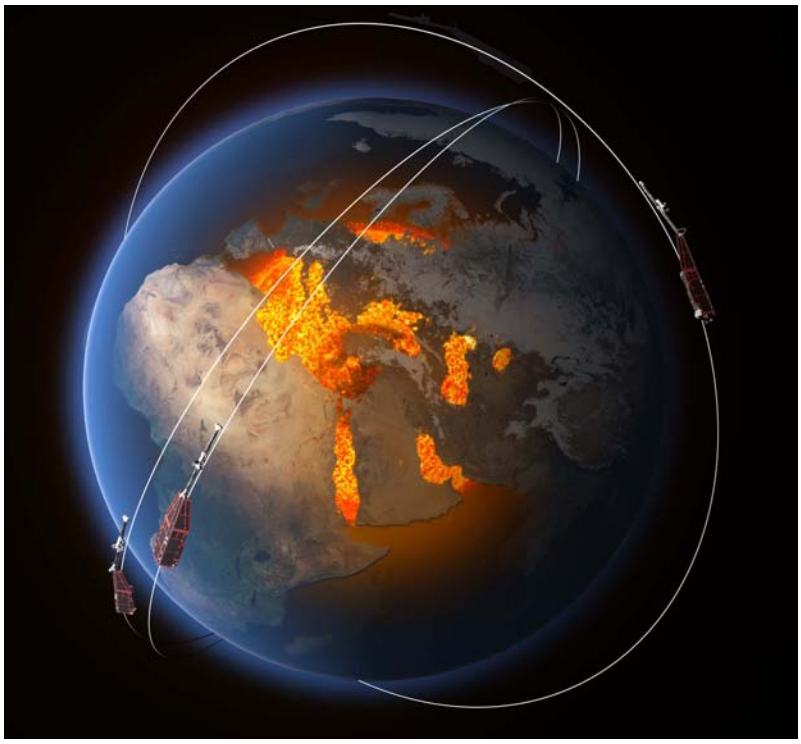

Figure 1.1: Illustration of the ESA *Swarm* constellation satellite mission, having amongst its science objectives studies of the core dynamics, geodynamo processes, and core-mantle interaction (Credit: ESA/ATG Medialab, https://earth.esa.int/web/guest/missions/esa-eo-missions/swarm/mission-overview).

When investigating the geomagnetic field evolution important questions arise: how do we determine reliable estimates of the MF, SV and SA on both global and local scales? How can such estimates be used to best map the core flow? What can we say about the observed time changes, such as the dipole decay, jerks and SA pulses? What does

this tell us about the processes operating in the core? In order to be able to answer some of these questions, pushing towards finer signal recovery, an essential issue is the ability to construct robust estimates of the field, together with uncertainty and resolution information, when mapping the field morphology and tracking its time evolution. It turns out that in order to properly describe the core-generated magnetic field, detailed knowledge of the electrical current system surrounding the Earth is required. This constitutes a very challenging problem and may in fact be the major limiting factor when trying to determine the core magnetic field. This means that alternative approaches have to be considered in order to investigate whether observed features are truly reliable, in order to give confidence that further geophysical interpretation can be carried out. The *Swarm* satellite constellation setup is particularly useful for such core field studies, due to the gradient concept where measurement differences along-track and cross-track (for the side-by-side flying *Swarm Alpha* and *Charlie* pair) can reduce the contamination from large-scale external fields. When pushing towards retrieval of finer field structures in time and space, appraisal techniques become important. Appraisal comprises of field spatial resolution and variance estimation, assessing the limitations of the data and the validity of field features observed at the CMB. Appraisal is crucial for advancing our knowledge of core dynamics, and especially when considering the new possibilities of tracking the field offered by the *Swarm* satellite constellation mission. Figure 1.1 presents an illustration of the *Swarm* satellite constellation orbiting the Earth, measuring the magnetic field.

1.1 Objective of Thesis

The objective of this thesis is to describe and to develop local methods of robustly estimating the core-generated magnetic field, and to used these to better characterize the secular variation and the secular acceleration. Magnetic field observations from the *Swarm* and CHAMP satellite missions will be used and, in particular, advantage will be taken of along-track and east-west (for *Swarm* only) data differences.

Two local techniques are described and investigated. The first technique is the Virtual Observatory (VO) method, generating time series of the magnetic field and its spatial derivatives at pre-specified locations at satellite altitude by using satellite magnetic field observations. Thereby the VO method tries to mimic the time series of ground observatories. The second technique is based on a modified Backus-Gilbert inversion approach called Subtractive Optimally Localized Averages (SOLA), where estimates of the field at the core-mantle boundary are determined by local field averages using satellite magnetic field observations. A fundamental aspect of the latter method is formal appraisal of spatial resolution and variance estimation.

1.2 Outline of Thesis

The outline of this thesis is as follows.

Chapter 2 presents an introduction to the Earth's magnetic field, providing an overview of the most important contributing sources and their magnetic signature. This is followed by a short description of different geomagnetic field disturbance diagnostics used in the thesis when selecting data. This chapter also includes sections on the basic mathematical description of the geomagnetic field and reviews some recent internal geomagnetic field models and their limitations.

Chapter 3 describes measurements from the CHAMP and *Swarm* satellite missions, and provides details of the data selection criteria and processing steps used. Two data sets

were built and used in this thesis. An exploratory data analysis was carried out for one of these data sets, and the chapter includes a description of how the data error covariance matrices used in this thesis were built.

Chapter 4 describes the virtual observatory (VO) method and how this was implemented. The work carried out relies on previous experience with the method and includes new modelling initiatives and analyses of these, along with recommendations on future usage of the VO method.

Chapter 5 describes a modified Backus-Gilbert inversion method called subtractive optimally localized averages (SOLA). The SOLA method is applied to the geomagnetic problem of determining the core-mantle boundary radial magnetic field and its time derivatives. Two different approaches to handling the field time-dependence are investigated.

Chapter 6 provides a summary of the results and findings of the VO and SOLA methods, and some conclusions.

Appendix A includes published and submitted papers, made in connection with the work of this thesis. Appendix B includes studies made of the VO method using synthetic data. Appendix C includes results of field computations with the VO method.

1.3 Units and Conventions

In this thesis a scalar is denoted using regular type, e.g. d, a vector is denoted by bold, e.g. $\mathbf{v}$ and a matrix is denoted by bold and two underlines, e.g. $\underline{\underline{\mathbf{G}}}$. The real three-dimensional Euclidean vector space is denoted by $\mathbb{R}^3$ in which a point in space using an orthogonal Cartesian coordinate system is given by the position vector $\mathbf{r}(x, y, z)$ or by its spherical polar coordinates $\mathbf{r}(r, \theta, \phi)$. The convention used here for spherical geometry is that θ denotes the polar angle also termed colatitude. A unit vector for the vector $\mathbf{r}$ having size $|\mathbf{r}|$ is denoted $\hat{\mathbf{r}}$ and given by $\hat{\mathbf{r}} = \frac{\mathbf{r}}{|\mathbf{r}|}$. Notation for differentiation follows the standard Leibniz's formulation, e.g. df/dx, and partial differentiation is written as $\partial f/\partial x$. Both Lagrange's and Newtons's notations will also be used, e.g. $f'(x)$ and $\dot{x}$ (where the dot notation refers to time derivatives), respectively.

This thesis implements units of the *Système Internationale* (International System, abbreviated as SI). The vector $\mathbf{B}$ is called the magnetic field (formally it is the magnetic induction or flux density), and the related field $\mathbf{H}$ referred to as the auxiliary field or magnetic displacement vector (Griffiths, 1999; Backus et al., 1996). The magnetic field measured above the Earth's surface is to a good approximation $\mathbf{B}$ and not $\mathbf{H}$, however since the permeability $\mu \sim \mu_0$ in the atmosphere due to the vanishing magnetic susceptibility the fields $\mathbf{B}$ and $\mathbf{H}$ are proportional (LEO satellites take measurements in the thermosphere, i.e. the lower ionospheric F-region) (Gubbins and Herrero-Bervera, 2007; Hrvoic and Newitt, 2011; Backus et al., 1996). The physical quantity $\mathbf{B}$ is in the Euclidean vector space, a geometric entity equipped with both length and direction, and is measured in the standard SI-unit Tesla where $[1T = \frac{Vs}{m^2}]$ (the auxiliary field $\mathbf{H}$ has units $[Am]$). In geomagnetism the magnetic fields occurring are often stated as being of the order micro Tesla, i.e. 1μ T$= 10^{-6}$T or nano Tesla, i.e. 1nT$= 10^{-9}$T. This thesis shall retain from using the auxiliary field $\mathbf{H}$ altogether, and instead reserve the letter H for the Heaviside function.

All programming work carried out in this thesis was done using Matlab version 2015b.

Chapter 2

The Earth's Magnetic Field

This Chapter provides an overview of the different sources which contribute to the geomagnetic field as measured above the Earth's surface. It also describes the fundamental principles used in present day geomagnetic field models and their limitations. Figure 2.1 presents an overview sketch of the spatial location of some the most important sources which contribute to the magnetic field (top plot) and an associated sketch (bottom plot) providing insights into their spectral domains, amplitudes, spatial wavelengths and temporal scales as observed at a typical satellite altitude of 350km. The sources are traditionally divided into their location relative to the Earth's surface as being either internal or external. Dynamo action in the liquid outer core and crustal magnetization in the upper layers of the Earth constitute the internal sources, whereas electrical current systems in the ionosphere and magnetosphere belong to the external sources. As illustrated in the plots the external ionospheric current systems are numerous and very complex in their nature and appearance, and they vary rapidly with location and time. Among these are E-region current phenomena including the polar and equatorial electrojects (PEJ and EEJ, respectively), the solar quiet (Sq) field, and F-region currents including plasma bubbles, interhemispheric field-aligned currents (IHFAC) and magnetospheric field-aligned coupling currents at polar regions (FAC). In addition to these sources, time variations in the external fields induce electrical currents within the Earth and oceans thereby producing secondary magnetic fields. Notice here the region in which satellite measurements are usually taken; the CHAMP and *Swarm* satellites fly between altitudes of roughly 200-500km, i.e. within the ionospheric F-region thus meaning that contributions from the ionospheric E-region currents would be observed as internal from a satellite perspective.

It is crucial to have an understanding of the length and time scales associated with the contributions to the magnetic field from all the different sources. The bottom plot in Figure 2.1 shows this in a schematic way; the bottom and top axes show the spherical harmonic degree and corresponding spatial wavelength, respectively, while the left and right axes show the mean field amplitude and the mean squared field amplitude (i.e. the power), respectively. Because satellites are moving at approximately 8km/s, it is not possible to decipher if the field measured is due to a temporal or a spatial change; this is illustrated by the upper most axis which illustrates that the magnetic signal from a source having a time period τ, would correspond to a certain spatial scale. For instance, a period of 150s would look like a spatial feature of 1200km Olsen and Stolle (2012). Also shown in this plot is the observed power spectrum for a given spherical harmonic degree n of the internal field from the core and crustal sources, by the combination of models CHAOS-4

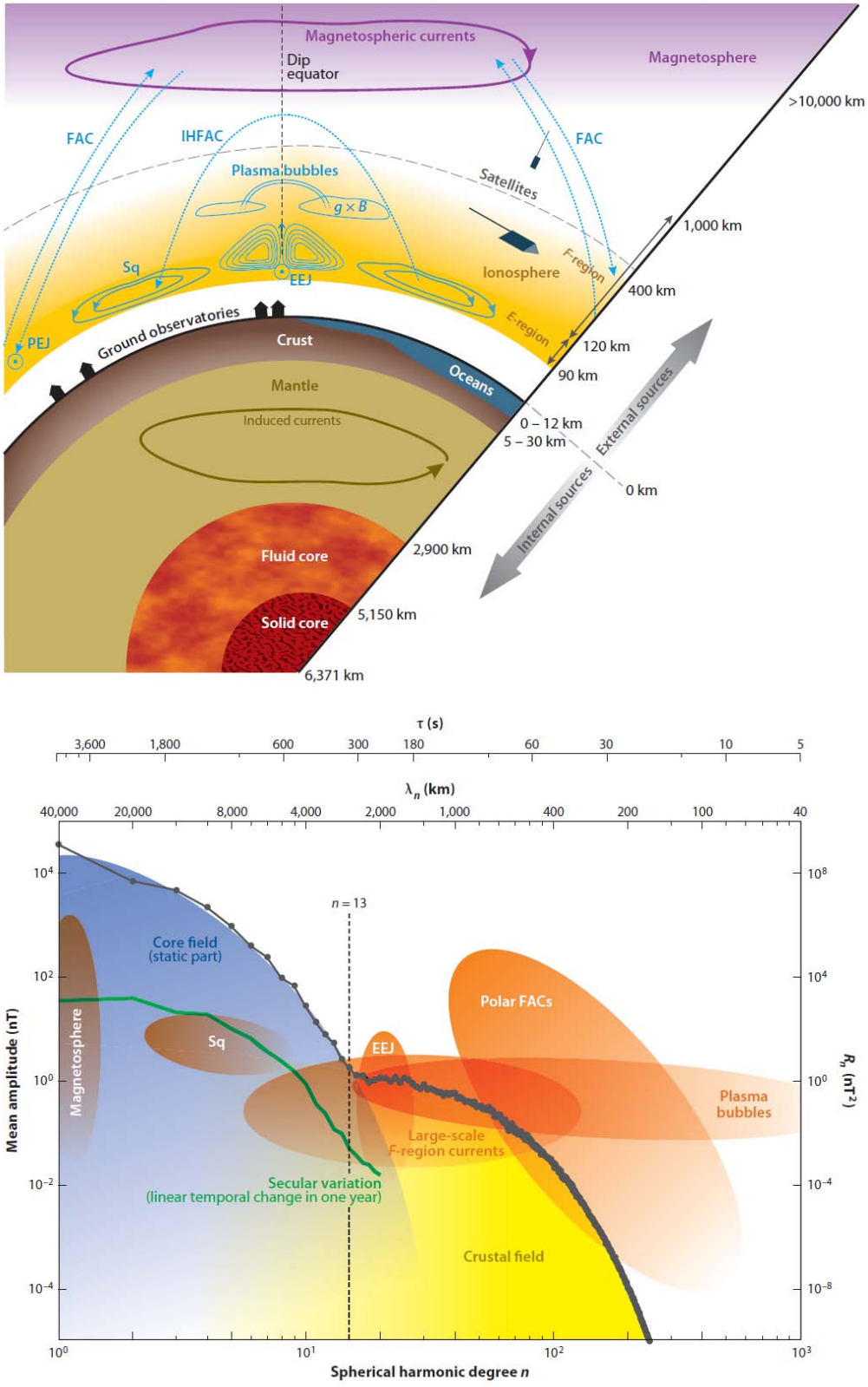

Figure 2.1: Sketches of the different sources making significant contributions to the magnetic field observed. The top plot shows the location of the sources while the bottom plot shows the corresponding spectral domains, amplitudes, spatial wavelengths and temporal scales as observed at a typical satellite altitude of 350km. Extracted from Olsen and Stolle (2012).

for $n \leq 90$, MF7 for $90 < n \leq 133$ and NGDC-720 for $n > 133$, plotted in black dots. The plots give of indications as to what can be expected from the internal and external sources; in particular the internal fields are seen to overlap in the spectral domain, as do internal and external sources. Lastly, a green curve is plotted which shows the time derivative of the core field, and what might be expected from this.

2.1 The Field Generated in the Outer Core

The main part of the Earth's internal magnetic field is believed to be produced by a self-sustaining dynamo process, called the geodynamo, converting kinetic energy into electromagnetic energy. The cooling of the Earth along with chemical differentiation at the inner-core boundary causes vigorous convection in the liquid metallic outer core of the Earth. Fluid motions gives rise to the geodynamo in the outer core, stretching, twisting and advecting the magnetic field (Buffett, 2000; Jones, 2015). The workings of the geodymano are governed by the laws of magnetohydrodynamics (MHD) which describe the motion of electrically conducting fluids in the presence of magnetic fields in a rotating system (e.g., Gubbins and Roberts, 1987; Finlay et al., 2010a). Magnetohydrodynamics combines the laws of electrodynamics (given by Maxwell's equations) with the force balance of a rotating fluid flow (given by the Navier-Stokes equation), coupled with the continuity equation (conservation of mass), the Poisson's equation for the gravity field and finally the heat equation. The related differential equations together with a number of simplifying assumptions (such as the Boussinesq approximation) and boundary conditions allow studies of the geodynamo to be carried out (Gubbins and Roberts, 1987; Roberts, 2015). The interplay of the different force terms in the Navier-Stokes equation along with magnetic field feed-back coupling is very complex, but insights can be gained by considering the relative importance of the force terms. For instance, considering slow motions and neglecting buoyancy, viscous effects and the Lorentz force leads to the geostrophic balance. Because the Earth is rapidly rotating, the flow tends to organize in columnar structures parallel to the rotation axis, such that the flow becomes invariant along these, as described by the Proudman-Taylor theorem.

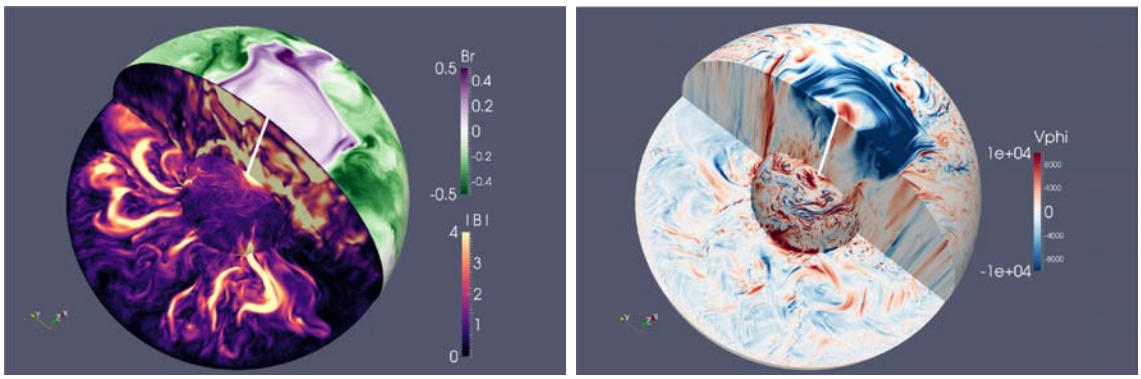

Figure 2.2: Snapshot example from a 3D geodynamo simulation showing the magnetic field intensity within the core and the radial magnetic field at the CMB (left plot) and the azimuthal (i.e. east-west) velocity (right plot) where the color scale indicates the direction of the flow. The inner sphere represents the inner core, and the white line in both plots represents the rotation axis. Extracted from Schaeffer et al. (2017).

However, the origin of the main field was a mystery that persisted up until the mid

1900s. Speculations into possible mechanisms flourished and the reader is referred to the interesting reviews given in (Chapman and Bartels, 1940, p. 701), (Rikitake, 1966, p. 13) and Parkinson (1983) for further details. In 1919 Larmor suggested that dynamo action could be responsible for the magnetic field of the sun (Larmor, 1919). Dynamo theory was developed starting with simple dynamo considerations (e.g., Elsasser, 1946; Bullard, 1955), and in 1963 Braginsky established the driving mechanism of the geodynamo (Gubbins, 2010), and later Glatzmaiers and Roberts (1995) succeeded in recreating important properties such as reversals of the geomagnetic field using a 3D geodynamo simulation. Throughout the intermediate years important studies where carried out in more detailed using simplified dynamo descriptions, trying to understand the fundamental processes and mechanisms responsible for the generation and behaviour of the geomagnetic field (e.g., Gubbins and Roberts, 1987; Merrill et al., 1998; Backus et al., 1996; Gubbins, 2010; Roberts, 2015). This included kinematic dynamo models having prescribed velocity fields, and mean-field dynamos (splitting the magnetic field and flow into a mean large scale part and a small turbulent part) where a small turbulent part of the flow would generate a large scale magnetic field (Roberts, 2015). Although much progress has been achieved since 1995, and characteristics such as drift of field features and secular variation, the role of diffusion, and complex polarity reversals have emerged from the simulations (e.g., Aubert et al., 2013; Sheyko et al., 2016; Aubert, 2018; Christensen and Wicht, 2015; Schaeffer et al., 2017), geodynamo model simulations are still relatively far from reaching real Earth conditions and unresolved issues include the validity of simplifying assumptions, the various dynamical interplays and understanding turbulence in the core (Christensen and Wicht, 2015).

In Figure 2.2 a snapshot example of a 3D dynamo simulations from Schaeffer et al. (2017) is given, showing the magnetic field intensity within the core and the radial magnetic field at the CMB (left plot) along with the azimuthal (east-west) fluid velocity (right plot). Both plots show the outer and inner core with a slice extracted such that the equatorial and meridional plans are visible. The plots illustrate some of the inner workings of the outer core producing the radial field at the CMB; for instance the columnar flow features going parallel to the rotation axis and the effects of the inner core causing differentiated motion behaviour inside the tangent cylinder compared to outside (i.e. an imaginary cylinder tangent at the equator of the inner core). In recent years, data assimilation, using the actual geomagnetic field observations, has begun to be a valuable tool in gaining significant insights into core dynamics, for instance identifying torsional oscillations and identifying magnetic diffusion associated with up- and downwellings (e.g., Beggan and Whaler, 2009, 2010; Gillet et al., 2010; Aubert, 2013; Barrois et al., 2018). As more satellite data becomes available and data assimilation technology progresses, the possibility to better forecast the evolution of the main field will become an increasing relevant topic (Hulot et al., 2015).

2.1.1 Time Variations of the Core Magnetic Field

The core-generated magnetic field changes on time scales ranging from months to centuries. The first and second time derivatives of the main field are called the secular variation (SV) and the secular acceleration (SA), respectively. The temporal changes includes a number of intriguing features such as the westward drift, noticeable east-west asymmetry of the field evolution between the Pacific and the Atlantic hemispheres, signatures of an accelerating high-latitude jet, geomagnetic jerks and decay of the geomagnetic dipole, all of which have been linked to the processes in the outer core (Jackson and Finlay, 2015; Livermore et al., 2017). Furthermore, on longer time-scales the geomagnetic field undergoes dramatic changes, called polar reversals, where the magnetic poles switch places, and at times so-

called field excursions can take place. In such processes the inner core is believed to play a significant role (Gubbins, 1999). The time change of the magnetic field is governed by the magnetic induction equation which is derived form Maxwell's equations and Ohm's law for a moving conductor, here assuming constant conductivity (e.g., Gubbins and Roberts, 1987; Holme, 2015)

$$\frac{\partial \mathbf{B}}{\partial t} = \nabla \times (\mathbf{u} \times \mathbf{B}) + \eta \nabla^2 \mathbf{B} \tag{2.1}$$

here $\mathbf{B}$ is the magnetic field, $\mathbf{u}$ is the fluid velocity (typical $\sim 10 - 20$km/yr) and $\eta = 1/(\mu_0 \sigma) = 1.69 m^2 s^{-1}$ is the magnetic diffusivity where μ_0 is the permeability of free space and σ is the fluid electrical conductivity (Gubbins and Roberts, 1987; Finlay et al., 2010a, e.g.). The second term of equation (2.1) represents the effect of magnetic diffusion due to the finite resistivity of the fluid. The characteristic time-scale associated with diffusion is $\sim$ 23.000yrs for a spherical conductor of the size of the Earth's core, which means that if there were no fluid flow, i.e. a stationary case where $\mathbf{u} = 0$, the field would diffuse away (e.g. Gubbins and Roberts, 1987). The first term is the advective effect to the field evolution, and considering a perfect conductor ($\sigma = \infty$) the second term drops to zero such that the magnetic field lines would be frozen into the fluid and moving along with it; this is also known as Alfvén's theorem. The time scales of the SV are years to centuries, thus shorter than the diffusion time. Furthermore, considering the non-dimensional magnetic Reynolds number, R_m, (i.e. the ratio of the advection to diffusion), applying typical length and flow scales, leads to $R_m \sim 300 - 1000$ (Gubbins and Roberts, 1987; Christensen and Tilgner, 2004). Even though this is a simplified scale analysis using a single system length scale, by assuming that time variations are sufficiently, short and the magnetic features are sufficiently large a reduction of equation (2.1) is commonly carried out leading to the frozen flux induction equation being the main tool for core flow inversions (Roberts and Scott, 1965; Holme, 2015). Thereby the main assumption is, that advection by the core flow is the primary cause of the observed secular variation. Several studies have investigated the validity of the frozen flux assumption looking for time changes in null-flux curves at the CMB (Jackson and Finlay, 2015), and some studies claim to have observed flux expulsion (e.g., Bloxham and Gubbins, 1985; Chulliat and Olsen, 2010).

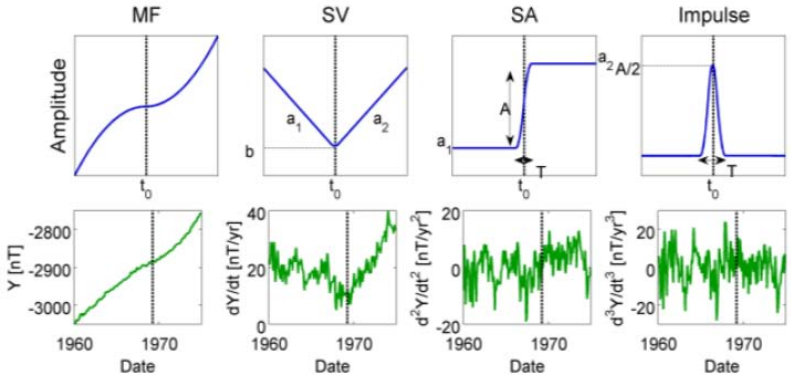

Figure 2.3: Comparison between an idealised jerk (top plots) as seen in the MF, SV and SA, and corresponding monthly mean time series of the Y-component and its derivatives at the Eskdalemuir (ESK) observatory in Scotland (bottom plots). The amplitude of the jerk is denoted A. Extracted from Brown et al. (2016).

However, the true nature of the dynamics underlying the observed time changes are still not clear, for instance, the westward drift which has been known for a long time

and has often been attributed to large-scale core flow (Parkinson, 1983; Holme, 2015). Another possible contribution to the westward drift are propagation of magnetic waves in the Earth's outer core as identified in the gufm1 field model (Finlay and Jackson, 2003; Jackson and Finlay, 2015) and it has been linked to inner-core superrotation (Livermore et al., 2013). Furthermore, geomagnetic jerks which are rapid field changes, also known as SV impulses, also not well understood. Jerks are seen as sharp changes in the rate of change of SV, or equivalently as abrupt changes in the SA at the Earth's surface, and are especially clear in the Y field component (e.g., Mandea et al., 2010; Jackson and Finlay, 2015). Jerk are identified in time series of the SV as "V" or "Λ" shaped features, and the SA as step changes "/" or "\" shaped features centred on zero (Mandea et al., 2010; Brown et al., 2016). Figure 2.3 illustrates the signature of the 1969 jerk in the Y component of the field as observed in Eskdalemuir in Scotland and its time derivatives.

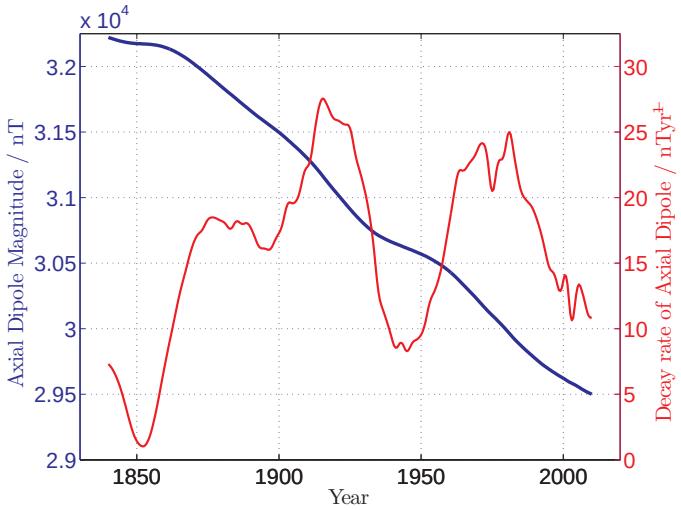

Figure 2.4: The plot shows the variation in magnitude (blue scale) and decay rate (red scale) of magnetic axial dipole g_1^0 from 1840-2010, from the COV-OBS model (Gillet et al., 2013). Extracted from (Finlay et al., 2014).

Another important feature is the decay of the geomagnetic axial dipole, which makes a large contribution to the SV observed during the last 180yrs. Figure 2.4 shows the magnitude of the axial dipole (in blue, left scale) and the corresponding decay rate (in red, right scale). It can be seen that since 1840 the axial dipole has decayed by 9%. Underlying mechanisms for the dipole decay has been proposed including; magnetic diffusion at the CMB through toroidal magnetic field flux expulsion associated with fluid upwelling (Gubbins, 1987), flow oscillations in a stably stratified layer at the top of the outer core (Buffett, 2014), and it has been linked to southward movement of field patches in the southern hemisphere and field reversal (Gubbins, 1987; Gubbins et al., 2006; Olson and Amit, 2006). Finlay et al. (2016a) suggested that meridional transport of field flux patches, linked to a planetary-scaled gyre motion observed in core flows in the southern hemisphere, together with asymmetries of the geomagnetic field related to the South Atlantic Anomaly, are responsible for the observed dipole decay, acting to redistribute energy into higher SH degrees. In their geodymamo simulations, the authors found no evidence of increased magnetic diffusion as an explanation for changes in the axial dipole moment. Figure 2.5 gives an illustration from the geodynamo simulation associated with the studies of Finlay et al. (2016a), showing part of the outer core dynamics and magnetic field as well as the surface core flow and magnetic field. In particular, the plot illustrates how

the equatorward surface flow of the eastern part of the gyre can be linked to columnar convection within the outer core.

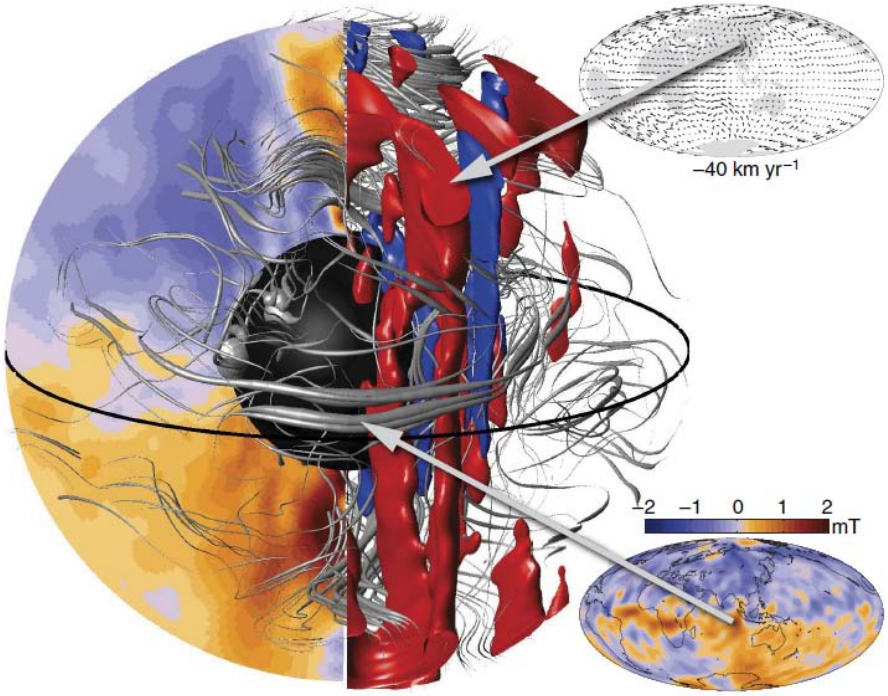

Figure 2.5: The plot gives an illustration from a geodynamo simulation showing the CMB radial magnetic field (in orange and blue color) and the associated core surface flow (global maps in the bottom and top subplots, respectively), the average azimuthal field within the core, columnar convection of the eastern part of the gyre is shown by iso-surfaces of constant axial flow velocity, and magnetic field lines within the core in grey threads (the thread thickness indicates their magnetic energy). The inner core is the back sphere in the center. Extracted from Finlay et al. (2016a).

Figure 2.6 shows global maps of the CMB quasi-geostrophic (QG) flow averages (i.e. a flow invariant along the rotation axis) from 2000-2010 along with the radial magnetic field (left plot), and the patterns of the advective contribution to the axial dipole moment (ADM) time change (right plot) which is computed based on the radial field and meridional flow. In order to better test these ideas, improved models of the CMB radial field and core surface flow (derived from the CMB SV) are required, especially for specific locations such as the meridional limbs of the gyre

2.2 The Crustal Field

The upper layers of the Earth's surface consists of magnetized rock giving rise to an associated magnetic field called the crustal (or lithospheric field) field. Magnetization is due to a net alignment of small elemental electrical currents inside matter, being classified according to how their directional magnetization responds relative to an applied magnetic field (Griffiths, 1999; Blakely, 1995). The crustal magnetic field is the sum of the contributions from induced and remanent magnetization; the ambient magnetic field enforces a temporary induced magnetization which is proportional in strength and direction to the

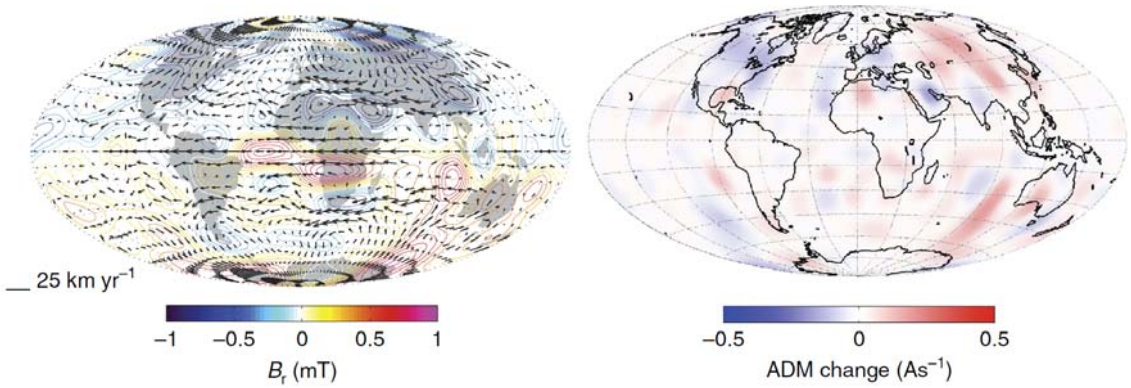

Figure 2.6: Global maps of the CMB QG flow (Gillet et al., 2015a) together with the radial magnetic field (left plot), and the advective contribution to the axial dipole moment (ADM) change (right plot). Extracted from Finlay et al. (2016a).

applied field, whereas the remanent magnetization remain after the removal of an applied field. Especially ferro magnetic materials retains their acquired magnetization if the applied magnetic field is removed, and are thought to be a major contributing source. It is believed that induced magnetization dominates the large-scale structures of the field, while remanent magnetization becomes important at smaller scales for instance at oceanic regions (Purucker and Whaler, 2007; Olsen et al., 2010b).

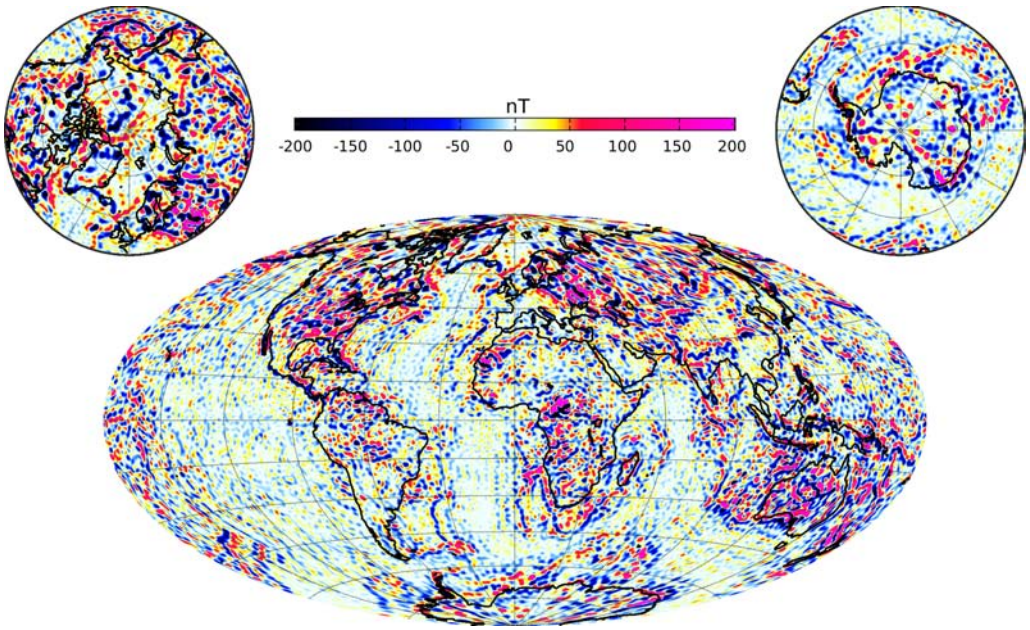

Figure 2.7: The radial component of the crustal magnetic field at the Earth's surface as predicted by the LCS-1 model plotted for SH degrees 1-185 Olsen et al. (2017).

In the present context of investigating the core-generated field, the magnetic field arising from the crust matters, because it makes a significant contribution to the magnetic field measured above the Earth's surface via ground or satellite measurements (Olsen et al., 2010b). At satellite altitudes the crustal field is less than 30nT in strength (Olsen and Stolle, 2012). Figure 2.7 presents the crustal field plotted at the Earth's surface for spher-

ical harmonic degrees 1-185 as predicted by the LSC-1 model (Olsen et al., 2017). The map of the crustal magnetic field reveals that it possesses complex and highly localized features, reflecting the underground geology. This makes the field interesting with regard to possible interpretations related to geological processes and for understanding the subsurface structure and its composition, geothermal heat flux determination, providing the signature of seafloor spreading along with geodynamics at subduction zones (i.e. plate tectonics) and resource exploration possibilities (Langel and Hinze, 1998; Maule et al., 2005; Purucker and Whaler, 2007). The internal power spectrum at the Earth's surface becomes flat at around spherical harmonic degree 15, corresponding to a wavelength of approximately 2500km, whereas the maximum degree in Figure 2.7 corresponds to wavelengths of ∼250km. The crustal magnetic field conceals the small-scale core field beyond a wavelength of ∼2500km, thus blocking potentially important insights into this regime.

2.3 Magnetospheric and Ionospheric Fields

The interaction of the solar wind and the associated interplanetary or heliospheric magnetic field (Owens and Forsyth, 2013; Balogh and Erdõs, 2013), with the internally generated magnetic field of the Earth, manifests itself by a range of complex couplings (Baumjohann and Nakamura, 2007; Lühr et al., 2017). Knowledge of the appearance and behaviour of these external sources is of great importance, because their signature in magnetic field measurements is the main limiting factor obscuring the internal field signal. Figure 2.8 presents a sketch of the near-Earth ionospheric and magnetospheric electrical current systems. Extensive reviews of the current systems in the ionosphere and magnetosphere are provided in (e.g., Baumjohann and Nakamura, 2007; Lühr et al., 2017; Olsen and Stolle, 2012, 2017; Alken et al., 2017).

Firstly, the interaction with the solar wind deforms the Earth's magnetic field, creating a magnetosphere, the boundary of which to outer space is termed the magnetospause. The interaction of the IMF and the Earth's magnetic field leads to magnetic reconnection, which is particularly pronounced during a southward oriented IMF. This brings solar plasma particles into electrical current systems inside the magnetosphere, the movement of which are determined by various drift forces, that results in the production of electrical currents and therefore magnetic fields (e.g., De Pater and Lissauer, 2001; Baumjohann and Nakamura, 2007). In the magnetosphere large-scale current systems includes the dayside magnetopause Chapman-Ferraro currents, cross-tail currents, the nightside tail current and the ring current (Lühr et al., 2017; Olsen and Stolle, 2017).

Secondly, the short-wavelength part of the solar illumination (the ultraviolet radiation) controls the ionization of the upper atmosphere and drives the ionospheric dynamo, causing complex electrical current patterns and phenomena to occur. At mid- and low latitudes the main sources are: i) solar quiet (Sq) currents of the ionospheric E-region dynamo generated by diurnal wind systems due to differentiated heating and cooling, having North and South hemispheric vortices, and ii) interhemispheric field-aligned currents (IHFAC) flowing between the two Sq vortices (Olsen and Stolle, 2012, 2017). Furthermore an intense electrical current flows along an equatorial band in the E-region called the equatorial electrojet (EEJ), being a dayside phenomena. At high latitudes the most important E-region current system occurs in the auroral oval and is known as the polar electrojet (PEJ). Considering the nightside, the E-region conductivity reduces significantly, however the Sq field and in particular its induced counterpart may still persist during night times (Olsen et al., 2005a). Ionospheric F-region systems include the diamagnetic effect of the equatorial ionization anomaly (also called the Appleton anomaly), gravity driven currents

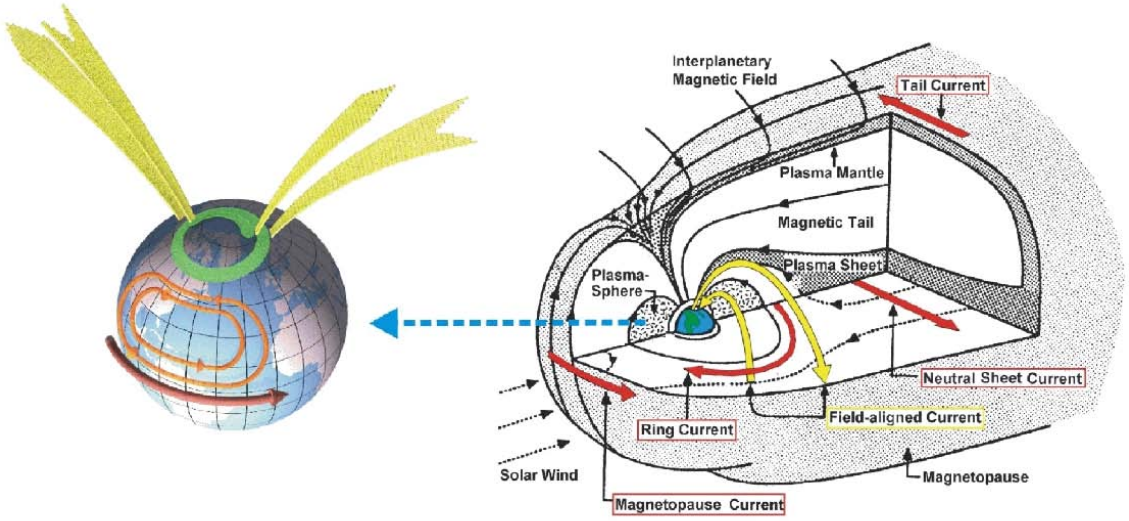

Figure 2.8: Sketch showing the major external electrical current systems of the ionopshere and magnetosphere. The right part shows the incoming solar wind interacting with the Earth's internal field to create the magnetospheric environment including the tail and ring current systems. The left part shows a close-up of the Earth and the major ionospheric electrical current systems including the EEJ (red), the Sq vortex (orange), auroral oval where the bulge is the PEJ (green). Field-align coupling current are illustrated in yellow. Extracted from Haagmans (2004).

at low latitudes and post-sunset equatorial plasma irregularities (also called Spread-F or plasma bubbles) (Lühr et al., 2002; Maus and Lühr, 2006; Stolle et al., 2006; Olsen and Stolle, 2012; Alken et al., 2017).

Thirdly, the solar induced electrical currents in the ionospheric regions are coupled to the magnetospheric systems via field-align currents especially at high latitudes (Olsen and Stolle, 2012, 2017). These F-region currents includes the mid latitude IHFACs from Sq imbalances, meridional currents connected to the EEJ and FACs at polar latitudes which follows the main field lines therefore only producing perpendicular magnetic fields. Lastly, the field from all these near-Earth primary current systems induces electrical currents within the Earth and Oceans, thereby producing secondary magnetic fields (e.g., Tyler et al., 2003; Manoj et al., 2006).

2.4 Geomagnetic Field Activity Diagnostics

This section describes different diagnostic tools for monitoring the disturbance/activity level of the geomagnetic field. Selecting magnetic field measurements which are completely free of external field contamination is an impossible task, however dedicated selection and processing of the measurements may significantly reduce such contamination. The goal is to distinguish so-called geomagnetically quiet times when the signals from external fields are much reduced, such that measurements will be less influenced by these fields. In this regard, inferring the geomagnetic activity level via appropriate diagnostics is vital (Kauristie et al., 2017). The dynamical coupling and behaviour of the magnetospheric and ionospheric systems causes a vast variety of electric currents to arise, the signature of which varies with location and time. Considering ionospheric currents at low and mid-latitudes,

being a product of solar irradiation, a typical criteria is to used data where the sun is below the horizon. A parade of magnetic activity indices exists, derived to monitor the variability of certain complicated current systems (Menvielle et al., 2011). In particular, the Kp index is used to monitor global field disturbance while the RC index targets the magnetospheric ring current and its Earth induced effect. The variability of high-latitude ionospheric currents, such as the auroral electrojet and polar cap currents, may be linked to the Interplanetary Magnetic Field (IMF) and the merging electric field (MEF) which depends on the solar wind (Kauristie et al., 2017). Furthermore, the F10.7 Solar Flux index is described, since this is used as a scaling parameter to estimate ionospheric Sq field predictions of the CM4 model, which was subtracted from the measurements used in this thesis.

2.4.1 Kp Index

The planetary Kp index is derived by GeoForschung Zentrum (GFZ) Potsdam, Germany, using the locally estimated K indices determined at 13 sub-auroral ground observatories by a procedure described in (e.g., Menvielle et al., 2011; Kauristie et al., 2017). The Kp index tries to quantify the global level of geomagnetic disturbances in 3-hour intervals converted to a scale ordered as: $0^o, 0^+, 1^-, 1^o, 1^+, 2^-, 2^o, 2^+, 3^-, 3^o, 3^+, ...9^-, 9^o$. Comparing geomagnetically quite and disturbed years, the most likely value of Kp can vary significantly, for instance during the quiet year 1997 $Kp < 2^o$ occurred 70% of the time while for the disturbed year 2003 it was only 25 % of the time (Kauristie et al., 2017). Thus, selecting data using restricted Kp criteria might have a severe effect on the amount of satellite data available for studying the core field.

Figure 2.9 presents a plot of the Kp index from 2000-2018, where the y-axis values $10, 20, ...90$ corresponds to the Kp values $1^o, 2^o, 3^o...9^o$. As can be observed in the plot, the time around 2003 had higher activity level, while the time around 2009 had lower activity level. It should be mentioned, that years of low solar activity coincide with a low geomagnetic activity level, while a high solar activity is seen as a maximum in Kp value approximately 2 years after the occurrence of solar maximum in the sunspot number (Kauristie et al., 2017). Also it should be noted that the locations of the observatories used to produce the Kp index are found mostly in the Northern hemisphere, having 11 stations in Western Europe and Northern America and just 2 stations in the Southern hemisphere (Menvielle et al., 2011).

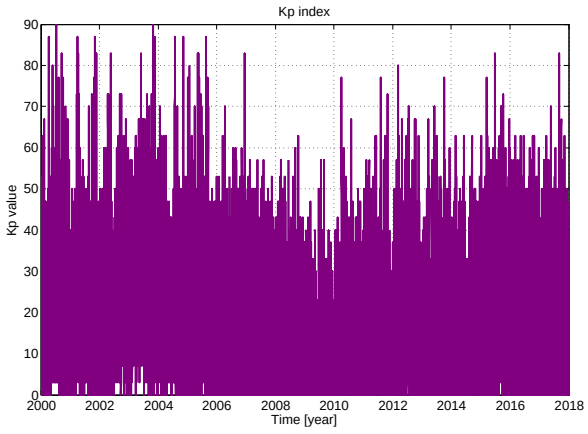

Figure 2.9: Time series of the Kp index during the period 2000-2018.

2.4.2 RC Index

The Ring Current (RC) index targets the equatorial magnetospheric ring current and its secondary Earth induced variations, having a stable baseline http://www.spacecenter.dk/files/magnetic-models/RC/. It was made with the specific intention to be used in internal field modelling by Olsen et al. (2014), and is believed to be well suited for that purpose (Lühr et al., 2017). To derive the index only night-side measurements were used in order to minimize Sq contamination. The RC index consists of an external, ϵ, and internal part ι, such that $RC(t) = \epsilon(t) + \iota(t)$. For this separation a global 1-D electrical conductivity model of the mantle of Grayver et al. (2017) was used. The primary field of the ring current parametrized by a P_1^0 geometry in a 3-D conducting Earth, would cause secondary contributions in all SH degrees and orders. However, assuming a 1-D conductivity model, has the consequence that each external SH coefficient induces only one internal SH coefficient having the same SH degree n and order m Olsen et al. (2005b). The version of the RC index used in this project was created on March 14th 2018, and was derived using 14 low and mid-latitude ground observatories: Alice Spring (Australia), Boulder (USA), Chambon la Foret (France), Fredericksburg (USA), Guam (Guam), Hermanus (South Africa), Honolulu (USA), Kakioka (Japan), Kourou (French Guiana), Learmouth (Australia), Mbour (Senegal), Niemegk (Germany), San Juan (Puerto Rico) and San Pablo de los Montes (Spain).

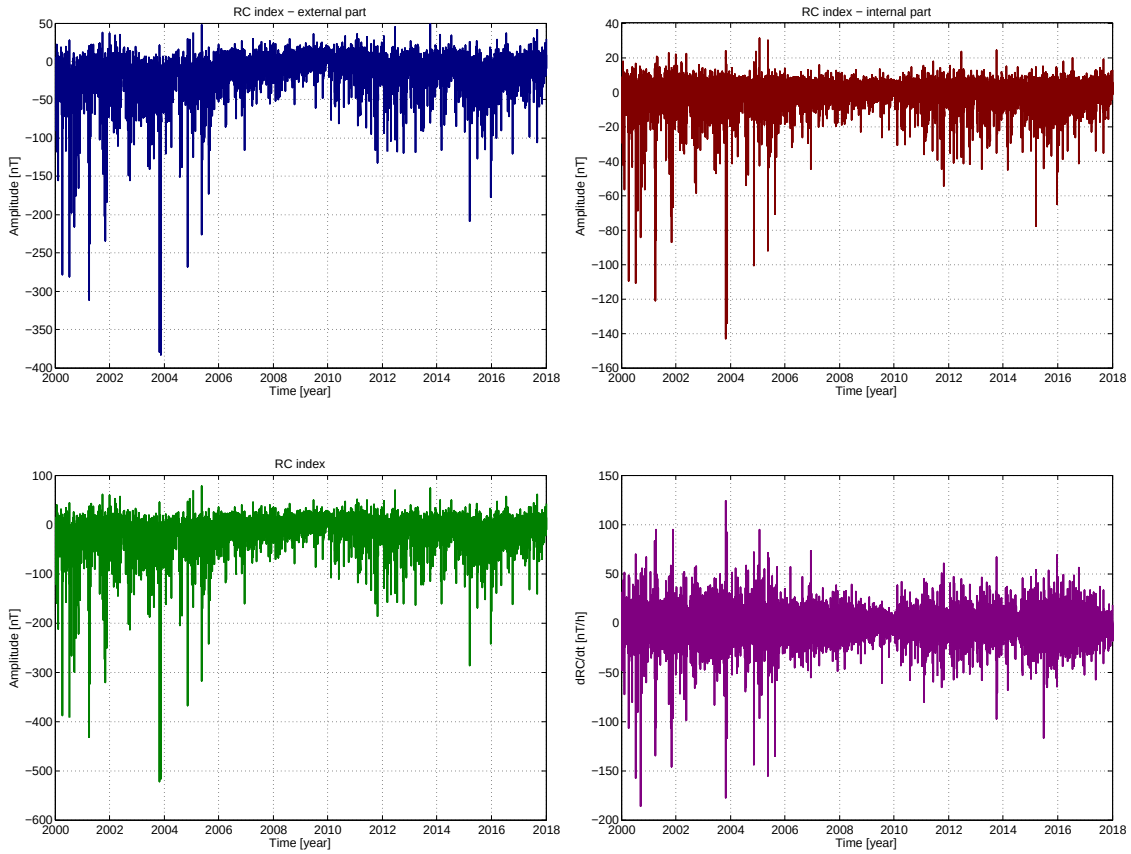

Figure 2.10: Time series of the external part ϵ (upper left), internal part ι (upper right), superposition RC (lower left) and time derivative dRC/dt (lower right) during the period 2000-2018.

Further details regarding the derivation of the RC index, see (Kauristie et al., 2017) and http://www.spacecenter.dk/files/magnetic-models/RC/. It should be noted that previous versions of the RC index may not have been derived from these specific stations. Figure 2.10 presents time series of the two components ϵ and ι, along with their summation RC and the time change dRC/dt during the period 2000-2018. It is evident that during the years 2000-2006, all the components saw large fluctuations.

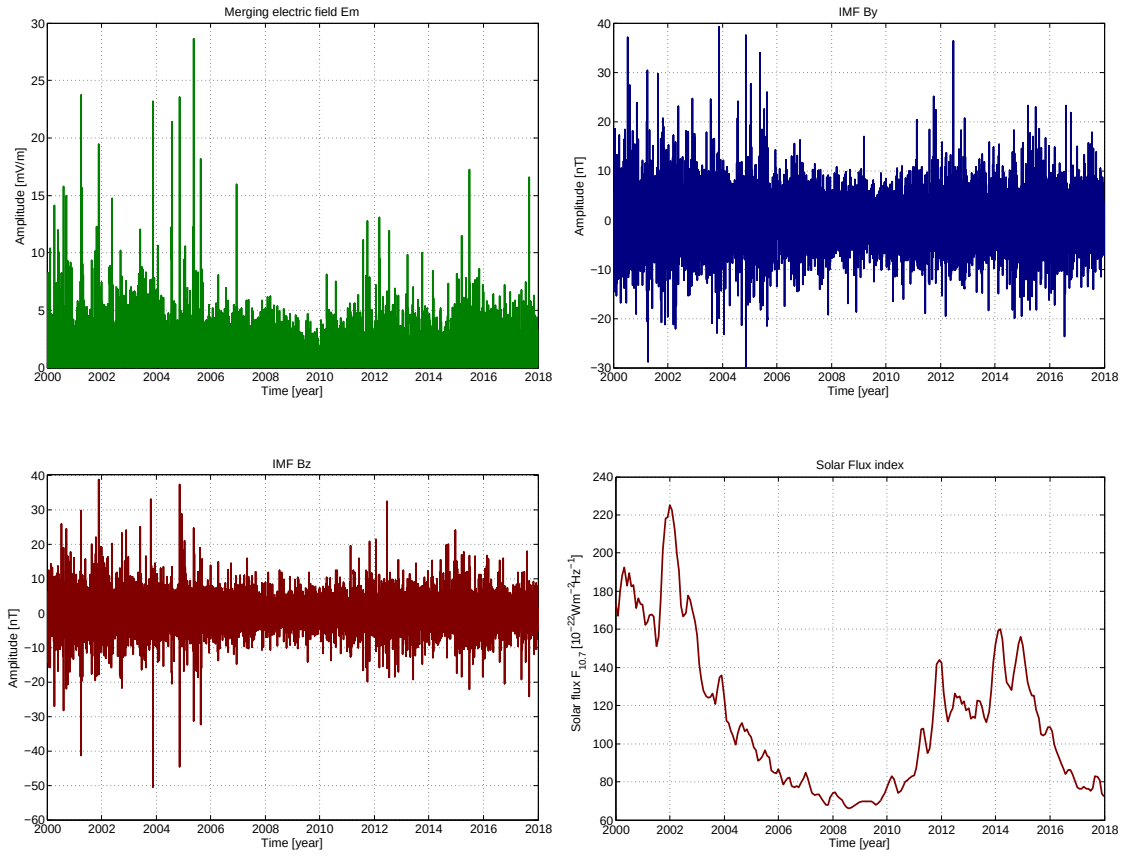

Figure 2.11: IMF and solar activity behaviour showing: the merging electric field at the magnetopause (top left), the IMF B_y (top right), the IMF B_z (bottom left) and a three month mean of the F10.7 solar flux index (bottom right) during the period 2000-2018.

2.4.3 Interplanetary Magnetic Field Behaviour

At high latitudes field-align (Birkeland) coupling currents of the magnetospheric-ionospheric system and the associated ionospheric closure currents, i.e. the Petersen and Hall currents and the PEJ, produces rapid fluctuations in the field; these also have an impact at mid- and low latitudes (Vennerstrom et al., 2007; Friis-Christensen et al., 2017). The amplitude and sign of these high latitude ionospheric electrical currents have been linked to the behaviour and orientation of the B_y and B_z components of the interplanetary magnetic field (IMF), in geocentric solar magnetospheric coordinates (GSM), and to the amplitude of the merging electric field (MEF), E_m, at the magnetospause (Friis-Christensen et al., 1985; Ritter et al., 2004; Friis-Christensen et al., 2017; Kauristie et al., 2017). Therefore, some geomagnetic field models where derived selecting data based on the IMF, including the POMME mod-

els (Maus et al., 2010), the GRIMM models (Lesur et al., 2010) and the CHAOS models (Finlay et al., 2016b). For example in CHAOS-6 it was required that IMF $B_z > 0$nT and that $E_m \leq 0.8$mV/m (Finlay et al., 2017). In this thesis 1-min values of the IMF and solar wind were extracted from the OMNI database http://omniweb.gsfc.nasa.gov, and 2 hourly mean values were computed. Figure 2.11 presents plots of the IMF B_y (upper right) and B_z (lower left) components, and of the merging electric field E_m (upper right) during the period 2000-2018.

2.4.4 F10.7 Solar Flux Index

The solar activity level is known to influence the ionospheric field and various parameters (for instance the sun spot number) may be used to track this activity. One such parameter is the F10.7 solar flux index, which measures the solar radio emission intensity of frequency 2800 MHz or equivalently a (microwave) wavelength of 10.7cm (Tapping, 2013). It correlates highly with the daily sunspot number. Since 1947 the National Research Council of Canada has provided observations using a radio telescope. From 1991 and onwards this was done at the Dominion Radio Astrophysical Observatory, Canada. The bottom right plot in Figure 2.11, shows a three month mean of the solar flux index between 2000 and 2018. The solar flux index was used in the data processing of Chapter 3, to compute and subtract the CM4 field model predictions the ionospheric field and its secondary Earth induced counterpart. For more details on the CM4 model and its ionospheric estimates see Section 2.6.

2.5 Mathematical Description of the Geomagnetic Field

This section is concerned with the mathematical aspects of describing the geomagnetic field. The laws of classical electrodynamics govern electric and magnetic vector fields and provides the basic formulations needed for further treatment and analysis. Assuming that current sources are absent in the region of interest, a potential field description emerges which makes up the backbone of modern day geomagnetic field description. However, the actual geomagnetic field may be a non-potential, thus requiring other descriptions to be considered such as the Mie-representation (Backus et al., 1996).

2.5.1 Classical Electrodynamics and Helmholtz's Theorem

Classical electrodynamic theory is well known and has be thoroughly described in the literature (e.g. Griffiths, 1999; Jackson, 2007), here the most important points related to geomagnetism are summarized. The electric and magnetic fields are described as vector fields, meaning that at each point in space (in $\mathbb{R}^3$) a vector can be assigned. Classical electrodynamic theory states that the electric and magnetic fields are governed by the Maxwell's equations together and the Lorentz force law along with appropriate boundary conditions (Griffiths, 1999). Maxwell's equations in a vacuum may be written

$$\nabla \cdot \mathbf{E} = \frac{q_c}{\epsilon_0} \tag{2.2}$$

$$\nabla \times \mathbf{E} = -\frac{\partial \mathbf{B}}{\partial t} \tag{2.3}$$

$$\nabla \cdot \mathbf{B} = 0 \tag{2.4}$$

$$\nabla \times \mathbf{B} = \mu_0 \mathbf{J} + \mu_0 \epsilon_0 \frac{\partial \mathbf{E}}{\partial t} \tag{2.5}$$

where ϵ_0 is the permittivity of free space, μ_0 is the permeability of free space, q_c is the electric charge density and $\mathbf{J}$ is the electric current density. $\mathbf{E}$ is the electric field vector and $\mathbf{B}$ is the magnetic field vector. The electric current density is determined as $\mathbf{J} = \mathbf{J}_b + \mathbf{J}_f$, where $\mathbf{J}_b$ represents bounded currents within and on the surface of a material due to a given magnetization, and $\mathbf{J}_f$ are called free currents due to free charges. Equations (2.2) and (2.3) are called Gauss's law and Faraday's law, respectively. Together they describe that electric fields can be produced by either electric charges or by time changing magnetic fields. Equations (2.4) and (2.5) describe how magnetic fields can be produced by either electric currents or by time changing electric fields. In addition to this the magnetic field is a solenoidal field as it is divergence free; in other words the net flux through any closed surface equals zero and no net magnetic charges can exist (Griffiths, 1999). As the Maxwell's equations are stated above they fully described the magnetic field and thereby also the geomagnetic field. However, important assumptions can be made which reduces the complexity of the description. The last term in Ampere's law, eq.(2.5), is called displacement currents such that $\mu_0\epsilon_0\frac{\partial \mathbf{E}}{\partial t} = \mathbf{J}_d$. It is possible to show that the displacement currents are negligible in the Earth's atmosphere, i.e. that $\mu_0\epsilon_0\frac{\partial \mathbf{E}}{\partial t} \ll \nabla \times \mathbf{B}$ provided that the time scale T, involved is long compared to the time it takes light to travel a distance of typical length scale L, i.e. $L/T \ll c$ (e.g. Backus et al., 1996; Sabaka et al., 2010). Thus Ampere's law is then reduced to the so-called pre-Maxwell form

$$\nabla \times \mathbf{B} = \mu_0 \mathbf{J} \tag{2.6}$$

All further description of the magnetic field is divided into whether or not the current $\mathbf{J}$ is zero, leading to potential and non-potential fields, respectively. The former assumes that no electrical currents are present in the region of interest where magnetic field measurements are taken, i.e. a source free region like the neutral atmosphere. In other words, the field is fully described using Maxwell's equations with $\nabla \times \mathbf{B} = 0$ and $\nabla \cdot \mathbf{B} = 0$, such that the field is a solenoidal irrotational field, and can be described by the negative gradient of an associated scalar potential ψ, which fulfils the Laplace differential equation, thereby being a Laplacian potential field. The latter case in which electrical currents are present in the region of interest, is known as a non-potential field. Satellites making magnetic field measurements are typically flying above the ionospheric E-region, but within the ionospheric F-region. Here electrical currents, such as for instance field-aligned currents, are present such that it is possible that $\nabla \times \mathbf{B} \neq 0$. Therefore the non-potential description may be viewed as a generalization of the potential case, and it involves either the Helmholtz or Mie representations.

2.5.2 Potential Field Description

Considering first the potential field assumption, in which the geomagnetic field is measured in a source free region, the field observed is the summation of the contributions from various sources, some of which are mentioned in Sections 2.1 to 2.3. Because electrical currents are known to exist within the ionosphere, data have to be selected and processed in such a way as to reduce contamination from these sources; this is the reason for some of the selection criteria used in Section 3.3 (Sabaka et al., 2010). In a geocentric reference frame described by the spherical polar coordinates (r, θ, ϕ), where r $(r \geq 0)$ denotes the radial distance from the center of the Earth, θ $(0 \leq \theta \leq \pi)$ denotes the geocentric colatitude and ϕ $(0 \leq \phi \leq 2\pi)$ denotes the eastern longitude, the magnetic vector field at any time t is written $\mathbf{B}(\mathbf{r}, t) = \mathbf{B}(r, \theta, \phi, t)$. The magnetic field is the sum of the fields contributing, and traditionally these are named according to their source location relative to some

measurement region or shell (for instance the Earth's surface) as being internal (int) or external (ext), (Langel, 1987, e.g.)

$$\mathbf{B} = \mathbf{B}^{int} + \mathbf{B}^{ext} \tag{2.7}$$

Because the geomagnetic field is fully described by the Maxwell's equations reduced to $\nabla \times \mathbf{B} = 0$ and $\nabla \cdot \mathbf{B} = 0$, the field has an associated scalar magnetic potential, ψ, such that

$$\mathbf{B} = -\nabla\psi(r, \theta, \phi) \tag{2.8}$$

which satisfies the Laplace's equation

$$\nabla^2\psi(r, \theta, \phi) = 0 \tag{2.9}$$

thus termed a Laplacian Potential. Furthermore, this potential may be written as the sum of its source potentials, i.e. $\psi = \psi^{int} + \psi^{ext}$. In other words, the geomagnetic field is a conserved vector field (being path independent when integrating) described such that at every point in space a vector is assigned having an associated scalar quantity called the magnetic potential. Therefore in the volume $V(a, b)$, bounded by spheres of inner and outer radius a and b such that $0 \leq a < b \leq \infty$, this potential can be formulated as $\nabla^2\psi = 0$, where ∇^2 is the Laplacian linear partial differential operator. The physical meaning underlying the Laplace equation, is that no sources nor sinks of the field can exist in the region $V(a, b)$, that is, no input or output of charges nor accumulation takes place; therefore none of the two types of sources to the magnetic field, namely electrical currents and alternating electric fields, may exist in $V(a, b)$. Only at the regions boundaries, $S(a)$ and $S(b)$, may the potential attain maximum or minimum values (Blakely, 1995). The Laplacian magnetic potential is harmonic in the region V because it fulfils the Laplace equation. This also means that any solution is given by harmonic functions; a function is said to be harmonic in some region, if it fulfils the Laplace equation at every point of that region. Harmonic functions have continuous single valued first and second derivatives, fulfilling the maximum principle (Blakely, 1995).

Some very important results that will be used later in Chapter 5, are the three Green's identities (some times called theorems) which can be derived from the divergence theorem applied to a vector field written as $\mathbf{F} = \Phi\nabla\Psi$. In particular, the second identity allows for the magnetic field potential to be expressed via volume and surface integrals: let Ψ and Φ be two scalar functions that are continuous and differentiable in the volume V bounded by the surface S (e.g., Barton, 1989; Blakely, 1995; Riley et al., 2004)

Green's second identity.

$$\int_V (\Phi\nabla^2\Psi - \Psi\nabla^2\Phi)dV = \int_S (\Phi\nabla\Psi - \Psi\nabla\Phi) \cdot \hat{\mathbf{n}}dS \tag{2.10}$$

where $\hat{\mathbf{n}}$ is the surface normal vector. This identity is essential for the developments in Chapter 5, when seeking solutions of the Neumann boundary value problem in terms of the Green's functions.

Solutions of the Laplace equation may be formed by a number of representations provided they are harmonic, including: spherical harmonics, harmonic splines, wavelets, Slepian functions, dipole and point sources (Schott and Thébault, 2011). The most widely used representation of the potential in spherical geometry is a series expansion in spherical

harmonic functions originally devised by Carl Friedrich Gauss in 1839 (Malin and Barraclough, 1991; Stern, 2002; Langel, 1987; Glassmeier and Tsurutani, 2014).

As mentioned a range of alternative representations to spherical harmonics have been investigated for studying the internal field, for instance: models based on icosodedral grids for the radial magnetic field at the CMB (Constable et al., 1993; O'Brien et al., 1997; Jackson et al., 2007b). Modelling techniques including point sources (i.e. monopoles) by (Hodder, 1982; O'Brien and Parker, 1994; Kother et al., 2015), harmonic splines introduced by Shure et al. (1982) and Parker and Shure (1982), a wavelet approach developed by Holschneider et al. (2003), and Slepian functions Plattner and Simons (2017) have been explored. Recently, Holschneider et al. (2016) introduced a technique based on specifying appropriate correlation functions for internal and external sources. This approach was used by Lesur et al. (2017) in order to derive the Gauss coefficients for the SV using ground observatory monthly means between 1957 and 2014.

The next section will be devoted to the spherical harmonic description of the geomagnetic field. The coefficients of the expansion are termed Gauss coefficients in honour of its inventor. Today most field models use this type of representation, and the IGRF/DGRF model series published by the International Association of Geomagnetism and Aeronomy (IAGA), are built from the Gauss coefficients of candidate field models. Section 2.6 describes some of the advanced geomagnetic field models produced. In particular, details of the CHAOS and the CM model series will be provided, as these models were used extensively in the data selection and processing (see Section 3.3) in this thesis.

Spherical Harmonic Representation

Here a description of the spherical harmonic representation is provided because this representation type will be frequently referred to and since spherical harmonic models have been built in this thesis. A description in spherical polar coordinates is natural, such that the Laplace equation can be written (Langel, 1987; Riley et al., 2004)

$$\nabla^2\psi = \frac{1}{r^2}\frac{\partial}{\partial r}\left(r^2\frac{\partial\psi}{\partial r}\right) + \frac{1}{r^2\sin\theta}\frac{\partial}{\partial\theta}\left(\sin\theta\frac{\partial\psi}{\partial\theta}\right) + \frac{1}{r^2\sin^2\theta}\frac{\partial^2\psi}{\partial\phi^2} = 0 \tag{2.11}$$

The solution of equation (2.11) at time t, can be written as an infinite summation of internal and external harmonic polynomials being spherical harmonics (Langel, 1987; Backus et al., 1996; Sabaka et al., 2010)

$$\begin{aligned}\psi(r,\theta,\phi,t) = a\sum_{n=1}^{\infty}\sum_{m=0}^{n}\left(\frac{a}{r}\right)^{n+1}\left[g_n^m(t)\cos(m\phi) + h_n^m(t)\sin(m\phi)\right]P_n^m(\cos\theta)\\ + a\sum_{n=1}^{\infty}\sum_{m=0}^{n}\left(\frac{r}{a}\right)^{n}\left[q_n^m(t)\cos(m\phi) + s_n^m(t)\sin(m\phi)\right]P_n^m(\cos\theta)\end{aligned} \tag{2.12}$$

where $a = 6371.2$km is a reference radius determined as the mean radius of the Earth (a enters as a scaling factor outside the summations to ensure the physical dimensions of equation (2.12)), $\{g_n^m(t), h_n^m(t), q_n^m(t), s_n^m(t)\}$ are the time-dependent Gauss coefficients measured in units nT of the internal and external contributions, and P_n^m are the Schmidt quasi-normalized associated Legendre functions of degree n and order m. Note that the Laplace equation does not involve time, however as the field varies this would materialise in time dependence of the coefficients. The Schmidt normalization is introduced such that the magnitude of the surface harmonics being squared and averaged over a sphere becomes

independent of their order (i.e. the Gauss coefficients reflects the relative importance played by each degree term in the series expansion) (Blakely, 1995). The first summation represents the internal expansion and the second summation is the external expansion relative to the measurement shell. The Schmidt quasi-normalized $P_n^m(\cos\theta)$ are connected to the Ferrers normalized $P_{n,m}(\cos\theta)$ via (Blakely, 1995; Sabaka et al., 2010)

$$P_n^m(\cos\theta) = \begin{cases} P_{nm}(\cos\theta) & \text{if } m = 0 \\ \left[2\frac{(n-m)!}{(n+m)!}\right]^{\frac{1}{2}} P_{nm}(\cos\theta) & \text{if } m > 0 \end{cases} \tag{2.13}$$

The angular part of the solution is made up of the normalized (surface) spherical harmonics given as (Sabaka et al., 2010)

$$Y_{n,c}^m(\theta,\phi) = P_n^m(\cos\theta)\cos(m\phi) \quad \text{and} \quad Y_{n,s}^m(\theta,\phi) = P_n^m(\cos\theta)\sin(m\phi) \tag{2.14}$$

The Schmidt normalized spherical harmonics eq. (2.14) satisfy the relations

$$\langle Y_{n,c}^m, Y_{l,c}^k\rangle = \langle Y_{n,s}^m, Y_{l,s}^k\rangle = \frac{1}{2n+1}\delta_{nl}\delta_{mk} \tag{2.15}$$

$$\langle Y_{n,c}^m, Y_{l,s}^k\rangle = 0 \tag{2.16}$$

where $\langle , \rangle$ denotes an inner product[1] over the sphere S and δ_{nl} denotes the Kronecker delta given as (e.g. Woan, 2000)

$$\delta_{nl} = \begin{cases} 1 & \text{if } n = l \\ 0 & \text{if } n \neq l \end{cases} \tag{2.19}$$

Therefore equation (2.12) can be written

$$\begin{aligned} \psi(r,\theta,\phi,t) = a\sum_{n=1}^{\infty}\sum_{m=0}^{n}\left(\frac{a}{r}\right)^{n+1}\left[g_n^m(t)Y_{n,c}^m(\theta,\phi) + h_n^m(t)Y_{n,s}^m(\theta,\phi)\right] \\ + a\sum_{n=1}^{\infty}\sum_{m=0}^{n}\left(\frac{r}{a}\right)^{n}\left[q_n^m(t)Y_{n,c}^m(\theta,\phi) + s_n^m(t)Y_{n,s}^m(\theta,\phi)\right] \end{aligned} \tag{2.20}$$

By using the potential representation, magnetic field measurements can be related to the Gauss coefficients for each field component (e.g. Langel, 1987; Sabaka et al., 2010). The internal Gauss coefficients $\{g_n^m(t), h_n^m(t)\}$ may then be determined using the radial field component only. However, in order to determine the internal and external Gauss coefficients separately, the horizontal components must be included as well (Langel, 1987).

A set of orthogonality relations follow which can be used to express the expansion coefficients as surface integrals given the value of the field on the surface of a sphere. In theory this field should be known continuously over the surface, however in practice field measurements are collected at discrete points. Thus compliance of the orthogonality

[1] The average value of a function f over the sphere S can be written (Backus et al., 1996)

$$\langle f\rangle = \frac{1}{4\pi}\oint f(\mathbf{r})dS \tag{2.17}$$

An inner product of two functions f and g may be defined such that (Backus et al., 1996; Aster et al., 2005)

$$\langle f, g\rangle = \frac{1}{4\pi}\oint f(\mathbf{r})^* g(\mathbf{r})dS \tag{2.18}$$

where $*$ denotes the complex conjugated.

properties rests on the actual measurements and whether or not the integral can be well approximated (Langel, 1987; Blakely, 1995). The reference radius of the Gauss coefficients is usually set to be the Earth's surface; knowing the Gauss coefficients it is then possible to perform a downward continuation of the field, for instance to the CMB. However, such a transformation constitutes an un-smoothing process (contrary to an upward continuation) in which noise may cause incorrect field features to blow up (Blakely, 1995).

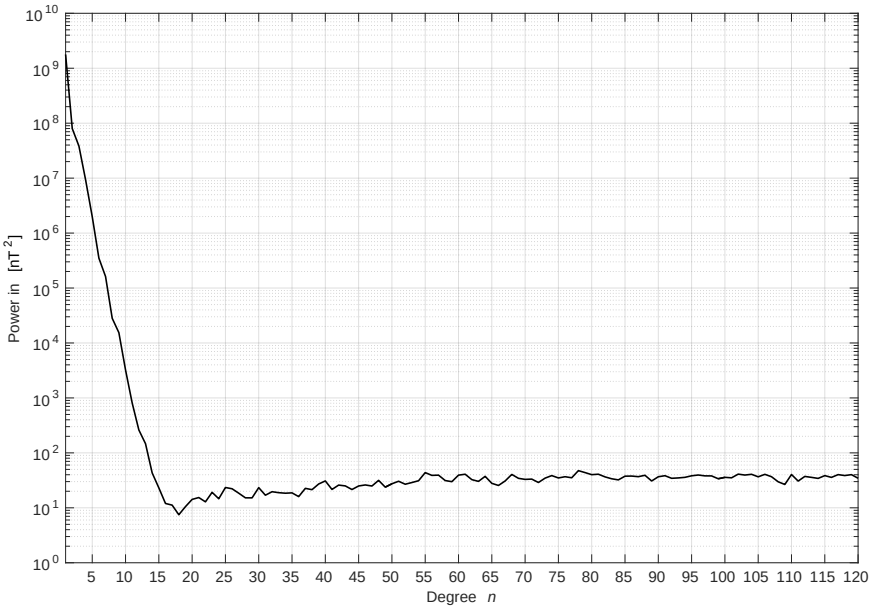

Figure 2.12: Lowes-Mauersberger spherical harmonic power spectrum plotted at the Earth's surface in 2016, as given by the CHAOS-6-x5 field model for SH degrees 1 to 120.

By using the spherical harmonic representation various analyses of the geomagnetic signal can be carried out. One tool is the power spectra of both internal (termed the Lowes–Mauersberger spectrum) and external origin, which can be computed (Lowes, 1966, 1974; Hulot et al., 2015) and used to study field amplitude as a function of wavelength. The internal power spectrum at the surface $S(r)$ with radius r is given by (Hulot et al., 2015)

$$\langle |\mathbf{B}^{int}|^2 \rangle_{S(r)} = R^i(r) = \sum_{n=1}^{\infty} R_n^i \tag{2.21}$$

where $R_n^i(r)$ is given by

$$R_n^i(r) = (n+1)\left(\frac{a}{r}\right)^{2n+4} \sum_{m=0}^{n} \left[(g_n^m)^2 + (h_n^m)^2\right] \tag{2.22}$$

The external power spectrum at the surface $S(r)$ with radius r is given by

$$\langle |\mathbf{B}^{ext}|^2 \rangle_{S(r)} = R^e(r) = \sum_{n=1}^{\infty} R_n^e \tag{2.23}$$

where $R_n^e(r)$ is given by

$$R_n^e(r) = n\left(\frac{r}{a}\right)^{2n-2} \sum_{m=0}^{n} \left[(q_n^m)^2 + (s_n^m)^2\right] \tag{2.24}$$

The internal spectrum plotted in a semi-logarithmic scale at the Earth's surface exhibits a distinct behaviour first investigated by Langel and Estes (1982); for SH degrees $n \lesssim 14$ there is a steep linear decline attributed to the core magnetic field after which the spectrum flattens out and is expected to fall eventually to zero beyond SH degree 200 which is attributed to the crustal magnetic field. Figure 2.12 shows the internal spectrum as predicted by the CHAOS-6-x5 field model up to SH degree 120. This behaviour means that the long-wavelength segment of the crustal field is concealed by the core field, while the small-wavelength part of the core field is conceals by the crustal field. The reason why the spectrum shows this linear decrease for SH degrees $n \lesssim 14$, is that higher order terms are geometrically attenuated. Plotting the spectrum at the CMB instead, the slope becomes nearly zero for SH degrees $n \lesssim 14$ while it becomes positive for for SH degrees $n \gtrsim 14$ (e.g., Backus et al., 1996, p. 181).

The degree correlation, ρ_n, between two SH models, having the sets of coefficients $\{g_n^m, h_n^m\}$ and $\{g_n^{m'}, h_n^{m'}\}$, makes it possible to compare the phase of the model coefficients (e.g., Langel and Hinze, 1998, p. 81)

$$\rho_n = \frac{\sum_{m=0}^{n}(g_n^m h_n^m + g_n^{m'} h_n^{m'})}{\sqrt{[\sum_{m=0}^{n}(g_n^m)^2 + (h_n^m)^2][\sum_{m=0}^{n}(g_n^{m'})^2 + (h_n^{m'})^2]}} \tag{2.25}$$

$$= \cos(\zeta_n) \tag{2.26}$$

where ζ_n is the angle in a $2n+1$ dimensional space between sets of coefficients $\{g_n^m, h_n^m\}$ and $\{g_n^{m'}, h_n^{m'}\}$. The degree correlation therefore measures the directional accordance between the vectors spanned by Gauss coefficients g_n^m and $g_n^{m'}$ for a given SH degree n. In the model degree space, an angle of $\zeta_n = 45°$ corresponds to $\rho_n = 0.7$. Correlated vectors are determined as having $\rho_n \geq 0.7$ ($\zeta_n \leq 45°$), such that below this level coefficients are regarded as being uncorrelated (e.g., Langel and Hinze, 1998; Sabaka and Olsen, 2006).

Another useful tool is the sensitivity matrix which can also be used to examine the differences between the two sets of coefficients, for every coefficient plotted in a SH degree versus order matrix. The differences are normalized by the mean spectral amplitude for a given degree n, and the elements of the sensitivity matrix are given as (Sabaka and Olsen, 2006)

$$M(n,m) = 100 \cdot \frac{g_n^m - g_n^{m'}}{\sqrt{\frac{1}{2n+1}\sum_{m=-n}^{n}(g_n^m)^2}} \tag{2.27}$$

The structure of the sensitivity matrix is illustrated in Figure 2.13, illustrating the coefficient patterns and their relation to the matrix; the zonal harmonics are situated along the center axis, the sectorial harmonics along the sides and the tesseral harmonics making up the body elements.

The Circle of Confusion

Looking at the power spectrum of the magnetic field plotted at the Earth's surface in Figure 2.12, the Gauss coefficients for the core-generated field may never be known beyond a maximum level of SH degree $L \simeq 13$. Likewise the SV and SA spectra may only be inferred to some level, see Section 2.6.1. Truncation of the spherical harmonic expansion, means that there is a maximum level to which features can be resolved when trying to infer the radial field at the CMB (Booker, 1969; Backus et al., 1996). The root of the problem is this: what can be inferred of the radial field on the surface S, knowing the

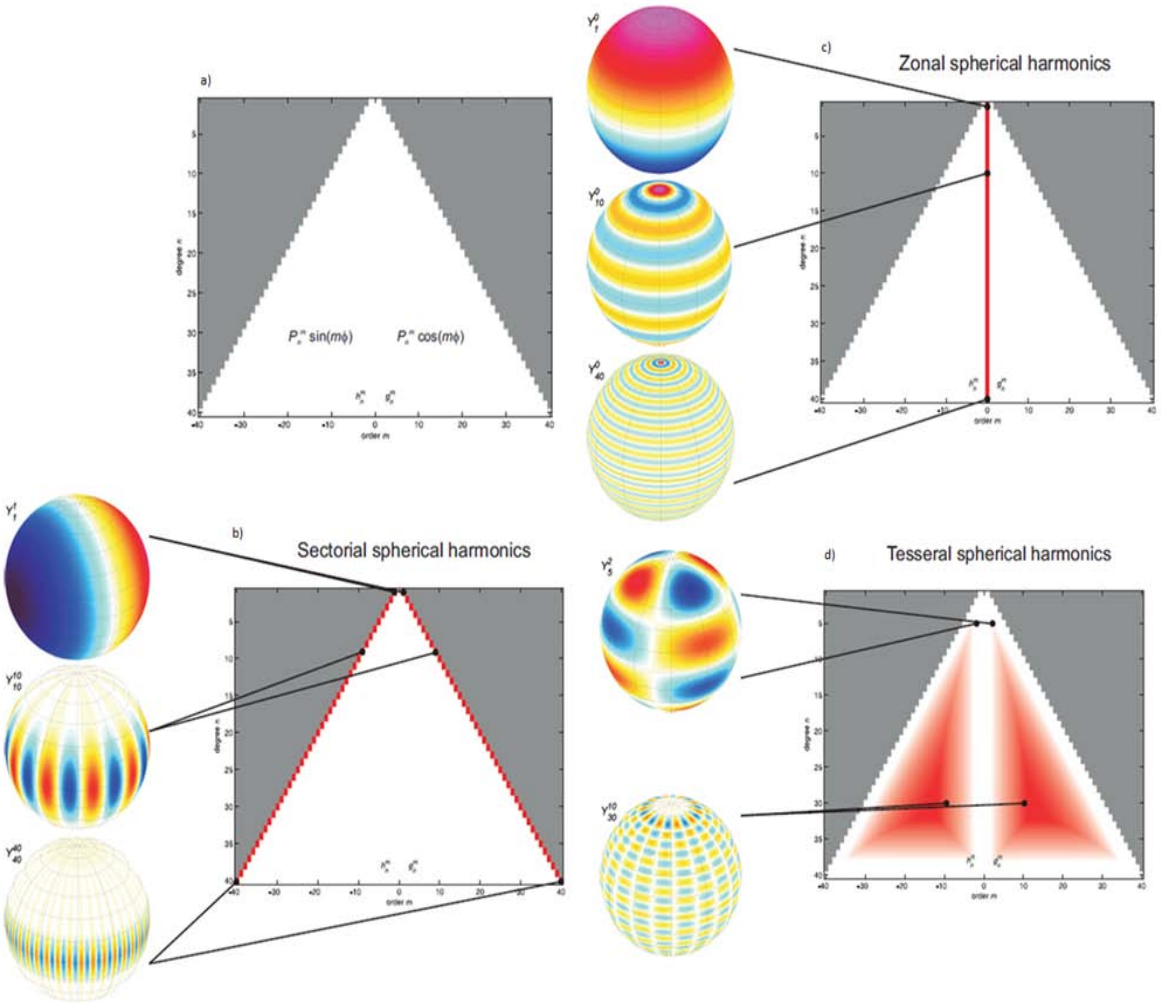

Figure 2.13: Sketch of the sensitivity matrix: a) the basic setup with coefficients g_n^m and h_n^m on the right and left hand side, respectively, b) the sectorial harmonics having $m = 0$ place along the matrix center, c) the zonal harmonics having $m = n$ place along the matrix sides and d) the tesseral harmonics placed in the matrix body. Plots extracted from Olsen (2009).

Gauss coefficients up to some truncated level, $n \leq L$? The internal radial magnetic field is determined as the gradient of the potential, equation (2.20), i.e.

$$B_r(r,\theta,\phi) = \sum_{n=1}^{\infty}\sum_{m=0}^{n}(n+1)\left(\frac{a}{r}\right)^{n+2}\left[g_n^m Y_{n,c}^m(\theta,\phi) + h_n^m Y_{n,s}^m(\theta,\phi)\right] \tag{2.28}$$

(Backus et al., 1996, sec. 4.4.4) considers a truncated approximation for the potential, such that the radial magnetic field, $\tilde{B}_L$, is written

$$\tilde{B}_L(\mathbf{r}) = \sum_{n=0}^{L}\sum_{m=0}^{n}(n+1)\left(\frac{a}{r}\right)^{n+2}\left[g_n^m Y_{n,c}^m(\theta,\phi) + h_n^m Y_{n,s}^m(\theta,\phi)\right] w_n^m \tag{2.29}$$

Notice here that the monopole term, i.e. $n = 0$ is included in the expansion; the Gauss coefficients for $n = 0$ are zero and thus not relevant, however the $n = 0$ term matters as will be clear below. The above approximating expansion includes some weighting constants

w_n^m, and the aim is to select w_n^m such that $\tilde{B}_L$ become a good approximation of B_r. Backus et al. (1996) shows that this can be done in a rms sense by minimizing the average value of the squared difference over a surface, i.e. $\langle |B_r - \tilde{B}_L|^2 \rangle$. If the solution does not need to be regularized, which means the minimization of a global norm of some property of the model (Parker, 1994), values of $w_n^m = 1$ gives the best approximation (Whaler et al., 2016). What does this mean in terms of resolution of the truncated expansion?

Because the Gauss coefficients can be expressed as inner products of the radial field and the spherical harmonics over the sphere (e.g. Langel, 1987; Blakely, 1995; Sabaka et al., 2010), Backus et al. (1996) shows that the approximating expansion can be written in terms of a so-called window function integrated with the field over the sphere, simplifying the consideration such that the weights are independent of m (i.e. $w_n^m = w_n$)

$$\tilde{B}_L(\mathbf{r}) = \oint_S W_L(\mathbf{r}|\mathbf{r}') B_r(\mathbf{r}') dS \tag{2.30}$$

where W_L is a weighting function called the averaging window, expressed as

$$W_L(\mathbf{r}|\mathbf{r}') = \sum_{n=0}^{L} w_n \frac{(2n+1)}{4\pi} P_l(\mu) \tag{2.31}$$

where $\mu = \cos\gamma = \cos\theta\cos\theta' + \sin\theta\sin\theta'\cos(\phi - \phi')$, γ being the angular distance. Backus et al. (1996) shows that selecting $w_0^0 = w_0 = 1$ will cause the integrated averaging window to be one, i.e. $\langle W_L(\mathbf{r}|\mathbf{r}') \rangle = 1$. This averaging window or kernel is axissymmetric, and if $w_n = 1$ it is called the Dirichlet kernel which would provide the best fit in a least-squares sense as seen above. In fact, this is exactly the same result obtained by Whaler and Gubbins (1981) in their studies of SH analysis of the geomagnetic field assuming the solution (i.e. the Gauss coefficients) is not regularized (i.e. $w_n = 1$) and therefore the resolution would be perfect (Whaler et al., 2016). Note here that Whaler and Gubbins (1981) discusses this for the non-dipole part of the field, while Whaler et al. (2016) provides an expression including the dipole term.

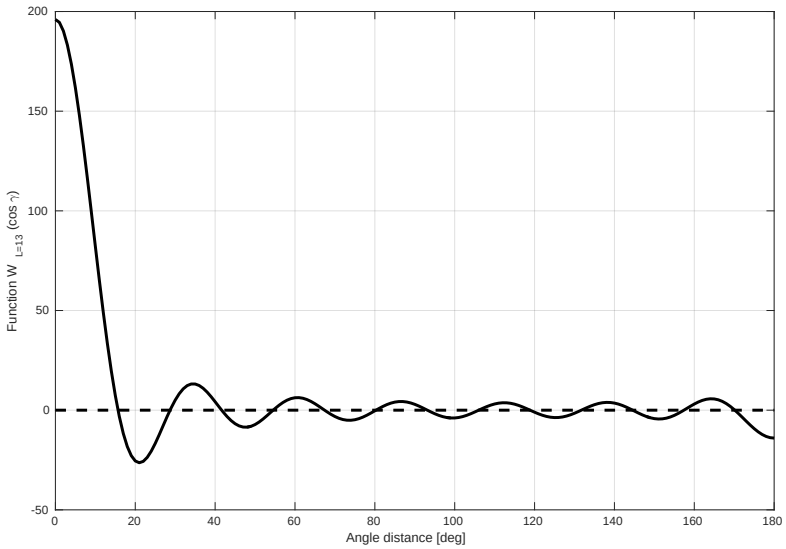

Figure 2.14: Plot of the Dirichlet kernel $W_{L=13}$.

The ideal window kernel would be the Dirac delta function, however in practise this is not possible since $\delta(\mathbf{r} - \mathbf{r}')$ contains all wavelengths in its spherical harmonic expansion

(see equation (5.4) in Section 5.2.1) whereas the expansion in equation (2.29) is truncated. Figure 2.14 shows a plot of the Dirichlet kernel setting the truncation at $L = 13$. As can be observed the radius of the window kernel peak (taken to be the distance from maximum amplitude to the point where the function first becomes zero) is around 16°, and oscillatory behaviour is evident in the window kernel. Decreasing L would lower the amplitude and broaden the radius of the peak. Therefore, using un-regularized Gauss coefficients up to some truncated degree, L, to plot the radial magnetic field at the CMB, will yield a blurred impression of the field features; this was referred to as the "circle of confusion" by Backus et al. (1996), having a radius of approximately 16° if choosing $L = 13$. Therefore: CMB field estimates at particular points, as determined via the Gauss coefficients, are contaminated by the field values everywhere else on the CMB if the expansion is truncated, and furthermore introducing regularization accentuates this problem (Whaler et al., 2016).

The Geomagnetic Gradient Tensor

In the following the magnetic field gradient tensor for a potential field is described. Time series of the tensor elements are estimated in the Virtual Observatory model as described in Chapter 4, and comparisons with the CHAOS-6-x5 field model predictions for these elements will be carried out. Furthermore, field models will be built from VO gradient data in Chapter 4. In the description below, the formulation follows that developed in a series of papers Olsen and Kotsiaros (2011); Kotsiaros (2012); Kotsiaros and Olsen (2012, 2014). The directional derivatives of each component of the geomagnetic vector field specifies a gradient tensor. As described in Olsen and Kotsiaros (2011) the elements of the gradient tensor may in general be written as the covariant derivative (i.e. the field derivatives in a general coordinate transformation) $B_{p;q}$ by

$$B_{p;q} = \frac{\partial B^p}{\partial y^p} + \Gamma^p_{kq} B^k \tag{2.32}$$

where B^p specifies the magnetic field component and y^p denotes the direction of differentiation. The labels p, q, k are specified by the chosen coordinate system. The Christoffel symbol is written as

$$\Gamma^p_{kq} = \frac{\partial \hat{\mathbf{e}}_k}{\partial y^q} \hat{\mathbf{e}}_p \tag{2.33}$$

where $\hat{\mathbf{e}}$ denotes a unit vector. Choosing spherical coordinates the components are $B^p = (B_r, B_\theta, B_\phi)$. The non-zero Christoffel symbols are given by

$$\Gamma^\theta_{r\theta} = \Gamma^\phi_{r\phi} = \frac{1}{r}, \quad \Gamma^\phi_{\theta\phi} = \frac{\cot\theta}{r}$$
$$\Gamma^r_{\theta\theta} = \Gamma^r_{\phi\phi} = -\frac{1}{r}, \quad \Gamma^\theta_{\phi\phi} = -\frac{\cot\theta}{r}$$

The differential directions in the spherical coordinates are given by

$$\frac{\partial}{\partial y^r} = \frac{\partial}{\partial r}, \quad \frac{\partial}{\partial y^\theta} = \frac{1}{r}\frac{\partial}{\partial \theta}, \quad \frac{\partial}{\partial y^\phi} = \frac{1}{r\sin\theta}\frac{\partial}{\partial \phi} \tag{2.34}$$

The 3×3 magnetic gradient tensor for the internal field is thus given by

$$\nabla \mathbf{B} = \begin{pmatrix} \frac{\partial B_r}{\partial r} & \frac{1}{r}\frac{\partial B_r}{\partial \theta} - \frac{1}{r}B_\theta & \frac{1}{r\sin\theta}\frac{\partial B_r}{\partial \phi} - \frac{1}{r}B_\phi \\ \frac{\partial B_\theta}{\partial r} & \frac{1}{r}\frac{\partial B_\theta}{\partial \theta} + \frac{1}{r}B_r & \frac{1}{r\sin\theta}\frac{\partial B_\theta}{\partial \phi} - \frac{\cot\theta}{r}B_\phi \\ \frac{\partial B_\phi}{\partial r} & \frac{1}{r}\frac{\partial B_\phi}{\partial \theta} & \frac{1}{r\sin\theta}\frac{\partial B_\phi}{\partial \phi} + \frac{1}{r}B_r + \frac{\cot\theta}{r}B_\theta \end{pmatrix}$$

Importantly, because the magnetic field is a solenoidal vector field, the divergence is zero, $\nabla \cdot \mathbf{B} = 0$. This means that the trace of the gradient tensor is zero, i.e. $tr(\nabla \mathbf{B}) = 0$, reducing the number of independent elements from 9 to 8. Furthermore, assuming the field is a Laplacian potential field, i.e. $\mathbf{J} = 0$, the curl of the field vanishes ($\nabla \times \mathbf{B} = 0$), thus reducing the number of independent tensor elements from 8 to 5; in other words, the magnetic gradient tensor is symmetric (in the general case in-situ electrical current density will cause non-symmetry of the tensor). It should be noted, that contributions from field components enter in some of the tensor elements. When investigating the large-scale part of the field for SH degrees below $n = 13$, these contributions need to be included and cannot be neglected as may be the case when considering the lithospheric field.

In spherical coordinates the 3×3 magnetic gradient tensor expressed in terms of the potential is

$$\nabla \mathbf{B} = \begin{pmatrix} -\frac{\partial^2 V_r}{\partial r^2} & -\frac{1}{r}\frac{\partial^2 \partial V}{\partial \theta \partial r} + \frac{1}{r^2}\frac{\partial V}{\partial \theta} & \cdots \\ -\frac{\partial^2 V_\theta}{\partial r \partial \theta} + \frac{1}{r^2}\frac{\partial V}{\partial \theta} & -\frac{1}{r^2}\frac{\partial^2 V}{\partial \theta^2} - \frac{1}{r}\frac{\partial V}{\partial r} & \cdots \\ -\frac{1}{r\sin\theta}\frac{\partial^2 V}{\partial r \partial \phi} + \frac{1}{r^2 \sin\theta}\frac{\partial V}{\partial \phi} & -\frac{1}{r^2\sin\theta}\frac{\partial^2 V}{\partial \theta \partial \phi} + \frac{\cos\theta}{r^2\sin^2\theta}\frac{\partial V}{\partial \phi} & \cdots \end{pmatrix}$$

$$\begin{pmatrix} \cdots & -\frac{1}{r\sin\theta}\frac{\partial^2 V}{\partial \phi \partial r} + \frac{1}{r^2\sin\theta}\frac{\partial V}{\partial \phi} \\ \cdots & -\frac{1}{r^2\sin\theta}\frac{\partial^2 V}{\partial \phi \partial \theta} + \frac{\cos\theta}{r^2\sin^2\theta}\frac{\partial V}{\partial \phi} \\ \cdots & -\frac{1}{r^2\sin^2\theta}\frac{\partial^2 V}{\partial \phi^2} - \frac{1}{r}\frac{\partial V}{\partial r} - \frac{\cos\theta}{r^2\sin^2\theta}\frac{\partial V}{\partial \theta} \end{pmatrix} \tag{2.35}$$

The internal gradient tensor elements, $[\nabla \mathbf{B}]_{jk}$, where $j, k = \{r, \theta, \phi\}$ may be expanded in terms of spherical harmonics as shown in Kotsiaros (2012)

$$[\nabla \mathbf{B}]_{jk} = \mathbb{R}\left\{ \frac{1}{a} \sum_{n=1}^{N} \sum_{m=0}^{n} \gamma_n^m(t) \exp(im\phi) \left(\frac{a}{r}\right)^{n+3} P_{n,jk}^m(\cos\theta) \right\} \tag{2.36}$$

where i is the imaginary number, $\gamma_n^m = g_n^m - ih_n^m$ contains the Gauss coefficients, $\exp(im\phi) = \cos m\phi + i \sin m\phi$, and $\mathbb{R}\{\cdots\}$ denotes the real part. The functions $P_{n,jk}^m(\cos\theta)$ are expressed as

$$\begin{aligned}
P_{n,rr}^m(\cos\theta) &= -(n+1)(n+2)P_n^m(\cos\theta) \\
P_{n,\theta\theta}^m(\cos\theta) &= (n+1)P_n^m(\cos\theta) + \frac{d^2 P_n^m(\cos\theta)}{d\theta^2} \\
P_{n,\phi\phi}^m(\cos\theta) &= \left[\frac{m^2}{\sin^2\theta} + (n+1)\right] P_n^m(\cos\theta) - \cot\frac{dP_n^m(\cos\theta)}{d\theta} \\
P_{n,r\theta}^m(\cos\theta) &= (n+2)\frac{dP_n^m(\cos\theta)}{d\theta} \\
P_{n,r\phi}^m(\cos\theta) &= \frac{m(n+2)}{\sin\theta} i P_n^m(\cos\theta) \\
P_{n,\theta\phi}^m(\cos\theta) &= \frac{m\cos\theta}{\sin^2\theta} i P_n^m(\cos\theta) - \frac{m}{\sin\theta} i \frac{dP_n^m(\cos\theta)}{d\theta}
\end{aligned}$$

A Matlab script for construction of the design matrix of the gradient spherical harmonics was kindly provided by Stavros Kotsiaros. This was used to produce gradient field models in Chapter 4.

2.5.3 Non-Potential Field Description

The potential field description is the fundamental building block used in Chapters 4 and 5. This is also the case for many of the present day geomagnetic field models being built,

see Section 2.6. However, the potential field assumption may break down because satellite measurements are conducted in regions where electrical currents may not vanish, such that the curl of the magnetic field is not zero. The situation is depicted in Figure 2.15: the satellite magnetic measurements are assumed to be taken in a shell, $S(r_1, r_3)$, situated in the ionospheric F-region at altitudes where in-situ ionospheric electrical currents, $\mathbf{J^{sh}}$, could be present especially at high latitudes (Olsen, 1997; Sabaka et al., 2010; Olsen et al., 2010b). Internal currents $\mathbf{J^i}$ and external currents $\mathbf{J^e}$ are below and above the measurements shell, respectively. Note also that satellites fly above the ionospheric E-region and observes contributions from this region as internal along with those of the crustal and core fields (on the contrary, ground observatory measurements only sees the crustal and core field as internal).

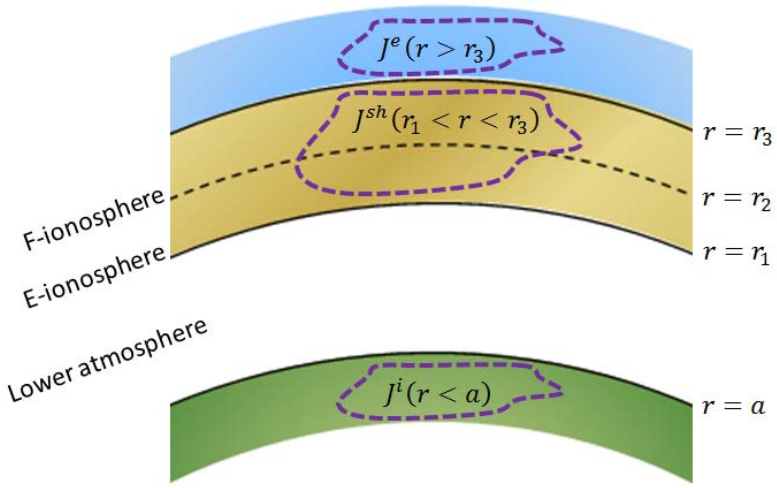

Figure 2.15: Illustration of the electrical currents and their location in connection to magnetic field observations. After Olsen (1997) and Sabaka et al. (2010).

Here it will be assumed that the electrical currents in the F-region mainly occurs as coupling currents between the ionospheric E-region and magnetospheric systems, though studies of satellite measurements have revealed greater complexity, see Section 2.3. Therefore these electrical currents are typically assumed poloidal in nature (i.e. purely radial), thus producing toroidal magnetic fields within the shell, and are found primarily at polar latitudes associated with FACs and also in a narrow band at the dipole equator (as the ionospheric systems tent to align with the morphology of the Earth's magnetic field as described in Section 2.3) associated with the coupling currents of the meridional Sq electrical current system. Decomposing the magnetic field measurements into their poloidal and toroidal parts, estimates of the in-situ electrical current density during evening and morning time in the ionospheric F-region was determined using Magsat satellite measurements (Magsat flew at altitudes between 350 to 550km above ground), also showing that a meridional current component is part of the low latitude system by Olsen (1997); Engels and Olsen (1998). This has also later been shown using CHAMP data (e.g., Maier, 2005). Therefore, in the case where the electrical currents in the ionospheric F-region are not assumed vanishing, a non-potential field formalism deviating from that of the usual potential field description needs to be considered (Backus et al., 1996; Olsen, 1997; Sabaka et al., 2010). Below a short description of the non-potential considerations is provided since, in Chapter 4, an analysis of the virtual observatory time series along these lines is conducted, looking into the contributions from internal, external and in-situ electric currents.

The Helmholtz Representation

The starting point is some vector function $\mathbf{B}(\mathbf{r})$ specified such that $\nabla \cdot \mathbf{B} = D$ and $\nabla \times \mathbf{B} = C$, where D and C are some scalar functions which go to zero faster than $1/r^2$ as $r \to \infty$. Then requiring that $\mathbf{B}(\mathbf{r}) \to 0$ as $r \to \infty$, unique solution to this function can be written according to the Helmholtz theorem (Backus et al., 1996; Griffiths, 1999; Sabaka et al., 2010)

$$\begin{aligned} \mathbf{B} &= -\nabla S + \nabla \times \mathbf{A} \\ &= -\nabla S + \nabla \times T\mathbf{r} + \nabla \times \nabla \times P\mathbf{r} \end{aligned} \tag{2.37}$$

where S, T, P and $\mathbf{A}$ are scalar and vector potentials, respectively. That is; if the field goes to zero at infinity then this field is uniquely determined from its divergence and curl. In fact another alternative Helmholtz representation can formulated (e.g. Sabaka et al., 2010). If the field is also irrotational (i.e. curl-free) the usual potential formalism described in Section 2.5.2 is applicable. If only the solenoidal constraint is placed on the field, an expression in terms of only two scalar potentials can be obtained. This representation, called the Mie representation or toroidal-poloidal decomposition, takes the form (Backus et al., 1996; Griffiths, 1999; Sabaka et al., 2010)

$$\begin{aligned} \mathbf{B} &= \nabla \times T\mathbf{r} + \nabla \times \nabla \times P\mathbf{r} \\ &= \mathbf{B}_{tor} + \mathbf{B}_{pol} \end{aligned} \tag{2.38}$$

where $\mathbf{B}_{tor}$ and $\mathbf{B}_{pol}$ are the toroidal and poloidal components, respectively. A requirement that the mean values of these scalar functions are zero when integrated on a sphere, is needed in order for the representation to be unique. An important aspect of this is that a toroidal magnetic field has no radial field component and is generated by a poloidal electrical current, while the poloidal magnetic field is generated by toroidal electrical currents which has no radial component. The toroidal and poloidal scalar functions can be expressed using a spherical harmonic expansion (e.g. Sabaka et al., 2010). There is a subtle link between the formalism using the Gauss coefficients and the formalism of the poloidal scalar function; the internal and external scalar potentials of equation (2.12), can be written as (Sabaka et al., 2010)

$$\psi^{int} = -\frac{\partial}{\partial r}\left(rP^{int}\right), \qquad \psi^{ext} = -\frac{\partial}{\partial r}\left(rP^{ext}\right) \tag{2.39}$$

where P^{int} and P^{ext} are the internal and external poloidal scalar functions.

The Mie Representation in a Thin Shell

Using the Mie-representation from above, allows for a description of the magnetic field in the current carrying (sampling) shell $S(r_1, r_3)$. The magnetic field at satellite altitude is written as (Backus, 1986; Backus et al., 1996; Olsen, 1997; Sabaka et al., 2010)

$$\mathbf{B} = \mathbf{B}^i_{pol} + \mathbf{B}^e_{pol} + \mathbf{B}^{sh}_{pol} + \mathbf{B}^{sh}_{tor} \tag{2.40}$$

where the superscripts i, e, sh denotes the internal, external and shell parts, respectively. The subscripts *pol* and *tor* denotes the poloidal and toroidal parts, respectively. $\mathbf{B}^i_{pol}$ and $\mathbf{B}^e_{pol}$ denotes the internal and external poloidal fields, respectively, while $\mathbf{B}^{sh}_{pol}$ and $\mathbf{B}^{sh}_{tor}$ denotes the non-potential fields due to currents in the shell. The situation is as illustrated in Figure 2.15: the internal, $\mathbf{B}^i_{pol}$, and external, $\mathbf{B}^e_{pol}$, magnetic fields are generated by

internal, $\mathbf{J}^i_{tor}$, and external, $\mathbf{J}^e_{tor}$, toroidal currents. What about the poloidal currents and their associated toroidal magnetic fields? Toroidal magnetic fields produced by poloidal currents do not exists outside the region of the current. In fact this is also the situation with the toroidal magnetic field of the outer core; it cannot be measured from outside the core surface; therefore outside the source regions $\mathbf{B}^i_{tor} = 0$ for $r > a$, and $\mathbf{B}^e_{tor} = 0$ for $r < r_3$. The terms $\mathbf{B}^{sh}_{pol}$ and $\mathbf{B}^{sh}_{tor}$ are the non-potential contributions to the field from in-situ ionospheric electrical currents in the shell.

Following the derivations of Backus (1986); Backus et al. (1996); Olsen (1997); Sabaka et al. (2010), the ionospheric F-region contribution is assumed to be that arising from field-aligned currents. The poloidal field is usually neglected since field-aligned currents have no toroidal component due to their assumed radial direction. Using the thin-shell approximation, in which $h/r_2 \to 0$ where $h = r_3 - r_1$ is the thickness of the shell which is considered thin as compared to the radius, r_2 , the magnetic field can be written (Olsen and Mandea, 2007)

$$\mathbf{B} = \mathbf{B}^i_{pol} + \mathbf{B}^e_{pol} + \mathbf{B}^{sh}_{tor} \tag{2.41}$$

It can be shown that these assumptions and knowledge of the field on the surface at $r = r_2$, allows for the determination of the expansion coefficients (i.e. the Gauss coefficients along with the toroidal coefficients). Therefore, the magnetic field can be written is terms of poloidal, $\{\psi^{int}, \psi^{ext}\}$ and toroidal, T^{sh}, scalar potentials (Olsen and Mandea, 2007)

$$\mathbf{B} = -\nabla\psi^{int} - \nabla\psi^{ext} + \nabla \times \hat{r}T^{sh} \tag{2.42}$$

where the potentials determined up to some maximum SH degree N are written

$$\psi^{int} = a \sum_{n=1}^{N} \sum_{m=0}^{n} [g^m_n(t)\mathrm{cos}m\phi + h^m_n(t)\mathrm{sin}m\phi] \left(\frac{a}{r}\right)^{n+1} P^m_n \tag{2.43}$$

$$\psi^{ext} = a \sum_{n=1}^{N} \sum_{m=0}^{n} [q^m_n(t)\mathrm{cos}m\phi + s^m_n(t)\mathrm{sin}m\phi] \left(\frac{r}{a}\right)^{n} P^m_n \tag{2.44}$$

$$T^{sh} = a \sum_{n=1}^{N} \sum_{m=0}^{n} [t^{m,c}_n(t)\mathrm{cos}m\phi + t^{m,s}_n(t)\mathrm{sin}m\phi] \left(\frac{r}{a}\right)^{n} P^m_n \tag{2.45}$$

and $\{t^{m,c}_n, t^{m,s}_n\}$ are the expansion coefficients associated with the toroidal scalar potential. The above description was used in Section 4.5.5, trying to investigate the contributions from the external and toroidal parts. The toroidal power spectrum at the surface $S(r)$ with radius r is given by (Hulot et al., 2015)

$$\langle |\mathbf{B}_{tor}|^2 \rangle_{S(r)} = R^t(r) = \sum_{n=1}^{\infty} R^t_n \tag{2.46}$$

where $R^t_n(r)$ is given by

$$R^t_n(r) = \left(\frac{n(n+1)}{2n+1}\right) \sum_{m=0}^{n} \left[(t^{m,c}_n)^2 + (t^{m,s}_n)^2\right] \tag{2.47}$$

2.6 Geomagnetic Field Models

Describing the Earth's magnetic field at any given time and location via some model is called geomagnetic field modelling (Olsen and Stolle, 2017). When producing a geomagnetic field model a large number of magnetic field observations are effectively converted

into a linear combination of elementary mathematical functions that best describes those observations. The set of numerical coefficients best defining this linear combination is then what one refers to as a geomagnetic field model; i.e the model parameters for that particular mathematical description (Sabaka et al., 2010). Traditionally, geomagnetic field modelling has been carried out implementing a spherical harmonic expansion model of the magnetic scalar potential and magnetic field, determining the expansion coefficients, i.e. the so-called Gauss coefficients as described in Section 2.5.2. The SH representation provides a way of distinguishing between the internal and external sources (relative to the measurement radius) in the signal and furthermore allocates the core and crustal fields to certain harmonic degrees, as mention in Section 2.5.2, such that the transition lies around SH degree 14 (Backus et al., 1996; Lesur et al., 2011a; Hulot et al., 2015). Therefore, small scale features of core field and large scale features of the crustal field are left undetermined by this spectral overlapping. Overall there may be two strategies for building an internally focused SH based field model: 1) using dedicated data selection and processing routines in order to obtain reliable models co-estimating the internal and large-scale external fields, and 2) simultaneously co-estimating the internal and external fields along with the toroidal field. In the following, a short review of recently built geomagnetic field models is given, all relying on the SH representation; specially the CHAOS and CM model series are in focus as these are used in the data processing in this thesis. The predictions of other field models are considered in Chapter 5, and therefore a brief discussion of these are also included here.

Internal field models vary with regard to the data type used and data selection schemes and model parametrization for example: the MEME08 model (Thomson et al., 2010), the GRIMM model series built from CHAMP measurements and HMV from ground observatories (Lesur et al., 2008, 2010, 2011b; Mandea et al., 2012), the POMME model series (Maus et al., 2006) see also `http://geomag.org/models/index.html`, the SIFM model series (Olsen et al., 2015, 2016) built entirely from *Swarm* data, and the CHAOS model series (Olsen et al., 2006, 2009, 2010c, 2014; Finlay et al., 2015, 2016b). Especially the CHAOS model series are of interest here, as the CHAOS external field estimates are removed from the data used in this thesis, see Section 3.3. In the CHAOS model, the contributions from the near-Earth magnetospheric electrical ring-current system and the remote-Earth magnetotail and magnetopause systems are represented. Details of the specific data type and selection criteria used will not be elaborated here; the reader is referred to the above papers. Typically uncertainty estimates are not provided in these field models, the reason being that such estimates are difficult to determine due to the imposed regularization and the data uncertainty not being well known (Finlay et al., 2015). Therefore the models are often assessed by comparison; quoted here is (Lesur et al., 2011a), section 11.4, p.292:

It is not clear how the different ways these fields are parameterized in MEME08, CHAOS or GRIMM affect the resulting core field model. Overall, the main differences between the three approaches remain the data selection techniques and these differences are particularly apparent at high latitudes. However, the fact that data sets covering different magnetic activity ranges, different local times and having such different noise levels, all lead to rather similar core field models give us confidence in the accuracy of the derived models.

The comprehensive model approach differs from the models mentioned above, in that these models try to co-estimate not only the internal and external parts of the SH expansion, but also non-potential contributions. The CM and CI model series rely on the same parametrization; besides ground observatory data the CM series uses measurements

from the Ørsted, SAC-C and CHAMP satellites (Sabaka et al., 2002, 2004, 2015), whereas the CI models use *Swarm* measurements only (Sabaka et al., 2013, 2018). These models are rather complex not only in their parametrization but also by the incorporation of the Selective Infinite Variance Weighting (SIVW) weighting scheme in the later models. The model parametrizations and their specific details are too numerous to be elaborate here, however the source contributions which are modelled include: the core-generated field, the crustal field, ionospheric E-region and large-scale magnetospheric fields along with their associated Earth induced contributions, the oceanic M_2 tidal field and the toroidal ionospheric F-region field. Here special notice should be given to the ionospheric field and its Earth induced counterpart, as their total predicted field from the CM4 model were removed from the data used in this thesis, see Section 3.3. The modelled ionospheric sources are the Sq electrical currents in the E-region assumed flowing in a shell at 110km altitude, thus below satellite data acquisition altitudes. Because mid- and low latitude ionospheric activity level is driven by the solar irradiation, a useful indicator to describe this is the solar flux index (see Section 2.4.4), which is used as a scaling parameter for the ionospheric fields in the CM models. The associated induced contributions are determined via an Earth 1D conductivity model, i.e. only having a radial dependence (in the latest CM5 and CIY4 models this was further refined to a 3D conductivity model). It should be noted, that the CM and CI models may be classified as quiet-time models, in that like the above mentioned SH models they rely on quiet-time data selection criteria.

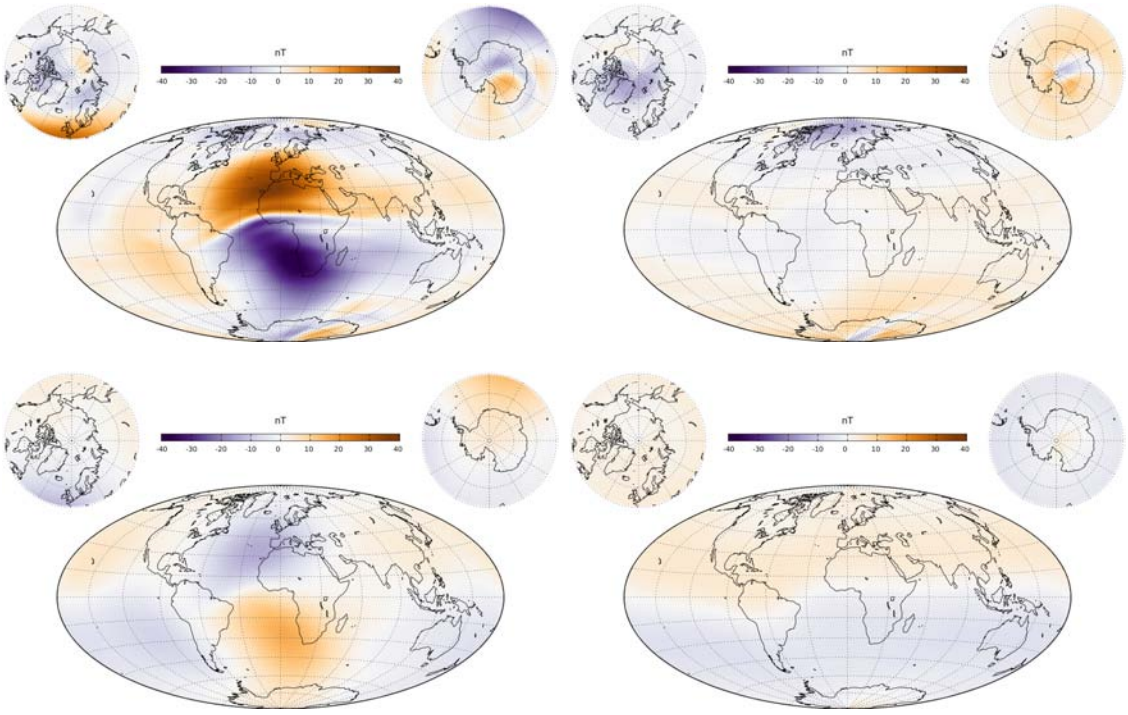

Figure 2.16: CM4 model predictions of the ionospheric E-region radial magnetic field component for 12 UT (left plots) and 00 LT (right plots), showing the primary part (top plots) and the secondary induced part (bottom plots) following Olsen et al. (2005a). Field predictions are shown for an example altitude above ground of 400km and a solar flux index of 150×10^{-22}W/m^{2}Hz.

Figure 2.16 shows example predictions at satellite altitude of the ionospheric radial magnetic field (top plots) and its associated secondary Earth induced counterpart (bot-

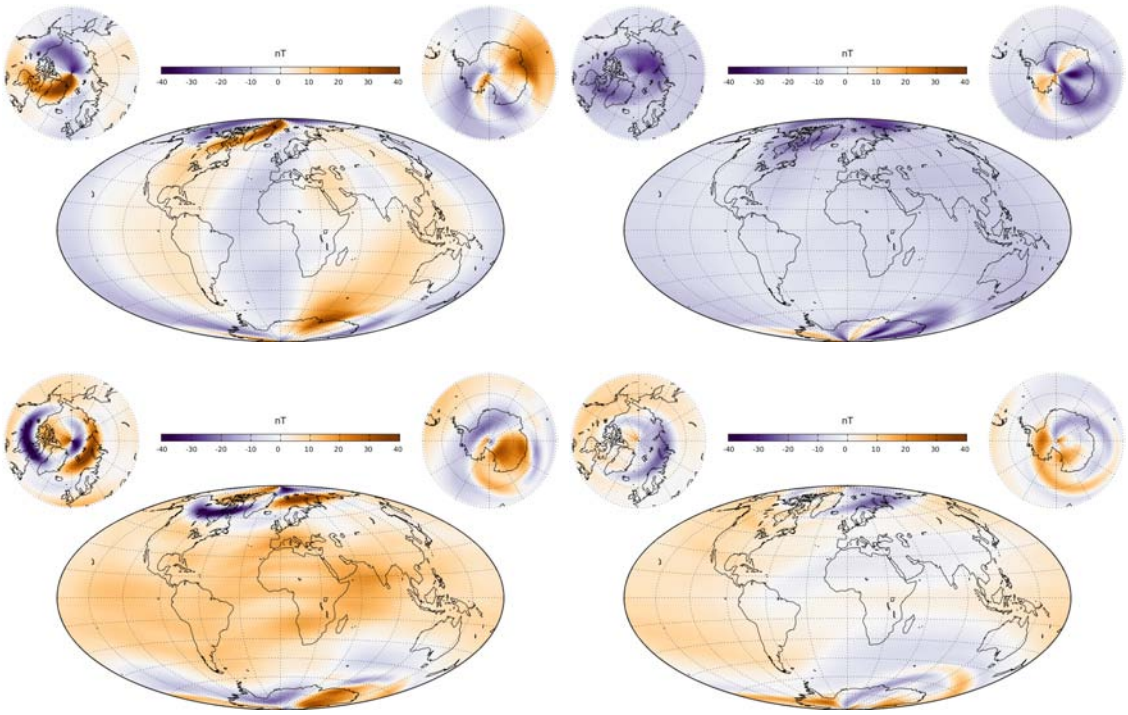

Figure 2.17: CM4 model predictions of the ionospheric F-region toroidal magnetic field for 12 UT (left plots) and 00 LT (right plots), showing the B_θ component (top plots) and the B_ϕ component (bottom plots). Field predictions are shown for an example altitude above ground of 400km and a solar flux index of 150×10^{-22}W/m^{2}Hz.

tom plots), as predicted by the CM4 model. The left plots show predictions for 12 UT when the primary Sq ionospheric field is clearly identified, and the right plots show the predicted fields for 00 LT (for all latitudes). The secondary induced field persists during night times, i.e. when the primary field has vanished, as stressed by Olsen et al. (2005a). Furthermore, high latitude electrical currents are always present. Another interesting feature of the CM4 model is the estimation of the toroidal magnetic field. Figure 2.17 shows the predictions of the horizontal field components at satellite altitude of the F-region toroidal magnetic field. Predictions at 12 UT (left plots) and 00 LT (right plots) illustrates what might also be expected from the discussions above, namely that, during day time these are present at mid and low-latitudes and are especially strong in the polar regions, whereas during night time they persist but are mostly confined to the polar regions. It should be noted, that these plots were made using a high solar flux index of 150×10^{-22}W/m^{2}Hz (see Figure 2.11 to compare). The intention here is to provide an idea of the spatial and temporal nature of the contributions from the ionospheric sources.

The spectral behaviour of the field and a subsequent cut-off at SH degree 13, may distort the large-scale features observed in the SH based models when plotting CMB maps. Therefore, dedicated attempts in constructing core field models have been made by mitigating the crustal contribution in the signal (Hulot et al., 2015). Such efforts include the C^{3}FM model series (Wardinski and Holme, 2006; Wardinski and Lesur, 2012) and models constructed based on icosodedral grids at the core surface forced to satisfy necessary conditions for frozen-flux and a magnetostrophic force balance implemented via topology preservation constraints in the work of (Constable et al., 1993; Jackson, 2003;

Jackson et al., 2007b; Gillet et al., 2007), and most recently used a correlation based approach wherein internal and external correlation functions are specified (Holschneider et al., 2016; Lesur et al., 2017).

2.6.1 Limitations of Present Modelling Approaches

The spherical harmonic representation is a very attractive method because it aligns with the natural spherical geometry, allows internal/external field separation and provides a global description of the field. Furthermore, knowing the Gauss coefficients allows downward (and upward) continuation of the field to be performed, such that the CMB field can be determined. In practice the infinite sum of the SH expansion is determined to some maximum degree N_{max}, having a total of $N_{max}(N_{max}+2)$ Gauss coefficients. The limit is set by the data quality and modelling capabilities, beyond which noise dominates the signal. Therefore, in the conventional approach the potential is represented on a global scale using a truncated SH expansion determined in a least-squares sense, perhaps also imposing temporal regularization, thus removing solution non-uniqueness (Oldenburg, 1984; Finlay et al., 2016b). Here regularization means minimizing a global norm of some property of the model (Parker, 1994). Since the SH functions have global support, ideally requiring evenly distributed data over the entire globe, they give equal weight to the entire data set assigning isotropic resolution even though this may not reflect the data. For instance, strict data selection could cause a sparse data coverage, and if data lacks an overall homogeneous distribution, the SH orthogonality properties will be disturbed (Backus et al., 1996; Sabaka et al., 2010). Thus influenced both by data distributions and model regularization, model uncertainties, which are likely biased due to the presence of unmodelled sources, are usually not stated. Model validation thus typically relies on comparing models constructed by different data schemes, external field parametrisation and regularization (Finlay et al., 2015, e.g.). Furthermore, the time dependence of the field is often described by regularized B-splines. However, the imposed regularization modifies the spline functions in a non-uniform manner which influences higher SH degrees the most (Constable and Parker, 1988; Olsen et al., 2009). Typically this means that the high degree part of the SV and SA estimates are averaged over long time windows, say 10 years (Olsen et al., 2009; Lesur et al., 2011a).

It is interesting to consider the behaviour of the spatial power spectra of the core field and it's time derivatives. Figure 2.18 shows the MF, SV and SA power spectra in 2016 at the Earth's surface (left plot) and at the CMB (right plot) as predicted by the CHAOS-6-x5 and CIY4 models. At the Earth's surface the MF and SV spectra of the two models agree well, whereas disagreement above SH degree 10 in the SA spectrum is evident. Looking at the spectra at the CMB, the MF power spectrum around degree 13 begins to increase due to non-core sources. Looking at the SV and SA spectra, their behaviour are blue which means that the power increases with SH degree; in order words, small scales dominate over the long scales. Furthermore, a situation arises in which the temporal behaviour of the field is know to a higher degree than the field itself. Geomagnetic field models built differently capture the same large-scale field behaviour which is very encouraging. A particular difficulty with the CMB power spectra of the SV and SA signals, is that truncation could perturb global field maps. In spite of studies having shown coherence in field structures in global maps, as the SH truncation degree of the SV and SA is increased (Holme et al., 2011; Aubert, 2018), care is needed when interpreting the resulting fields at the CMB.

The temporal spectra of the Gauss coefficients are considered to scale with frequency differently looking at the dipole and non-dipole terms separately. The non-dipole terms

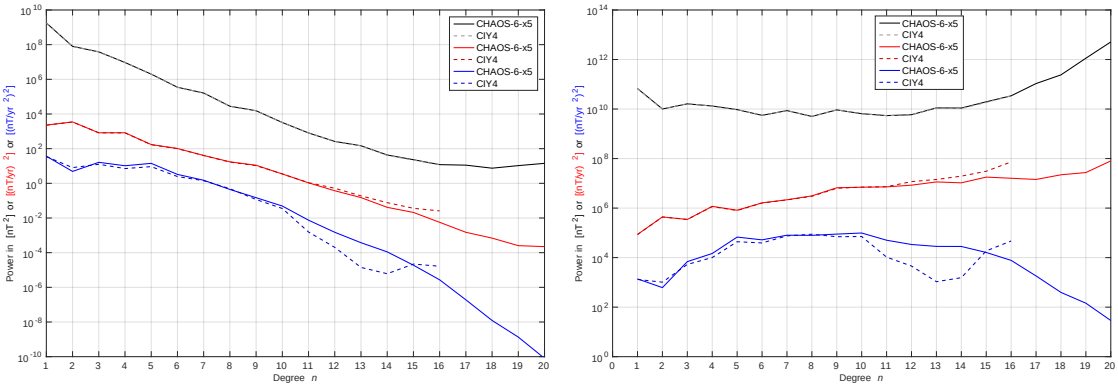

Figure 2.18: Lowes-Mauersberger spherical harmonic power spectra in 2016 as given by the CHAOS-6-x5 and CIY4 field models showing: the main field (black and dotted grey), secular variation (red and dotted red) and secular acceleration (blue and dotted blue) plotted at the Earth's surface (left plot) and the CMB (right plot).

are assumed to scale as f^0 for long frequencies and as f^{-4} for intermediate frequencies (De Santis et al., 2003; Gillet et al., 2013; Bouligand et al., 2016), where f is the frequency. This means that the SV and SA spectra for intermediate frequencies would follow f^{-2} and f^0 behaviours, respectively. It is expected that the temporal spectra will turn over, eventually converging (Bouligand et al., 2016). Thus, with regard to the SA, this may raise some concerns; it has been argued that the temporal spectra is such that higher order time derivatives of the field may be formally undefined as the time window used to estimate these goes towards zero (Gillet et al., 2013; Bouligand et al., 2016; Lesur et al., 2017). In other words, an instantaneous SA may not be well defined due to lack of spectral convergence. SH based field models thus provide band limited estimates; in particular, the SA is truncated in the spectral domain and only determined from within a certain frequency band of say a few years.

2.7 Summary

The geomagnetic field has many sources which vary with time and position. In this thesis we are interested in the core-generated magnetic field and its time variations. In order to extract the core field signal from satellite magnetic field measurements, a selection scheme based on dark, geomagnetically quiet-times is needed. In addition to this, knowledge of the IMF and MEF can be used as disturbance/activity diagnostics. In this thesis, the large-scale magnetospheric fields and their Earth induced counterpart as estimated by the CHAOS-6 model, are subtracted from the satellite data. Furthermore, because contributions from ionospheric and secondary Earth induced currents persists during dark time, the CM4 model predictions of the magnetic field from such sources are subtracted.

Traditionally, the magnetic field is assumed to be measured in a source free region, thereby allowing for a potential field description to be used. This potential is typically modelled using a spherical harmonic representation. However, there are shortcomings to the SH representation: 1) the noise is not the same at different latitudes due to the various field sources (noise is locally larger in the poles), and because the SH are global functions, the noise at higher latitudes can map into the all harmonics, 2) the SH expansion is truncated

in the spectral domain which might disturb the harmonics coefficients, 3) the truncated SH representation assigns isotropic spatial resolution which may not reflect the actual situation globally, 4) the time-dependence of the SH models are usually represented by B-splines using temporal regularization, which affects the higher SH degrees the most, and 5) appraisal is not provided in the SH based field models (as data errors are not well accounted for).

Based on the limitations mentioned above, we are motivated to seek and investigate new methods of determining local estimates of the magnetic field. In this thesis two local techniques are investigated. The first technique is the Virtual Observatory method which provides time series of the field at specified locations using a local fit to the potential using satellite data, and the second technique is a modified Backus-Gilbert inversion approach where estimates of the field are determined as local spatial averages at the CMB, providing appraisal consisting of spatial resolution and variance estimation.

Chapter 3

Measurements of the Magnetic Field

3.1 Introduction

The objective of this chapter is to describe and present an initial exploratory analysis of the satellite data used throughout this thesis. The data used consists of vector magnetic field measurements from the CHAMP and *Swarm* low Earth orbiting (LEO) satellite missions, and therefore these two satellite missions will be described in detail in Section 3.2. From the satellite observations two data subsets were built using slightly different selection criteria. These data sets are used in the virtual observatory (VO) and subtractive optimally localized average (SOLA) methods described in Chapters 4 and 5, respectively. Section 3.3 describes the data selection criteria and processing steps used to produce the two data sets. In Section 3.4 an exploratory data analysis is conducted for one of these data subsets (as the datasets are rather similar), in particular, describing the spatial structure of the data residuals for each field component computed as the differences with respect to predictions of the CHAOS-6-x5 field model (Finlay et al., 2016b). A data error covariance matrix derived from these residuals provides information on the statistical behaviour of the data, giving a measure of the joint variability between elements in the data set, having variance as diagonal elements. Often when doing geomagnetic field modelling data errors are assumed to be spatially and temporally uncorrelated, thus associated covariance matrices are diagonal. However, data errors are known to be correlated. Here an attempt is made to build a simple data error covariance matrix accounting for along-track serial error correlations based on an exponential correlation model. This is to be used with the subtractive optimally localized average method in Chapter 5. Section 3.5 describes ground observatory magnetic measurements as these will are used later for comparisons with the virtual observatory time series produced in Chapter 4.

3.2 Satellite Magnetic Measurements

Magnetic measurements from space can be characterized as spatio-temporal data; the observations are made at particular positions in space over a period of time. The observations in question are high precision absolute magnetic field measurements (Olsen et al., 2010a; Olsen and Stolle, 2012). When LEO satellites are taking magnetic field measurements they are travelling at velocities of around 8 km/s, which means that a magnetic field variation

detected along the satellite track will be a combination of both temporal and geographical changes in the field, and with a single satellite it is not possible to decipher whether such a variation is due a spatial or temporal change (in contrast, at ground magnetic observatories measurements are taken at one location, and therefore only temporal changes in the field are observed). Moreover, the observations are made over a range of altitudes due to the satellite orbit. In addition, the LEO satellites are flying within the ionospheric F-region where electrical currents can flow, especially at polar latitudes and on the day side. This means that the observed field may not strictly be a Laplacian potential as often assumed (Olsen et al., 2010b; Olsen and Stolle, 2012). Also, because the LEO satellites fly above the ionospheric E-region, electrical currents existing there produce magnetic fields that are seen as internal contributions by the satellites. Clearly as the satellites orbit the Earth, temporal correlations in the data will be present. Due to the satellite orbital inclination, measurement gaps will occur around the geographic poles. The polar gaps will influence spherical harmonic models, in particular affecting the near-zonal coefficients, i.e. $m \approx 0$ (Olsen et al., 2010a).

Despite some of the above mentioned difficulties, the advantages of using satellite data are numerous. Most importantly, sampling with the same instrument for long time periods providing good global spatial coverage (except for the polar gaps). This makes satellite measurements ideal for studying the slowly changing internal magnetic field and its spatial and temporal behaviour, for example if a spherical harmonic model is sought (Backus et al., 1996). The satellites considered in this project, are flying at $\approx$ 400km altitude, and thus their sensitivity towards finer spatial internal field structures is reduced, however this also means that the crustal and Earth induced magnetic fields have less amplitude which is advantageous in connection with internal field modelling focusing on the core-generated field. The determination of the magnetic field is dependent on the field components measured; using only intensity measurements is not enough to remove non uniqueness of the problem (Backus, 1970d; Backus et al., 1996; Sabaka et al., 2010).

A particular challenge when using satellite measurements is the spacecraft orientation (attitude) and in-flight calibration. The CHAMP and *Swarm* satellites carry both scalar and vector magnetometers; the intensity of the field is measured using absolute scalar magnetometers, whereas the vector magnetometers are non-absolute instruments and therefore need to be calibrated and aligned (Olsen et al., 2003; Tøffner-Clausen et al., 2016). In a process called calibration, the raw vector field magnetometer measurements are converted into scaled magnetic field components having units of nT. This is done in-orbit using information from the intensity readings. Afterwards the calibrated measurements are rotated from the magnetometer frame into an Earth-Centered-Earth-Fixed (ECEF) coordinate system in a process step called data alignment. This requires precise determination of the rotations, the so-called Euler angles, between the magnetometer frame and the star tracker frame (Olsen and Kotsiaros, 2011). It should be noted, that unmodelled toroidal magnetic fields may disturb the determination of the Euler angles (Olsen and Stolle, 2017). Anisotropic errors in attitude also influences the rotation (Holme and Bloxham, 1996), and in field models, such as the CHAOS-6, information on this is included in a data error covariance matrix. In the CHAOS-6 field model these Euler angles are co-estimated (Finlay et al., 2016b), and these Euler angles were used in this thesis when handling data.

The CHAMP and *Swarm* Satellite Missions

The German CHAMP (CHAllenging Minisatellite Payloads) single satellite mission lasted from its launch on the 15th of July 2000 to its re-entry in the atmosphere on the 19th of September 2010. CHAMP was a geoscientific satellite, designed to perform gravity and magnetic field observations. The satellite initially had an altitude of 454km which declined to an altitude of 250km at the end of the mission, having an orbit inclination of 87.3°. CHAMP carried an Overhauser scalar magnetometer (OVM) measuring the field intensity and two fluxgate vector magnetometers (FGM) measuring the direction and strength of the field (Reigber et al., 2002; Yin and Lühr, 2011; Lühr et al., 2013). The instruments were placed on a boom, such that contaminating effects from other onboard systems could be minimized. Additionally CHAMP carried two star imager heads in order to reduce attitude errors (Olsen and Kotsiaros, 2011). The top plot of Figure 3.1 shows a sketch of the CHAMP and the instruments on board the satellite.

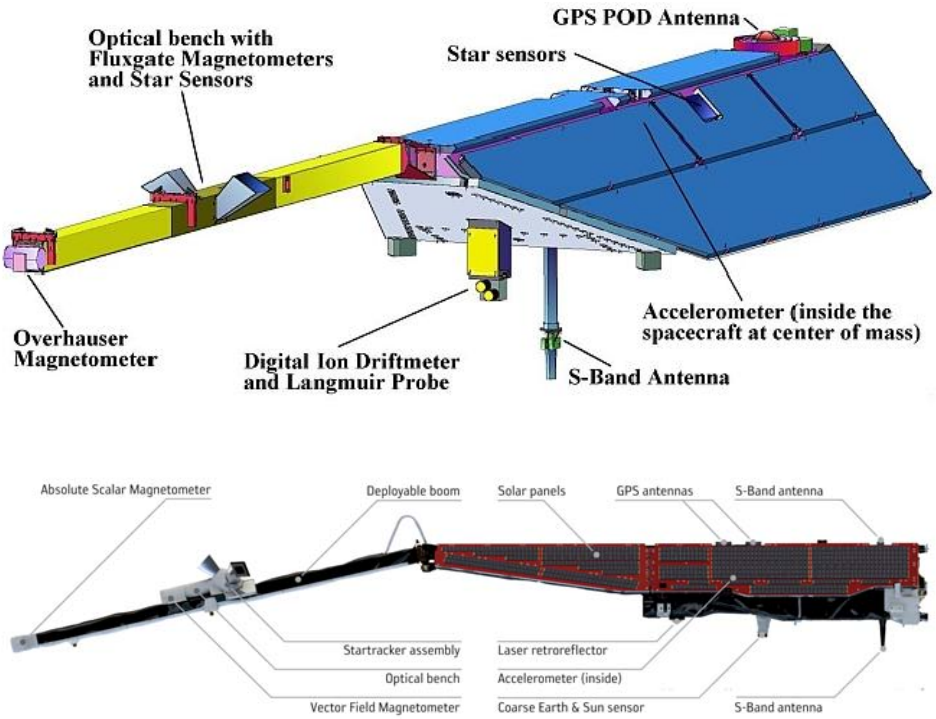

Figure 3.1: Illustrations of the CHAMP satellite (top) (Credit: GFZ, https://directory.eoportal.org/web/eoportal/satellite-missions/c-missions/champ), and *Swarm* satellites (bottom) (Credit: ESA/AOES Medialab, https://www.esa.int/spaceinimages/Images/2012/11/Swarm_instruments_side_view), showing the structure and instrumentation of the two spacecraft.

The three *Swarm* satellites *Alpha*, *Bravo* and *Charlie* were launched on the 22nd of November 2013, in a mission led by the European Space Agency (ESA). The aim of the *Swarm* mission is to provide the best ever survey of the geomagnetic field and its temporal evolution, the mission scientific objectives are research into the sources of the core-generated field, the crustal field, the ionospheric and magentospheric fields, and to get a better characterization and understanding of these fields (Friis-Christensen et al., 2006). An important aspect of the three satellite constellation is the orbital concept in

which the *Swarm Alpha* and *Charlie* satellites are flying side-by-side allowing for east-west measurement differences to be computed, that is the so-called gradient concept. The *Swarm Alpha* and *Charlie* have an orbit inclination of 87.35°, while *Bravo* has an inclination of 87.75°, for further details see `https://directory.eoportal.org/web/eoportal/satellite-missions/s/swarm` and `https://earth.esa.int`. The bottom plot of Figure 3.1 shows a sketch of one the *Swarm* satellite and the instruments on board.

The *Swarm* satellites all carry the same instrumentation on-board; an absolute scalar magnetometer (ASM) taking measurements of the magnetic field intensity, a vector fluxgate magnetometer (VFM) taking measurements of the directions and strength of the field and a three-head star tracker (STR) providing satellite orientation (attitude) information such that measurements can be rotated from the magnetometer frame to the geocentric coordinate frame (Tøffner-Clausen et al., 2016). A specific aim with the ASM instrument is to be able to calibrate the VFM. Scalar residuals between measurement readings of the ASM and the modulus of the VFM, have shown that the vector field measurements were contaminated by an initially unexpected and unknown source of peak to peak amplitude of approximately 5nT. Investigations into these residuals, revealed disturbances related to the incidence angles of the Sun on the satellites. This was named the Sun-driven disturbance field and investigations led to the determination and removal of an empirical model such that the effect could be mitigated; this has been implemented from L1b magnetic field data versions 0401 and onwards (Tøffner-Clausen et al., 2016).

The accuracy of the CHAMP and *Swarm* satellites vector field measurements are ~ 0.3nT (Lühr et al., 2013; Friis-Christensen et al., 2006). It should be noted that unmodelled external fields often dominate over the instrumental errors (Finlay et al., 2016b), and in data error covariances used in field modelling as described in Section 3.4.2. Figure 3.2 shows the mean altitude above the surface of the Earth of the CHAMP (left plot) and *Swarm* Alpha and Bravo (right plot) satellites. The mean altitude during the current lifetime of the CHAMP and *Swarm* satellites are approximately 370km and 490km, respectively.

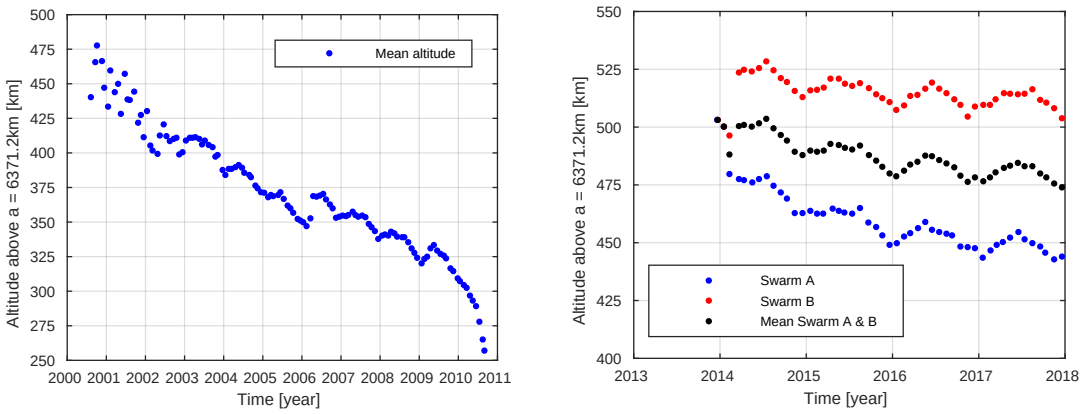

Figure 3.2: Mean altitude above ground of the CHAMP satellite (left plot) and the *Swarm* Alpha (in red) and Bravo (in blue) satellites along with their mean altitude (in black) (right plot).

3.3 Satellite Data Selection Criteria

This section describes the data selection criteria and processing steps applied to the satellite measurements to produce the two data subsets used in the VO and SOLA methods. The art of selecting satellite measurements that are contaminated as little as possible by external magnetic fields and their secondary Earth induced counterparts, and at the same time have good spatial and temporal coverage is challenging, and it is the primary limiting factor when modelling the internal geomagnetic field (Olsen et al., 2013; Finlay et al., 2017). Various approaches have been investigated in order to minimize the external contamination (Finlay et al., 2017; Kauristie et al., 2017; Lühr et al., 2017). This project aims at using geomagnetic data having low activity levels, i.e. deemed quiet time, selected such that the sun was below the horizon to minimize the magnetic signal from ionospheric currents, i.e. deemed dark times. Furthermore, in order to reduce contamination from polar cap electrical currents, restrictions on components of the IMF and MEF were used. These criteria follow a commonly used philosophy when selecting data for implementation in geomagnetic field models such as the CHAOS model series (Olsen et al., 2015; Finlay et al., 2016b, 2017). As a final step estimates of the crustal field, the large-scale external magnetospheric field and its Earth induced counterpart from the CHAOS-6-x5 model, and of the Sq part of the ionospheric field and its Earth induced counterpart from the CM4 model, were subtracted from the measurements.

From the CHAMP and *Swarm* vector measurements a 15s subsampling of the low rate (5Hz for CHAMP and 1Hz for *Swarm*) calibrated vector magnetic field data in the Vector Field Magnetometer (FGM/VFM) frame (in units of nT) as provided by the CHAMP MAG-L3 and *Swarm* Level 1b MAG-L (MAGX_LR_1B) version 0503 data products were extracted. Descriptions of the CHAMP and *Swarm* data products are given in `http://www-app2.gfz-potsdam.de/pb1/op/champ/more/docs_CHAMP.html` and by Olsen et al. (2013) and Nielsen (2017), respectively. CHAMP measurements were taken from 19th of July 2000 to the 1st of September 2010 and *Swarm* measurements were taken from 1st December 2013 up to 31th of December 2017. The FGM/VFM data were afterwards transformed into an Earth-Centered Earth-Fixed (ECEF) local Cartesian North-East-Centre (NEC) coordinate frame. This was done by data alignment such that the FGM/VFM data were first rotated into the Common Reference Frame (CRF) of the star tracker. To do this, the Euler rotation angles as determined by the CHAOS-6-x5 model were used. Measurements from known disturbed days where satellite manoeuvres took place were removed. Also gross data outliers for which the vector field components deviated more than 500nT from predictions of the CHAOS-6-x5 field model for SH degrees $n \in [1, 13]$ were removed. Next, the following selection criteria and processing steps were employed: (1) only dark region data requiring the sun to be at least 10° below horizon in order to reduce ionospheric field contamination; (2) for quiet time conditions it was required that the geomagnetic planetary activity index $\mathrm{K_p}$ was below either 2^o or 3^o (see Table 3.1); (3) for the magnethospheric ring current and its Earth induced contribution given by the *RC* disturbance index, the time derivative $|d\mathrm{RC}/dt|$ was required below either 2nT/hr or 3nT/hr (see Table 3.1) (Olsen et al., 2014); (4) restricting the merging electric field at the magnetopause such that $\mathrm{E_m} \leq 0.8\mathrm{mV/m}$ with $E_m = 0.33 v^{4/3} B_t^{2/3} \sin(|\varpi|/2)$ where v is the solar wind speed, $\varpi = \arctan(B_y/B_z)$ is the IMF clock angle and $B_t = \sqrt{B_y^2 + B_z^2}$ is the magnitude of the interplanetary magnetic field (IMF) having components in the geocentric solar magnetospheric (GSM) coordinate y-z plane (Newell et al., 2007), calculated using 2 hourly means based on 1-min values of the IMF and solar wind extracted form the

OMNI database http://omniweb.gsfc.nasa.gov; (5) requiring that IMF $B_z > 0$nT and IMF $|B_y|$ smaller than either 6nT or 10nT, in order to reduce sub-storm auroral electrojet contamination originating from field-aligned currents (Ritter et al., 2004; Friis-Christensen et al., 2017). Finally, CHAOS-6 model estimates of the crustal field for SH degrees 14-120[1] and the external magnetospheric (plus induced) field, together with the CM4 (Sabaka et al., 2004) estimates of the ionospheric field and its induced counterpart scaled by the F10.7 solar flux index were subtracted[2]. Table 3.1 summarises the data selection criteria and processing steps used to built two data subsets, named Data Set 1 and Data Set 2, used in Chapters 4 and 5, respectively. During the project many experiments with changing the selection criteria were performed; for instance an asymmetric morning/evening linear tapering using degrees relative to the horizon of $[0°, 10°]$ and $[-20°, -10°]$, respectively, instead of a clear cut-off for the sun being 10° below horizon. However, in this document it was decided to focus on the data subsets described in Table 3.1.

	Data set 1	*Data set 2*
Used in	*VO models (Chapter 4)*	*SOLA models (Chapter 5)*
CHAMP data	*MAG-L3*	*MAG-L3*
Swarm data	*Level 1b MAG-L, vs.0503*	*Level 1b MAG-L, vs.0503*
Data type	*vector only*	*vector only*
Subsampling rate	15Hz	15Hz
Kp	$< 3^o$	$< 2^o$
$\|dRC/dt\|$	$<$ 3nT/h	$<$ 2nT/h
Em	$\leq$ 0.8mV/m	$\leq$ 0.8mV/m
IMF B_z	$>$ 0nT	$>$ 0nT
IMF $\|B_y\|$	$<$ 10nT	$<$ 6nT
Solar angle	$< -10°$	$< -10°$
Outliers removed	$>$ 500nT from CHAOS	$>$ 500nT from CHAOS
CHAOS-6-x5	Crustal field for $n \in [14, 120]$ subtracted	
CHAOS-6-x5	Magnetospheric (plus induced) fields subtracted	
CM4	Ionospheric (plus induced) fields subtracted	
Weights applied	SWA and SWC by a factor 1/2	—

Table 3.1: Data sets - data selection criteria and processing.

This thesis uses both vector field data and sums and differences of the magnetic field components $B_k = \hat{\mathbf{k}} \cdot \mathbf{B}(\mathbf{r})$ in geographic spherical polar coordinates where $(k = r, \theta, \phi)$, such that Δd_k and Σd_k are data differences and sums, respectively. The along-track (AT) and east-west (EW) data differences are denoted by $\Delta d_k = (\Delta d_k^{\mathrm{AT}}, \Delta d_k^{\mathrm{EW}})$, and the data sums constructed by $\Sigma d_k = (\Sigma d_k^{\mathrm{AT}}, \Sigma d_k^{\mathrm{EW}})$. Note that in some circumstances it is necessary to consider data sums as well as differences to ensure sufficient information on longer wavelengths (Sabaka et al., 2015). The along-track data differences are calculated

[1] In finalizing the thesis it was noted, that the time-dependent part of CHAOS-6-x5 for degrees 14-20 were removed in calculating the datasets. An improvement would be to instead remove only the static part for one selected epoch, since this would not remove the SV signal above degree 14. Also the static crustal field for CHAOS-6 should only be used up to SH degree 110.

[2] It should be noted that an updated version CIY4 has now been released; the induced secondary field associated with the ionospheric primary field is now more advanced and reflects a 3-D conductivity structure that consists of an ocean–continent contrast in the upper layer with a 1-D mantle underneath (Sabaka et al., 2018). However this updated model was not used in this project.

using 15s differences $\Delta d_k^{\mathrm{AT}} = [B_k(\mathbf{r}, t) - B_k(\mathbf{r} + \delta\mathbf{r}, t + 15s)]$. With a satellite speed of ≈ 7.7km/s this corresponds to an along-track distance of 115km (Olsen et al., 2015). The along-track summations were calculated as $\Sigma d_k^{AT} = [B_k\mathbf{r}, t) + B_k(\mathbf{r} + \delta\mathbf{r}, t + 15s)]/2$. The east-west differences were calculated as $\Delta d_k^{\mathrm{EW}} = [B_k^{\mathrm{SWA}}(\mathbf{r}_1, t_1) - B_k^{\mathrm{SWC}}(\mathbf{r}_2, t_2)]$ having an East-West orbit separation between the *Swarm Alpha* (SWA) and *Charlie* (SWC) satellites of $\approx 1.4°$ corresponding to 155km at the equator (Olsen et al., 2015). The east-west sums were calculated as $\Sigma d_k^{\mathrm{EW}} = [B_k^{\mathrm{SWA}}(\mathbf{r}_1, t_1) + B_k^{\mathrm{SWC}}(\mathbf{r}_2, t_2)]/2$. For a particular orbit of *Swarm Alpha* the corresponding *Swarm Charlie* data were selected to be the one closest in colatitude with the condition that $|\Delta t| = |t_1 - t_2| < 50s$.

3.4 Analysis of Data Set 2

In this section a more detailed analysis of the *Swarm* and CHAMP data from Data Set 2 is presented in order to give insights into the satellite measurements and their content. Because Data Set 1 and 2 are quite similar the analysis is presented for one of these sets. In particular, Quasi-Dipole (QD) latitude dependent Huber weighted data uncertainties are derived which are used to built the data error covariance matrices implemented in the modelling described in Chapter 5. In addition to this, the off-diagonal elements of the covariance matrix were modelled by an exponential correlation model in an effort to account for along-track serial error correlation in the data.

3.4.1 Exploratory Data Analysis

The satellite data used in this project are a function of time and space. Data residuals with respect to the CHAOS-6-x5 model field predictions are used here to construct a data error covariance matrix. This is of course an incomplete approach; the CHAOS-6 is an imperfect model. However, analysis of residuals to CHAOS-6 provides the means of deriving a data error covariance matrix with the assumption that the structure of these data residuals is indicative of the amount of unmodelled field disturbance present in the data.

An analysis of these data residuals, computed as $\epsilon_i = (d_i - d_{model,i})$ for $i = 1, ..., N$ data, are presented below. Here d_i are either magnetic field observations or differences of magnetic observations from Data Set 2, and $d_{model,i}$ are the predictions of the CHAOS-6-x5 model for SH degrees $n \in [1, 13]$ at the given data positions and times. Note here that Data Set 2 differs from that used to construct the CHAOS-6-x5 model by data selection and handling procedures; in particular, CHAOS-6-x5 uses both ground and satellite (including Ørsted and SAC-C) based measurements. Furthermore, the ionospheric field and its induced counterpart as estimated from the CM4 model were subtracted from Data Set 2, which is not the case for the data used in the CHAOS-6-x5 model. Some basic statistics on the vector data residuals for the *Swarm* and CHAMP satellites are presented in Tables 3.2; the number of vector measurements are approximately 1.6mio and 1.2mio for the three *Swarm* and the CHAMP satellites, respectively. Ideally data residuals would be random and normally distributed with a zero mean and they would be uncorrelated. This is not the case in practise. The minimum and maximum values of the field components are similar for all satellites (though a threshold of ±500nT has been implemented), as are the means and standard deviations.

Figure 3.3 presents the spatial structure of the vector data residuals plotted against geographic colatitude for each field component. It is evident that large residuals are present in the polar regions from geographic colatitudes 0° to 40° and 140° to 180°. Even though large residuals are found in all three vector components, the residual level in the radial

Component	No. data	min [nT]	max [nT]	Mean [nT]	Median [nT]	std [nT]
Swarm						
δB_r	1616182	−119.41	115.62	−0.24	−0.18	4.96
δB_θ	1616182	−447.71	495.58	−0.34	−0.37	12.69
δB_ϕ	1616182	−416.66	441.19	0.13	0.17	15.05
CHAMP						
δB_r	1167303	−467.21	353.32	−0.27	−0.12	7.67
δB_θ	1167303	−427.78	430.75	−0.09	−0.15	13.47
δB_ϕ	1167303	−473.42	493.85	0.15	0.15	14.32

Table 3.2: *Swarm* and CHAMP vector data residual statistics.

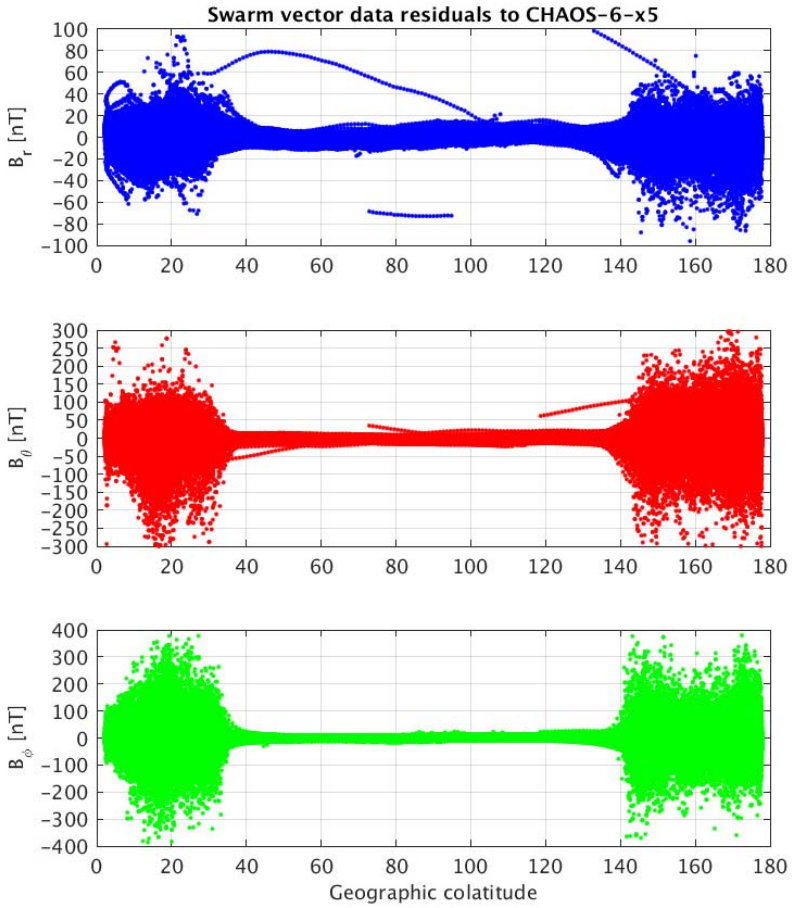

Figure 3.3: *Swarm* data residuals vs. colatitude.

component is seen to be significantly lower than for the two horizontal components. Furthermore, in the radial component some satellite tracks having higher residual amplitudes can be seen outside the polar regions. Figures 3.4 and 3.5 present histograms of the data and data difference residuals for the CHAMP and *Swarm* satellites, respectively, showing the frequency of residual values (notice that the x-axis has been limited to ±50nT such that large outliers are not visible). The plot shows the residuals for each field component for the data (top plots) and data differences (bottom plots). Each of these histograms also include the best fit of a normal distribution shown in red, stating the mean, μ, and the standard deviation, σ. Notice here the behaviour of the standard deviation (i.e. the

measure of distribution spread) becoming broader for the two horizontal components as compared to the radial field component; that is, the variability differs between the components.

Exploring further, Figures 3.6 and 3.7 present normal probability plots for each field component for the CHAMP and *Swarm* satellites, respectively. As before plots are shown for residuals of the data (top plots) and data differences (bottom plots). These plots are used to examine whether residuals are normally distributed or not. The blue crosses are the actual residuals distribution while the red stipulated line shows a fitted normal distribution. For instance considering *Swarm* data; from these plots it can be seen that more residuals than expected by a Gaussian distribution are negative; according to the Gaussian pdf 1% of the vector data residuals should be less than -8nT,-10nT and -5nT for the r-, θ- and ϕ components, respectively, however the blue curve indicates that the real numbers are ≈3%, ≈5% and ≈8%. Considering the CHAMP data; according to the Gaussian pdf 1% of the vector data residuals should be less than -8nT,-11nT and -7nT for the r-, θ- and ϕ components, respectively, however the blue curve indicates that the real numbers are ≈4%, ≈7% and ≈8%. Figure 3.8 presents global scatter plots of the *Swarm* data residuals for each field component larger than 10nT in size. Looking at the plots it should be noted that the scale in each plot is not the same.

By visual inspection of the normal probability plots and histograms, it appears that the residuals are in fact not normally distributed; the residuals have a long tail. Testing each component for normality, a one-sample Kolmogorov-Smirnov test, using the build-in Matlab function *kstest*, was performed (other similar tests exist, for instance the Anderson-Darling and Lilliefors tests) (Aster et al., 2005). The Kolmogorov-Smirnov method tests the following null hypothesis: namely that the residuals originate from a standard normal distribution (against that it does not). In all cases the hypothesis was rejected at a 5% significance level (i.e. the typical chosen significance level, rejecting the null hypothesis if there is less than 5% probability that it is true) (Barlow, 1989; Taylor, 1997).

Thus, from the above analysis data residuals do not follow a normal distribution; why is this and what does it mean? There could be various causes (for instance insufficient data), however the reason here is long tails in the distribution i.e. more high or low values than expected that have an abnormal distance from other points, and thereby disturbing the statistics (Barlow, 1989; Taylor, 1997). Here long tailed distributions are the cause of the non-normality. The overall patterns show residuals concentrated at the polar regions extending equatorward by approximately $30° - 40°$. The residual asymmetry, as compared to the North-South axis around the polar region, indicates that quasi-dipole coordinates would provide a suitable description. As can be observed, the radial magnetic field residuals are smaller than the horizontal component residuals. Moreover, the θ-component exhibits a pattern of residuals along the magnetic equator which may be attributed to removal of the ionospheric field predictions of the CM4 model. The long tailed distribution of the data errors needs to be handled in an appropriate manner and the following section describes an approach of doing this.

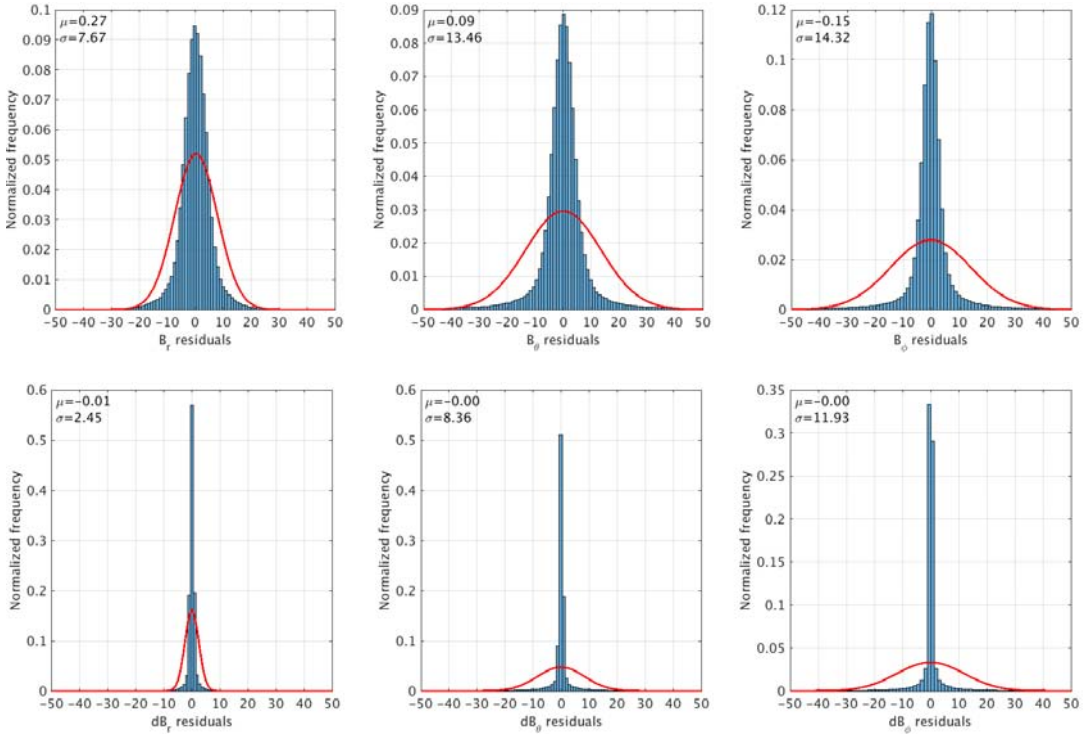

Figure 3.4: Histograms of CHAMP data (top) and data differences (bottom) residuals.

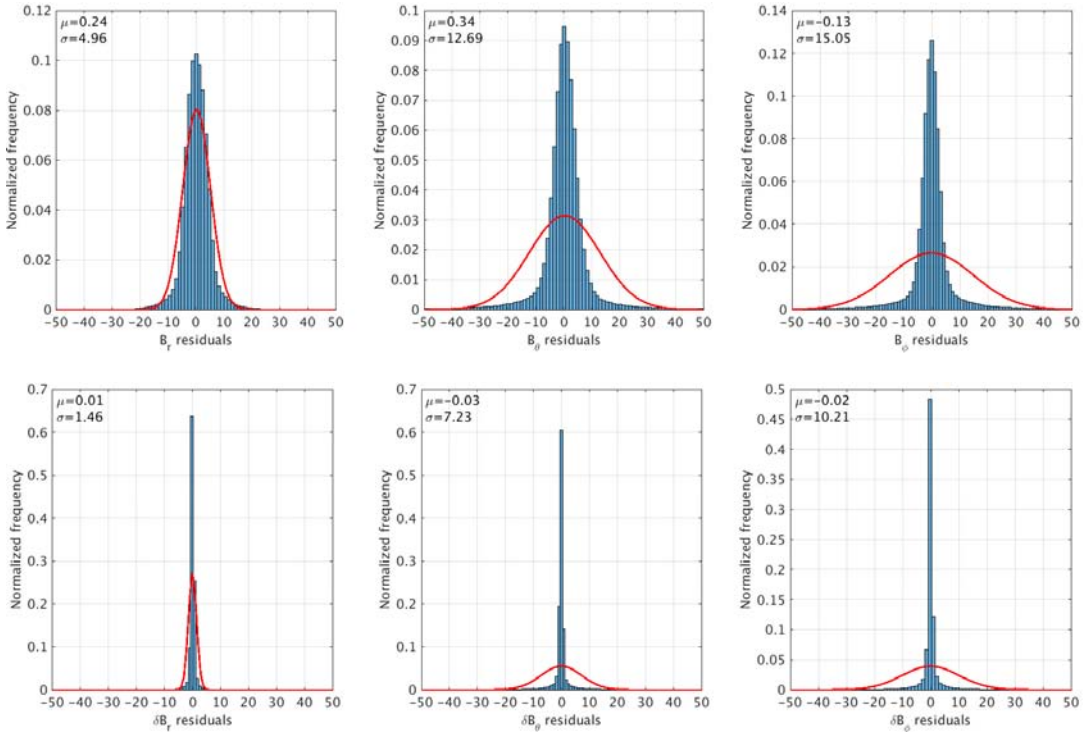

Figure 3.5: Histograms of *Swarm* data (top) and data differences (bottom) residuals.

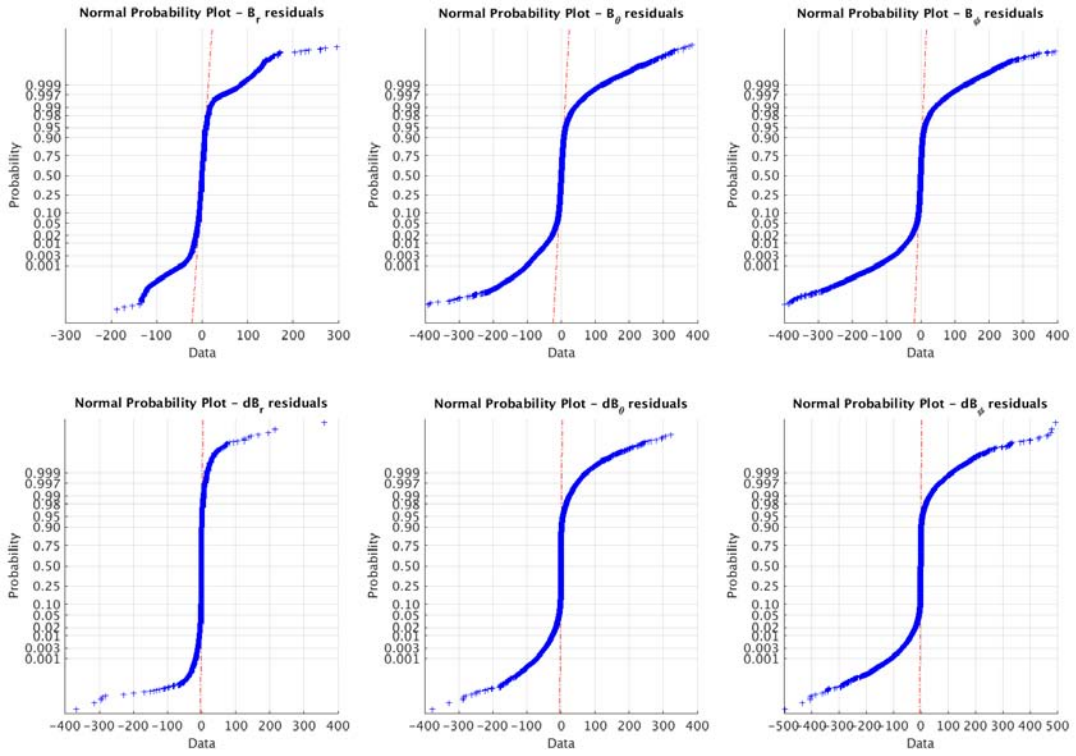

Figure 3.6: Normal plots of CHAMP data (top) and data differences (bottom) residuals.

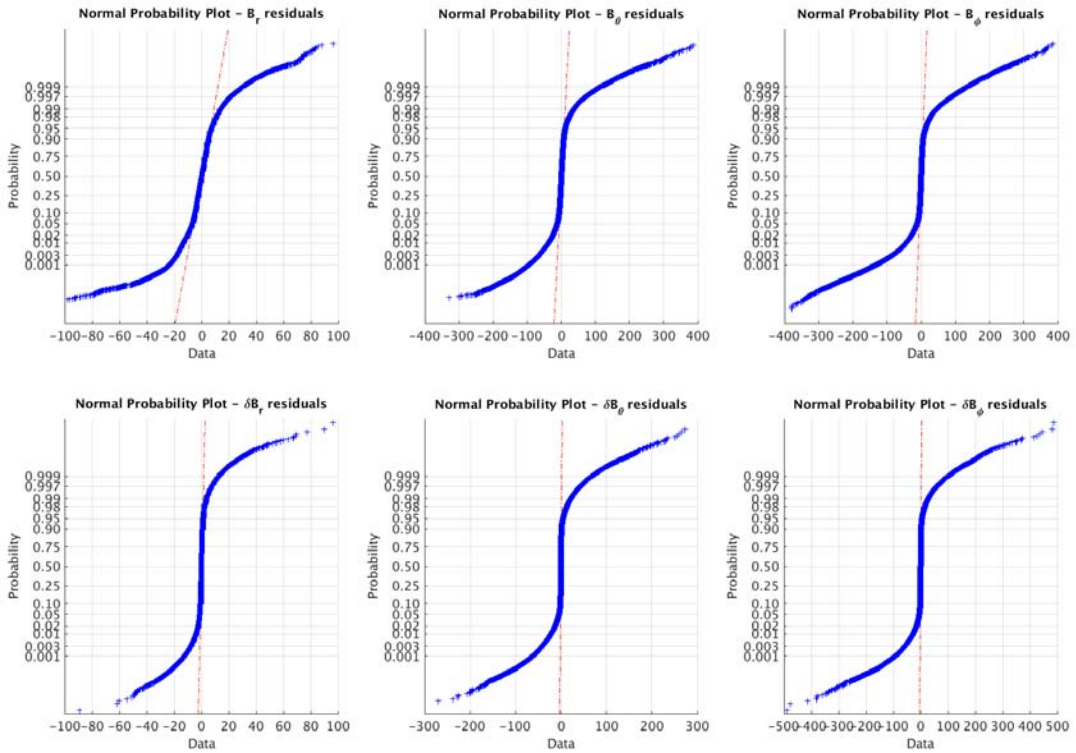

Figure 3.7: Normal plots of *Swarm* data (top) and data differences (bottom) residuals.

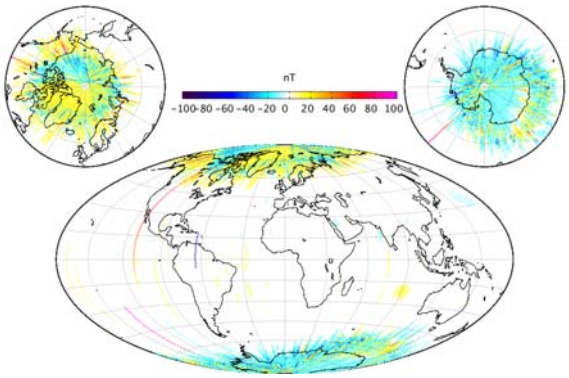

(a) Data residuals B_r component.

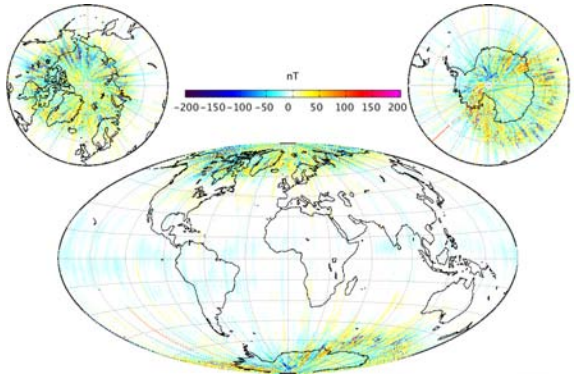

(b) Data residuals B_θ component.

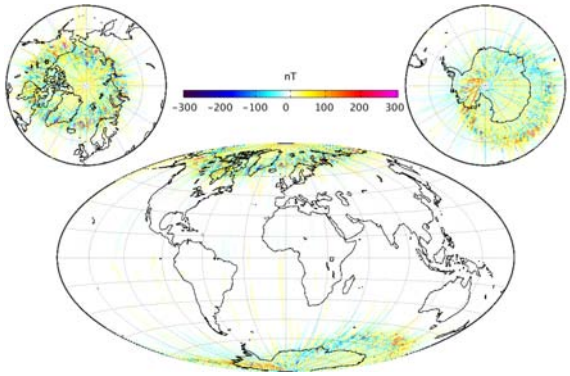

(c) Data residuals B_ϕ component.

Figure 3.8: Global scatter plot of *Swarm* vector data residuals > 10nT in size.

3.4.2 Latitude-dependent Data Error Covariance Matrix

In this section a procedure for providing data variance estimates is described, which is used to construct covariance matrices used in the SOLA model in Chapter 5. Knowledge of data error estimates and possible error correlation, are encapsulated in a data error covariance matrix, which can be written $E_{ij} = \mathrm{Cov}(x_i, x_j)$, where i and j are elements of the residuals (response variable) x. The diagonal elements of the covariance matrix are the variances which are the squared standard deviation; these provide an estimate for the data uncertainty. However, if the data errors are correlated this will result in non-zero off-diagonal elements as well (e.g., Barlow, 1989; Crawley, 2015). Thus, a dense covariance matrix can incorporate both uncertainty and correlation information on the data set.

The idea is as follows: 1) use all data from Data Set 2 to construct quasi-dipole (QD) latitude (Richmond, 1995) dependent data uncertainty estimates, $\sigma(QD)$, and robust weights, w, in latitude bins for vector data and vector data sums and differences. The reason for using the QD latitude and not the geographical latitude is that the QD system is a well-suited coordinate system for describing unmodelled ionospheric signals (Sabaka et al., 2002; Laundal and Richmond, 2017); 2) for Data Set 2, construct diagonal elements of the data error covariance matrices based on these binned values:

Step 1) estimates of the QD latitude binned standard deviations were determined using

all data as

$$\sigma(QD) = \sqrt{\frac{\sum_i w_i (x_i - \mu_w)^2}{\sum_i w_i}} \tag{3.1}$$

where x_i is the residual for a given field component determined as the difference to the CHAOS-6-x5 field predictions for SH degrees 1-13, $x = (d - d_{CHAOS})$. The weighted residual mean is given by (e.g., Finlay et al., 2010b)

$$\mu_w = \frac{\sum_i w_i x_i}{\sum_i w_i} \tag{3.2}$$

Different types of weight functions may be used, for instance Huber or Tukey's biweight. For a long tailed error distribution, Huber weights are appropriate determined as (Constable, 1988; Olsen, 2002)

$$w_i = \begin{cases} 1 & \text{if } \epsilon_i \leq c_w \\ c_w/\epsilon_i & \text{if } \epsilon_i > c_w \end{cases}$$

where the normalized residuals are $\epsilon_i = x_i/\sigma$ and $c_w = 1.5$ is the selected breakpoint for the Huber distribution. Figure 3.9 presents the calculated data uncertainty estimates as a function of QD latitude for CHAMP and *Swarm* vector data, and vector data differences and sums. It can be seen that large uncertainty estimates are confined to polar latitudes (i.e. QD latitudes 60° to 90° and −60° to −90° for the northern and southern polar regions, respectively). Furthermore, the estimates are larger for the horizontal field components, and are seen to exhibit a noticeable asymmetry between the northern and southern polar regions. Such behaviours have been observed in previous studies (Kotsiaros et al., 2015; Kother et al., 2015).

Step 2) built a diagonal covariance matrix using $\sigma^2_{w,i} = \sigma^2_i/w_i$. Here a covariance matrix is built based on the data used, i.e. vector data or vector data sums and differences. The matrix determined this way is purely diagonal. As described, the Huber weights, are in addition to latitude-dependent uncertainties, used in order to handle a long-tailed residual distribution. The Huber weights assign a value less than 1 to data lying in the tail based on some predefined cut-off point which is here set to 1.5σ. Thus, the smaller the Huber weight, the bigger the data error variance estimate will become. Below, the covariance matrix, $\underline{\underline{E}}$, is illustrated for an example of using vector data sums and differences, where Δ and Σ denotes sums and differences, respectively

$$\underline{\underline{E}} = \begin{pmatrix} [E^{\Delta B_r}] & & & & & \\ & [E^{\Sigma B_r}] & & & & \\ & & [E^{\Delta B_\theta}] & & & \\ & & & [E^{\Sigma B_\theta}] & & \\ & & & & [E^{\Delta B_\phi}] & \\ & & & & & [E^{\Sigma B_\phi}] \end{pmatrix}$$

Figures 3.10 and 3.11 present Huber weights less than 1 and the obtained data error covariances, for an example case of data sums and differences from March 2017. The amount of Huber weights less than one are approximately 11%, 12%, 9% for residuals of components B_r, B_θ, B_ϕ, respectively. For main field estimates in the SOLA approach, see Chapter 5, an additional weight factor of $1/\sin\theta$, where θ is geographic co-latitude, was implemented. This was done in order to account for there being more data close to the poles and in order to simulate an equal-area distribution (on the sphere the differential longitudinal element in spherical polar coordinates is given by $r\sin\theta d\phi$) (Olsen et al., 2014).

Thus, closer to the polar regions, the data error variances are effectively enhanced by this factor. For SOLA estimates of the SV, data were selected to obtain a good coverage in a global regular grid, so this factor was not used; details are given in Chapter 5.

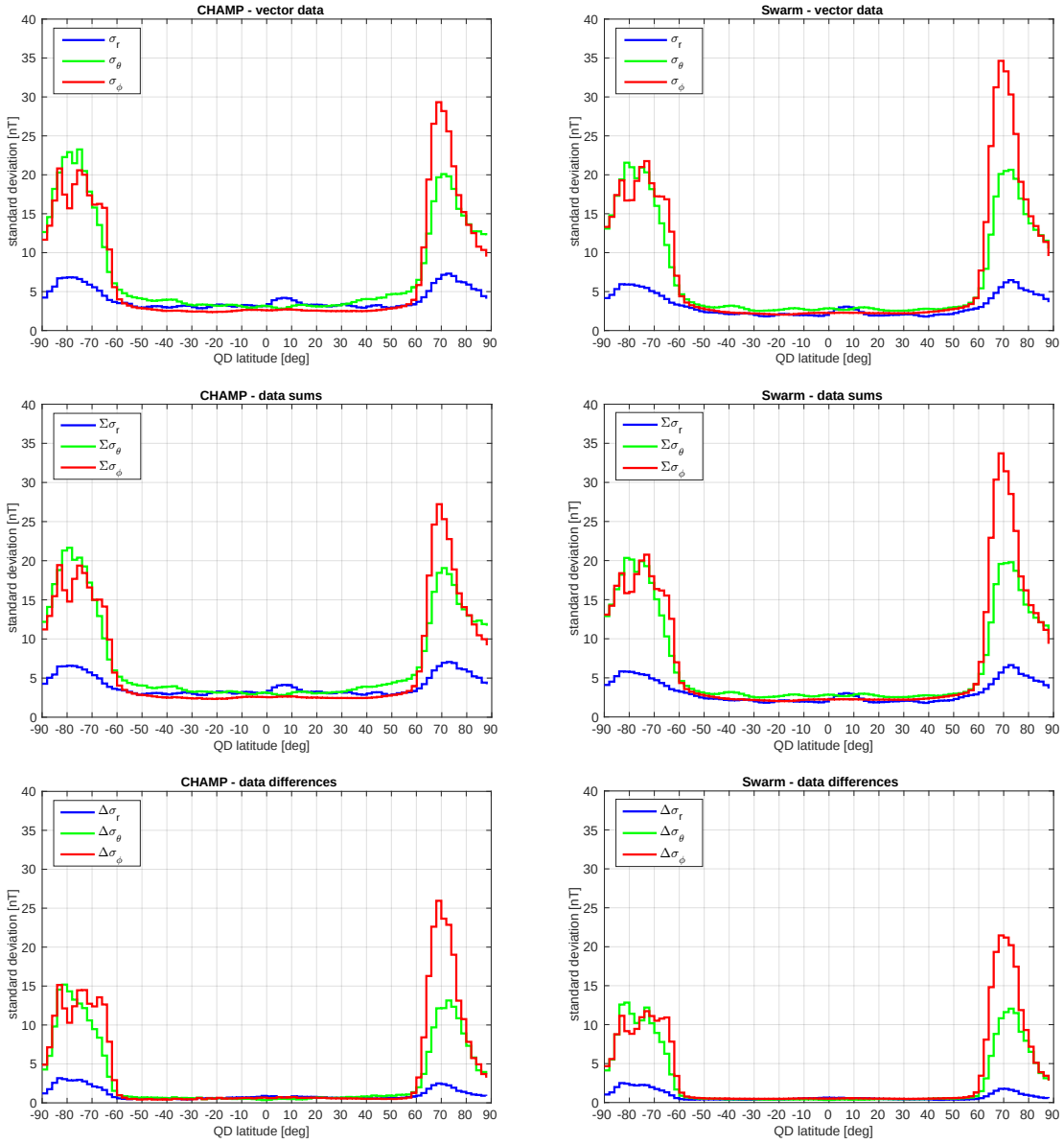

Figure 3.9: Latitude-dependent Huber weighted standard deviations in 2° bands (Northern hemisphere having positive QD) for CHAMP data (left figures) and *Swarm* data (right figures). Top: using vector data, center using data sums and bottom using data differences.

3.4.3 Along-Track Serial Error Correlation

From the description of the geomagnetic field and its various contributing sources in Chapter 2 together with the data residual analysis presented above, it is to be expected that the obtained signal exhibits correlation in a least the following ways (Lowes and Olsen, 2004)

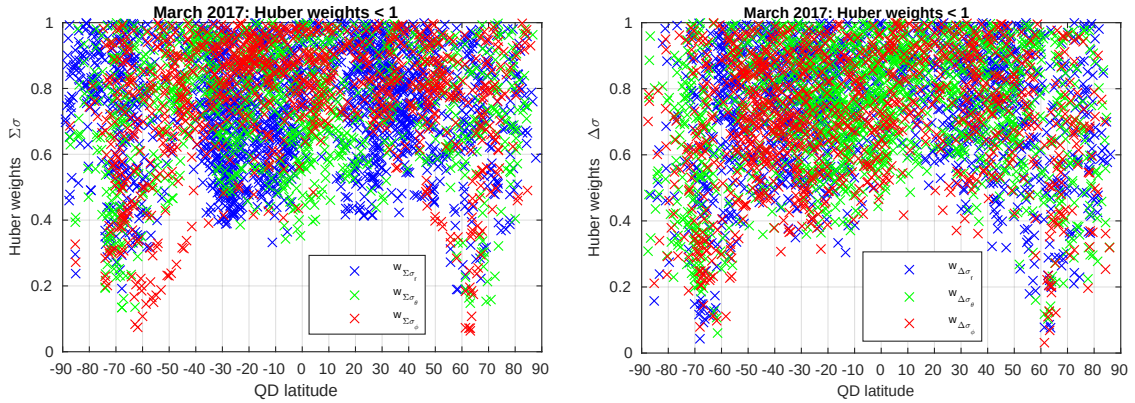

Figure 3.10: Huber weights <1 for March 2017 data example case of each field component for vector data sums (left) and difference (right).

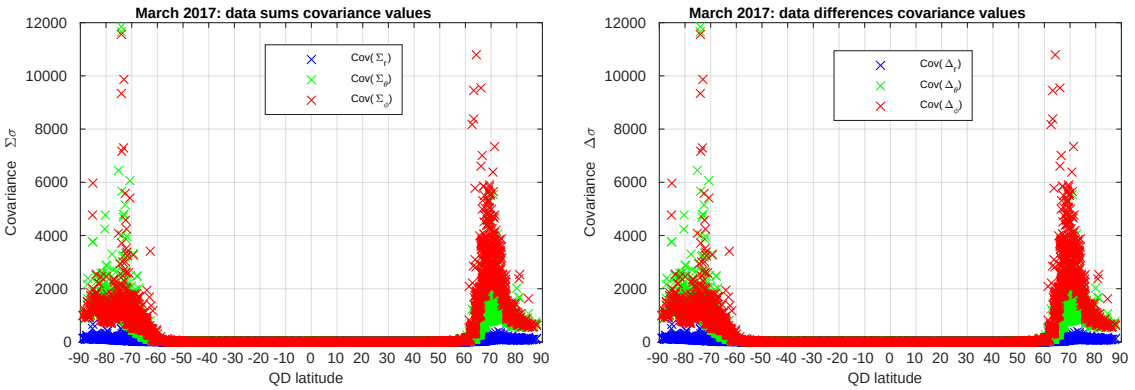

Figure 3.11: Data error variances for March 2017 data example case of each field component for vector data sums (left) and difference (right). Units in [nT^2].

i) along-track (approximately latitudinal) correlation due to unmodelled magnetospheric signal

ii) orbital recurrence (latitudinal and longitudinal) correlation due to unmodelled magnetospheric noise, having an estimated correlation time of 3-6 hr

iii) leakage of unmodelled crustal and ionospheric (plus induced) fields

It is generally recognized that large-scale magnetospheric contamination will have associated time scales of minutes to hours, i.e. longer than the sampling frequency for the satellite observations. This means that noise in the measurements will not be independent for adjacent data points, i.e. cases (i), and for measurements with orbital recurrence, i.e. case (ii). For case (i) Lowes and Olsen (2004) estimated a serial correlation time of 5-10 min. At satellite altitudes the amplitude of the small scale crustal field remaining after having subtracted the CHAOS-6-x5 model predictions, is thought to be very small (Lowes and Olsen, 2004).

Reduction of the ionospheric contamination relies on night time data selection (i.e. the sun below horizon). However, this is mostly the case at low and mid-latitudes; at polar latitudes ionospheric contamination may still be present during night times. Furthermore,

secondary Earth induction effects (i.e. induced currents in the conducting mantle and oceans producing secondary magnetic fields) may still persist during night times, long after the primary inducing sources have seized to exist (Olsen et al., 2005a). The CM4 field model predictions of the ionospheric and its Earth induced fields were therefore removed, but it should be noted that this is only an approximation, and in particular the polar ionospheric signal is not well accounted for.

Here an attempt was made to account for the serial correlation in case (i); an along-track correlation having a correlation time of 10 min based on the findings of (Lowes and Olsen, 2004). Various correlation models exists, for instance exponential and spherical types. Here an exponential covariance model was attempted (e.g. Cressie, 1993)

$$E_{ij} = E_{ii}(1-\gamma), \qquad \gamma = 1 - e^{-\Delta t_{ij}/\tau} \tag{3.3}$$

$$= \sigma^2_{w,i} e^{\frac{-\Delta t_{ij}}{\tau}} \tag{3.4}$$

where $\Delta t_{ij} = t_i - t_j$ is the time differences between each satellite observation, $\tau = 600$s is the correlation time (i.e. 10 min), and γ is called the variogram (Cressie, 1993). The exponential correlation model was build using the Matlab tool Synthetic_Variogram by T. Mejer-Hansen `http://mgstat.sourceforge.net/htmldoc/index.html`.

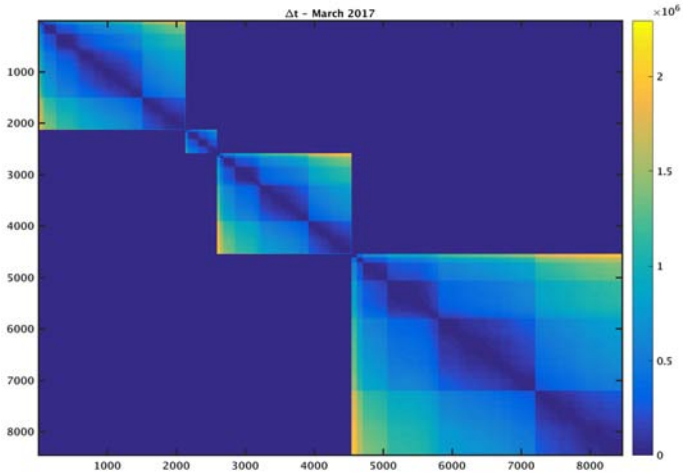

Figure 3.12: Δt_{ij} matrix example for March 2017 using data sums and differences.

Figure 3.12 shows the Δt_{ij} matrix using the March 2017 data example case. The Δt_{ij} describes the time lag, in seconds, between each observation for each of the *Swarm* satellites; the upper left block is for *Swarm Alpha* data, the second block is for *Swarm Bravo* (which for this month is slightly smaller than for the other satellites), the third is for *Swarm Charlie* and the last is *Alpha-Charlie* data. From the Δt_{ij} matrix the non-diagonal elements of the covariance matrix can be determined by the exponential correlation model. Notice that the obtained covariance matrix is required to be symmetric, i.e. $E_{ij} = E_{ji}$, and positive definite, i.e. the eigenvalues of the covariance matrix should be greater than 0, which can be investigated by performing a principal component analysis (PCA) obtaining the eigenvalues. In order to invoke a simple check for the symmetric positive definite criteria, a Cholesky decomposition on the covariance matrix was performed since only matrices with these criteria have a unique Cholesky decomposition (Aster et al., 2005).

The left plot in Figure 3.13 presents the non-zero elements of the obtained covariance matrix for the March 2017 data example, using a correlation time of 10min. The right

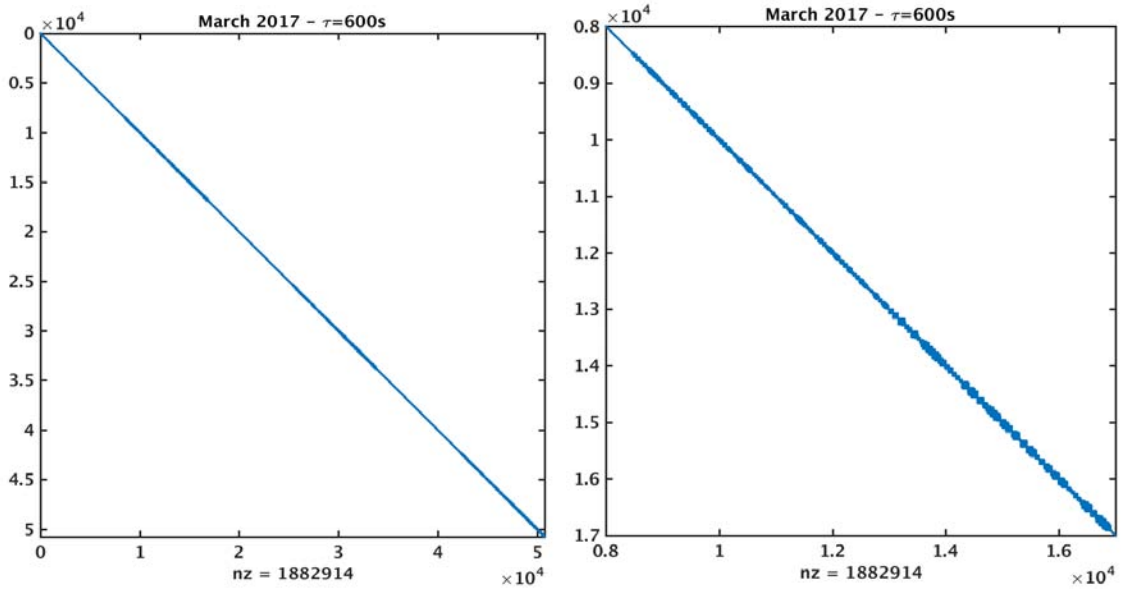

(a) Full covariance matrix having non-zero elements shown in blue.

(b) Full covariance matrix: zoom at radial data sums part, $E^{\Sigma B_r}$ having non-zero elements shown in blue.

Figure 3.13: Full covariance matrix example for March 2017 using data sums and differences including an exponential correlation model. For this example case approximately 1.9 mio out of 2600 mio elements of $\underline{\underline{E}}$ are non zero (the size of $\underline{\underline{E}}$ is 141 Mb).

plot of Figure 3.13 shows a zoom in on part of the covariance matrix, which illustrates the non-diagonal behaviour of the obtained covariance matrix. Three big lumps along the covariance matrix where the off-diagonal elements increases are due to the data sums for each of the three components being placed here; the variances for the data sums are larger which yields these slightly bigger lump structures.

3.5 Ground Observatory Data

Ground observatories (GO) provide absolute records the geomagnetic field as measured by calibrated magnetometers. At the present time there are around 180 operating ground observatories being part of the INTERMAGNET (International Real-time Magnetic Observatory Network.) Magnetic Observatory (IMO) network. Observatories part of INTERMAGNET are required to fulfil certain standards regarding accuracy and resolution, and Figure 3.14 shows a global map of the ground observatories (Mandea and Korte, 2010). As can be seen in the map, the ground observatories are unevenly distributed, and there are many in Europe. Magnetic ground observatory measurements are of great importance for several reasons: 1) they provide continuous temporal monitoring of the magnetic field with high accuracy, 2) having monitored the magnetic field from the middle of 19th century, they provide important insights into historic (Jackson et al., 2000; Gillet et al., 2013, 2015a) and present day field variations (Finlay et al., 2016b), and 3) observatory data products such as the K_p, D_{st} and RC indices are typically implemented in the selection criteria of satellite measurements to identify geomagnetically quiet times, and 4) they measure the field below the ionosphere.

Observatory data used in this thesis consists of annual differences of so-called revised

monthly mean values of the north, east and vertical downward (NEC) field components, which have been derived from hourly mean values (HMV) by a procedure described in Olsen et al. (2014). The measurements covered the period 2000-2018 and the HMV data was extracted from the BGS database `ftp://ftp.nerc-murchison.ac.uk/geomag/Swarm/AUX_OBS`, version 0111. Quality control procedures of the observatory measurements ensures inspection for data spikes, baseline jumps and other errors (Macmillan and Olsen, 2013). The revised monthly mean values were computed as follows; 1) estimates of the large-scale magnetospheric plus Earth induced fields from the CHAOS-6-x5 model predictions along with estimates of the ionospheric Sq plus Earth induced fields from the CM4 model predictions were removed from the HMV. 2) Afterwards monthly mean values were calculated using a robust method implementing Huber weights by an iterative-reweighting scheme (Olsen et al., 2014; Finlay et al., 2015). From these revised monthly mean values, the annual differences were computed at time t as $\mathbf{SW}(t)^{obs}_{NEC} = \mathbf{B}(t+0.5yr)_{NEC} - \mathbf{B}(t-0.5yr)_{NEC}$. Because the annual differences are used in this thesis to represent SV, the bias from the unmodelled crustal field are not considered important.

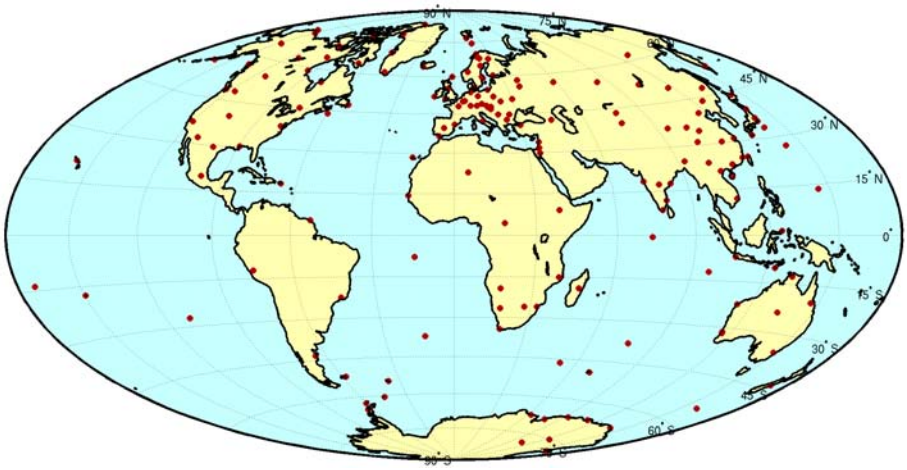

Figure 3.14: Locations of magnetic ground observatories marked with red symbols using a Hammer projection.

Chapter 4

Virtual Observatory Modelling

4.1 Introduction

The objective of this chapter is to describe, implement and advance on previous developments of a geomagnetic field data processing and modelling technique known as the Virtual Observatory (VO). The intention of the VO technique is to create time series of the field at pre-specified locations using satellite measurements by a local procedure in which a mean core field over a chosen time window at satellite altitude is determined.

The purpose of the VO data is to capture genuine short-period variations of the internal signal, thus producing a high time resolution core field signal recovery. Figure 4.1 shows an illustration of the VO concept. Here advantage will be taken of the latest measurements from the *Swarm* and CHAMP satellites in order to reconstruct VO time series of the last 15 years. However, care must be taken since signals from external sources are present in the measurements influencing the short-period core field signal; thus questions of whether the obtained signals are truly of internal origin making appropriate data selection and processing vital. This chapter presents investigations into a range of the possibilities, presented by VO modelling. In particular various improvements in the method setup and the computation of field gradients and their temporal behaviour will be explored. Note that it is not a specific goal of this chapter to model the spatial and temporal variations of the magnetic field on a global scale, but rather to produce good quality local VO's. Section 4.2 provides a summary of previous implementations and applications of the VO method. Section 4.3 describes the VO method setup used in this project and Section 4.4 describes the VO solution outputs. Sections 4.5 and 4.6 present results of the field and field gradient computations, respectively. Section 4.8 gives recommendations for future VO modelling improvements based on the results of this thesis. Section 4.8 provides a summary of the lessons learnt and conclusions of these investigations.

4.2 Prior use of the Virtual Observatory Model

The paper by Mandea and Olsen (2006) was the first to propose the modelling concept of virtual observatories. The intention of the authors was to extract and investigate short-period core field variations directly from satellite measurements. The idea was to produce satellite monthly means at specified locations mimicking ground observatory monthly means. The logic behind replicating ground observations using satellite data was the

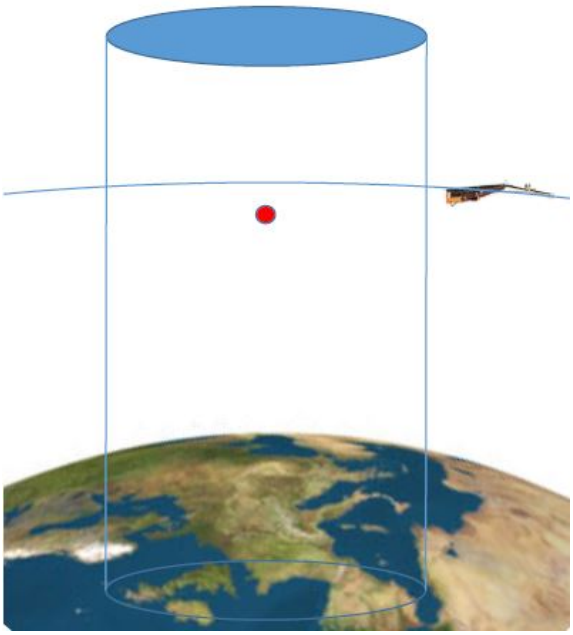

Figure 4.1: Illustration of the VO concept, satellite measurements from within a target cylinder are used to infer time series at the VO location given by a red dot. Courtesy of C. Finlay.

recognition of the excellent temporal coverage provided by the continuous field monitoring offered at the ground observatories. The VO approach used measurements in the VO target point vicinity from which an a-priori core field model evaluated at the time of the measurements was subtracted. The residual field was assumed to be a Laplacian field being fitted by a local Cartesian quadratic potential. To obtain the main field an a priori core field model prediction at the target VO location at a monthly mean time was added back afterwards. The authors used CHAMP satellite measurements from 2000-2005 comparing model results with ground observatory measurements at the observatories NGK, HER and KAK (see Figure 4.5 for a map showing the location of these observatories). In order to make processing of the satellite data similar to that of the ground data, the authors used measurements from all local times having all geomagnetic activity conditions, thus deviating from the data selection methodology usually implemented when using satellite data that typically relies on dark geomagnetic quiet times e.g. (Thomson et al., 2010; Finlay et al., 2015; Sabaka et al., 2015). The reasoning behind this were that short-period external fields was assumed to have zero mean value over the period of a month. Mandea and Olsen (2006) showed that the secular variation could indeed be usefully reproduced from the VO approach yielding mean correlation coefficients between field change records at ground and at the virtual observatories in the dX/dt, dZ/dt and dY/dt components of 0.65, 0.21, 0.73, respectively. Thus, the authors found that the dY/dt component gave no significant correlation which they attributed to possible in-situ ionospheric currents.

A second paper by Olsen and Mandea (2007) used the virtual observatory approach to capture the global patterns of the secular variation on a regular grid of VO's with special focus on resolving abrupt changes in the secular variation termed geomagentic jerks. In addition to removal of the static field estimates, the authors also subtracted a time-dependent model for SH degrees $n \leq 8$. The authors used from all local time CHAMP measurements

from 2001-2005 again with a mindset of constructing a model derived from data being uniformly distributed in space and time. In agreement with the results of Mandea and Olsen (2006), the authors found that the predictions of the virtual observatory approach contained more short-period variations than those of the CHAOS temporally smoothed model predictions. Considerable scatter about the monthly mean values was seen causing the authors to separate the observed signal into internal and external field contributions using spherical harmonic analysis in order to investigate if part of the short-period signal could be explained by magnetospheric field variations.

The authors performed a spherical harmonic analysis describing the magnetic field as the sum of poloidal and toroidal contributions; a Laplacian potential expansion into internal and external sources combined with a non-potential toroidal scalar expansion, see Section 2.5.3. The external expansion was designed to capture magnetospheric contributions and most energy was found in the SH degree $n = 1$ coefficients (i.e. due to the ring current). The toroidal expansion was added in recognition of the presence of in-situ currents at satellite altitude; it was found that there were significant non-zero coefficients for the SH degrees $n = 1$ and order $m = 0$ (the toroidal coefficients having $m = 0$ affect only the Y field component, and are thought to be related to field-align currents). Note, that ground observations cannot contain toroidal contributions, since measurements are performed in the non-conducting lower atmosphere. The authors found strong variation in the time derivatives of the external, $\dot{q_n^m}$, and toroidal, $\dot{t_n^m}$, coefficients and noticed that an induced counterpart of $\dot{q_n^m}$ might have significance. The authors found that short-period variations were not fully described by the model even when including modelled external and toroidal fields. In addition, the authors demonstrated application of the VO time series data in geomagnetic jerk investigations, determining the occurrence time of the 2003 jerk event in the northern and southern hemispheres, finding a simultaneous occurrence.

Beggan et al. (2009) attempted to find the best procedure for virtual observatory modelling based on residuals obtained after fitting an outer core fluid flow model, considering various data selection criteria, VO grid types and removal of the CM4 external and ionospheric field predictions of the primary and secondary (induced) magnetospheric, ionospheric and toroidal estimates. The authors considered both CHAMP and Østed satellite measurements. Despite a sampling frequency of 1Hz for CHAMP measurements, lack of suitable data during some months forced the authors to perform a spatial interpolation in order to fill the VO time series. The SV data were inverted for toroidal and poloidal flow using the linear relationship between SV and flow spherical harmonic coefficients. The authors' aim was to do short-term forecasting by core flows. The authors found evidence for significant contamination by external fields in the obtained flow signal, especially pronounced when using all time data, suggesting that the assumption of zero mean of the external field is not correct. Using instead night-side data and removal of CM4 external magnetospheric and ionospheric field predictions improved the flow model. Furthermore, the authors attributed enhanced residuals to satellite orbital drift and VO grid usage; that is, i) because the CHAMP satellite precessed in local time of approximately 2.5 hours per month, the data used to create monthly VO's therefore did not sample all local times. Thereby the VO's generated month by month contained different local times which experiences distinct external magnetic field environments that apparently mapped into the VO time series. Thus when calculating annual differences, to obtain SV time series, an LT effect might be present, ii) due to a global grid of equally spaced latitude and longitudes overlaps in data bins could occur. Both of these effects were shown to result in sectorial banding of the residuals, i.e. the SH coefficients $m = n$.

Beggan and Whaler (2009), Beggan and Whaler (2010) and Whaler and Beggan (2015) also used the virtual observatory approach in order to produce forecasting models of the core field. Whaler and Beggan (2015) used two different sets of magnetic field measurements covering the period 2000–2010 to generate SV and SA estimates. The first was vector monthly mean values based on night-time data from up to 160 global magnetic observatories. Monthly field component time series from CHAMP vector measurements on a grid of 648 points with equal latitude and longitude spacings of 10°, from 5° to 175° in colatitude and 0° to 350° in longitude. The authors used the CHAOS-3 model predictions to remove an estimate of the main field before the inversion for the VO solution. The authors found that the flow model fit to the GO and VO data were poorer for the SA than the SV data, and for VO than ground observatory data. The authors further found that spatial data residuals were severely biased, both for ground observatory and VO data, regardless of whether two- or one-norm data misfit measures were used during the flow inversion. The authors noted that Beggan et al. (2009) had identified spatial patterns in the SV residuals which they attributed primarily to external field contamination referring also to Shore (2013). They believed that external field contamination was the likely cause of the large outliers observed near the polar regions, especially in the VO data time series. The large-scale patterns in the residuals were common to both ground observatory and VO data, suggesting that the ground data also had significant external field contamination.

Olsen et al. (2009) and Olsen et al. (2010c) used the virtual observatory technique to assess the temporal resolution of the CHAOS-2 and CHAOS-3 field models, respectively. Olsen et al. (2009) showed that time series of annual differences of monthly means in dZ/dt of the CHAOS-2 model predictions were able to capture some of the short-period variations seen in the virtual observatory time series. Because the VO grid time series was built using all time data, it was regarded an independent data set from that of the CHAOS-2 model. Olsen et al. (2010c) calculated virtual observatory monthly means determining time series of the Gauss coefficients. In order to minimize effects of external currents that depend on local time, the authors applied a 4-month running mean to the Gauss coefficients. This reduced the scatter of the coefficients seen in Olsen and Mandea (2007). They found scatter in the individual monthly solutions to be largest in the lower-order zonal harmonics, i.e. $m = 0$, indicating the influence of ionospheric field contributions in the polar ionosphere. Furthermore, the authors saw the signature of semi-annual variations in some SH degree $n = 1$ coefficients (e.g. h_3^1, g_4^1) thought to be caused by contributions from polar ionospheric currents. However, temporal changes in the higher degree sectorial harmonics, i.e. $m = n$ representing low latitude field changes, showed rapid field fluctuations were not well described by the CHAOS-3 model predictions due to the applied temporal regularization implemented. Hence, small scale low latitude rapid field fluctuations were observed in the VO model which were not captured by the CHAOS-3 spline model.

Shore (2013) addressed a series of issues in VO modelling concluding that "the temporal simplifications are by far the most damaging to the VOs", i.e. that external fields are not averaging to a zero-mean over the course of a month as originally assumed by Mandea and Olsen (2006). The author tested different approaches of reducing the effects of external sources and used these results to provide a more complete description of the external field variations. The author found indications that contaminations were mainly due to the symmetric ring current along with a mixture of contaminations related to patterns termed UT and LT bias. The author ascribed the UT bias to variations in the temporal density

within each VO, and found this could potentially cause the sectorial banding patterns. Furthermore, as in Beggan et al. (2009) the assumption that each VO contains the same LT sampling was found to be incorrect since various magnetic environments such as noon and midnight might be sampled differently, thus causing a LT bias resulting in "tiling" patterns (also termed the LT effect). The author proposed suggestions to mitigate some of the contamination in the VO approach; i) multiple satellite measurements providing an improved coverage of temporal variations at different local times, ii) magnetospheric field removal, iii) binning data for time windows of 4.5 months in order to ensure sampling of all LT.

Saturnino (2015) modified the VO modelling procedure by using a so-called equivalent source dipole (ESD) model representation. A grid of ESD's were constructed for each virtual observatory, inverting for the dipole magnetization and thus the corresponding field at the VO. One advantage was that no a-priori field model had to be subtracted and the possibility of downward (or upward) field continuation. The author applied *Swarm* measurements for a series of individual observatories and for a global grid. The author found good correlation between the Y and Z components. No data selection was applied and no external field corrections were attempted; thus the obtained virtual observatory time series were prone to contaminating signals.

In summary, previous investigations using the virtual observatory approach have shown it to be a robust procedure for estimating high resolution time series of the secular variation. In particular, Olsen and Mandea (2007) showed that the technique performs better than global spherical harmonic field model in that respect; typical field models are based on an analysis of globally distributed measurements whereas the virtual observatory model is based on measurements extracted in the vicinity of a particular location. Moreover, SH field models typically incorporate temporal regularization procedures in order to produce stable solutions (for instance the CHAOS field model minimizes the second time derivative of the squared magnetic field average over the Earth's surface, thus observed field accelerations exceeds model predictions Olsen et al. (2010c)). However, as shown by Beggan et al. (2009); Shore (2013); Olsen et al. (2010c) external field contamination is likely to leak into the virtual observatory time series. It is a difficult matter to reduce the effect of these external fields without affecting the VO approach; in particular using geomagnetically quite dark time data selection criteria heavily reduces the number of data available for inverting the local VO time series.

4.3 Virtual Observatory Model Formulation

The original approach devised by Mandea and Olsen (2006), for producing core field time series, used satellite measurements on a monthly basis from within a target cylinder centred on a target point called a virtual observatory located close to the mean satellite altitude.

Here the method produces a field "mean" at the target point for each time window (not necessarily in monthly windows); the procedure used in this thesis is as shown in the flowchart Figure 4.2. In the following sections each step is explained in more detail.

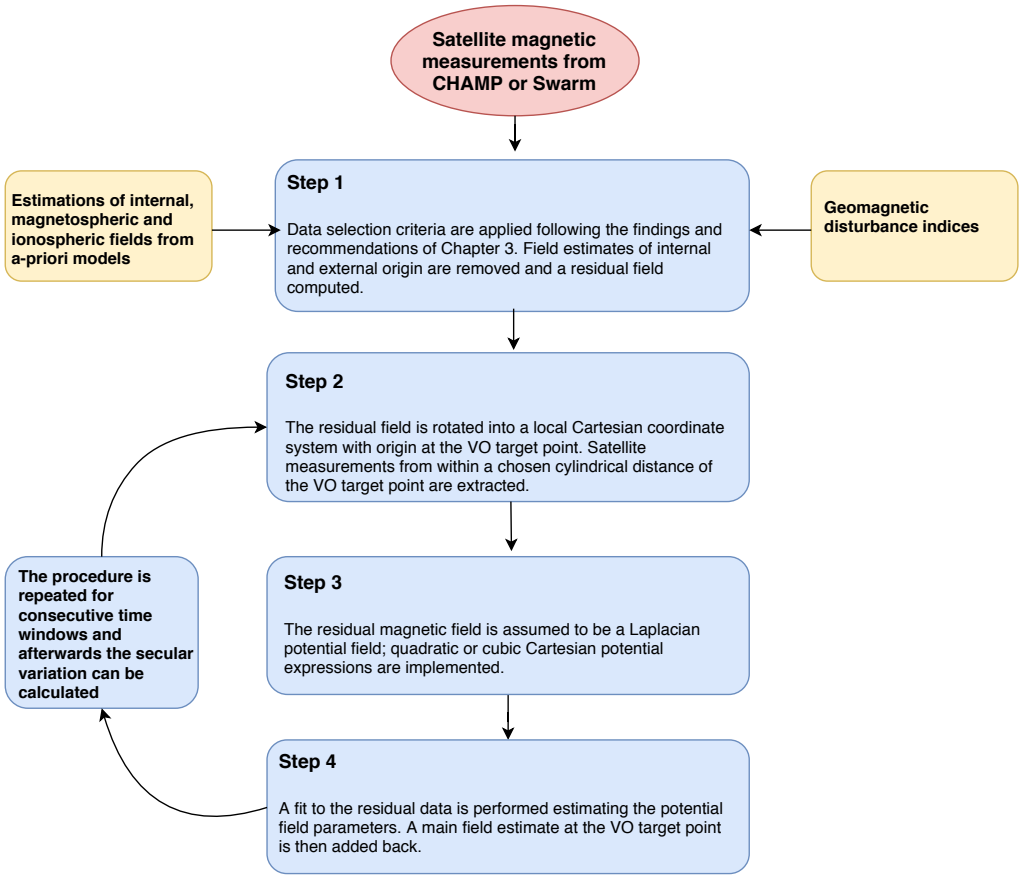

Figure 4.2: VO methodology flowchart illustrating the main steps.

4.3.1 Step 1. Data Selection and Residual Field Determination

The CHAMP and *Swarm* measurements, selection criteria and data processing applied are described in details in Section 3.3, and are denoted Data Set 1. Contrary to the original implementation, here the focus is on using dark time data, since the assumption of external zero mean field might not be valid (Beggan et al., 2009; Shore, 2013). Within a pre-specified time window for a given fixed VO target location, data from within a target cylinder, having some specified horizontal dimension, surrounding that particular VO location, are extracted. The VO position vector is given in spherical polar coordinates as $\mathbf{r}_{VO} = (r, \theta, \phi)_{VO}$, where $r = r_a + h_{VO}$ such that h_{VO} specifies the height above ground of the VO. During the CHAMP and the *Swarm* periods $h_{VO} = 370$km and $h_{VO} = 490$km, respectively such that the VO's are located at approximately the mean orbital height of the satellites (see Section 3.2). Depending on the type of investigation carried out, the radius of the target cylinder, d_{VO}, also termed data search range, may be adjusted to fit the specific requirements of the investigations. Note that this may influence the truncation of the potential field expansion as described in Step 3.

From the magnetic field measurements, $\mathbf{B}^{satellite}$, in the ECEF frame, field residuals are obtained as

$$\delta\mathbf{B} = \mathbf{B}^{satellite} - \mathbf{B}^{MF} - \mathbf{B}^{crust} - \mathbf{B}^{mag} - \mathbf{B}^{iono} \tag{4.1}$$

where $\mathbf{B}^{MF}$ is taken as SH degrees $n \in [1, 13]$ from the time-dependent part of the CHAOS-6-x5 model. $\mathbf{B}^{crust}$ is taken as the sum of the SH degrees $n \in [14, 20]$ of the time-dependent

part evaluated for each data time and the SH degrees $n \in [21, 110]$ of the static part of the CHAOS-6-x5 model. Note here that in contrast to the original approach an estimate of the crustal field is subtracted, the reason being that VO main field time series may be need in some applications such as core dynamics data assimilation (this has no implications for the computation of the SV field determined as annual differences). The suggestions put forward by Shore (2013) regarding the removal of external field estimates are here incorporated; $\mathbf{B}^{mag}$ is taken as CHAOS-6-x5 magnetospheric primary and secondary (induced) field model predictions, and $\mathbf{B}^{iono}$ is taken as CM4 ionospheric primary and secondary (induced) field estimates, see Chapter 2 for more details. The computed residual field, $\delta\mathbf{B}$, is then assumed to be a potential field. In their first paper, Mandea and Olsen (2006) did not remove a time-dependent core field, however, this they did in their second paper, Olsen and Mandea (2007).

In the final step 4, CHAOS-6-x5 model estimates for SH degrees $n \in [1, 16]$ are added back to the residual field for the VO target times. The reason for choosing SH degrees up to $n = 16$ is that these are thought to be stably estimated. The reason for subtracting the time-dependent estimates of the CHAOS-6-x5 model from the data and afterwards adding it back for the target times, is that this allows an effective pre-whitening of the data. Pre-whitening in this context means some operation acting on the data time series equalizing the amplitude of all frequencies in order for it to behave like white noise (in white noise all frequencies have the same intensity thus yielding a constant power spectra) in a statistical sense ("pre" here referring to the whitening prior to any other operation) (e.g. Kearey et al., 2013). This procedure allows for Huber weights counteracting big outliers present in the data to be effectively determined. Note here that considering a pre-specified VO time window of say four months, the associated time dependence within the four months will be lost. Using a time window of 4 months (i.e. 60 days around each epoch t) instead of the 1 month windows used in the original approach, may be advantageous; firstly more data is used minimizing data gaps and secondly a better LT coverage may be obtained arguably minimizing the LT bias Shore (2013). In the following calculations have been done using 4 month time windows. The same procedure applies to time series of magnetic field gradients, see Section 4.6.

4.3.2 Step 2. Coordinate Transformations

The satellite data are given in the Earth-Centered-Earth-Fixed coordinate frame by their spherical polar components, i.e. (r, θ, ϕ), after having performed appropriate transformations of the calibrated measurements, for more details see Section 3.3. In the virtual observatory approach, the residual field and the associated positions are transformed from the geocentric coordinate system into a local Cartesian coordinate system having origin at the individual VO target points, i.e. $(x_0, y_0, z_0)_{VO} = (0, 0, 0)$. The procedure is as follows:

1. Transform the residual field components and positions, as well as VO positions from spherical polar to Cartesian coordinates in the ECEF frame, i.e. $(r, \theta, \phi)_{ECEF}$ to $(x, y, z)_{ECEF}$. The Cartesian and spherical polar position coordinates are connected via (e.g. Riley et al., 2004)

$$\mathbf{r} = \begin{bmatrix} x \\ y \\ z \end{bmatrix} = r \begin{bmatrix} \sin\theta\cos\phi \\ \sin\theta\sin\phi \\ \cos\theta \end{bmatrix} \tag{4.2}$$

where $r \geq 0$, $0 \leq \theta \leq \pi$ and $0 \leq \phi < 2\pi$. The Cartesian unit vectors are connected to the spherical unit vectors via (e.g. Riley et al., 2004)

$$\begin{bmatrix} \hat{x} \\ \hat{y} \\ \hat{z} \end{bmatrix} = \begin{bmatrix} \sin\theta\cos\phi & \cos\theta\cos\phi & -\sin\phi \\ \sin\theta\sin\phi & \cos\theta\sin\phi & \cos\phi \\ \cos\theta & -\sin\theta & 0 \end{bmatrix} \begin{bmatrix} \hat{r} \\ \hat{\theta} \\ \hat{\phi} \end{bmatrix} \tag{4.3}$$

2. Transform the residual field components and positions from the ECEF frame to a local topocentric Cartesian right-handed system where x points towards geographic south, y points towards east and z points upwards, here termed the SEU (South,East,Up) VO target frame, i.e. from $(x, y, z)_{ECEF}$ to $(x, y, z)_{SEU}$, centred on the VO target point under consideration. Constructing an appropriate rotation matrix transforming from the SEU to the ECEF frame can be done by considering Figure 4.9: 1) rotate by angle β about the y-axis and 2) rotate by angle γ about the z-axis. The rotation matrices about the y- and z axes are then (e.g., Seeber, 2003, p. 11)

$$\underline{\underline{R}}_y(\beta) = \begin{bmatrix} \cos\beta & 0 & -\sin\beta \\ 0 & 1 & 0 \\ \sin\beta & 0 & \cos\beta \end{bmatrix} \qquad \underline{\underline{R}}_z(\gamma) = \begin{bmatrix} \cos\gamma & \sin\gamma & 0 \\ -\sin\gamma & \cos\gamma & 0 \\ 0 & 0 & 1 \end{bmatrix} \tag{4.4}$$

Thus the complete rotation matrix is given by

$$\underline{\underline{R}}^{ECEF}_{SEU} = \underline{\underline{R}}_z(\gamma)\underline{\underline{R}}_y(\beta) = \begin{bmatrix} \cos\gamma\cos\beta & \sin\gamma & -\cos\gamma\sin\beta \\ -\sin\gamma\sin\beta & \cos\gamma & \sin\gamma\sin\beta \\ \sin\beta & 0 & \cos\beta \end{bmatrix} \tag{4.5}$$

Note that rotation matrix does not change the length of the position vector and multiplication is not commutative (i.e. $\underline{\underline{R}}_z(\gamma)\underline{\underline{R}}_y(\beta) \neq \underline{\underline{R}}_y(\beta)\underline{\underline{R}}_z(\gamma)$). Inserting the relevant rotation angles for the VO application $\beta = -\theta$ and $\gamma = -\phi$ gives

$$\underline{\underline{R}}^{ECEF}_{SEU} = \underline{\underline{R}}_z(\gamma)\underline{\underline{R}}_y(\beta) = \begin{bmatrix} \cos\phi\cos\theta & -\sin\phi & \cos\phi\sin\theta \\ \sin\phi\sin\theta & \cos\phi & \sin\phi\sin\theta \\ -\sin\theta & 0 & \cos\theta \end{bmatrix} \tag{4.6}$$

Transforming instead from the ECEF to the SEU frame requires the transpose (or equivalently the inverse) of the rotation matrix (e.g., Seeber, 2003, p. 11), i.e.

$$\underline{\underline{R}}^{SEU}_{ECEF} = \left(\underline{\underline{R}}^{ECEF}_{SEU}\right)^T = \left(\underline{\underline{R}}^{ECEF}_{SEU}\right)^{-1} = \begin{bmatrix} \cos\phi\cos\theta & \sin\phi\sin\theta & -\sin\theta \\ -\sin\phi & \cos\phi & 0 \\ \cos\phi\sin\theta & \sin\phi\sin\theta & \cos\theta \end{bmatrix} \tag{4.7}$$

Thus the coordinates are rotated as

$$\begin{bmatrix} x \\ y \\ z \end{bmatrix}_{SEU} = \begin{bmatrix} \cos\theta\cos\phi & \cos\theta\sin\phi & -\sin\phi \\ -\sin\phi & \cos\phi & 0 \\ \sin\theta\cos\phi & \sin\theta\sin\phi & \cos\theta \end{bmatrix} \begin{bmatrix} x \\ y \\ z \end{bmatrix}_{ECEF} \tag{4.8}$$

Afterwards the radius of the VO target point is subtracted from the z coordinate, to obtain the z position relative to the VO. The height, h_{VO}, of the VO's were here chosen to be 370km and 490km during the CHAMP and *Swarm* periods, respectively.

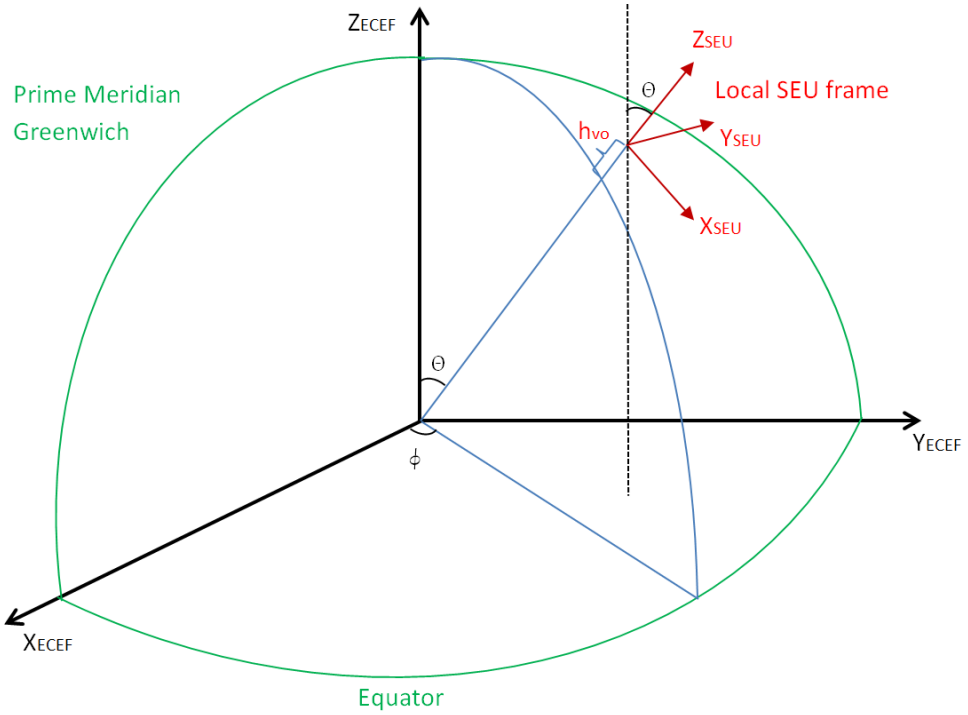

Figure 4.3: The ECEF geocentric (in black) and local SEU topocentric (in red) Cartesian frames.

4.3.3 Step 3. Cartesian Potential Representation

The magnetic potential at a given VO can be represented as an expansion in terms of Cartesian coordinates of an ECEF local topocentric coordinate system. Quadratic and cubic potential expansions are described here; because the data search range may be larger than in the original implementation a cubic expression might be needed for a more accurate description. Especially in the polar regions lack of data might be an issue of concern when using geomagnetically quiet dark time, selection criteria; this motivates the use of a larger search radius.

Quadratic Potential Description

It is assumed that the residual magnetic field, $\delta\mathbf{B}$, is a Laplacian potential field outside the source region, i.e. fulfilling the quasi-stationary approximation and neglecting electrical currents present at satellite altitude ($\mathbf{J} = 0$). In a local topographic Cartesian coordinate system, choosing the normal basis $(\hat{\mathbf{x}}, \hat{\mathbf{y}}, \hat{\mathbf{z}})_{SEU}$ for $\mathbb{R}^3$, the Laplace equation of the magnetic scalar potential, V, can be written (Blakely, 1995)

$$\nabla^2 V(x, y, z) = \frac{\partial^2 V}{\partial x^2} + \frac{\partial^2 V}{\partial y^2} + \frac{\partial^2 V}{\partial z^2} = 0 \tag{4.9}$$

Harmonic polynomials satisfy the Laplace partial differential equation and in Cartesian coordinates these can be written as the summation (Backus et al., 1996)

$$\begin{aligned} V(x,y,z) &= \sum_{a+b+c=l}^{l} C_{a,b,c} x^a y^b z^c \\ &= C_{000} + C_{100}x + C_{010}y + C_{001}z + C_{200}x^2 + C_{020}y^2 + C_{002}z^2 \\ &+ C_{110}xy + C_{101}xz + C_{011}yz + C_{110}yx + C_{101}zx + C_{011}zy \\ &+ C_{300}x^3 + C_{030}y^3 + C_{003}z^3 + \cdots \end{aligned} \tag{4.10}$$

where $C_{a,b,c}$ are the expansion coefficients, $\{a,b,c\} \in \mathbb{N}_+$, and l is the expansion order. Hence, the solution is expressed as a sum of harmonic polynomials; harmonic because it satisfies the Laplace's equation and polynomial since the expression consists of variables and coefficients involve only the operations of addition, subtraction, multiplication, having non-negative integer exponents. The position vector is written $\mathbf{r} = x\hat{\mathbf{x}} + y\hat{\mathbf{y}} + z\hat{\mathbf{z}}$, and because the variables are thought of as coordinates of a point, the polynomials are scalar fields in $\mathbb{R}^3$. The first term in eq.4.10 is a constant and can be left out of the equation when studying the magnetic field (the first term vanishes since the gradient is applied, i.e. $\mathbf{B} = -\nabla V$). Olsen and Mandea (2007) expanded the potential to second order, i.e. a quadratic description; writing here the expansion coefficients in the notation of Olsen and Mandea (2007) the potential, equation (4.10), becomes

$$\begin{aligned} V(x,y,z) &= \nu_x x + \nu_y y + \nu_z z + \nu_{xx}x^2 + \nu_{yy}y^2 + \nu_{zz}z^2 \\ &+ \nu_{xy}xy + \nu_{xz}xz + \nu_{yz}yz + \nu_{yx}yx + \nu_{zx}zx + \nu_{zy}zy \end{aligned} \tag{4.11}$$

The scalar potential $V(x,y,z)$ thus varies quadratically with the spatial coordinates and is specified in terms of 12 parameters. The directional derivatives of the potential are

$$\begin{aligned} \frac{\partial V}{\partial x} &= \nu_x + 2\nu_{xx}x + \nu_{xy}y + \nu_{xz}z + \nu_{yx}y + \nu_{zx}z \\ \frac{\partial V}{\partial y} &= \nu_y + 2\nu_{yy}y + \nu_{xy}y + \nu_{yz}z + \nu_{yx}x + \nu_{zy}y \\ \frac{\partial V}{\partial z} &= \nu_z + 2\nu_{zz}z + \nu_{xz}z + \nu_{yz}y + \nu_{zx}x + \nu_{zy}y \end{aligned}$$

The geomagnetic field is a solenoidal irrotational vector field since it fulfills the two conditions: 1) $\nabla \times \mathbf{B} = 0$ (irrotational) and 2) $\nabla \cdot \mathbf{B} = 0$ (solenoidal, i.e. no isolated monopoles) (Blakely, 1995; Backus et al., 1996). Implementing these constraints reduces the number of independent parameters of equation (4.11), thus simplifying the potential expression:

1. $\underline{\nabla \times \mathbf{B} = \nabla \times \nabla V = 0}$ The cross product is

$$\nabla \times \nabla V = \begin{pmatrix} \hat{x} & \hat{y} & \hat{z} \\ \frac{\partial}{\partial x} & \frac{\partial}{\partial y} & \frac{\partial}{\partial z} \\ \nabla V_x & \nabla V_y & \nabla V_z \end{pmatrix}$$

$$\begin{aligned} \nabla \times \nabla V &= \hat{x}\left[\frac{\partial}{\partial y}\nabla V_z - \frac{\partial}{\partial z}\nabla V_y\right] - \hat{y}\left[\frac{\partial}{\partial x}\nabla V_z - \frac{\partial}{\partial z}\nabla V_x\right] + \hat{z}\left[\frac{\partial}{\partial x}\nabla V_y - \frac{\partial}{\partial y}\nabla V_x\right] \\ &= \hat{x}\Big[(\nu_{yz} + \nu_{zy}) - (\nu_{yz} + \nu_{zy})\Big] - \hat{y}\Big[(\nu_{xz} + \nu_{zx}) - (\nu_{xz} + \nu_{zx})\Big] \\ &+ \hat{z}\Big[(\nu_{xy} + \nu_{yx}) - (\nu_{xy} + \nu_{yx})\Big] \end{aligned}$$

For this to fulfil $\nabla \times \mathbf{B} = \nabla \times \nabla V = 0$ requires each term in the brackets to be zero. Thus

$$\nu_{xy} = \nu_{yx} \qquad \nu_{xz} = \nu_{zx} \qquad \nu_{yz} = \nu_{zy}$$

2. $\underline{\nabla \cdot \mathbf{B} = \nabla \cdot \nabla V = 0}$ Using the above the potential can be written

$$\begin{aligned} V(x,y,z) = \nu_x x + \nu_y y + \nu_z z + \nu_{xx} x^2 + \nu_{yy} y^2 + \nu_{zz} z^2 \\ + 2\nu_{xy} xy + 2\nu_{xz} xz + 2\nu_{yz} yz \end{aligned}$$

Taking the derivative of the potential:

$$\begin{aligned} \frac{\partial V}{\partial x} &= \nu_x + 2\nu_{xx} x + 2\nu_{xy} y + 2\nu_{xZ} z \\ \frac{\partial V}{\partial y} &= \nu_y + 2\nu_{yy} y + 2\nu_{xy} y + 2\nu_{yz} z \\ \frac{\partial V}{\partial z} &= \nu_z + 2\nu_{zz} z + 2\nu_{xz} z + 2\nu_{yz} y \end{aligned} \tag{4.12}$$

Taking the second derivative:

$$\frac{\partial^2 V}{\partial x^2} = 2\nu_{xx} \qquad \frac{\partial V^2}{\partial y^2} = 2\nu_{yy} \qquad \frac{\partial V^2}{\partial z^2} = 2\nu_{zz}$$

Because of the requirement $\nabla^2 V = 0$ we get:

$$\begin{aligned} 2\nu_{xx} + 2\nu_{yy} + 2\nu_{zz} = 0 \Rightarrow \\ \nu_{zz} = -(\nu_{xx} + \nu_{yy}) \end{aligned} \tag{4.13}$$

Combining the outcome of conditions 1) and 2) yields a quadratic potential of the form

$$\begin{aligned} V(x,y,z) = \nu_x x + \nu_y y + \nu_z z + \nu_{xx} x^2 + \nu_{yy} y^2 - (\nu_{xx} + \nu_{yy}) z^2 \\ + 2(\nu_{xy} xy + \nu_{xz} xz + \nu_{yz} yz) \end{aligned} \tag{4.14}$$

Thus, assuming that the magnetic field is a potential field, the number of parameters characterizing the potential is reduced from 12 to 8: $(\nu_x, \nu_y, \nu_z, \nu_{xx}, \nu_{yy}, \nu_{xy}, \nu_{xz}, \nu_{yz})$. This should match the number of Gauss coefficients of the corresponding spherical harmonic expansion being $n(n+2)$ for SH degree n, i.e. $2(2+2) = 8$ for $n = 2$. The residual magnetic field can be determined as $\delta\mathbf{B} = -\nabla V$ and the directional derivatives are those given by eq.4.12. For the measurements within the VO target search range this potential is then used as the basis of the fit. At the given VO target point, having the origin coordinates $(x_0, y_0, z_0) = (0, 0, 0)$, the residual magnetic field is simply determined as $\delta\mathbf{B} = -\nabla V = -(\nu_x, \nu_y, \nu_z)$, i.e. it depends only on three of the estimated parameters.

With the assumption of a spherical Earth, the solution obtained can then be transformed into the usual geocentric ECEF spherical polar coordinate system or the NEC system from the coefficients of the expansion as $(Z, X, Y)_{NEC} = (-B_r, -B_\theta, B_\phi) = (-Z, -X, Y)_{SEU} = (\nu_z, \nu_x, -\nu_y)$.

Cubic Potential Description

In case when the search range around the VO target point is larger the quadratic potential fit ($V \propto x^2, y^2, z^2; \nabla V \propto x, y, z; \nabla^2 V \propto constant$) from above might need to be replaced by a cubic fit ($V \propto x^3, y^3, z^3; \nabla V \propto x^2, y^2, z^2; \nabla^2 V \propto x, y, z$). Expanding in the potential solution as for the quadratic case, the potential is now first written using a total of 39 expansion coefficients. Arguing as before using the requirements $\nabla \times \mathbf{B} = 0$ and $\nabla \cdot \mathbf{B} = 0$ reduces this number to 15 parameters

$$\begin{aligned} V(x,y,z) &= \nu_x x + \nu_y y + \nu_z z + \nu_{xx}x^2 + \nu_{yy}y^2 - (\nu_{xx} + \nu_{yy})z^2 \\ &+ 2\nu_{xy}xy + 2\nu_{xz}xz + 2\nu_{yz}yz - (\nu_{xyy} + \nu_{xzz})x^3 \\ &+ 3\nu_{xxx}x^2y + 3\nu_{xxz}x^2z + 3\nu_{xyy}xy^2 + 3\nu_{xzz}xz^2 + 6\nu_{xyz} \\ &- (\nu_{xxy} + \nu_{yzz})y^3 + 3\nu_{yyz}y^2z + 3\nu_{yzz}yz^2 - (\nu_{xxz} + \nu_{yyz})z^3 \end{aligned} \tag{4.15}$$

and the required directional derivatives are

$$\begin{aligned} \frac{\partial V}{\partial x} &= \nu_x + 2\nu_{xx}x + 2\nu_{xy}y + 2\nu_{xz}z + 6\nu_{xxy}xy + 6\nu_{xxz}xz \\ &+ (3y^2 - 3x^2)\nu_{xyy} + (3z^2 - 3x^2)\nu_{xzz} \\ \frac{\partial V}{\partial y} &= \nu_y + 2\nu_{yy}y + 2\nu_{xy}x + 2\nu_{yz}z + (3x^2 - 3y^2)\nu_{xxz} + 6\nu_{xyy}xy \\ &+ 6\nu_{yyz}yz + (3z^2 - 3y^2)\nu_{yzz} \\ \frac{\partial V}{\partial z} &= \nu_z - 2\nu_{xx}z - 2\nu_{yy}z + 2\nu_{xz}x + 2\nu_{yz}y + (3x^2 - 3z^2)\nu_{xxz} + 6\nu_{xzz}xz \\ &+ (3y^2 - 3z^2)\nu_{yyz} + 6\nu_{yzz}yz \end{aligned} \tag{4.16}$$

As for the quadratic case at the given VO target point, having the origin coordinates $(x_0, y_0, z_0) = (0, 0, 0)$, the residual field is simply determined as $\delta\mathbf{B} = -\nabla V = -(\nu_x, \nu_y, \nu_z)$.

Field Gradients

It is also possible to produce VO time series of magnetic field spatial gradients and their temporal variation. Here a procedure is described for computing the 3×3 magnetic gradient tensor using the VO models. Results of these computations are presented in Section 4.6. As mentioned in Section 2.5.2 the elements of the gradient tensor serve as filters providing information of the field structure in specific directions. The geomagnetic field is irrotational, i.e.

$$\nabla \times \nabla V = \hat{x}\left[\frac{\partial}{\partial y}\nabla V_z - \frac{\partial}{\partial z}\nabla V_y\right] - \hat{y}\left[\frac{\partial}{\partial x}\nabla V_z - \frac{\partial}{\partial z}\nabla V_x\right] + \hat{z}\left[\frac{\partial}{\partial x}\nabla V_y - \frac{\partial}{\partial y}\nabla V_x\right]$$

requiring each bracket to be zero. Thus, the potential assumption involves the restrictions

$$\frac{\partial^2 V}{\partial y \partial z} = \frac{\partial^2 V}{\partial z \partial y}, \quad \frac{\partial^2 V}{\partial x \partial z} = \frac{\partial^2 V}{\partial z \partial x}, \quad \frac{\partial^2 V}{\partial x \partial y} = \frac{\partial^2 V}{\partial y \partial x}$$

or equivalently

$$\frac{\partial B_z}{\partial y} = \frac{\partial B_z}{\partial z}, \quad \frac{\partial B_z}{\partial x} = \frac{\partial B_x}{\partial z}, \quad \frac{\partial B_y}{\partial x} = \frac{\partial B_x}{\partial y}$$

Adding to these the derivatives

$$\frac{\partial B_x}{\partial x}, \quad \frac{\partial B_y}{\partial y}, \quad \frac{\partial B_z}{\partial z}$$

a total of five derivatives may be of interest. In the local Cartesian coordinate system the magnetic gradient tensor is written

$$\nabla \mathbf{B} = \begin{pmatrix} \frac{\partial B_z}{\partial z} & \frac{\partial B_z}{\partial x} & \frac{\partial B_z}{\partial y} \\ \frac{\partial B_x}{\partial z} & \frac{\partial B_x}{\partial x} & \frac{\partial B_x}{\partial y} \\ \frac{\partial B_y}{\partial z} & \frac{\partial B_y}{\partial x} & \frac{\partial B_y}{\partial y} \end{pmatrix} \tag{4.17}$$

The field gradient tensor using the VO potential model fit is thus written

$$\nabla \mathbf{B} = \begin{pmatrix} -2(\nu_{xx} + \nu_{yy}) & 2\nu_{xz} & 2\nu_{yz} \\ 2\nu_{xz} & 2\nu_{xx} & 2\nu_{xy} \\ 2\nu_{yz} & 2\nu_{xy} & 2\nu_{yy} \end{pmatrix} \tag{4.18}$$

Notice here that the tensor is symmetric and that tensor trace is zero, $tr(\nabla \mathbf{B}) = -2(\nu_{xx} + \nu_{yy}) + 2\nu_{xx} + 2\nu_{yy} = 0$.

4.3.4 Step 4. Model Estimation

Determining the magnetic scalar potential expansion coefficients amounts to estimating model parameters $\mathbf{m}$ of a linear inverse problem

$$\mathbf{d} = \underline{\underline{\mathbf{G}}}\mathbf{m} \tag{4.19}$$

where $\mathbf{d}$ is the data vector containing the residual field values in the SEU system, $\delta\mathbf{B} = (\delta X, \delta Y, \delta Z)$, and the design matrix $\underline{\underline{\mathbf{G}}}$ describes the mathematical formulation relating the model and the data, and $\mathbf{m}$ contains the parameters of the potential, such that $\mathbf{m} = (\nu_x, \nu_y, \nu_z, \nu_{xx}, ...)^T$. The inversion was carried out using the Matlab robust multilinear regression tool *robustfit* using an algorithm based on an iteratively reweighted least squares solution incorporating a weighting function `https://se.mathworks.com/help/stats/robustfit.html`, implementing a Huber weighting function having a tuning constant of 1.5 (Constable, 1988; Sabaka et al., 2004). In order to produce a viable solution a limit on the minimum number of data points required for the inversion N_{VO} was specified.

Use of satellite vector data sums and differences instead of regular vector data was also implemented in accordance with the procedure described by Kotsiaros et al. (2015) and Olsen et al. (2015). The idea of using data differences was to try and remove any large-scale external signal from the measurements, however it was found during initial model runs that data sums needs to be included as well in order to ensure sufficient information on longer wavelengths of the field (see also Sabaka et al. (2004), Olsen et al. (2007) and Sabaka et al. (2015). Data are defined as $\mathbf{d} = \{\Delta d_x, \Delta d_y, \Delta d_z, \Sigma d_x, \Sigma d_y, \Sigma d_z\}$, where Δ and Σ denotes differences and sums, respectively. The design matrix using sums and differences was constructed as $\underline{\underline{\mathbf{G}}} = \{\Delta G_x; \Delta G_y; \Delta G_z; \Sigma G_x; \Sigma G_y; \Sigma G_z)\}$ where $\Delta G_k = [G_k(\mathbf{r}_1) - G_k(\mathbf{r}_2)]$ and $\Sigma G_k = [G_k(\mathbf{r}_1) + G_k(\mathbf{r}_2)]/2$ where $k = (x, y, z)$ are the difference and sums data kernels, respectively. Considering sums and differences of vector data in spherical coordinates, it is important to note that the design matrix $\underline{\underline{\mathbf{G}}}$ contains all information regarding data positions and how these are connected to the model $\mathbf{m}$; this means, that when considering differences, the ΔG's are not formed by assuming averaging positions for the data nor by assuming them to be at the same position.

Using a quadratic potential description, the estimation of 8 model parameters $\mathbf{m} = (\nu_x, \nu_y, \nu_z, \nu_{xx}, \nu_{yy}, \nu_{xy}, \nu_{xz}, \nu_{yz})$ from the field residuals was implemented using a design

matrix linking the parameters and data, i.e. eq.4.12, such that the system of equations is written

$$\begin{pmatrix} \delta X(r_1) \\ \delta X(r_n) \\ \vdots \\ \delta Y(r_1) \\ \delta Y(r_n) \\ \vdots \\ \delta Z(r_1) \\ \delta Z(r_n) \\ \vdots \end{pmatrix} = \begin{pmatrix} -1 & 0 & 0 & -2x_1 & 0 & -2y_1 & -2z_1 & 0 \\ -1 & 0 & 0 & -2x_n & 0 & -2y_n & -2z_n & 0 \\ \vdots & \vdots & \vdots & \vdots & \vdots & \vdots & \vdots & \vdots \\ 0 & -1 & 0 & 0 & -2y_1 & -2x_1 & 0 & -2z_1 \\ 0 & -1 & 0 & 0 & -2y_n & -2x_n & 0 & -2z_n \\ \vdots & \vdots & \vdots & \vdots & \vdots & \vdots & \vdots & \vdots \\ 0 & 0 & -1 & 2z_1 & 2z_1 & 0 & -2x_1 & -2y_1 \\ 0 & 0 & -1 & 2z_n & 2z_n & 0 & -2x_n & -2y_n \\ \vdots & \vdots & \vdots & \vdots & \vdots & \vdots & \vdots & \vdots \end{pmatrix} \begin{pmatrix} \nu_x \\ \nu_y \\ \nu_z \\ \nu_{xx} \\ \nu_{yy} \\ \nu_{xy} \\ \nu_{xz} \\ \nu_{yz} \end{pmatrix} \quad (4.20)$$

where $\delta\mathbf{B} = (\delta X, \delta Y, \delta Z)$ is the data vector (i.e. the residual field) containing each of the three vector field components at a given VO location and $(j = 1, ..., n)$ is an index of the observations.

In a similar manner as with the quadratic potential described above, the estimation of the 15 model parameters $\mathbf{m} = (\nu_x, \nu_y, \nu_z, \nu_{xx}, \nu_{yy}, \nu_{xy}, \nu_{xz}, \nu_{yz}, \nu_{xxy}, \nu_{xxz}, \nu_{xyy}, \nu_{xzz}, \nu_{yyz}, \nu_{yzz}, \nu_{xyz})$ of the cubic potential description is written

$$\begin{pmatrix} \delta X(r_1) \\ \delta X(r_n) \\ \vdots \\ \delta Y(r_1) \\ \delta Y(r_n) \\ \vdots \\ \delta Z(r_1) \\ \delta Z(r_n) \\ \vdots \end{pmatrix} = \begin{pmatrix} -1 & 0 & 0 & -2x_1 & 0 & -2y_1 & -2z_1 & 0 & -6x_1y_1 & \dots \\ -1 & 0 & 0 & -2x_n & 0 & -2y_n & -2z_n & 0 & -6x_ny_n & \dots \\ \vdots & \vdots & \vdots & \vdots & \vdots & \vdots & \vdots & \vdots & \vdots & \dots \\ 0 & -1 & 0 & 0 & -2y_1 & -2x_1 & 0 & -2z_1 & -3x_1^2 - 3y_1^2 & \dots \\ 0 & -1 & 0 & 0 & -2y_n & -2x_n & 0 & -2z_n & -3x_n^2 - 3y_n^2 & \dots \\ \vdots & \vdots & \vdots & \vdots & \vdots & \vdots & \vdots & \vdots & \vdots & \dots \\ 0 & 0 & -1 & 2z_1 & 2z_1 & 0 & -2x_1 & -2y_1 & 0 & \dots \\ 0 & 0 & -1 & 2z_n & 2z_n & 0 & -2x_n & -2y_n & 0 & \dots \\ \vdots & \vdots & \vdots & \vdots & \vdots & \vdots & \vdots & \vdots & \vdots & \dots \end{pmatrix}$$

$$\begin{pmatrix} -6x_1z_1 & -3y_1^2 - 3x_1^2 & -3z_1^2 - 3x_1^2 & 0 & 0 & 0 \\ -6x_nz_n & -3y_n^2 - 3x_n^2 & -3z_n^2 - 3x_n^2 & 0 & 0 & 0 \\ \vdots & \vdots & \vdots & \vdots & \vdots & \vdots \\ 0 & -6x_1y_1 & 0 & -6y_1z_1 & -3z_1^2 - 3y_1^2 & 0 \\ 0 & -6x_ny_n & 0 & -6y_nz_n & -3z_n^2 - 3y_n^2 & 0 \\ \vdots & \vdots & \vdots & \vdots & \vdots & \vdots \\ -3x_1^2 - 3z_1^2 & 0 & -6x_1z_1 & -3y_1^2 - 3z_1^2 & -6y_1z_1 & 0 \\ -3x_n^2 - 3z_n^2 & 0 & -6x_nz_n & -3y_n^2 - 3z_n^2 & -6y_nz_n & 0 \\ \vdots & \vdots & \vdots & \vdots & \vdots & \vdots \end{pmatrix} \begin{pmatrix} \nu_x \\ \nu_y \\ \nu_z \\ \nu_{xx} \\ \nu_{yy} \\ \nu_{xy} \\ \nu_{xz} \\ \nu_{yz} \\ \nu_{xxy} \\ \nu_{xxz} \\ \nu_{xyy} \\ \nu_{xzz} \\ \nu_{yyz} \\ \nu_{yzz} \\ \nu_{xyz} \end{pmatrix}$$

where $\delta\mathbf{B} = (\delta X, \delta Y, \delta Z)$ is the data vector, containing each of the three vector field components at a given VO location and $(j = 1, ..., n)$ is the number of observations.

The final step is to add back the CHAOS-6-x5 model predictions, $\mathbf{B}_{VO}^{MF}$, for SH degrees $n \in [1, 16]$, to the mean residual field determined for the VO position and target time under consideration, $\delta\mathbf{B}_{VO}$, obtaining a main field estimate

$$\mathbf{B}_{VO}(t) = \delta\mathbf{B}_{VO}(t) + \mathbf{B}_{VO}^{MF}(t) \tag{4.21}$$

The procedure is then repeated for each time window to obtain time series. The secular variation at a particular VO location for a given time window at epoch t, was computed as the annual difference between the field component values at time $t + 6$months and that at time $t - 6$months (Mandea and Olsen, 2006)

$$\mathbf{SV}_{VO}(t) = \mathbf{B}_{VO}(t + 0.5yr) - \mathbf{B}_{VO}(t - 0.5yr)$$

Estimates of the secular acceleration were likewise computed as annual differences of the secular variation

$$\mathbf{SA}_{VO}(t) = \mathbf{SV}_{VO}(t + 0.5yr) - \mathbf{SV}_{VO}(t - 0.5yr)$$

4.4 Virtual Observatory Model Computations

The VO modelling investigations reported here, comes in two categories:

1. VO's located above existing ground observatories (GO), a procedure discussed in Section 4.4.1. This allows for a clear comparison between annual differences of the VO's and GO's enabling an assessment of the VO time series (the times series of the GO annual differences are constructed based on revised monthly means as explained in Section 3.5)

2. 2) VO's located in a global grid, a procedure discussed in Section 4.4.3. This allows for global VO time series to be used in various applications, e.g. spherical harmonic analyses, field modelling, jerk analysis, data assimilation studies and core flows studies.

The VO data files produced contain time series of the main magnetic field as well as main field gradient components. The components are provided in a geocentric spherical coordinate system (r, θ, ϕ), in units of [nT] and [nT/km], respectively. Output data files named version 0105 were used for the results reported in this Chapter. These files were build using Data Set 1 (see Section 3.3), using a cubic potential description having a search range $d_0 = 700$km and using 4 month time windows. Some examples of synthetic case studies can be found in Appendix B. From these studies, it became clear that increasing the search range would require an increase in potential description, i.e. going from a quadratic to a cubic expansion, in order to obtain an adequate fit.

An important issue when using dark geomagnetically quiet time data selection criteria, is that this reduces the amount of data significantly. This can cause gaps in the VO time series, and thus one may wish to implement a bigger search range. Of course the data subsampling rate could be changed, but these data are not necessarily independent samples of the field of interest due to correlation of noise along-track. The original approach took data from all times with no data selection criteria and used a search range of 400km. In this project a search range of 700km was used to generate dataset 0105, as this was found to be reasonable based on the synthetic test studies and minimized overlap of data

cylinders for grids of 300 equally distributed VO's (see Section 4.4.3). To do the inversion, a minimum limit of 30 data was here required, in order to secure enough data to do the robust weighting. Table 4.1 lists the various elements of the VO data files version 0105.

Figure 4.4 provides an example of an output file version 0105 for a VO solution above the German observatory Niemegk. The output files contain the information as described in Table 4.1; the VO positions, times, main field and main field gradients, the number of data along with statistics providing the mean and rms values of the residuals being computed as the differences between the data and the VO model predictions.

The results of the VO computations for the chosen setup are given in: 1) Section 4.5 presenting secular variation and acceleration time series of the field above selected ground observatories and an SH analysis of external field contributions, and 2) Section 4.6 presenting secular variation and acceleration time series of the field gradients above selected ground observatories also testing the possibility of doing global field modelling using the field gradient data. The output example includes the diagnostics listed in Table 4.1, in particular the example list statistics being rms and mean values of the residuals between data and model fit.

Name	*column*	*Symbol*	*Units*	*Content*
theta	1	θ	degrees	Colatitude of VO target point
phi	2	ϕ	degrees	Longitude of VO target point
Year	3			Year of VO solution
Month	4			Center month of time window for VO solution
Time	5	t	[days]	Modified Julian date
r	6	r	[km]	Radius of VO target point
Br	7	B_r	[nT]	Magnetic field r component
Bthe	8	B_θ	[nT]	Magnetic field θ component
Bp	9	B_ϕ	[nT]	Magnetic field ϕ component
dBrdr	10	$\nabla_r B_r$	[nT/km]	Magnetic field r gradient of r component
dBthedthe	11	$\nabla_\theta B_\theta$	[nT/km]	Magnetic field θ gradient of θ component
dBpdp	12	$\nabla_\phi B_\phi$	[nT/km]	Magnetic field ϕ gradient of ϕ component
dBthedr	13	$\nabla_\theta B_r$	[nT/km]	Magnetic field θ gradient of r component
dBpdr	14	$\nabla_\phi B_r$	[nT/km]	Magnetic field ϕ gradient of r component
dBthedp	15	$\nabla_\theta B_\phi$	[nT/km]	Magnetic field θ gradient of ϕ component
N_data	16	N_{VO}		Number of data used for solution
diff Mean	17-19	$mean_\Delta$	[nT]	Huber weighted mean of residuals between difference data and fit
diff root-mean-square	20-22	rms_Δ	[nT]	Huber weighted rms of residuals between difference data and fit
sums Mean	23-25	$mean_\Sigma$	[nT]	Huber weighted mean of residuals between sums data and fit
sums root-mean-square	26-28	rms_Σ	[nT]	Huber weighted rms of residuals between sums data and fit

Table 4.1: Output file description for VO dataset 0105.

4.4.1 VO Solutions at Ground Observatory Sites

The VO time series have been computed above the selected ground observatories marked with blue dots in Figure 4.5 and listed in Table 4.2. Table 4.3 presents an example case of output statistics for a VO above the German Niemegk observatory. Listed are the mean and rms misfit between the VO model $\mathbf{d}_{model}$, predictions $\underline{\underline{G}}\mathbf{m}$ and the contributing satellite data $\mathbf{d}_{obs} = \delta\mathbf{B}$ (an estimation measure of the imperfection of the model fit to the data) in [nT]. The mean and rms are a mean over all epoch stating the (Huber) weighted values computed from the residuals $\mathbf{e} = \mathbf{d}_{obs} - \mathbf{d}_{model}$ using the VO model described in Section 4.3.4. During the *Swarm* time, no distinction was made between data from the three satellites. The mean values are all very close to zero. The rms values for the sums are seen to be slightly larger during CHAMP time than *Swarm* time, however most values are below 2nT. For the differences the rms misfits are approximately 0.5nT.

```
% Virtual Observatory Model
% Data type used: N-S and E-W gradient data - observatory locations
% NS data sampling time [sec]: 15
% EW data sampling time [sec]: 15
% |dRC/dt|< data selection: 3
% kp< index data selection: 3
% Data time used: dark
% Include external field correction: yes
% Potential spatial degree: cubic
% Search radius: 700
% Target point altitude: 490
% Inversion limit: 30
% Inversion: difference and sums used
%
% theta     |   phi    | Year  Month |   Time       |     r    |       Br            Bt            Bp     |  dBrdr     dBtdt     dBpdp     dBtdr     dBpdr     dBtdp |
% [deg]     |  [deg]   |             |  [mjd2000]   |    [km]  |     Predicted field - NEC frame [nT]       |      Predicted gradient field - NEC frame [nT/km]        |
%
 38.11980     12.68300     2013    3          NaN        NaN          NaN           NaN           NaN      NaN       NaN       NaN       NaN       NaN       NaN
 38.11980     12.68300     2013    7          NaN        NaN          NaN           NaN           NaN      NaN       NaN       NaN       NaN       NaN       NaN
 38.11980     12.68300     2013   11          NaN        NaN          NaN           NaN           NaN      NaN       NaN       NaN       NaN       NaN       NaN
 38.11980     12.68300     2014    3    5204.8125    6861.20   -36500.43635   -15477.59508     543.67276  15.87805  -8.67699  -7.20106  -5.92513  -0.76851   0.07399
 38.11980     12.68300     2014    7    5326.5625    6861.20   -36506.19764   -15480.10200     555.20085  15.88240  -8.67856  -7.20384  -5.92535  -0.77404   0.07352
 38.11980     12.68300     2014   11    5448.3125    6861.20   -36515.01934   -15479.19722     569.08053  15.89337  -8.68210  -7.21127  -5.92624  -0.78005   0.07318
 38.11980     12.68300     2015    3    5570.0625    6861.20   -36523.50958   -15480.61303     580.14843  15.89403  -8.68476  -7.20927  -5.92681  -0.78417   0.07376
 38.11980     12.68300     2015    7    5691.8125    6861.20   -36529.89113   -15482.85526     593.95927  15.89814  -8.68770  -7.21044  -5.92655  -0.78892   0.07510
 38.11980     12.68300     2015   11    5813.5625    6861.20   -36540.80411   -15481.61657     609.65894  15.90695  -8.69072  -7.21623  -5.92595  -0.79371   0.07443
 38.11980     12.68300     2016    3    5935.3125    6861.20   -36550.41164   -15483.45266     622.24056  15.91311  -8.69388  -7.21923  -5.92691  -0.80069   0.07507
 38.11980     12.68300     2016    7    6057.0625    6861.20   -36559.56860   -15483.17580     637.22456  15.91964  -8.69650  -7.22315  -5.92749  -0.80532   0.07532
 38.11980     12.68300     2016   11    6178.8125    6861.20   -36571.83404   -15484.36565     653.80946  15.92715  -8.70053  -7.22663  -5.92576  -0.81124   0.07536
 38.11980     12.68300     2017    3    6300.5625    6861.20   -36582.62241   -15483.82216     666.59210  15.93516  -8.70382  -7.23134  -5.92667  -0.81891   0.07553
 38.11980     12.68300     2017    7    6422.3125    6861.20   -36592.69871   -15483.94449     683.74953  15.94178  -8.70785  -7.23393  -5.92661  -0.82506   0.07697
 38.11980     12.68300     2017   11    6544.0625    6861.20   -36605.26761   -15483.31228     699.78487  15.94890  -8.71110  -7.23780  -5.92699  -0.83164   0.07604
```

```
N_{data}  | Mean_dr  Mean_dt  Mean_dp | rms_dr  rms_dt  rms_dp | Mean_sr  Mean_st  Mean_sp | rms_sr  rms_st  rms_sp |
 # data   |          diff  Mean       |  diff root-mean-square |          sums  Mean       |  sums root-mean-square |

       0       NaN       NaN       NaN       NaN       NaN       NaN       NaN       NaN       NaN       NaN       NaN       NaN
       0       NaN       NaN       NaN       NaN       NaN       NaN       NaN       NaN       NaN       NaN       NaN       NaN
      27       NaN       NaN       NaN       NaN       NaN       NaN       NaN       NaN       NaN       NaN       NaN       NaN
     326    0.1351   -0.0332   -0.0096    0.3732    0.3397    0.3501    0.0000    0.0000    0.0000    1.4774    1.2455    0.7116
     288    0.0267   -0.1090    0.0645    0.4163    0.5206    0.6144   -0.0000    0.0000    0.0000    1.1962    1.3232    0.7661
     426    0.1815    0.0275   -0.1146    0.6000    0.5427    0.5760   -0.0000    0.0000    0.0000    2.3223    2.0515    1.4590
     252   -0.0380    0.0709    0.0117    0.3578    0.4692    0.5183    0.0000    0.0000   -0.0000    1.5783    1.3614    0.7607
     341   -0.0231   -0.1320   -0.0250    0.3889    0.5518    0.6280   -0.0000   -0.0000   -0.0000    1.3946    1.9268    0.8355
     445   -0.0044    0.0102   -0.0779    0.3464    0.4853    0.5217   -0.0000   -0.0000   -0.0000    1.8485    1.1249    1.0261
     482    0.0444    0.1374   -0.0758    0.4163    0.5651    0.6815   -0.0000    0.0000    0.0000    1.8198    1.8282    0.7568
     184    0.0060    0.0151    0.0493    0.3805    0.5466    0.6300   -0.0000   -0.0000    0.0000    1.0637    1.6404    0.7929
     295   -0.0143   -0.2493   -0.0476    0.4567    0.5854    0.6686    0.0000   -0.0000    0.0000    1.7070    1.1943    0.9147
     354    0.1053   -0.1004    0.0657    0.4353    0.5022    0.5727   -0.0000   -0.0000    0.0000    1.3017    1.4670    0.8838
     196   -0.0131   -0.1518    0.0420    0.4516    0.5771    0.6283   -0.0000    0.0000    0.0000    1.6514    1.5711    0.9263
     709    0.1386   -0.0507    0.0158    0.5208    0.5026    0.5418    0.0000    0.0000    0.0000    1.7381    1.9097    1.6188
```

Figure 4.4: VO model output example for solution above German Niemegk observatory.

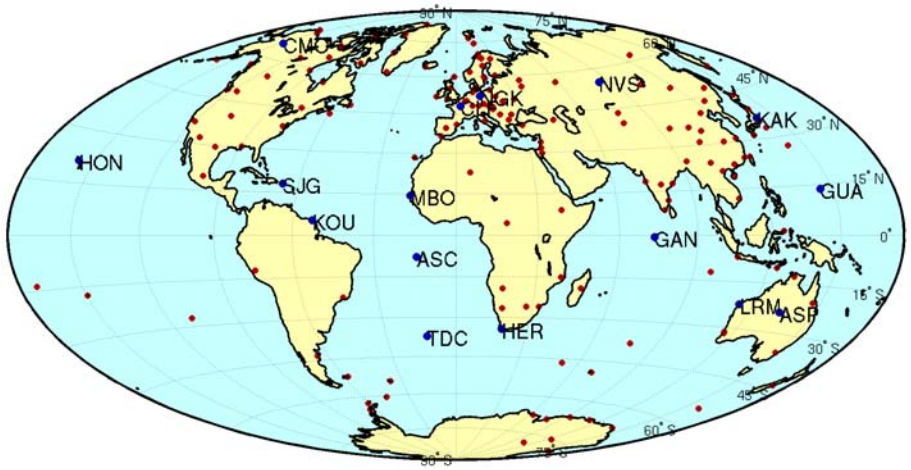

Figure 4.5: Plot of selected ground observatories used in the VO comparison analysis using a Hammer projection. All ground observatories are marked with red symbols and emphasized with blue symbols are the selected ground observatories used for time series comparisons.

Observatory name	*IAGA code*	*Colatitude*	*East longitude*
Ascension Island	*ASC*	97.95°	345.62°
Alice Springs	*ASP*	113.77°	133.88°
Chambon la Foret	*CLF*	41.98°	2.27°
College	*CMO*	25.13°	212.14°
Gan	*GAN*	89.3054°	73.1537°
Guam	*GUA*	76.41°	144.87°
Hermanus	*HER*	124.43°	19.23°
Honolulu	*HON*	68.68°	202.0°
Kakioka	*KAK*	53.77°	140.18°
Kourou	*KOU*	84.79°	307.27°
Learmonth	*LRM*	112.22°	114.1°
Mbour	*MBO*	75.62°	343.03°
Niemegk	*NGK*	37.93°	12.68°
Novosibirsk	*NSV*	35.15°	83.23°
San Juan	*SJG*	71.89°	293.85°
Tristan da Cunha	*TDC*	127.067°	347.685°

Table 4.2: List of selected ground observatories in alphabetic order. Source http://www.intermagnet.org/.

	CHAMP		Swarm	
Component	Mean [nT]	rms [nT]	Mean [nT]	rms [nT]
$\sum B_r$	0.00	2.20	0.00	1.59
$\sum B_\theta$	0.00	1.66	0.00	1.55
$\sum B_\phi$	0.00	1.29	0.00	0.95
ΔB_r	0.01	0.68	0.05	0.43
ΔB_θ	-0.02	0.52	-0.05	0.52
ΔB_ϕ	-0.03	0.54	-0.01	0.58

Table 4.3: VO model misfit statistics example case for NGK station during CHAMP and *Swarm* periods.

4.4.2 On the Main Field Pre-Whitening

In this section the VO method is tested subtracting only the static field using CHAOS-6-x5 for SH degrees 14-120, but without subtracting or adding back any main field model. Thus a main field pre-whitening has not been performed. Figure 4.6 presents VO example cases computed at selected ground observatories. The plots show the revised monthly mean of the GO's (black dots), and both VO's without the MF pre-whitening (blue dots) and with a CHAOS-6-x5 model pre-whitening (red dots), and the CHAOS-6-x5 model predictions (green) for SH degrees $n \in [1, 13]$ at the VO altitudes of 370km and 490km during the CHAMP and *Swarm* eras, respectively. From these plots it is evident, that there are considerable scatter in the VO's without the main field pre-whitening. As stated in Section 4.3.1, the pre-whitening allows for Huber weights to be used counteracting outliers. This leads to the conclusion that a pre-whitening using the main field is needed in order to computed the VO's robustly.

Next, investigations into the VO dependence on the chosen field model used to perform the pre-whitening, are presented. Figure 4.7 presents examples of VO time series computed by subtracting the static field using CHAOS-6-x5 for SH degrees 14-120 (here the static part for n=14-20 was computed for 2010), as well as subtracting and adding back two different main field models. In these computations the IGRF-12 (Thébault et al., 2015) and CHAOS-6-x5 (Finlay et al., 2016b) models were used for SH degrees n=1-13. The plots show the IGRF-12 (blue dots) and CHAOS-6-x5 (red dots) MF pre-whitening based VO's, the GO's (black dots), and the CHAOS-6-x5 (green) and IGRF-12 (magenta) model predictions.

Investigating further into this, Tables 4.4 and 4.6 presents the rms misfit between the VO SV time series as determined using the IGRF-12 and CHAOS-6-x5 model pre-whitening, respectively, and four month averages of the ground observatory data. This is given for each vector component and shown separately for the CHAMP and *Swarm* satellites. Tables 4.5 and 4.7 presents the correlation degree between the VO SV time series as determined using the IGRF-12 and CHAOS-6-x5 model pre-whitening, respectively, and four month averages of the ground observatory data. The correlation coefficient provides a measure in the interval $[-1, 1]$ of the linear dependence between two random variables, such that +1 and -1 corresponds to a strong and no coherence, respectively (e.g., Barlow, 1989; Taylor, 1997; Aster et al., 2005). Again this is shown separately for the CHAMP and *Swarm* satellites. Here the Pearson correlation coefficient between the two random variables X and Y has been used, defined as (e.g., Aster et al., 2005, p. 259)

$$\rho(X, Y) = \frac{\mathrm{Cov}(X, Y)}{\sqrt{\mathrm{Var}(X)\mathrm{Var}(Y)}} \tag{4.22}$$

where $\mathrm{Var}(X)$ and $\mathrm{Var}(Y)$ are the variances, and $\mathrm{Cov}(X, Y)$ is the covariance of X and Y. It should be noticed that due to the short time series during *Swarm* time, these correlations may not be well determined. From these numbers it can be seen that the correlation between the ground observatory and VO SV data are very good. The correlation coefficients using IGRF-12 and CHAOS-6-x5 pre-whitening are nearly identical, as are the rms levels. From the plots and the tables, it can be seen that the differences between VO's computed based on the IGRF-12 and CHAOS-6-x5 models are very small; therefore it is concluded that the computed VO's are independent on which field model is used for the pre-whitening. In the following computations, the CHAOS-6-x5 field model has been used for the pre-whitening.

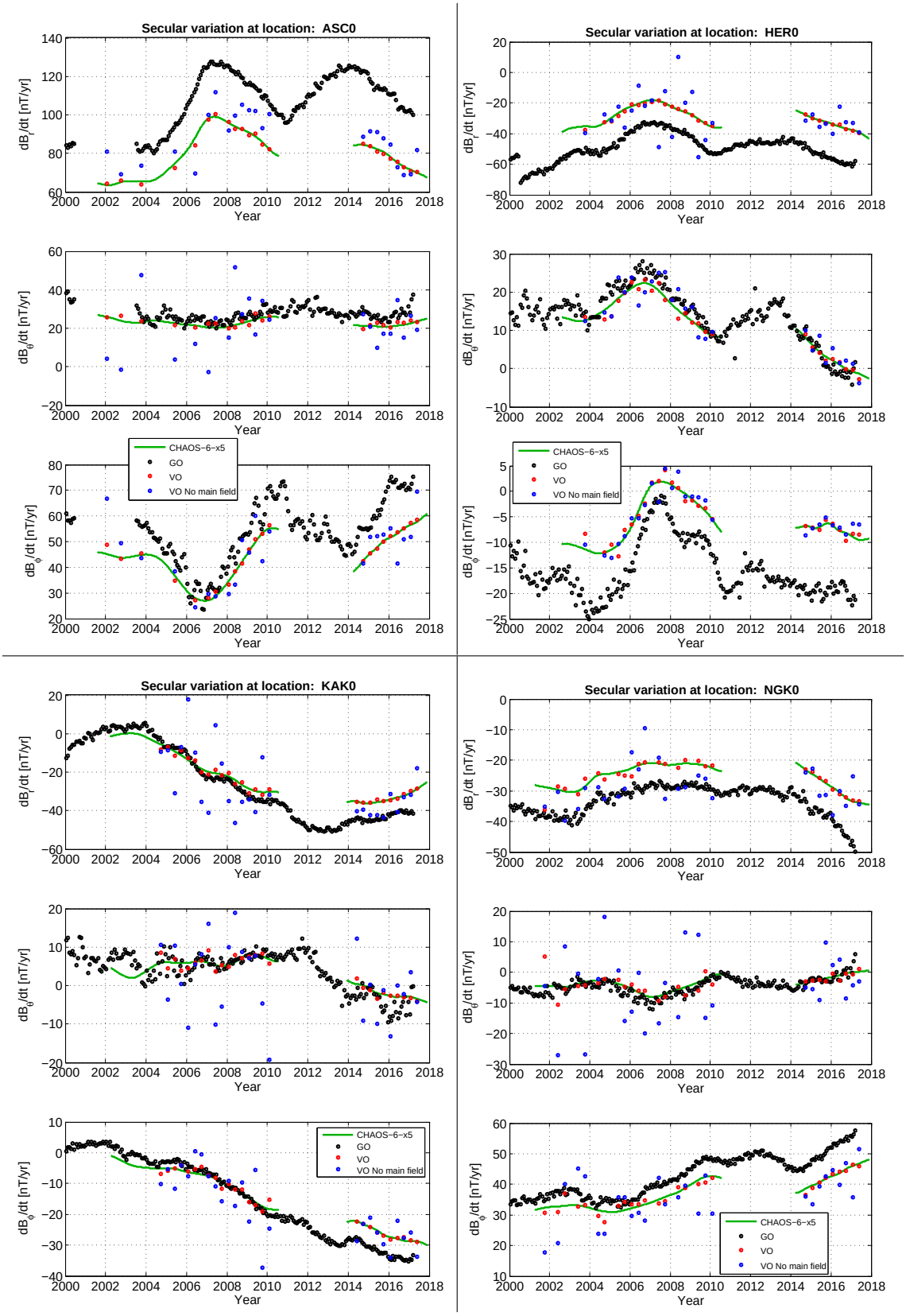

Figure 4.6: Time series of SV showing VO's using 4 month data windows at satellite altitudes with (red dots) and without (blue dots) CHAOS-6-x5 MF corrections, GO's (black dots) and CHAOS-6-x5 model predictions (green) using SH degrees up to $n = 13$.

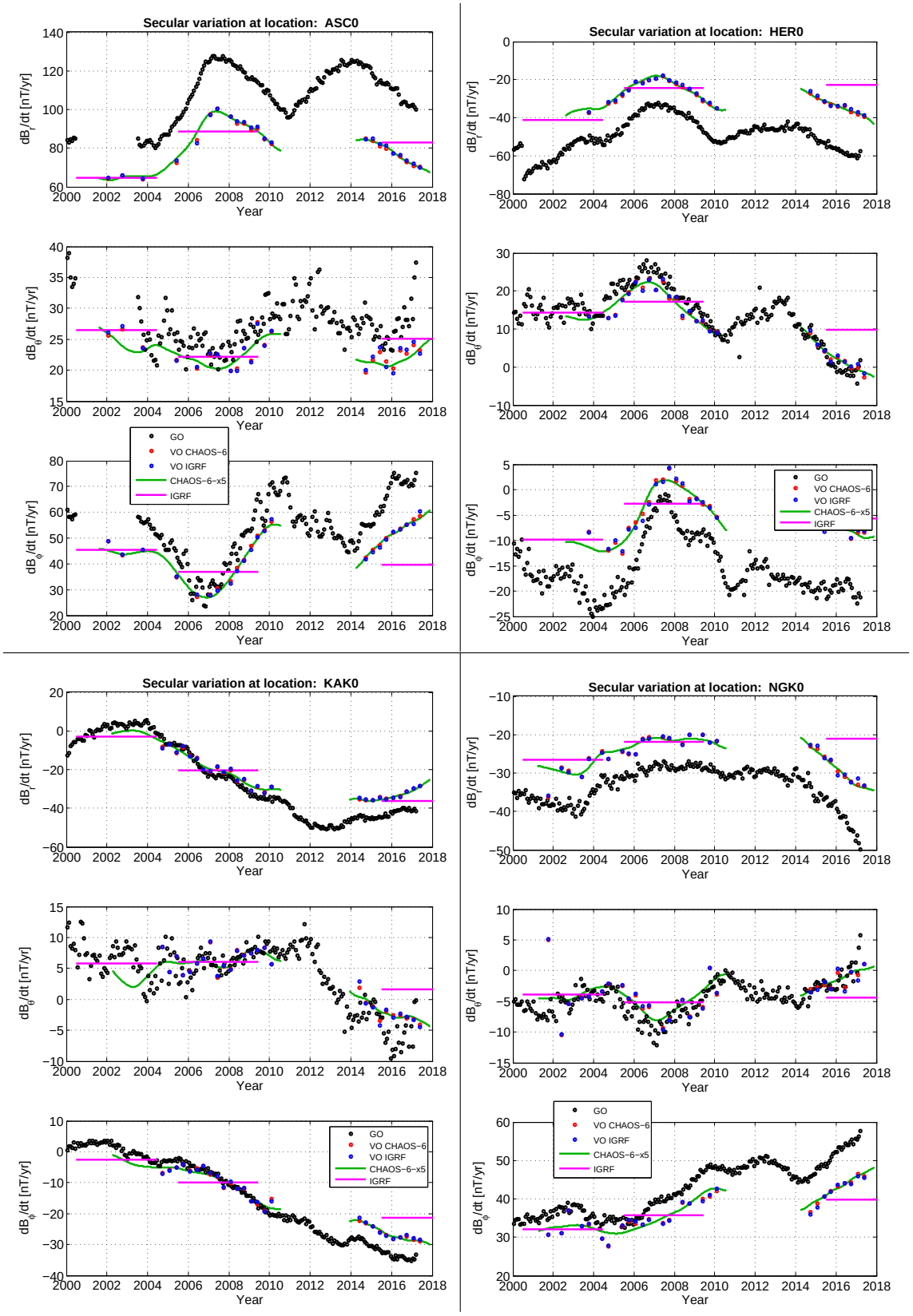

Figure 4.7: Time series of SV showing VO's using 4 month data windows at satellite altitudes with IGRF (blue dots) and CHAOS-6-x5 (red dots) MF corrections, GO's (black dots), CHAOS-6-x5 and IGRF model predictions (green and magenta) using SH degrees up to $n = 13$.

	CHAMP			Swarm		
Observatory	rms_r	rms_θ	rms_ϕ	rms_r	rms_θ	rms_ϕ
ASC	3.26	1.95	3.97	2.55	2.10	1.61
ASP	2.27	2.78	2.28	0.88	2.25	1.39
CLF	1.69	2.26	1.28	1.16	2.34	1.79
CMO	4.08	7.72	5.36	2.74	9.31	9.12
GAN	-	-	-	0.93	2.10	1.96
GUA	1.45	2.49	2.49	1.40	2.47	1.68
HER	2.71	2.26	1.97	1.29	1.97	1.96
HON	2.05	2.44	2.41	3.15	1.80	1.70
KAK	2.72	1.75	1.58	1.32	2.51	1.15
KOU	4.17	2.33	2.65	3.36	1.72	1.78
LRM	3.26	3.07	2.56	2.37	2.46	2.00
MBO	2.24	1.94	3.34	1.23	1.49	1.59
NGK	2.06	3.13	2.23	1.87	1.35	1.42
NSV	1.55	3.01	2.76	3.64	1.96	1.15
SJG	1.75	2.75	3.01	2.08	2.08	1.62
TDC	-	-	-	1.30	1.62	2.65

Table 4.4: VO time series based on IGRF-12 pre-whitening misfit statistics during CHAMP and *Swarm* periods. Units are in [nT].

	CHAMP			Swarm		
Observatory	ρ_r	ρ_θ	ρ_ϕ	ρ_r	ρ_θ	ρ_ϕ
ASC	0.97	0.74	0.96	0.98	0.45	0.98
ASP	0.76	0.81	0.96	0.82	0.51	0.94
CLF	0.87	0.73	0.96	0.94	-0.45	0.93
CMO	0.81	0.45	0.73	0.97	0.71	0.12
GAN	-	-	-	0.98	0.98	0.97
GUA	0.74	0.90	0.95	0.88	0.73	0.07
HER	0.93	0.94	0.96	0.96	0.94	-0.65
HON	0.91	0.46	0.64	0.96	0.86	0.50
KAK	0.98	0.55	0.97	0.89	0.42	0.89
KOU	0.97	0.91	0.90	0.93	0.83	0.81
LRM	0.96	0.93	0.98	0.96	0.44	0.77
MBO	0.93	0.86	0.96	0.87	0.71	0.98
NGK	0.91	0.50	0.88	0.92	0.62	0.96
NSV	0.96	0.92	0.81	0.96	0.86	0.95
SJG	0.96	0.93	0.85	0.93	0.55	0.11
TDC	-	-	-	0.79	0.90	0.86

Table 4.5: VO time series based on IGRF-12 pre-whitening correlation coefficients during CHAMP and *Swarm* periods.

	CHAMP			Swarm		
Observatory	rms_r	rms_θ	rms_ϕ	rms_r	rms_θ	rms_ϕ
ASC	3.68	1.93	4.32	3.08	2.27	2.18
ASP	2.14	2.68	2.13	0.75	2.39	1.50
CLF	1.64	2.28	1.35	1.16	2.00	1.65
CMO	4.02	7.72	5.20	3.08	7.26	7.15
GAN	-	-	-	1.22	2.48	2.29
GUA	1.46	2.57	2.34	1.35	1.74	1.55
HER	2.81	2.39	2.21	1.48	2.11	2.05
HON	1.96	2.45	2.50	3.36	1.98	1.22
KAK	2.68	1.77	1.64	1.19	2.18	0.82
KOU	4.67	2.51	2.76	3.87	1.39	1.51
LRM	3.00	2.85	2.45	2.35	2.29	1.72
MBO	2.30	2.00	3.57	1.08	1.26	2.42
NGK	2.20	3.10	2.16	1.64	1.01	1.43
NSV	1.61	2.90	2.90	3.36	1.69	1.18
SJG	1.85	2.91	3.30	2.17	1.67	1.60
TDC	-	-	-	0.60	1.53	2.71

Table 4.6: VO time series based on CHAOS-6-x5 pre-whitening misfit statistics during CHAMP and *Swarm* periods. Units are in [nT].

	CHAMP			Swarm		
Observatory	ρ_r	ρ_θ	ρ_ϕ	ρ_r	ρ_θ	ρ_ϕ
ASC	0.96	0.75	0.95	0.98	0.26	0.96
ASP	0.76	0.82	0.97	0.92	0.44	0.95
CLF	0.88	0.72	0.96	0.96	-0.24	0.95
CMO	0.80	0.45	0.75	0.96	0.72	0.25
GAN	-	-	-	0.92	0.97	0.96
GUA	0.74	0.89	0.96	0.92	0.85	0.19
HER	0.92	0.93	0.95	0.98	0.95	-0.64
HON	0.92	0.46	0.62	0.97	0.80	0.55
KAK	0.98	0.54	0.97	0.93	0.53	0.94
KOU	0.97	0.90	0.89	0.93	0.89	0.85
LRM	0.97	0.94	0.98	0.97	0.53	0.85
MBO	0.93	0.85	0.95	0.91	0.78	0.98
NGK	0.89	0.50	0.89	0.96	0.80	0.97
NSV	0.95	0.93	0.80	0.98	0.89	0.96
SJG	0.95	0.93	0.81	0.92	0.78	-0.04
TDC	-	-	-	0.95	0.92	0.90

Table 4.7: VO time series based on CHAOS-6-x5 pre-whitening correlation coefficients during CHAMP and *Swarm* periods.

4.4.3 Global Grids of VO Solutions

A global grid of VO time series provides an excellent opportunity for studies of the core field in particular regions as shown by Olsen and Mandea (2007); field models, geomagnetic jerks studies and inference of outer core fluid flow can be investigated by such a VO grid arrangement. Beggan et al. (2009) investigated both regular and equal area grid arrangements, and found that a regular grid partly enhanced sectorial banding and large residuals were found in the polar regions (orbital drift was also believed to be responsible). This project also applies two different grid arrangements: 1) a regular 5° colatitude and longitude spaced grid similar to the one used by Olsen and Mandea (2007), in which $(\theta = 0°, 5°, ..., 180°; \phi = 0°, 5°, ...350°)$. The sole purpose of using this grid was to perform a SHA to investigate the behaviour of the expansion coefficients of the internal, and in particular of external and toroidal fields. A problem of this type of grid is the overlap of VO target cylinders causing data to be binned into multiple VOs. 2) an equal area grid based on the equal area (EQ) sphere partitioning algorithm of Leopardi (2006) has also been used to setup a VO grid of a given size. This partition, $EQ(d, N)$, of the unit sphere into N regions, termed recursive zonal equal area sphere partitioning, is defined by the sphere dimensions, here being a positive integer, $d \in \mathbb{N}_+$ and number of regions of equal area $N \in \mathbb{N}_+$. The VO grid locations used are then the center point of each region. The EQ partition allows for any number of sphere partitions to be specified, making it very usable for this particular implementation. Figure 4.8 a) illustrates the EQ sphere partitioning for $N = 300$, and b) the associated locations of the $P_{VO} = 300$ EQ globally distributed VO's. The minimum spherical distance between any two points of the $N = 300$ EQ grid is ≈ 1400km (corresponding roughly to SH degree $n = 16$). The Matlab Recursive Zonal Equal Area Sphere Partitioning Toolbox implements the algorithm for this grid, `http://eqsp.sourceforge.net/`.

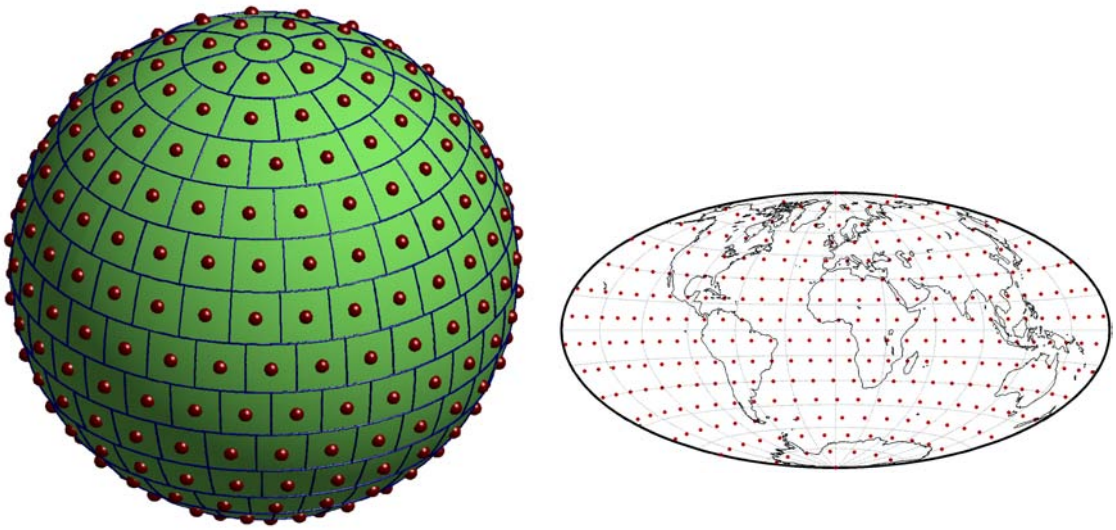

(a) EQ sphere partitioning $EQ(2, 300)$ of Leopardi (2006). Red dots are center points.

(b) EQ grid having 300 globally distributed VOs illustrated by red dots, using a Hammer projection.

Figure 4.8: Equal area grid construction.

Table 4.8 presents the VO model misfit statistics similar to Table 4.3 but now for the global grid, split into polar and non-polar location of the VO's, again being a mean over all the epochs. As can be seen from the table, the polar rms values for both sums

and differences are higher than the non-polar, and the CHAMP values are slightly higher than the *Swarm* values. Presumably, these high numbers are due to unmodelled field contributions. However, at non-polar regions the rms values are all below 2nT.

		CHAMP		Swarm	
	Component	Mean [nT]	rms [nT]	Mean [nT]	rms [nT]
Polar	$\sum B_r$	0.00	6.68	0.00	5.04
	$\sum B_\theta$	0.00	6.59	0.00	5.40
	$\sum B_\phi$	0.00	3.30	0.00	2.48
	ΔB_r	0.00	4.33	0.05	2.93
	ΔB_θ	0.00	5.23	0.00	3.45
	ΔB_ϕ	-0.01	10.16	-0.02	6.80
Non-polar	$\sum B_r$	0.00	1.87	0.00	1.45
	$\sum B_\theta$	0.00	1.49	0.00	1.18
	$\sum B_\phi$	0.00	1.35	0.00	0.94
	ΔB_r	-0.01	0.51	0.02	0.34
	ΔB_θ	0.00	0.58	0.00	0.44
	ΔB_ϕ	0.00	0.64	0.00	0.50

Table 4.8: VO model misfit statistics - example case for a global grid of 300 VO's during CHAMP and *Swarm* periods.

4.5 VO Model Results I: Field Computations

This section presents the main results obtained for the magnetic field and its temporal variations using the VO method applied to Data Set 1 and producing VO model version 0105. Section 4.5.1 presents examples of VO time series of annual differences of the main field and secular variation computed at the selected ground observatory sites listed in Section 4.4.1. An example of correlation analysis applied to the model parameters is provided in Section 4.5.2. Sections 4.5.3 and 4.5.4 present results of VO application to an EQ global grid, looking into data error estimates. Section 4.5.5 provides a spherical harmonic analysis performed for a regular grid of globally distributed VO's with the intention of investigating the amplitude of the external and toroidal contributions in the time series.

4.5.1 Time Series at Ground Observatory Sites

Figures 4.9 to 4.16 present time series of annual differences of the main field (i.e. the SV) and of the secular variation (i.e. the SA) at the selected ground observatories listed in Table 4.2. The figures are listed in alphabetic ordering of the observatories; shown with black dots are the revised monthly mean of the GOs, in red dots the VO estimates and with the green curves the CHAOS-6-x5 model predictions at the ground for SH degrees $n \in [1, 16]$. For each station the left (top or bottom) plots show the SV estimates while the right (top or bottom) plots show the SA estimates of the three field components. The VO's have been relocated to the ground in order to ease the GO and VO comparison. This was done by subtracting the field difference determined by the CHAOS-6-x5 model between ground and the VO altitudes. In Appendix C the same plots as those presented in the following are provided without this relocation of the VO's, such that the VO's are

plotted at altitudes 370km and 490km during CHAMP and *Swarm* times, respectively.

A number of interesting observations can be made from these plots. Firstly, comparing the VO's and GO's there seems to be remarkably good agreement of the temporal field behaviour at most stations as also indicated by the correlation degree in Table 4.7. Secondly, the VO's provide insight into places were GO data are lacking for instance at the GAN or TDC stations. Thirdly, it can be seen that the CHAOS-6-x5 model predictions overall are in a remarkably good agreement with most of the variations seen in the VO time series; as the VO approach is very different from that of the CHAOS-6-x5 model, the VO time series may be used as an assessment of field models and their temporal resolution (Olsen et al., 2009). Such well agreement are seen at e.g. the Ascension Island (ASC), Kakioka (KAK) and Learmonth (LRM) observatories. However it seems as though there is a slight difference between the CHAMP and *Swarm* periods, which is also to be expected based on the rms values listed in Table 4.6. However, CHAOS-6-x5 may not capture all variations equally well; for instance at Honolulu (HON) observatory there is a clear dip in the dB_ϕ/dt component around 2007 that is seen in the VO's but not in CHAOS-6-x5.

The VO time series capture important rapid temporal features, i.e geomagnetic jerks here being interpreted as a sign change in the acceleration, seen as "V" or "Λ" shape features in the SV signal and as step changes "/" or "\" shape features centred on zero in the SA signal (Mandea et al., 2010; Brown et al., 2016). For example the 2007 jerk, having about 3 years on either side of the event, is clearly seen in the VO time series at the Ascension Island (ASC), Hermanus (HER), Mbour (MBO) and Tristan da Cunha (TDC) observatories, were the above mentioned behaviour is observed. In the VO time series at Honolulu (HON) observatory a steep change in the SA can be observed around 2017; this may be the first signs of a jerk happening. Also in the VO time series at Kourou (KOU) observatory, a "V" shape feature in the θ components of the SV can be seen at 2016, with an associated steep change in the SA which could indicate jerk happening. Hence, the satellite based VO's are shown to provide the same important temporal insight as the ground observatories. However, because the particular VO series plotted here are based on 4 month time windows some temporal resolution is lost.

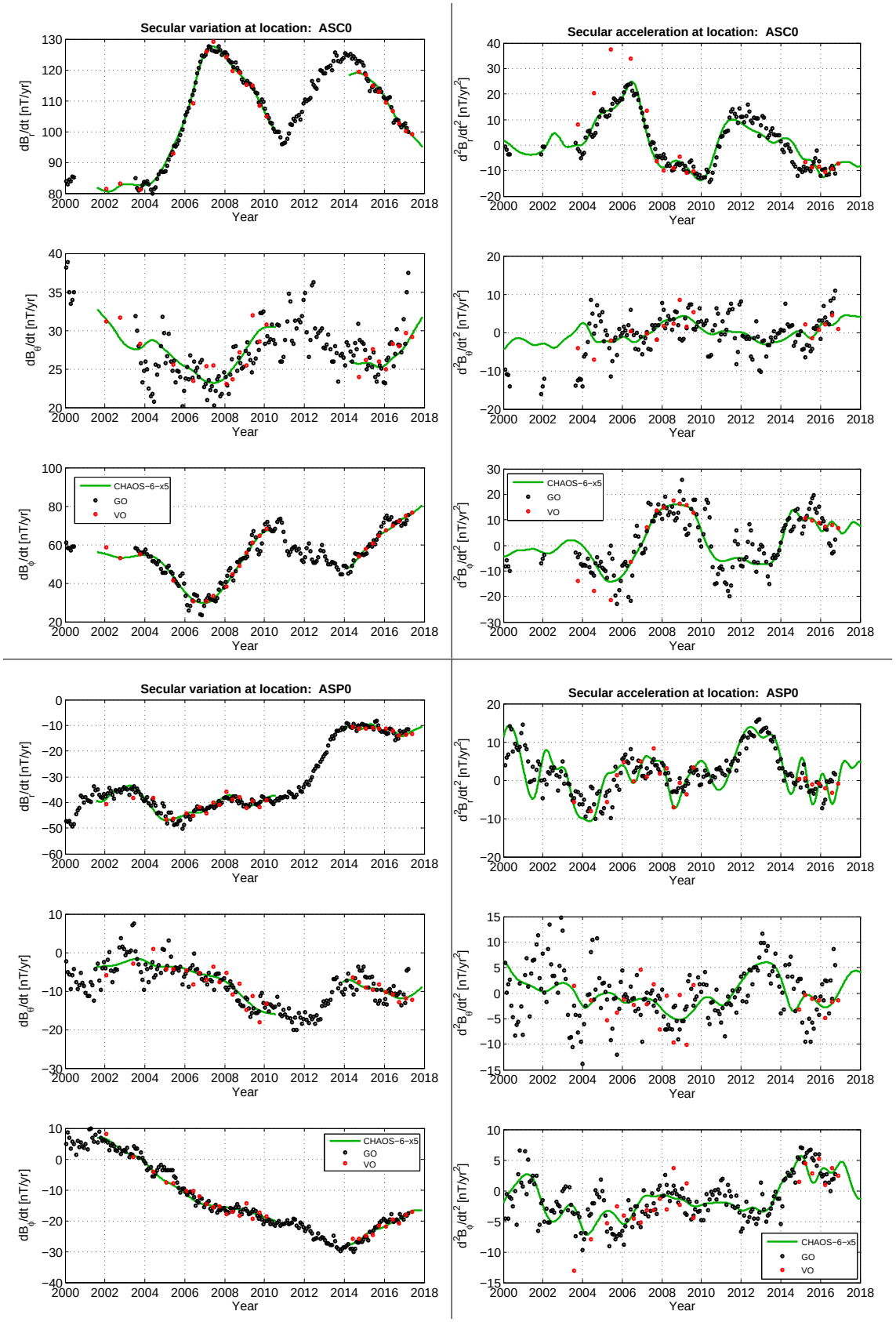

Figure 4.9: Time series of SV (left) and SA (right) showing VO's (red dots) using 4 month data windows re-plotted at ground, GO's (black dots) and CHAOS-6-x5 model predictions (green) using SH degrees up to $n = 16$.

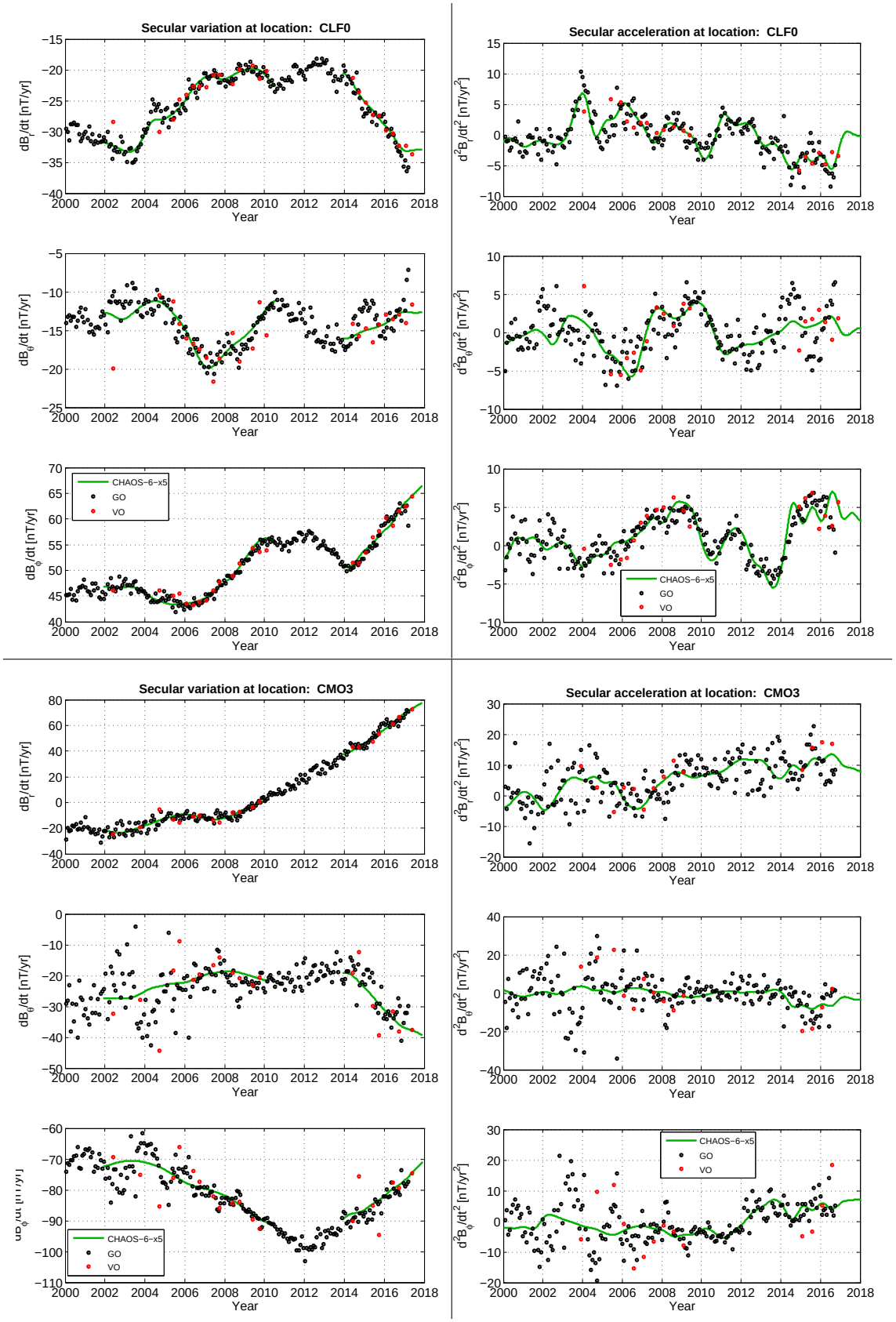

Figure 4.10: Time series of SV (left) and SA (right) showing VO's (red dots) using 4 month data windows re-plotted at ground, GO's (black dots) and CHAOS-6-x5 model predictions (green) using SH degrees up to $n = 16$.

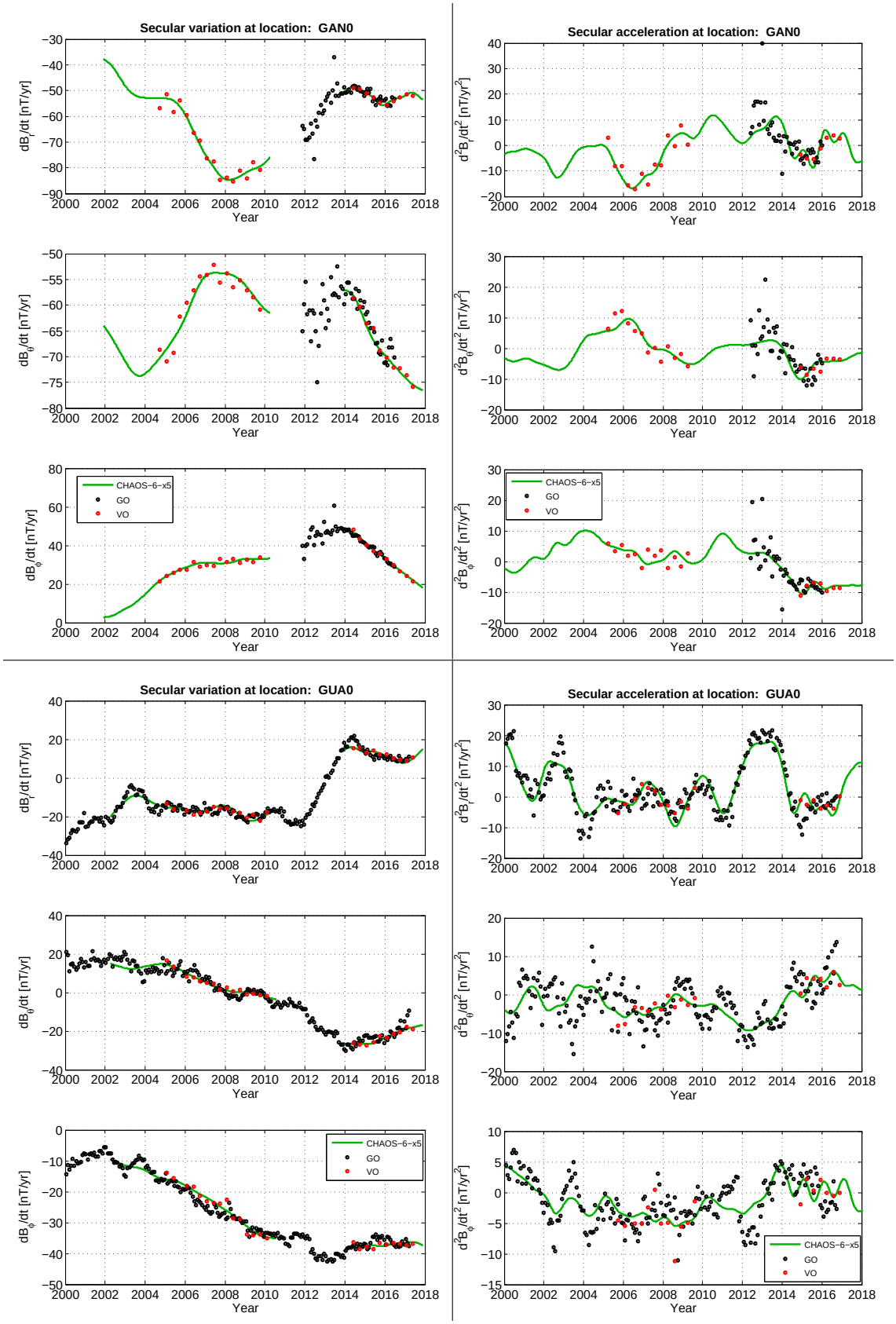

Figure 4.11: Time series of SV (left) and SA (right) showing VO's (red dots) using 4 month data windows re-plotted at ground, GO's (black dots) and CHAOS-6-x5 model predictions (green) using SH degrees up to $n = 16$.

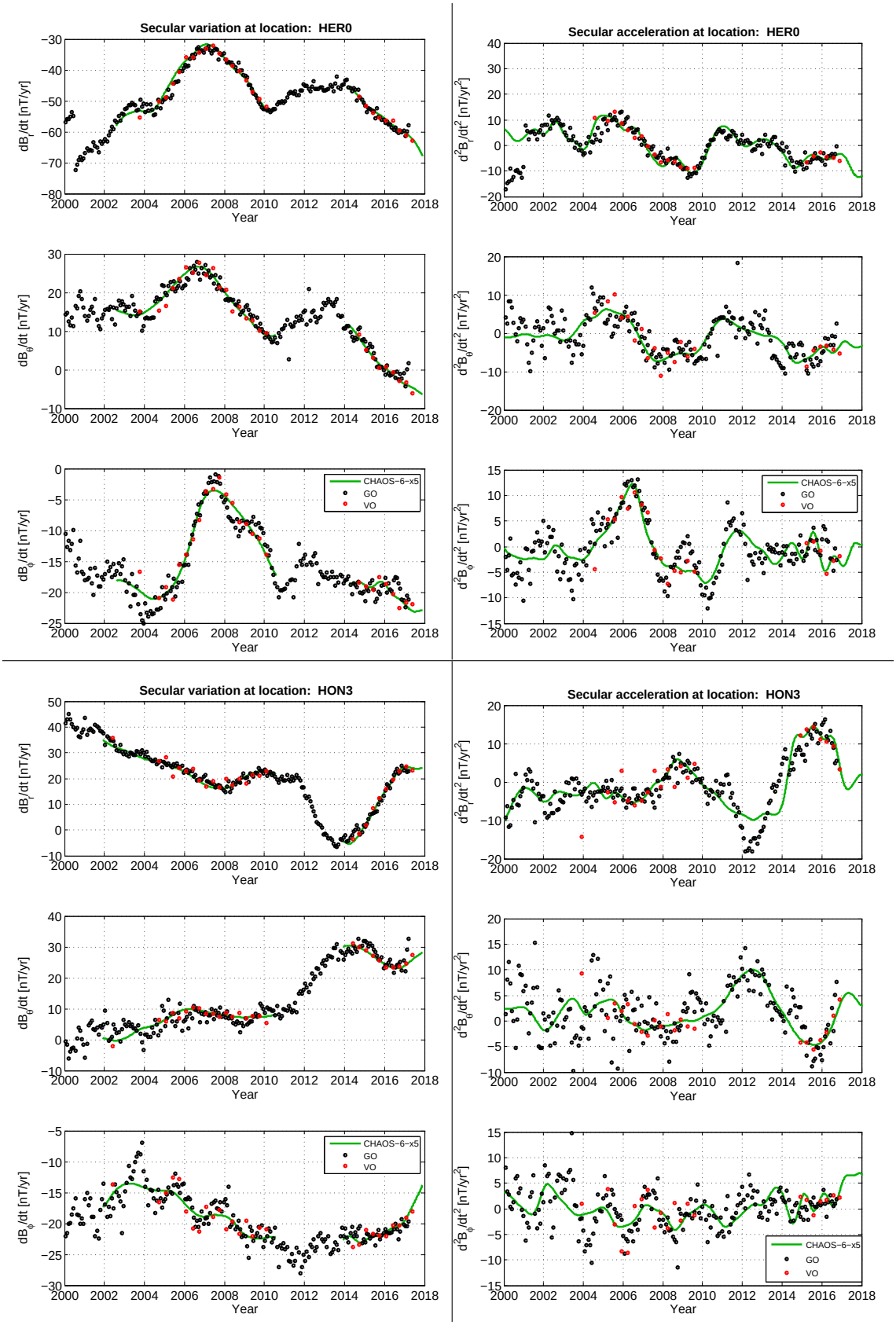

Figure 4.12: Time series of SV (left) and SA (right) showing VO's (red dots) using 4 month data windows re-plotted at ground, GO's (black dots) and CHAOS-6-x5 model predictions (green) using SH degrees up to $n = 16$.

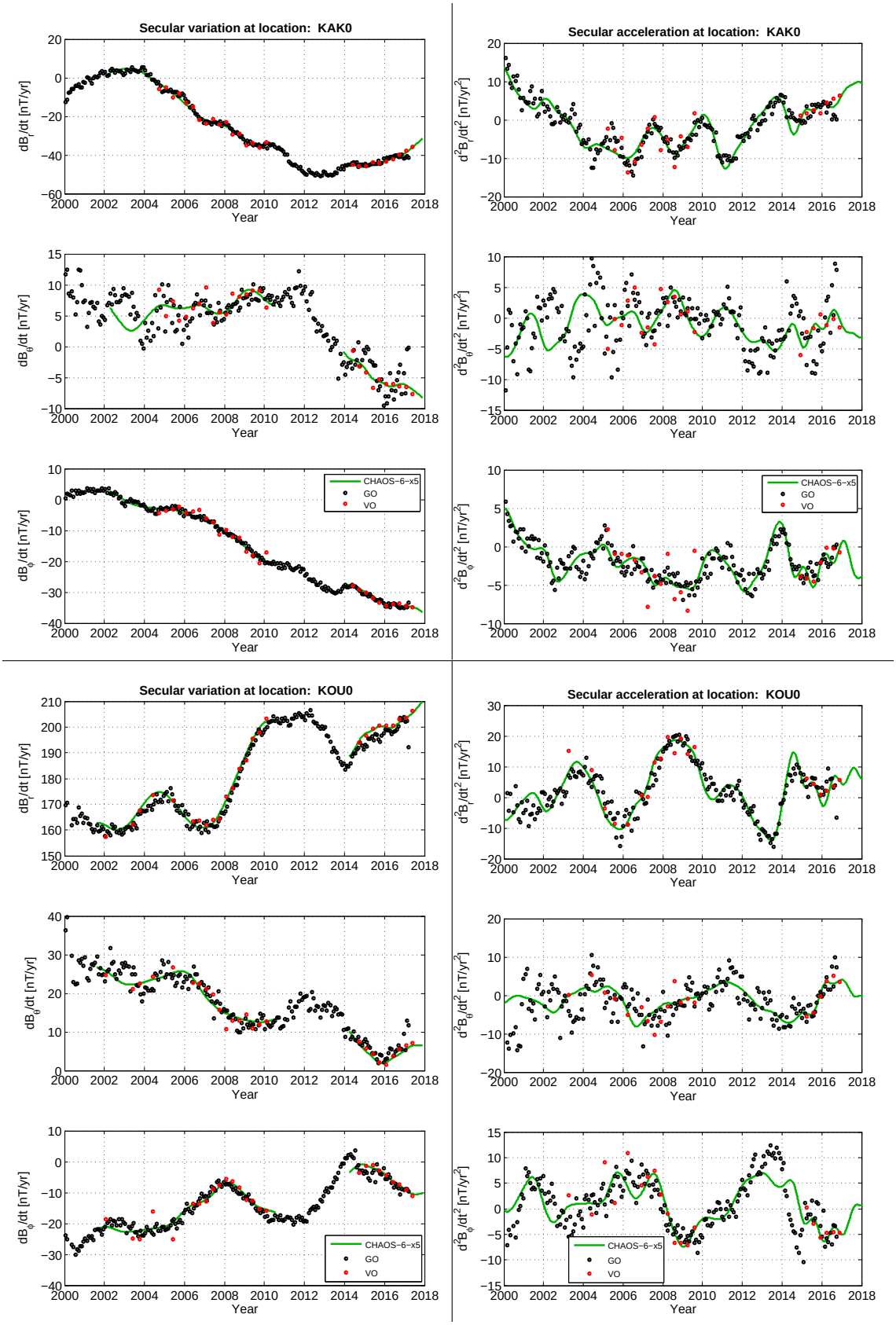

Figure 4.13: Time series of SV (left) and SA (right) showing VO's (red dots) using 4 month data windows re-plotted at ground, GO's (black dots) and CHAOS-6-x5 model predictions (green) using SH degrees up to $n = 16$.

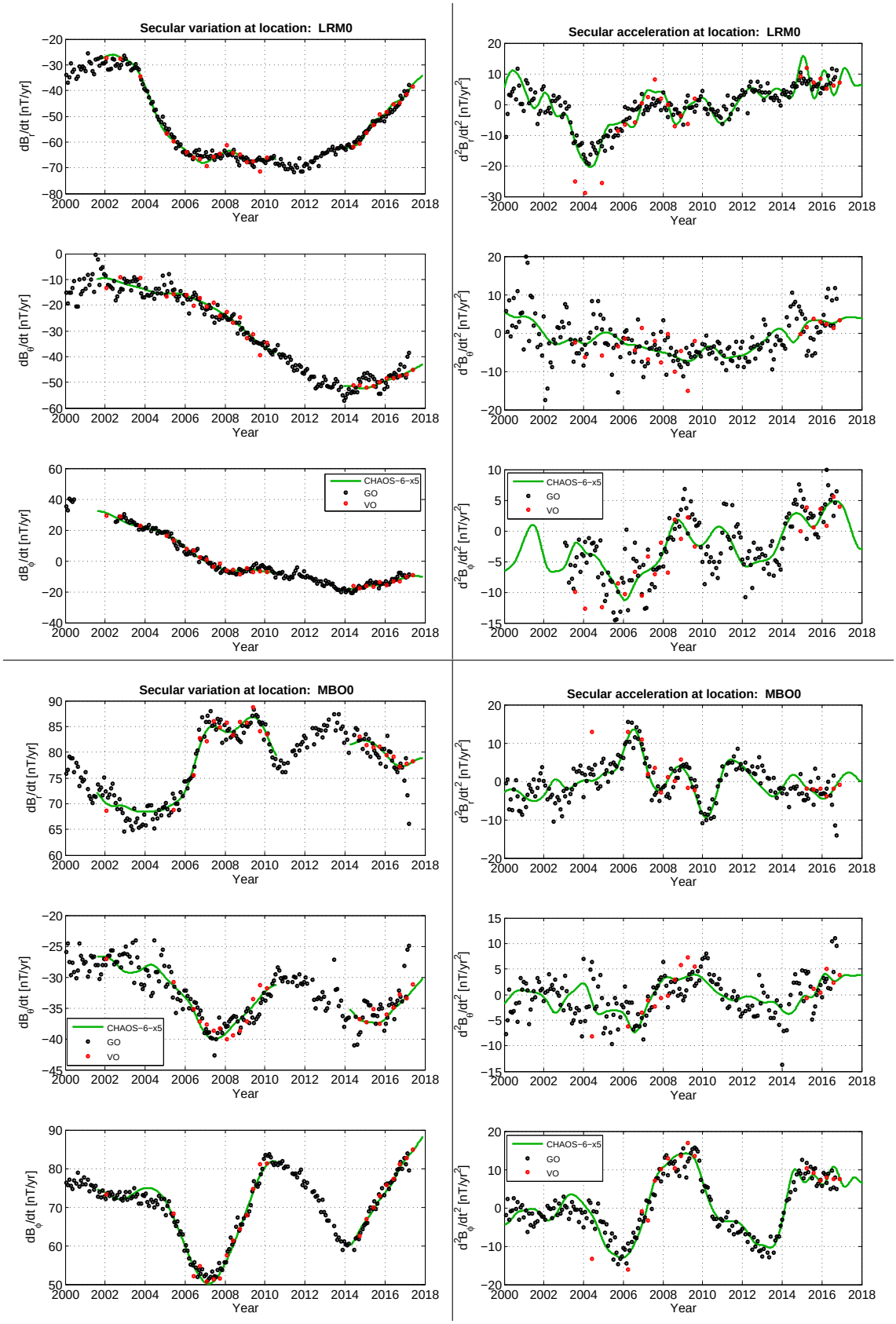

Figure 4.14: Time series of SV (left) and SA (right) showing VO's (red dots) using 4 month data windows re-plotted at ground, GO's (black dots) and CHAOS-6-x5 model predictions (green) using SH degrees up to $n = 16$.

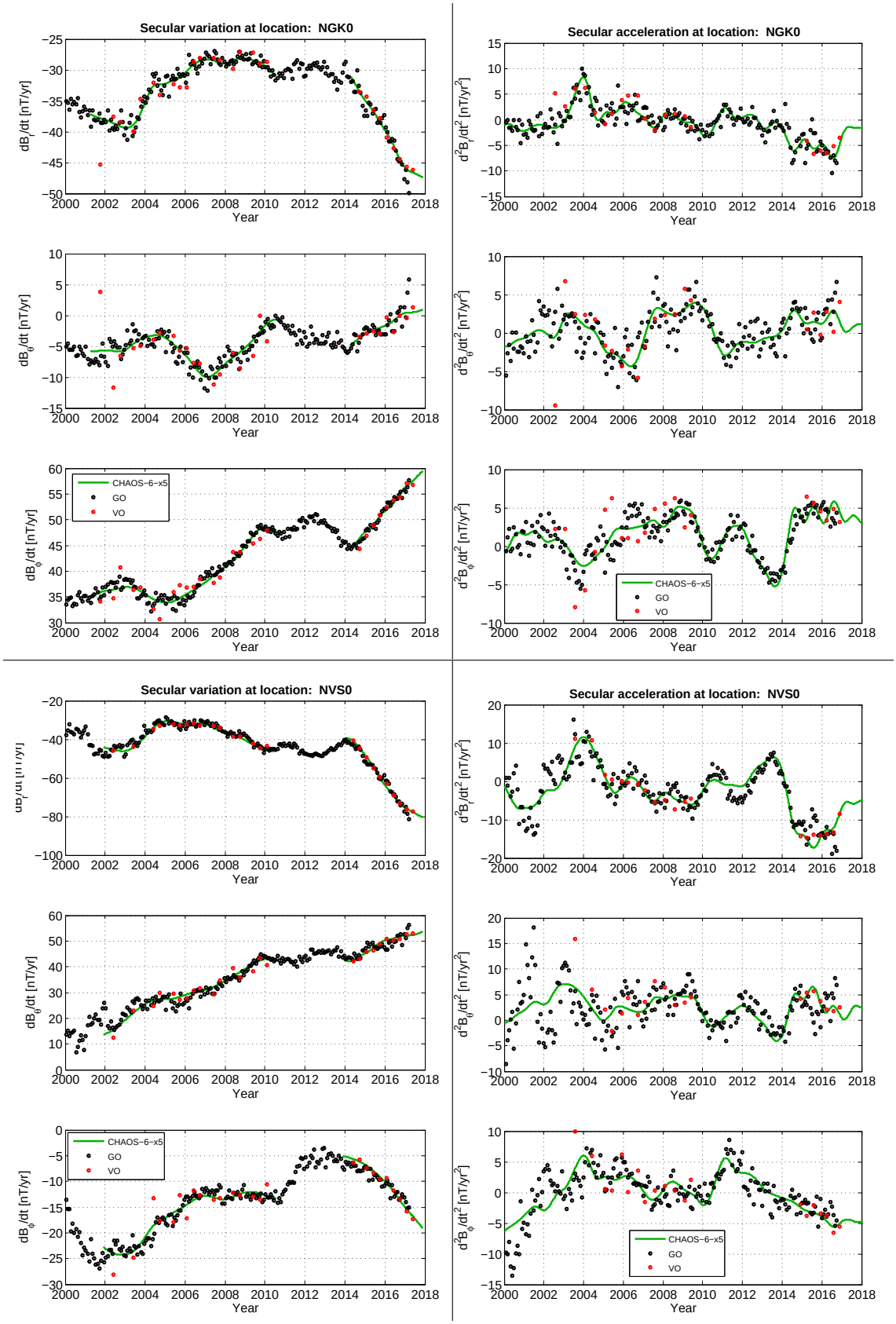

Figure 4.15: Time series of SV (left) and SA (right) showing VO's (red dots) using 4 month data windows re-plotted at ground, GO's (black dots) and CHAOS-6-x5 model predictions (green) using SH degrees up to $n = 16$.

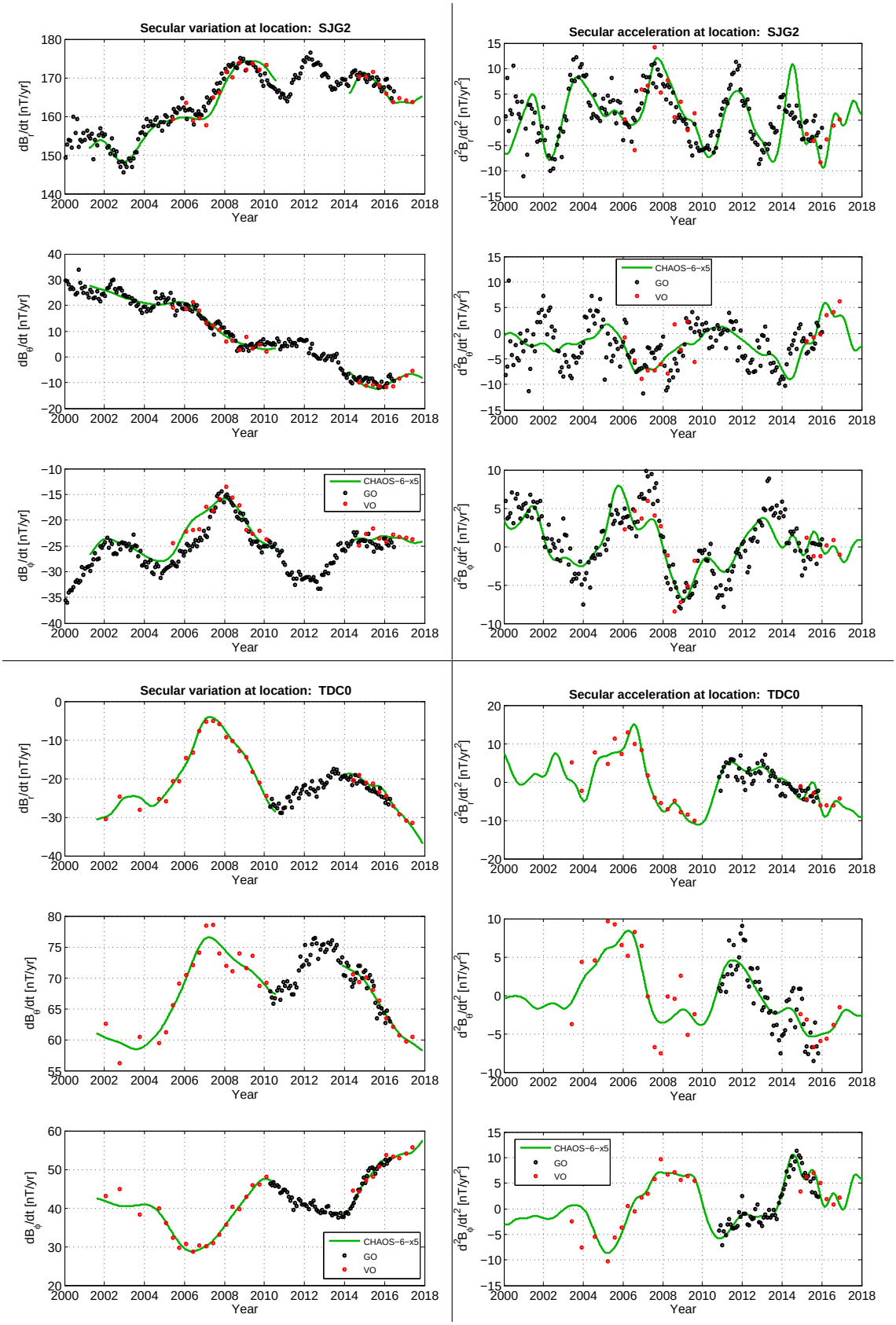

Figure 4.16: Time series of SV (left) and SA (right) showing VO's (red dots) using 4 month data windows re-plotted at ground, GO's (black dots) and CHAOS-6-x5 model predictions (green) using SH degrees up to $n = 16$.

4.5.2 Model Covariance and Correlation Matrices

It is possible to investigate the uncertainty associated with the model parameters when using the cubic potential description. The covariance of the random variables, X and Y can be written (e.g., Aster et al., 2005, p. 257)

$$\mathrm{Cov}(X,Y) = E\left[(X - E[X])(Y - E[Y])\right] = E[XY] - E[X]E[Y] \tag{4.23}$$

where $E[X], E[Y]$ is the expectation value of the variables, being a sum of the variables weighted by their probability density function. The variance is defined by $\mathrm{Var}(X) = E[X^2] - E[X]^2$, such that $\mathrm{Cov}(X,X) = \mathrm{Var}(X)$. A useful tool measuring the relation between variables is the correlation matrix, being a normalized scaled version of the covariance matrix written (e.g., Aster et al., 2005, p. 259)

$$\rho(X,Y) = \frac{\mathrm{Cov}(X,Y)}{\sqrt{\mathrm{Var}(X)\mathrm{Var}(Y)}} \tag{4.24}$$

where $-1 \geq \rho \leq 1$. The correlation matrix is dimensionless and symmetric under interchanging X and Y. If $\rho(X,Y) = 0$ the variables are uncorrelated, if $\rho = 1$ (or $\rho = -1$) the variables are completely (inversely) correlated (e.g., Barlow, 1989; Taylor, 1997).

Figures 4.17 and 4.18 present example model correlation matrices, $\rho_r, \rho_\theta, \rho_\phi$, computed for each field component, for a VO solution above the Niemegk ground observatory. Figure 4.17 a) and b) show correlations using regular vector data for time windows January-April and May-August during 2017, respectively. Overall the correlation matrix exhibits the same patterns in a) and b) for the three components, though the first three parameters used to generated the VO model field series are not correlated to each other in any case. It is seen that the correlation appears to be enhanced slightly for the May-August time window. Figure 4.17 c) and d) show correlations using data sums and difference for time windows January-April and May-August during 2017, respectively. These plot look very similar to a) and b) which is to be expected since the data sums, which are rather similar to the data itself, are included. Figure 4.18 presents correlations using data differences only for for time window January-April (left) and May-August (right). As also stated in Section 4.3.4, it should be notated that using the differences alone turned out not to constrain the first three model parameters, and thus the data sums are needed as well.

These correlations suggests that some model parameters could be constraint considering only certain data components and potentially using differences alone for some parameters, in a similar manner as discussed in (Olsen et al., 2007, 2010b; Kotsiaros and Olsen, 2014) (in the case of optimal gradient observation combination). That is, identification of data subsets being suitable for determining particular model parameters, a procedure know as Selectetive Infinite-Variance Weighting (SIVW) method(Olsen et al., 2007; Sabaka et al., 2013, 2015). However, such possibilities have not been pursued further in this thesis.

4.5.3 Time Series for the Global Grids

This section briefly summarises the availability of reliable, global VO time series, version 0105, using an EQ grid of 300 VO's. Figure 4.19 shows the number of available VO data points of the EQ grid during CHAMP and *Swarm* periods (having a possible maximum of 300). It is evident that the intervals 2004-2010 and 2014-2018 are well covered. The major dip at 2003 is related to the solar activity level peaking around this time, see Section 2.4.4. Despite the dark geomagnetic quite time selection criteria used, stable VO time

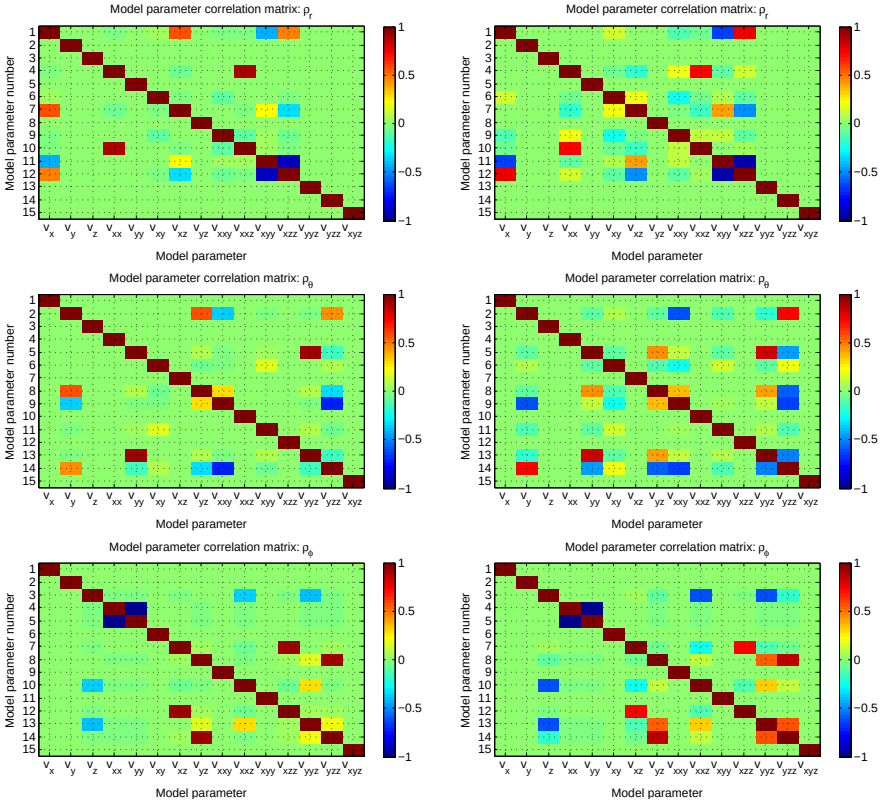

(a) Using regular vector data: year 2017, months jan-apr.

(b) Using regular vector data: year 2017, months may-aug.

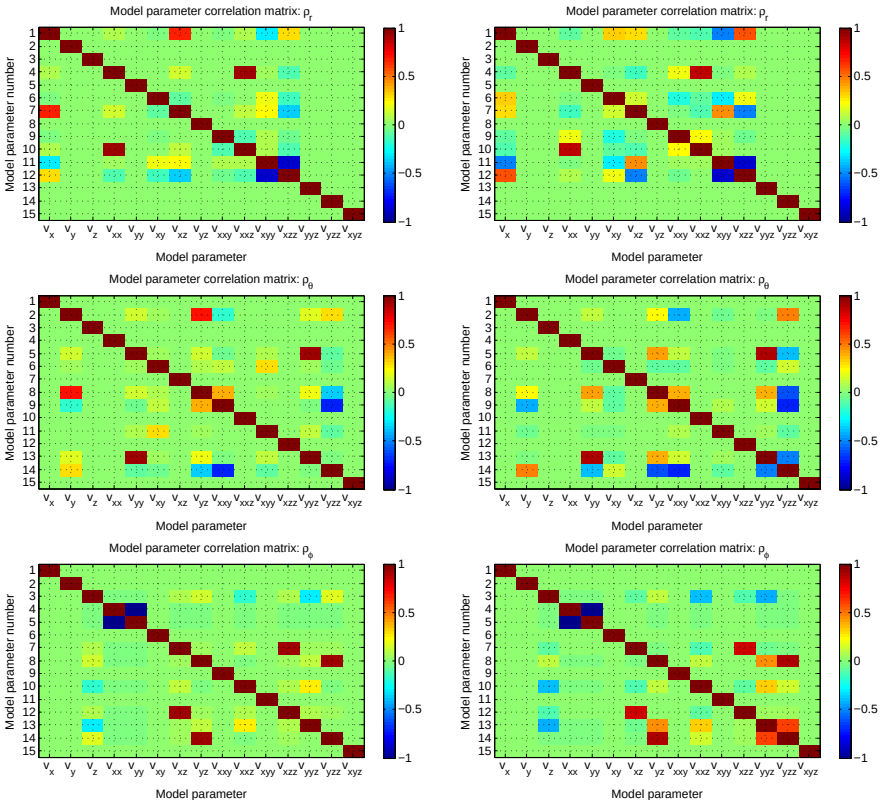

(c) Using sums and differences data: year 2017, months jan-apr.

(d) Using sums and differences data: year 2017, months may-aug.

Figure 4.17: Model correlation matrix for location NGK.

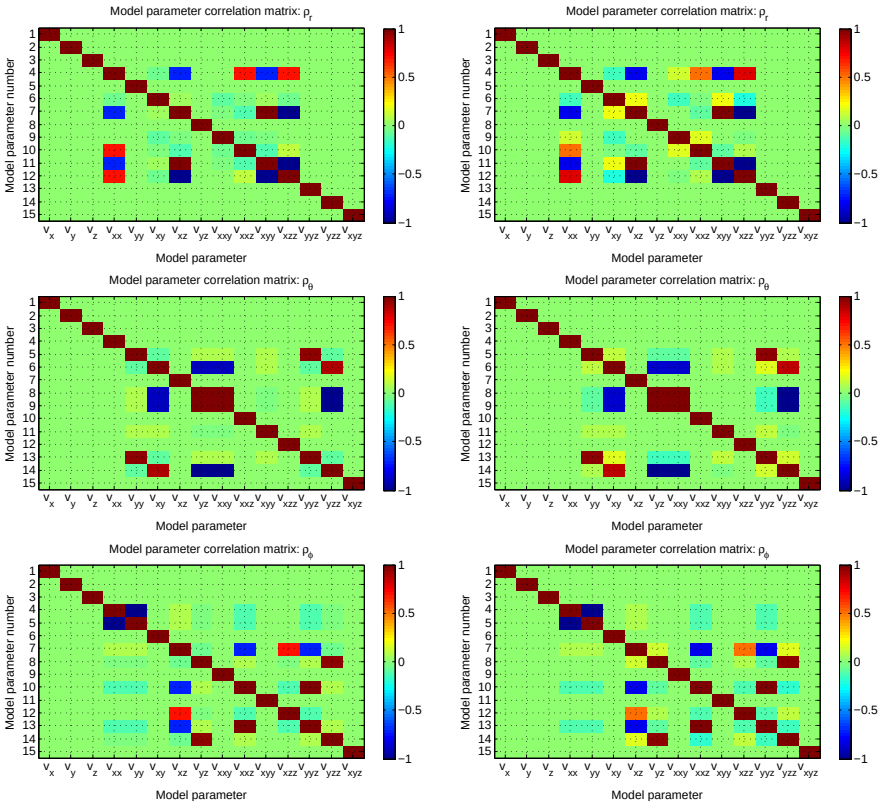

(a) Using differences data: year 2017, months jan-apr.

(b) Using differences data: year 2017, months may-aug.

Figure 4.18: Model correlation matrix for location NGK.

series of good global coverage can be obtained, particular during the operation of the *Swarm* mission.

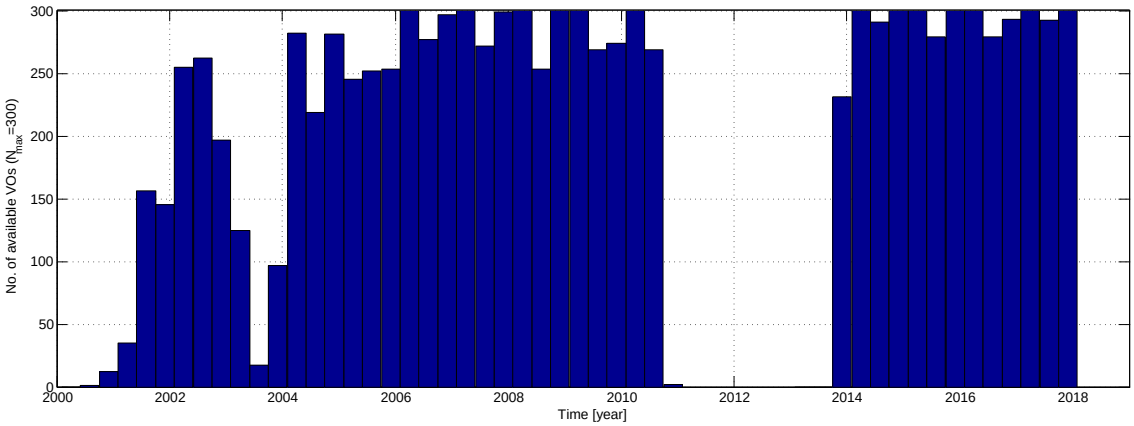

Figure 4.19: Number of acceptable VO's.

4.5.4 Data Error Covariance Matrices

Derivation of uncertainty estimates for the MF and SV time series is of importance when the VO's are used in various studies, for example core flow inversion and data assimilation. Uncertainty estimates for each field component were determined as the square root of the diagonal (variance) elements of the covariance matrix. Diagonal entities of the covariance matrices for the VO time series of the MF and SV were computed as devised by C. Finlay in a manner similar to the computation for ground observatory revised monthly means (Olsen et al., 2014; Barrois et al., 2018). The data errors were assumed to be independent time, though different errors are attributed to CHAMP and *Swarm* periods. For each VO time series, the difference to the CHAOS-6-x5 model predictions, δB, was detrended using the Matlab build-in function *detrend* which has an algorithm removing the linear trend, $\widehat{\delta B}$, as estimated through a least-squares fit https://se.mathworks.com/help/matlab/ref/detrend.html. For instance in the case of SV, the detrended signal, x_i, is written

$$x_i = \frac{\delta B_i}{dt} - \frac{\widehat{\delta B_i}}{dt} \tag{4.25}$$

where i denotes the time instance. The function *mcdcov* from the LIBRA (Library for Robust Analysis) tool box, developed at ROBUST@Leuven, was used to compute the covariance matrices for the three field components https://wis.kuleuven.be/stat/robust/LIBRA. This function uses a minimum covariance determinant (MCD) estimator which takes a subset of the data and seeks a covariance matrix with the smallest determinant (Verboven and Hubert, 2005). In the MF and SV cases the covariance matrix, $C_e = \mathrm{cov}(x_i, x_j)$, has dimension $3P \times 3P = 900 \times 900$ since there are 300 VO's having three components. The square root of the diagonal covariance elements was the used.

It should be noted that the errors between the VO time series and their components are expected to be correlated (e.g., Finlay, 2017). Properly dealing with this requires the determination of a full covariance matrix including off-diagonal elements. This is difficult due to the short length of the time series. This perspective has therefore not been pursued in this project, but may be important for future applications.

Figures 4.20 and 4.21 presents the estimated variances for each component of the main field (in units of [nT^2]) and secular variation (in units of [(nT/yr)^2]) during CHAMP and *Swarm* periods. It is observed that the horizontal components of both the MF and SV variances contain larger estimates moving towards polar latitudes, possibly related to enhanced contamination due to presence of e.g. field-align currents (which would not disturb the radial as much as the horizontal components) and the polar electrojet currents.

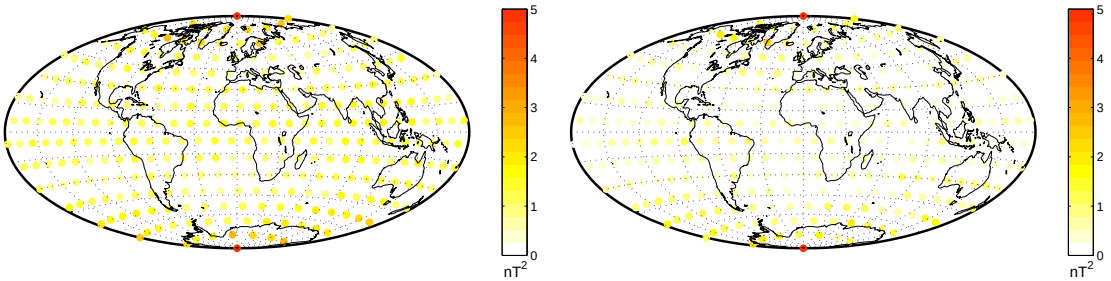

(a) B_r variance estimates.

(b) B_r variance estimates.

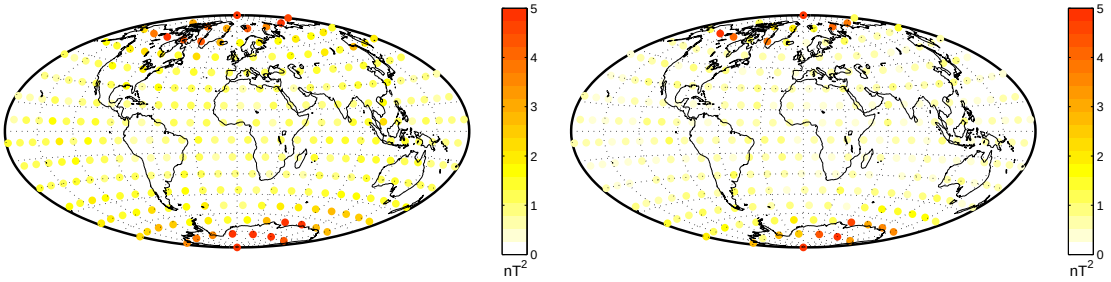

(c) B_θ variance estimates.

(d) B_θ variance estimates.

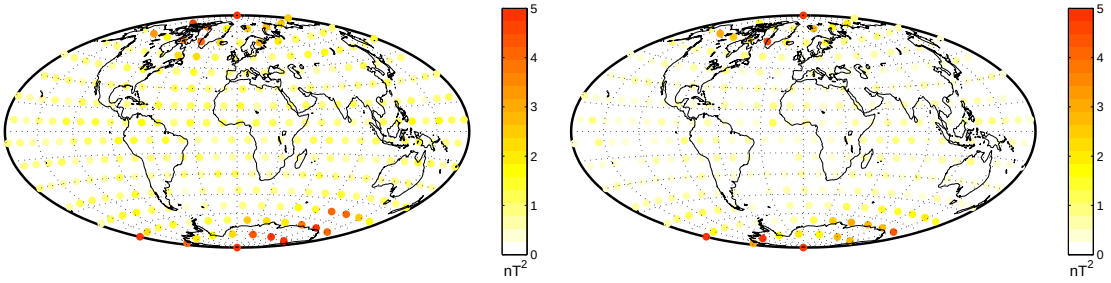

(e) B_ϕ variance estimates.

(f) B_ϕ variance estimates.

Figure 4.20: MF variance estimates during the CHAMP (left column) and *Swarm* (right column) eras.

4.5.5 SHA of Global Grid VO Model Time series

In this section a SH model, using B-spline representation of the time-dependence, built from VO MF data provided on a regular global grid, is described. The main objective here was to estimate the amplitude and behaviour of the external and toroidal model coefficients as described by the potential, equation (2.42), using equations (2.43) to (2.45) for the expansions, given in Section 2.5.3. Olsen and Mandea (2007) also performed such a SH analysis, investigating whether some parts of the short-period VO signal could be explained by these external and toroidal coefficients. Indeed the authors found strong variations in the external term dq_1^0/dt and toroidal term $dt_1^{0,c}/dt$, exceeding the internal coefficients in amplitude. It should be stressed that Olsen and Mandea (2007) intentionally did not employ data selection criteria and did not remove estimated external field contributions, contrary to this study, since they implicitly assumed external fields average to zero on a monthly basis. Here a similar investigation was performed conducting a spherical harmonic transform analysis on the quiet-time, dark, VO data set 0105, determining the expansion coefficients.

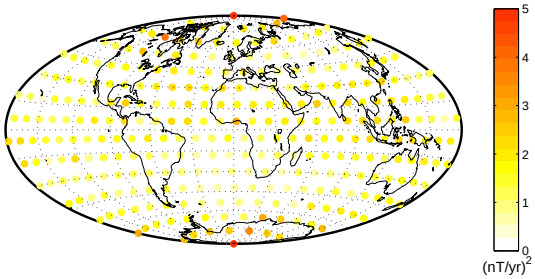

(a) dB_r/dt variance estimates.

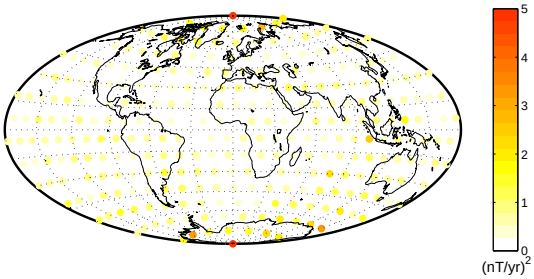

(b) dB_r/dt variance estimates.

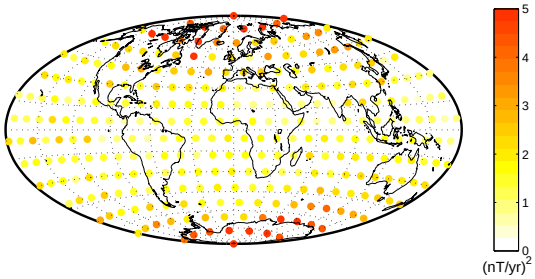

(c) dB_θ/dt variance estimates.

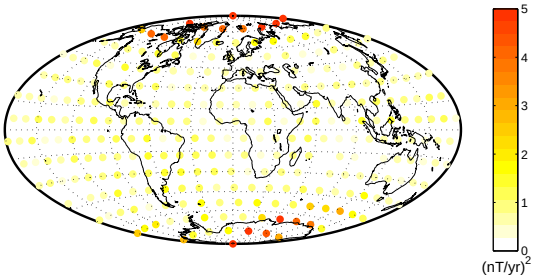

(d) dB_θ/dt variance estimates.

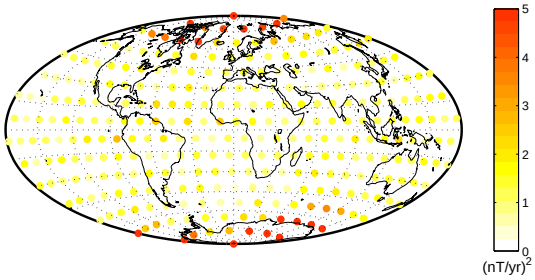

(a) dB_ϕ/dt variance estimates.

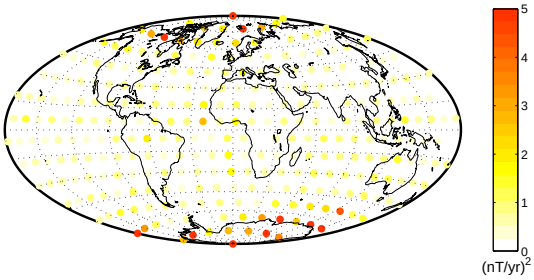

(b) dB_ϕ/dt variance estimates.

Figure 4.21: SV variance estimates during the CHAMP (left column) and *Swarm* (right column) eras.

The analysis was carried out for both CHAMP and *Swarm* data periods using VO model version 0105. The procedure was as follows: for each time in the 4 month VO MF data series, an inversion for the expansion coefficients was performed truncated to SH degree $n = 20$. The spherical harmonic transform Olsen and Mandea (2007) of the equally spaced VO data determining the internal and external coefficients along with toroidal coefficients, as described in Section 2.5.3, was performed using the DTU in-house algorithm *SH_analysis.m* supplied by N. Olsen.

When trying to approximate a function (in this case the time-dependence of the Gauss coefficients) polynomials are useful; one example is the well-known Taylor series. However, considering a long time window, piecewise polynomials termed splines may be more a appropriate method. In this case the time window is subdivided into smaller sections defined by a knot sequence, such that a polynomial belonging to that section approximates the function while requiring the assembled solution to have continuous derivatives. This means that locally the splines minimize the influence from the entire data set, since they are collections of piecewise polynomials linked together. Here the time-dependence of the

internal $\{g_n^m(t), h_n^m(t)\}$, external $\{q_n^m(t), s_n^m(t)\}$ and toroidal $\{t_n^{m,c}(t), t_n^{m,s}(t)\}$ coefficients was approximated by fourth-order (cubic) B-splines during the CHAMP and *Swarm* time intervals such that for instance g_n^m are described as

$$g_n^m(t) = \sum_{l=1}^{L} g_{n,l}^m M_l(t) \tag{4.26}$$

where $M_l(t)$ are the B-spline functions having L basis functions (Green and Silverman, 1993; De Boor, 2001). Changing the spline order or the number of knots the corresponding fit will change accordingly; to low order will not capture enough structure while to many knot points may result in over fitting. Spline representation have often be employed in present day field modelling (e.g. Constable and Parker, 1988; Finlay et al., 2016b). Here cubic splines were used for the the internal, external and toroidal coefficients obtained during the CHAMP and *Swarm* data intervals, i.e. they were built having two continuous derivatives, a temporal knot space every 6 months and using four-folded knots at the end points, an approach mimicking that described in Olsen et al. (2009); during CHAMP time the end points were $t = 2002.4$ and $t = 2010.4$ yielding 15 interior knots at $\{2002.9, ..., 2009.9\}$ and 4 exterior knots at each end point given a total of 19 basic B-spline functions. Since the internal coefficients were determined for $n \in [1, 20]$ this resulted in 8360 internal coefficients. VO data prior to 2002.4 had significant gaps and were therefore excluded, also VO gaps during the selected time interval were filled by CHAOS-6-x5 model estimates; during *Swarm* time end points were $t = 2014.5$ and $t = 2018.0$ yielding 6 interior knots at $\{2015.0, ..., 2017.5\}$ and 4 exterior knots at each end point given a total of 10 basic B-spline functions. Since the internal coefficients were determined for $n \in [1, 20]$ this yielded 4400 coefficients. The spline fit approach used here was conducted using various Matlab tools, see *https://se.mathworks.com/help/curvefit/types-of-splines-ppform-and-b-form.html* and *https://se.mathworks.com/help/curvefit/constructing-and-working-with-b-form-splines.html* and *https://se.mathworks.com/help/curvefit/spcol.html*: *augknt* was used to generate the knot sequences as well as providing boundary knots, the B-spline collocation matrix was build using the *spcol* function. A piecewise polynomial form was formed using *fn2fm* applying *spmak* to put together the spline in B-form. The expansion coefficients was then determined using the Matlab function *fnval* on the piecewise polynomial form. To solve the problem a damped least squares solution was implemented

$$\min||\underline{\underline{\mathbf{G}}}\mathbf{m} - \mathbf{d}||_2^2 + \alpha^2||\underline{\underline{\mathbf{L}}}\mathbf{m}||_2^2 \tag{4.27}$$

where $\underline{\underline{\mathbf{G}}}$ is the spline design matrix, $\mathbf{m}$ is the model vector, $\mathbf{d}$ is the data vector (i.e. the estimated coefficients at the given epochs) and $\underline{\underline{\mathbf{L}}}$ approximates the first derivative of the spline design matrix (note that other constraints could be implemented such as the third derivative). Thus the solution is written

$$\mathbf{m} = (\underline{\underline{\mathbf{G}}}^T \underline{\underline{\mathbf{W}}}\ \underline{\underline{\mathbf{G}}} + \alpha^2 \underline{\underline{\mathbf{L}}}^T \underline{\underline{\mathbf{L}}}^{-1}) \underline{\underline{\mathbf{G}}}^T \underline{\underline{\mathbf{W}}}\mathbf{d} \tag{4.28}$$

were $\underline{\underline{\mathbf{W}}}$ is a weighting matrix containing Huber weights (a data covariance matrix was not implemented). The model parameters were estimated using a regularized iteratively reweighted least squares procedure using Huber weights with elements refined each iteration (Olsen, 2002; Olsen et al., 2009). A series of α values were investigated with a solution converging after about 10 iterations. The value of α was selected based on visual inspections of the power spectrum and global field maps. The Huber weights were determined from the residuals e_i^k between the ith data, d_i^{obs}, and model $d_i^{model,k}$ element, for the kth

iteration as $e_i^k = d_i^{obs} - d_i^{model,k}$. Normalized residuals ϵ_i^k were determined as

$$\epsilon_{i,k} = \frac{|e_i^k|}{\sigma_i} \tag{4.29}$$

where σ_k is the estimated standard deviation computed by the weighted root mean square of the data. For the kth iteration the weights were determined as $w_{i,k} = max(c_w/\epsilon_{i,k}, 1)$ or equivalently

$$w_{i,k} = \begin{cases} 1 & ,\text{if } |\epsilon_{i,k}| < c_w \\ \frac{c_w}{\epsilon_{i,k}} & ,\text{if } |\epsilon_{i,k}| \geq c_w \end{cases} \tag{4.30}$$

The Huber tuning constant was selected to be $c_w = 1.5$. An initial setup was required allowing for the iterative calculations to be performed, selected as a model vector of zeros. The weighted residual means and root mean square deviations were determined as Olsen et al. (2009)

$$mean = \frac{\sum_i w_i e_i}{\sum_i w_i} \tag{4.31}$$

$$rms = \sqrt{\frac{\sum_i w_i e_i^2}{\sum_i w_i}} \tag{4.32}$$

Cubic spline fits to the external and toroidal parts were performed as well, using the same value for α as for the internal part. The resulting field model produced was called *VO_vect_SH.01*. Figures 4.22 and 4.23 present time series of the first time derivatives of the internal Gauss coefficients of the spline model (in green), $\{dg_n^m/dt, dh_n^m/dt\}$, for SH degrees $n \in [1, 7]$ in units of [nT/yr]. Also shown are 12-month running mean of the first differences (i.e. a moving average (boxcar) filter having a filter length of 12 months) in blue dots and the CHAOS-6-x5 predictions (in red). Figure 4.24 a) and b) presents the external coefficients $\{dq_n^m/dt, ds_n^m/dt\}$ and toroidal coefficients $\{dt_n^{m,c}/dt, dt_n^{m,s}/dt\}$ of the spline models, respectively, for SH degrees $n \in [1, 2]$ in units of [nT/yr]. Importantly, considering these external and toroidal coefficients no strong variation was found, demonstrating that the adopted strategy of data selection and processing along with VO model setup has successfully reduced, but not completely removed, the major contaminating contributions in the signal. Looking at the external and toroidal parts and comparing with those of Olsen and Mandea (2007), it is clear that a significant reduction of these terms has taken place. This is probably a result of removing the model estimates of the external field, and using dark, quiet time data.

Figure 4.25 presents the power spectra of the secular variation (in blue) and acceleration (in red) of the VO field model (stipulated lines) and CHAOS-6-x5 models plotted at the core surface in year 2016. Figure 4.26 a) and b) presents the SV and SA degree correlations and SV coefficient differences between the VO and CHAOS-6-x5 models. From these figures it is evident, that the SV and SA coefficients show coherence with the CHAOS-6-x5 model up to SH degrees $n = 12$ and $n = 7$. Maps of the *VO_vect_SH.01* model radial SV and SA fields up to SH degrees $n = 12$ and $n = 7$, respectively, are presented in Figure 4.27. Also shown for comparison are maps of the predictions of the CHAOS-6-x5 model up to the same degrees. Clearly, both SV and SA patches observed in the VO model agree with those present in the CHAOS-6-x5 model. However, it is also evident that contamination in the polar regions has leaked into the VO model SV and SA estimates. The reason for the distinct SA field patches around Antarctica may be due to lack of data at the South Pole. It should be noted that the CHAOS-6-x5 model is based on scalar data in the polar regions, whereas the model *VO_vect_SH.01* is based on all three field vector components.

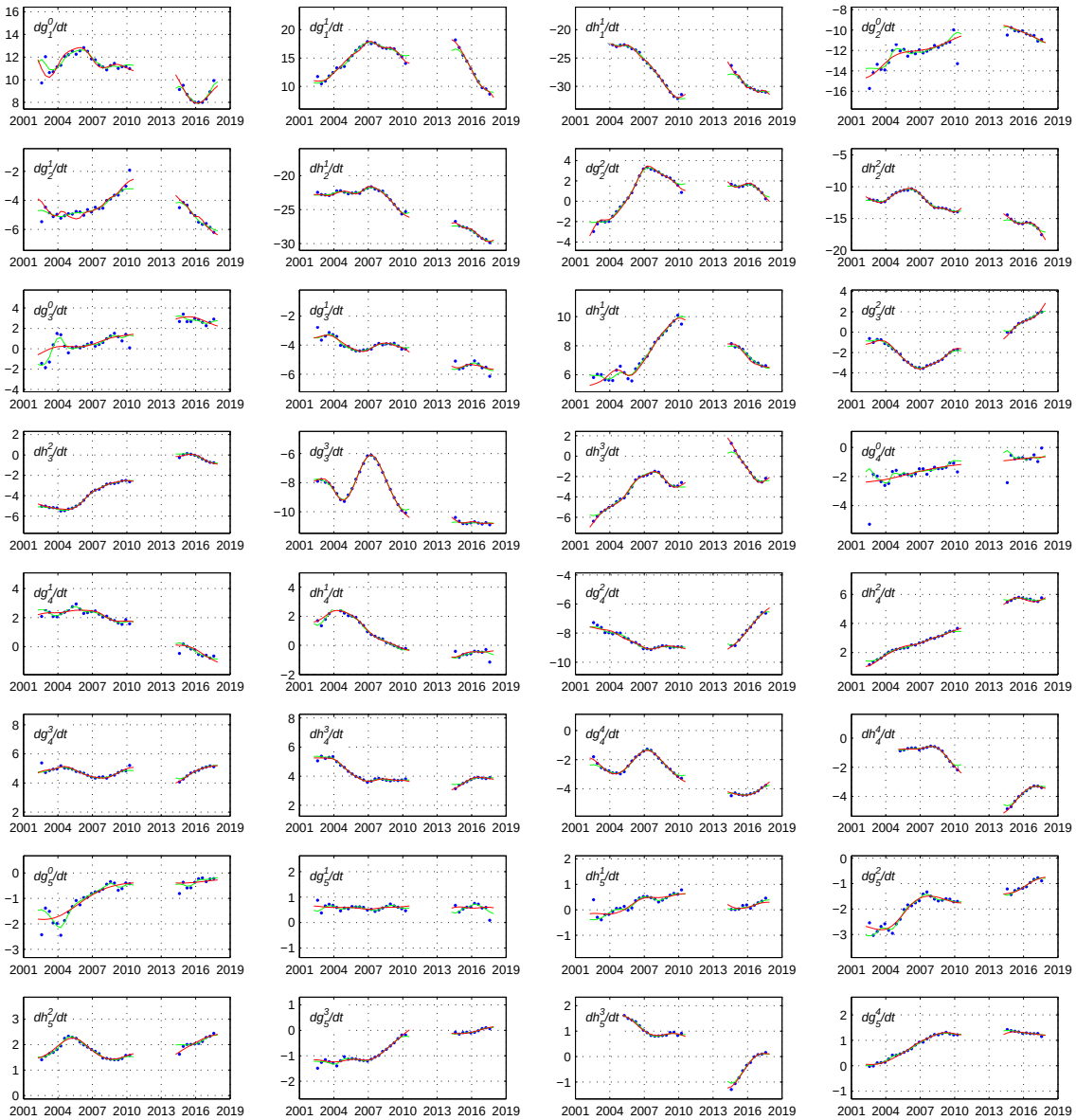

Figure 4.22: The first time derivatives of the internal Gauss coefficients, $\{dg_n^m/dt, dh_n^m/dt\}$ in [nT/yr]. The blue symbols are 12-month running mean of the first differences and the CHAOS-6-x5 model predictions are in red. The green curve is the model *VO_vect_SH.01* using cubic B-spline with 6-month knot spacing fit to the 4-monthly values.

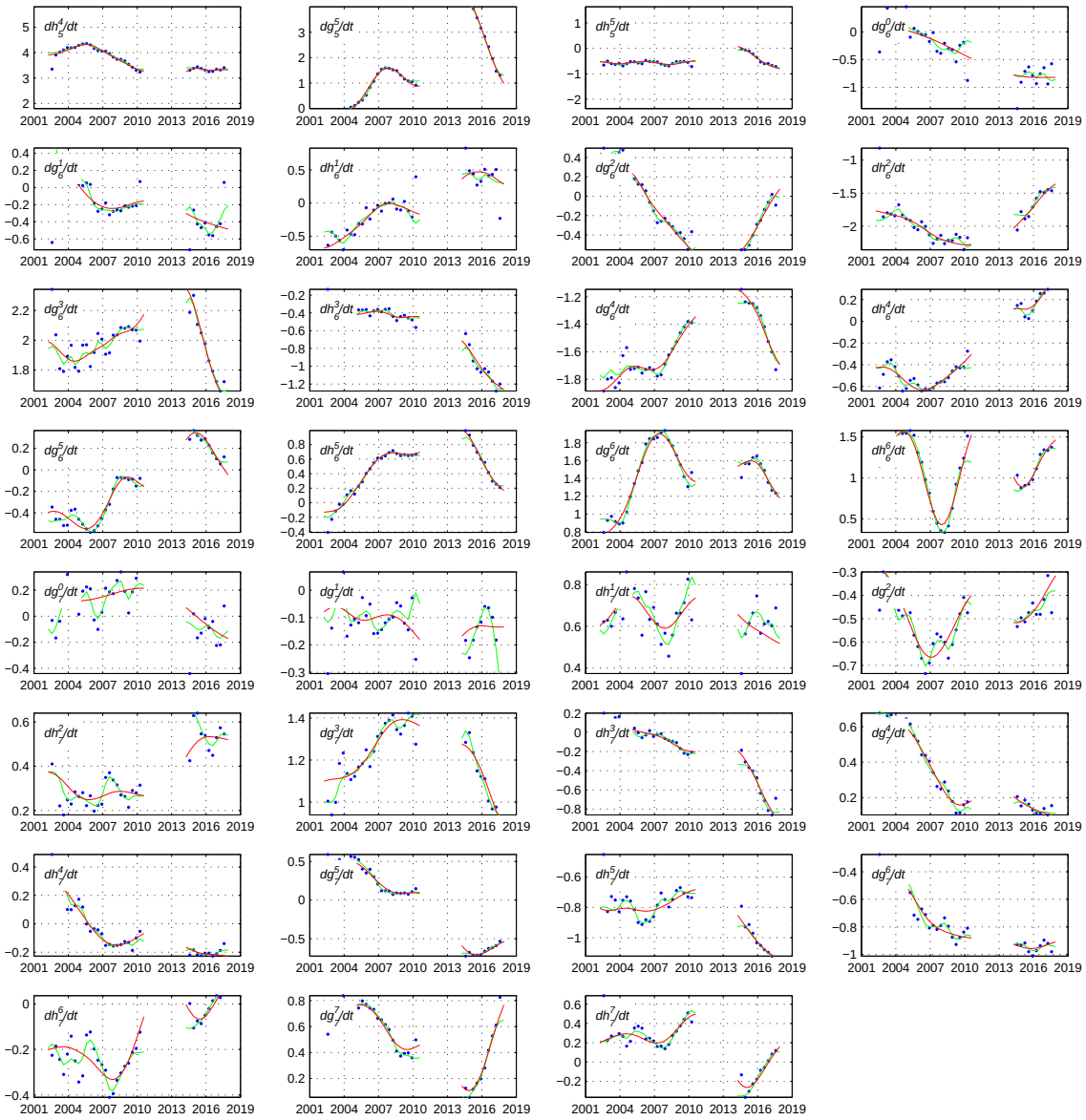

Figure 4.23: Continuation of Figure 4.22.

The VO concept is especially well suited for investigating global patterns of sharp changes in the first time derivative of the field. Following figure 2 of Olsen and Mandea (2007), Figures 4.28, 4.29 and 4.30 present global VO times series of the field components dZ/dt, dX/dt and dY/dt, respectively. These are shown at VO altitudes for segments of $10^\circ \times 20^\circ$ from the $5^\circ \times 5^\circ$ regular grid during the CHAMP (plots a) and *Swarm* (plots b) eras. The left and right end points of each curve corresponds to epochs 2002 and 2010.5 for CHAMP and epochs 2014.5 and 2018 for *Swarm*, respectively. The locations of the VO's are marked by black dots, the blue curves are the 12-month running mean of the first differences of the internal field (as estimated through the SHA), while in red and green are the internal field predictions from the CHAOS-6-x5 and VO models, respectively. These plots demonstrates the usefulness of the VO method to globally consider both the short and longer period variations of the field; i) the polar regions are seen to exhibit noticeable variations related to contamination, ii) both the *VO_vect_SH.01* and the CHAOS-6-x5

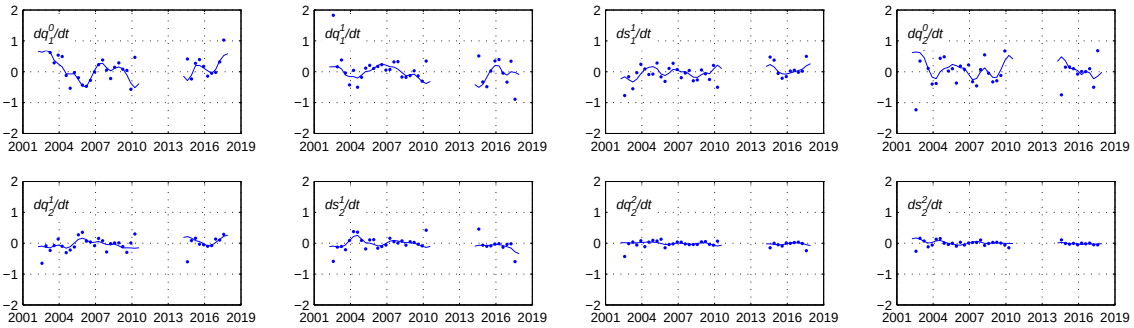

(a) First time derivatives of the external coefficients $\{dq_n^m/dt, ds_n^m/dt\}$.

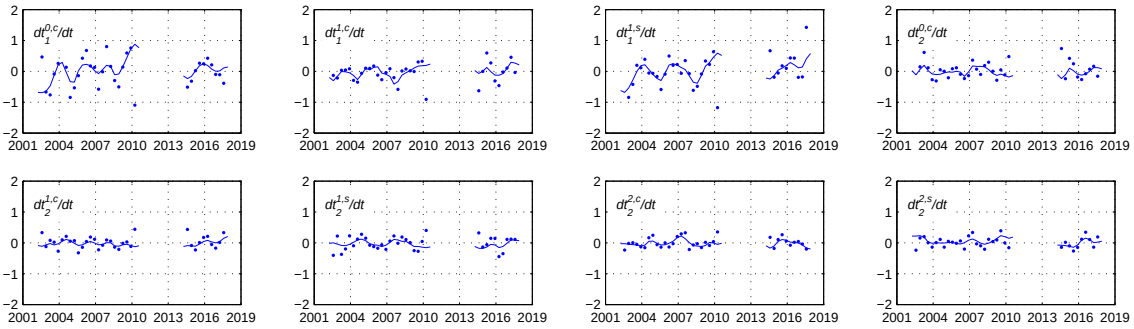

(b) First time derivatives of the toroidal coefficients $\{dt_n^{m,c}/dt, dt_n^{m,s}/dt\}$.

Figure 4.24: First time derivatives of a) external, $\{dq_n^m/dt, ds_n^m/dt\}$, and b) toroidal, $\{dt_n^{m,c}/dt, dt_n^{m,s}/dt\}$, coefficients in (nT/yr). The blue symbols are 12-month running mean of first differences of the external and toroidal fields as estimated through the SHA. Note the scale as compared to the internal Gauss coefficients in Figures 4.22 and 4.23.

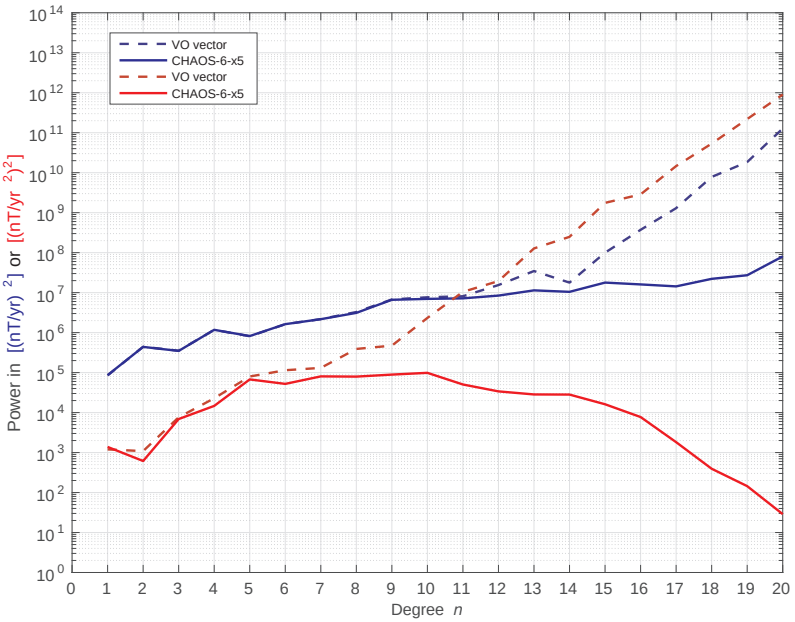

Figure 4.25: Core surface power spectra for secular variation and acceleration in 2016. The SV and SA of the *VO_vect_SH.01* (dotted) and CHAOS-6-x5 models are showing in blue and red, respectively.

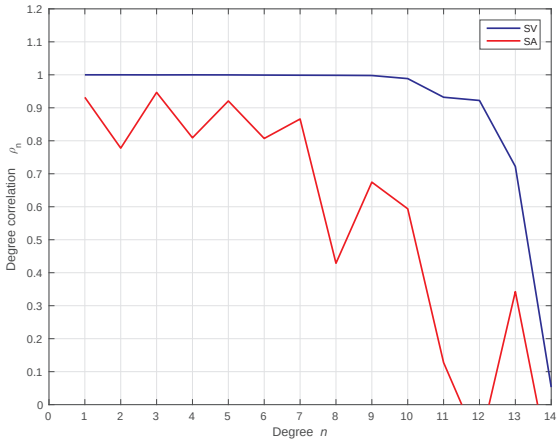

(a) Degree correlation between the VO and CHAOS-6-x5 model for SV coefficients $n = 1 - 20$ for 2016.0.

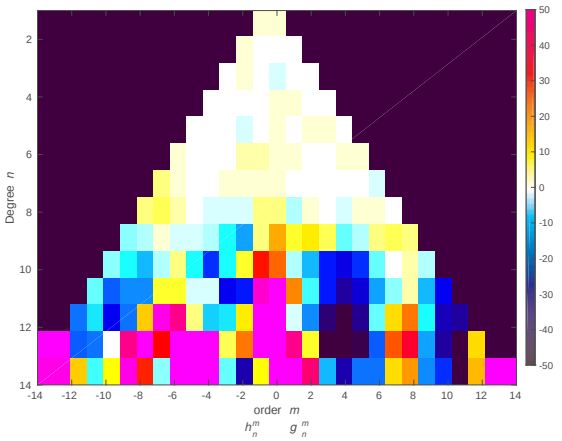

(b) Sensitivity matrix in units (nT/yr), showing VO and CHAOS-6-x5 model differences for SV coefficients $n = 1 - 14$ for 2016.0.

Figure 4.26: Radial SV and SA degree correlation (left) and SV sensitivity matrix (right) between *VO_vect_SH.01* and CHAOS-6-x5 models in 2016.

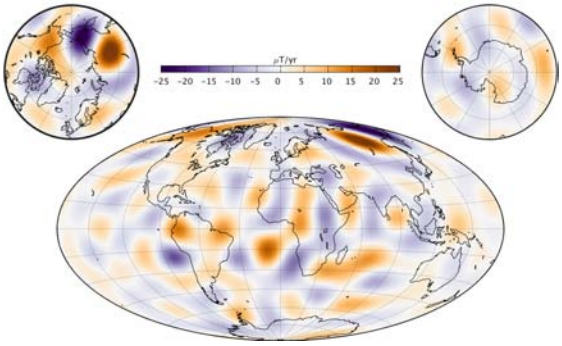

(a) *VO_vect_SH.01* model SV radial field up to SH degree $n = 12$ at CMB in 2016.0.

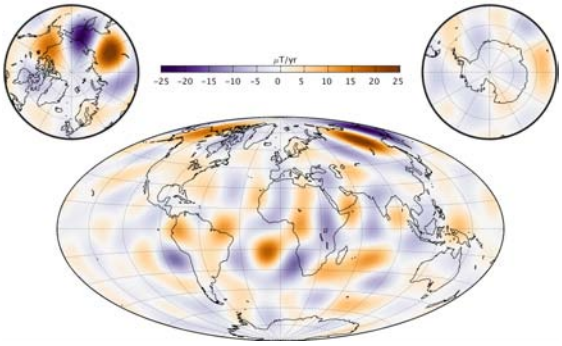

(b) CHAOS-6-x5 model SV radial field up to SH degree $n = 12$ at CMB in 2016.0.

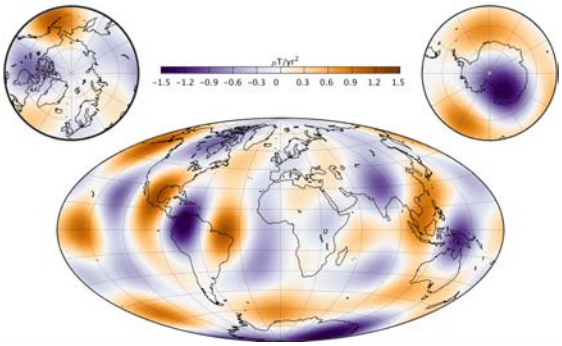

(c) *VO_vect_SH.01* model SA radial field up to SH degree $n = 7$ at CMB in 2016.0.

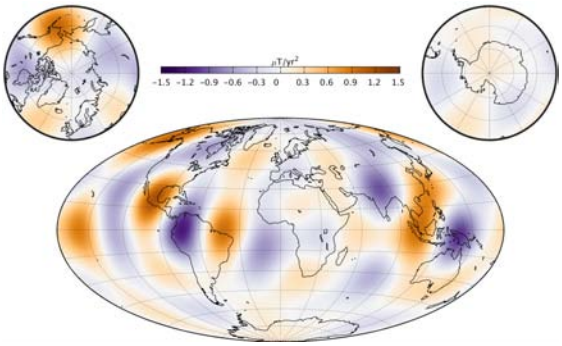

(d) CHAOS-6-x5 model SA radial field up to SH degree $n = 7$ at CMB in 2016.0.

Figure 4.27: Global radial SV (top) and SA (bottom) fields at the CMB in 2016.0, comparing the *VO_vect_SH.01* (left figures) and CHAOS-6-x5 (right figures) models.

models generally reproduce the data seen although some short time variations are not captured, iii) jerk events such as the 2007 jerk seen as a strong "V" dip in the dZ/dt and "Λ" in the dY/dt VO curves in the region around the South Atlantic ocean during CHAMP time, may easily be identified in such plots. Interestingly, the *VO_vect_SH.01* model gives indication of a jerk-like "V" change in the dZ/dt and possibly in the dY/dt slope of the VO time series in the Pacific region around 2016, and also changes around South America may be observed in dZ/dt. In order to properly asses these changes, longer time series are needed. Interestingly, global maps of the radial SA in Figure 4.27, show activity in the Pacific and South American regions around 2016.

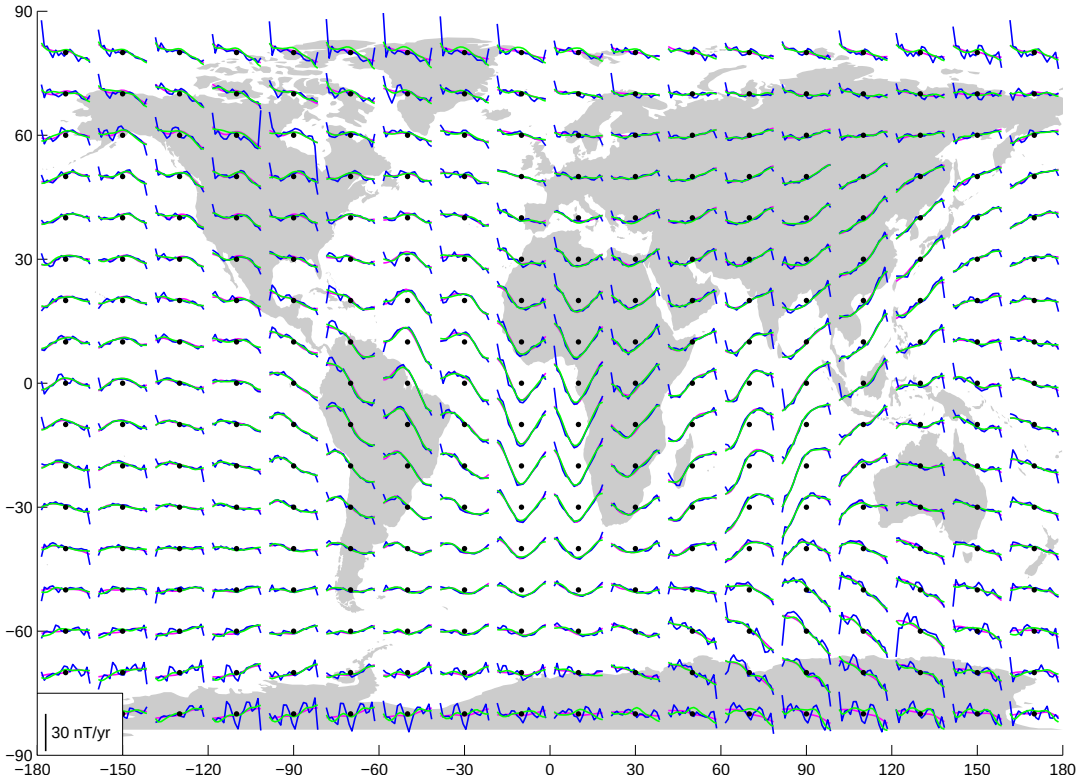

(a) dZ/dt during CHAMP period from 2002-2010 at 370km altitude.

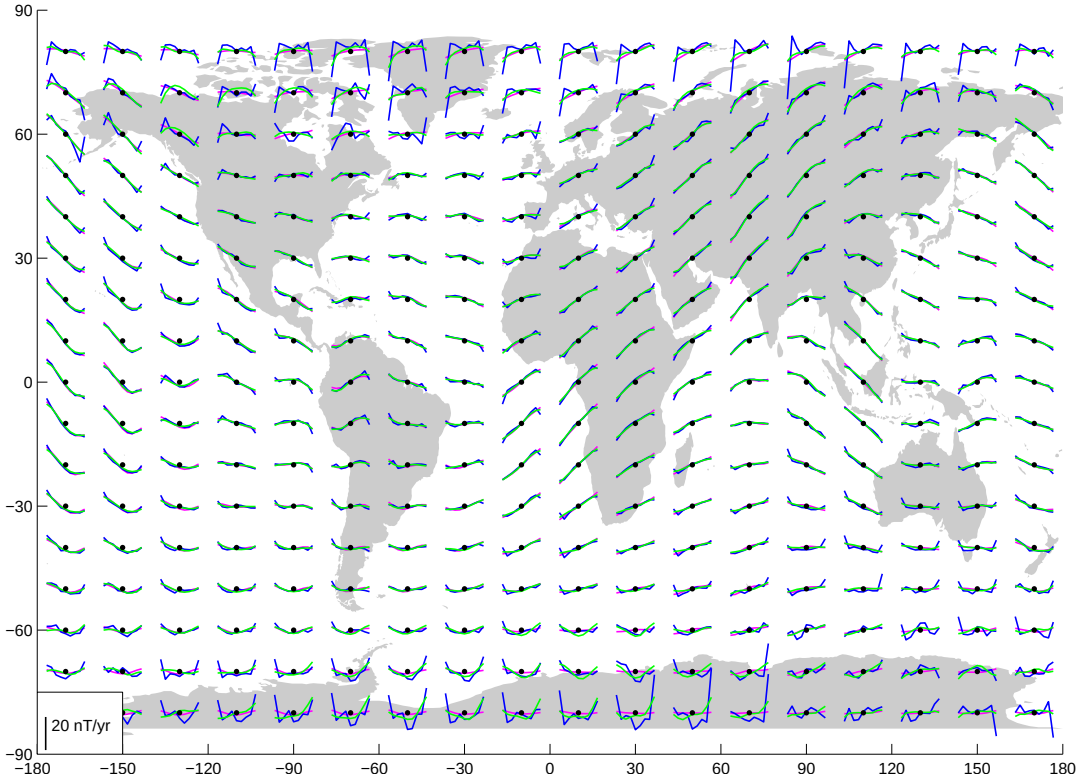

(b) dZ/dt during *Swarm* period from 2014-2017 at 490km altitude.

Figure 4.28: Global time series of dZ/dt for CHAMP (top) and *Swarm* (bottom) periods in a regular grid. Blue symbols are the 12-month running mean of the first differences of the internal field (as estimated through the SHA), in red and green are the internal field predictions from the CHAOS-6-x5 and *VO_vect_SH.01* models.

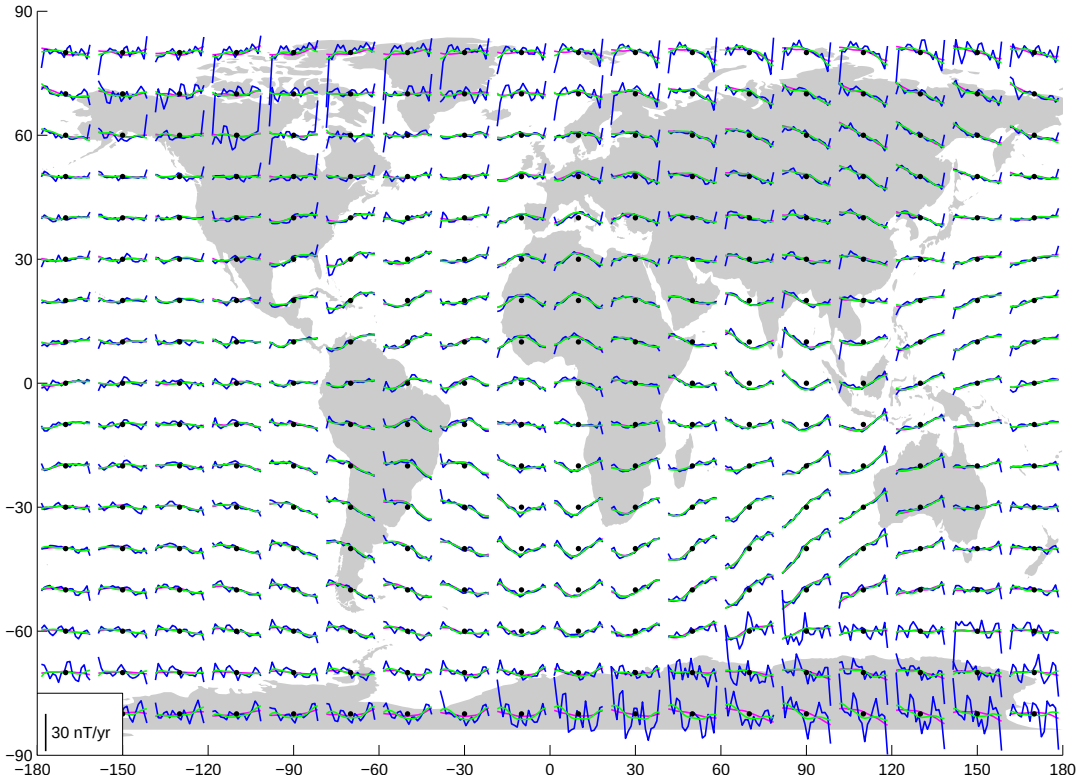

(a) dX/dt during CHAMP period from 2002-2010 at 370km altitude.

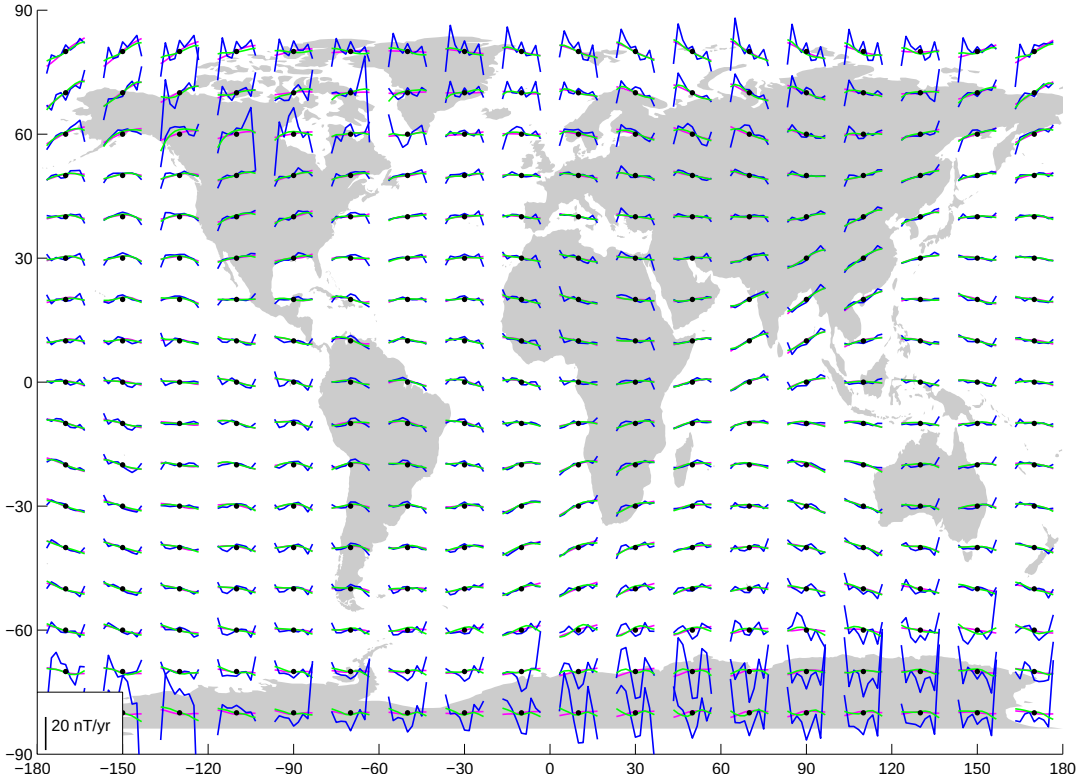

(b) dX/dt during *Swarm* period from 2014-2017 at 490km altitude.

Figure 4.29: Global time series of dX/dt for CHAMP (top) and *Swarm* (bottom) periods in a regular grid. Blue symbols are the 12-month running mean of the first differences of the internal field (as estimated through the SHA), in red and green are the internal field predictions from the CHAOS-6-x5 and *VO_vect_SH.01* models.

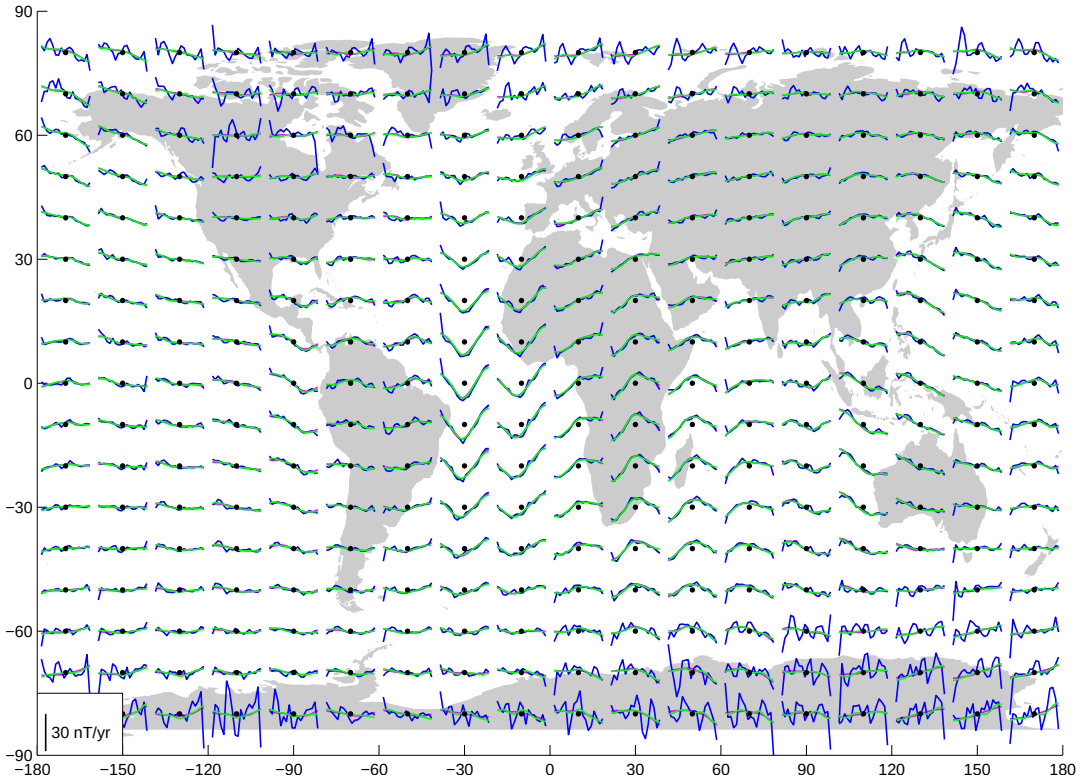

(a) dY/dt during CHAMP period from 2002-2010 at 370km altitude.

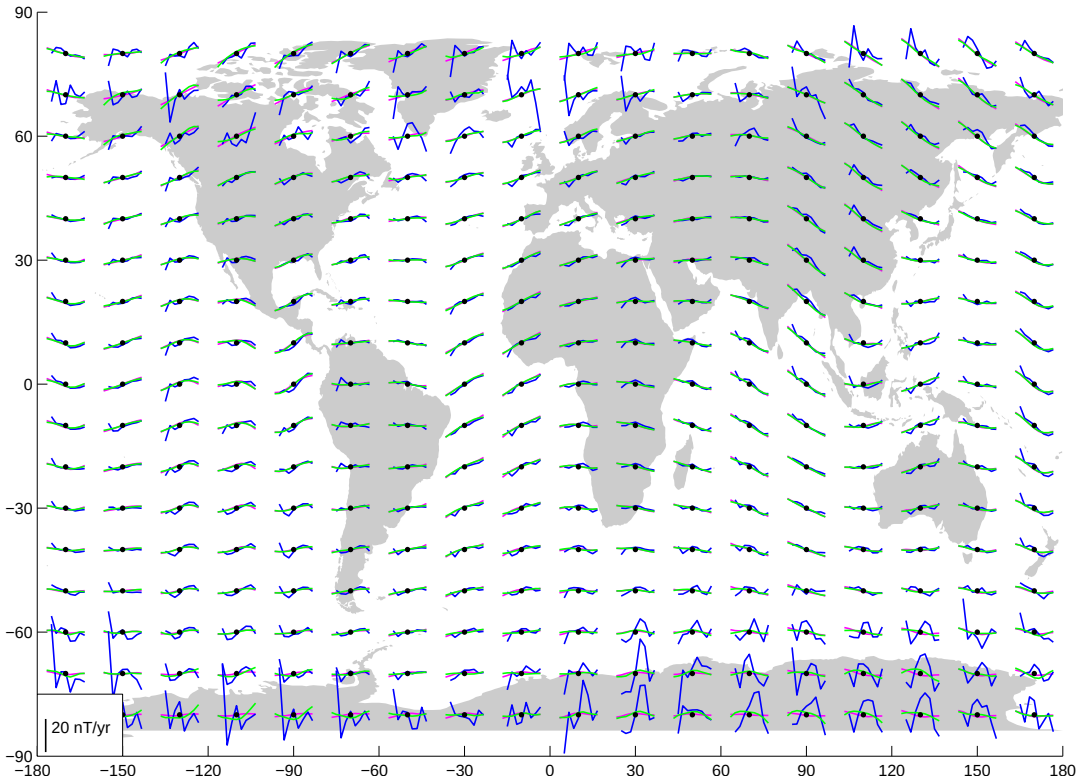

(b) dY/dt during *Swarm* period from 2014-2017 at 490km altitude.

Figure 4.30: Global time series of dY/dt for CHAMP (top) and *Swarm* (bottom) periods in a regular grid. Blue symbols are the 12-month running mean of the first differences of the internal field (as estimated through the SHA), in red and green are the internal field predictions from the CHAOS-6-x5 and *VO_vect_SH.01* models.

4.6 VO Model Results II: Field Gradient Computations

This section presents results of gradient computations obtained for the magnetic field and its temporal variations using the VO method. Section 4.6.1 presents examples of VO time series of annual differences of the main and secular variation gradient fields computed at some of the selected ground observatory sites listed in Section 4.4.1. Section 4.6.2 presents results of VO application to an EQ global grid, determining data error covariance estimates obtained for the field gradients. Section 4.6.3 presents a spherical harmonic analysis performed for an EQ grid of globally distributed VO's with the specific intention to investigate the construction of field models based on field gradients. The field gradients were constructed as described in Section 4.3.3, by the VO model parameters.

4.6.1 Time Series at Ground Observatory Sites

Figures 4.31 to 4.35 presents VO time series of annual differences of the gradient field, i.e. the SV of the gradients, and the SA of the gradients computed from annual differences of the SV of the gradients, at the selected ground observatories. Shown with red dots are the VO estimates and with the blue curves the CHAOS-6-x5 model predictions at the VO altitudes during CHAMP and *Swarm* periods for SH degrees $n \in [1, 16]$. The plots are organized such that they show the upper right structure of the gradient tensor (in order to make a visual pleasing presentation of the tensor content, the lower left triangle of the tensor is not shown, since the tensor is symmetric).

For each station the top plots show the SV gradient estimates while the bottom plots show the SA gradient estimates; here six field gradient components are shown. As with the field cases the VO model results and the CHAOS-6-x5 model predictions overall show good agreement. Interestingly, the VO gradient time series are able to track rapid temporal changes seen as "V" or "Λ" shape features in the SV gradient components and as step changes "/" or "\" shape features centred on zero in the SA gradient components. Considering the 2007 jerk, this is easily identified at the VO time series above the Ascension Island (ASC), Hermanus (HER), Mbour (MBO) and Tristan da Cunha (TDC) observatories, via the above mentioned behaviour. It appears that jerks are most easily identified in the components $d(\partial B_r/dr)/dt$, $d(\partial B_\theta/dr)/dt$ and $d(\partial B_\phi/dr)/dt$. Furthermore, another interesting feature is observed at the VO time series at the Gan (GAN) observatory located in the Indian Ocean, seen as changing behaviour of the $d(\partial B_\phi/d\theta)/dt$ and associated $d^2(\partial B_\phi/d\theta)/dt^2$ components.

From the uncertainty estimates, presented in the next section, it is expected that these are higher during the CHAMP than the *Swarm* era, and pronounced in the $d(\partial B_r/dr)/dt$ SV component, and the $d^2(\partial B_r/dr)/dt^2$, $d^2(\partial B_\phi/r)/dt^2$ and $d^2(\partial B_\phi/\phi)/dt^2$ SA gradient components.

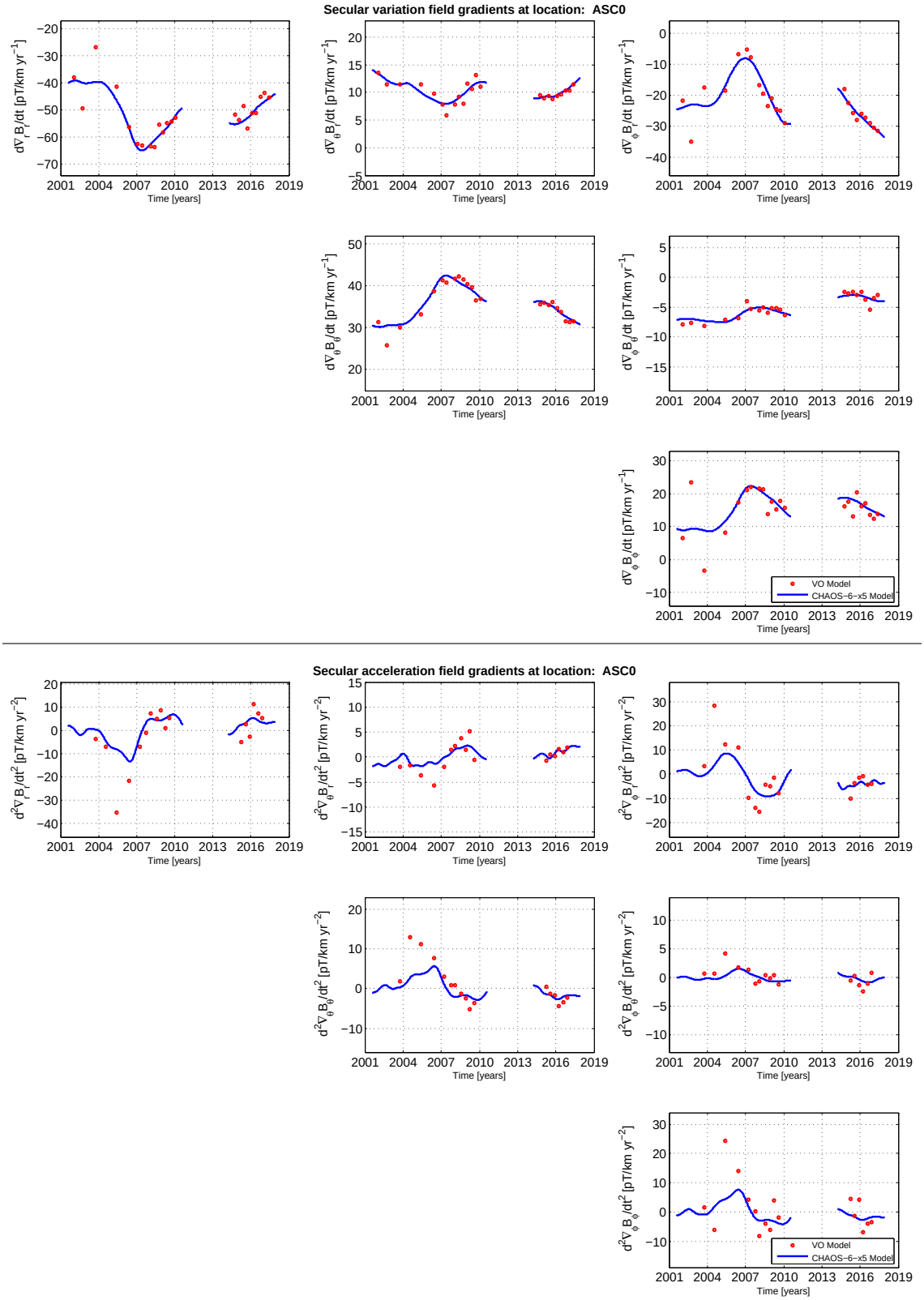

Figure 4.31: SV (top) and SA (bottom) field gradients at selected observatories showing VO (red dots) and CHAOS-6-x5 (blue curve) estimates. CHAOS-6-x5 estimates were computed using SH degrees up to $n = 16$. Because the gradient tensor is symmetric the three lower left components have been omitted for clarity.

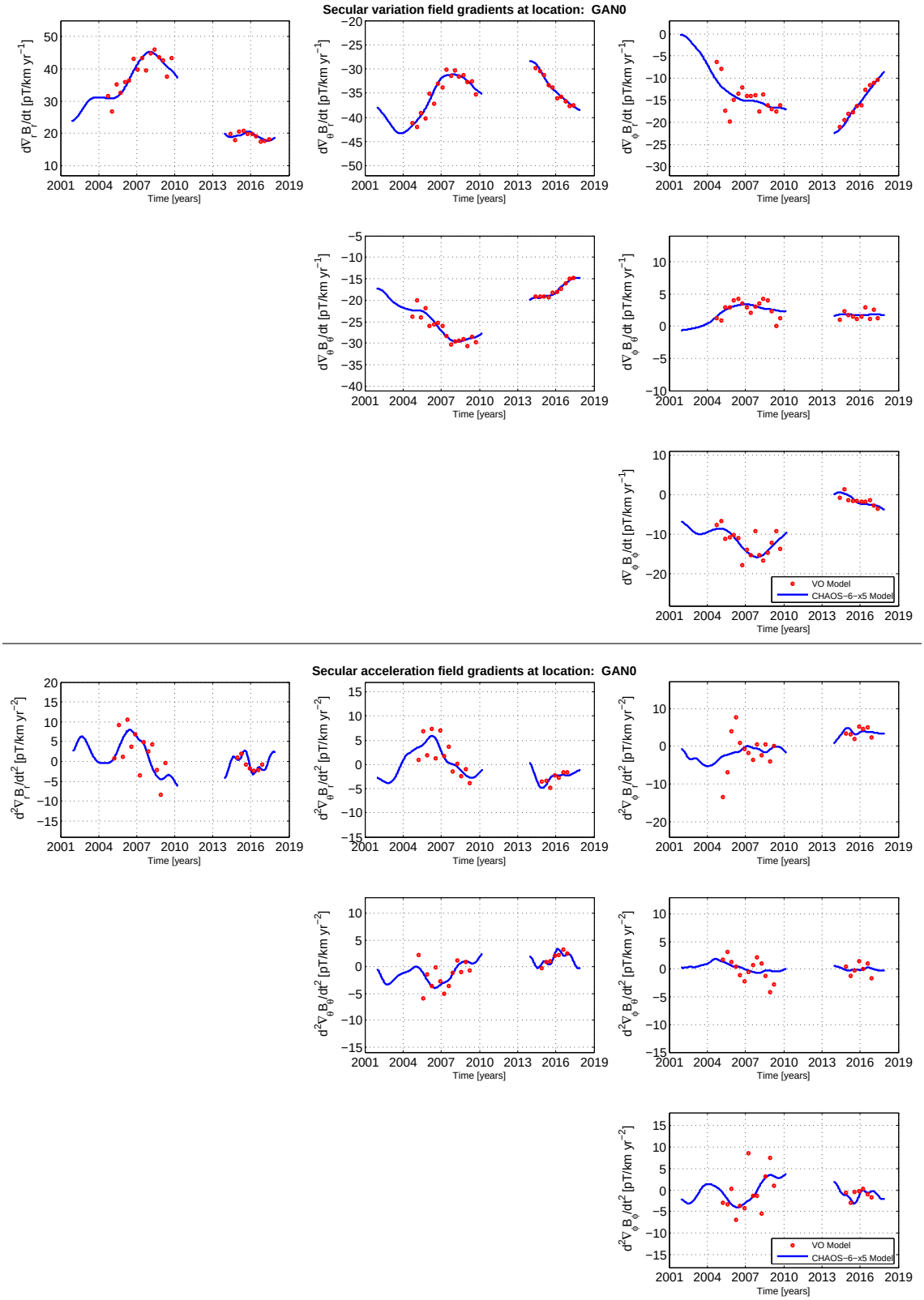

Figure 4.32: SV (top) and SA (bottom) field gradients at selected observatories showing VO (red dots) and CHAOS-6-x5 (blue curve) estimates. CHAOS-6-x5 estimates were computed using SH degrees up to $n = 16$. Because the gradient tensor is symmetric the three lower left components have been omitted for clarity.

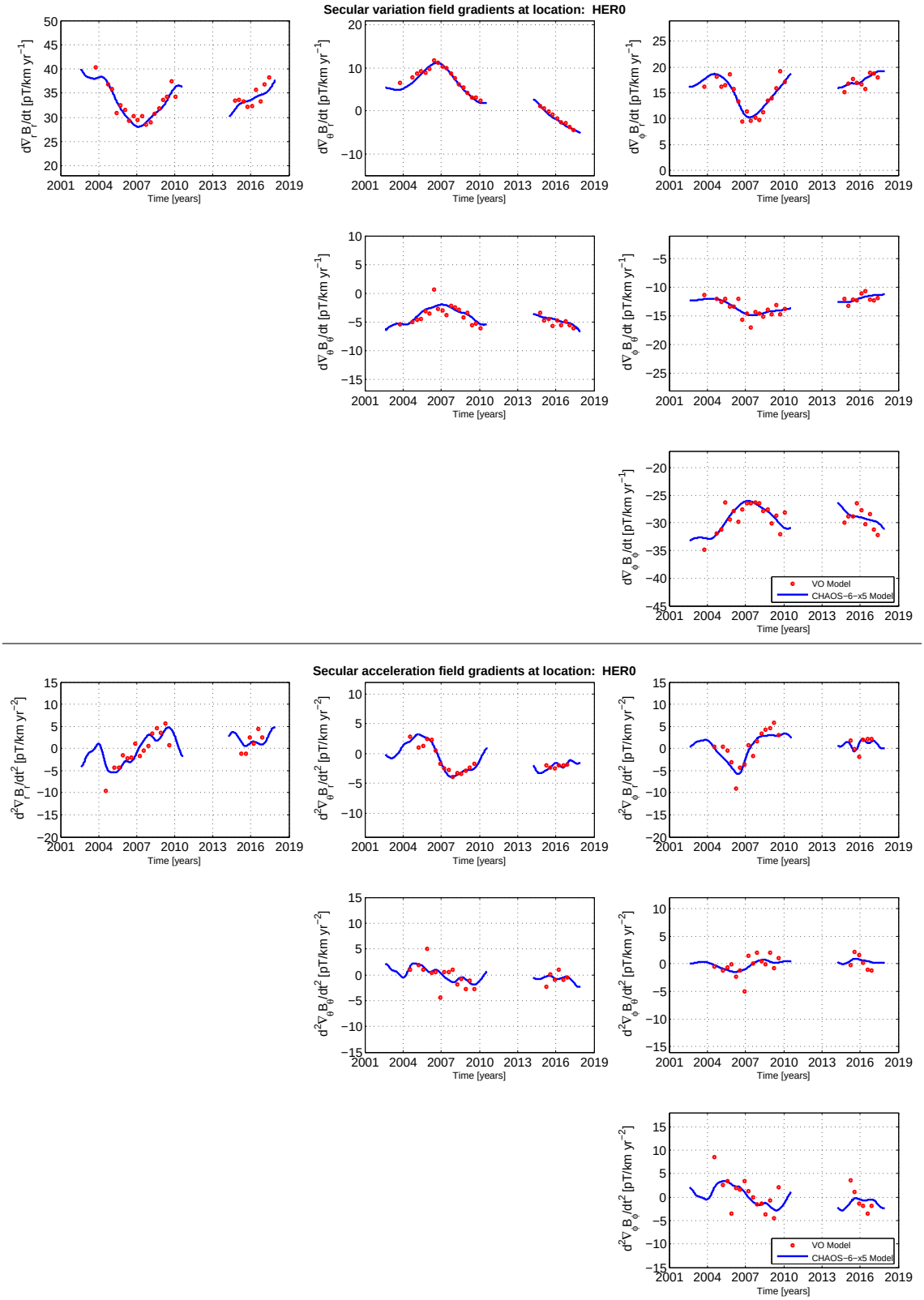

Figure 4.33: SV (top) and SA (bottom) field gradients at selected observatories showing VO (red dots) and CHAOS-6-x5 (blue curve) estimates. CHAOS-6-x5 estimates were computed using SH degrees up to $n = 16$. Because the gradient tensor is symmetric the three lower left components have been omitted for clarity.

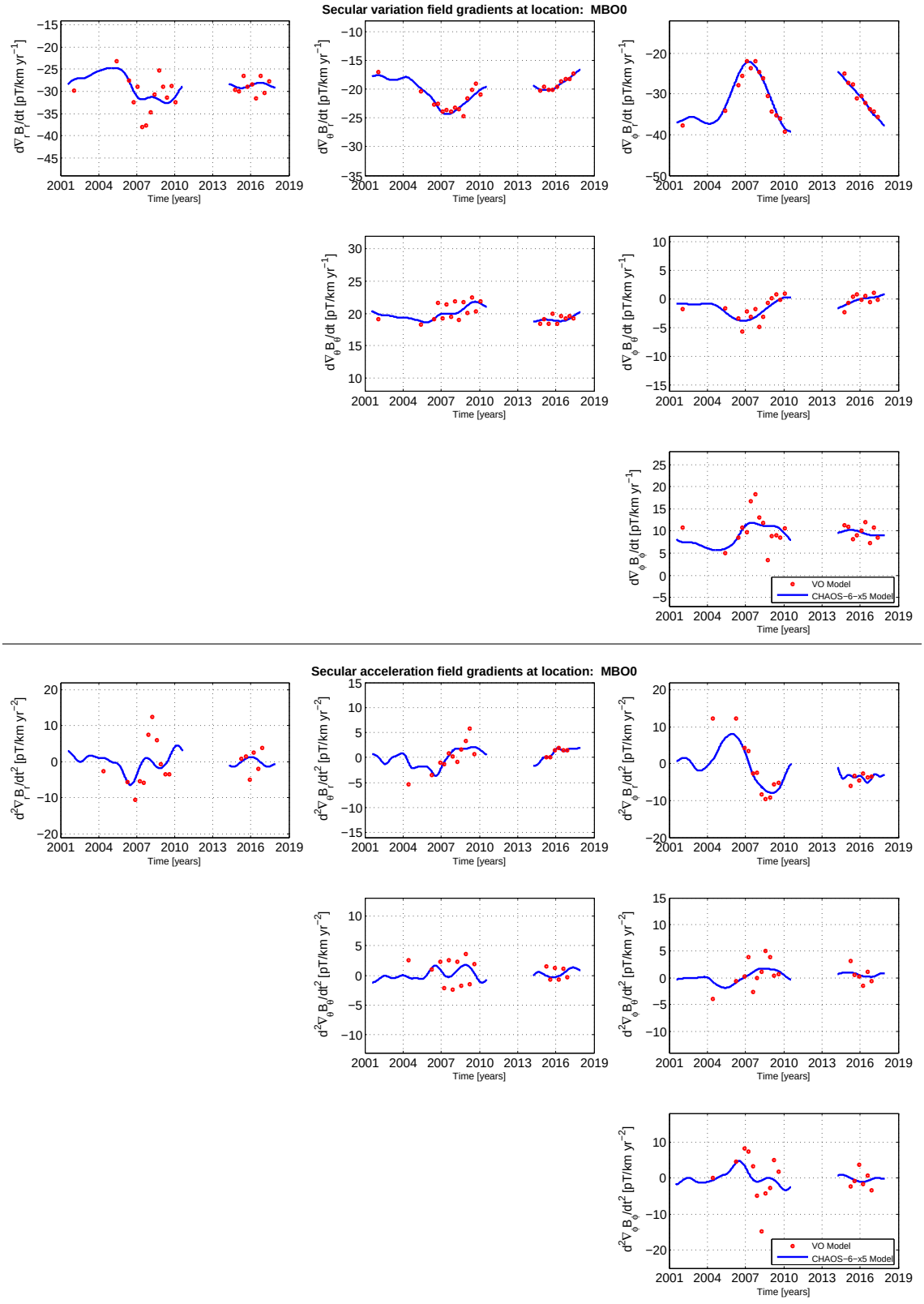

Figure 4.34: SV (top) and SA (bottom) field gradients at selected observatories showing VO (red dots) and CHAOS-6-x5 (blue curve) estimates. CHAOS-6-x5 estimates were computed using SH degrees up to $n = 16$. Because the gradient tensor is symmetric the three lower left components have been omitted for clarity.

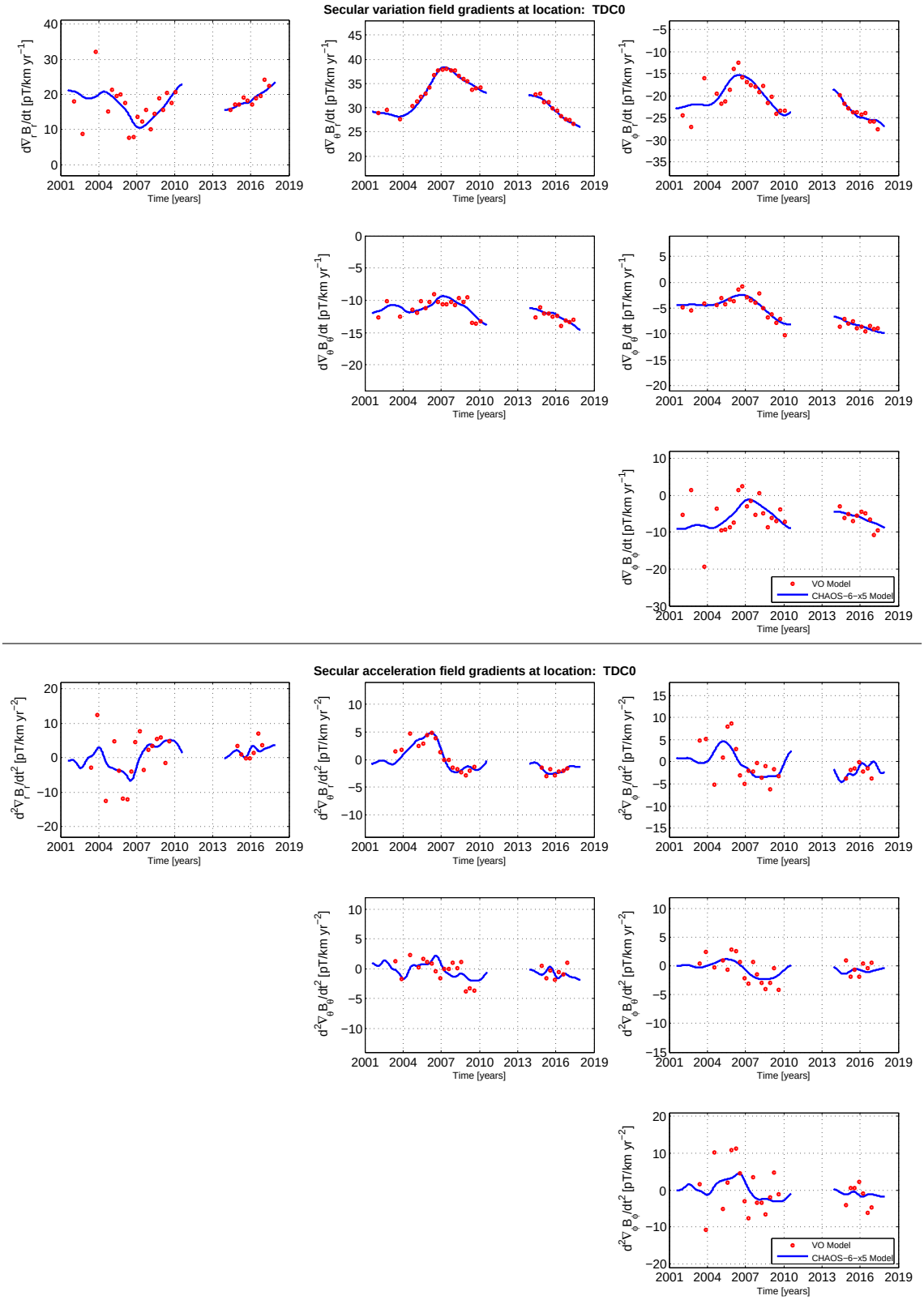

Figure 4.35: SV (top) and SA (bottom) field gradients at selected observatories showing VO (red dots) and CHAOS-6-x5 (blue curve) estimates. CHAOS-6-x5 estimates were computed using SH degrees up to $n = 16$. Because the gradient tensor is symmetric the three lower left components have been omitted for clarity.

4.6.2 Data Error Covariance Matrices

Similar to the approach of Section 4.5.4, diagonal covariance matrices for the VO gradient time series of the MF and SV gradients have been computed using a similar procedure to that adopted for the MF and SV field cases. However, the size of the covariance matrices are now $6P \times 6P = 1800 \times 1800$ since there are 300 VOs having six components. The derivation follows the same procedure described previously in Section 4.5.4. Again it should be noted that the errors are expected to be correlated which in principle should be described by a full covariance matrix having off-diagonal elements. Figures 4.36 and 4.38 presents the variances for each component of the main field gradients, in units of $[(\mathrm{pT/km})^2]$ during *Swarm* and CHAMP times, respectively. Figures 4.37 and 4.39 present the variances for each component of the SV gradients, in units of $[(\mathrm{pT/kmyr}^{-1})^2]$, during *Swarm* and CHAMP time, respectively. It appears that the horizontal gradients of the radial field may be less disturbed at polar regions which may be beneficial for internal field modelling. For the SV gradient components during *Swarm* time there seems to be smaller deviations from CHAOS predictions at mid and low latitudes, compared to the CHAMP era when there were larger uncertainty estimates.

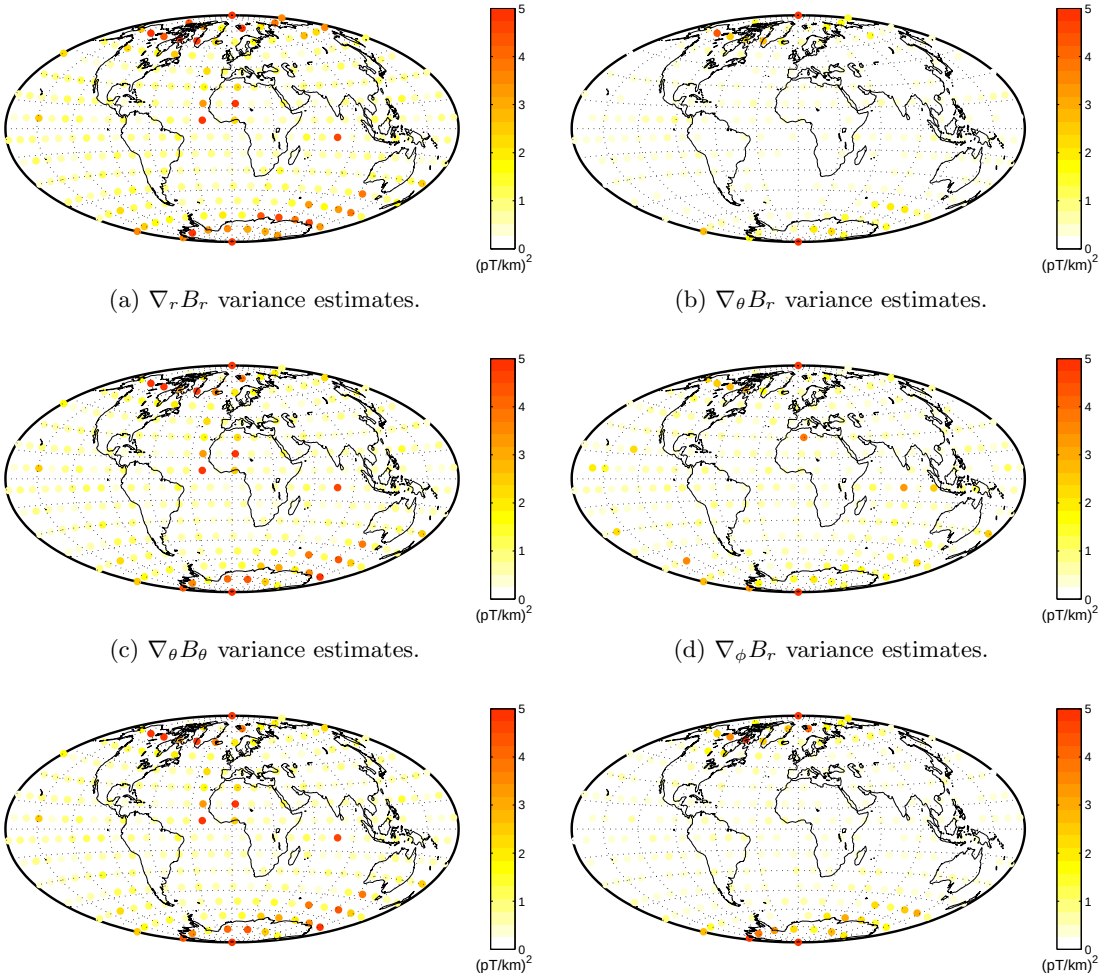

(a) $\nabla_r B_r$ variance estimates.

(b) $\nabla_\theta B_r$ variance estimates.

(c) $\nabla_\theta B_\theta$ variance estimates.

(d) $\nabla_\phi B_r$ variance estimates.

(e) $\nabla_\phi B_\phi$ variance estimates.

(f) $\nabla_\theta B_\phi$ variance estimates.

Figure 4.36: MF gradient variance estimates during *Swarm* time.

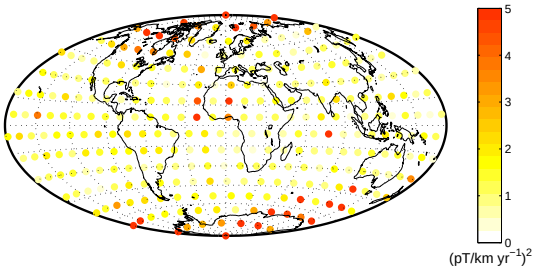

(a) $d\nabla_r B_r/dt$ variance estimates.

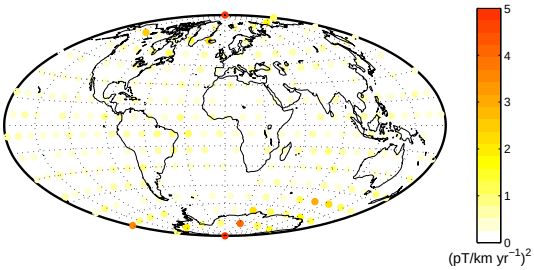

(b) $d\nabla_\theta B_r/dt$ variance estimates.

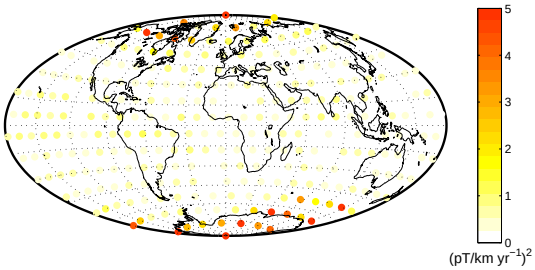

(c) $d\nabla_\theta B_\theta/dt$ variance estimates.

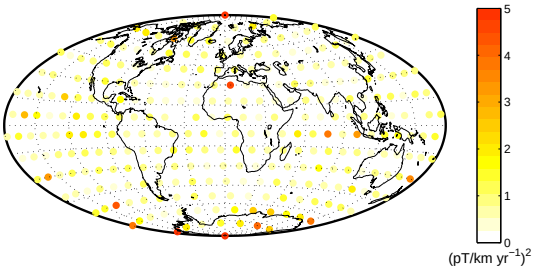

(d) $d\nabla_\phi B_r/dt$ variance estimates.

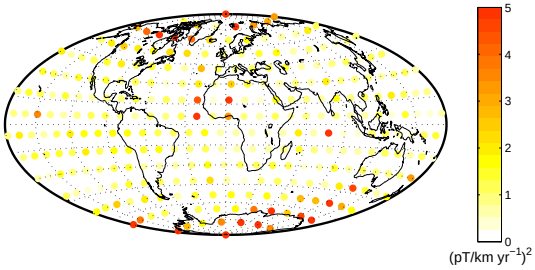

(e) $\nabla_\phi dB_\phi/dt$ variance estimates.

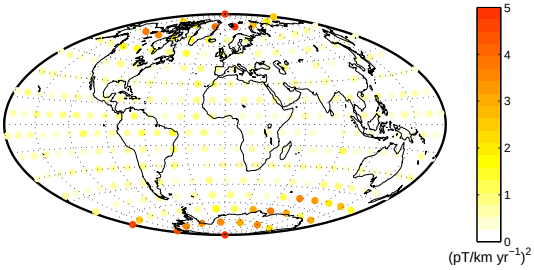

(f) $d\nabla_\theta B_\phi/dt$ variance estimates.

Figure 4.37: SV gradient variance estimates during *Swarm* time.

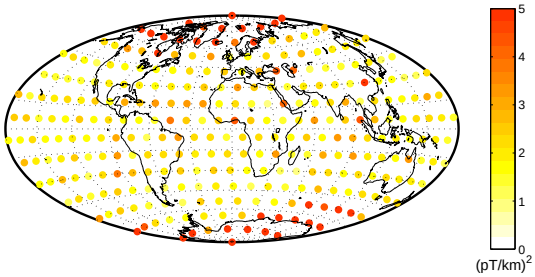

(a) $\nabla_r B_r$ variance estimates.

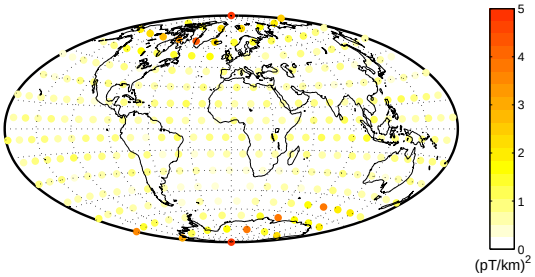

(b) $\nabla_\theta B_r$ variance estimates during *Swarm*.

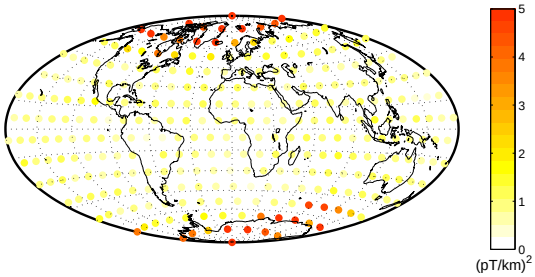

(c) $\nabla_\theta B_\theta$ variance estimates.

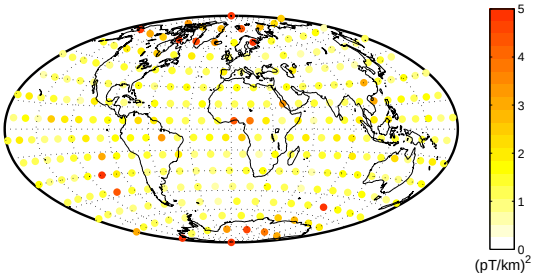

(d) $\nabla_\phi B_r$ variance estimates.

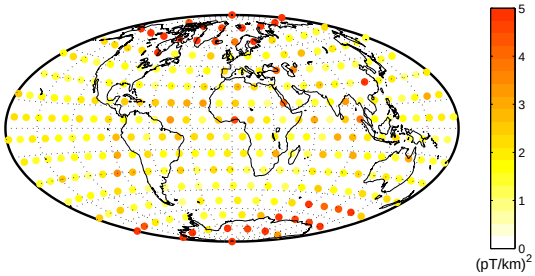

(e) $\nabla_\phi B_\phi$ variance estimates.

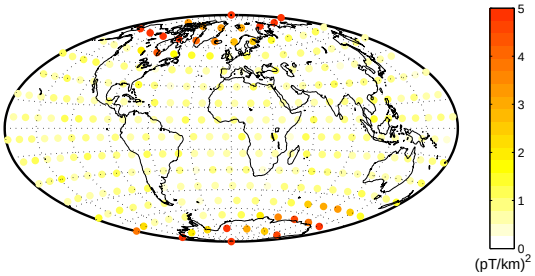

(f) $\nabla_\theta B_\phi$ variance estimates.

Figure 4.38: MF gradient variance estimates during CHAMP time.

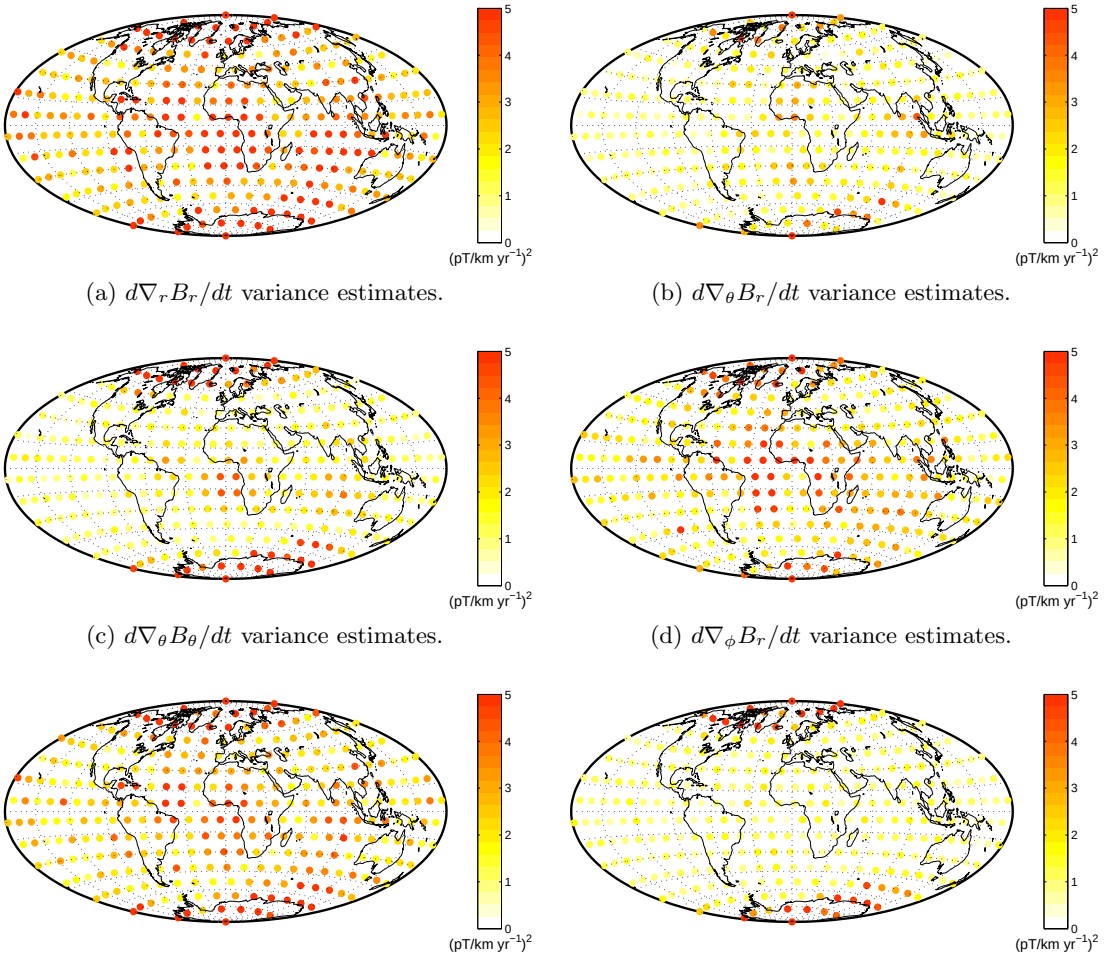

(a) $d\nabla_r B_r/dt$ variance estimates.

(b) $d\nabla_\theta B_r/dt$ variance estimates.

(c) $d\nabla_\theta B_\theta/dt$ variance estimates.

(d) $d\nabla_\phi B_r/dt$ variance estimates.

(e) $d\nabla_\phi B_\phi/dt$ variance estimates.

(f) $d\nabla_\theta B_\phi/dt$ variance estimates.

Figure 4.39: SV gradient variance estimates during CHAMP time.

4.6.3 SH Field Model from VO Gradient Data

In this section results using a purely internal SH field model are reported, with a B-spline-representation of the time-dependence, built from *Swarm* VO gradient data, from version 0105, provided in an EQ grid having 300 VO's. The main purpose here is to demonstrate that field models can indeed be constructed from VO gradients and to investigate whether these might offer improved insight into field structures. The procedure for computing the gradient models follow that of Section 4.5.5; that is, for each epoch in the VO data series an inversion for the expansion coefficients was performed truncating the expansion at SH degree $n = 20$. However, in this particular case, SV rather than MF (which was used in Section 4.5.5) VO time series was used. The three vector components, $\{\dot{B}_r, \dot{B}_\theta, \dot{B}_\phi\}$, along with the six gradient components, $\{\nabla_r \dot{B}_r, \nabla_\theta \dot{B}_\theta, \nabla_\phi \dot{B}_\phi, \nabla_r \dot{B}_\theta, \nabla_r \dot{B}_\phi, \nabla_\theta \dot{B}_\phi\}$, were used to invert for the internal expansion coefficients. As the VO data was given in an EQ grid the model coefficients were estimated using a least squares solution (instead of using the SH transform algorithm as used in Section 4.5.5). Here a Matlab script for constructing the gradient design matrices was kindly provided by Stavros Kotsiaros. Afterwards an order five spline approximation was used to describe the time-dependence using 6 month knot spacing and five-folded knots at the end points $t = 2014.5$ and $t = 2017.5$, thus yielding

5 interior knots at (2015,2015.5,...,2017.0) and five exterior knots at each end point given a total of 10 B-spline basis functions. Since the internal coefficients were determined for $n \in [1, 20]$, this gave a total of 4400 model coefficients. The resulting field models produced were: the *VO_vect_SH.02* model using vector data only, the *VO_grad_SH.02* model using gradient data only, and the *VO_vectgrad_SH.02* model using both vector and gradient data.

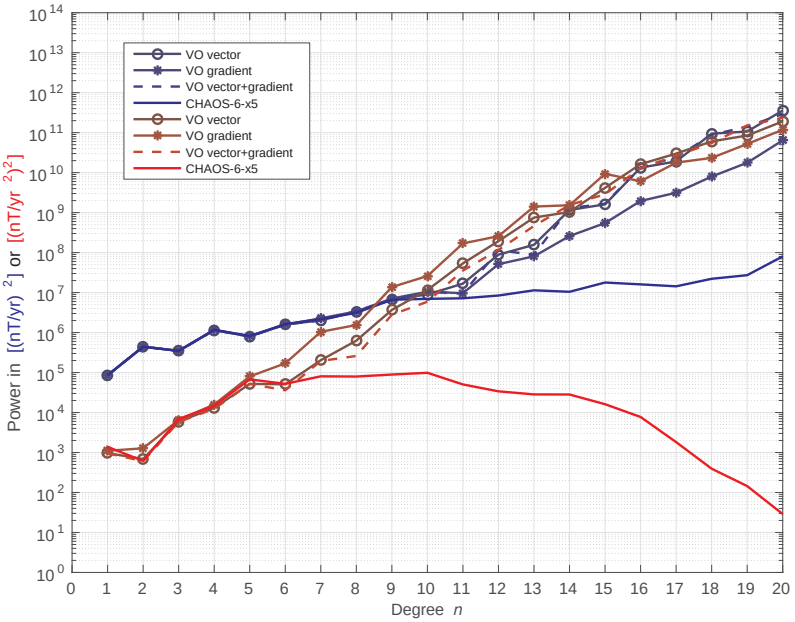

Figure 4.40: Core surface power spectra for secular variation (blue curves) and acceleration (red curves) in 2016. Spectra are shown for models *VO_vect_SH.02* (curve with circle), *VO_grad_SH.02* (curve with stars) and *VO_vectgrad_SH.02* (dashed curve). Also shown is the CHAOS-6-x5 model.

Figure 4.40 presents the power spectra of the secular variation (in blue) and acceleration (in red) of the VO (dashed lines) and CHAOS-6-x5 models evaluated at the core surface in 2016.0. The spectra are shown for models build using vector data only, field gradient data only and a combination of vector and field gradient data. Figure 4.41 a) and b) presents the SV and SA degree correlations and SV coefficient differences between the VO and CHAOS-6-x5 models, respectively. The figures compare models based on vector data only, gradient data only and a combination of vector and gradient data. For the SV case it seems that including the gradients indeed improves the model reconstruction for SH degrees 1 to 6. However, in the SA case a gradient only model appears to have lower correlation seemingly due to slightly increased power. The near zonal coefficients for higher degrees are apparently worse. This could be related to polar gaps of the VO distribution. From these figures the SV and SA coefficients show coherence with the CHAOS-6-x5 model up to SH degrees $n = 11$ and $n = 6$, respectively.

Figures 4.42 and 4.43 presents time series of the first time derivatives of the internal Gauss coefficients, $\{dg_n^m/dt, dh_n^m/dt\}$, for SH degrees $n \in [1, 7]$ in units of [nT/yr]. Shown with blue dots are the inverted coefficient values along with the VO (in green) and CHAOS-6-x5 (in red) model predictions. These are plotted for a model based on both vector and gradient field data. Using the *VO_vectgrad_SH.02* model, built using both vector and gradient data, CMB maps of the radial SV field up to SH degrees $n = 11$ and radial SA

field up to SH degrees $n = 6$ and $n = 7$ in 2016.0, are presented in Figure 4.44. Also shown for comparison are maps of the predictions of the CHAOS-6-x5 model up to the same degrees. SV field patches observed in the VO model agree well with those of the CHAOS-6-x5 model. However, contamination in the polar regions is clearly present. The reason for this could be the differences in data used between the two models; CHAOS-6-x5 used only scalar data in the polar regions. Looking at the SA map for SH degrees up to $n = 6$ shows good agreement with the field features appearing in CHAOS-6-x5, though the SA has slightly less power. Pushing towards SH degree $n = 7$ the SA patches at mid and low latitudes still exhibits agreements with CHAOS-6-x5 though it seems that patches become slightly different and noise becomes prominent in the polar regions.

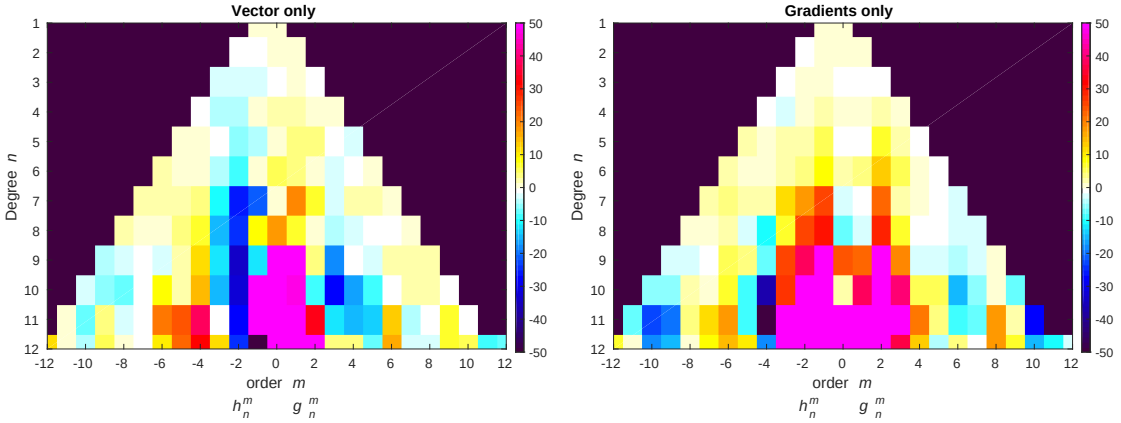

(a) Sensitivity matrix in units (nT/yr), showing *VO_vect_SH.02* and CHAOS-6-x5 model differences for SV coefficients $n = 1 - 12$ for 2016.0.

(b) Sensitivity matrix in units (nT/yr), showing *VO_grad_SH.02* and CHAOS-6-x5 model differences for SV coefficients $n = 1 - 12$ for 2016.0.

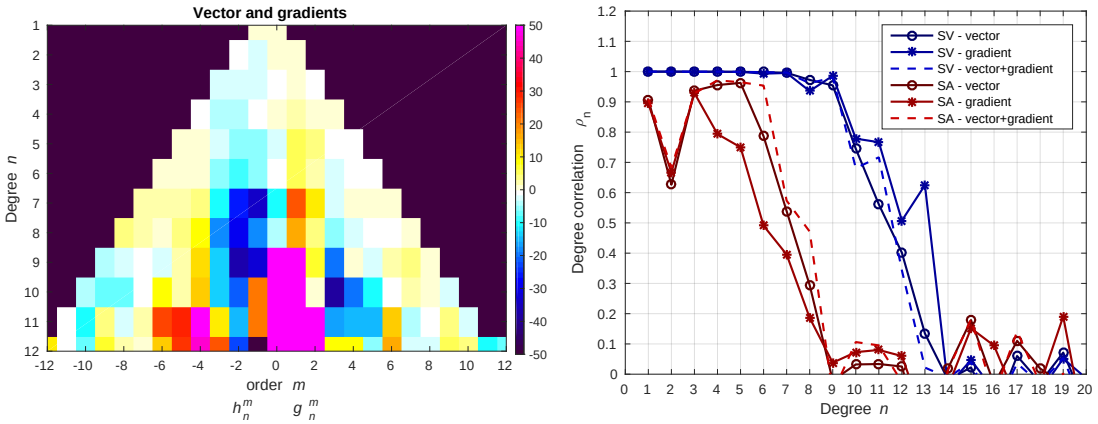

(c) Sensitivity matrix in units (nT/yr), showing *VO_vectgrad_SH.02* and CHAOS-6-x5 model differences for SV coefficients $n = 1 - 12$ for 2016.0.

(d) Degree correlation between the VO and CHAOS-6-x5 model for SV coefficients $n = 1 - 20$ for 2016.0.

Figure 4.41: SV sensitivity matrix between VO and CHAOS-6-x5 models: using vector data only (top left), field gradient data only (top right) and vector and field gradient data (bottom left). Bottom right plot shows SV degree correlation between VO and CHAOS-6-x5.

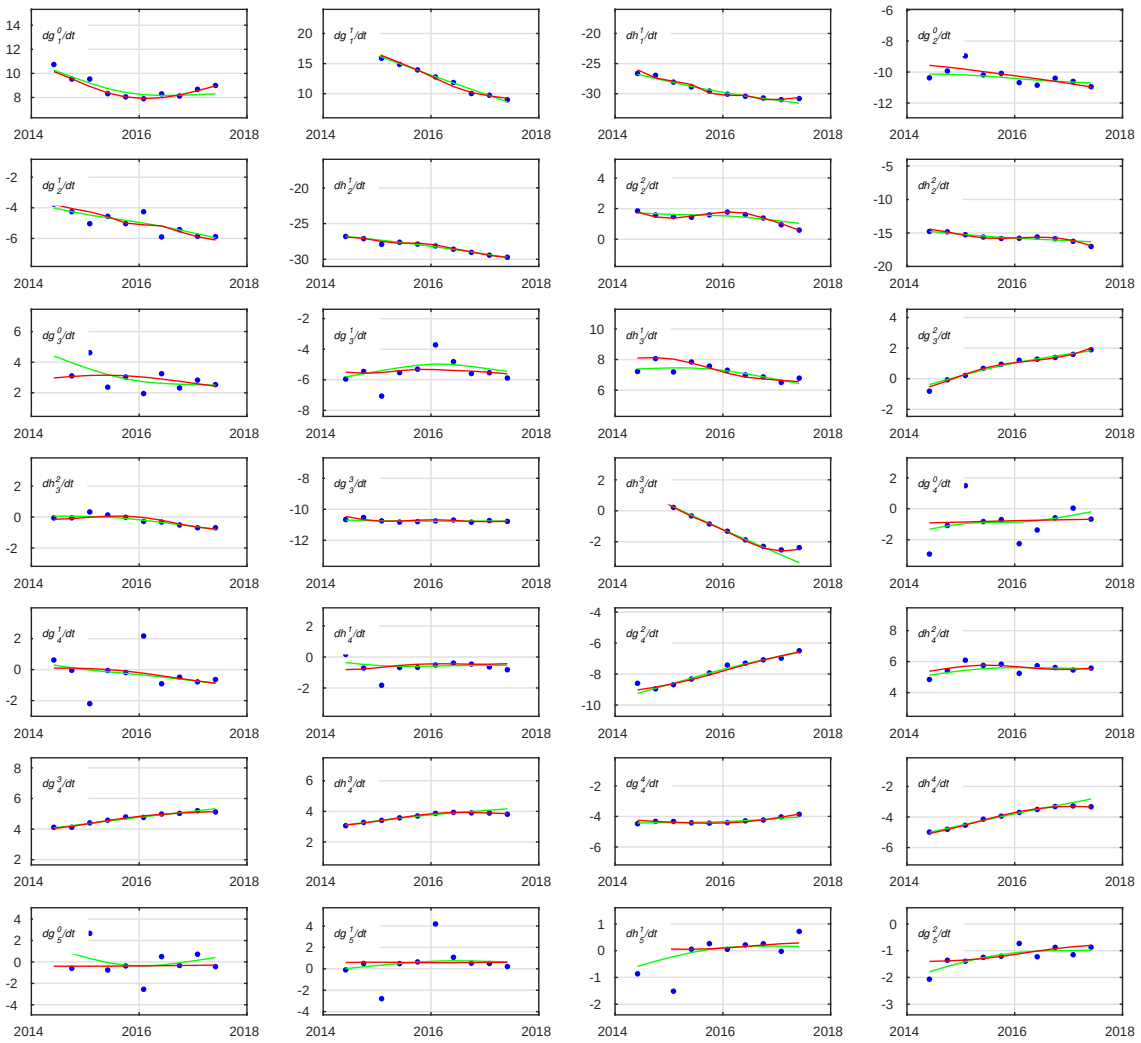

Figure 4.42: The first time derivatives of the internal Gauss coefficients, $\{dg_n^m/dt, dh_n^m/dt\}$ in [nT/yr] of the *VO_vectgrad_SH.02* model. The blue symbols are inverted coefficient values while the *VO_vectgrad_SH.02* and the CHAOS-6-x5 model predictions are in green and red, respectively.

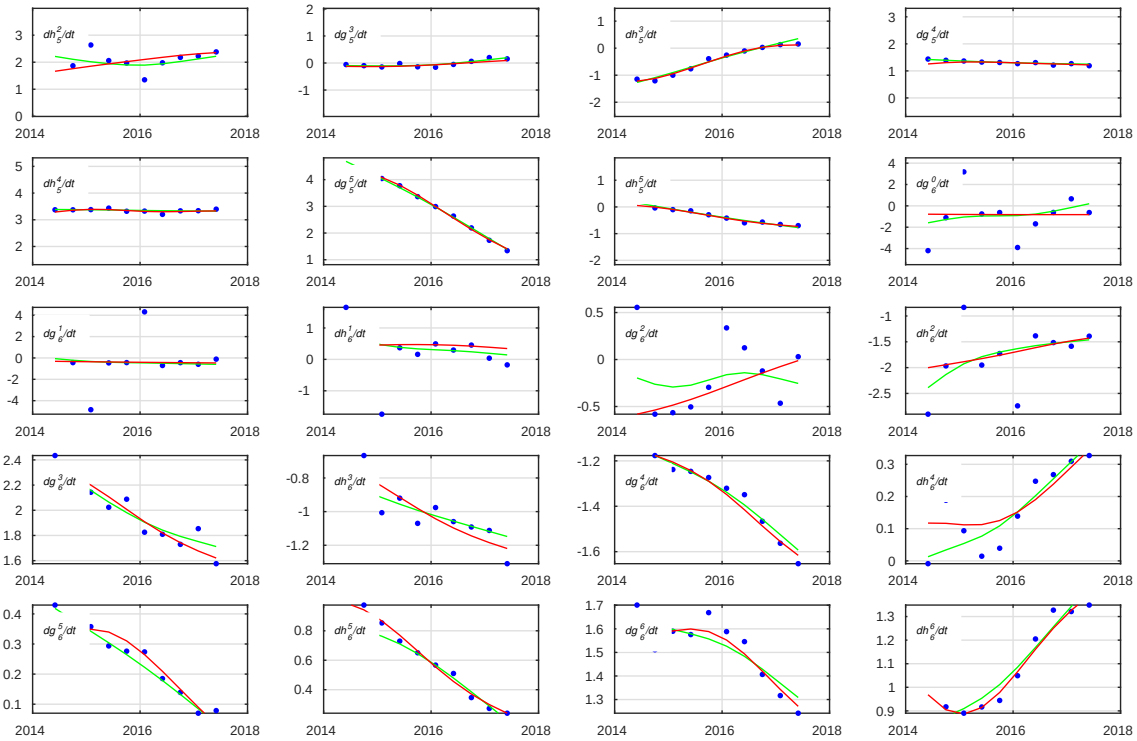

Figure 4.43: Continuation of Figure 4.43.

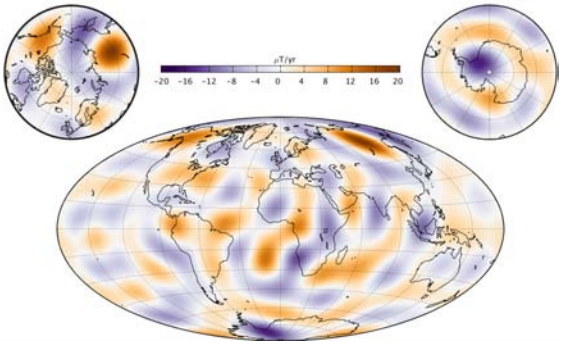

(a) *VO_vectgrad_SH.02* radial SV radial up to SH degree $n = 11$ at CMB in 2016.0.

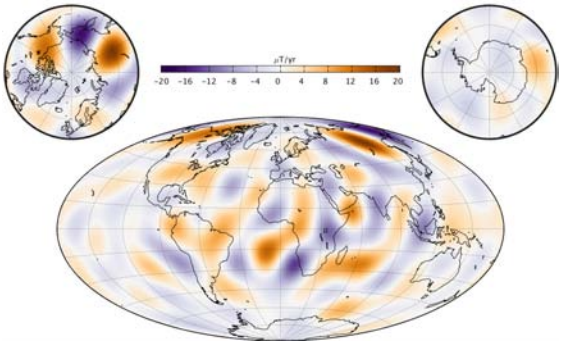

(b) CHAOS-6-x5 model radial SV up to SH degree $n = 11$ at CMB in 2016.0.

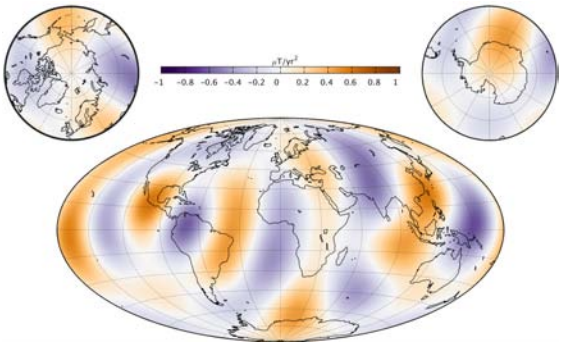

(c) *VO_vectgrad_SH.02* radial SA up to SH degree $n = 6$ at CMB in 2016.0.

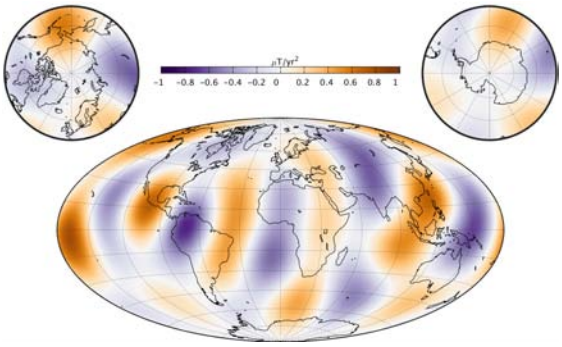

(d) CHAOS-6-x5 model radial SA up to SH degree $n = 6$ at CMB in 2016.0.

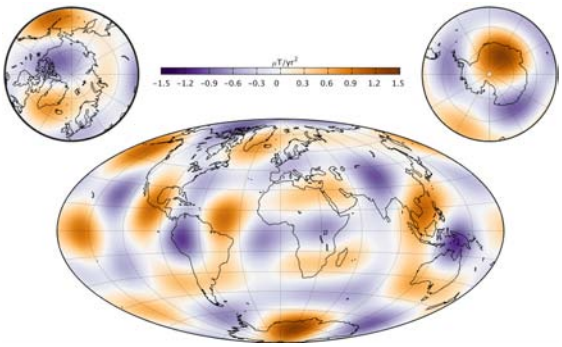

(e) *VO_vectgrad_SH.02* radial SA up to SH degree $n = 7$ at CMB in 2016.0.

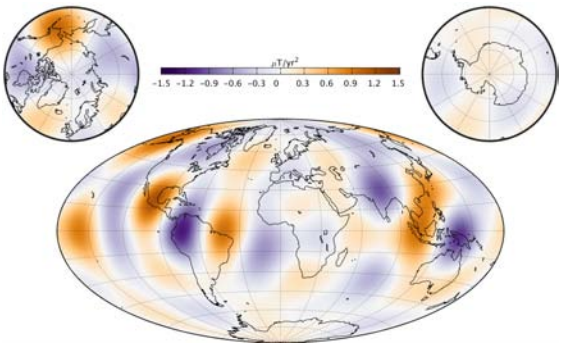

(f) CHAOS-6-x5 model radial SA up to SH degree $n = 7$ at CMB in 2016.0.

Figure 4.44: Global maps of the SV (top) and SA (center and bottom) radial fields at the CMB in 2016.0, of the *VO_vectgrad_SH.02* (left plots) and CHAOS-6-x5 (right plots) models.

4.7 Recommendations

This section collections the recommendations for future VO modelling, these are:

- Data selection: it is recommended to select data using dark (i.e. the sun 10° below horizon) quiet-time criteria in order to reduce the contamination of external fields.
- Data processing: it is recommended to use the ESA L2 product, CI inversion estimates of the ionospheric fields along with the induced counterparts (Sabaka et al.,

2018). The latest version CIY4 incorporates Earth induced fields using a 3D conductivity model. It is also recommended to investigate whether the CIY4 oceanic lunar semi-diurnal magnetic signal could be beneficial to remove (at satellite altitudes this is a signal of 2.5nT prominent in the Indian Ocean, the sea around Antarctica and in the North Atlantic Ocean). It is recommended to use the CHAOS model estimates of the magnetospheric field and its induced counterpart.

- Data processing: as a technical recommendation, the removal of the internal field from the measurements should be done as follows: i) subtract the time-dependent internal field for SH degrees 1-14, ii) subtract the static internal field for epoch 2010 (where the CHAMP satellite was at it lowest) for SH degrees 15-20, and iii) subtract the internal static field for SH degrees 21-110.

- Data processing: the VO modelling was found to be independent on which field model was used to perform the pre-whitening. It is recommended to use a geomagnetic field model, that is considered the most optimal at reproducing the observations on which it is built; in case a standardized procedure is required, the IGRF model should be considered.

- VO model setup: the VO's should be placed at mean satellite altitudes; in this project this were 370km and 490km altitude above ground during the CHAMP and *Swarm* eras, respectively. It is recommended to investigated whether the VO's should be computed separately for the *Swarm* Alpha and Charlie satellites and the Bravo satellite.

- VO model setup: it is recommended to use a cubic potential expansion.

- VO model setup: if the VO's are to be used in applications of inferring the core flow or in data assimilation, equal area global grids having at least 300 VO's should be used in order to obtain sufficiently spatial resolution. For such a grid, the search radius should be no more than 700km in order to avoid VO data overlap.

- VO model setup: it is recommended to use a 4 month time window from which data are binned into the VO epochs.

- Error estimates: it is recommended to investigate computing off-diagonal elements of the covariance matrices of the VO time series, which could be important for future application studies.

- Model correlation matrices: it is recommended to further explore the possible to improve on the VO modelling by taking advantage of a Selectetive Infinite-Variance Weighting (SIVW) approach by applying a weight matrix. That is, trying to use an optimal combination of observation components which may be suitable to constrain certain model parameters (Olsen et al., 2007; Sabaka et al., 2015; Kotsiaros and Olsen, 2014).

- Field gradients: it is recommended to further explore the prospects of field gradient computations and their time derivatives, and to investigate possible applications in regards to core flow studies and jerk investigations.

- Internal/external field separation: it is recommended to investigate whether an internal/external separation modelling could be performed, and if ionospheric field

parametrization could be incorporated in order to mitigate such signals. Furthermore, considerations on how to mitigate the in-situ ionospheric tororidal field is suggested.

4.8 Summary

In this Chapter the local modelling technique called the Virtual Observatory method has been described, implemented and new initiatives trying to improve on previous results have been undertaken, including: 1) optimization of the data selection and modelling procedure based on previous experience, such as subtracting crustal and external field estimations, 2) improved the VO method setup using a cubic potential description and using longer data time windows, 3) extending the method to compute field gradients and their time derivatives, 4) providing uncertainty estimates for field and gradient outputs.

The main results and findings of the work conducted in this thesis are:

- VO's computed with improved data selection criteria and processing, and modelling set up, agree well with the ground observatory measurements and field model predictions. Comparing SV estimates computed from 4 month averages of GO's with those of the VO's, results in rms misfit of a few nano Tesla and correlation coefficients for the radial components not below 0.74 and 0.91 during the CHAMP and *Swarm* eras, respectively. The correlation coefficients for the horizontal field components show equally high numbers thus confirming the high coherence of the VO time series with those of the GO's.
- It is concluded that an internal field model is required in other to perform a prewhitening of the data. It was found that the VO time series are independent on which field model is chosen for this purpose.
- External and toroidal field contributions are much reduced but still present especially at polar latitudes.
- VO time series above the Honolulu observatory, shows a steep change in the SA observed around 2017. This is also seen in the dZ/dt component in global VO time series; this may be the first signs of a jerk in the Pacific region in the *Swarm* era. Global maps of the SV and in particular the SA may support this suspicion showing increased activity.
- VO time series above the Kourou (KOU) observatory, shows a "V" shape feature in the θ components of the SV seen around 2016, with an associated steep change in the SA which could indicate a jerk in the *Swarm* era. This is also seen in the dX/dt component in global VO time series.
- Field gradients can be computed using the VO's. Using the gradient field data, it has been demonstrated that spherical harmonic based field models can be built, which may add additional information on the field structures compared to vector only based field models. The VO time series may be used to produce dedicated time dependent models of the core field. The 2007 jerk is clearly identified in the gradient SV and SA time series, confirming the usability of gradients in studies of jerks.

The potential applications of the VO time series are significant as has already been shown in previous studies (e.g. Olsen and Mandea, 2007; Beggan et al., 2009; Beggan and

Whaler, 2009, 2010; Whaler and Beggan, 2015; Olsen et al., 2009, 2010c). During this project various collaborations involving the usage of an EQ grid of globally distributed VO time series, has been carried out. Among these studies, the VO data was used in the assimilation study of (Barrois et al., 2018) trying to infer both core surface magnetic and velocity fields. The associated article *Assimilation of ground and satellite magnetic measurements: inference of core surface magnetic and velocity field changes* can be found in Appendix A. Also the VO data produced in this project was used in studying the time-dependent core flow at low latitudes between 2000 and 2017 (Kloss and Finlay, 2018), and in core flow studies (Whaler, 2017).

Several of the issues concerning VO field reconstruction are shared by all conventional SH field reconstructions. These arguments should not prevent a pragmatic approach to estimating VO time series. Major disturbing signals due to ionospheric and magnetospheric sources might be subtracted to some extent by applying improved data selection from the CHAMP and *Swarm* satellites (e.g., Finlay et al., 2017; Friis-Christensen et al., 2017), removal of modelled external field predictions (e.g., Laundal et al., 2018), or usage of gradient data for determining particular model parameters (e.g., Kotsiaros and Olsen, 2014; Sabaka et al., 2015).

Chapter 5

Optimal Localized Field Estimation

5.1 Introduction

The objective of this chapter is to introduce, describe and implement a technique for obtaining localized spatial average estimates of the radial magnetic field and its time derivatives at the core-mantle boundary (CMB). An important perspective offered by the technique described here is formal appraisal of the spatial resolution and variance of the estimated field averages. The formalism proposed offers a powerful alternative to conventional core field modelling, which is typically based on global spherical harmonic basis functions, where noise in the polar regions maps into all harmonics, and which requires model regularization and spectral truncation, making inference of resolution and variance troublesome.

The central idea is that Green's second identity allows solutions to the Laplace equation to be formulated by imposing inhomogeneous boundary conditions of the Neumann type. This provides a mathematical relationship between vector magnetic field measurements and the radial magnetic field at the CMB. The Green's function method under the Neumann boundary conditions allows both internal and external sources to be described. Investigating the field at the CMB from satellite measurements constitutes an inverse problem, which can be solved using a modified Backus-Gilbert approach. The Backus-Gilbert approach is an optimally localized averaging (OLA) method; a field estimate is constructed as a linear combination of the data providing a unique spatial average value. In this project a specific extension building on the Subtractive Optimally Localized Averages (SOLA) method developed in helioseismology has been used; this involves seeking averaging kernels as close as possible to a specified spatial target kernel. The formalism presented here is able to account for both internal and external field sources, and it can incorporate data error covariance information such as along-track serial error correlation as described in Section 3.4.2.

Section 5.2 presents the background theory of the Neumann boundary value problem (NBVP), and derivations of the exterior and interior Green's functions. Section 5.3 describes the optimal localized averaging method, and in particular presents the SOLA method. Two different approaches to implement the SOLA method in the time-dependent

geomagnetic problem are here described: 1) Section 5.4 derives a formalism wherein the time dependence of the field is approximated by a Taylor series expansion, 2) Section 5.5 derives an alternative formalism where the temporal function, relating data and the source field in time, is approximated by a local polynomial. Applications to the method are presented using magnetic field observations collected by the low-Earth-orbiting CHAMP and *Swarm* satellites missions based on the Data Set 2 described in Sections 3.3 and 3.4. Studies of the SA at the CMB are reported in Section 5.4.5. These shed fresh light on rapid field changes in the equatorial region and jerks at the CMB. A summary is given in Section 5.6.

5.2 The Laplace Equation - The Neumann Problem

Here, the fundamental theory of potential fields is presented following closely the treatments by Barton (1989), Jackson (2007) and Riley et al. (2004). The fundamental equation that describe and governs the geomagnetic potential is the second order partial differential Laplace equation, see Section 2.5. The Laplace equation is a special case of a more general equation but may be written (e.g., Riley et al., 2004, p. 686)

$$\mathcal{L}\psi(\mathbf{r}) = \nabla^2\psi(\mathbf{r}) = -\rho(\mathbf{r}) \tag{5.1}$$

where $\mathcal{L}$ represents the partial differential operator, ψ is the potential function and ρ is some source function (for instance in electrostatics ρ would be the charge density). Choosing here the Laplace operator $\mathcal{L} = \nabla^2$, the Poisson's equation (5.1) appears, which is classified as being of elliptic type. This problem is well-posed in the Hadamard sense if it satisfies: i) existence of a solution, ii) uniqueness of the solution found, iii) stability of solution (Barton, 1989). We wish to find a well-posed solution, $\psi(\mathbf{r})$, within some region, V, to the Poisson's equation in the homogeneous case for which $\rho(\mathbf{r}) = 0$; in this case it reduces to the Laplace equation. The volume, V, is bounded by the surface, S, which here consists of two disconnected parts, S_1 and S_2, such that $S = S_1 + S_2$ and $\int_S dS = \int_{S_1} dS_1 + \int_{S_2} dS_2$. In the three dimensional space considered here, S_1 and S_2 are concentric spheres with V in the gap between as shown in Figure 5.1. It is important to note that some parts or all of S, are allowed to be at infinity; e.g. considering the case of an infinite volume, the radius of the surface S_2 goes to infinity. The normal vector is denoted $\hat{\mathbf{n}}$ and points out of V (Barton, 1989; Riley et al., 2004). The elliptic classification specifies under which conditions well-posed problems are given; for the elliptic case appropriate conditions are inhomogeneous (i.e. $\neq 0$) boundary conditions of either the Dirichlet (DBC) type specifying the potential ψ on S, also termed the first boundary value problem, or the Neumann boundary conditions (NBC) type specifying the normal derivatives $\partial_n\psi$ on S, also termed the secondary boundary value problem on a closed surface (such as a sphere), allowing for parts of S to be at infinity. Cauchy boundary conditions, which are a combination of the Dirichlet and Neumann boundary conditions, overdetermine the problem (Kellogg, 1954; Barton, 1989; Jackson, 2007; Riley et al., 2004). The uniqueness theorem below is especially important, since it states that a solution satisfying the Laplace equation using the boundary conditions is the correct and only one regardless of how it is found (e.g., Riley et al., 2004, p. 639)

Uniqueness theorem. *If ψ is real and its first and second partial derivatives are continuous in a region V and on its boundary S, and $\nabla^2\psi = -\rho$ in V, and either $\psi = g$ (DBC) or $\partial\psi/\partial n = f$ (NBC) on S, where ρ, f and g are prescribed functions, then ψ is unique (at least to within an additive constant).*

The problem considered here, i.e. the geomagnetic case, is inhomogeneous with NBC prescribed on the surface S, i.e. the normal derivative of the potential (i.e. the radial field) $\partial\psi/\partial n$. A homogeneous problems requires both $\rho = 0$ and all boundary conditions to be zero; in fact a homogeneous problem with the NBC does not exist as will be shown in Section 5.2.2.

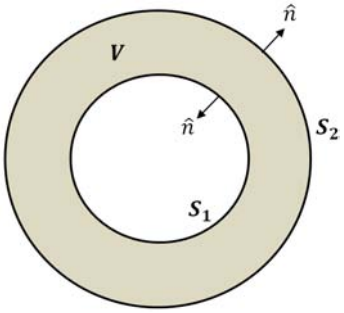

Figure 5.1: Illustration of volume V and surface $S = S_1 + S_2$.

5.2.1 The Concept and Properties of Green's Functions

The method of Green's functions provides a suitable procedure for solving the Laplace equation. The fundamental concept is to assume that a certain function, called the Green's function, $N(\mathbf{r}|\mathbf{r}')$, exists and fulfils (Barton, 1989; Riley et al., 2004)

$$-\nabla^2 N(\mathbf{r}|\mathbf{r}') = \delta(\mathbf{r} - \mathbf{r}') \tag{5.2}$$

where both $\mathbf{r}$ and $\mathbf{r}'$ lies within V, and $\delta(\mathbf{r} - \mathbf{r}')$ is the singularity Dirac delta function in three dimensions. The 3D Dirac delta function can be written (e.g., Barton, 1989, p. 32)

$$\delta(\mathbf{r} - \mathbf{r}') = \frac{1}{r'^2}\delta(r - r')\delta(\phi - \phi')\delta(\theta - \theta') = \frac{1}{r'^2}\delta(r - r')\delta(\Omega - \Omega') \tag{5.3}$$

where $\delta(\Omega - \Omega')$ represents the angular part which can be expanded in terms of spherical harmonics

$$\delta(\Omega - \Omega') = \sum_{l=0}^{\infty}\sum_{m=-l}^{l} Y_{lm}^*(\theta', \phi')Y_{lm}(\theta, \phi) = \frac{1}{4\pi}\sum_{l=0}^{\infty}(2l + 1)P_l(\mu) \tag{5.4}$$

where Y_{lm} are the complex surface spherical harmonics being functions of the angular part only determined as (Barton, 1989)

$$Y_{lm}(\theta, \phi) = (-1)^m N_{lm} P_{l,m}(\cos\theta)\exp^{im\phi} \quad for\ l \geq 0\ and\ -l \leq m \leq 1 \tag{5.5}$$

where $P_{l,m}$ are the associated Legendre functions satisfying the Ferrers normalization, $\mu = \cos\gamma = \cos\theta\cos\theta' + \sin\theta\cos\theta'\sin(\phi - \phi')$, the asterisk denotes complex conjugation, and where the pre-factor

$$N_{lm} = \sqrt{\frac{(2l + 1)}{4\pi}\frac{(l - m)!}{(l + m)!}} \tag{5.6}$$

such that the inner product of the complex surface spherical harmonics is written

$$\langle Y_{lm}, Y_{n,k}\rangle \equiv \int_0^{2\pi}\int_0^{\pi} Y_{lm}^* Y_{nk} dS = \delta_{ln}\delta_{mk} \tag{5.7}$$

In the above l and m are the degree and order, respectively. Note here that some definitions includes a factor $1/4\pi$ in front of this integral (Sabaka et al., 2010) and correspondingly not in the N_{lm} expression of equation (5.6). However this only slightly modifies the computations, such as the spherical harmonic addition theorem equation (5.8); it does not influence the end result. In the above the spherical harmonic addition theorem has been used to re-write the expansion (e.g., Barton, 1989, p. 32)

$$\sum_{m=-1}^{l} Y_{lm}^{*}(\theta',\phi')Y_{lm}(\theta,\phi) = \frac{2l+1}{4\pi}P_l(\mu) \tag{5.8}$$

Properties of the Dirac delta function include (e.g., Woan, 2000, p. 50)

$$\delta(\mathbf{r}-\mathbf{r}') = 0, \quad \textit{if } \mathbf{r} \neq \mathbf{r}' \tag{5.9}$$

$$\int_V \delta(\mathbf{r}-\mathbf{r}')dV = 1 \tag{5.10}$$

$$f(\mathbf{r})\delta(\mathbf{r}-\mathbf{r}') = f(\mathbf{r}')\delta(\mathbf{r}-\mathbf{r}') \tag{5.11}$$

$$\int_V f(\mathbf{r})\delta(\mathbf{r}-\mathbf{r}')dV = f(\mathbf{r}') \tag{5.12}$$

where $f(\mathbf{r})$ is some arbitrary continuous function. It is important to be clear about the notation used: i) $\mathbf{r}$ denotes the position in V of the sought-after potential solution, $\psi(\mathbf{r})$, and is termed the field point, ii) $\mathbf{r}'$ denotes the position in V or on the boundary S where for instance boundary conditions are given, and is termed the source point (Barton, 1989). Furthermore, it should be stressed that the differentiation, ∇', along with the volume and surface integrals $\int_V dV'$ and $\int_S dS'$, respectively, are carried out with respect to $\mathbf{r}'$.

The Green's function, also termed the response or influence function, may be considered as the response of a system to a δ-point source or unit impulse (represented by the Dirac delta function) at the position $\mathbf{r} = \mathbf{r}'$. Considering Green's second theorem, see equation (2.10), Section 2.5, and writing the source potential $\Phi = \psi(\mathbf{r}')$ and the Green's function $\Psi = N(\mathbf{r}'|\mathbf{r})$, yields

$$\int_V \left[\psi(\mathbf{r}')\nabla'^2 N(\mathbf{r}'|\mathbf{r}) - N(\mathbf{r}'|\mathbf{r})\nabla'^2\psi(\mathbf{r}')\right] dV(\mathbf{r}') = \int_S \left[\psi(\mathbf{r}')\frac{\partial N(\mathbf{r}'|\mathbf{r})}{\partial n} - N(\mathbf{r}'|\mathbf{r})\frac{\partial \psi(\mathbf{r}')}{\partial n}\right] dS(\mathbf{r}') \tag{5.13}$$

where the notation $\nabla\psi(\mathbf{r}')\cdot\hat{\mathbf{n}}dS = (\partial\psi(\mathbf{r}')/\partial n)dS$ has been used, i.e. the rate of change of $\psi(\mathbf{r}')$ in the normal direction. Inserting equations 5.1 and 5.2, and using equation 5.12 allows for equation 5.13 to be re-written as

$$\psi(\mathbf{r}) = -\int_V N(\mathbf{r}'|\mathbf{r})\rho(\mathbf{r}')dV(\mathbf{r}') - \int_S \left[\psi(\mathbf{r}')\frac{\partial N(\mathbf{r}'|\mathbf{r})}{\partial n} - N(\mathbf{r}'|\mathbf{r})\frac{\partial \psi(\mathbf{r}')}{\partial n}\right] dS(\mathbf{r}') \tag{5.14}$$

Equation 5.14 provides an expression of the potential at $\mathbf{r}$ described in terms of the Green's function which is comprised of an integration over the volume source $\rho(\mathbf{r}')$ where $\mathbf{r}' \in V$ and two surface integrations containing boundary conditions for which $\mathbf{r}' \in S$. Note that calling equation 5.14 a solution would be misleading, since the expression contains both the potential and its derivative on the surface (Jackson, 2007). Restrictions regarding the continuity of the Green's function and discontinuity of its first derivative need to be considered when constructing appropriate expressions for $N(\mathbf{r}'|\mathbf{r})$. Equation 5.2 means

that $\nabla^2 N(\mathbf{r}|\mathbf{r}')$ ought to match the behaviour of the Dirac delta function at $\mathbf{r} = \mathbf{r}'$; for instance, the Dirac delta is a singularity class function of which integration yields the Heaviside step function, which is piecewise continuous (e.g., Barton, 1989, p. 18). Thus the derivative $\partial N(\mathbf{r}|\mathbf{r}')/\partial r$ should be discontinuous and $N(\mathbf{r}|\mathbf{r}')$ continuous, fulfilling the jump and continuity conditions (e.g., Barton, 1989, p. 46). Considering the radial dependence, these are stated below, where the jump condition is found by integrating equation (5.2) on both sides from $r' - \eta_1$ to $r' + \eta_2$, letting $\eta_1, \eta_2 \to 0$, i.e.

$$\int_{r'-\eta_1}^{r'+\eta_2} \nabla^2 N(r|r')dr = \int_{r'-\eta_1}^{r'+\eta_2} -\frac{1}{r'^2}\delta(r-r')dr$$

$$\left.\frac{\partial N(r|r')}{\partial r}\right|_{r=r'+\eta_2} - \left.\frac{\partial N(r|r')}{\partial r}\right|_{r=r'-\eta_1} = -\frac{1}{r'^2} \quad \text{for } \eta_1, \eta_2 \to 0 \qquad \text{jump condition} \tag{5.15}$$

$$N(r'+\eta_2|r') - N(r'-\eta_1|r') = 0 \qquad \text{for } \eta_1, \eta_2 \to 0 \qquad \text{continuity condition} \tag{5.16}$$

5.2.2 Neumann Problem Considerations

Before deriving the expressions for the Green's functions, some important considerations regarding the Neumann problem must be addressed. The Neumann Green's function should fulfil the symmetry $N(\mathbf{r}|\mathbf{r}') = N(\mathbf{r}'|\mathbf{r})$. This requirement means that the positions $\mathbf{r}$ and $\mathbf{r}'$ are interchangeable such that the potential at $\mathbf{r}$ due to a source at $\mathbf{r}'$ is equivalent to the potential at $\mathbf{r}'$ due to a source at $\mathbf{r}$. Applying the divergence theorem (also known as Gauss's theorem) to equation 5.1 yields

$$\int_V \nabla^2 \psi dV = -\int_V \rho dV = \int_S \nabla\psi \cdot \hat{\mathbf{n}} dS = \int_S f dS \tag{5.17}$$

where $\partial\psi/\partial n = f$ is some prescribed value on S. Equation 5.17 is a consistency conditions that must be fulfilled. However, this means that the Green's function cannot fulfil homogeneous NBCs (as is the case for DBCs). This can be seen by considering

$$\int_V \nabla^2 N(\mathbf{r}|\mathbf{r}')dV = \int_S \nabla N(\mathbf{r}|\mathbf{r}') \cdot \hat{\mathbf{n}} dS = \int_S \frac{\partial N(\mathbf{r}|\mathbf{r}')}{\partial n} dS = -1 \tag{5.18}$$

which is not possible if $\partial N(\mathbf{r}|\mathbf{r}')/\partial n = 0$ (Barton, 1989; Riley et al., 2004). There are two ways of fixing this: either i) to change equation 5.2 by adding some appropriate term defining a pseudo Green's function or ii) to change the boundary condition for the Green's function making it inhomogeneous. Proceeding with option ii) a suitable boundary condition is (Barton, 1989; Riley et al., 2004)

$$\frac{\partial N(\mathbf{r}|\mathbf{r}')}{\partial n} = -\frac{1}{A} \qquad \textit{for } \mathbf{r} \textit{ on } S \tag{5.19}$$

where A is the area of the surface. To summaries four important properties of the Green's functions under the NBC are

- The requirement $\nabla^2 N(\mathbf{r}|\mathbf{r}') = \delta(\mathbf{r} - \mathbf{r}')$
- Inhomogeneous boundary conditions $\frac{\partial N(\mathbf{r}|\mathbf{r}')}{\partial n} = -\frac{1}{A}$
- Symmetry $N(\mathbf{r}|\mathbf{r}') = N(\mathbf{r}'|\mathbf{r})$
- Fulfils jump and continuity conditions

Furthermore, symmetry allows for swapping $\mathbf{r}$ and $\mathbf{r}'$. The solution to the Laplace equation under the NBCs, having set $\rho = 0$ and $\partial N(\mathbf{r}|\mathbf{r}')/\partial n = -1/A$, can be written

$$\begin{aligned}\psi(\mathbf{r}) &= \frac{1}{A}\int_S \psi(\mathbf{r}')dS(\mathbf{r}') + \int_S N(\mathbf{r}'|\mathbf{r})\frac{\partial\psi(\mathbf{r}')}{\partial n}dS(\mathbf{r}') \\ &= \langle\psi(\mathbf{r}')\rangle_S + \int_S N(\mathbf{r}'|\mathbf{r})\frac{\partial\psi(\mathbf{r}')}{\partial n}dS(\mathbf{r}') \end{aligned} \tag{5.20}$$

where $\langle\psi(\mathbf{r}')\rangle_S$ means the ψ average over the surface, which is a constant to which the potential can be determined using the Green's function. For the exterior problem, described shortly, A becomes infinite because V is bounded by S_2 at infinity, such that $1/A = 0$ and $\partial N(\mathbf{r}|\mathbf{r}')/\partial n = 0$ vanishes on the total surface S. This is however not the case for the interior problem. The presence of a constant is not important for application since we are interested in the magnetic field which is the gradient of the potential.

The following two sections are concerned with the detailed derivations of closed form expressions for the Green's functions for the exterior and interior problems under the Neumann boundary value condition (NBC) in a spherical geometry. The motivation for including these derivations here is that they are not easily available in the literature and may seem abstruse to deduce. The notation and formulation adopted here follows that of Barton (1989) and Jackson (2007). Even though the exterior and interior problems are treated separately here, a joint formulation exists (Jackson, 2007; Kim and Jackson, 1993). It can be shown that this expression reduces the exterior/interior Green's functions under appropriate considerations. Here, instead treating the problem as two separate cases (i.e. the exterior/interior), closed-form expressions were obtained; adding the two expressions is possible since the total field (and thus the total potential) is just a superposition of the fields produced by the two sources under consideration.

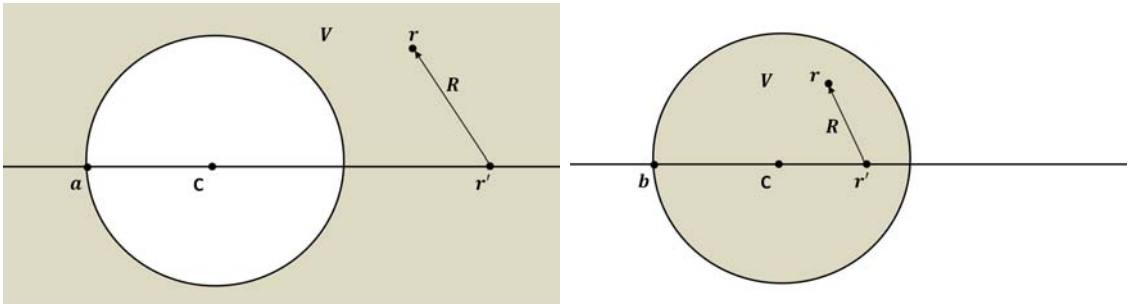

(a) Exterior problem. (b) Interior problem.

Figure 5.2: Illustration of Neumann boundary value problem. After Barton (1989) Figures 5.3 and 5.4.

The form of the Green's functions can be derived through various approaches (e.g., Barton, 1989; Jackson, 2007; Constable et al., 1993). Here an expansion of spherical harmonics will be used from which closed-form expressions can be obtained. The exterior and interior cases are illustrated in Figure 5.2: a) the exterior problem for a sphere, seeking the Green's function $N_{ext}(\mathbf{r}|\mathbf{r}')$ in V bounded by the (source) sphere S_1 with radius a and S_2 at infinity, requiring that $\psi(\mathbf{r}) \to 0$ as $\mathbf{r} \to \infty$ and b) the interior problem for a sphere, seeking the Green's function $N_{int}(\mathbf{r}|\mathbf{r}')$ in V bounded by the (source) sphere S,

applying Neumann boundary conditions to both. However, the derivation of $N_{ext}(\mathbf{r}|\mathbf{r}')$ and $N_{int}(\mathbf{r}|\mathbf{r}')$ differs significantly due to the fact that exterior problem has one surface at infinity. Looking at the geometric setup in Figure 5.2 a) and b) for the exterior and interior cases, respectively, the following notations are used: the origin C is at the center of a sphere of radius a (which should not be confused with the notation for the Earth's surface in Chapter 2), $\mathbf{r}$ is the field point, $\mathbf{r}'$ is the source point, the angular distance, γ, between these two positions is $\mu = \cos\gamma = \cos\theta\cos\theta' + \sin\theta\cos\theta'\sin(\phi - \phi')$. The vector distance is $\mathbf{R} = \mathbf{r} - \mathbf{r}'$, such that $R = |r - r'| = \sqrt{r^2 + r'^2 - 2rr'\mu}$. Note that in general the distances r and r' are not fixed, thus requiring the two case $r > r'$ and $r < r'$ to be investigated separately. Table 5.1 summaries the some basic geometric considerations.

	Exterior problem	*Interior problem*
Radius	$r > a,\ r' \geq a$	$r < b,\ r' \leq b$
NBC on Green's function	$\frac{\partial N_{ext}}{\partial r} = 0$ for $r = a,\ r \to \infty$	$\frac{\partial N_{int}}{\partial r} = \frac{1}{4\pi b^2}$ for $r = b$
NBC on potential	$\frac{\partial \psi(\mathbf{r})}{\partial n} = B_r(\mathbf{r})$	$\frac{\partial \psi(\mathbf{r})}{\partial n} = -B_r(\mathbf{r})$
Behaviour	$\psi(\mathbf{r}) \to 0$ as $\lvert\mathbf{r}\rvert \to \infty$	$\psi(\mathbf{r}) \to 0$ as $\lvert\mathbf{r}\rvert \to 0$

Table 5.1: 3D Neumann boundary value problem for a sphere.

The Neumann Green's function, $N(\mathbf{r}|\mathbf{r}') = N(r, \theta, \phi|r', \theta', \phi') = N(r, \Omega|r', \Omega')$, is derived using a complete orthogonal set of functions over the interval $0 \leq \theta \leq \pi$ (i.e. $-1 \leq \mu \leq 1$); a spherical harmonic expansion in which the radial and angular dependences are assumed separable (e.g., Barton, 1989; Jackson, 2007)

$$N(\mathbf{r}|\mathbf{r}') = \sum_{l=0}^{\infty} \sum_{m=-l}^{l} g_l(r|r') Y_{lm}^*(\theta', \phi') Y_{lm}(\theta, \phi) = \frac{1}{4\pi} \sum_{l=0}^{\infty} g_l(r|r')(2l+1) P_l(\mu) \tag{5.21}$$

where Y_{lm} are the surface spherical harmonics and P_l are the Legendre polynomials. The spherical harmonic addition theorem, equation (5.8), has been used to re-write the expansion. The $g_l(r|r')$ is a function expressing the radial dependence and the spherical harmonics express the angular dependence. Because the Green's function exhibits axial symmetry, such that $m = 0$, the angular part can be expressed by the Legendre polynomials. For each case (i.e. exterior/interior) expressions for g_l are sought and inserted into equation 5.21 for further inference. Expressing the operator ∇^2 in spherical polar coordinates (see (e.g. Woan, 2000)) and substituting for equations (5.21), (5.3) and (5.4) into equation 5.2 yields

$$\frac{1}{4\pi} \sum_{l=0}^{\infty} \left[\frac{(2l+1)P_l(\mu)}{r^2} \frac{d}{dr}\left(r^2 \frac{dg_l}{dr} \right) + \frac{g_l}{r^2 \sin\theta} \frac{d}{d\theta}\left(\sin\theta \frac{dP_l(\mu)}{d\theta} \right) \right] = - \frac{1}{4\pi} \frac{1}{r'^2} \delta(r - r') \sum_{l=0}^{\infty} (2l+1) P_l(\mu) \tag{5.22}$$

The angular part on the left-hand side, having $m = 0$, satisfies the differential equation (e.g., Riley et al., 2004, p. 666)

$$\frac{1}{\sin\theta} \frac{d}{d\theta}\left(\sin\theta \frac{dP_l(\mu)}{d\theta} \right) = -l(l+1) P_l(\mu) \tag{5.23}$$

which can be inserted into equation 5.22, giving

$$\frac{1}{4\pi}\sum_{l=0}^{\infty}\left[\frac{1}{r^2}\frac{d}{dr}\left(r^2\frac{dg_l}{dr}\right)-\frac{l(l+1)g_l}{r^2}\right](2l+1)P_l(\mu)= \\ -\frac{1}{4\pi}\frac{1}{r'^2}\delta(r-r')\sum_{l=0}^{\infty}(2l+1)P_l(\mu) \tag{5.24}$$

For each value of l, equating the left and right hand side of equation 5.24 provides an ordinary differential equation such that

$$\frac{1}{r^2}\frac{d}{dr}\left(r^2\frac{dg_l}{dr}\right)-\frac{l(l+1)g_l}{r^2}=-\frac{1}{r'^2}\delta(r-r')\Rightarrow \\ -\frac{d^2g_l}{dr^2}-\frac{2}{r}\frac{dg_l}{dr}+\frac{l(l+1)g_l}{r^2}=\frac{1}{r'^2}\delta(r-r') \tag{5.25}$$

This means that g_l is a solution to the homogeneous equation 5.25 except at $r = r'$. Considering the cases $r < r'$ and $r > r'$, the structure of g_l is split into the form

$$g_l(r)=\begin{cases}A_lr^l+D_l/r^{l+1} & \text{for } r<r'\\ B_lr^l+C_l/r^{l+1} & \text{for } r>r'\end{cases} \tag{5.26}$$

In the next two sections derivations of the exterior and interior Green's functions are provided based on the preliminary formulations given above; i.e. the structure of the g_l term, imposing boundary conditions along with the jump and continuity conditions, is the first step, the next step is to derive closed-form expressions of the Green's functions.

5.2.3 Exterior Neumann Green's Function for a Sphere

The intention is to solve for the potential in V outside the surface S_1 bounded by the surface S_2 at infinity, i.e the volume becomes infinite, as illustrated in the geometric setup seen in Figure 5.2 a). As stated by equation 5.26, the cases $r < r'$ and $r > r'$ are considered separately; outside the sphere S_1 for $r > r'$ the solution is bounded as $r \to \infty$, thus requiring $B_l = 0$ for all values of l since otherwise the term r^l would blow up. Recall that $1/A$ of the total surface is zero since S_2 is infinity, thus imposing the boundary condition $\partial N/\partial r = 0$ at $r = a$.

1. Case $l = 0$ The boundary condition imposes that $\partial N(r|r')/\partial r = 0$ such that differentiating equation 5.21 gives

$$\frac{\partial}{\partial r}\left(\left[A_0+D_0\frac{1}{r}\right]Y_{00}^2\right)\Bigg|_{r=a}=0 \qquad \Rightarrow \qquad \text{thus, } D_0=0 \tag{5.27}$$

where $Y_{00} = 1/\sqrt{4\pi}$. Hence, for $l = 0$, the solution is

$$g_0(r|r')=H(r'-r)A_0+H(r-r')\frac{C_0}{r} \tag{5.28}$$

where H is the Heaviside function such that $H(r' - r)$ and $H(r - r')$ picks out the solutions for cases $r' > r$ and $r > r'$, respectively. Furthermore $H(r'-r)+H(r-r') = 1$. Because the Green's function is continuous at $r = r'$ the continuity conditions requires

$$g_0(r'+\eta_2|r')=g_0(r'-\eta_1|r') \qquad \Rightarrow \qquad \text{thus, } A_0=\frac{C_0}{r'} \tag{5.29}$$

Hence, inserting this it is possible to write

$$\begin{aligned} g_0(r|r') &= H(r'-r)\frac{C_0}{r'} + H(r-r')\frac{C_0}{r} \\ &= C_0\left[H(r'-r) + H(r-r')\right] + \frac{H(r'-r)}{r'} + \frac{H(r-r')}{r} \\ &= C_0 + \frac{H(r'-r)}{r'} + \frac{H(r-r')}{r} \end{aligned} \tag{5.30}$$

The constant C_0 is an arbitrary additive constant, left undetermined by the boundary conditions, appearing in any Neumann problem.

2. Case $l \geq 1$ The boundary condition imposes that $\partial g_l(r|r')/\partial r = 0$ at $r = a$ such that

$$\frac{\partial}{\partial r}\left(A_l r^l + D_l/r^{l+1}\right)\Big|_{r=a} = 0 \qquad \Rightarrow \qquad \text{thus, } D_l = A_l \frac{l}{l+1} a^{2l+1} \tag{5.31}$$

The solution may therefore be written

$$\begin{aligned} g_l(r|r') &= H(r'-r)\left(A_l r^l + D_l \frac{1}{r^{l+1}}\right) + H(r-r')C_l \frac{1}{r^{l+1}} \\ &= H(r'-r)A_l\left[r^l + \frac{l}{l+1}\frac{a^{2l+1}}{r^{l+1}}\right] + H(r-r')C_l\frac{1}{r^{l+1}} \end{aligned} \tag{5.32}$$

Using equation 5.32, the continuity condition requires

$$C_l = A_l\left[r'^{2l+1} + \frac{l}{l+1}a^{2l+1}\right] \tag{5.33}$$

Inserting this into equation 5.32 gives

$$\begin{aligned} g_l(r|r') = {} & H(r'-r)A_l\left[r^l + \frac{l}{l+1}\frac{a^{2l+1}}{r^{l+1}}\right] \\ & + H(r-r')A_l\left[r'^{2l+1} + \frac{l}{l+1}a^{2l+1}\right]\frac{1}{r^{l+1}} \end{aligned} \tag{5.34}$$

The derivative $\partial g_l/\partial r$ fulfils the jump condition by integrating equation 5.25 with respect to r from $r' - \eta_1$ to $r' + \eta_2$ (e.g., Barton, 1989, p. 47)

$$\begin{aligned} &\int_{r'-\eta_1}^{r'+\eta_2}\left[-\frac{d^2 g_l}{dr^2} - \frac{2}{r}\frac{dg_l}{dr} + \frac{l(l+1)g_l}{r^2}\right]dr = \int_{r'-\eta_1}^{r'+\eta_2}\frac{1}{r'^2}\delta(r-r')dr \Rightarrow \\ &\frac{dg_l(r'+\eta_2|r')}{dr} - \frac{dg_l(r'-\eta_1|r')}{dr} = -\frac{1}{r'^2} \end{aligned} \tag{5.35}$$

This jump condition is used to solve for the coefficient A_l

$$\begin{aligned} \frac{dg_l(r'+\eta_2|r')}{dr} &= -A_l\left[(l+1)\frac{r'^{2l+1}}{r^{l+2}} + \left(\frac{l}{l+1}\right)(l+1)\frac{a^{2l+1}}{r^{l+2}}\right] \\ \frac{dg_l(r'-\eta_1|r')}{dr} &= A_l\left[lr^{l-1} - \left(\frac{l}{l+1}\right)(l+1)\frac{a^{2l+1}}{r^{l+2}}\right] \end{aligned}$$

subtracting the two expressions, finding

$$\frac{dg_l(r'+\eta_2|r')}{dr} - \frac{dg_l(r'-\eta_1|r')}{dr} = -A_l r'^{l-1}(2l+1) = -\frac{1}{r'^2} \Rightarrow$$
$$A_l = \left(\frac{1}{2l+1}\right)\frac{1}{r'^{l+1}} \tag{5.36}$$

Inserting this into equation 5.34 gives

$$\begin{aligned} g_l(r|r') &= H(r'-r)\left(\frac{1}{2l+1}\right)\left[\frac{r^l}{r'^{l+1}} + \frac{1}{a}\left(1-\frac{1}{l+1}\right)\left(\frac{a^2}{r'r}\right)^{l+1}\right] \\ &+ H(r-r')\left(\frac{1}{2l+1}\right)\left[\frac{r'^l}{r^{l+1}} + \frac{1}{a}\left(1-\frac{1}{l+1}\right)\left(\frac{a^2}{r'r}\right)^{l+1}\right] \\ &= \left(\frac{1}{2l+1}\right)\left[\frac{1}{a}\left(1-\frac{1}{l+1}\right)\left(\frac{a^2}{r'r}\right)^{l+1}\right] + \\ &\left(\frac{1}{2l+1}\right)\left[H(r'-r)\frac{r^l}{r'^{l+1}} + H(r-r')\frac{r'^l}{r^{l+1}}\right] \end{aligned} \tag{5.37}$$

Recall that in the above expressions, the Heaviside function $H(r'-r)$ and $H(r-r')$ picks out the $r' > r$ and $r > r'$ cases, respectively.

Taking the $r > r'$ part, the complete expression for the Green's function for $l \geq 0$ equation 5.21, a closed-form expression can be derived

$$\begin{aligned} N(\mathbf{r}|\mathbf{r}') &= \frac{1}{4\pi}\sum_{l=0}^{\infty} g_l(r|r')(2l+1)P_l(\mu) \\ &= \frac{1}{4\pi}\left(\left(C_0+\frac{1}{r}\right)P_0(\mu) + \sum_{l=1}^{\infty}P_l(\mu)\left[\left(\frac{r'^l}{r^{l+1}}\right) + \frac{1}{a}\left(1-\frac{1}{l+1}\right)\left(\frac{a^2}{r'r}\right)^{l+1}\right]\right) \\ &= \frac{1}{4\pi}\left[\sum_{l=0}^{\infty}P_l(\mu)\left(\frac{r'^l}{r^{l+1}}\right) + \frac{1}{a}\sum_{l=0}^{\infty}P_l(\mu)\left(\frac{a^2}{r'r}\right)^{l+1} - \frac{1}{a}\sum_{l=0}^{\infty}P_l(\mu)\left(\frac{1}{l+1}\right)\left(\frac{a^2}{r'r}\right)^{l+1}\right] + \frac{C_0}{4\pi} \\ &= \frac{1}{4\pi}\left[\frac{1}{R} + \frac{a}{r'\tilde{R}} - \frac{1}{a}F_1\right] + \frac{C_0}{4\pi} \end{aligned} \tag{5.38}$$

where the following useful substitutions have been used

$$\frac{1}{R} = \sum_{l=0}^{\infty}P_l(\mu)\left(\frac{r'^l}{r^{l+1}}\right), \frac{1}{\tilde{R}} = \frac{1}{r}\sum_{l=0}^{\infty}P_l(\mu)\left(\frac{a^2}{r'r}\right)^l, F_1 = -\sum_{l=0}^{\infty}P_l(\mu)\left(\frac{1}{l+1}\right)\left(\frac{a^2}{r'r}\right)^{l+1}$$

For the last expression the substitution $\zeta = a^2/(r'r)$ can be used such that

$$F_1(\zeta) = -\sum_{l=0}^{\infty}P_l(\mu)\left(\frac{1}{l+1}\right)\zeta^{l+1} \tag{5.39}$$

such that the derivative may be calculated

$$\frac{\partial F_1(\zeta)}{\partial \zeta} = -\sum_{l=0}^{\infty}P_l(\mu)\zeta^l = -\frac{1}{\left[1+\zeta^2-2\zeta\mu\right]^{1/2}} \tag{5.40}$$

This is a well known generating function for the polynomials $P_l(\mu)$ (Barton, 1989). Integrating allows for F_1 to be re-written to a closed-form

$$\begin{aligned}\int_{\zeta_1=0}^{\zeta_1=\zeta} F_1(\zeta)d\zeta &= -\int_{\zeta_1=0}^{\zeta_1=\zeta} \frac{1}{[1+\zeta^2-2\zeta\mu]^{1/2}}d\zeta \Rightarrow \\ F_1(\zeta) &= -\ln\left[2\left[1+\zeta^2-2\zeta\mu\right]^{1/2}+2\zeta-2\mu\right]\Bigg|_{\zeta_1=0}^{\zeta_2=\zeta} \\ &= \ln\left[\frac{1-\mu}{[1+\zeta^2-\zeta\mu]^{1/2}+\zeta-\mu}\right] \\ &= \ln\left[\frac{r'r(1-\mu)/a^2}{1+r'\tilde{R}/a^2-r'r\mu/a^2}\right] \end{aligned} \tag{5.41}$$

Having used $F_1(\zeta=0)=0$. Inserting equation 5.41 into equation 5.38 leads to

$$N(\mathbf{r}|\mathbf{r}') = \frac{1}{4\pi}\left[\frac{1}{R}+\frac{a}{r'\tilde{R}}+\frac{1}{a}\ln\left[\frac{r'r(1-\mu)/a^2}{1+r'\tilde{R}/a^2-r'r\mu/a^2}\right]\right]+\frac{C_0}{4\pi} \tag{5.42}$$

where for completeness the arbitrary constant C_0 for the $l=0$ case has been included. However, since this only adds a constant term to the potential in equation 5.20 and the interest is for the derivative of the potential, it will be omitted from the exterior Neumann Green's function below. Setting the source radius $r'=a$ means that $\tilde{R}=R$ and that

$$N(\mathbf{r}|\mathbf{r}')\Big|_{r'=a} = \frac{1}{4\pi}\left[\frac{2}{R}+\frac{1}{a}\ln\left[\frac{r(1-\mu)/a}{1+R/a-r\mu/a}\right]\right] \tag{5.43}$$

The exterior Green's function times the radius squared, where $r'=a$, can be written after some rearrangement (e.g., Barton, 1989, p. 423)

$$r'^2 N(\mathbf{r}|\mathbf{r}')\Big|_{r'=a} = \frac{a^2}{4\pi}\left[\frac{2}{R}+\frac{1}{a}ln\left[\frac{1-\mu}{R/r+a/r-\mu}\right]\right] \tag{5.44}$$

The multiplication with a factor r'^2, comes from the surface integration of equation 5.20 for which the differential surface element perpendicular to $\hat{\mathbf{n}}$ is written $dS = r'^2\sin\theta' d\theta' d\phi'$. This Green's function is identical to the one given by (Gubbins and Roberts, 1983) except for a minus sign due to potential sign conventions (they use $\mathbf{B}=\nabla\psi$).

5.2.4 Interior Neumann Green's Function for a Sphere

The intention here is to solve for the potential in V outside the surface S_1 having radius $a \to 0$ bounded by the surface S_2 at b, i.e the volume does not become infinite as for the exterior case, as illustrated in the geometric setup seen in Figure 5.2 b). The derivation follows the same logic as for the exterior case by equation 5.26, studying cases $r < r'$ and $r > r'$; the solution is bounded as $r \to 0$, requiring $D_l = 0$ for all cases of l since the term $1/r^{l+1}$ would blow up. Recall here the boundary condition $\partial N/\partial r = 1/4\pi b^2$ at $r=b$. As before, terms with $l=0$ and $l \geq 0$ are considered separately.

1. Case $l=0$ The boundary condition means that $\partial N/\partial r = 1/4\pi b^2$ such that differentiating equation 5.21 gives

$$\frac{\partial}{\partial r}\left(\left[B_0+C_0\frac{1}{r}\right]Y_{00}^2\right)\Bigg|_{r=b} = \frac{1}{4\pi b^2} = \frac{C_0}{4\pi b^2} \quad \Rightarrow \quad \text{thus, } C_0 = 1 \tag{5.45}$$

where $Y_{00} = 1/\sqrt{4\pi}$. Hence, for the $l = 0$ solution

$$g_0(r|r') = H(r' - r)A_0 + H(r - r')\left(B_0 + \frac{1}{r'}\right) \tag{5.46}$$

As before the Green's function is continuous at $r = r'$ such that the continuity conditions require

$$g_0(r' + \eta_2|r') = g_0(r' - \eta_1|r') \qquad \Rightarrow \qquad \text{thus, } A_0 = B_0 + \frac{1}{r'} \tag{5.47}$$

The jump condition is found by integrating equation 5.25 with respect to r, i.e. equation 5.35

$$\frac{dg_l(r' + \eta_2|r')}{dr} - \frac{dg_l(r' - \eta_1|r')}{dr} = -\frac{1}{r'^2} \tag{5.48}$$

The g_0 term is thus written

$$\begin{aligned} g_0(r' + \eta_2|r') &= H(r' - r)\left(B_0 + \frac{1}{r'}\right) + H(r - r')\left(B_0 + \frac{1}{r}\right) \\ &= B_0\left(H(r' - r) + H(r - r')\right) + H(r' - r)\frac{1}{r'} + H(r - r')\frac{1}{r} \end{aligned} \tag{5.49}$$

As before the constant B_0 is an arbitrary additive constant, left undetermined by the boundary conditions, appearing in any Neumann problem.

2. Case $l \geq 1$ The boundary condition imposes that $\partial N/\partial r = 1/4\pi b^2$ where

$$\begin{aligned} \partial N/\partial r &= \frac{\partial}{\partial r}\left(\sum_{l=0}^{\infty}\sum_{m=-1}^{l} g_l(r|r')Y_{lm}^*(\theta', \phi')Y_{lm}(\theta, \phi) - \frac{1}{4\pi r}\right)\Bigg|_{r=b} \\ &= \frac{\partial}{\partial r}\left(\sum_{l=0}^{\infty}\sum_{m=-1}^{l}\left[B_l r^l + C_l\frac{1}{r^{l+1}}\right]Y_{lm}^*(\theta', \phi')Y_{lm}(\theta, \phi) - \frac{1}{4\pi r}\right)\Bigg|_{r=b} \\ &= \left(\sum_{l=0}^{\infty}\sum_{m=-1}^{l}\left[B_l l r^l - C_l(l+1)\frac{1}{r^{l+2}}\right]Y_{lm}^*(\theta', \phi')Y_{lm}(\theta, \phi) + \frac{1}{4\pi r^2}\right)\Bigg|_{r=b} \\ &= \frac{1}{4\pi}\left(\sum_{l=0}^{\infty}\left[B_l l r^l - C_l(l+1)\frac{1}{r^{l+2}}\right](2l+1)P_l(\mu)\right) + \frac{1}{4\pi r^2}\Bigg|_{r=b} \end{aligned}$$

and the last term is the monopole $l = 0$ term. For this to be true $\partial g_l(r = b|r')/\partial r = 0$, i.e.

$$B_l l r^l - C_l(l+1)\frac{1}{r^{l+2}} = 0 \qquad \Rightarrow \qquad \text{thus, } C_l = B_l\frac{l}{l+1}b^{2l+1} \tag{5.50}$$

and the solution may be written

$$\begin{aligned} g_l(r|r') &= H(r' - r)A_l r^l + H(r - r')\left(B_l r^l + C_l\frac{1}{r^{l+1}}\right) \\ &= H(r' - r)A_l r^l + H(r - r')B_l\left(r^l + \frac{l}{l+1}\frac{b^{2l+1}}{r^{l+1}}\right) \end{aligned} \tag{5.51}$$

Using equation 5.51, the continuity condition requires

$$A_l = B_l\left[1 + \frac{l}{l+1}\left(\frac{b}{r'}\right)^{2l+1}\right] \tag{5.52}$$

Inserting this into equation 5.51 gives

$$g_l(r|r') = H(r'-r)B_l\left[1+\frac{l}{l+1}\left(\frac{b}{r'}\right)^{2l+1}\right]r^l + H(r-r')B_l\left(r^l+\frac{l}{l+1}\frac{b^{2l+1}}{r^{l+1}}\right) \tag{5.53}$$

The jump condition is thus used to solve for the coefficient B_l

$$\frac{dg_l(r'+\eta_2|r')}{dr} = lr^{l-1}B_l\left[1+\left(\frac{(2l+1)l}{l+1}\right)\frac{b^{2l+1}}{r'^{2l+2}}\right]$$
$$\frac{dg_l(r'-\eta_1|r')}{dr} = B_l\left[lr^{l-1}-\frac{l(l+1)}{l+1}\frac{b^{2l+1}}{r'^{l+2}}\right]$$

subtracting the two expressions gives

$$\frac{dg_l(r'+\eta_2|r')}{dr} - \frac{dg_l(r'-\eta_1|r')}{dr} = -\frac{1}{r'^2} \Rightarrow$$
$$B_l = \frac{(l+1)}{l(2l+1)}\frac{r'^l}{b^{bl+1}} \tag{5.54}$$

Inserting this into equation 5.51 gives

$$\begin{aligned} g_l(r|r') &= H(r'-r)\left(\frac{1}{2l+1}\right)\left[\left(1+\frac{1}{l}\right)\left(\frac{rr'}{b^2}\right)^l\frac{1}{b}+\frac{r^l}{r'^{l+1}}\right] \\ &+ H(r-r')\left(\frac{1}{2l+1}\right)\left[\left(1+\frac{1}{l}\right)\left(\frac{rr'}{b^2}\right)^l\frac{1}{b}+\frac{r'^l}{r^{l+1}}\right] \\ &= \left(\frac{1}{2l+1}\right)\left[\left(1+\frac{1}{l}\right)\left(\frac{rr'}{b^2}\right)^l\frac{1}{b}+\frac{r_<^l}{r_>^{l+1}}\right] \end{aligned} \tag{5.55}$$

where the notation $r_< = min(r,r')$ and $r_> = max(r,r')$ has been used.

Putting together the $l=0$ (equation 5.49) and $l \geq 1$ (equation 5.55) solutions , taking the $r < r'$ part, and placing in the complete expression for the Green's function for $l \geq 0$ equation 5.21 becomes

$$\begin{aligned} N(\mathbf{r}|\mathbf{r}') &= \frac{1}{4\pi}\sum_{l=0}^{\infty} g_l(r|r')(2l+1)P_l(\mu) \\ &= \frac{1}{4\pi}\left[\left(B_0+\frac{1}{r'}\right)+\sum_{l=1}^{\infty}P_l(\mu)\left[\left(\frac{r^l}{r'^{l+1}}\right)+\left(1+\frac{1}{l+1}\right)\frac{1}{b}\left(\frac{rr'}{b^2}\right)^l\right]\right] \\ &= \frac{1}{4\pi}\left[B_0+\frac{1}{R}+\frac{1}{b}\sum_{l=1}^{\infty}P_l(\mu)\left(1+\frac{1}{l+1}\right)\left(\frac{rr'}{b^2}\right)^l\right] \\ &= \frac{1}{4\pi}\left[B_0+\frac{1}{R}+\frac{b}{r'\tilde{R}}-\frac{1}{b}+\frac{1}{b}F_2\right] \end{aligned} \tag{5.56}$$

where the following useful substitutions have been used

$$\frac{1}{R} = \sum_{l=0}^{\infty}P_l(\mu)\left(\frac{r^l}{r'^{l+1}}\right) = \frac{1}{r'}+\sum_{l=1}^{\infty}P_l(\mu)\left(\frac{r^l}{r'^{l+1}}\right), F_2 = \sum_{l=1}^{\infty}P_l(\mu)\frac{1}{l}\left(\frac{rr'}{b^2}\right)^l$$
$$\frac{b}{4\pi r'\tilde{R}} = \frac{1}{4\pi b}\sum_{l=0}^{\infty}P_l(\mu)\left(\frac{rr'}{b^2}\right)^l = \frac{b}{4\pi b}\left[1+\sum_{l=1}^{\infty}P_l(\mu)\left(\frac{rr'}{b^2}\right)^l\right]$$

An expression for F_2 is obtained using the substitution $\xi = (rr')/b^2$ such that

$$F_2(\xi) = \sum_{l=1}^{\infty} P_l(\mu) \left(\frac{1}{l}\right) \xi^l \tag{5.57}$$

taking the derivative multiplied by ξ gives

$$\begin{aligned} \xi \frac{\partial F_2(\xi)}{\partial \xi} &= \sum_{l=1}^{\infty} P_l(\mu)\xi^l = \sum_{l=0}^{\infty} P_l(\mu)\xi^l - 1 \\ &= \frac{1}{\left[1 + \xi^2 - 2\xi\mu\right]^{1/2}} - 1 \end{aligned} \tag{5.58}$$

This is a generating function for the polynomials $P_l(\mu)$ minus the $l = 0$ term. Next dividing by ξ and integrating allows for F_2 to be re-written to a closed-form

$$\begin{aligned} \int_{\xi_1=0}^{\xi_1=\xi} F_2(\xi) d\xi &= -\int_{\xi_1=0}^{\xi_1=\xi} \left[\frac{1}{\xi\left[1 + \xi^2 - 2\xi\mu\right]^{1/2}} - \frac{1}{\xi}\right] d\xi \Rightarrow \\ F_2(\xi) &= \left[-\ln\left[\frac{2\left[1 + \xi^2 - 2\xi\mu\right]}{\xi} + \frac{2}{\xi} - 2\mu\right] - \ln\xi\right]\Bigg|_{\xi_1=0}^{\xi_2=\xi} \\ &= \ln\left[\frac{2}{\left[1 + \xi^2 - 2\xi\mu\right]^{1/2} + 1 - \xi\mu}\right] \\ &= \ln\left[\frac{2}{r'\tilde{R}/b^2 + 1 - rr'\mu/b^2}\right] \end{aligned} \tag{5.59}$$

where $F_2(\xi = 0) = 0$. Inserting equation 5.59 into equation 5.56 gives

$$N(\mathbf{r}|\mathbf{r}') = \frac{1}{4\pi}\left[B_0 + \frac{1}{R} + \frac{b}{r'\tilde{R}} - \frac{1}{b} + \frac{1}{b}\ln\left[\frac{2}{r'\tilde{R}/b^2 + 1 - rr'\mu/b^2}\right]\right] \tag{5.60}$$

As for the exterior case the constant B_0 is omitted since we are interested in the magnetic field. Setting the source radius $r' = b$ means that $\tilde{R} = R$ such that

$$N(\mathbf{r}|\mathbf{r}')\Big|_{r'=b} = \frac{1}{4\pi}\left[\frac{2}{R} - \frac{1}{b} + \frac{1}{b}\ln\left[\frac{2}{R/b + 1 - r\mu/b}\right]\right] \tag{5.61}$$

Finally, as for the exterior case, this is multiplied by a factor r'^2 such that (e.g., Barton, 1989, p. 421)

$$r'^2 N(\mathbf{r}|\mathbf{r}')\Big|_{r'=b} = \frac{b^2}{4\pi}\left[\frac{2}{R} - \frac{1}{b} + \frac{1}{b}\ln\left[\frac{2}{R/b + 1 - r\mu/b}\right]\right] \tag{5.62}$$

Here similar expressions have been used before in geomagnetism, referred to as the interior Poisson's kernel (Holschneider et al., 2016).

5.2.5 Geomagnetic Field Modelling using Green's Functions

The satellite magnetic measurements are made at geocentric radius r in the volume V of a spherical shell bounded by $r_c \leq r \leq r_m$. The volume V is bounded by a surface S having the disconnected parts S_C and S_M; S_C is closed and finite at radius r_c and S_M is closed and finite at radius r_m. The region is assumed to contain no magnetization and no

electric nor displacement currents, thus being described by a potential field, see Section 2.5. Thus the magnetic vector field $\mathbf{B}$ in the volume can be represented by the gradient of a scalar potential, $\mathbf{B} = -\nabla\psi$, which fulfils the Laplace equation $\nabla^2\psi = 0$ (e.g., Backus et al., 1996). The Laplace equation subject to prescribed values of the outward normal derivative on the surface S_C/S_M constitutes the exterior/interior Neumann boundary value problem described in Section 5.2. Thus two surfaces are considered here as being the origin of two distinct magnetic field sources; one of internal nature producing a core field, $\mathbf{B}_C$, and one of external nature producing a large-scale magnetospheric field, $\mathbf{B}_M$. Caution is needed for geomagnetists regarding the notation; the 'exterior' problem involves fields produced by internal sources while the 'interior' problem involves fields produced by external sources. Maxwell's equations are linear with respect to these sources, and thus the total field is a superposition of the magnetic fields, i.e. $\mathbf{B} = \mathbf{B}_C + \mathbf{B}_M = -\nabla\psi_C - \nabla\psi_M$, where ψ_C here describes the internal (core) sources and ψ_M describes the external (large-scale magnetospheric) sources. As shown in Section 5.2 the potential for each of these sources can be described by the integral 5.20 involving the appropriate Green's functions and the radial field at the source surface. The potential is thus written

$$\begin{aligned}\psi(\mathbf{r},t) &= \psi_C + \psi_M \\ &= \oint_{S_C} N_C(\mathbf{r}|\mathbf{r}')B_r(\mathbf{r}',t)r_c^2 dS_C + \oint_{S_M} N_M(\mathbf{r}|\mathbf{r}')B_r(\mathbf{r}',t)r_m^2 dS_M \end{aligned} \tag{5.63}$$

where $dS_C, dS_M = \sin\theta' d\theta' d\phi'$. Note that the squared radius r_c/r_m has deliberately been placed outside dS_C/dS_M (as explained in Sections 5.2.3 and 5.2.4), redefining the Green's functions; in the exterior case defined by equation 5.44 where $a = r_c$ and in the interior case defined by equation 5.62 where $b = r_m$. Therefore in the ECEF geographic spherical polar coordinate system the magnetic field components, $(k = r, \theta, \phi)$, at some observation location, $\mathbf{r}$, are linked to the radial field at surfaces S_C and S_M having positions vector, $\mathbf{r}'$, taken here to be the CMB ($r' = r_c = 3480$km) and the magnetosphere ($r' = r_m = 4r_a$) (where $r_a = 6371.2$km is the mean Earth reference radius), respectively, using the gradient of the potential equation 5.63

$$\begin{aligned}B_k(\mathbf{r},t) &= -\oint_{S_C} \nabla_k N_C(\mathbf{r}|\mathbf{r}')B_r(\mathbf{r}',t)r_c^2 dS_C - \oint_{S_M} \nabla_k N_M(\mathbf{r}|\mathbf{r}')B_r(\mathbf{r}',t)r_m^2 dS_M \\ &= \oint_{S_C} G_{C,k}(\mathbf{r}|\mathbf{r}')B_r(\mathbf{r}',t)dS_C + \oint_{S_M} G_{M,k}(\mathbf{r}|\mathbf{r}')B_r(\mathbf{r}',t)dS_M \end{aligned} \tag{5.64}$$

where $(k = r, \theta, \phi)$, and $N_C(\mathbf{r}|\mathbf{r}')$, having absorbed the term r_c^2, is the exterior Neumann Green's function and $N_M(\mathbf{r}|\mathbf{r}')$, having absorbed the term r_m^2, is the interior Neumann Green's function. Equation 5.64 consists of two homogeneous Fredholm integral equations of the first kind for the unknown radial fields at the CMB and the magnetosphere. Integral equations have the unknown and desired function, i.e. the radial field at the source surfaces in this case, under the integral sign and the functions of positions, $G_{C,k}(\mathbf{r}|\mathbf{r}')$ and $G_{M,k}(\mathbf{r}|\mathbf{r}')$, being the directional derivatives of the Green's functions with respect to $\mathbf{r}$, are referred to here as the data kernels. The Fredholm class of equations consists of definite integrals having fixed integration limits (e.g., Parker, 1977; Riley et al., 2004; Press et al., 2006). The kernels can be derived using the chain rule (Gubbins and Roberts, 1983). The exterior data kernels (associated with internal sources) are given by

$$G_{C,r} = -\frac{\partial N_C}{\partial r} = \frac{1}{4\pi}\frac{h^2(1-h^2)}{f^3} \tag{5.65}$$

$$G_{C,\theta} = -\frac{1}{r}\frac{\partial N_C}{\partial \theta} = -\frac{1}{r}\frac{\partial N_C}{\partial \mu}\frac{\partial \mu}{\partial \theta} = -\frac{1}{r}\frac{\partial N_C}{\partial \mu}[\cos\theta\sin\theta'\cos(\phi-\phi') - \sin\theta\cos\theta'] \tag{5.66}$$

$$G_{C,\phi} = -\frac{1}{r\sin\theta}\frac{\partial N_C}{\partial \phi} = -\frac{1}{r\sin\theta}\frac{\partial N_C}{\partial \mu}\frac{\partial \mu}{\partial \phi} = \frac{1}{r}\frac{\partial N_C}{\partial \mu}[\sin\theta'\sin(\phi-\phi')] \tag{5.67}$$

where the derivative with respect to μ is

$$\frac{1}{r}\frac{\partial N_C}{\partial \mu} = \frac{h}{4\pi}\left[\frac{1-2h\mu+3h^2}{f^3} + \frac{\mu}{f(f+h-\mu)} - \frac{1}{1-\mu}\right] \tag{5.68}$$

The corresponding interior data kernels (associated with external sources) are given by

$$G_{M,r} = -\frac{\partial N_M}{\partial r} = \frac{1}{4\pi}\left[h + \frac{h^2(1-h)}{f^3}\right] \tag{5.69}$$

$$G_{M,\theta} = -\frac{1}{r}\frac{\partial N_M}{\partial \theta} = -\frac{1}{r}\frac{\partial N_M}{\partial \mu}\frac{\partial \mu}{\partial \theta} = -\frac{1}{r}\frac{\partial N_M}{\partial \mu}[\cos\theta\sin\theta'\cos(\phi-\phi') - \sin\theta\cos\theta'] \tag{5.70}$$

$$G_{M,\phi} = -\frac{1}{r\sin\theta}\frac{\partial N_M}{\partial \phi} = -\frac{1}{r\sin\theta}\frac{\partial N_M}{\partial \mu}\frac{\partial \mu}{\partial \phi} = \frac{1}{r}\frac{\partial N_M}{\partial \mu}[\sin\theta'\sin(\phi-\phi')] \tag{5.71}$$

where the derivative with respect to μ is

$$\frac{1}{r}\frac{\partial N_M}{\partial \mu} = -\frac{h}{4\pi}\left[\frac{2h^2}{f^3} + \frac{r'/f}{r'-\mu r + rf)}\right] \tag{5.72}$$

where in the above expressions $h = r'/r$, $f = R/r$, $R = \sqrt{r^2 + r'^2 - 2rr'\mu}$ and $\mu = \cos\gamma = \cos\theta\cos\theta' + \sin\theta\sin\theta'\cos(\phi-\phi')$, γ being the angular distance. Similar expressions for the exterior data kernels has been given by Gubbins and Roberts (1983); Constable et al. (1993). However, it should be noted that in Gubbins and Roberts (1983) these expressions include the monopole term that was removed by Constable et al. (1993). However, here it proves useful to retain the monopole term when building Backus-Gilbert averaging kernels (Whaler, 1984).

As described in Section 3.3 both vector field data and sums and differences of the magnetic field components $B_k = \hat{\mathbf{k}} \cdot \mathbf{B}(\mathbf{r})$ in geographic spherical polar coordinates where $(k = r, \theta, \phi)$, are used in this thesis. The notation is as follows: Δd_k and Σd_k denotes the data differences and sums, respectively, which are constructed as $\Delta d_k = (\Delta d_k^{\mathrm{AT}}, \Delta d_k^{\mathrm{EW}})$, and the data sums constructed by $\Sigma d_k = (\Sigma d_k^{\mathrm{AT}}, \Sigma d_k^{\mathrm{EW}})$ for the along-track (AT) and East-West (EW) data. Using vector data, the data kernels are denoted $\{G_{C,k}; G_{M,k}\}$, while using data sums the notation is $\{\sum G_{C,k}; \sum G_{M,k}\}$ and using data differences the notation is $\{\Delta G_{C,k}; \Delta G_{M,k}\}$; these are computed as $\Delta G_{C,k} = [G_{C,k}(\mathbf{r}_1|\mathbf{r}') - G_{C,k}(\mathbf{r}_2|\mathbf{r}')]$ and $\sum G_{C,k} = [G_{C,k}(\mathbf{r}_1|\mathbf{r}') + G_{C,k}(\mathbf{r}_2|\mathbf{r}')]/2$. Figure 5.3 presents specific examples of the exterior and interior data kernels using an observation altitude above ground of 400km.

The data and the data sums kernels are effectively the same when considering the individual field components, i.e. $G_{C,r}$ and $\sum G_{C,r}$ gives the same kernel behaviour in the plots. Therefore, the left plots collects the data and data sums kernels, while the right plots collect the data difference kernels. The top plots show the exterior kernels while the bottom plots show the interior kernels. These plots illustrate how a measurement samples part of the model; for instance the radial magnetic data d_r samples the radial core field, via the kernel $G_{C,r}$, most strongly directly below the observation site while the radial data differences Δd_r samples the radial core field, via the kernel $\Delta G_{C,r} = [G_{C,r}(\mathbf{r}_1|\mathbf{r}') - G_{C,r}(\mathbf{r}_2|\mathbf{r}')]$, with highest amplitude at an angular distance of approximately 20° having no sensitivity directly beneath the observation site.

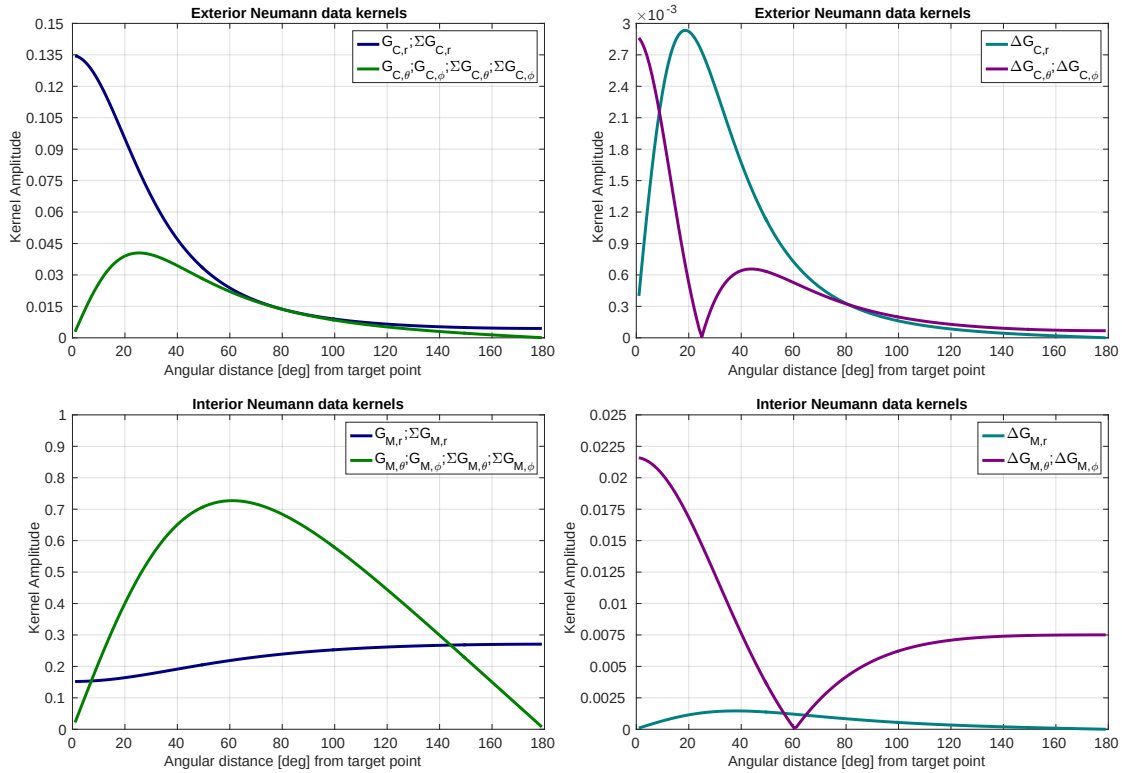

Figure 5.3: Sampling of satellite measurements of the CMB field versus angular distance from target point as determined by data kernels using an observation altitude of $r_{obs} = r_a + 400\text{km}$. Top: exterior data kernels plotted using a source radius $r' = r_c$. Bottom: interior data kernels plotted using a source radius $r' = 4r_a$.

5.3 Optimal Localized Averaging

In this section we move on to describe an approach for estimating localized averages, as determined by appropriate averaging kernels, of the radial magnetic field and its time derivatives at the core-mantle boundary. This approach offers interesting perspectives regarding the appraisal of the data resolving power; that is, the evaluation of resolution and uncertainty of the field estimate through the averaging kernels. In order to shed light on this technique, pointing out its applicability regarding investigations of the core generated magnetic field, a short introduction to inverse problems and their resolution is given below before proceeding to the actual implementation.

5.3.1 Inverse Problems and Studies of Resolution

Trying to determine the radial CMB field from magnetic data using equation 5.64 is a continuous linear inverse problem. A series of issues needs to be addressed in the Hadamard sense. Considering the (linear) problem of finite measurements, a discretized form of equation 5.64 can be written as a system of equations (e.g., Aster et al., 2005, p. 2)

$$\mathbf{d} = \underline{\underline{G}}\mathbf{m} \tag{5.73}$$

where $\mathbf{d} \in Y$ is a vector of measurements i.e. vector data or data sums and differences, $\mathbf{m} \in X$ is the desired model strived for and $\underline{\underline{G}}$ is the design matrix mapping $\underline{\underline{G}} : X \rightarrow Y$, where Y and X are data and model (Hilbert) spaces, respectively. For instance, having n measurements, the general data space would here be $Y = \mathbb{R}^n$ (Mueller and Siltanen, 2012; Schuster, 2007). The Hadamard criteria for a well-posed problem reads (e.g., Mueller and Siltanen, 2012, p. 36)

- Existence of a solution. There should be at least one solution
- Uniqueness of the solution. There should be at most one solution
- Stability of solution. The solution must depend continuously on the data

For a well-posed problem $\underline{\underline{G}}^{-1}$ exists and the straight forward solution would be $\mathbf{m} = \underline{\underline{G}}^{-1}\mathbf{d}$, such that $\underline{\underline{G}}^{-1}\underline{\underline{G}} = \underline{\underline{I}}$ where $\underline{\underline{I}}$ is the identity matrix. Contrary to this is (the more common case) of the ill-posed problem in which $\underline{\underline{G}}$ is not invertible and usually a $\underline{\underline{G}}^{\dagger}$, termed the generalized inverse, is calculated such that a model estimate is given by $\widehat{\mathbf{m}} = \underline{\underline{G}}^{\dagger}\mathbf{d}$ (Nolet, 2008; Voronin and Zaroli, 2018).

The Fredholm integral equation of the first kind encountered here in the geomagnetic problem is usually being very ill-conditioned (e.g., Parker, 1977; Riley et al., 2004; Press et al., 2006). Furthermore, instability is accentuated due to the availability of insufficient and erroneous data, and because the kernel function decays with depth, such that the possibility to decipher the field at greater depths decreases (Oldenburg, 1984). The linear inverse problem can be investigated in three ways: 1) model construction in which a model is sought that fits the data, 2) appraisal in which an unique average of the model is written as a linear combination of the data and 3) inference in which data are used to predict values of some linear functional of the model (Oldenburg, 1984). For instance, the usual approach applied in geomagnetic field modelling is the construction; the magnetic potential is represented on a global scale using a truncated spherical harmonic expansion determined in a least-squares sense imposing temporal regularization (e.g., Olsen et al., 2006; Finlay et al., 2016b), see Section 2.6.

Following Nolet (2008) and Voronin and Zaroli (2018), considering for a moment an error-free setup such that $\mathbf{d} = \underline{\underline{G}}\mathbf{m}^{true}$ where $\mathbf{m}^{true}$ denotes the true model, the solution estimate, $\widehat{\mathbf{m}}$, may be written

$$\widehat{\mathbf{m}} = \underline{\underline{G}}^{-1}\underline{\underline{G}}\mathbf{m}^{true} = \underline{\underline{R}}\mathbf{m}^{true} \tag{5.74}$$

The matrix $\underline{\underline{R}}$ is called the (model) resolution matrix, and represents the lens trough which the true model is observed. Thus, the resolution matrix describes to what level the true model is blurred by the generalized inverse when estimating the model. The estimate, $\widehat{\mathbf{m}}$, is called unbiased if each row in $\underline{\underline{R}}$ sums to one, i.e $\underline{\underline{R}} = \underline{\underline{I}}$. If for instance an estimate is constructed using a truncated singular value decomposition such that $\underline{\underline{G}}^{-1} = \underline{\underline{V}}_k\underline{\underline{\Lambda}}_k^{-1}\underline{\underline{U}}_k^T$,

the truncation may cause the resolution matrix to become biased such that $\underline{\underline{R}} = \underline{\underline{V}}_k \underline{\underline{V}}_k^T \neq \underline{\underline{I}}$ resulting in row sums being less than one, i.e. $\sum_{j=1} R_{ij} < 1$. Likewise, applying (subjective) regularization results in damped model estimates that may also introduce a bias, making obtained resolution difficult to interpret.

By considering model resolution in this way one tries to estimate to what level the obtained model reconstruction is trustworthy; the resolution length denotes the critical scale to which field structures may be inferred. Thus, consideration of resolution provides valuable insight revealing the capabilities of estimated models. There may be two approaches for estimating the resolution length: 1) using the construction approach from which smooth models may be obtained such that a qualitative appreciation can be gained, though often biased due to the applied regularization, and 2) using the Backus-Gilbert appraisal approach from which quantitative statements may be made (Backus and Gilbert, 1970; Oldenburg, 1984; Parker, 1994). Considering the conventional SH approach to field modelling, assessments of resolution suffer from what Backus et al. (1996) deemed the "circle of confusion", see Section 2.5.

In the following, we pursue a formalism based on the appraisal approach mentioned above. The geomagnetic inverse problem is explored by the Backus-Gilbert method of appraisal which provides the only unique information directly obtainable from the data, thus enabling investigation into whether all models constructed contain certain spatial (magnetic field) features of interest. In the case of accurate data, any specific linear data combination will provide a unique value of the model (i.e. the magnetic field); this can be shown to be equivalent to an unique spatial average value, determined by the inner product of an averaging kernel with the true model (field) around some particular target location of interest (Oldenburg, 1984; Pujol, 2013). In the case of inaccurate data, a variance is assigned to the averaged estimate computed such that a trade-off between spatial resolution and the variance of the estimated average arises. Any model determined, for instance in the regularized least-squares sense, which reproduces the data must attain this estimated average. To emphasise: an important difference between the construction and appraisal approaches should be understood; whereas the regularized least-squares solution refers to a damped version of the true model, the Backus-Gilbert estimates refers to averages of the actual true (undamped) model. Because the regularized least-squares solution is related to a damped version of the true model, interpretation of its resolution is not straightforward; a bias is effectively introduced in the resolution as discussed above (Nolet, 2008; Zaroli, 2016). It should be noted that the average values obtained in the appraisal approach are not designed to fit the original data. The Backus-Gilbert estimate can however in some circumstances be closer to the true value than least-squares solutions, provided the quantity being estimated is sufficiently smooth (Parker, 1977; Pujol, 2013).

5.3.2 Outline of the Optimal Localized Averaging (OLA)

The appraisal philosophy has been implemented in a class of methods called optimally localized averaging (OLA). The OLA theory was referred to as quelling by its authors and is also termed approximate inverse or mollifying method in the mathematical literature and named Backus-Gilbert theory in the geophysical literature (Backus and Gilbert, 1970; Schuster, 2007; Nolet, 2008). An important modification of the original Backus-Gilbert formalism has been developed independently by Louis and Maass (1990) and Pijpers and Thompson (1992), being termed Subtractive Optimally Localized Averages (SOLA) by the latter. The SOLA approach estimates the coefficients of linear data combinations by

minimizing a norm measuring the squared distance between the averaging kernel (i.e. the resolution) and some a prior chosen target averaging kernel; this turns out to significantly reduce the computationally burden of the method when making a large number of estimates from a given data set. The Backus-Gilbert technique has been applied to a wide range of geophysical topics (e.g., Tanimoto, 1985, 1986; Masters, 1979; Masters and Gubbins, 2003; Parker, 1994; Pujol, 2013; Zaroli, 2016; Zaroli et al., 2017). In geomagnetism, Whaler and Gubbins (1981) used the Backus-Gilbert method to invert for an average vertical field component which was then downward continued to the CMB, using the Gauss coefficients derived from 80 ground observatories as data. Later Whaler (1984) used the Backus-Gilbert theory to estimate null-flux patch integrals of the radial SV component at the CMB.

Similar to the classical 1D case, we here construct model averages as linear combinations of the data, which can be shown to be equivalent to unique spatial average values at some target point $\mathbf{r}_0$ (Backus and Gilbert, 1968, 1970; Nolet, 2008)

$$\widehat{m}^k(\mathbf{r}_0) = \sum_n^N q_n^{(k)}(\mathbf{r}_0) d_n \tag{5.75}$$

where here $k \in [1, ..., M]$ are some target node points in case multiple points are considered, i.e. $\mathbf{r}_0^1, \mathbf{r}_0^2, ...\mathbf{r}_0^M$, $q_n^{(k)}(\mathbf{r}_0)$ are some weighting coefficients to be determined and d_n are the data for $(n = 1, ..., N)$ expressed by the data kernels, G, and model, m, i.e.

$$d_n = \int_S G_n(\mathbf{r}) m(\mathbf{r}) dS \tag{5.76}$$

where dS denotes a surface integral. Inserting equation 5.76 into equation 5.75 gives

$$\widehat{m}^k = \sum_n^N q_n^{(k)} \int_S G_n(\mathbf{r}) m(\mathbf{r}) dS = \int_S \mathcal{K}^k(\mathbf{r}|\mathbf{r}_0) m(\mathbf{r}) dS \tag{5.77}$$

The function $\mathcal{K}^k$ is termed an averaging or resolution kernel and this define the resolution of the estimate, given by

$$\mathcal{K}^k(\mathbf{r}|\mathbf{r}_0) = \sum_n^N q_n^{(k)}(\mathbf{r}_0) G_n = R_k \tag{5.78}$$

This means that for a given target node point, k, the resolution is determined from the coefficients, q_n^k, of length data. Varying the coefficients results in changing the estimate and the associated averages which is always required to sum up to 1, i.e. $\sum R_k = 1$, to ensure that an unbiased estimate of the resolution is obtained.

The generalized formulation of the Backus-Gilbert method involves determining the coefficients, q_n^k, by minimizing some suitable measure of the averaging kernel (Pijpers and Thompson, 1992; Pujol, 2013)

$$\oint_S \mathcal{J}(\mathbf{r}_0)[\mathcal{K}^k(\mathbf{r}_0|\mathbf{r}') - \mathcal{T}^k(\mathbf{r}_0|\mathbf{r}')]^2 dS \tag{5.79}$$

where $\mathcal{J}$ is a weight function and $\mathcal{T}$ is some a priori target function. Selecting $(\mathcal{J} = 12(\mathbf{r} - \mathbf{r}_0)^2; \mathcal{T} = 0)$ corresponds to the original Backus-Gilbert approach of minimizing a product of a weight function and averaging kernel (the factor of 12 is dependent on

the dimensionality of the problem), this approach is also known as Multiplicative OLA (MOLA). MOLA is the traditional approach by which the coefficients are sought such that the target averaging kernel is the Dirac delta function, i.e. peaking at the target point r_0^k.

The alternative Subtractive OLA (SOLA) approach, pioneered and publicized in a series of papers by Pijpers and Thompson (1992, 1994), instead uses a norm measuring the squared distance between the averaging kernel, $\mathcal{K}^k$, and some appropriate target function, $\mathcal{T} \neq 0$, taking $\mathcal{J} = 1$. The advantage of using SOLA over the MOLA, is that significant computational time can be gained when performing calculation of multiple estimates. Coefficients are determined in the SOLA approach by minimizing the above objective function, eq. (5.79), with the possibility to include data error covariance information, $\underline{\underline{E}}$, subject to the constraint that the averaging kernel integrates to 1, i.e.

$$\begin{aligned} \min \quad & \oint_S [\mathcal{K}^k(\mathbf{r}_0|\mathbf{r}') - \mathcal{T}^k(\mathbf{r}_0|\mathbf{r}')]^2 dS + \lambda_k^2 \underline{\underline{E}} \\ \textit{subject to 1.} \quad & \int \mathcal{K}^k(r|r_0) dS = 1 \end{aligned} \tag{5.80}$$

Here the first term may be regarded as a misfit of the averaging kernel and the target kernel, however, by construction the averaging kernel is always unbiased. A range of well-characterized solutions can be obtained by varying the averaging kernel width via the trade-off parameter λ; here it is desirable to have a low averaging kernel width while at the same time having a sufficiently low uncertainty estimate for the determined field averages. The variance, $\widehat{\sigma}^2(\mathbf{r}_0)$, of the estimate propagated from the data error covariance matrix is determined as[1]

$$\widehat{\sigma}^2(\mathbf{r}_0) = \sum_{l,n}^{N} q_l q_n E_{ln} = \mathbf{q}^T \underline{\underline{E}} \mathbf{q} \tag{5.81}$$

The SOLA approach offers an additional flexibility, in that the target form $\mathcal{T}$ can take different forms i.e. Gaussian or boxcar types (Masters and Gubbins, 2003). Additionally the target kernel could be subject to the constraint of integrating to 1 and/or to 0, the latter case will be explored in an application example in Section 5.4.4 where multiple target kernels are in involved. The left plot in Figure 5.4 shows a sketch of the averaging kernel centred on some target location $\mathbf{r}_0$, and how the kernel width was determined.

5.3.3 Appraisal - Averaging Kernel Diagnostics

The main concern of the SOLA method is appraisal of the solution, that is to obtain information regarding the resolvability offered by the available geomagnetic field observations. A crucial insight is that the estimated average field is the only unique information offered by the data; that is, the average estimate along with the averaging kernel constitutes our knowledge of the magnetic field in the vicinity of the target location in question (Oldenburg, 1984; Parker, 1994). Appraisal here therefore consists of computing the field average averaging kernel and determining its width together with a measure of the uncertainty (variance) of the estimate. The original Backus-Gilbert method defined the width as the full width at half maximum (FWHM). In this project the width of the kernel was determined as the meridional distance between points at which the averaging kernel reaches zero amplitude moving away from its maximum value.

[1] Note that contamination from averaging kernel side lobs and from leakage of co-estimating fields have not been included in the variance estimates described in this project.

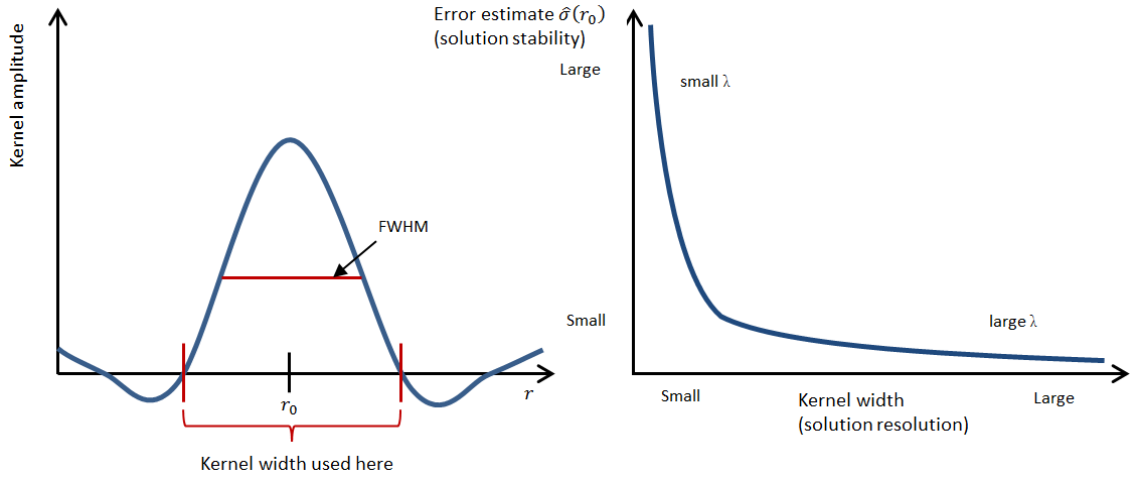

Figure 5.4: Illustration of the Backus-Gilbert appreciation of the inverse problem. The left plot shows a sketch of the averaging kernel and the right plot illustrates a trade-off curve showing estimated variance versus kernel width.

A family of solution estimates with different levels of trade-off between fitting the target function and giving an estimate with low variance, are obtained, as illustrated in the right plot in Figure 5.4. A small λ corresponds to fitting only the target function which decreases the width of the averaging kernel, increasing the spatial resolution, but at the expense of the statistical reliability and solution stability, on the other hand increasing λ broadens the averaging kernel lowering the spatial resolution, but allows a more reliable estimate having smaller variance.

5.3.4 A Preliminary Synthetic Test

This section describes a synthetic case study of the SOLA approach, testing its application to estimates of the radial main field at the CMB where the answer is known. In particular, the behaviour of the averaging kernel width and the variance estimates as a function of the number of satellite data are investigated. Experiments with varying number of data for satellite altitudes of 300km and 500km were conducted. Synthetic vector data were generated on an approximately equal area grid using the equal area (EQ) sphere partitioning algorithm of Leopardi (2006), described in Section 4.4.3. The magnetic field at the grid was generated using a synthetic dynamo model of the magnetic field (Aubert et al., 2017) for SH degrees $n \leq 30$. The top left plot of Figure 5.5 shows the input model of Aubert et al. (2017) for SH degrees $n \leq 30$. Using the terminology of Section 5.3.2, the SOLA estimates, $\widehat{m}$, are here estimates of the radial magnetic field at the CMB, and the data kernels are expressed by the exterior data kernels of Section 5.2.5 (i.e. equations (5.65) to (5.67)), and as a target, $\mathcal{T}(\mathbf{r}_0|\mathbf{r}')$, a Fisher function on a sphere having the width parameter κ was used, see Section 5.4 for further details regarding the Fisher function. In these studies $\kappa = 200$ and $\lambda = 10^{-4}\text{nT}^{-1}$ were used. In studies with the real data in Section 5.4, further investigations into the behaviour of the averaging kernel width and variance estimates as a function of κ were carried out. Details of the numerical implementation used for this test are given in Section 5.4.1.

Figure 5.6 present the key results of the SOLA method applied to synthetic data at 300km and 500km altitudes for various number of approximately equal area distributed data, $1000, 2000, ..., 40000$. The plot shows the averaging kernels for an example location

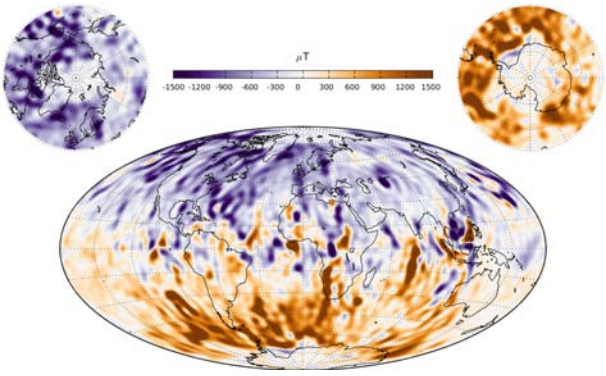

(a) Radial CMB field from the model of Aubert et al. (2017) for SH degrees $n \leq 30$.

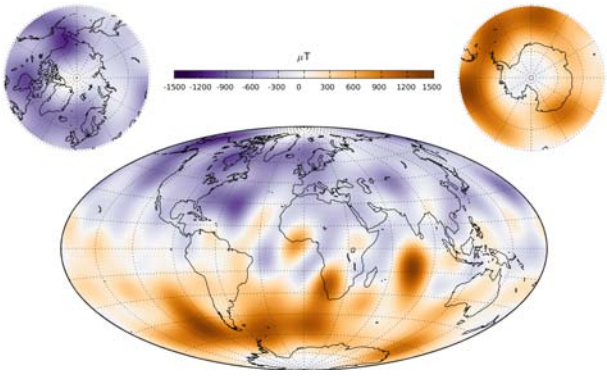

(b) Radial CMB field from the model of Aubert et al. (2017) for SH degrees $n \leq 13$.

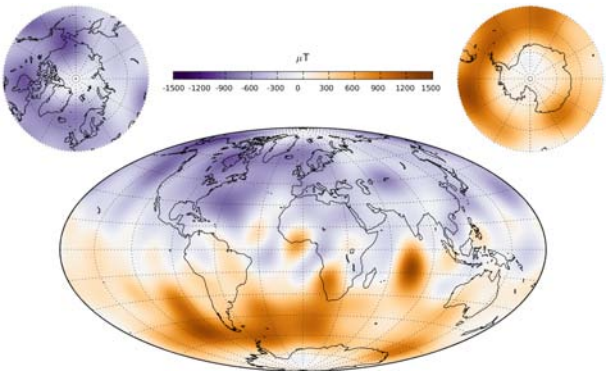

(c) Radial CMB field from SOLA using 1000 data.

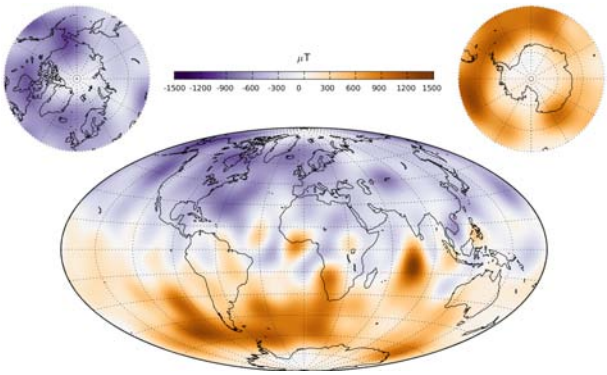

(d) Radial CMB field from SOLA using 40000 data.

Figure 5.5: Radial core field at the CMB: a) and b) show predictions from the model of Aubert et al. (2017) truncated at SH degrees 30 and 13, respectively. c) and d) show the collected global estimates from the SOLA method having $\kappa = 200$ using 1000 and 40000 data points, respectively. Units in $[\mu\mathrm{T}]$.

at latitude 0° and longitude -168°. The blue curve shows the kernel using only 1000 data and the red curve shows the kernel using 40000 data, while the black kernels are shown for intermediate steps of 3000 data. The left plot in Figure 5.7 presents the width of the averaging kernels (see Figure 5.4) as a function of the number of data, showing in blue data at for 300km altitude and red data for 500km altitude. The right plot in Figure 5.7 presents the behaviour of the uncertainty estimate as a function of the number of data. Random noise was added to the synthetic data, and a diagonal covariance matrix was used having variances of $1\mathrm{nT}^2$. The averaging kernels obtained using the two altitudes did behave very similarly. As can be seen, the kernel amplitude increases and the width decreases slightly when increasing the number of data. The variance is also seen to decrease as the number of data increases. It is also seen that both the kernel width and uncertainty estimates appear to be converging, so little improvements is gained by adding further data beyond 30.000. Notice also that the FWHM of the averaging does not change significantly for all the data sets used. It thus seems as there is a limit of approximately 27°, beyond which no further increase in spatial resolution may be gained by adding more data. Looking at global collections of SOLA field estimates at the CMB in Figure 5.5, plots c) and d) built using 1000 and 40000 data for an altitude of 300km, respectively, the same overall field structures are seen. However, looking carefully there are some small differences in

amplitude and resolution between the two. This is expected based on Figures 5.6 and 5.7. A kernel width of approximately 27° would correspond roughly to SH degree 13. Comparing with the core field at the CMB from the model of Aubert et al. (2017) for SH degrees $n \leq 13$ and the two maps computed using the SOLA method, it is clear that our SOLA approach succeeds in reproducing the field features observed in the model of Aubert et al. (2017).

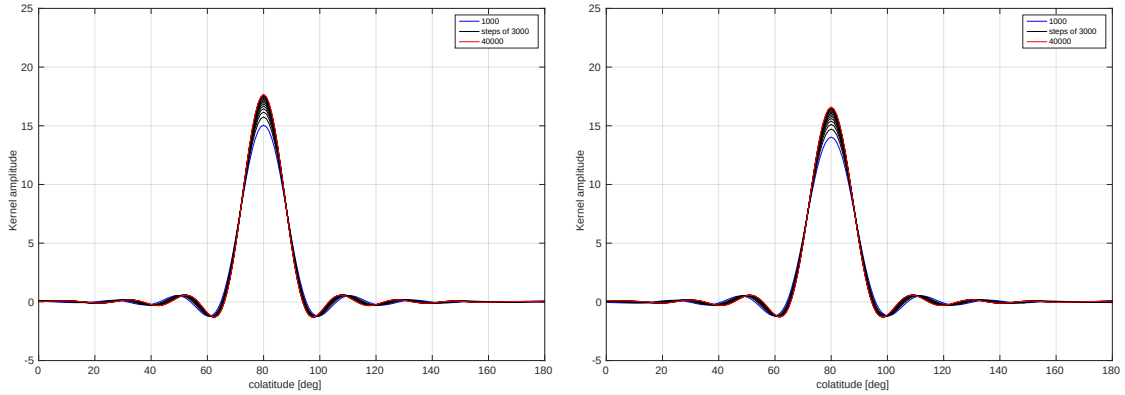

Figure 5.6: SOLA averaging kernel behaviour for the synthetic data test, based on $\kappa = 200$ and for increasing numbers of data at altitudes of 300km (left) and 500km (right). The kernels are shown using 1000 data points (blue kernel) increasing to 40000 (red kernel) in steps of 3000.

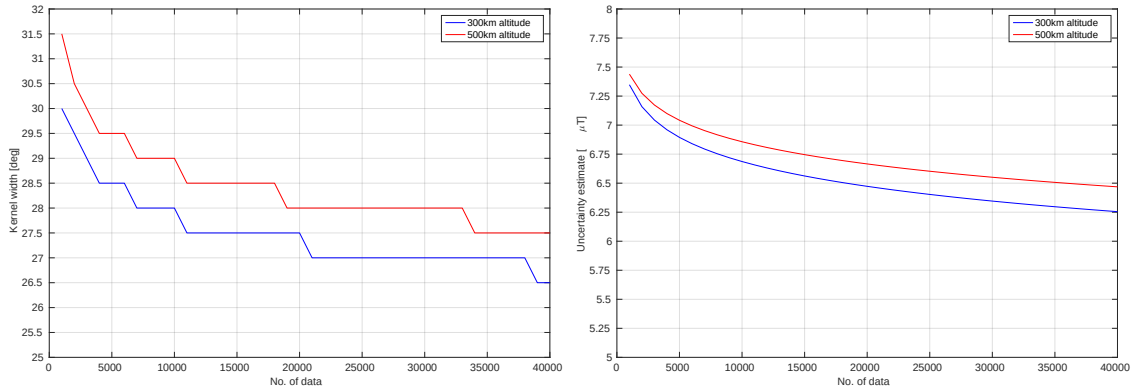

Figure 5.7: SOLA averaging kernel widths (left) and estimate uncertainty (right) for the synthetic data test, based on $\kappa = 200$, as a function of the number of data, for altitudes of 300km (blue) and 500km (red).

In the following sections the SOLA technique is implemented using real satellite data such that at specified locations on the CMB, local spatial averages of the radial magnetic field are computed and appraisal is carried out. The CMB magnetic field is related to the observations via the Green's functions described in Section 5.2. Section 5.4 presents a general formalism where the potential is described by both internal and external source contributions. The time dependence of the field is handle by a Taylor series expansion in time. Section 5.5 presents a treatment of the time dependence using kernel polynomial approximation.

5.4 Estimation of Time-dependent CMB Field: A Taylor Expansion Approach

In this section the SOLA method described in Section 5.3.2 is applied to the geomagnetic problem of inferring the time-dependent radial magnetic field and its time derivatives at the CMB. Here a Taylor series expansion is used to parametrize the time dependence of the field. The numerical implementation of the theory is described in Section 5.4.1 and 5.4.2. Applications of the SOLA method to estimates of the radial MF field using Swarm data, and to the radial SV field using Swarm and CHAMP data, are presented in Sections 5.4.3 and 5.4.4, respectively. The accumulated radial SA was computed as SV epoch differences and results of this are presented in Section 5.4.5.

Using the SOLA method outlined in Section 5.3.2 to the linear system, described by equation (5.64), an estimate of the radial field, $\widehat{B_r}$, is determined as a spatial average optimally localized at a particular location and time of interest $(\mathbf{r}_0, t_0) = (r_c, \theta_0, \phi_0, t_0)$. Following Backus and Gilbert (1970) the estimate can be written as an inner product of the radial field of interest with some averaging kernel, determined as a linear combination of the data; equation (5.75) in this application becomes

$$\widehat{B_r}(\mathbf{r}_0, t_0) = \sum_{n}^{N} q_n(\mathbf{r}_0, t_0) d_n(\mathbf{r}, t) \tag{5.82}$$

where $(n = 1, ..., N)$ are the data from a specified time window and q_n are weighting coefficients to be determined. Using equation (5.64), the data d_n at a particular position $\mathbf{r}_n$ and time t_n for the field component k, are given as the vector data or data sums and differences (see Section 5.2.5), and are related to the radial magnetic field, $B_r(\mathbf{r}', t)$, at the source regions; here taken to be the CMB and the magnetosphere. In this section, we allow the field at the CMB to be time-dependent, adopting a first order Taylor expansion assumed to be valid close to a reference time t_0, i.e.

$$\begin{aligned} d_{k,n}(\mathbf{r}, t) &= \oint_{S_C} G^*_{C,k}(\mathbf{r}_n|\mathbf{r}') B_r(\mathbf{r}', t_n) dS_C + \oint_{S_M} G^*_{M,k}(\mathbf{r}_n|\mathbf{r}') B_r(\mathbf{r}', t_n) dS_M \\ &\approx \oint_{S_C} G^*_{C,k}(\mathbf{r}_n|\mathbf{r}') \left[B_r(\mathbf{r}', t_0) + \dot{B}_r(\mathbf{r}', t_0) \Delta t_n \right] dS_C \\ &\quad + \oint_{S_M} G^*_{M,k}(\mathbf{r}_n|\mathbf{r}') B_r(\mathbf{r}', t_n) dS_M \end{aligned} \tag{5.83}$$

A difference here compared to equation (5.64) is the notation G^*; because the actual data kernels which are used in the computations are either related to the vector data, or to the data sums and differences, a more general notation including a * will be used to describe any given data kernel, and not the complex conjugate. Therefore, $G^*_k(\mathbf{r}_n|\mathbf{r}')$ are the appropriate data kernels for the vector field components or the sums and differences of vector field components, see Section 5.2.5. Here the time differences are with respect to some reference time, t_{ref}, such that as $\Delta t_n = t_n - t_{ref}$. In general the reference time and the target time need not to be the same; however for simplicity it was decided to select the reference time to be the target time, i.e. $t_{ref} = t_0$.

Inserting equation (5.83), via the chosen data (i.e. vector field or vector field sums and differences), into equation (5.82), the field estimate at the target time t_0 is then given by

$$\widehat{B_r}(\mathbf{r}_0,t_0) = \oint_{S_C} \sum_n^N q_n(\mathbf{r}_0,t_0) G^*_{C,k}(\mathbf{r}_n|\mathbf{r}') B_r(\mathbf{r}',t_0) dS_C + \oint_{S_C} \sum_n^N q_n(\mathbf{r}_0,t_0) G^*_{C,k}(\mathbf{r}_n|\mathbf{r}') \dot{B}_r(\mathbf{r}',t_0) \Delta t_n dS_C + \oint_{S_M} \sum_n^N q_n(\mathbf{r}_0,t_0) G^*_{M,k}(\mathbf{r}_n|\mathbf{r}') B_r(\mathbf{r}',t_n) dS_M \quad (5.84)$$

The weighting coefficients, q_n, define spatial averaging kernels that are linear combinations of the data kernels, i.e.

$$\mathcal{K}_C(\mathbf{r}_0,t_0|\mathbf{r}',t_0) = \sum_n^N q_n(\mathbf{r}_0,t_0) G^*_C(\mathbf{r}_n|\mathbf{r}') \quad (5.85)$$

$$\mathcal{K}_{\dot{C}}(\mathbf{r}_0,t_0|\mathbf{r}',t) = \sum_n^N q_n(\mathbf{r}_0,t_0) G^*_C(\mathbf{r}_n|\mathbf{r}') \Delta t_n \quad (5.86)$$

$$\mathcal{K}_M(\mathbf{r}_0,t_0|\mathbf{r}',t) = \sum_n^N q_n(\mathbf{r}_0,t_0) G^*_M(\mathbf{r}_n|\mathbf{r}') \quad (5.87)$$

Here the notation $\mathcal{K}_{\dot{C}}$ include the time difference Δt_n from the Taylor expansion to the data kernel defining $G^*_{\dot{C}} = G^*_C \Delta t_n$. Therefore the estimated radial field consists of spatial integrals over the source spheres of the true field convolved with the averaging kernels, i.e.

$$\widehat{B_r}(\mathbf{r}_0,t_0) = \oint_{S_C} \mathcal{K}_C(\mathbf{r}_0,t_0|\mathbf{r}',t) B_r(\mathbf{r}',t_0) dS_C + \oint_{S_C} \mathcal{K}_{\dot{C}}(\mathbf{r}_0,t_0|\mathbf{r}',t) \dot{B}_r(\mathbf{r}',t_0) dS_C + \oint_{S_M} \mathcal{K}_M(\mathbf{r}_0,t_0|\mathbf{r}',t) B_r(\mathbf{r}',t) dS_M \quad (5.88)$$

The SOLA field estimates then consist of integrals of the true model weighted by spatial averaging kernels such that the kernel width expresses the area over which the true model has been averaged; varying the coefficients, q_n, changes the shape of the averaging kernels accordingly. Incorporating the time differences in the averaging kernel may be thought of as assigning temporal weights to that kernel. The desired weights may act in such a way as to produce SOLA estimates of the SV field; for instance, selecting data from a time window of two years centred on the reference time will assign equal weights having opposite signs for data equal times such that field differences are effectively computed. In order for the estimate to be a meaningful physical average and to avoid a biased result, a normalization of the averaging kernels was implemented requiring a unimodular constraint to be fulfilled, that is

$$\oint_{S_C} \mathcal{K}_C(\mathbf{r}_0,t_0|\mathbf{r}',t) dS_C + \oint_{S_C} \mathcal{K}_{\dot{C}}(\mathbf{r}_0,t_0|\mathbf{r}',t) dS_C + \oint_{S_M} \mathcal{K}_M(\mathbf{r}_0,t_0|\mathbf{r}',t) dS_M = 1 \quad (5.89)$$

In practice, the target term of interest (the CMB field, the CMB SV or the magnetospheric field) should integrate to one and the other terms should integrate to zero. Note here that the monopole term was retained in equations (5.65) to (5.71); this was necessary in order to prevent the averaging kernels from integrating to zero in violation of the unimodular constraint (Whaler, 1984).

Following the SOLA approach as outlined in Section 5.3.2, in order to determine the coefficients, an objective function is defined which is minimized

$$\Theta = \oint_{S_C} [\mathcal{K}_C(\mathbf{r}_0|\mathbf{r}') - \mathcal{T}_C(\mathbf{r}_0|\mathbf{r}')]^2 dS_C + \oint_{S_C} [\mathcal{K}_{\dot{C}}(\mathbf{r}_0|\mathbf{r}') - \mathcal{T}_{\dot{C}}(\mathbf{r}_0|\mathbf{r}')]^2 dS_C + \oint_{S_M} [\mathcal{K}_M(\mathbf{r}_0|\mathbf{r}') - \mathcal{T}_M(\mathbf{r}_0|\mathbf{r}')]^2 dS_M + \lambda^2 \mathbf{q}^T \underline{\underline{\mathbf{E}}} \mathbf{q} \tag{5.90}$$

where λ (units of $[\mathrm{nT}^{-1}]$) is a trade-off parameter and $\underline{\underline{\mathbf{E}}}$ is the data error covariance matrix because data contains noise. Regarding the spatial target kernel, $\mathcal{T}$, different possibilities exists; for instance a Fisher function or a disc box car function could be used. The Fisher function on a sphere using the angular distance $\Psi(\mathbf{r}_0|\mathbf{r}')$ was here chosen

$$\mathcal{T}(\Psi) = \frac{\kappa}{4\pi \mathrm{sinh}\kappa} e^{\kappa cos\Psi} \tag{5.91}$$

where κ is the width of the Fisher function (Fisher, 1953). Here $\mathrm{cos}\Psi = \mathrm{cos}\theta_0 \mathrm{cos}\theta' + \mathrm{sin}\theta_0 \mathrm{sin}\theta' \mathrm{cos}(\phi_0 - \phi')$, Ψ being the angular distance between points $\mathbf{r}_0$ and $\mathbf{r}'$ on the sphere. The target kernels were the same for all targets, i.e. $\mathcal{T}_C, \mathcal{T}_{\dot{C}}, \mathcal{T}_M = \mathcal{T}$. Furthermore, it was enforced that $\mathcal{T}(\Psi)$ should integrate to one for the term of interest in equation (5.85) and zero for the remaining terms. Which terms to include in the objective function depends on the desired field estimate; for instance estimating the radial field over a time window short enough, such that field time-dependence could be ignored, means that the second term was not included. On the other hand estimation of the radial SV field involved retaining the second term as well while setting the target kernels $\mathcal{T}_C, \mathcal{T}_M$ to zero. The diagonal elements of the data error covariance matrix, $\underline{\underline{\mathbf{E}}}$, were constructed using latitude-dependent data error estimates, σ_n, and the Huber weights, w_n accounting for a long-tailed error distribution (see Section 3.4.2 for more details)

$$\sigma_{w,n}^2 = \frac{\sigma_n^2}{w_n} \tag{5.92}$$

In experiments when only MF was estimated, satellite data simply sampled at 15sec intervals from one month was used, and it was assumed that there was no time variation of the field. As described in Section 3.4.3, satellite data are expected to have an along-track (latitudinal) correlation due to noise from unmodelled currents, with an estimated correlation time of 5-10 min based on the findings of Lowes and Olsen (2004). Therefore an exponential data error covariance model was used in this case, having a correlation time of 10 min such that the data error covariance matrix was written as equation 3.4.2 (see Section 3.4.3 for further details), i.e.

$$E_{ln} = \sigma_{w,n}^2 e^{\frac{-\Delta t_{ln}}{\tau}} \tag{5.93}$$

where $\Delta t_{ln} = t_l - t_n$ are the time differences and $\tau = 600$s is the assumed correlation time, i.e. 10min. As stated in Section 3.4.3, the covariance matrix is required to be symmetric (i.e. $E_{ln} = E_{nl}$) and positive definite (i.e. its eigenvalues must be greater than 0). When estimating the main field, see Section 5.4.3, a weight by a factor $\mathrm{sin}\theta$ was included, where θ is the geographic co-latitude to account for there being more data (when sampled in regular intervals along-track) close to the poles and in order to approximate an equal-area distribution (e.g., Olsen et al., 2014). When estimating the radial SV, see Section 5.4.4, data were selected such as to obtain a good global coverage and not sampled at regular intervals along-track, since data in this case were not temporally continuous, the temporal data error correlation could be neglected.

5.4.1 Method for Numerical Implementation

The minimization of the objective function equation (5.90) was performed by taking the derivative with respect to q_n, such that $\partial\Theta/\partial q_n = 0$, i.e.

$$\frac{d}{dq_n}\left(\oint_{S_C}[\mathcal{K}_C^2 + T_C^2 - 2\mathcal{K}_C T_C]dS_C + \oint_{S_C}[\mathcal{K}_{\dot{C}}^2 + T_{\dot{C}}^2 - 2\mathcal{K}_{\dot{C}} T_{\dot{C}}]dS_C \right.$$
$$\left. + \oint_{S_M}[\mathcal{K}_M^2 + T_M^2 - 2\mathcal{K}_M T_M]dS_M + \lambda^2 \mathbf{q}^T \underline{\underline{E}}\mathbf{q}\right) = 0 \Rightarrow$$
$$\frac{d}{dq_n}\left(\oint_{S_C}\left[\left(\sum q_n G_n\right)^2 + T_C^2 + 2\sum q_n G_n T_C\right]dS_C + \oint_{S_C}\left[\left(\sum q_n G_n\right)^2 + T_{\dot{C}}^2 + \right.\right.$$
$$\left.\left. + 2\sum q_n G_n T_{\dot{C}}\right]dS_C + \oint_{S_M}\left[\left(\sum q_n G_n\right)^2 + T_M^2 + 2\sum q_n G_n T_M\right]dS_M + \lambda^2 \sum q_n^2 \sigma^2\right) = 0$$

Following Larsen and Hansen (1997) the resulting set of equations subject to the constraint equation (5.89) may be written in matrix-vector form as

$$\left[\underline{\underline{\mathbf{K}}}_C \underline{\underline{\mathbf{W}}}\, \underline{\underline{\mathbf{K}}}_C^T + \underline{\underline{\mathbf{K}}}_{\dot{C}} \underline{\underline{\mathbf{W}}}\, \underline{\underline{\mathbf{K}}}_{\dot{C}}^T + \underline{\underline{\mathbf{K}}}_M \underline{\underline{\mathbf{W}}}\, \underline{\underline{\mathbf{K}}}_M^T + \lambda^2 \underline{\underline{\mathbf{E}}}\right]\mathbf{q}(\mathbf{r}_0)$$
$$= \underline{\underline{\mathbf{K}}}_C \underline{\underline{\mathbf{W}}}\mathbf{t}_C(\mathbf{r}_0) + \underline{\underline{\mathbf{K}}}_{\dot{C}} \underline{\underline{\mathbf{W}}}\mathbf{t}_{\dot{C}}(\mathbf{r}_0) + \underline{\underline{\mathbf{K}}}_M \underline{\underline{\mathbf{W}}}\mathbf{t}_M(\mathbf{r}_0)$$
$$\textit{subject to} \quad \left[\mathbf{e}_p^T \underline{\underline{\mathbf{W}}}\, \underline{\underline{\mathbf{K}}}_C^T + \mathbf{e}_p^T \underline{\underline{\mathbf{W}}}\, \underline{\underline{\mathbf{K}}}_{\dot{C}}^T + \mathbf{e}_p^T \underline{\underline{\mathbf{W}}}\, \underline{\underline{\mathbf{K}}}_M^T\right]\mathbf{q}(\mathbf{r}_0) = 1 \qquad (5.94)$$

Here the $\mathbf{K}$ matrices having size $N \times M$, are defined such that

$$(\mathbf{K})_{np} = \left[G_{C,n}^*(\mathbf{r}_p), G_{\dot{C},n}^*(\mathbf{r}_p), G_{M,n}^*(\mathbf{r}_p)\right], \quad n = 1, ..., N \quad p = 1, ..., M \qquad (5.95)$$

and $\mathbf{W}$ is a diagonal matrix of size $M \times M$ where M is the number of integration points on the sphere

$$(\mathbf{W})_{pp} = l_p, \quad p = 1, ..., M \qquad (5.96)$$

and three vectors have been introduced: $\mathbf{e}_p = (1, ..., 1)^T$, $\mathbf{t}(\mathbf{r}_0)$ having elements related to the targets $(\mathbf{t}(\mathbf{r}_0))_p = \mathcal{T}(\mathbf{r}_0|\mathbf{r}_p)$ and $\mathbf{k}(\mathbf{r}_0)$ having elements $(\mathbf{k}(\mathbf{r}_0))_p = \mathcal{K}(\mathbf{r}_0|\mathbf{r}_p)$ for $p = 1, ..., M$. The discretized averaging kernel was calculated as $\mathbf{k}(\mathbf{r}_0) = \underline{\underline{\mathbf{K}}}^T \mathbf{q}(\mathbf{r}_0)$. The required angular integrations over the CMB and magnetosphere were performed numerically using Lebedev angular quadrature (Lebedev and Laikov, 1999), see Section 5.4.2, such that

$$\int_S F(\mathbf{r}')dS \approx \sum_{p=1}^{M} l_p F(\mathbf{r}_p) \qquad (5.97)$$

It was found that using $M = 1730$ Lebedev points, corresponding to SH degree and order 71, were sufficient to perform the integrations to the required accuracy. The normal equations for the coefficients, $\mathbf{q} = (q_1, ..., q_N)$, were finally solved using a Lagrange multiplier μ as proposed by (Pijpers and Thompson, 1994)

$$\begin{pmatrix} \underline{\underline{\mathbf{K}}}_C \underline{\underline{\mathbf{W}}}\, \underline{\underline{\mathbf{K}}}_C^T + \underline{\underline{\mathbf{K}}}_{\dot{C}} \underline{\underline{\mathbf{W}}}\, \underline{\underline{\mathbf{K}}}_{\dot{C}}^T + \underline{\underline{\mathbf{K}}}_M \underline{\underline{\mathbf{W}}}\, \underline{\underline{\mathbf{K}}}_M^T + \lambda^2 \underline{\underline{\mathbf{E}}} & \underline{\underline{\mathbf{K}}}_C \underline{\underline{\mathbf{W}}}\mathbf{e}_p + \underline{\underline{\mathbf{K}}}_{\dot{C}} \underline{\underline{\mathbf{W}}}\mathbf{e}_p + \underline{\underline{\mathbf{K}}}_M \underline{\underline{\mathbf{W}}}\mathbf{e}_p \\ \mathbf{e}_p^T \underline{\underline{\mathbf{W}}}\, \underline{\underline{\mathbf{K}}}_C^T + \mathbf{e}_p^T \underline{\underline{\mathbf{W}}}\, \underline{\underline{\mathbf{K}}}_{\dot{C}}^T + \mathbf{e}_p^T \underline{\underline{\mathbf{W}}}\, \underline{\underline{\mathbf{K}}}_M^T & 0 \end{pmatrix}$$
$$\begin{pmatrix} \mathbf{q}(\mathbf{r}_0) \\ \mu \end{pmatrix} = \begin{pmatrix} \underline{\underline{\mathbf{K}}}_C \underline{\underline{\mathbf{W}}}\mathbf{t}_C(\mathbf{r}_0) + \underline{\underline{\mathbf{K}}}_{\dot{C}} \underline{\underline{\mathbf{W}}}\mathbf{t}_{\dot{C}}(\mathbf{r}_0) + \underline{\underline{\mathbf{K}}}_M \underline{\underline{\mathbf{W}}}\mathbf{t}_M(\mathbf{r}_0) \\ 1 \end{pmatrix}$$

The first matrix term on the left hand side is independent of estimate position $\mathbf{r}_0$. This is important because it needs only to be computed once which significantly reduces the amount of computations required (under the original Backus-Gilbert settings this would have to be computed for every target location). The linear system was solved for the vector containing $(q_1, ..., q_N, \mu)$ such that averaging kernels and uncertainty estimates could be re-computed. It should be noted that an alternative LSQR solution schemes could also have been implemented to solve the problem (Larsen and Hansen, 1997; Zaroli, 2016) but we did not find it necessary. When estimating the radial MF at a given location, data from within a month were used, such that the term involving $\underline{\underline{\mathbf{K}}}_{\dot{C}}$ was neglected and the target kernel terms $\mathbf{t}_{\dot{C}}(\mathbf{r}_0), \mathbf{t}_M(\mathbf{r}_0)$ were set to zero. When estimating the radial SV the target kernel terms $\mathbf{t}_C(\mathbf{r}_0), \mathbf{t}_M(\mathbf{r}_0)$ were set to zero.

5.4.2 Lebedev Quadrature for Integration Over a Sphere

The numerical integrations over the source spheres were performed numerically using Lebedev angular quadrature weights (Lebedev and Laikov, 1999). The fundamental issue of quadrature is to evaluate a definite integral, here being a surface integration over the three-dimensional sphere having surface S

$$I[F] = \int_S F(\mathbf{r}')dS = \int_0^{2\pi} \int_0^{\pi} F(r', \theta', \phi')\sin\theta d\theta d\phi \tag{5.98}$$

Lebedev introduced a quadrature that approximates the surface integral defined by a fixed set of weights, l_p, and base points, M_p (Lebedev, 1975, 1976, 1977). The Lebedev angular quadrature on a grid $\mathbf{r}_p = (r_p, \theta_p, \phi_p)$ is here written

$$S_{M_p}[F] = \sum_{p=1}^{M_p} l_p F(\mathbf{r}_p) \tag{5.99}$$

that is, a weighted sum of the function at given points. Note here that no distinction between the base points were made, e.g. vertices, center of faces etc. in contrast to the complete description (Lebedev, 1976). The grid weights and positions were computed from the condition that the quadrature exactly integrates all spherical harmonics up to a given degree. Furthermore, a requirement is that the points are invariant with respect to the octahedron rotation group (Lebedev, 1976). Lebedev and Laikov extended the rules to $L_{max} = 131$ (Lebedev and Laikov, 1999). A Matlab tool getLebedevSphere `https://se.mathworks.com/matlabcentral/fileexchange/27097-getlebedevsphere` was used to derived the Lebedev rules, specifying the rules $M_p = \{6, 14, 26, 38, 50, 74, 86, 110, 146, 170, 194, 230, 266, 302, 350, 434, 590, 770, 974, 1202, 1454, 1730, 2030, 2354, 2702, 3074, 3470, 3890, 4334, 4802, 5294, 5810\}$ with corresponding SH degree $L_{max} = \{3, 5, 7, 9, 11, 13, 15, 17, 19, 21, 23, 25, 27, 29, 31, 35, 41, 47, 53, 59, 65, 71, 77, 83, 89, 95, 101, 107, 113, 119, 125, 131\}$ (Lebedev and Laikov, 1999; Parrish, 2010). Using getLebedevSphere each set can integrate a spherical harmonic up to degree L_{max} to an accuracy of 10^{-14}. There may be 6, 8, 12, 24 or 48 equivalent positions included in the grid (i.e. a minimum grid has $M_p = 6$) assigned the same weights. Figure 5.8 presents a plot showing the distribution of 1730 Lebedev points used for the calculations of Sections 5.4.3 and 5.4.4.

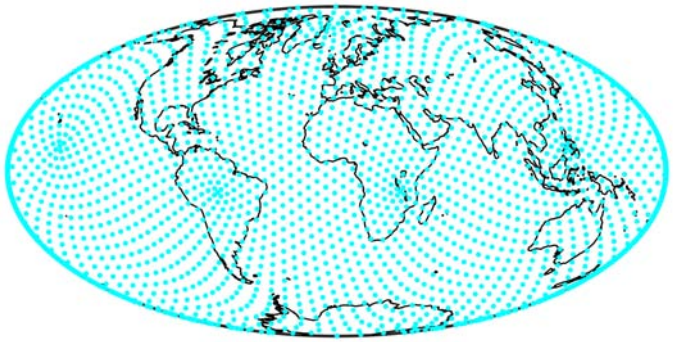

Figure 5.8: 1730 globally distributed Lebedev quadrature points.

5.4.3 Application to Estimation of the Main Field at the CMB

As a first application with the real data, the SOLA method is illustrated here by computing radial field estimates at a sequence of target locations at the CMB using along-track and east-west sums and differences of *Swarm* field measurements taken from March 2017 of Data Set 2, see Section 3.3. Using the sums and differences of the vector field, the data vector was given as $\mathbf{d} = \{\Delta d_r, \Sigma d_r, \Delta d_\theta, \Sigma d_\theta, \Delta d_\phi, \Sigma d_\phi\}$. The data kernels were constructed as

$$G^* = \{\Delta G_{C,r}; \Sigma G_{C,r}; \Delta G_{C,\theta}; \Sigma G_{C,\theta}; \Delta G_{C,\phi}; \Sigma G_{C,\phi}\}$$

where $\Delta G_{C,k} = [G_{C,k}(\mathbf{r}_1|\mathbf{r}') - G_{C,k}(\mathbf{r}_2|\mathbf{r}')]$ and $\Sigma G_{C,k} = [G_{C,k}(\mathbf{r}_1|\mathbf{r}') + G_{C,k}(\mathbf{r}_2|\mathbf{r}')]/2$, for the component $(k = r, \theta, \phi)$, are the data kernels for the differences and sums, respectively. Because the focus was on estimating the radial component of the CMB field itself, the second term was omitted from the objective function equation (5.90) and the constraint equation (5.89). The exponential data error covariance model was included along with an equal area weighting factor as described in Section 5.4. Sections 3.4.2 and 3.4.3 provide more detail on the data also explaining the construction of the data error covariance matrix, $\underline{\underline{E}}$, and the data error correlation model used, including plots for the March 2017 data used here.

In Figure 5.9 the behaviour of the MF averaging kernel, $\mathcal{K}_C$, is investigated as a function of the target kernel width parameter κ, and the trade-off parameter λ, by considering a series of example averaging kernels at QD latitude 0° and longitude −168°. The plots include the error estimate for the field average (see equation (5.81)) and the approximate kernel width in degrees (see Figure 5.4). Increasing κ (i.e. going from left to right in the plot columns) will cause the kernel to become narrower while increasing the amplitude of the estimate, but also its variance. However, increasing κ also induces more side-lobe oscillations in the kernel structure around the target location. Increasing λ (i.e. going from top to bottom in the plot rows) will decrease the kernel amplitude and increase its width, reducing the side lobe oscillations. In order to obtain a good resolution it is desirable to select a narrow, high amplitude, kernel, while at the same time trying to keep the side lobe oscillations to a minimum. Figure 5.10 presents the behaviour of the external averaging kernel, $\mathcal{K}_M$, for the corresponding computations presented in Figure 5.9, i.e. the target is the internal field and the external kernels show the level on contamination. The MF averaging kernels are all well behaved showing only minor side lobes compared to the kernel maximum amplitudes; this motivates us to push towards a high κ value.

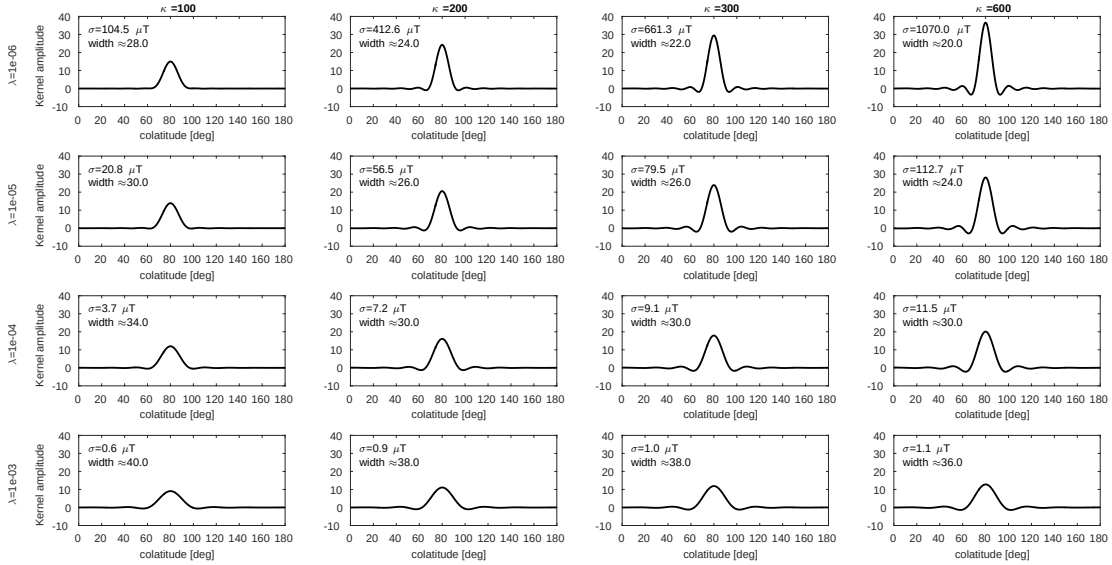

Figure 5.9: Main field application using data from March 2017 shown at target location QD latitude 0°: behaviour of the averaging kernel as a function of Fisher function width κ and trade-off parameter λ. The value of κ increases from the left column where $\kappa = 100$ to the right column where $\kappa = 600$. The value of λ increases from the top row of $\lambda = 10^{-6}\mathrm{nT}^{-1}$ to the bottom row having $\lambda = 10^{-3}\mathrm{nT}^{-1}$. In each plot the estimated uncertainty $\widehat{\sigma}$ and kernel width in degrees are stated.

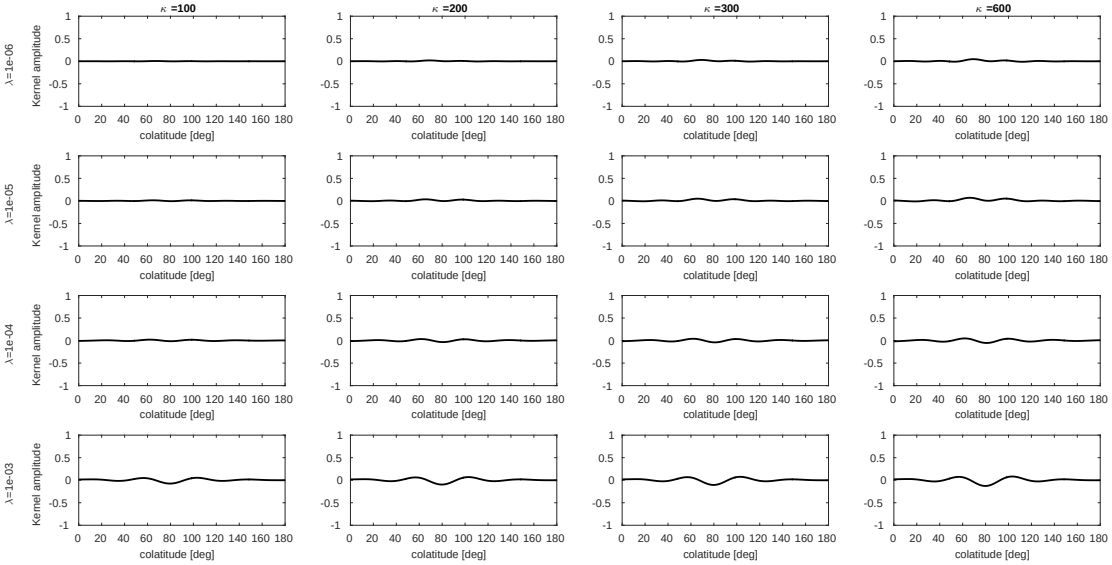

Figure 5.10: Main field application using data from March 2017 shown at target location QD latitude 0°: behaviour of the external averaging kernel as a function of Fisher function width κ and trade-off parameter λ. The value of κ increase from left column having $\kappa = 100$ to right column having $\kappa = 600$. The value of λ increases from top row of $\lambda = 10^{-6}\mathrm{nT}^{-1}$ to bottom row having $\lambda = 10^{-3}\mathrm{nT}^{-1}$. In each plot the estimated uncertainty $\widehat{\sigma}$ and kernel width in degrees are stated.

Next an investigation into how the SOLA method performs at four different QD latitudes was conducted: $(0°, 35°, 70°, 85°)$. The reason for choosing these specific QD latitudes was to look at the behaviour of the SOLA method in regions of unmodelled field disturbance with different amplitudes, and with different data coverage, investigating their influence on the uncertainty and kernel width; in the Arctic region QD latitudes 70° and 85° are located approximately within and poleward of the auroral oval, respectively, while QD 35° represents mid-latitudes and QD 0° represents low-latitudes. The left plot in Figure 5.11 presents the local error estimate versus the trade-off parameter λ. Interestingly this plot shows that the error estimates are of the same size independent of the QD latitude for the various trade-off parameters. Therefore this plot may be used to pinpoint a suitable λ which yields more or less uniform error estimates for regional or global collections of target points.

The right plot in Figure 5.11 presents the local error estimate versus the averaging kernel width in degrees, which shows a characteristic L-curve shape as described in Section 5.3.3 (the curves for latitudes 0° and 35° coincide making them difficult to see). A distinct right-shift of the L-curves can be observed as the QD latitude increases. At low and mid-latitudes the kernel widths are seen to be significantly smaller than those in the polar regions and there are polar gaps in the data coverage. This behaviour may be expected since the date error estimates are larger in the polar regions; this means that in order to obtain the same model variance the averaging kernel needs to become broader. Based on the information contained in Figures 5.9 and 5.11 it was decided to proceed using a Fisher parameter $\kappa = 600$ and regularization parameter $\lambda = 1 \times 10^{-4}\mathrm{nT}^{-1}$ in the following calculations of the CMB main field using the SOLA method.

Figure 5.12 presents the SOLA method applied to a global grid of target points at the CMB having 1° spacing in latitude and longitude. As stated above $\kappa = 600$ and $\lambda = 1{\times}10^{-4}\mathrm{nT}^{-1}$ was used for an application of March 2017 data from Data Set 2, using sums and differences of all three vector field components. The top left plot shows a global collection of radial magnetic field estimates. Associated plots show the error estimates (top right), the kernel widths (bottom left) and the spatial distribution of the data under consideration (bottom right). It is observed that the morphology of the radial field patches and their amplitudes are very similar to those seen in the CHAOS-6-x5 field model predictions for SH degrees 1 to 13.

Among the interesting field structures seen, are three distinct field lobs resolved at high latitudes in the Northern Hemisphere, and a strong field patch in the Indian Ocean, west of Australia. The error estimates remain homogeneous as is expected from Figure 5.11 being approximately $10\mu T$ which corresponds to about 5% of the mean CMB field amplitude. This is a rigorous error estimate for these particular spatial averages given the chosen data error model. Such error estimates are not easy to obtain for regularized or truncated SH field models. The kernel widths are seen to be more or less uniform at non-polar latitudes and are seen to exhibit coherence with the data distribution. Distinct behaviour of the kernels are found in the polar regions; in particular, a striking region of increased kernel width coinciding with the auroral oval (where the applied data error estimates are also larger) can be observed.

On the CMB, at radius r_c, the wavelength λ_n associated with a particular SH degree n is $\lambda_n = (2\pi r_c)/n$ ($1° \approx 61$km). Averaging kernels having widths of $\approx 30°$ correspond roughly to SH degree 12; therefore the spatial resolution obtained in our localized SOLA estimates is comparable to that of standard field models truncated to avoid crustal effects.

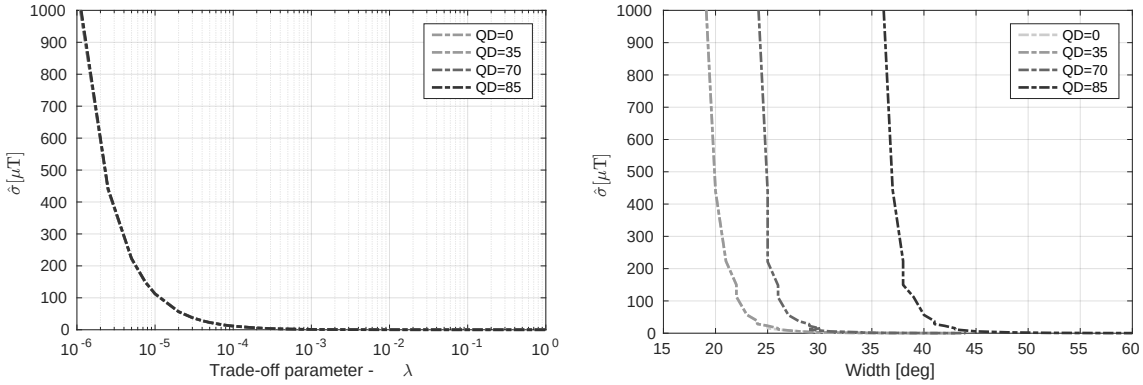

Figure 5.11: SOLA MF application using *Swarm* data from March 2017 at target locations of QD latitudes 0°, 35°, 70° and 85°. Left: error estimates $\hat{\sigma}(\mathbf{r}_0)$ versus trade-off parameter λ. Right: error estimates $\widehat{\sigma}(\mathbf{r}_0)$ versus averaging kernel width in degrees.

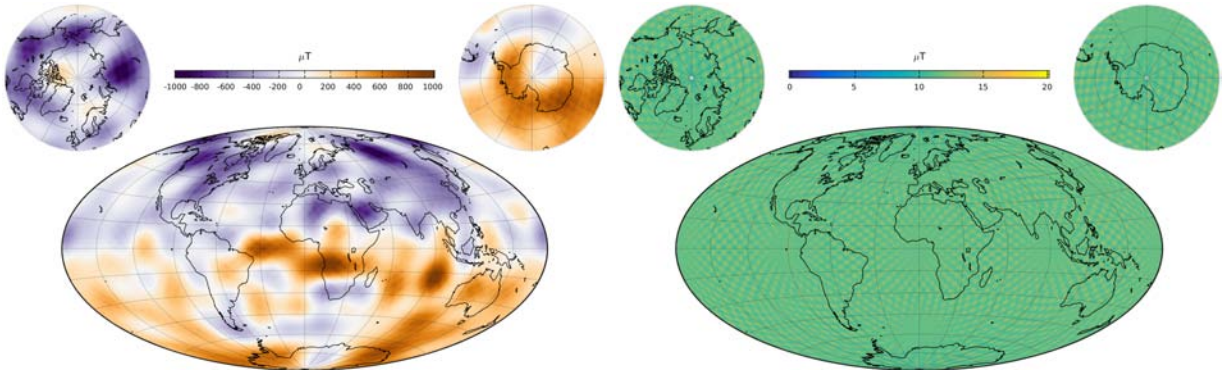

(a) Map collecting local estimates of CMB radial field $\widehat{B_r}(\mathbf{r}_0, t_0)$ in [μT] derived from *Swarm* data using the SOLA approach

(b) Map collecting local error estimates $\widehat{\sigma}(\mathbf{r}_0, t_0)$ in [μT].

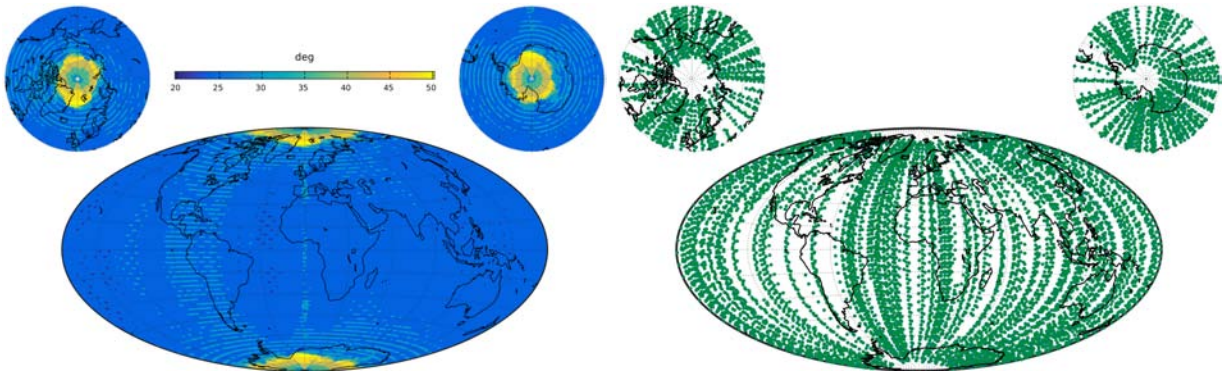

(c) Map collecting widths of averaging kernel $\mathcal{K}_C(\mathbf{r}_0|\mathbf{r}')$ for local estimates in [deg].

(d) Location of observations used in March 2017 example.

Figure 5.12: SOLA application to CMB field estimation using March 2017 sums and differences for the *Swarm* data with $\kappa = 600$ and $\lambda = 10^{-4}\mathrm{nT}^{-1}$ showing: (a) radial MF estimates for a global 1° spaced collection of target locations, (b) uncertainty estimates for each target point, (c) averaging kernel widths for each target location and (d) *Swarm* data distribution.

5.4.4 Application to Estimation of the Secular Variation at the CMB

In this section an application of the SOLA method to the radial magnetic field secular variation at the CMB is investigated. Initially a data time window of two years of *Swarm* vector field data from 2015.0 to 2017.0 was considered. Here only the radial magnetic field component of the data was considered in order to reduce external field contamination at high latitudes and in an effort to maximize the data coverage for a given number of data points. Using the vector field, the data vector was given as $\mathbf{d} = \{d_r\}$, and the data kernels were constructed as $G^* = \{G_{C,r}\}$. Using 2 month time windows starting from year 2015.0 a regularly $3.5^\circ \times 4^\circ$ latitude/longitude spaced global distribution of data was constructed by randomly selecting data in time from within the two month window for a given spatial cell. The total data set covering the period 2015.0 to 2017.0 was then generated by accumulating these 2 month globally distributed data sets from the entire two years, resulting in a total of 43540 data points. In these computations serial data error correlation was not accounted for as data were selected randomly from within the 2 months.

The behaviour of the SV averaging kernel, $\mathcal{K}_{\dot{C}}$, is first reported in Figure 5.13 as a function of the target kernel width parameter κ and the trade-off parameter λ by considering a series of example averaging kernels at QD latitude 0° and longitude -168° stating the error estimate and the approximate kernel width in degrees. As in the MF case all the kernels were well behaved showing only minor oscillations.

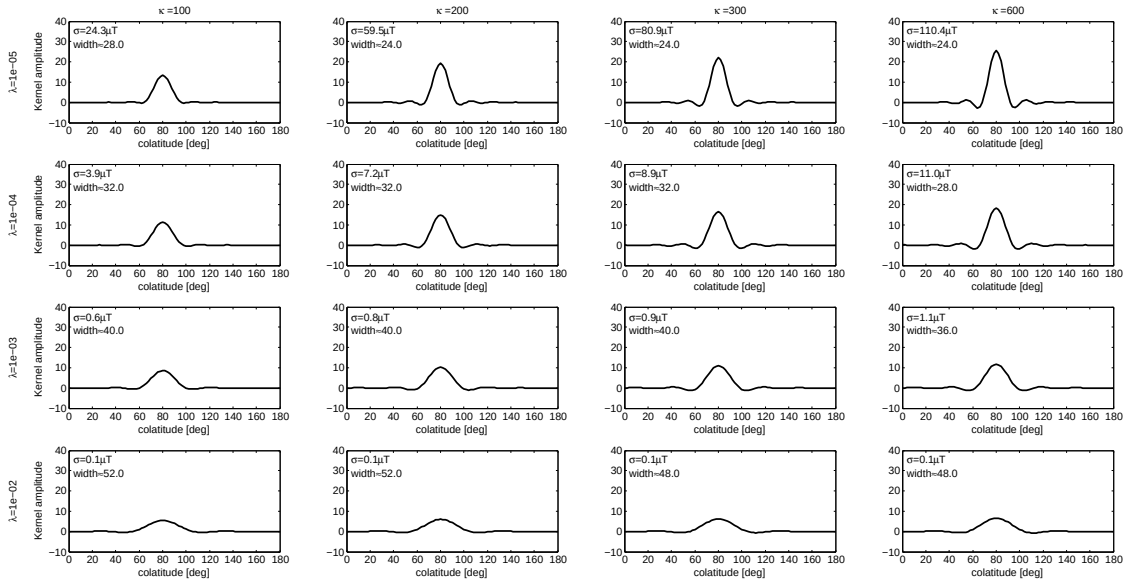

Figure 5.13: Application of SOLA to SV radial field estimates using 2 years of *Swarm* radial field observations between $2015.0 - 2017.0$ shown at target location QD latitude 0°: behaviour of the SV averaging kernel as a function of Fisher function width κ and trade-off parameter λ. The value of κ increases from the left column having $\kappa = 100$ to the right column having $\kappa = 600$. The value of λ increases from the top row of $\lambda = 10^{-6}\mathrm{nT}^{-1}$ to the bottom row having $\lambda = 10^{-3}\mathrm{nT}^{-1}$. In each plot the estimated uncertainty $\widehat{\sigma}$ and kernel width in degrees are stated.

Next the L-curve behaviour for the same QD positions investigated in the MF case in Section 5.4.3 is conducted, Figure 5.14 presents the error estimate versus the trade-off parameter λ (left plot) and versus the averaging kernel width in degrees (right plot). As

in the MF case the error estimates are seen to be independent of location for a given λ value; for a given value of λ a corresponding $\widehat{\sigma}(\mathbf{r}_0)$ is fixed. Furthermore, in both plots blue, red and green dots marked selected λ values which are chosen for further study in Figures 5.15 and 5.16. Here we considered in detail three different λ values in order to explore the resolvability of the SV with different choices of average kernel.

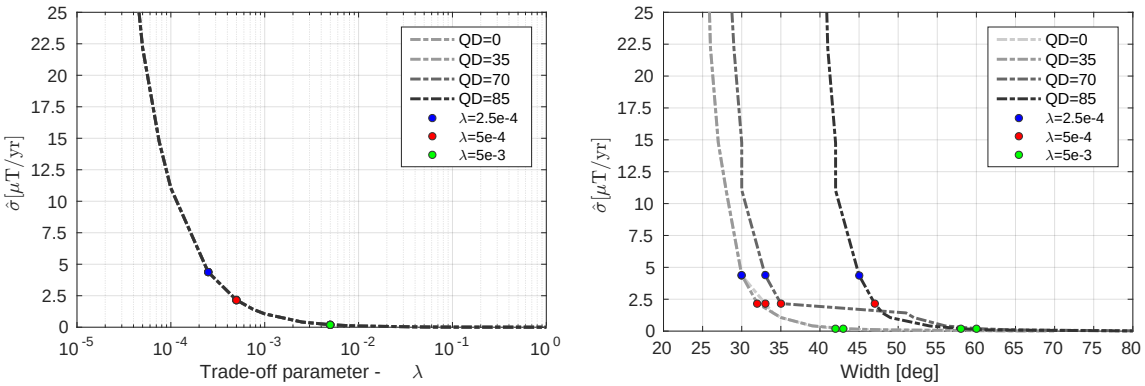

Figure 5.14: Application of SOLA to SV radial field estimates using 2 years of *Swarm* data between 2015.0 − 2017.0 with $\kappa = 600$. Plots showing $\widehat{\sigma}(\mathbf{r}_0)$ trade-off curves at various target locations for QD latitudes 0°, 35°, 70° and 85° as a function of λ (left) and kernel width (right).

Figure 5.15 presents global collections of the radial SV field estimates at the CMB having a 1° spacing (left plots) and associated error estimates (right plots) obtained using $\lambda = 2.5 \times 10^{-4}\text{nT}^{-1}$ (the blue dot in Figure 5.14) in the top plots, $\lambda = 5 \times 10^{-4}\text{nT}^{-1}$ (the red dot in Figure 5.14) in the center plots and $\lambda = 5 \times 10^{-3}\text{nT}^{-1}$ (the green dot in Figure 5.14) in the bottom plots. Figure 5.16 presents the associated kernel widths along with example plots of averaging kernels at QD latitude 0° and longitude −168° having widths of $\approx 30°$, 33° and 42°; comparing the three kernels it is clear that using $\lambda = 2.5 \times 10^{-4}\text{nT}^{-1}$ results in higher amplitudes and a narrower averaging kernel. The effect of increasing λ, and thus broadening the averaging kernel, is clearly seen in the these plots; the field structures become smeared out as the kernel width is increased, i.e. going from the top plots to the bottom plots, decreasing the kernel amplitude while a decrease in the associated error estimates is also observed. The kernel widths increase noticeably towards the polar regions, resembling the results in the MF case study, peaking at areas matching those of the auroral oval where data error estimates are larger.

Remembering that the SOLA method involves no direct regularization of higher spatial frequencies of the signal nor truncation in the spectral domain, it is interesting to compare the global SV estimates to the radial SV field predictions of the CHAOS-6-x5 model. Figure 5.17 shows the 2016 radial SV predictions of the CHAOS-6-x5 model for SH degrees 1-10 (left) and 1-16 (right). The left plot corresponds roughly to the SOLA SV field estimates using $\lambda = 5 \times 10^{-3}\text{nT}^{-1}$ (i.e. plot e of Figure 5.15). Although the data used and the data selection criteria and processing are not the same, similar SV structures can clearly be identified and the amplitude is alike; in particular these include high amplitude features appearing at low latitudes stretching in the longitudinal band of ±90°, lower activity in the pacific region (at least for the broader averaging kernels) and a sequence of high latitude patches encircling the north pole.

Looking at results for a decreasing kernel width, remembering that noise may become

more influential in the average field estimates, in particular at mid-latitudes and polar regions, a clear change in the eastern pacific region and around South America is evident for $\lambda = 2.5 \times 10^{-4} \mathrm{nT}^{-1}$. This is interesting as recent spherical harmonic based field models find distinct SA features in these regions (Chulliat et al., 2015; Finlay et al., 2016b). When probing smaller spatial scales, high SV amplitudes are found at eastern longitudes under Asia, Indonesia and west of Australia, and in the Atlantic Ocean west of Africa.

It is stressed that no spectral truncation nor regularization are embedded in the SOLA estimates as in the case for the CHAOS-6-x5 model; this is particularly interesting due to the blue nature of the SV power spectrum because the SH truncation in the field model removes higher harmonics which are expected to be significant, while in contrast the SOLA approach averages over these features, and they may not necessarily locally average to zero. Interpretation of maps from regularized field models such as CHAOS-6-x5, is complicated by the fact that the applied regularization implicitly averages higher SH degrees over longer times (e.g., Olsen et al., 2009). The SOLA SV estimates all refer to averages over the specified time window (e.g. 2 years).

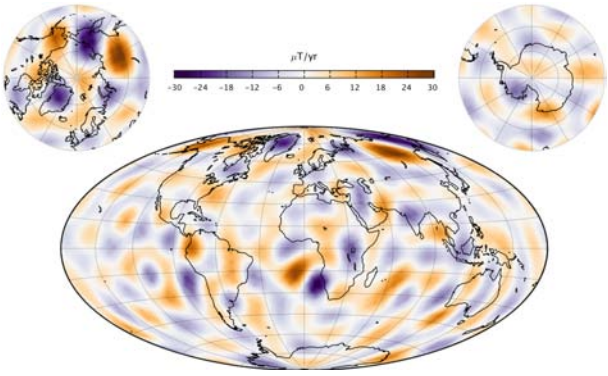

(a) Local estimates of CMB radial SV for $\lambda = 2.5 \times 10^{-4}\text{nT}^{-1}$. $\widehat{\sigma} \approx 5\mu T/yr$.

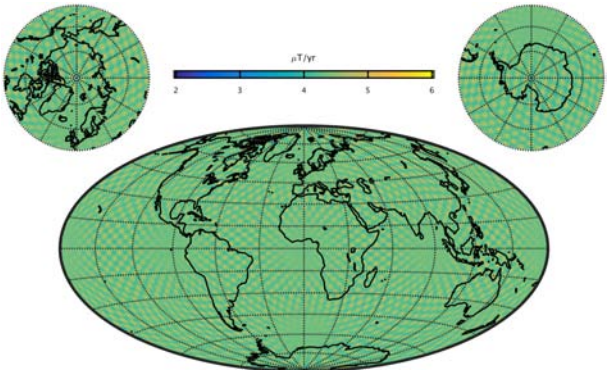

(b) SOLA model error estimates.

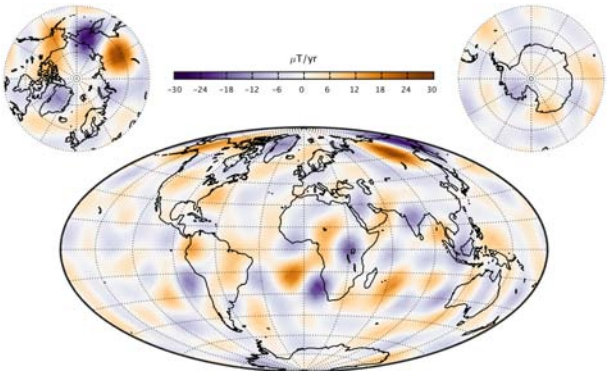

(c) Local estimates of CMB radial SV for $\lambda = 5 \times 10^{-4}\text{nT}^{-1}$. $\widehat{\sigma} \approx 2.5\mu T/yr$.

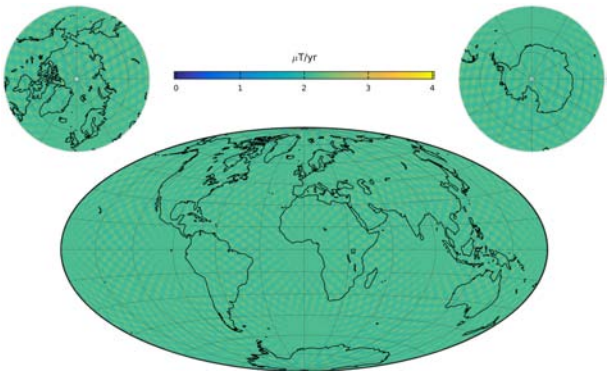

(d) SOLA model error estimates.

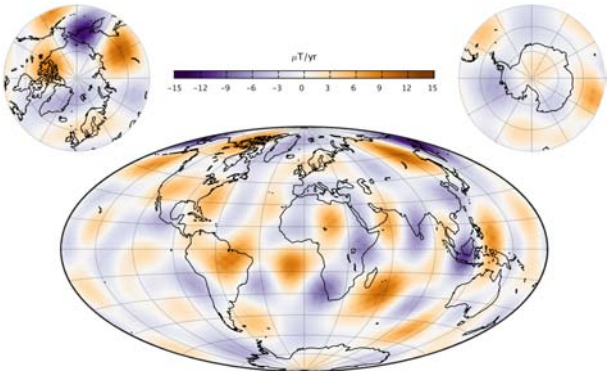

(e) Local estimates of CMB radial SV for $\lambda = 5 \times 10^{-3}\text{nT}^{-1}$. $\widehat{\sigma} \approx 0.25\mu T/yr$.

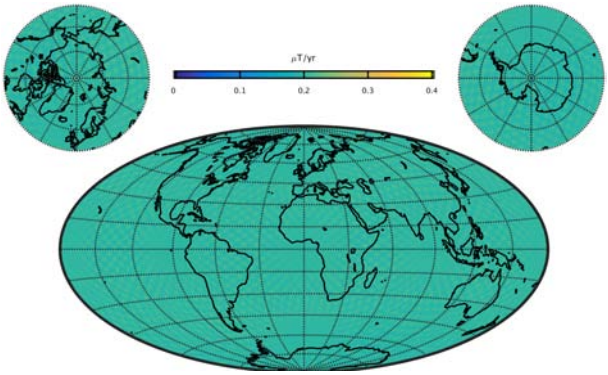

(f) SOLA model error estimates.

Figure 5.15: Application of the SOLA method to radial SV field estimation from 2 years of *Swarm* data between $2015.0 - 2017.0$ using a global 1° spaced collection of target locations having $\kappa = 600$. The plots show the radial SV estimates (left plots) and associated error estimates (right plots). Results shown are: (a-b) using $\lambda = 2.5 \times 10^{-4}\text{nT}^{-1}$, (c-d) using $\lambda = 5 \times 10^{-4}\text{nT}^{-1}$ and (e-f) using $\lambda = 5 \times 10^{-3}\text{nT}^{-1}$. Notice that the scale is not the same in the plots.

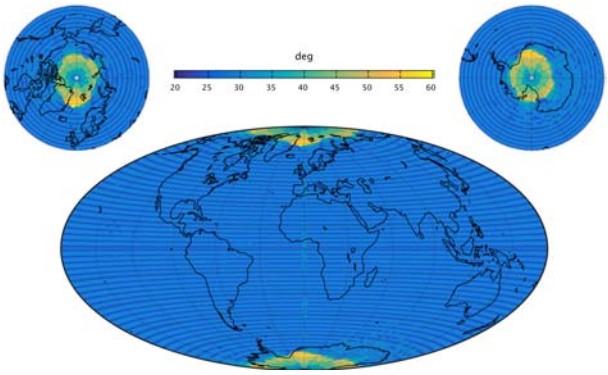

(a) Width of averaging kernel using $\lambda = 2.5 \times 10^{-4}\text{nT}^{-1}$.

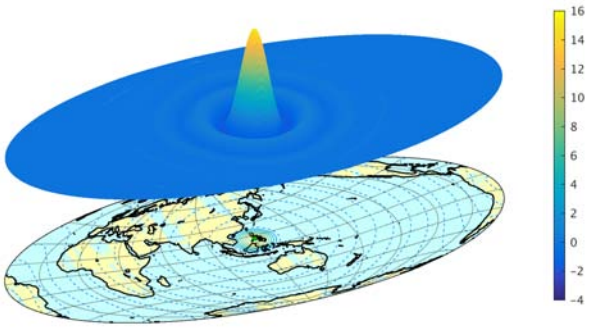

(b) SV averaging kernel for $\lambda = 2.5 \times 10^{-4}\text{nT}^{-1}$. Kernel width $\approx 30°$.

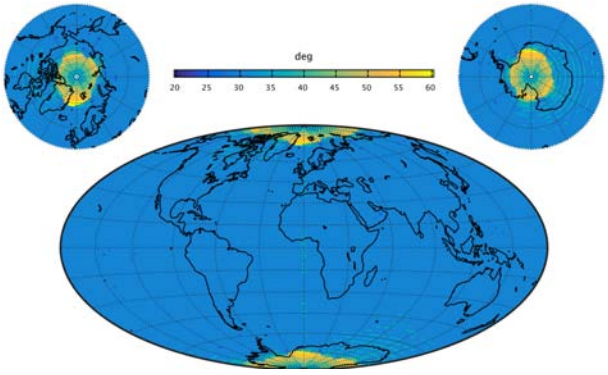

(c) Width of averaging kernel using $\lambda = 5 \times 10^{-4}\text{nT}^{-1}$.

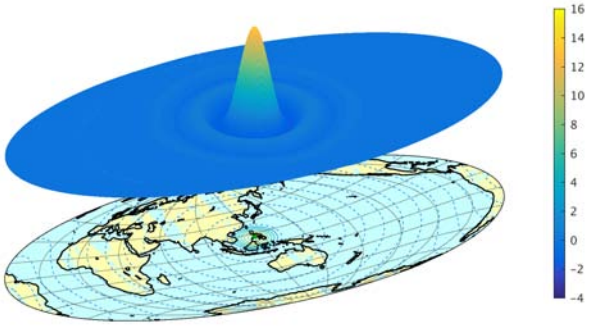

(d) SV averaging kernel using $\lambda = 5 \times 10^{-4}\text{nT}^{-1}$. Kernel width $\approx 33°$.

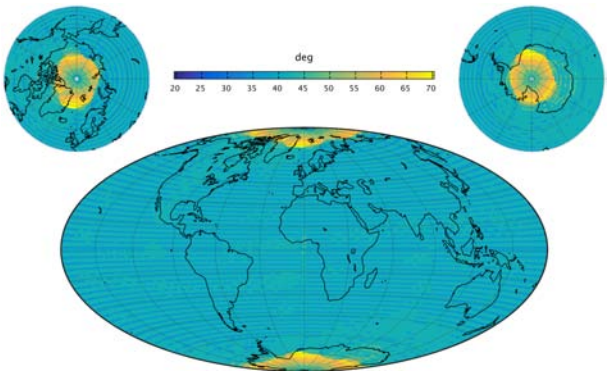

(e) Width of averaging kernel using $\lambda = 5 \times 10^{-3}\text{nT}^{-1}$.

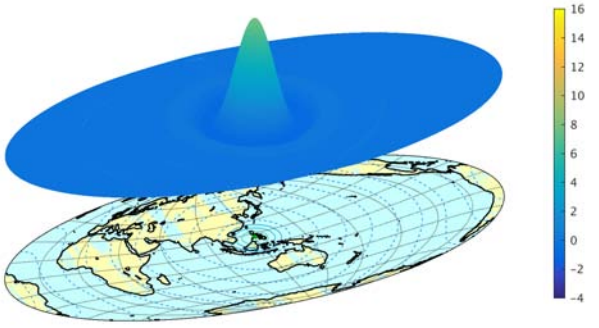

(f) SV averaging kernel using $\lambda = 5 \times 10^{-3}\text{nT}^{-1}$. Kernel width $\approx 42°$.

Figure 5.16: Application of the SOLA method to radial SV field estimation from 2 years of *Swarm* data between 2015.0 − 2017.0 using a global 1° spaced collection of target locations and with $\kappa = 600$. The plots show the width of the averaging kernels (left plots) and example kernels at QD latitude 0° and longitude −168° (right plots). Results shown are: (a-b) using $\lambda = 2.5 \times 10^{-4}\text{nT}^{-1}$, (c-d) using $\lambda = 5 \times 10^{-4}\text{nT}^{-1}$ and (e-f) using $\lambda = 5 \times 10^{-3}\text{nT}^{-1}$.

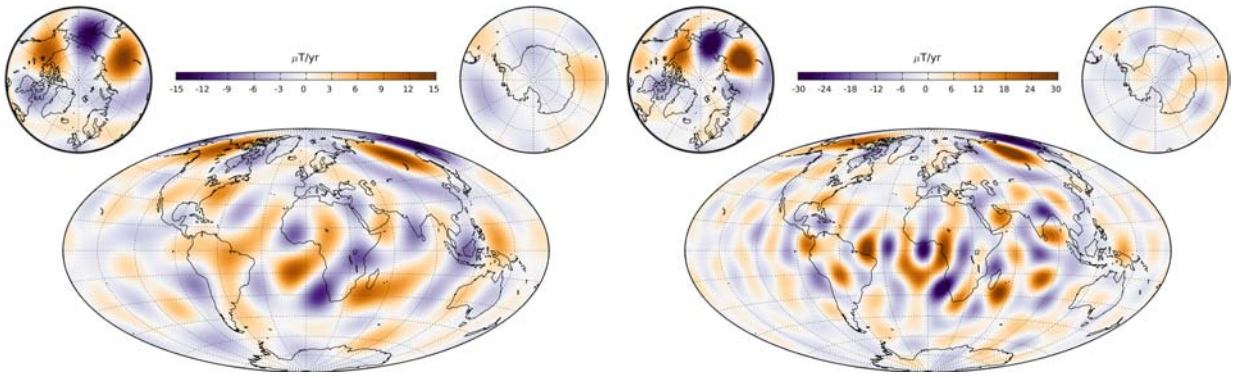

Figure 5.17: Global maps of the radial SV field at the CMB in 2016 from the CHAOS-6-x5 model based on SH degrees 1-10 (left) and 1-16 (right).

5.4.5 The Secular Acceleration at the CMB

In this section the accumulated radial SA magnetic field, computed as the change in the radial SV field between different epochs are presented. The calculations are presented for 1yr and 2yr differences of the SOLA radial SV estimates, which have been computed from 2yr and 1yr data time windows, discussed in Section 5.4.4. The SA error estimate, $\widehat{\sigma}(\mathbf{r}_0, t)_{SA}$, at time t, is here computed as the square root of the squared sums of the SV error estimates (assuming these are independent) for the epochs being differenced (Barlow, 1989; Taylor, 1997), i.e.

$$\widehat{\sigma}(\mathbf{r}_0, t)_{SA} = \sqrt{\widehat{\sigma}(\mathbf{r}_0, t_1)^2_{SV} + \widehat{\sigma}(\mathbf{r}_0, t_2)^2_{SV}} \tag{5.100}$$

Figure 5.18 presents global collections of the radial SA field computed as the accumulated change in the radial SV between years 2015 and 2017. In order to determine this, the radial SV in 2017.0 was computed from two years of data using $\lambda = 1 \times 10^{-3}\mathrm{nT}^{-1}$ shown in the top plots, $\lambda = 3 \times 10^{-3}\mathrm{nT}^{-1}$, shown in the center plots, and $\lambda = 5 \times 10^{-3}\mathrm{nT}^{-1}$, shown in the bottom plots (i.e. in the bottom plot seeking SA maps based on the detail level as given in the bottom plot of Figure 5.15). Next the averaging kernels obtained using these values of λ, were used as the target kernels for the SV in 2015.0 in order to ensure the quantities being differenced had been averaged in the same fashion. Associated error estimates are given in the right plots. Even though the $\lambda = 1 \times 10^{-3}\mathrm{nT}^{-1}$ result may contain some genuine features, noise is prominent and the error level is high. The $\lambda = 3 \times 10^{-3}\mathrm{nT}^{-1}$ and $\lambda = 5 \times 10^{-3}\mathrm{nT}^{-1}$ results are very alike, though the $\lambda = 3 \times 10^{-3}\mathrm{nT}^{-1}$ has stronger field amplitudes.

Figure 5.19 presents similar radial SA field predictions from the CHAOS-6-x5 (left plot) and CIY4 (right plot) models for SH degrees 1 to 10 in 2016.0. Looking at these plots the SOLA maps using $\lambda = 3 \times 10^{-3}\mathrm{nT}^{-1}$ and $\lambda = 5 \times 10^{-3}\mathrm{nT}^{-1}$ agrees remarkably well with the SH models capturing many of the same features. Even small scale SA field features can be found in between the models, though the high latitude SA signal is perhaps not as prominent in the SOLA maps. Thus the SA predictions of regularized SH based models up to SH degree 10 are essentially reproduced by the SOLA approach which does not involve any regularization nor truncation at all.

Figure 5.20 shows the MF, SV and SA power spectra plotted at the CMB of the CHAOS-6-x5 and CYI4 field models in 2016. Also shown are the SOLA power spectra computed from the global collections of the local SOLA estimates for various values of the

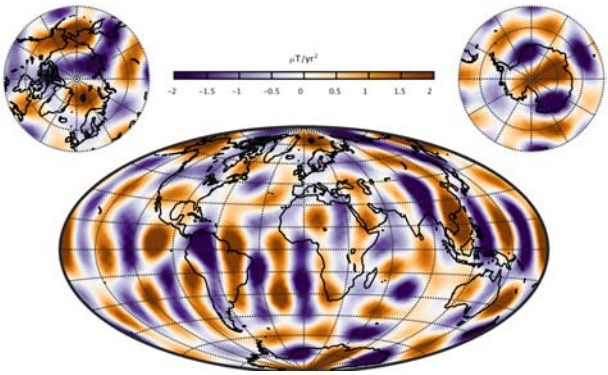

(a) SOLA model based on $\lambda = 1 \times 10^{-3}\mathrm{nT}^{-1}$.

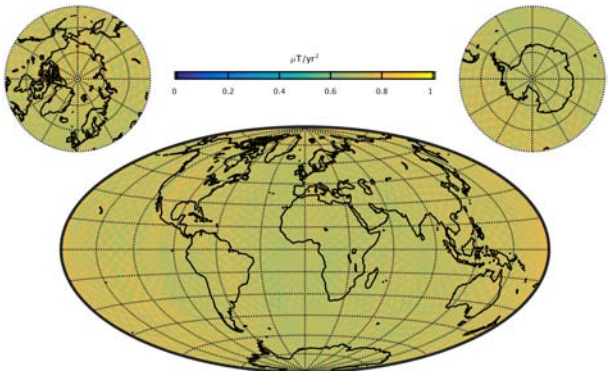

(b) SOLA model error estimates.

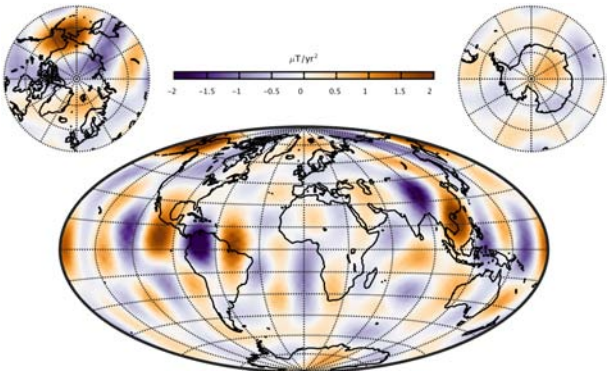

(c) SOLA model based on $\lambda = 3 \times 10^{-3}\mathrm{nT}^{-1}$.

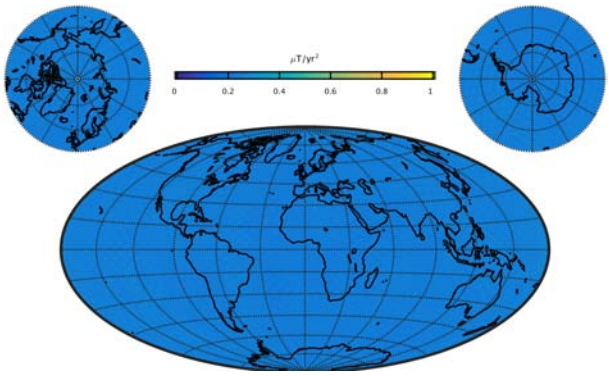

(d) SOLA model error estimates.

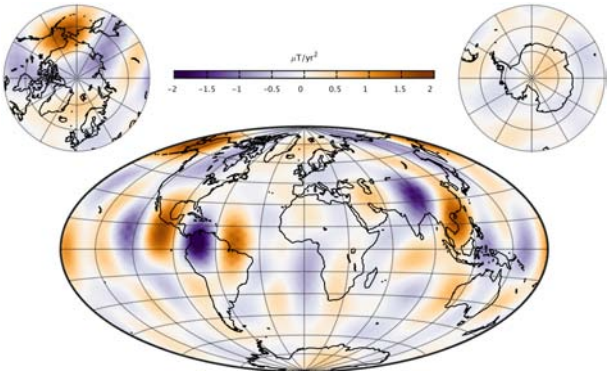

(e) SOLA model based on $\lambda = 5 \times 10^{-3}\mathrm{nT}^{-1}$.

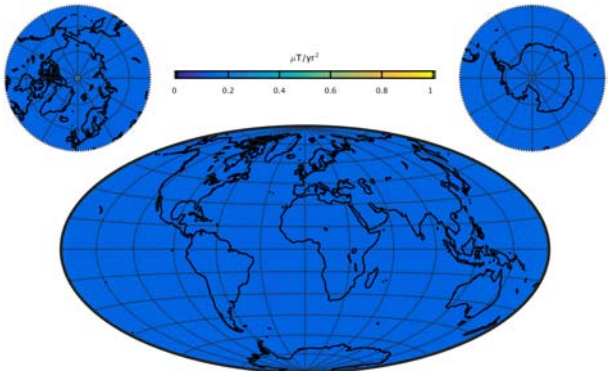

(f) SOLA model error estimates.

Figure 5.18: Global maps of the radial SA field (left plots) computed as accumulated change in radial SV at the CMB of SOLA SV estimates from years 2015.0 to 2017.0, also showing the associated error estimates (right plots).

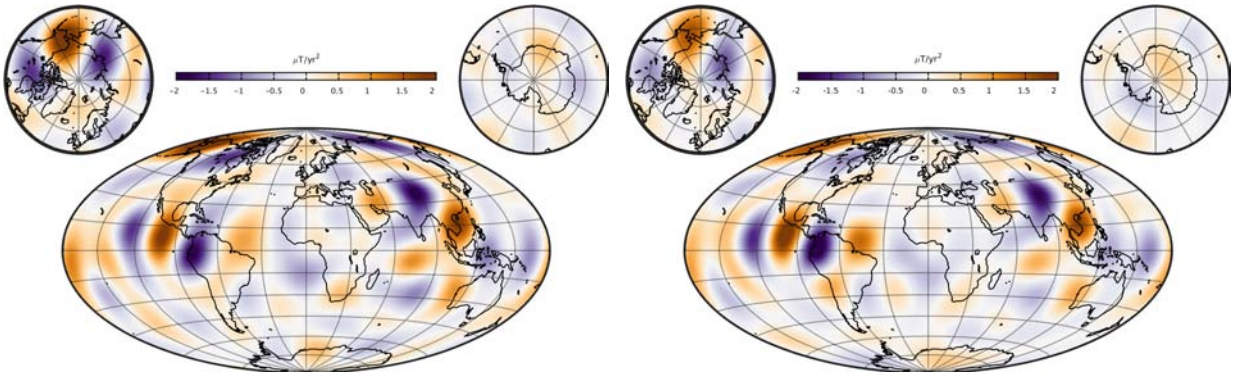

(a) CHAOS-6-x5 model predictions. (b) CIY4 model predictions.

Figure 5.19: Global maps of the radial SA at the CMB in 2016.0 from predictions of the CHAOS-6-x5 (left plot) and CIY4 (right plot) models based on SH degrees 1-10.

trade-off parameter λ. The spectra shows that it is possible to produced SH models from the SOLA estimates that fully matches those of conventional SH based field models, and that varying the spatial averaging kernel width of the local estimates by changing λ, will change the spectral appearance accordingly. Therefore, using the global diagnostics of the SH power spectrum, shows the full strength of our localized SOLA technology.

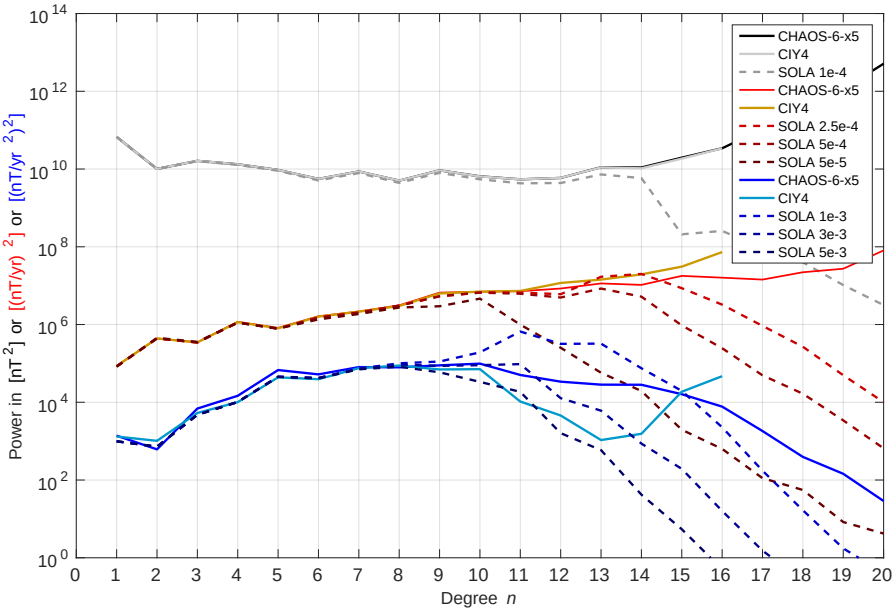

Figure 5.20: Lowes-Mauersberger power spectra in 2016 plotted at the CMB showing the main field (black and dotted grey), secular variation (red and dotted red) and secular acceleration (blue and dotted blue) as given by the CHAOS-6-x5 and CIY4 field models and the SOLA method for various values of the trade-off parameter λ.

Next the SA was computed centred on the years 2008 and 2006 for $\lambda = 5 \times 10^{-3}\mathrm{nT}^{-1}$ and compared with other field models. The same procedure was used here as above; the averaging kernels for 2017 were used as target kernels for the years 2005 to 2007 and 2005 to 2007. Figure 5.21 and 5.22 presents the results for the 2yr accumulated radial

SA for windows centred on 2008 and 2006, respectively. In both figures the SOLA based SA estimates (plot a) and the associated error estimates (plot b) are shown, along with the SA predictions for SH degrees 1 to 10 of CHAOS-6-x5 (Finlay et al., 2016b) (plot c), the GRIMM (Lesur et al., 2008, 2010, 2011b) (plot d) and the POMME10 (Maus et al., 2006) and http://geomag.org/models/pomme10.html (plot e) field models. As in the previous example, the SOLA based SA estimates are in remarkable agreement with the other models up to SH degree 10.

Figure 5.23 presents line plots centred on the years 2006 (plot a and b), 2008 (plot c and d) and 2016 (plot e and f) along the geographic equator for the SOLA based SA estimates using 2 year SV epoch differences based on 2yr data windows having the global data grids refiled every 2 month (right plots), and from 1 year SV epoch differences based on 1yr data windows having 1 month data refilling (left plots). SOLA estimates for $\lambda = 5 \times 10^{-3}\mathrm{nT}^{-1}$ (blue curve) and $\lambda = 3 \times 10^{-3}\mathrm{nT}^{-1}$ (green curve) are shown along with the associated error estimates. Also shown are the predictions of the CHAOS-6-x5 model for SH degrees 1 to 10 (red curve) and 1 to 16 (dark red curve). In particular it seems that the 2yr SOLA based SA estimates correlate well with the CHAOS-6-x5 model predictions for SH degrees 1 to 10.

Next, the evolution of the radial SA at the CMB along the geographic equator is investigated by looking at time-longitude plots. SOLA based SA estimates were computed from 2 year SV epoch differences constructed from 1 year time windows moved in steps of 2 months, and also from 1 year SV epoch differences constructed from 1 year time windows moved in 1 month steps. Figure 5.24 shows a segment of the averaging kernels along the equator for selected years, obtained for the case of 2 year SV differences. As can be seen, all the kernels obtained appear very similar throughout making the differencing meaningful. The percentage error of the kernel differences has been computed as $100 \times \sqrt{(\mathcal{K}_1 - \mathcal{K}_2)^2/\mathcal{K}_1^2}$. Figure 5.25 presents the mean of the percentage errors computed for kernels along the geographical equator, calculated for both 2yr and 1yr SV differences, and for both $\lambda = 5 \times 10^{-3}\mathrm{nT}^{-1}$ and $\lambda = 3 \times 10^{-3}\mathrm{nT}^{-1}$. It can be seen that in all cases, the mean percentage error is below 1%. The differences are seen to be slightly larger during the early CHAMP period, which is properly related to the amount of data determining the kernels.

Figures 5.26 and 5.27 present time-longitude plots along the geographic equator based on differencing SV SOLA estimates looking at and 2yr and 1yr SV differences, respectively. The 2yr and 1yr SV estimates were built using 2 and 1 month sliding data windows, respectively. The figures show the evolution of the SA field (left plots) for $\lambda = 5 \times 10^{-3}\mathrm{nT}^{-1}$ (top plot) and $\lambda = 3 \times 10^{-3}\mathrm{nT}^{-1}$ (bottom plots), and the associated error estimates (right plots). The reason for not showing results prior to 2004 in Figure 5.27 is that using a 1 month sliding time window there is a severe lack of data during this time under the chosen data dark, quiet time selection criteria. Note that the scales are not the same in the two figures. Comparing plots (a) and (c) many coherent SA evolution structures can be identified. This is important as it illustrates the ability of the SOLA based SA to track temporal changes, and as can be seen, much higher temporal resolution is gained in (c) using 1 year SV differences. The uncertainty estimates increase in 2004 and 2005, which is probably related to there being less data at these times. Striped looking patterns in the error estimates are also be observed, which is probably related to the regular gridding of the data used in the dataset for estimating the SV. This behaviour could be reduced in the future by seeking a different data setup.

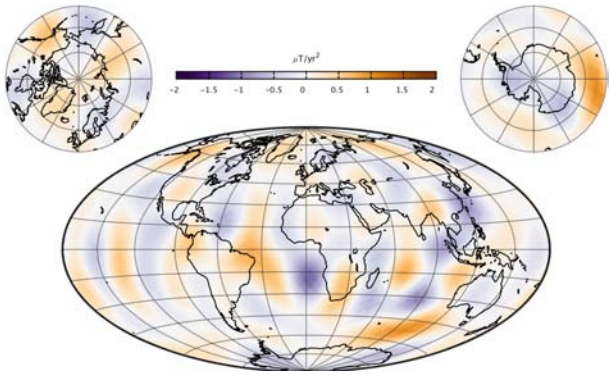

(a) SOLA model based on $\lambda = 5 \times 10^{-3}\mathrm{nT}^{-1}$.

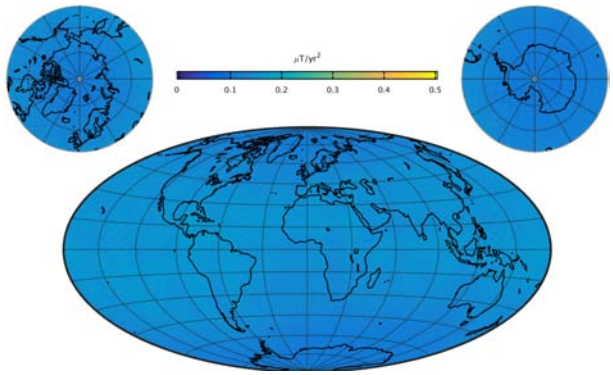

(b) SOLA model error estimates.

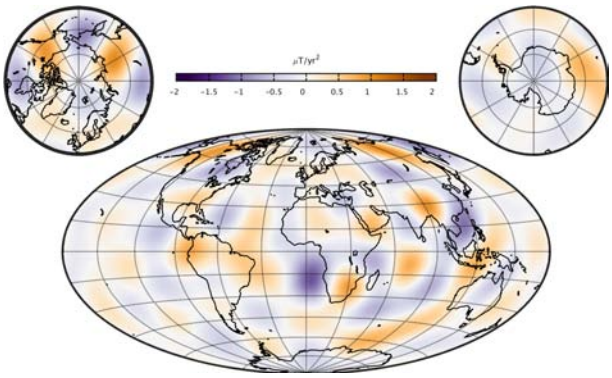

(c) CHAOS-6-x5 model predictions.

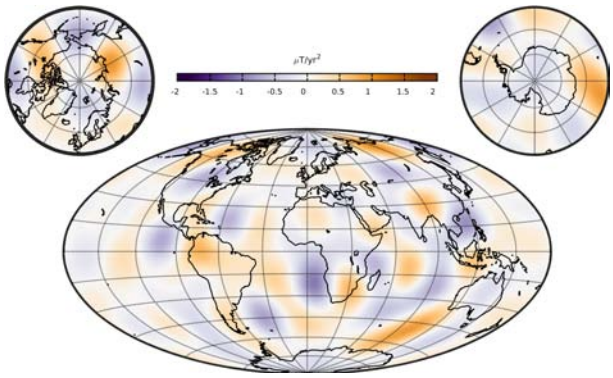

(d) GRIMM model predictions.

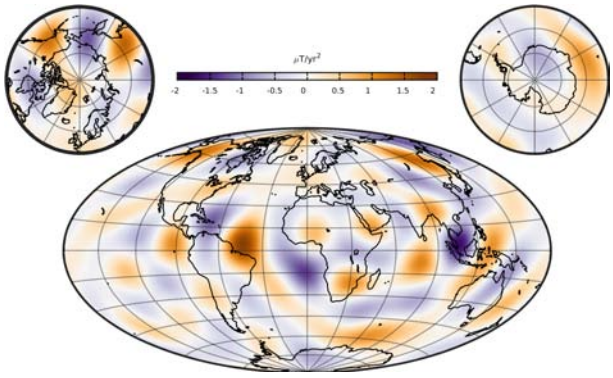

(e) POMME10 model predictions.

Figure 5.21: Global maps of the radial SA at the CMB in 2008.0 showing: the SOLA based estimates using the SA accumulated over a 2yr window centred on 2008.0 (a) and associated error estimates (b) along with the radial SA field predictions of the CHAOS-6-x5 (c), the GRIMM (d) and the POMME10 (e) models based on SH degrees 1-10.

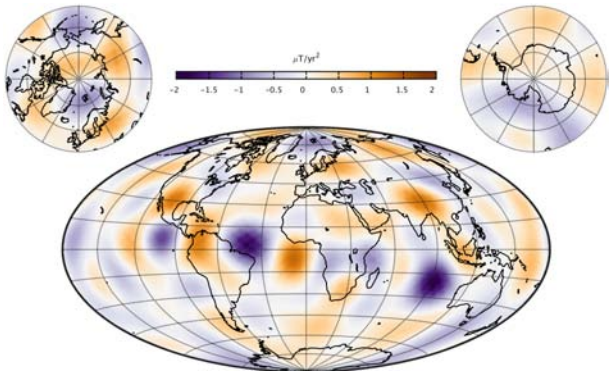

(a) SOLA model based on $\lambda = 5 \times 10^{-3}\mathrm{nT}^{-1}$.

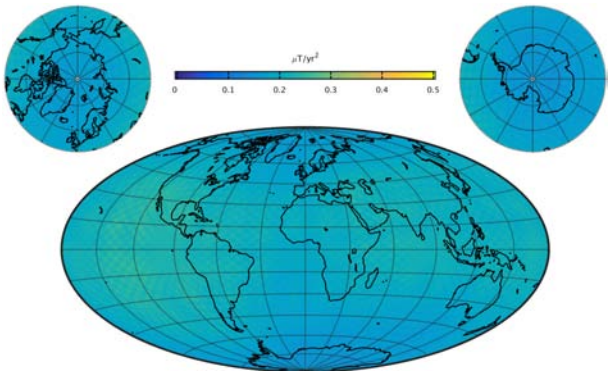

(b) SOLA model error estimates.

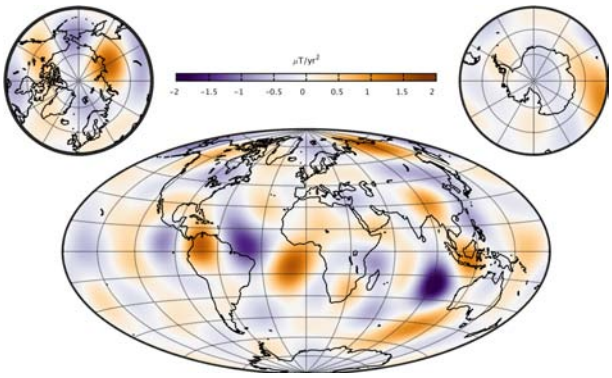

(c) CHAOS-6-x5 model predictions.

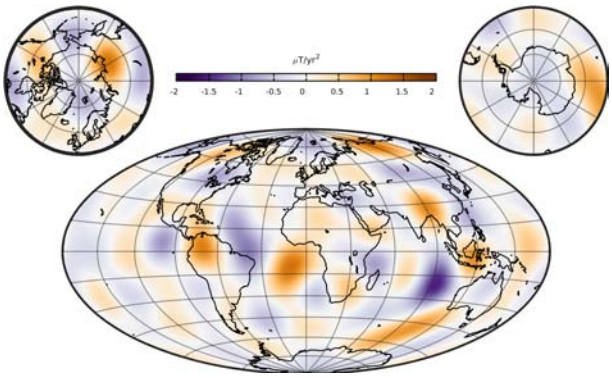

(d) GRIMM model predictions.

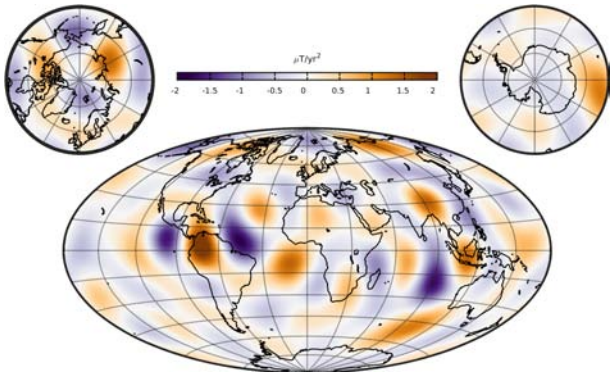

(e) POMME10 model predictions.

Figure 5.22: Global maps of the radial SA at the CMB in 2006.0 showing: the SOLA based estimates using the SA accumulated over a 2yr window centred on 2006.0 (a) and associated error estimates (b) along with the radial SA field predictions of the CHAOS-6-x5 (c), the GRIMM (d) and the POMME10 (e) models based on SH degrees 1-10.

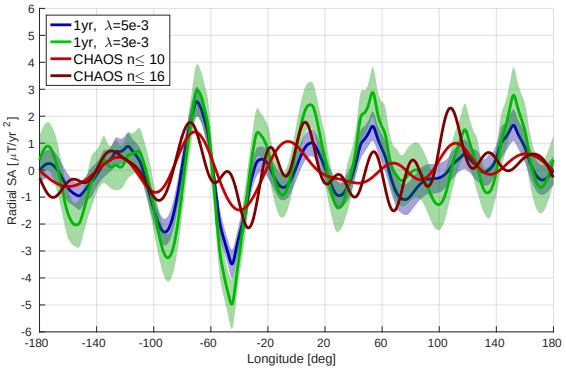

(a) SA in 2006 from 1yr ΔSV.

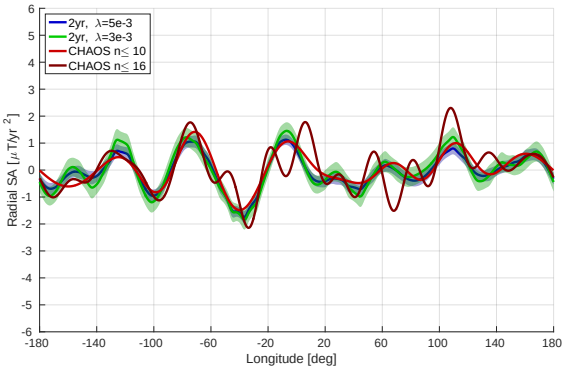

(b) SA in 2006 from 2yr ΔSV.

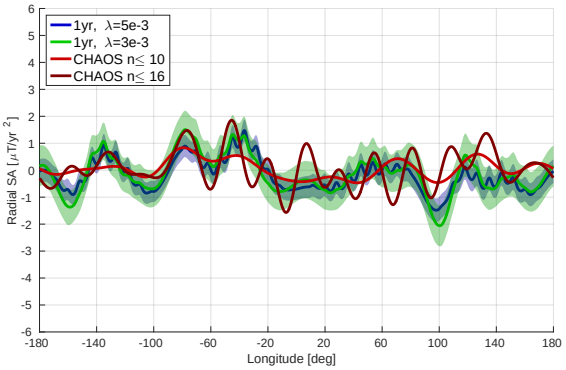

(c) SA in 2008 from 1yr ΔSV.

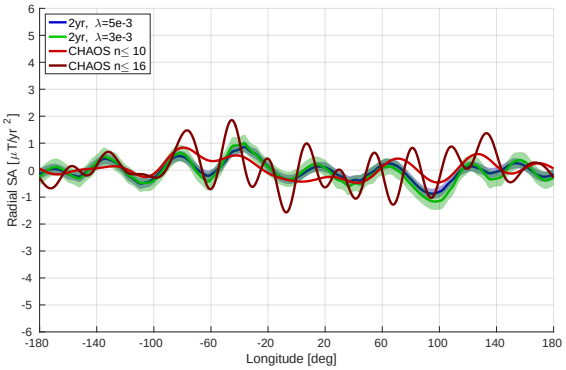

(d) SA in 2008 from 2yr ΔSV.

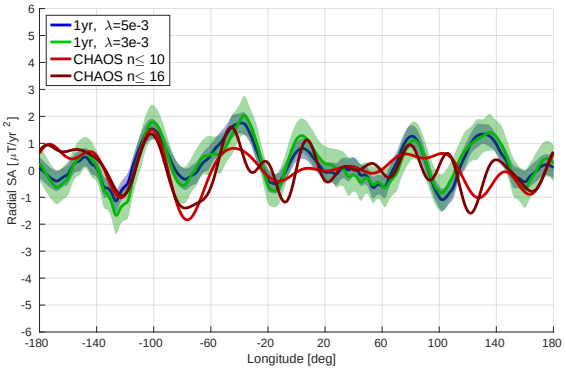

(e) SA in 2016 from 1yr ΔSV.

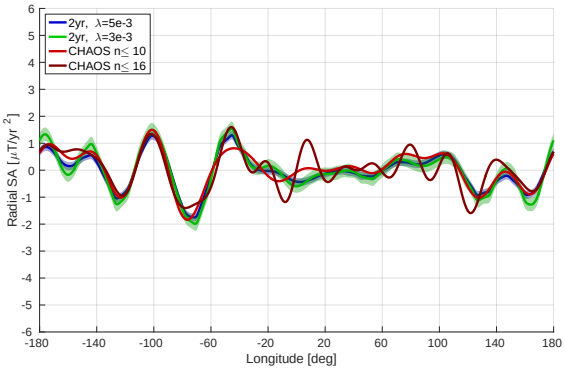

(f) SA in 2016 from 2yr ΔSV.

Figure 5.23: Line plots along the geographic equator at the CMB showing the radial SA field based on 1yr (left column) and 2yr (right column) SV differences including error estimates (shaded regions). The plots show estimates based on $\lambda = 5 \times 10^{-3}\mathrm{nT}^{-1}$ (blue curves) and $\lambda = 3{\times}10^{-3}\mathrm{nT}^{-1}$ (green curves), as well as the CHAOS-6-x5 model predictions for SH degrees 1 to 10 (in red) and 1 to 16 (in dark red).

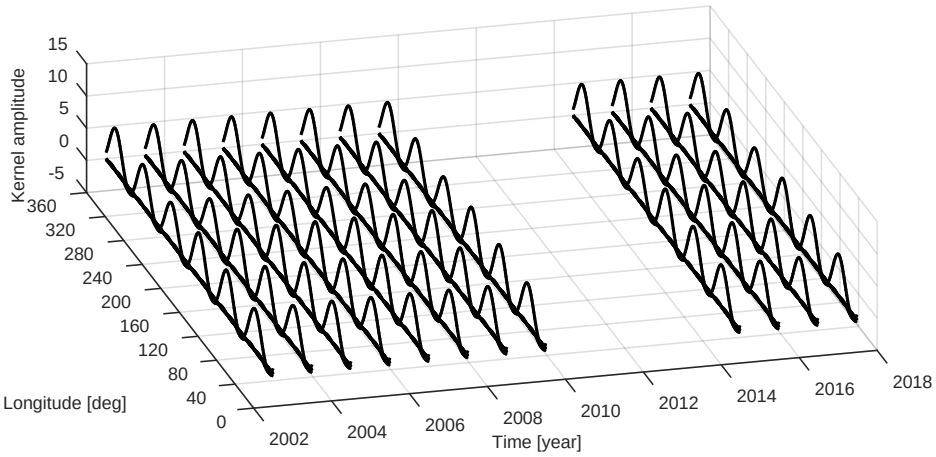

Figure 5.24: A segment of the averaging kernels along the geographic equator for selected years for the SV over 2yr windows.

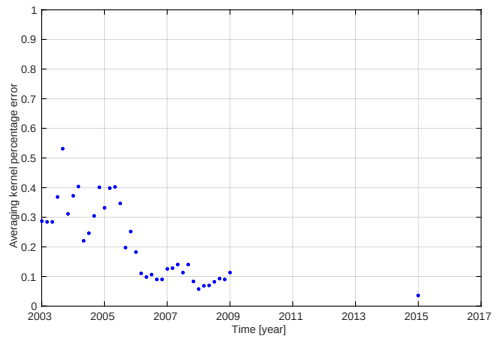

(a) 2yr ΔSV using $\lambda = 5 \times 10^{-3}\text{nT}^{-1}$.

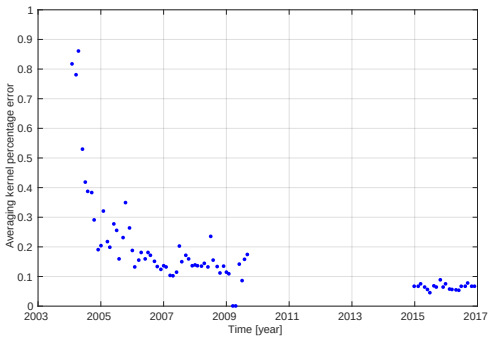

(b) 1yr ΔSV error estimates, $\lambda = 5 \times 10^{-3}\text{nT}^{-1}$.

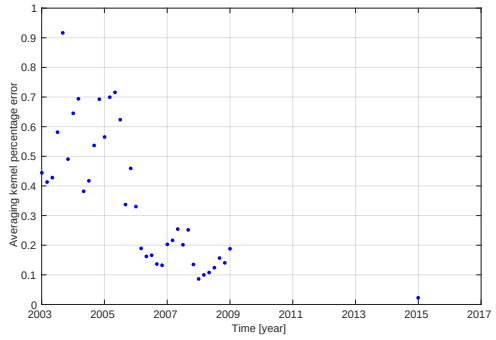

(c) 2yr ΔSV using $\lambda = 3 \times 10^{-3}\text{nT}^{-1}$.

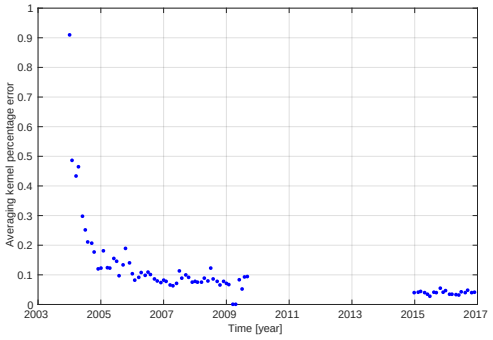

(d) 1yr ΔSV error estimates, $\lambda = 3 \times 10^{-3}\text{nT}^{-1}$.

Figure 5.25: Averaging kernel mean percentages errors along the geographical equator. Results are shown for $\lambda = 5 \times 10^{-3}\text{nT}^{-1}$ (left plots) and $\lambda = 3 \times 10^{-3}\text{nT}^{-1}$ (right plots).

Figure 5.28 presents time-longitude plots along the geographic equator from CHAOS-6-x5 model predictions for SH degrees 1 to 10 (left plot) and 1 to 16 (right plot). The SA patterns observed in Figures 5.26 and 5.27 plots (a) and (c), correspond qualitatively to those found in the CHAOS-6 model and also in previous studies by Chulliat et al. (2015); in particular, the prominent features appearing between 2005 and 2009 in the longitude band from $-100°$ to $20°$. At 25°W in mid 2007, a distinctive SA 'cross-over' event may be observed, having strong, oppositely signed and adjacent, SA features rapidly changing sign within a year. The SA rapidly going trough zero is the characteristic feature of a geomagnetic jerk; here we are seeing the localized signature of such an event at the CMB. Furthermore, we see evidence of SA activity in the Pacific region in 2016.

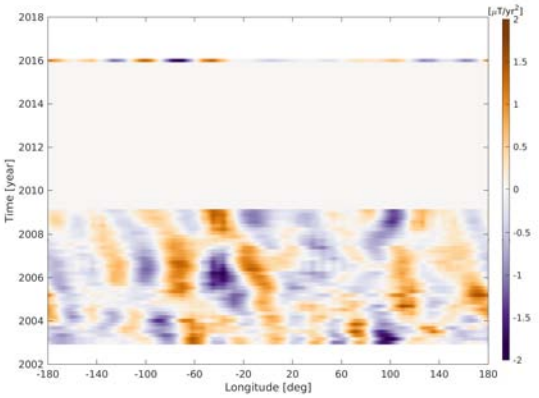

(a) 2yr accumulated SA using $\lambda = 5 \times 10^{-3}\mathrm{nT}^{-1}$.

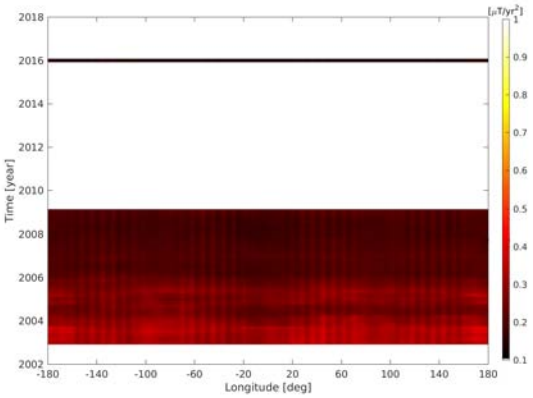

(b) 2yr accumulated SA error estimates, $\lambda = 5 \times 10^{-3}\mathrm{nT}^{-1}$.

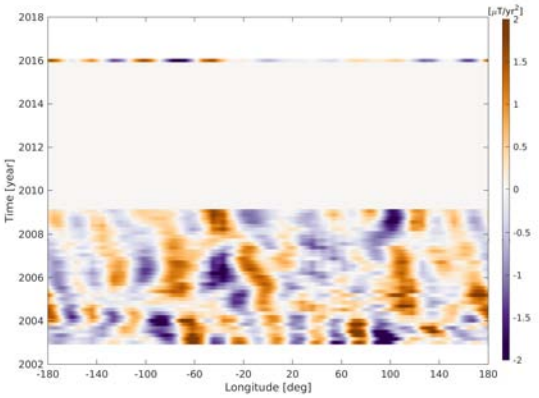

(c) 2yr accumulated SA using $\lambda = 3 \times 10^{-3}\mathrm{nT}^{-1}$.

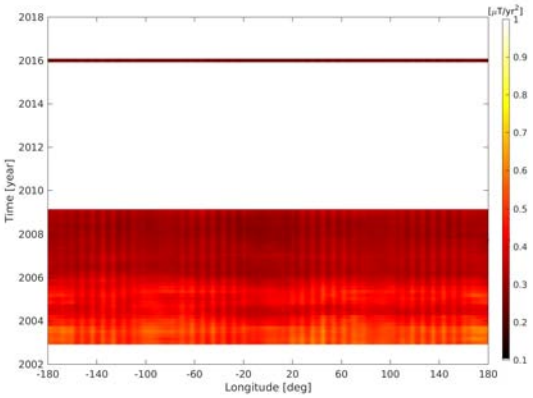

(d) 2yr accumulated SA error estimates, $\lambda = 3 \times 10^{-3}\mathrm{nT}^{-1}$.

Figure 5.26: Time-longitude plots along the geographical equator at the CMB showing the accumulated radial SA (left plots) and associated error estimates (right plots) as determined from 2yr differences of SV based on 2yr time windows, moved in 2 month steps. Results shown for $\lambda = 5 \times 10^{-3}\mathrm{nT}^{-1}$ (top) and $\lambda = 3 \times 10^{-3}\mathrm{nT}^{-1}$ (bottom).

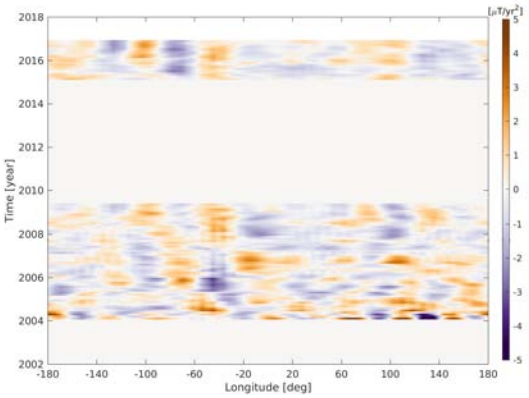

(a) 1yr accumulated SA using $\lambda = 5 \times 10^{-3}\mathrm{nT}^{-1}$.

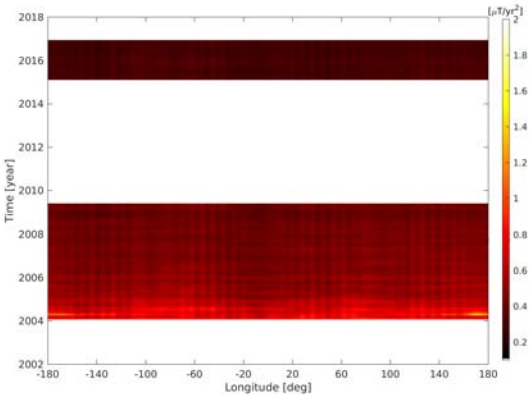

(b) 1yr accumulated SA error estimates, $\lambda = 5 \times 10^{-3}\mathrm{nT}^{-1}$.

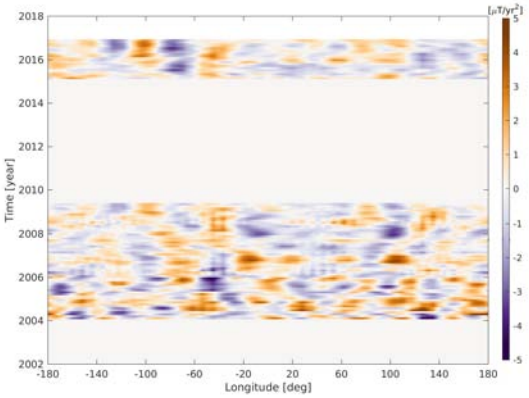

(c) 1yr accumulated SA using $\lambda = 3 \times 10^{-3}\mathrm{nT}^{-1}$.

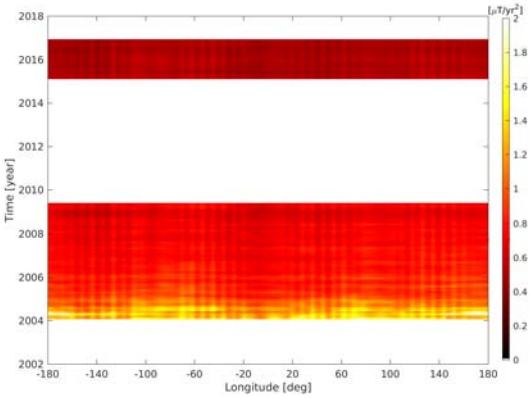

(d) 1yr accumulated SA error estimates, $\lambda = 3 \times 10^{-3}\mathrm{nT}^{-1}$.

Figure 5.27: Time-longitude plots along the geographical equator at the CMB showing the accumulated radial SA (left plots) and associated error estimates (right plots) as determined from 1yr differences of SV based on 1yr time windows, moved in 1 month steps. Results shown for $\lambda = 5 \times 10^{-3}\mathrm{nT}^{-1}$ (top) and $\lambda = 3 \times 10^{-3}\mathrm{nT}^{-1}$ (bottom).

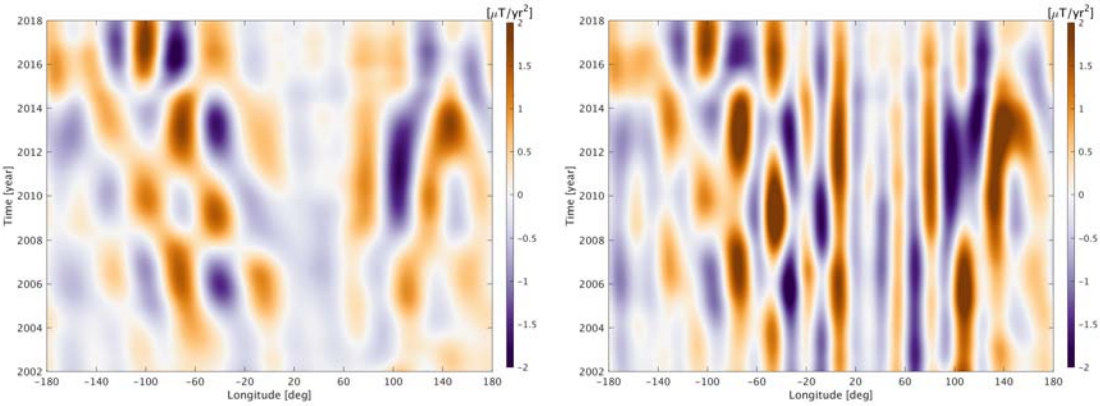

Figure 5.28: Time-longitude plots of the CHAOS-6-x5 model predictions for SH degrees 1 to 10 (left) and 1 to 16 (right).

5.5 Estimation of Time-dependent CMB Field: A Kernel Polynomial Approach

In this section we briefly report experiments with an alternative approach to the one given Section 5.4, regarding the time-dependence of the field. Here the data are related to the source field via both spatial and temporal kernels, and we attempt to localize in both space and time. The spatial (data) kernel is as before consisting of the Green's functions, while the temporal kernel is represented using local polynomials. A formalism is derived such that not just the MF and SV signals, but also the SA signal may be computed directly. Ignoring the spatial dependence, a simple synthetic case study was performed using a time series from one location in order to illustrate the method. Studies using geomagnetic real data turned out to be very unstable; it was possible to localize the spatial and temporal kernels, but only at the expense of stability. Therefore, the setup and numerical consideration regarding the real case study will be presented, but detailed results will not be shown.

It is assumed that the magnetic data, $d_n = d(\mathbf{r}_n, t_n)$, where $n = 1, ..., N$, may be expressed by the convolution

$$d_n = \int \oint_{S_C} G(\mathbf{r}|\mathbf{r}')H(t|t')B_r(\mathbf{r}', t')dS_C dt \tag{5.101}$$

Thus, the spatial and temporal kernels are separated, with $G(\mathbf{r}|\mathbf{r}')$ being the exterior spatial data kernels connecting positions of the data at $\mathbf{r}$ to the field at position $\mathbf{r}'$ and $H(t|t')$ being the smooth temporal kernel function connecting data at time t to the source field at time t'. Equation 5.101 resembles the internal part of equation (5.83) stated in Section 5.4, where the temporal kernel $H(t|t')$ implicit was taken to be a Taylor series expansion over a short time window. That is; if data were to be extracted from a short period of time, for instance a month, $H(t|t') \approx 1$, and thus the time dependence could be neglected in the similar case of the MF estimation in Section 5.4.3.

Next, consider some scattered observations, $\{(t_1, d_1), ..., (t_n, d_n)\}$, at one location and the source at that same location, i.e. $G(\mathbf{r}_n|\mathbf{r}') = 1$, such that using the explanatory variable, t, it is possible to write (Ledolter, 2013)

$$d_n = m(t_n) + \epsilon_n \tag{5.102}$$

where $m()$ is some function and ϵ_n are independent errors having zero mean. The method of non-parametric regression tries to estimate the unknown function m (Hastie et al., 1993). The idea is as follows; without making any assumptions regarding the functional form of $m(\cdot)$, an estimate at some specified time, t_0, is sought by using polynomial smoothing within some window centred on t_0. The function $m(\cdot)$ is unknown and the method of (local) polynomial smoothing is based on approximating $m(t)$ (locally) by a pth order polynomial in $t - t_0$ (Hastie et al., 1993; Gutierrez et al., 2003), i.e.

$$\begin{aligned}\widehat{m}(t) &\approx m(t_0) + m^1(t_1)(t - t_0) + \cdots + \frac{m^p(t_0)}{p!}(t - t_0)^p \\ &= \beta_0 + \beta_1(t - t_0) + \cdots + \beta_p(t - t_0)^p\end{aligned} \tag{5.103}$$

where $\beta = (\beta_0, \beta_1, ..., \beta_p)$ are the model coefficients for the polynomial description of order $p \in [0, p]$. The least squares solution (i.e. the model coefficients) is found by

$$\widehat{\beta} = (\underline{\underline{K}}^T \underline{\underline{K}})^{-1} \underline{\underline{K}}^T \mathbf{d} \tag{5.104}$$

Here $\underline{\underline{K}}$ is a matrix formed by the polynomial description such that

$$\underline{\underline{K}} = \begin{pmatrix} 1 & (t_1 - t_{tar}) & \cdots & (t_1 - t_{tar})^p \\ \vdots & \vdots & & \vdots \\ 1 & (t_n - t_{tar}) & \cdots & (t_n - t_{tar})^p \end{pmatrix} \tag{5.105}$$

A weighting matrix could be included assigning the largest weights close to t_0 to make a local regression (for instance a Gaussian kernel) (Hastie et al., 1993), but this was not explicitly done here. In forward problem the predicted data $\mathbf{d}^{pre}$ may then be written as

$$\mathbf{d}^{pre} = m(\mathbf{t}^{pre}) = \underline{\underline{K}}^{pre}\hat{\beta} = \underline{\underline{K}}^{pre}(\underline{\underline{K}}^T\underline{\underline{K}})^{-1}\underline{\underline{K}}^T\mathbf{d} \tag{5.106}$$

That is, the data, $\mathbf{d}$, may be regarded as the "model" and $\underline{\underline{K}}^{pre}(\underline{\underline{K}}^T\underline{\underline{K}})^{-1}\underline{\underline{K}}^T$ forms a kernel matrix linking the observed data in time; i.e. this is the kernel H. The first and second derivatives can be directly computed, and are only shown here for comparison, as

$$\begin{aligned} \dot{\mathbf{d}}^{pre} &= \dot{\underline{\underline{K}}}^{pre}\hat{\beta} = \dot{\underline{\underline{K}}}^{pre}(\underline{\underline{K}}^T\underline{\underline{K}})^{-1}\underline{\underline{K}}^T\mathbf{d} \\ \ddot{\mathbf{d}}^{pre} &= \ddot{\underline{\underline{K}}}^{pre}\hat{\beta} = \ddot{\underline{\underline{K}}}^{pre}(\underline{\underline{K}}^T\underline{\underline{K}})^{-1}\underline{\underline{K}}^T\mathbf{d} \end{aligned} \tag{5.107}$$

where the derivatives matrices are given by

$$\begin{aligned} \dot{\underline{\underline{K}}}^{pre} &= p(t - t_{tar})^{p-1} \\ \ddot{\underline{\underline{K}}}^{pre} &= p(p-1)(t - t_{tar})^{p-2} \end{aligned} \tag{5.108}$$

Discretizing the problem, the matrix $\underline{\underline{K}}$ is determined by the data times and order of the polynomial having dimensions $N \times P$, i.e. the number of data times order of the polynomial. The matrix $\underline{\underline{K}}^{pre}$ is determined by the numerical integration having dimensions $N_{int} \times P$, i.e. integration points times the order of the polynomial. Therefore the $\underline{\underline{H}}$ matrix is built as

$$\underline{\underline{H}} = \underline{\underline{K}}^{pre}(\underline{\underline{K}}^T\underline{\underline{K}})^{-1}\underline{\underline{K}}^T \tag{5.109}$$

having dimensions $N \times N_{int}$. In the next sections computations of the MF, SV and SA fields are considered separately in order to clarify this type of approach also incorporating the spatial kernel. However the important point to remember is that in each case $H(t|t')$ is the same and it can be represented within the above formulation. The only thing that changes in each field case, is the temporal target kernel and the constraints applied to it (i.e. the formulations in equations 5.108 are not used to make the SOLA estimates).

5.5.1 Main Field Case

Using the SOLA formulation, the main field estimate is written as the linear combination of the data

$$\widehat{B_r}(\mathbf{r}_0, t_0) = \sum_n^N q_n d_n \tag{5.110}$$

where q_n are the weight coefficients and the summation runs over the data being magnetic field measurements and t_0 denotes the target time of interest. The data may be expressed by the convolution, equation 5.101, above. Thus, an estimate at time t_0 and position $\mathbf{r}_0$ is given such that

$$\begin{aligned} \widehat{B_r}(\mathbf{r}_0, t_0) = \sum_n^N q_n d_n &= \sum_n^N q_n(\mathbf{r}_0, t_0) \int \oint_{S_C} G(\mathbf{r}|\mathbf{r}')H(t|t')B_r(\mathbf{r}', t')dS_C dt \\ &= \int \oint_{S_C} A_{MF}(\mathbf{r}_0, t_0|\mathbf{r}', t')B_r(\mathbf{r}', t')dS_C dt \end{aligned} \tag{5.111}$$

A spatial-temporal averaging kernel may thus be written as

$$A_{MF}(\mathbf{r}_0, t_0|\mathbf{r}', t') = \sum_n^N q_n(\mathbf{r}_0, t_0) G(\mathbf{r}_n|\mathbf{r}') H(t_n|t') \tag{5.112}$$

That is, the weights, q_n, are assigned to the data determining the shape of the main field averaging kernel, A_{MF}, which thus acts as a filter or a weighted average in space and time. The coefficients, q_n, can be estimated by minimization of an objective function as in Section 5.3.2

$$\Theta = \int \oint_{S_C} [A_{MF} - T_{MF}]^2 dS_C dt + +\lambda^2 \mathbf{q}^T \underline{\underline{E}} \mathbf{q} \tag{5.113}$$

where T_{MF} is some specified target function and $\underline{\underline{E}}$ is the covariance matrix. It is assumed that the target function may be written as a joint target function $T_{MF}(\Psi, t) = T_{Space}(\Psi) T_{Time}(t)$, where T_{Space} and T_{Time} are the space and time domain target functions, respectively. In the space domain a Fisher type target kernel as in Section 5.3.2 could be used, i.e.

$$\mathcal{T}_{\text{Fisher}}(\Psi) = \frac{\kappa}{4\pi \text{sinh}\kappa} \text{e}^{\kappa cos\Psi} \tag{5.114}$$

where κ is the Fisher target width. Here $\text{cos}\Psi = \text{cos}\theta_0 \text{cos}\theta' + \text{sin}\theta_0 \text{sin}\theta' \text{cos}(\phi_0 - \phi')$, Ψ being the angular distance between points $\mathbf{r}_0$ and $\mathbf{r}'$ on the sphere. In the time domain a Gaussian type target kernel could be used, i.e.

$$T_{\text{Gaussian}}(t_0|t) = \frac{1}{\sqrt{2\pi\tau^2}} \text{e}^{-\frac{(t-t_0)^2}{2\tau^2}} \tag{5.115}$$

where τ is some specified width of the function. The coefficients may then be found by using the requirement that $d\Theta/dq = 0$, i.e.

$$\frac{d}{dq}\left(\int \oint_{S_C} [A_{MF}^2 + T_{MF}^2 - 2A_{MF}T_{MF}] dS_C dt + \lambda^2 \mathbf{q}^T \underline{\underline{E}} \mathbf{q} \right) = 0$$
$$\frac{d}{dq}\left(\int \oint_{S_C} \left[\left(\sum q_n G_n H_n \right)^2 + T_{MF}^2 + 2 \sum q_n G_n H_n T_F T_G \right] dS_C dt + \lambda^2 \sum q_n^2 \sigma^2 \right) = 0$$

thus

$$\int \oint_{S_C} 2 \sum c_n G_n^2 H_n^2 dS_C dt - \int \oint_{S_C} 2 G_n H_n T_F T_G dS_C dt + 2\lambda^2 \sum q_n \sigma^2 = 0 \leftrightarrow$$
$$\int \oint_{S_C} \sum q_n G_n^2 H_n^2 dS_C dt + \lambda^2 \sum q_n \sigma^2 = \int \oint_{S_C} G_n H_n T_F T_G dS_C dt$$

Here $T_F = \mathcal{T}_{\text{Fisher}}$ and $T_G = T_{\text{Gaussian}}$. It is possible to imposed individually (unimodular) constraints in space and time to the spacial-temporal averaging kernel as

$$\oint_{S_C} A_{MF} dS_C = 1 \tag{5.116}$$
$$\int A_{MF} dt = 1 \tag{5.117}$$

The resulting set of equations subject to the constraints can be written

$$\left[\underline{\underline{\mathbf{G}}}\ \underline{\underline{\mathbf{W}}}\ \underline{\underline{\mathbf{G}}}^T \underline{\underline{\mathbf{K}}}\ \underline{\underline{\mathbf{W}}}\ \underline{\underline{\mathbf{K}}}^T + \lambda^2 \underline{\underline{\mathbf{E}}} \right] \mathbf{q}(\mathbf{r}_0) = \underline{\underline{\mathbf{G}}}\ \underline{\underline{\mathbf{W}}} \mathbf{t}_F(\mathbf{r}_0) \underline{\underline{\mathbf{K}}}\ \underline{\underline{\mathbf{W}}} \mathbf{t}_G(t_0) \tag{5.118}$$

$$\textit{subject to 1.} \quad \mathbf{e}^T \underline{\underline{\mathbf{W}}}\ \underline{\underline{\mathbf{G}}}^T \mathbf{q}(\mathbf{r}_0, t_0) \mathbf{H}(t, t_0) = 1 \tag{5.119}$$

$$\textit{subject to 2.} \quad \mathbf{e}^T \underline{\underline{\mathbf{W}}}\, \underline{\underline{\mathbf{K}}}^T \mathbf{q}(\mathbf{r}_0, t_0)\mathbf{G}(\mathbf{r}, \mathbf{r}_0) = 1 \tag{5.120}$$

where $\mathbf{H}$ and $\mathbf{G}$ are vectors having length $(1, ..., N)$, relating individual data times and positions to the target time and position, respectively. The coefficients of the solution are determined using the Lagrange multipliers $\{\mu_1, \mu_2\}$

$$\begin{pmatrix} \underline{\underline{\mathbf{G}}}\, \underline{\underline{\mathbf{W}\mathbf{G}}}^T \underline{\underline{\mathbf{K}}}\, \underline{\underline{\mathbf{W}\mathbf{K}}}^T + \lambda^2 \underline{\underline{\mathbf{E}}} & \underline{\underline{\mathbf{G}}}\, \underline{\underline{\mathbf{W}}}\mathbf{e} & \underline{\underline{\mathbf{G}}}\, \underline{\underline{\mathbf{W}}}\mathbf{e} \\ \mathbf{e}^T \underline{\underline{\mathbf{W}}}\, \underline{\underline{\mathbf{G}}}^T & 0 & 0 \\ \mathbf{e}^T \underline{\underline{\mathbf{W}}}\, \underline{\underline{\mathbf{K}}}^T & 0 & 0 \end{pmatrix} \begin{pmatrix} \mathbf{q}(\mathbf{r}_0) \\ \mu_1 \\ \mu_2 \end{pmatrix} = \begin{pmatrix} \underline{\underline{\mathbf{G}}}\, \underline{\underline{\mathbf{W}}}\mathbf{t}_G(\mathbf{r}_0) \underline{\underline{\mathbf{K}}}\, \underline{\underline{\mathbf{W}}}\mathbf{t}_G(t_0) \\ 1 \\ 1 \end{pmatrix}$$

where t_G and t_F are vectors relating the target position and time to the integration points, respectively. In order to try and improve stability of the calculations, additional Lagrange constrains were added, requiring a symmetry constraint on the MF temporal averaging kernel about the target time. In the numerical studies, the temporal integration was done using Trapezoidal quadrature (Riley et al., 2004) and the spatial integration was performed using Lebedev quadrature, see Section 5.4.2.

5.5.2 Secular Variation Field Case

The secular variation may be estimated in a similar approach as above, by a linear combination of the data

$$\widehat{\dot{B}_r}(\mathbf{r}_0, t_0) = \sum_n^N q'_n d_n \tag{5.121}$$

where q'_n are the (SV) weight coefficients and the summation runs over the data $n = 1, ..., N$. As for the MF case data may be expressed by equation 5.101, such that

$$\begin{aligned} \widehat{\dot{B}_r}(\mathbf{r}_0, t_0) = \sum_n^N q'_n d_n &= \sum_n^N q'_n(\mathbf{r}_0, t_0) \int \oint_{S_C} G(\mathbf{r}|\mathbf{r}')H(t|t')B_r(\mathbf{r}', t')dS_C dt \\ &= \int \oint_{S_C} A_{SV}(\mathbf{r}_0, t_0|\mathbf{r}', t')B_r(\mathbf{r}', t')dS_C dt \end{aligned} \tag{5.122}$$

A spatial-temporal SV averaging kernel may thus be written as

$$A_{SV}(\mathbf{r}_0, t_0|\mathbf{r}', t') = \sum_n^N q'_n(\mathbf{r}_0, t_0)G(\mathbf{r}_n|\mathbf{r}')H(t_n|t') \tag{5.123}$$

where the weights, q'_n, determines the shape of the SV averaging kernel that acts as a filter in time and an average in space. Here H is computed using equation (5.109). The coefficients are again estimated by minimization of an objective function here written

$$\Theta = \int \oint_{S_C} [A_{SV} - T_{SV}]^2 dS_C dt + +\lambda^2 \mathbf{q}'^T \underline{\underline{E}}\mathbf{q}' \tag{5.124}$$

where T_{SV} is a target function written as the product $T_{SV} = T_{Space}(dT_{Time}/dt)$, where T_{Space} and (dT_{Time}/dt) are the space and time domain target functions, respectively. The required time derivative of the Gaussian target kernel, equation 5.115, is

$$\begin{aligned} \frac{d}{dt}T_{Gaussian} &= \frac{d}{dt}\left(\frac{1}{\sqrt{2\pi\tau^2}}\exp^{-\frac{(t-t_0)^2}{2\tau^2}}\right) \\ &= -\frac{2\sqrt{2}(t-\tau)}{4\sqrt{\pi}\tau^3}\exp^{-\frac{(t-t_0)^2}{2\tau^2}} \end{aligned} \tag{5.125}$$

The solution scheme follows that of the main field with the exception that the integral of the temporal averaging kernel is enforced to equal zero. Furthermore, Lagrange constrains are such that the SV temporal averaging kernel should be anti symmetric about the target time.

5.5.3 Secular Acceleration Field Case

The secular acceleration may also be estimated in a similar approach, i.e. by a linear combination of the data

$$\widehat{\ddot{B}_r}(\mathbf{r}_0, t_0) = \sum_n^N q_n'' d_n \tag{5.126}$$

where q_n'' are the (SA) weight coefficients and the summation runs over the data $n = 1, ..., N$. As for the MF case data may be expressed by equation 5.101, such that

$$\begin{aligned}\widehat{\ddot{B}_r}(\mathbf{r}_0, t_0) = \sum_n^N q_n' d_n &= \sum_n^N q_n''(\mathbf{r}_0, t_0) \int \oint_{S_C} G(\mathbf{r}|\mathbf{r}') H(t|t') B_r(\mathbf{r}', t') dS_C dt \\ &= \int \oint_{S_C} A_{SA}(\mathbf{r}_0, t_0|\mathbf{r}', t') B_r(\mathbf{r}', t') dS_C dt \end{aligned} \tag{5.127}$$

A spatial-temporal SA averaging kernel may thus be written as

$$A_{SA}(\mathbf{r}_0, t_0|\mathbf{r}', t') = \sum_n^N q_n''(\mathbf{r}_0, t_0) G(\mathbf{r}_n|\mathbf{r}') H(t_n|t') \tag{5.128}$$

where the weights, q_n'', determines the shape of the SA averaging kernel acting as a filter in time and an average in space just as in the MF ans SV cases. Here H is computed using equation (5.109). The coefficients are estimated by minimization of the objective function

$$\Theta = \int \oint_{S_C} [A_{SA} - T_{SA}]^2 dS_C dt + + \lambda^2 \mathbf{q}''^T \underline{\underline{E}} \mathbf{q}'' \tag{5.129}$$

where T_{SA} is a target function written as the product $T_{SA} = T_{Space}(d^2 T_{Time}/dt^2)$, where T_{Space} and $(d^2 T_{Time}/dt^2)$ are the space and time domain target functions, respectively. The second time derivative of the Gaussian target kernel, equation 5.115, is

$$\begin{aligned}\frac{d^2}{dt^2} T_{Gaussian} &= \frac{d^2}{dt^2} \left(\frac{1}{\sqrt{2\pi\tau^2}} \exp^{-\frac{(t-t_0)^2}{2\tau^2}} \right) \\ &= \frac{1}{4\tau^4} \left[\exp^{-\frac{(t-t_0)^2}{2\tau^2}} (2t - 2t_0)^2 \right] - \frac{1}{\tau^2} \exp^{-\frac{(t-t_0)^2}{2\tau^2}} \end{aligned} \tag{5.130}$$

The solution scheme follows that of the MF and SV also requiring that the integration of the SA averaging kernel should equal zero. Furthermore, Lagrange constrains are applied such that the SA temporal averaging kernel should be symmetric about the target time.

5.5.4 Synthetic Test Studies

In this section a synthetic test is described using the above formulations for the MF, SV and SA. For this study it was assumed that the data and source locations were the same,

i.e. $G(\mathbf{r}_i|\mathbf{r}') = 1$. This means that the temporal averaging kernels can be written

$$A_{MF}(t_0|t') = \sum_n^N q_n(\mathbf{r}_0, t_0) H(t_n|t') = \mathbf{q}^T \underline{\underline{H}} \tag{5.131}$$

$$A_{SV}(t_0|t') = \sum_n^N q'_n(\mathbf{r}_0, t_0) H(t_n|t') = \mathbf{q}'^T \underline{\underline{H}} \tag{5.132}$$

$$A_{SA}(t_0|t') = \sum_n^N q''_n(\mathbf{r}_0, t_0) H(t_n|t') = \mathbf{q}''^T \underline{\underline{H}} \tag{5.133}$$

Thus the spatial target and averaging kernels drop out, simplifying the problem. Synthetic time series were generated such that each month there was a data point mimicking a real case scenario. Figure 5.29 presents plots of synthetic data of the generated MF, SV and SA fields; in this case study the SA was constant at 211 nT/yr^2. Figure 5.30 presents the least-squares solutions, i.e. equations (5.106) and (5.107), which are seen to match the data in all three cases. In this example case the order of the polynomial description was $P = 14$ and the temporal integration was done using Trapezoidal quadrature (Riley et al., 2004) having a total number of integration points $N_{int} = 8001$, to ensure high numerical accuracy.

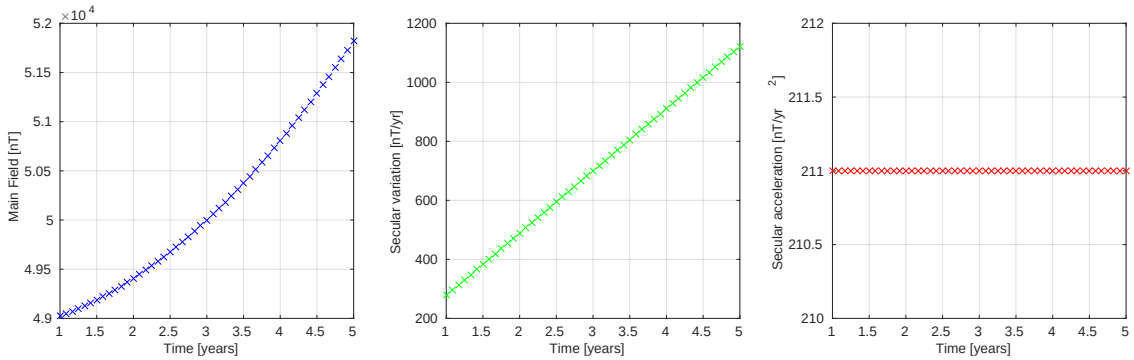

Figure 5.29: Synthetic studies showing the MF (left), the SV (center) and SA (right) data.

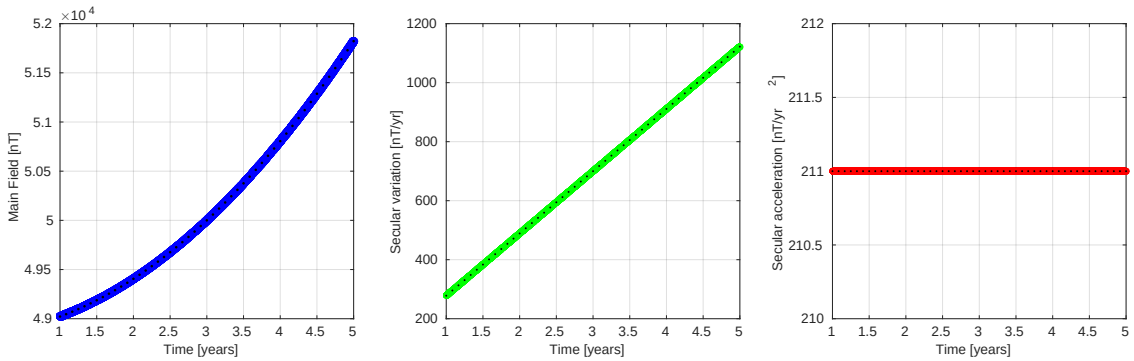

Figure 5.30: Least squares solution of the MF (left), SV (center) and SA (right) fields.

Figure 5.31 presents the temporal target kernels for the MF, SV and SA (left plot), the obtained averaging kernels (center plot) and their differences (right plot). In this example the covariance matrix had a diagonal of values 0.5nT^2 (the value here is not vital as the

solution just scales with λ), the width of the temporal kernels were taken as $\tau = 0.55$yr and $\lambda = 10^{-9}$. The obtained averaging kernels all looked close to their target kernels, however their differences, though symmetric about the target time, indicate a small bias most notably in the SA kernel. In Table 5.2 results obtained from a run using the above mentioned values are presented. It can be seen that the reconstructions of the MF, SV and SA fields are reasonable. However, it was found that the SV and SA determination was very dependent on even slight disturbances in the associated kernel structures, the reason being that a slight shift in these kernels will have a big impact on the estimates. For this reason, it was concluded that additional constraints are needed to get an appropriate robust SA determination by this method.

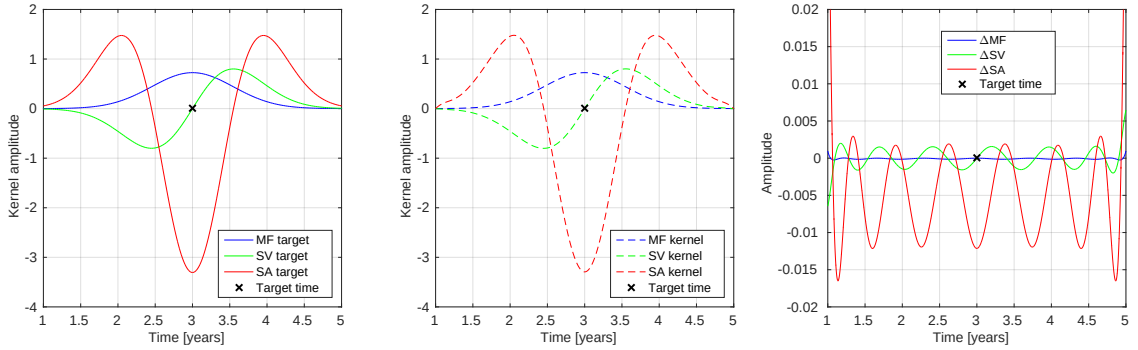

Figure 5.31: Synthetic studies showing the target kernels (left), the obtained averaging kernels (center), and their differences (right). The black cross shows the target time. Note the change of scale in the right plot.

Field	Truth	SOLA estimate	Error [%]
Main field [nT]	50000	50031.79	0.06
Secular variation field [nT/yr]	700	696.41	0.51
Secular acceleration field [nT/yr^2]	211	197.27	6.51

Table 5.2: Example results from a synthetic test run.

5.5.5 Problems with Instability

Experiments using real data revealed that the solutions obtained using the above scheme were very unstable. In order to obtain estimates, a large trade-off parameter for the covariance was required at the expense of an associated high variance and solution stability. Part of the explanation for this is perhaps the strong requirements that the SV and SA kernels should be anti-symmetric and symmetric around the target time and unbiased. As can be seen from the synthetic case studies, there are small differences (asymmetries and biases) between the targets and obtained kernels. Because the main field is so large compared to the SV and SA signals, even a small off-set in the kernels applied to the observed data have a large impact on the SV and SA estimates; for instance a difference in amplitude of say 0.001 in the SA kernel would correspond to 500nT, assuming a background main field of 50000nT. It may be that additional constraints on the kernel behaviour, besides those investigated, could mitigate such issues. Further studies into the effect of

data gaps or uneven data distribution in time could be made to better understand the kernel behaviour.

5.6 Summary

This chapter has been devoted to the development and implementation of a modified Backus-Gilbert method called SOLA, to the geomagnetic problem of estimating the radial magnetic field and its time evolution at the core-mantle boundary. The SOLA method is a subclass belonging to the OLA methods, which aims at determining localized average estimates, and was originally developed in helioseimology in order to overcome the computational expensive burden of the original Backus-Gilbert method. In this thesis the SOLA formalism was implemented with the aim of determining local averages of the core-generated magnetic field at the CMB along with its time derivatives. Under the settings of the Neumann boundary value problem, exterior and interior Green's functions have been formulated relating both internal and external source to the magnetic measurements. Furthermore, data error covariance matrices were incorporated in the formulation, which allowed latitude dependent data errors and along-track serial error correlation to be accounted for.

Two different approaches to handling the field time dependence have been described: 1) a Taylor series expansion of the field at the CMB, and 2) a polynomial approximation of the temporal kernel relating measurement and source field times. The latter approach turned out to be very unstable using real data, and thus only synthetic case studies have been presented here. The former approach turned out to be more successful providing stable results, and applications to estimates of the radial MF and the radial SV have been presented as global collections of estimates at the CMB. These global collections of both the MF and SV SOLA estimates showed good coherence with the results from more conventional spherical harmonic based field models. Also the accumulated radial SA field was determined using 1 and 2 year epoch differences between SV estimates. Maps of collected estimates were in good agreement with field morphology seen in maps of the radial SA fields as predicted by models such as the CHAOS-6-x5, CIY4, GRIMM and POMME. The SOLA estimates however involves no spectral truncation and no applied regularization (neither in space or time) which heavily influences the SA above SH degree 9 in models such as CHAOS-6-x5 (Finlay et al., 2016b). Time-longitude plots of the SA field at the CMB along the geographical equator have been studied. Coherence of the SA signal in these plots for different SV time windows was evident, and they were found to be useful for tracking the evolution of the SA field. As an example, a rapid change (cross-over) in oppositely signed SA features was observed in 2007 at longitude 25°W. Such a sign change is characteristic of a geomagnetic jerk event which has here been imaged locally at the CMB.

Chapter 6

Conclusions

In this section the main results and findings from the work carried out and presented in this thesis are collected. In this thesis two different methods of locally estimating the core-generated magnetic field have been described and implemented. The first method considered is the Virtual Observatory (VO) method, providing a way of using satellite measurements to make time series of the field and its time derivatives at pre-specified locations mimicking the time series from ground observatories. The second method considered in this thesis builds on a modified Backus-Gilbert inversion approach called Subtractive Optimally Localized Averages (SOLA). The SOLA method enables estimates of local averages of the field and its first time derivative directly at the core-mantle boundary from satellite measurements. The work carried out in this thesis used dark geomagnetic, quiet-time, measurements from the CHAMP and *Swarm* satellite missions.

The VO Technique

Chapter 4 described, implemented and advanced on previous developments of the VO modelling technique. Using a cubic potential expansion, VO time series at epochs of 4 month spacing were produced, resulting in high correlation levels with the time series at ground observatories in all three vector field components. In addition to this, a simple procedure for estimating uncertainties of the VO time series has been devised. The VO technique involves a pre-whitening step where the internal part of a geomagnetic field model is removed. We found that results for the VO time series were independent of which field model is used for this pre-whitening. VO time series of field gradients and their first and second time derivatives VO's were also produced. We found that these gradient time series show promising results, and found that geomagnetic jerk events can be clearly identified in such time series. This offers new possibilities for tracking and uncovering the short time changes of the core-generated field locally. Furthermore, we have shown that internal field models can be built using VO gradient time series. Although unmodelled contamination has been reduced via optimization of data selection and handling procedures, further mitigation of external and in-situ measured toroidal field contamination should be explored further as these constitute the major limits on the method.

Scientific findings using the VO time series include; i) a change in the SV signal mostly seen in the X-component in South America, observed around 2016 having an associated steep change in the SA signal which could indicate a geomagnetic jerk taking place during

the *Swarm* from 2014-2018, ii) a change in the SV signal and a steep change in the radial SA around 2017 can be observed in the Pacific region, which may be the first signs of a geomagnetic jerk taking place, iii) using the internal field models built from VO field and field gradient time series, global maps of the radial SV and SA fields supports evidence of changing field activity in the Pacific region. Recent studies have indicated that jerks have taken place in the *Swarm* era (Brown and Macmillan, 2018). The properties of such field changes are of great interest; are these local or global events and over how long time intervals do they occur, and what is the time between events? We conclude that the VO modelling technique is a flexible and highly versatile tool, which can be tailored to meet the specific requirements of particular researchers whether conducting local or global field analysis. The VOs have also proven useful for core flow inversions and data assimilations (Whaler, 2017; Barrois et al., 2018). As satellite magnetic field measurements continuously accumulate with time, the VO method may eventually help shed light on some of the outstanding scientific questions regarding the core field.

Future Possibilities using the VO Technique

The VO time series could be used for several future applications and investigations, in particular:

- As the *Swarm* satellite constellation mission progresses, rapid field change events can be studied in great detail using the VO approach. Events such as geomagnetic jerks are clearly seen in the annual differences of both the field and gradient time series.
- Measurements from other satellites such as the DMSP (Alken et al., 2014) or Cryosat missions, may prove useful when trying to fill the gap between the CHAMP and *Swarm* eras. Using these measurements and applying the VO method could prove beneficial when investigating the core field evolution during the CHAMP/*Swarm* satellite data void.
- The VO field time series have already been used for core flow inversions and in data assimilation studies, inferring both the the core magnetic field and fluid flow. Using VO field gradient time series could prove very useful in such studies as well.
- The VO technique could prove useful in both core field modelling, and perhaps in external field modelling on month to year time-scales as well. Such studies may be further explored in the future as more satellite data are collected.

The SOLA Technique

Chapter 5 introduced, described and implemented the SOLA technique for computing localized spatial average estimates of the radial magnetic field and its first time derivative at the core-mantle boundary. A key point in using this approach is formal appraisal of the spatial resolution and the variance of the field estimates.

The field time dependence was investigated by two different approaches; 1) a Taylor series expansion of the field at the CMB, and 2) a local polynomial approximation of the temporal kernel relating measurement times and source field times. When using real data, the second approach turned out to be unstable for estimating field derivatives and therefore only synthetic case studies are presented in this thesis. The first approach proved

successful at providing stable results when applied to real data, and results from this are discussed below.

Initial synthetic studies revealed that the spatial averaging kernel width only changed slightly even with a dramatic increase in the amount of satellite data, apparently reaching an upper limit of the resolvability offered by data collected at a given distance from the source region. From synthetic test results it was shown that 1000 data points were enough to obtain useful SOLA estimates at the CMB. The SOLA technique was formulated accounting for both internal and external field sources. Furthermore, we showed how one could incorporate information from data error covariance matrices such as along-track serial correlation.

We presented results for an example of a global collection of SOLA estimates for the radial main field (MF), having widths of the spatial resolution kernel varying between $\sim 18^\circ$ and $\sim 54^\circ$ depending on latitude, with a standard deviation of $\sim 10\mu$T. We also presented global collections of SOLA estimates for the radial secular variation (SV) at the CMB, with widths of the spatial resolution kernel of $\sim 42^\circ$, $\sim 33^\circ$ and $\sim 30^\circ$ at the equator, with corresponding standard deviations of $\sim 0.25\mu$T/yr, $\sim 2.5\mu$T/yr and $\sim 5\mu$T/yr. We found that the morphology of the MF and SV maps agrees well with results from spherical harmonic based field models, however our method does not involve any direct spectral truncation or temporal regularization. By regularization we mean minimizing a global norm of the model (Parker, 1994). Changing the averaging kernel widths, a clear coherence in field morphology was observed as would be expected for well resolved features (Holme et al., 2011; Aubert, 2018). The Backus-Gilbert approach was originally not intended to be used for such global estimate collections. However, the union of a collection of point estimates has been considered by some authors to constitute a sensible approach (Parker, 1994; Nolet, 2008; Zaroli, 2016). In principle, such a union would require studies of trade-off curves for each target location. However, the findings of this thesis showed that the same trade-off parameter can be used for all target points provided the data error budget is set appropriately. This in turn causes the variances of the estimates and the averaging kernel widths to vary with position, thus reflecting uneven data distribution and/or enhanced data errors in certain regions. Surprisingly, it was discovered that the variances changed very little with position when performing such global estimates. Averaging kernel widths stated may give only a crude summary of the actual averaging scale, since the kernels can be prone to oscillatory behaviour especially for small values of the trade-off parameter (Parker, 1994). However, we found that the averaging kernels generally behaved very well showing no significant side lobes, and that the kernel widths gave a very useful diagnostic of the resolution.

We computed the local accumulated secular acceleration (SA) by subtracting the SV SOLA estimates, based on two year data time windows, from epochs 2 years apart. These had averaging kernel widths of $\sim 42^\circ$ degrees at the equator and a standard deviation of $\sim 0.2\text{T/yr}^2$. Comparisons with SH based field models CHAOS-6-x5, CIY4, GRIMM and POMME, showed remarkably good agreements in terms of the field morphology, with the SOLA based SA. Also the power spectra of the MF, SV and SA as determined from global collections of the local SOLA estimates, matched well those of conventional SH based field models. Using a global diagnostics such as the SH power spectrum, however misses the key strength of our localized SOLA technology. The direct control of the spatial averaging kernel and the time window length, enables investigations into the robustness of the inferred SA field as a function of length-scale and time-scale. Investigating the time evolution of the radial SA along the geographical equator and pushing towards higher temporal resolution, we computed both 2 and 1 year SV epoch differences constructed using two and one

year time windows, respectively. We were able to track coherent structures of the radial SA and their evolution in time-longitude plots. These findings of rapid field acceleration changes were achieved down to an averaging width of ∼30° degrees at the CMB. One particular finding observed at 25°W around mid 2007, was a distinctive SA 'cross-over' event having adjacent and strong oppositely signed SA features rapidly changing sign within a year. Such features may have important implications for understanding the origin of geomagnetic jerks. Using shorter time windows makes such possible SA cross-over events more easily seen, thereby confirming hints of its presence in field models like the CHAOS-6 (Chulliat et al., 2015). The origin of such SA field features, likely involves rapid change in sign of the azimuthal core flow acceleration (Gillet et al., 2015a; Finlay et al., 2016b; Kloss and Finlay, 2018). Recently, studies have suggested that geomagnetic jerks might be explained by rapid hydromagnetic Alfven waves emerging at the core surface, which are caused by sudden buoyancy releases inside the outer core (Aubert and Finlay, 2018). In addition to this, possible correlation between the SA and gravity anomalies measured by the GRACE satellite have been reported (Mandea et al., 2012). In revealing such new aspects of the core dynamics, it is very important that the SA behaviour and its temporal characteristics are robustly estimated. Interestingly, both the SV and SA SOLA based global maps from 2016 indicate field activity in the Pacific region; this agrees well with the findings made using the VO method as described above. The SOLA technique proves to be well suited for robust studies of the localized radial SA and its time evolution, while at the same time providing the appraisal needed, and may pave the way into further investigations that may allow insights into geophysical processes happening at even shorter time scales.

We stress that the SOLA method does not involve the traditional form of regularization applied in field model construction (neither in space or time) which is known to heavily influence the SA above SH degree 9 (Finlay et al., 2016b). Furthermore, we have full control over the time window length and spatial averaging kernel. Returning to the issue of determining the SA signal as discussed in Section 2.6.1, recall that a SH based model gives a band-limited SA via the spectral domain truncation and temporal frequency band considered. Likewise, what is provided in Chapter 5 of this thesis are SA estimates that are spatial averaged (also effectively band limited, since spatial averaging may be considered a smoothing operation in which small scales are attenuated) and temporally averaged over a given time window. Although the SOLA results presented in this these have been global collections of localized field estimates, the technique works equally well for regional or local collections (e.g. local time series, time-longitude plots, regional field evolution).

In summary, the SOLA technique presented in this thesis offers a useful alternative for estimating the geomagnetic field as compared to conventional geomagnetic field modelling; instead of relying on a regularized truncated spherical harmonics representation being downward continued to the CMB, the SOLA approach performs spatial averages of the field over a given time window directly at the CMB. The most important advantage of the SOLA method is that it automatically provides the associated spatial averaging kernels and variance estimates thereby allowing for a detailed appraisal of the field averages; a major strength of this is that an unbiased resolution estimate can be obtained (which is not the case when regularization is applied). In contrast, it is difficult to interpret variances for point estimates derived from regularized SH models, and workers rarely compute the associated spatial averaging kernels. A wide range of well-characterized estimates can be realized by varying the kernel width via the trade-off parameter λ, thus providing full

control over the solution; it is desirable to have a low kernel width while at the same time having a sufficiently low uncertainty estimates for the field averages. Another advantage offered by the SOLA method, is the possibility to pre-specify other types of target kernels in order to devise a particular form of the spatial averaging; in this thesis a Fisher function was used, however other possibilities exists such as for example a disc boxcar averaging function (Masters and Gubbins, 2003) depending on the desired application. It should be noted, that the SOLA estimate may under some circumstances be closer to the true value than the least-squares solution, provided the quantity being estimated is sufficiently smooth (Parker, 1977; Pujol, 2013).

One shortcoming of the SOLA technique is that the number of solution coefficients equals the number of data, i.e. it requires the solution of a linear system of size (number of data x number of data), which becomes challenging when considering very large datasets. Considering satellite measurements, a large amount of data becomes available especially if one wishes to use data sums and differences for each vector field component, and even more so getting data from multiple satellites. In the results presented here, the problem was not insurmountable, and it was mitigated by computing field estimates from within a short time window (i.e. as done in the MF case) and/or to perform strong data decimation in order to obtain a data set with good spatial and temporal coverage (i.e. as done in the SV case).

The most severe source of error in the determination of the core-generated field is probably the incomplete separation of the crustal field and contamination from magnetospheric and ionospheric E-region fields and in-situ measured toroidal fields. The SOLA technique presented in this thesis relies on a potential field formulation allowing for internal and external field separation, however it is unable to perform a core/crust/ionosphere separation with satellite data alone. This means that bias from incompletely separated non-core field sources cannot be excluded in the maps presented throughout this thesis, and its effects are difficult to quantify. Including measurements from several altitudes may help mitigate this issue, as will experiments carried out for different external field selection criteria. Considering magnetosphere-ionospheric coupling (in-situ) currents in the F-region that produce toroidal fields, it may be possible to modify the SOLA formalism to a non-potential description by adding a toroidal field term.

Future Possibilities using the SOLA Technique

The SOLA technique described may be used in a number of promising applications and investigations in future studies, in particular:

- As the *Swarm* satellite mission progresses, rapid field evolution can be studied robustly and in great detail in specific locations of interest using this method. In such studies the ability to estimate the field and its time derivatives locally providing associated appraisal becomes very important, in particular in the quest to understand the underlying dynamics behind the features observed in the SA field.

- Measurements from other satellites including the DMSP (Alken et al., 2014) or Cryosat missions, may prove useful when trying to fill the gap between the CHAMP and *Swarm* eras. Using these measurements and applying the SOLA method could prove beneficial when investigating the core field during the CHAMP/*Swarm* satellite data void.

- The SOLA technique could be applied to estimation at locations other than the CMB. For instance on a grid at mean satellite altitude, being an alternative means of producing the virtual observatories. As such the estimates obtained having associated averaging and variance information may be well suited for data assimilation applications

- The SOLA technique allows for other types of magnetic observations to be used, for instance ground observatory measurements. The SOLA technique is a local method and does not need not to produce global results (as the SH method). Therefore, the SOLA technique may be particularly useful in certain regions such as Europe, North America and Australia where there are excellent coverage with ground-based measurements. This could provide an opportunity to study the local field evolution under Europe at high resolution, providing important means of validating results obtained with satellite data.

- Investigating the longer term evolution of the geomagnetic field, the SOLA technique could perhaps also be applied in archeomagnetism and paleomagnetism where the data coverage is more sparse, and appraisal information would certainly be very valuable. For instance the method could be used to investigate what is happening at the CMB during archeomagnetic spike events (Ben-Yosef et al., 2009; Shaar et al., 2016; Korte and Constable, 2018). Performing such studies would demand linearization approaches in order to handle nonlinear intensity and directional data (Snieder, 1991).

- Finally, there is the exciting possibility that the SOLA technique may be applied to local core flow studies. This would require a formulation of the local core flow in SOLA terms, but this could prove very beneficial for confirming the observations made by present day global core flow inversion.

Bibliography

Alken, P., Maus, S., Lühr, H., Redmon, R. J., Rich, F., Bowman, B., and O'Malley, S. M. (2014). Geomagnetic main field modeling with DMSP. *Journal of Geophysical Research: Space Physics*, 119(5):4010–4025.

Alken, P., Maute, A., and Richmond, A. D. (2017). The F-Region Gravity and Pressure Gradient Current Systems: A Review. *Space Science Reviews*, 206(1-4):451–469.

Aster, R. C., Borchers, B., and Thurber, C. H. (2005). *Parameter Estimation and Inverse Problems*. Elsevier Academic Press, London, UK.

Aubert, J. (2013). Flow throughout the Earth's core inverted from geomagnetic observations and numerical dynamo models. *Geophysical Journal International*, 192(2):537–556.

Aubert, J. (2018). Geomagnetic acceleration and rapid hydromagnetic wave dynamics in advanced numerical simulations of the geodynamo. *Geophysical Journal International*, 214(1):531–547.

Aubert, J. and Finlay, C. C. (2018). Geomagnetic jerks and rapid hydromagnetic waves focusing at Earth's core surface. Study of the Earth's Deep Interior (SEDI) session S5-P19.

Aubert, J., Finlay, C. C., and Fournier, A. (2013). Bottom-up control of geomagnetic secular variation by the Earth's inner core. *Nature*, 502:219–223.

Aubert, J., Gastine, T., and Fournier, A. (2017). Spherical convective dynamos in the rapidly rotating asymptotic regime. *Journal of Fluid Mechanics*, 813:558–593.

Backus, G. (1970a). Inference from Inadequate and Inaccurate Data, I. *Proceedings of the National Academy of Sciences*, 65(1):1–7.

Backus, G. (1970b). Inference from Inadequate and Inaccurate Data, II. *Proceedings of the National Academy of Sciences*, 65(2):281–287.

Backus, G. (1970c). Inference from Inadequate and Inaccurate Data, III. *Proceedings of the National Academy of Sciences*, 67(1):282–289.

Backus, G. (1986). Poloidal and Toroidal Fields in Geomagnetic Field Modelling. *Reviews of geophysics*, 24:75–109.

Backus, G. and Gilbert, F. (1968). The Resolving Power of Gross Earth Data. *Geophysical Journal International*, 16(2):169–205.

Backus, G. and Gilbert, F. (1970). Uniqueness in the inversion of inaccurate gross Earth data. *Philosophical Transactions of the Royal Society of London A: Mathematical, Physical and Engineering Sciences*, 266(1173):123–192.

Backus, G., Parker, R. L., and Constable, C. (1996). *Foundations of geomagnetism*. Cambridge University Press.

Backus, G. E. (1970d). Non-Uniqueness of the External Geomagnetic Field Determined by Surface Intensity Measurements. *Journal of Geophysical Research*, 75(31):6339–6341.

Balogh, A. and Erdõs, G. (2013). The heliospheric magnetic field. *Space Science Reviews*, 176(1-4):177–215.

Barlow, R. J. (1989). *Statistics: a guide to the use of statistical methods in the physical sciences*, volume 29. John Wiley & Sons.

Barrois, O., Gillet, N., and Aubert, J. (2017). Contributions to the geomagnetic secular variation from a reanalysis of core surface dynamics. *Geophysical Journal International*, 211(1):50–68.

Barrois, O., Hammer, M. D., Finlay, C. C., Martin, Y., and Gillet, N. (2018). Assimilation of ground and satellite magnetic measurements: inference of core surface magnetic and velocity field changes. *Geophysical Journal International*, 215:695–712.

Barton, G. (1989). *Elements of Green's functions and propagation: potentials, diffusion, and waves*. Oxford University Press.

Baumjohann, W. and Nakamura, R. (2007). Magnetospheric contributions to the terrestrial magnetic field. In *Treatise on Geophysics*, volume 5, chapter 3, pages 77–91. Elsevier.

Beggan, C. and Whaler, K. (2010). Forecasting secular variation using core flows. *Earth, planets and space*, 62(10):821–828.

Beggan, C. D. and Whaler, K. A. (2009). Forecasting change of the magnetic field using core surface flows and ensemble Kalman filtering. *Geophysical Research Letters*, 36(18).

Beggan, C. D., Whaler, K. A., and Macmillan, S. (2009). Biased residuals of core flow models from satellite-derived virtual observatories. *Geophysical Journal International*, 177(2):463–475.

Ben-Yosef, E., Tauxe, L., Levy, T. E., Shaar, R., Ron, H., and Najjar, M. (2009). Geomagnetic intensity spike recorded in high resolution slag deposit in Southern Jordan. *Earth and Planetary Science Letters*, 287(3):529–539.

Blakely, R. J. (1995). *Potential Theory in Gravity and Magnetic Applications*. Cambridge Press, Cambridge.

Bloxham, J. and Gubbins, D. (1985). The secular variation of Earth's magnetic field. *Nature*, 317(6040):777.

Bloxham, J., Gubbins, D., and Jackson, A. (1989). Geomagnetic secular variation. *Phil. Trans. R. Soc. Lond. A*, 329(1606):415–502.

Bloxham, J. and Jackson, A. (1991). Fluid flow near the surface of Earth's outer core. *Reviews of Geophysics*, 29(1):97–120.

Booker, J. R. (1969). Geomagnetic data and core motions. *Proc. R. Soc. Lond. A*, 309(1496):27–40.

Bouligand, C., Gillet, N., Jault, D., Schaeffer, N., Fournier, A., and Aubert, J. (2016). Frequency spectrum of the geomagnetic field harmonic coefficients from dynamo simulations. *Geophysical Supplements to the Monthly Notices of the Royal Astronomical Society*, 207(2):1142–1157.

Brown, W., Beggan, C., and Macmillan, S. (2016). Geomagnetic Jerks in the Swarm Era. *ESA Living Planet Symposium, Czech, Prague*, pages 9–13.

Brown, W. and Macmillan, S. (2018). Geomagnetic jerks during the Swarm era and impact on IGRF-12. [Poster] In: EGU General Assembly 2018, Vienna, Austria, 8-13 April 2018. British Geological Survey.

Buffett, B. (2014). Geomagnetic fluctuations reveal stable stratification at the top of the Earth's core. *Nature*, 507(7493):484.

Buffett, B. A. (2000). Earth's core and the geodynamo. *Science*, 288(5473):2007–2012.

Bullard, E. (1955). The stability of a homopolar dynamo. In *Mathematical Proceedings of the Cambridge Philosophical Society*, volume 51, pages 744–760. Cambridge University Press.

Chapman, S. and Bartels, J. (1940). *Geomagnetism*. Clarendon Press.

Christensen, U. R. and Tilgner, A. (2004). Power requirement of the geodynamo from ohmic losses in numerical and laboratory dynamos. *Nature*, 429(6988):169.

Christensen, U. R. and Wicht, J. (2015). Numerical dynamo simulations. In *Treatise on Geophysics*, volume 8, pages 245–277. Elsevier/Academic Press, 2 edition.

Chulliat, A., Alken, P., and Maus, S. (2015). Fast equatorial waves propagating at the top of the Earth's core. *Geophysical Research Letters*, 42(9):3321–3329.

Chulliat, A. and Maus, S. (2014). Geomagnetic secular acceleration, jerks, and a localized standing wave at the core surface from 2000 to 2010. *Journal of Geophysical Research: Solid Earth*, 119(3):1531–1543.

Chulliat, A. and Olsen, N. (2010). Observation of magnetic diffusion in the Earth's outer core from Magsat, Ørsted and CHAMP data. *Journal of Geophysical Research: Solid Earth*, 115(B5).

Constable, C. and Parker, R. (1988). Smoothing, splines and smoothing splines; their application in geomagnetism. *Journal of Computational Physics*, 78(2):493–508.

Constable, C. G. (1988). Parameter estimation in non-Gaussian noise. *Geophysical Journal International*, 94(1):131–142.

Constable, C. G., Parker, R. L., and Stark, P. B. (1993). Geomagnetic field models incorporating frozen-flux constraints. *Geophysical Journal International*, 113(2):419–433.

Crawley, M. J. (2015). *Statistics: an introduction using R*. John Wiley & Sons.

Cressie, N. A. C. (1993). *Statistics for spatial data*. John Wiley & Sons.

De Boor, C. (2001). A practical guide to splines, revised edition, vol. 27 of applied mathematical sciences. *Mechanical Sciences*.

De Pater, I. and Lissauer, J. J. (2001). *Planetary sciences*. Cambridge University Press.

De Santis, A., Barraclough, D. R., and Tozzi, R. (2003). Spatial and temporal spectra of the geomagnetic field and their scaling properties. *Physics of the Earth and Planetary Interiors*, 135(2-3):125–134.

Elsasser, W. M. (1946). Induction effects in terrestrial magnetism part I. Theory. *Physical Review*, 69(3-4):106.

Engels, U. and Olsen, N. (1998). Computation of magnetic fields within source regions of ionospheric and magnetospheric currents. *Journal of atmospheric and solar-terrestrial physics*, 60(16):1585–1592.

Finlay, C. C. (2017). Satellite magnetic field observations as a tool for studying the Earth's core: opportunities and challenges. 4D-deep Earth science meeting, ESA/ESTEC, 27th September, 2017.

Finlay, C. C., Aubert, J., and Gillet, N. (2014). Gyre-driven decay of the geomagnetic dipole. [Poster] In: 14th international symposium on Study of Earth's Deep Interior (SEDI).

Finlay, C. C., Aubert, J., and Gillet, N. (2016a). Gyre-driven decay of the Earth's magnetic dipole. *Nature communications*, 7:10422.

Finlay, C. C., Dumberry, M., Chulliat, A., and Pais, M. A. (2010a). Short timescale core dynamics: theory and observations. *Space science reviews*, 155(1-4):177–218.

Finlay, C. C. and Jackson, A. (2003). Equatorially dominated magnetic field change at the surface of Earth's core. *Science*, 300(5628):2084–2086.

Finlay, C. C., Lesur, V., Thébault, E., Vervelidou, F., Morschhauser, A., and Shore, R. (2017). Challenges handling magnetospheric and ionospheric signals in internal geomagnetic field modelling. *Space Science Reviews*, 206(1-4):157–189.

Finlay, C. C., Maus, S., Beggan, C. D., Hamoudi, M., Lowes, F. J., Olsen, N., and Thébault, E. (2010b). Evaluation of candidate geomagnetic field models for IGRF-11. *Earth, planets and space*, 62(10):8.

Finlay, C. C., Olsen, N., Kotsiaros, S., Gillet, N., and Tøffner-Clausen, L. (2016b). Recent geomagnetic secular variation from Swarm and ground observatories as estimated in the CHAOS-6 geomagnetic field model. *Earth, Planets and Space*, 68(1):1–18.

Finlay, C. C., Olsen, N., and Tøffner-Clausen, L. (2015). DTU candidate field models for IGRF-12 and the CHAOS-5 geomagnetic field model. *Earth, Planets and Space*, 67(1):1–17.

Fisher, N. I., Lewis, T., and Embleton, B. J. (1987). *Statistical analysis of spherical data*. Cambridge university press.

Fisher, R. (1953). Dispersion on a sphere. In *Proceedings of the Royal Society of London A: Mathematical, Physical and Engineering Sciences*, volume 217.1130, pages 295–305. The Royal Society.

Friis-Christensen, E., Finlay, C. C., Hesse, M., and Laundal, K. M. (2017). Magnetic field perturbations from currents in the dark polar regions during quiet geomagnetic conditions. *Space Science Reviews*, 206(1-4):281–297.

Friis-Christensen, E., Kamide, Y., Richmond, A. D., and Matsushita, S. (1985). Interplanetary magnetic field control of high-latitude electric fields and currents determined from greenland magnetometer data. *Journal of Geophysical Research: Space Physics*, 90(A2):1325–1338.

Friis-Christensen, E., Lühr, H., and Hulot, G. (2006). Swarm: A constellation to study the Earth's magnetic field. *Earth, planets and space*, 58(4):351–358.

Gillet, N., Barrois, O., and Finlay, C. C. (2015a). Stochastic forecasting of the geomagnetic field from the COV-OBS.x1 geomagnetic field model, and candidate models for IGRF-12. *Earth, Planets and Space*, 67(1):71.

Gillet, N., Jackson, A., and Finlay, C. C. (2007). Maximum entropy regularization of time-dependent geomagnetic field models. *Geophysical Journal International*, 171(3):1005–1016.

Gillet, N., Jault, D., Canet, E., and Fournier, A. (2010). Fast torsional waves and strong magnetic field within the Earth's core. *Nature*, 465(7294):74.

Gillet, N., Jault, D., Finlay, C., and Olsen, N. (2013). Stochastic modeling of the Earth's magnetic field: inversion for covariances over the observatory era. *Geochemistry, Geophysics, Geosystems*, 14(4):766–786.

Gillet, N., Jault, D., and Finlay, C. C. (2015b). Planetary gyre, time-dependent eddies, torsional waves, and equatorial jets at the Earth's core surface. *Journal of Geophysical Research: Solid Earth*, 120(6):3991–4013.

Glassmeier, K. H. and Tsurutani, B. T. (2014). Carl Friedrich Gauss-General Theory of Terrestrial Magnetism-a revised translation of the German text. *History of Geo-and Space Sciences*, 5(1):11.

Glatzmaiers, G. A. and Roberts, P. H. (1995). A three-dimensional self-consistent computer simulation of a geomagnetic field reversal. *Nature*, 377(6546):203.

Grayver, A. V., Munch, F. D., Kuvshinov, A. V., Khan, A., Sabaka, T. J., and Tøffner-Clausen, L. (2017). Joint inversion of satellite-detected tidal and magnetospheric signals constrains electrical conductivity and water content of the upper mantle and transition zone. *Geophysical Research Letters*.

Green, P. J. and Silverman, B. W. (1993). *Nonparametric regression and generalized linear models: a roughness penalty approach*. CRC Press.

Griffiths, D. J. (1999). *Introduction to Electrodynamics*. Printice Hall, New Jersey.

Gubbins, D. (1987). Mechanism for geomagnetic polarity reversals. *Nature*, 326(6109):167.

Gubbins, D. (1999). The distinction between geomagnetic excursions and reversals. *Geophysical Journal International*, 137(1):F1–F3.

Gubbins, D. (2010). Terrestrial magnetism: historical perspectives and future prospects. *Space science reviews*, 155(1-4):9–27.

Gubbins, D. and Herrero-Bervera, E. (2007). *Encyclopedia of geomagnetism and paleomagnetism*. Springer Science & Business Media.

Gubbins, D., Jones, A. L., and Finlay, C. C. (2006). Fall in Earth's magnetic field is erratic. *Science*, 312(5775):900–902.

Gubbins, D. and Roberts, N. (1983). Use of the frozen flux approximation in the interpretation of archaeomagnetic and palaeomagnetic data. *Geophysical Journal International*, 73(3):675–687.

Gubbins, D. and Roberts, P. H. (1987). Magnetohydrodynamics of the Earth's core. *Geomagnetism, Vol. 2, p. 1-183*, 2:1–183.

Gutierrez, R. G., Linhart, J. M., Pitblado, J. S., et al. (2003). From the help desk: Local polynomial regression and stata plugins. *Stata Journal*, 3(4):412–419.

Haagmans, R. (2004). Swarm - The Earth's Magnetic Field and Environment Explorers. ESA Publications Division.

Hammer, M. D. and Finlay, C. C. (2018). Local averages of the core-mantle boundary magnetic field from satellite observations. *Geophysical Journal International*. Submitted to GJI.

Hastie, T., Loader, C., et al. (1993). Local regression: Automatic kernel carpentry. *Statistical Science*, 8(2):120–129.

Hodder, B. M. (1982). Monopoly. *Geophysical Journal of the Royal Astronomical Society*, 70(1):217–228.

Holme, R. (2015). Large-scale flow in the core. In *Treatise on Geophysics*, volume 8, pages 91–113. Elsevier/Academic Press, 2 edition.

Holme, R. and Bloxham, J. (1996). The treatment of attitude errors in satellite geomagnetic data. *Physics of the earth and planetary interiors*, 98(3-4):221–233.

Holme, R., Olsen, N., and Bairstow, F. L. (2011). Mapping geomagnetic secular variation at the core-mantle boundary. *Geophysical Journal International*, 186(2):521–528.

Holschneider, M., Chambodut, A., and Mandea, M. (2003). From global to regional analysis of the magnetic field on the sphere using wavelet frames. *Physics of the Earth and Planetary Interiors*, 135(2-3):107–124.

Holschneider, M., Lesur, V., Mauerberger, S., and Baerenzung, J. (2016). Correlation-based modeling and separation of geomagnetic field components. *Journal of Geophysical Research: Solid Earth*, 121(5):3142–3160.

Hrvoic, I. and Newitt, L. R. (2011). Instruments and methodologies for measurement of the Earth's magnetic field. In *Geomagnetic Observations and Models*, pages 105–126. Springer.

Hulot, G., Sabaka, T. J., Olsen, N., and Fournier, A. (2015). The present and future geomangetic field. In *Treatise on Geophysics*, volume 5, pages 33–78. Elsevier/Academic Press, 2 edition.

Jackson, A. (2003). Intense equatorial flux spots on the surface of the Earth's core. *Nature*, 424(6950):760.

Jackson, A., Constable, C., and Gillet, N. (2007a). Maximum entropy regularization of the geomagnetic core field inverse problem. *Geophysical Journal International*, 171(3):995–1004.

Jackson, A., Constable, C. G., Walker, M. R., and Parker, R. L. (2007b). Models of Earth's main magnetic field incorporating flux and radial vorticity constraints. *Geophysical Journal International*, 171(1):133–144.

Jackson, A. and Finlay, C. (2015). Geomagnetic secular variation and its applications to the core. In *Treatise on geophysics*, volume 5, pages 137–184. Elsevier Science, 2 edition.

Jackson, A., Jonkers, A. R. T., and Walker, M. R. (2000). Four centuries of geomagnetic secular variation from historical records. *Philosophical Transactions of the Royal Society of London A: Mathematical, Physical and Engineering Sciences*, 358(1768):957–990.

Jackson, J. D. (2007). *Classical electrodynamics*. John Wiley & Sons.

Jones, C. A. (2015). Thermal and compositional convection in the outer core. In *Treatise on Geophysics*, volume 8. Elsevier/Academic Press, 2 edition.

Kauristie, K., Morschhauser, A., Olsen, N., Finlay, C. C., McPherron, R. L., Gjerloev, J. W., and Opgenoorth, H. J. (2017). On the usage of geomagnetic indices for data selection in internal field modelling. *Space Science Reviews*, 206(1-4):61–90.

Kearey, P., Brooks, M., and Hill, I. (2013). *An introduction to geophysical exploration*. John Wiley & Sons.

Kellogg, O. D. (1954). *Foundations of Potential Theory*. Dover Publications.

Kim, K.-J. and Jackson, J. D. (1993). Proof that the Neumann Green's function in electrostatics can be symmetrized. *American Journal of Physics*, 61(12):1144–1146.

Kloss, C. and Finlay, C. C. (2018). Time-dependent low latitude core flow and geomagnetic field acceleration pulses. *Geophysical Journal International*. Submitted to GJI.

Korte, M. and Constable, C. G. (2018). Archeomagnetic intensity spikes: global or regional geomagnetic field features? *Frontiers in Earth Science*, 6:17.

Kother, L., Hammer, M. D., Finlay, C. C., and Olsen, N. (2015). An equivalent source method for modelling the global lithospheric magnetic field. *Geophysical Journal International*, 203(1):553–566.

Kotsiaros, S. (2012). *Determination of Earth's magnetic field from satellite constellation magnetic field observations*. PhD thesis, DTU Space.

Kotsiaros, S., Finlay, C. C., and Olsen, N. (2015). Use of along-track magnetic field differences in lithospheric field modelling. *Geophysical Journal International*, 200(2):878–887.

Kotsiaros, S. and Olsen, N. (2012). The geomagnetic field gradient tensor. *GEM-International Journal on Geomathematics*, 3(2):297–314.

Kotsiaros, S. and Olsen, N. (2014). End-to-end simulation study of a full magnetic gradiometry mission. *Geophysical Journal International*, 196(1):100–110.

Langel, R. A. (1987). The main field. In *Geomagnetism*. Academic Press.

Langel, R. A. and Estes, R. H. (1982). A geomagnetic field spectrum. *Geophysical Research Letters*, 9(4):250–253.

Langel, R. A. and Hinze, W. J. (1998). *The magnetic field of the Earth's lithosphere: The satellite perspective*. Cambridge University Press, Cambridge.

Larmor, J. (1919). How could a rotating body such as the sun become a magnet. *Rep. Brit. Adv. Sci.*, pages 159–160.

Larsen, R. M. and Hansen, P. C. (1997). Efficient implementations of the SOLA mollifier method. *Astronomy and Astrophysics Supplement Series*, 121(3):587–598.

Laundal, K. M., Finlay, C. C., Olsen, N., and Reistad, J. P. (2018). Solar wind and seasonal influence on ionospheric currents from Swarm and CHAMP measurements. *Journal of Geophysical Research: Space Physics*.

Laundal, K. M. and Richmond, A. D. (2017). Magnetic coordinate systems. *Space Science Reviews*, 206(1-4):27–59.

Lebedev, V. I. (1975). Values of the nodes and weights of ninth to seventeenth order gauss-markov quadrature formulae invariant under the octahedron group with inversion. *USSR Computational Mathematics and Mathematical Physics*, 15(1):44–51.

Lebedev, V. I. (1976). Quadratures on a sphere. *USSR Computational Mathematics and Mathematical Physics*, 16(2):10–24.

Lebedev, V. I. (1977). Spherical quadrature formulas exact to orders 25–29. *Siberian Mathematical Journal*, 18(1):99–107.

Lebedev, V. I. and Laikov, D. N. (1999). A quadrature formula for the sphere of the 131st algebraic order of accuracy. In *Doklady. Mathematics*, volume 59, pages 477–481. MAIK Nauka/Interperiodica.

Ledolter, J. (2013). *Data mining and business analytics with R*. John Wiley & Sons.

Leopardi, P. (2006). A partition of the unit sphere into regions of equal area and small diameter. *Electronic Transactions on Numerical Analysis*, 25(12):309–327.

Lesur, V., Olsen, N., and Thomson, A. W. P. (2011a). Geomagnetic core field models in the satellite era. In *Geomagnetic observations and models*, pages 277–294. Springer.

Lesur, V., Wardinski, I., Baerenzung, J., and Holschneider, M. (2017). On the frequency spectra of the core magnetic field Gauss coefficients. *Physics of the Earth and Planetary Interiors*.

Lesur, V., Wardinski, I., Hamoudi, M., and Rother, M. (2010). The second generation of the GFZ reference internal magnetic model: GRIMM-2. *Earth, planets and space*, 62(10):6.

Lesur, V., Wardinski, I., Hamoudi, M., Rother, M., and Kunagu, P. (2011b). Third version of the GFZ Reference Internal Magnetic Model: GRIMM-3. *Abstract, 25th IUGG General Assembly (Melbourne)*.

Lesur, V., Wardinski, I., Rother, M., and Mandea, M. (2008). GRIMM: the GFZ Reference Internal Magnetic Model based on vector satellite and observatory data. *Geophys. J. Int.*, 173:382–394.

Livermore, P. W., Hollerbach, R., and Finlay, C. C. (2017). An accelerating high-latitude jet in Earth's core. *Nature Geoscience*, 10(1):62.

Livermore, P. W., Hollerbach, R., and Jackson, A. (2013). Electromagnetically driven westward drift and inner-core superrotation in Earth's core. *Proceedings of the National Academy of Sciences*, 110(40):15914–15918.

Louis, A. K. and Maass, P. (1990). A mollifier method for linear operator equations of the first kind. *Inverse problems*, 6(3):427.

Lowes, F. J. (1966). Mean-square values on sphere of spherical harmonic vector fields. *Journal of Geophysical Research*, 71(8):2179–2179.

Lowes, F. J. (1974). Spatial power spectrum of the main geomagnetic field, and extrapolation to the core. *Geophysical Journal International*, 36(3):717–730.

Lowes, F. J. and Olsen, N. (2004). A more realistic estimate of the variances and systematic errors in spherical harmonic geomagnetic field models. *Geophysical Journal International*, 157(3):1027–1044.

Lühr, H., Maus, S., Rother, M., and Cooke, D. (2002). First in-situ observation of nighttime F region currents with the CHAMP satellite. *Geophysical research letters*, 29(10).

Lühr, H., Xiong, C., Olsen, N., and Le, G. (2017). Near-Earth magnetic field effects of large-scale magnetospheric currents. *Space Science Reviews*, 206(1-4):521–545.

Lühr, H., Yin, F., and Bock, R. (2013). Magnetic properties of CHAMP and their effects on in-orbit calibration. *Journal of Sensors and Sensor Systems*, 2(1):9–17.

Macmillan, S. and Olsen, N. (2013). Observatory data and the Swarm mission. *Earth, Planets and Space*, 65(11):15.

Maier, T. (2005). Wavelet Mie representations for solenoidal vector fields with applications to ionospheric geomagnetic data. *SIAM Journal on Applied Mathematics*, 65(6):1888–1912.

Malin, S. R. C. and Barraclough, D. R. (1991). Humboldt and the Earth's magnetic field. *Quarterly Journal of the Royal Astronomical Society*, 32:279.

Mandea, M., Holme, R., Pais, A., Pinheiro, K., Jackson, A., and Verbanac, G. (2010). Geomagnetic jerks: rapid core field variations and core dynamics. *Space science reviews*, 155(1-4):147–175.

Mandea, M. and Korte, M. (2010). *Geomagnetic observations and models*, volume 5. Springer.

Mandea, M. and Olsen, N. (2006). A new approach to directly determine the secular variation from magnetic satellite observations. *Geophysical research letters*, 33(15).

Mandea, M., Panet, I., Lesur, V., De Viron, O., Diament, M., and Le Mouël, J.-L. (2012). Recent changes of the Earth's core derived from satellite observations of magnetic and gravity fields. *Proceedings of the National Academy of Sciences*, 109(47):19129–19133.

Mandea, M. and Purucker, M. (2018). The varying core magnetic field from a space weather perspective. *Space Science Reviews*, 214(1):11.

Manoj, C., Kuvshinov, A., Maus, S., and Lühr, H. (2006). Ocean circulation generated magnetic signals. *Earth, Planets and Space*, 58(4):429–437.

Masters, G. (1979). Observational constraints on the chemical and thermal structure of the Earth's deep interior. *Geophysical Journal of the Royal Astronomical Society*, 57(2):507–534.

Masters, G. and Gubbins, D. (2003). On the resolution of density within the Earth. *Physics of the Earth and Planetary Interiors*, 140(1):159–167.

Maule, C. F., Purucker, M. E., Olsen, N., and Mosegaard, K. (2005). Heat flux anomalies in Antarctica revealed by satellite magnetic data. *Science*, 309(5733):464–467.

Maus, S. and Lühr, H. (2006). A gravity-driven electric current in the Earth's ionosphere identified in CHAMP satellite magnetic measurements. *Geophysical research letters*, 33(2).

Maus, S., Manoj, C., Rauberg, J., Michaelis, I., and Lühr, H. (2010). NOAA/NGDC candidate models for the 11th generation International Geomagnetic Reference Field and the concurrent release of the 6th generation Pomme magnetic model. *Earth, planets and space*, 62(10):2.

Maus, S., Rother, M., Stolle, C., Mai, W., Choi, S., Lühr, H., Cooke, D., and Roth, C. (2006). Third generation of the Potsdam Magnetic Model of the Earth (POMME). *Geochemistry, Geophysics, Geosystems*, 7(7).

Menvielle, M., Iyemori, T., Marchaudon, A. e. l., and Nos é, M. (2011). Geomagnetic indices. In *Geomagnetic Observations and Models*, pages 183–228. Springer.

Merrill, R. T., McElhinny, M. W., and McFadden, P. L. (1998). *The magnetic field of the Earth: paleomagnetism, the core, and the deep mantle*, volume 63. Academic Press.

Mueller, J. L. and Siltanen, S. (2012). *Linear and nonlinear inverse problems with practical applications*, volume 10. Siam.

Newell, P. T., Sotirelis, T., Liou, K., Meng, C.-I., and Rich, F. J. (2007). A nearly universal solar wind-magnetosphere coupling function inferred from 10 magnetospheric state variables. *Journal of Geophysical Research: Space Physics*, 112(A1).

Nielsen, J. B. (2017). Swarm Level 1b Product Definition. Technical Report SW-RS-DSC-SY-0007, Issue 5.20, National Space Institute, Technical University of Denmark.

Nolet, G. (2008). *A breviary of seismic tomography: imaging the interior of the Earth and sun*. Cambridge University Press, Cambridge, UK.

O'Brien, M. S., Constable, C. G., and Parker, R. L. (1997). Frozen-flux modelling for epochs 1915 and 1980. *Geophysical Journal International*, 128(2):434–450.

O'Brien, M. S. and Parker, R. L. (1994). Regularized geomagnetic field modelling using monopoles. *Geophysical Journal International*, 118(3):566–578.

Oldenburg, D. W. (1976). Calculation of fourier transforms by the Backus-Gilbert method. *Geophysical Journal International*, 44(2):413–431.

Oldenburg, D. W. (1984). An introduction to linear inverse theory. *IEEE Transactions on Geoscience and Remote Sensing*, GE-22(6):665–674.

Olsen, N. (1997). Ionospheric F region currents at middle and low latitudes estimated from Magsat data. *Journal of Geophysical Research: Space Physics*, 102(A3):4563–4576.

Olsen, N. (2002). A model of the geomagnetic field and its secular variation for epoch 2000 estimated from Ørsted data. *Geophysical Journal International*, 149(2):454–462.

Olsen, N. (2009). Geomagnetic Field Modelling Lessons learned from Ørsted and CHAMP and prospects for Swarm. RAS Discussion Meeting on Swarm.

Olsen, N., Clausen, L. T., Sabaka, T. J., Brauer, P., Merayo, J. M., Jørgensen, J. L., Léger, J.-M., Nielsen, O. V., Primdahl, F., and Risbo, T. (2003). Calibration of the ørsted vector magnetometer. *Earth, planets and space*, 55(1):11–18.

Olsen, N., Finlay, C. C., Kotsiaros, S., and Tøffner-Clausen, L. (2016). A model of Earth's magnetic field derived from 2 years of Swarm satellite constellation data. *Earth, Planets and Space*, 68(1):124.

Olsen, N., Friis-Christensen, E., Floberghagen, R., Alken, P., Beggan, C. D., Chulliat, A., Doornbos, E., Da Encarnação, J. T., Hamilton, B., Hulot, G., et al. (2013). The Swarm satellite constellation application and research facility (SCARF) and Swarm data products. *Earth, Planets and Space*, 65(11):1189–1200.

Olsen, N., Hulot, G., Lesur, V., Finlay, C. C., Beggan, C., Chulliat, A., Sabaka, T. J., Floberghagen, R., Friis-Christensen, E., Haagmans, R., et al. (2015). The Swarm Initial Field Model for the 2014 geomagnetic field. *Geophysical Research Letters*, 42(4):1092–1098.

Olsen, N., Hulot, G., and Sabaka, T. J. (2010a). Measuring the Earth's magnetic field from space: concepts of past, present and future missions. *Space science reviews*, 155(1-4):65–93.

Olsen, N., Hulot, G., and Sabaka, T. J. (2010b). Sources of the Geomagnetic Field and the Modern Data That Enable Their Investigation. In *Handbook of geomathematics*, pages 105–124. Springer.

Olsen, N. and Kotsiaros, S. (2011). Magnetic satellite missions and data. In *Geomagnetic Observations and Models*, pages 27–44. Springer.

Olsen, N., Lowes, F., and Sabaka, T. J. (2005a). Ionospheric and induced field leakage in geomagnetic field models, and derivation of candidate models for DGRF 1995 and DGRF 2000. *Earth, planets and space*, 57(12):1191–1196.

Olsen, N., Lühr, H., Finlay, C. C., Sabaka, T. J., Michaelis, I., Rauberg, J., and Tøffner-Clausen, L. (2014). The CHAOS-4 geomagnetic field model. *Geophysical Journal International*, 197(2):815–827.

Olsen, N., Lühr, H., Sabaka, T. J., Mandea, M., Rother, M., Tøffner-Clausen, L., and Choi, S. (2006). CHAOS - a model of the Earth's magnetic field derived from CHAMP, Ørsted, and SAC-C magnetic satellite data. *Geophysical Journal International*, 166(1):67–75.

Olsen, N. and Mandea, M. (2007). Investigation of a secular variation impulse using satellite data: The 2003 geomagnetic jerk. *Earth and Planetary Science Letters*, 255(1):94–105.

Olsen, N. and Mandea, M. (2008). Rapidly changing flows in the Earth's core. *Nature geoscience*, 1(6):390.

Olsen, N., Mandea, M., Sabaka, T. J., and Tøffner-Clausen, L. (2009). CHAOS-2 - a geomagnetic field model derived from one decade of continuous satellite data. *Geophysical Journal International*, 179(3):1477–1487.

Olsen, N., Mandea, M., Sabaka, T. J., and Tøffner-Clausen, L. (2010c). The CHAOS-3 geomagnetic field model and candidates for the 11th generation IGRF. *Earth, planets and space*, 62(10):719–727.

Olsen, N., Ravat, D., Finlay, C. C., and Kother, L. K. (2017). LCS-1: a high-resolution global model of the lithospheric magnetic field derived from CHAMP and Swarm satellite observations. *Geophysical Journal International*, 211(3):1461–1477.

Olsen, N., Sabaka, T. J., and Gaya-Pique, L. R. (2007). Study of an improved comprehensive magnetic field inversion analysis for Swarm. *DNSC Scientific Report*, 1:2007.

Olsen, N., Sabaka, T. J., and Lowes, F. (2005b). New parameterization of external and induced fields in geomagnetic field modeling, and a candidate model for IGRF 2005. *Earth, planets and space*, 57(12):1141–1149.

Olsen, N. and Stolle, C. (2012). Satellite geomagnetism. *Annual Review of Earth and Planetary Sciences*, 40:441–465.

Olsen, N. and Stolle, C. (2017). Magnetic signatures of ionospheric and magnetospheric current systems during geomagnetic quiet conditions - An overview. *Space Science Reviews*, 206(1-4):5–25.

Olson, P. and Amit, H. (2006). Changes in Earth's dipole. *Naturwissenschaften*, 93(11):519–542.

Owens, M. J. and Forsyth, R. J. (2013). The heliospheric magnetic field. *Living Reviews in Solar Physics*, 10(1):5.

Parker, R. L. (1977). Understanding inverse theory. *Annual Review of Earth and Planetary Sciences*, 5:35.

Parker, R. L. (1994). *Geophysical Inverse Theory*. Princeton University Press, Princeton, New Jersey, USA.

Parker, R. L. and Shure, L. (1982). Efficient modelling of the Earth's magnetic field with harmonic splines. *Geophys. Res. Lett.*, 9:812–815.

Parkinson, W. D. (1983). *Introduction to Geomagnetism*. Scottish Academic Press, Edinburgh.

Parrish, R. (2010). Matlab code: getlebedevsphere. The Sherrill Group, CCMST Georgia Tech.

Pijpers, F. P. and Thompson, M. J. (1992). Faster formulations of the optimally localized averages method for helioseismic inversions. *Astronomy and Astrophysics*, 262:L33–L36.

Pijpers, F. P. and Thompson, M. J. (1994). The SOLA method for helioseismic inversion. *Astronomy and Astrophysics*, 281:231–240.

Plattner, A. and Simons, F. J. (2017). Internal and external potential-field estimation from regional vector data at varying satellite altitude. *Geophysical Journal International*, 211(1):207–238.

Press, W., Teukolsky, S., Vetterling, W., and Flannery, B. (2006). *Numerical Recipes in Fortran 77*. Cambridge University Press, Cambridge.

Pujol, J. M. (2013). The Backus-Gilbert method and their minimum-norm solution. *Geophysics*, 78(3):W9–W30.

Purucker, M. and Whaler, K. (2007). Crustal magnetism. *Treatise on geophysics*, 5:195–237.

Reigber, C., Lühr, H., and Schwintzer, P. (2002). CHAMP mission status. *Advances in space research*, 30(2):129–134.

Richmond, A. D. (1995). Ionospheric Electrodynamics Using Magnetic Apex Coordinates. *Journal of geomagnetism and geoelectricity*, 47(2):191–212.

Rikitake, T. (1966). *Electromagnetism and the Earth's Interior*. Number 2. Elsevier.

Riley, K. F., Hobson, M., and Bence, S. (2004). *Mathematical Methods for Physics and Engineering*. Cambridge University Press, Cambridge.

Ritter, P., Lühr, H., Maus, S., and Viljanen, A. (2004). High-latitude ionospheric currents during very quiet times: their characteristics and predictability. In *Annales Geophysicae*, volume 22, pages 2001–2014.

Roberts, P. H. (2015). Theory of the Geodynamo. In *Treatise on Geophysics*, volume 8, pages 57–90. Elsevier/Academic Press.

Roberts, P. H. and Scott, S. (1965). On analysis of the secular variation. *Journal of geomagnetism and geoelectricity*, 17(2):137–151.

Sabaka, T. J., Hulot, G., and Olsen, N. (2010). Mathematical properties relevant to geomagnetic field modeling. In *Handbook of Geomathematics*, pages 503–538. Springer.

Sabaka, T. J. and Olsen, N. (2006). Enhancing comprehensive inversions using the Swarm constellation. *Earth, Planets and Space*, 58:371–395.

Sabaka, T. J., Olsen, N., and Langel, R. A. (2002). A comprehensive model of the quiet-time, near-earth magnetic field: phase 3. *Geophysical Journal International*, 151(1):32–68.

Sabaka, T. J., Olsen, N., and Purucker, M. E. (2004). Extending comprehensive models of the Earth's magnetic field with Ørsted and CHAMP data. *Geophysical Journal International*, 159(2):521–547.

Sabaka, T. J., Olsen, N., Tyler, R. H., and Kuvshinov, A. (2015). CM5, a pre-Swarm comprehensive geomagnetic field model derived from over 12 yr of CHAMP, Ørsted, SAC-C and observatory data. *Geophysical Journal International*, 200(3):1596–1626.

Sabaka, T. J., Tøffner-Clausen, L., and Olsen, N. (2013). Use of the Comprehensive Inversion method for Swarm satellite data analysis. *Earth, Planets and Space*, 65(11):1201–1222.

Sabaka, T. J., Tøffner-Clausen, L., Olsen, N., and Finlay, C. C. (2018). A Comprehensive Model of the Earth's Magnetic Field Determined From 4 Years of Swarm Satellite Observations. *Earth, Planets and Space*. in Press.

Saturnino, D. (2015). *Describing temporal variations of the geomagnetic field using a modified virtual observatory scheme: application to Swarm data*. PhD thesis, University of Nantes.

Schaeffer, N., Jault, D., Nataf, H.-C., and Fournier, A. (2017). Turbulent geodynamo simulations: a leap towards Earth's core. *Geophysical Journal International*, 211(1):1–29.

Schott, J.-J. and Thébault, E. (2011). Modelling the Earth's magnetic field from global to regional scales. In *Geomagnetic Observations and Models*, pages 229–264. Springer.

Schuster, T. (2007). *The method of approximate inverse: theory and applications*, volume 1906. Springer.

Seeber, G. (2003). *Satellite geodesy: foundations, methods, and applications*. Walter de gruyter.

Shaar, R., Tauxe, L., Ron, H., Ebert, Y., Zuckerman, S., Finkelstein, I., and Agnon, A. (2016). Large geomagnetic field anomalies revealed in Bronze to Iron Age archeomagnetic data from Tel Megiddo and Tel Hazor, Israel. *Earth and Planetary Science Letters*, 442:173–185.

Sheyko, A., Finlay, C. C., and Jackson, A. (2016). Magnetic reversals from planetary dynamo waves. *Nature*, 539(7630):551.

Shore, R. M. (2013). *An improved description of Earth's external magnetic fields and their source regions using satellite data*. PhD thesis, The University of Edinburgh.

Shure, L., Parker, R. L., and Backus, G. E. (1982). Harmonic splines for geomagnetic modelling. *Phys. Earth Planet. Int.*, 28:215–229.

Snieder, R. (1991). An extension of Backus-Gilbert theory to nonlinear inverse problems. *Inverse Problems*, 7(3):409.

Stern, D. P. (2002). A millennium of geomagnetism. *Reviews of geophysics*, 40(3).

Stolle, C., Lühr, H., Rother, M., and Balasis, G. (2006). Magnetic signatures of equatorial spread f as observed by the champ satellite. *Journal of Geophysical Research: Space Physics*, 111(A2).

Tanimoto, T. (1985). The Backus-Gilbert approach to the three-dimensional structure in the upper mantle-I. Lateral variation of surface wave phase velocity with its error and resolution. *Geophysical Journal International*, 82(1):105–123.

Tanimoto, T. (1986). The Backus-Gilbert approach to the 3-D structure in the upper mantle–II. SH and SV velocity. *Geophysical Journal of the Royal Astronomical Society*, 84(1):49–69.

Tapping, K. F. (2013). The 10.7 cm solar radio flux (F10.7). *Space Weather*, 11(7):394–406.

Taylor, J. (1997). *Introduction to error analysis, the study of uncertainties in physical measurements*. University Science Books.

Thébault, E., Finlay, C. C., Beggan, C. D., Alken, P., Aubert, J., Barrois, O., Bertrand, F., Bondar, T., Boness, A., Brocco, L., et al. (2015). International geomagnetic reference field: the 12th generation. *Earth, Planets and Space*, 67(1):79.

Thomson, A. W. P., Hamilton, B., Macmillan, S., and Reay, S. J. (2010). A novel weighting method for satellite magnetic data and a new global magnetic field model. *Geophysical Journal International*, 181(1):250–260.

Tøffner-Clausen, L., Lesur, V., Olsen, N., and Finlay, C. C. (2016). In-flight scalar calibration and characterisation of the Swarm magnetometry package. *Earth, Planets and Space*, 68(1):129.

Tyler, R. H., Maus, S., and Lühr, H. (2003). Satellite observations of magnetic fields due to ocean tidal flow. *Science*, 299(5604):239–241.

Vennerstrom, S., Christiansen, F., Olsen, N., and Moretto, T. (2007). On the cause of IMF By related mid-and low latitude magnetic disturbances. *Geophysical Research Letters*, 34(16).

Verboven, S. and Hubert, M. (2005). Libra: a matlab library for robust analysis. *Chemometrics and intelligent laboratory systems*, 75(2):127–136.

Voronin, S. and Zaroli, C. (2018). Survey of computational methods for inverse problems, recent trends in computational science and engineering. *Serdar Celebi, IntechOpen*.

Wardinski, I. and Holme, R. (2006). A time-dependent model of the Earth's magnetic field and its secular variation for the period 1980–2000. *Journal of Geophysical Research: Solid Earth*, 111(B12).

Wardinski, I. and Lesur, V. (2012). An extended version of the C3FM geomagnetic field model: application of a continuous frozen-flux constraint. *Geophysical Journal International*, 189(3):1409–1429.

Whaler, K. A. (1984). Fluid upwelling at the core - mantle boundary - resolvability from surface geomagnetic data. *Geophysical Journal International*, 78(2):453–473.

Whaler, K. A. (1986). Geomagnetic evidence for fluid upwelling at the core-mantle boundary. *Geophysical Journal International*, 86(2):563–588.

Whaler, K. A. (2017). Probing the core surface flow with satellite data. IAGA Joint Assembly Session A02 - Earth's core dynamics and planetary dynamos (DIV I).

Whaler, K. A. and Beggan, C. D. (2015). Derivation and use of core surface flows for forecasting secular variation. *Journal of Geophysical Research: Solid Earth*, 120(3):1400–1414.

Whaler, K. A. and Gubbins, D. (1981). Spherical harmonic analysis of the geomagnetic field: an example of a linear inverse problem. *Geophysical Journal International*, 65(3):645–693.

Whaler, K. A., Olsen, N., and Finlay, C. C. (2016). Decadal variability in core surface flows deduced from geomagnetic observatory monthly means. *Geophysical Journal International*, 207(1):228–243.

Woan, G. (2000). *The Cambridge handbook of physics formulas*. Cambridge University Press.

Yin, F. and Lühr, H. (2011). Recalibration of the CHAMP satellite magnetic field measurements. *Measurement Science and Technology*, 22(5):055101.

Zaroli, C. (2016). Global seismic tomography using Backus-Gilbert inversion. *Geophysical Journal International*, 207:876–888.

Zaroli, C., Koelemeijer, P., and Lambotte, S. (2017). Toward seeing the Earth's interior through unbiased tomographic lenses. *Geophysical Research Letters*, 44(22).

Appendix

Appendix A

Published and Submitted Papers

This appendix contains published and submitted publications written during the PhD project and includes:

- Magnus Danel Hammer and Christopher Charles Finlay, 2019. Local Averages of the Core-mantle Boundary Magnetic Field from Satellite Observations. *Geophysical Journal International*, 216, 1901-1918.
- Olivier Barrois, Magnus Danel Hammer, Christopher Charles Finlay, Yannick Martin and Nicolas Gillet, 2018. Assimilation of ground and satellite magnetic measurements: inference of core surface magnetic and velocity field changes. *Geophysical Journal International*, 215(1), 695-712.

Geophysical Journal International

Geophys. J. Int. (2019) **216,** 1901–1918 doi: 10.1093/gji/ggy515
Advance Access publication 2018 December 11
GJI Geomagnetism, rock magnetism and paleomagnetism

Local averages of the core–mantle boundary magnetic field from satellite observations

Magnus D. Hammer and Christopher C. Finlay

Division of Geomagnetism, Technical University of Denmark - DTU Space, Kgs. Lyngby, Denmark. E-mail: magdh@space.dtu.dk

Accepted 2018 December 6. Received 2018 November 16; in original form 2018 July 02

SUMMARY

We introduce a formalism for estimating local spatial averages of the core–mantle boundary (CMB) radial magnetic field and its time derivatives, based on magnetic field observations collected by low-Earth-orbit satellites. This provides a useful alternative to conventional core field modelling based on global spherical harmonic basis functions, where noise in the polar regions maps into all harmonics, and model regularization and spectral truncation are required. A powerful perspective offered by the proposed technique is formal appraisal of the spatial resolution and variance of the resulting field averages. We use the Green's functions for the Neumann boundary value problem to link the satellite observations to the radial magnetic field on the CMB and estimate field averages using a modified Backus–Gilbert inversion approach. Our approach builds on the Subtractive Optimally Localized Averages (SOLA) method developed in helioseismology, that seeks averaging kernels as close as possible to a chosen target kernel. We are able to account for both internal and external field sources and can incorporate data error covariance information, for example describing along-track serial error correlation. As a proof of concept we present a global map collecting local estimates of the radial main field (MF) constructed on a grid at the CMB with one degree spacing in latitude and longitude, derived from 1 month of three component vector magnetic field data collected by the *Swarm* satellite trio, using data from dark and geomagnetically quiet times. Using sums and differences of the field components taken along track and in the east–west direction we obtain estimates with spatial resolution kernel widths varying between 18° and 54° depending on the latitude, and a standard deviation of approximately 10 μT (i.e. 5 per cent of the mean CMB field amplitude). The morphology of our CMB radial field map agrees well with results from conventional spherical harmonic field models. In a second application, we determine local estimates of the average rate of change, or secular variation (SV), of the radial field at the CMB, initially considering 2-yr time windows, and performing the analysis on data collected by either the *Swarm* or CHAMP satellites. We obtain stable local estimates of the SV at the CMB, and present maps of estimates with averaging kernel widths of approximately 42°, 33° and 30° on the equator, with corresponding standard derivations of 0.25, 2.5 and 5 μT yr^{-1}. By subtracting SV estimates constructed at different epochs we are able to calculate the local aggregated secular acceleration (SA) and to study its time changes. Differencing SV estimates 2 yr apart, and considering an averaging kernel width of 42° on the equator, we obtain SA maps similar to those found in the CHAOS-6-x7 field model truncated at SH degree 10. Using our approach we are able to directly control the width of the spatial averaging kernel and the length of the time window, enabling us to directly study the robustness of the inferred SA. Pushing to higher resolution in time, considering 1 yr differences of SV estimates constructed using 1 yr windows, we are able to track the evolution of coherent SA structures in time-longitude plots at the equator. At 25°W in mid 2007 we find a distinctive SA 'cross-over' event, with strong, oppositely signed and adjacent, SA features rapidly changing sign within a year. Our method is well suited for studying such spatio-temporally localized SA events at high resolution; there will be further opportunities for such investigations as the time-series of data provided by the *Swarm* mission lengthens.

Key words: Rapid time variations; Satellite magnetics; Inverse theory.

1 INTRODUCTION

The ability to construct reliable estimates of the core-generated magnetic field, tracking its morphology and time evolution, is essential in efforts to improve our knowledge of core dynamics. With the advent of the low-Earth-orbit CHAMP and *Swarm* satellite missions collecting magnetic measurements over multiple years, it has become possible to image small scale features of the core field that exhibit rapid temporal variations (Lesur *et al.* 2008; Olsen & Mandea 2008; Finlay *et al.* 2016). The first and second time derivative of the main field undergoes subdecadal changes that may be probed down to a period of about 1 yr (Chulliat *et al.* 2015). New techniques have been developed that use spatial differences of the magnetic field observations in order to to enhance the recovery of small scale field features, since compared to using vector data, they are less sensitive to unmodelled large-scale external field contamination (Kotsiaros *et al.* 2015; Olsen *et al.* 2015; Finlay *et al.* 2016). Spherical harmonic (SH) models derived using *Swarm* observations have shown that the first time derivative of the field, or secular variation (SV), can be obtained up to approximately SH degree 11 from 1 yr of measurements (Olsen *et al.* 2015, 2016). Studies of geodynamo simulations have also recently suggested that the second time derivative of the field, or secular acceleration (SA), might be expected to exhibit distinctive equatorial localization (Aubert 2018). Moreover, considering 3-yr data time windows, pulse like features in the radial SA at the core–mantle boundary (CMB) concentrated along the geographical equator, have recently been observed (Chulliat & Maus 2014; Chulliat *et al.* 2015) possibly indicative of a wave propagating or arriving at the core surface. The basic structure of the SA at short length and timescales, and the details of the responsible core dynamics are however still unclear and further investigations are urgently needed.

Assuming the region between the CMB and the observation site is an insulator, the magnetic field can be described by the gradient of a scalar magnetic potential. In the conventional, so-called construction, approach to field modelling the potential is represented on a global scale using a truncated SH expansion determined using a least-squares solution (Langel 1987; Parker 1994) that is often also regularized in order to obtain stable solutions at the CMB (Bloxham *et al.* 1989). Here we use the term regularization to denote the modification of the least-squares solution to the inverse problem such that a global norm of the model parameters is added to the data misfit norm in the cost function being minimized. Since the SH functions are of global support, assuming equal data errors, they give equal weight to the entire data set assigning isotropic resolution. Regularized B-splines are often used to describe the model time dependence; the temporal regularization modifies the spline functions in a non-uniform manner influencing higher SH degrees the most (Constable & Parker 1988; Olsen *et al.* 2009). Moreover, model uncertainties are usually not provided and validation typically relies on comparing models constructed using different data selection schemes, external field parametrizations and regularizations.

Various alternatives to SH modelling have been investigated for studying the CMB magnetic field, for instance constructing models based on icosodedral grids for the radial field at the core surface that can be forced to satisfy necessary conditions for frozen-flux and a magnetostrophic force balance implemented via topology preservation constraints (Constable *et al.* 1993; Jackson *et al.* 2007). Techniques such as harmonic splines introduced by Shure *et al.* (1982) and Parker & Shure (1982), a wavelet approach developed by Holschneider *et al.* (2003), and Slepian functions (Plattner & Simons 2017) have also been explored. Most recently, Holschneider *et al.* (2016) have introduced an attractive new technique, based on specifying appropriate correlation functions for internal and external sources, that has been used by Lesur *et al.* (2017) to determine the Gauss coefficients for the SV from ground observatory monthly means between 1957 and 2014.

A difficulty with core field studies is that the CMB spectra of the SV and SA signals are blue (i.e. power increases with SH degree). Although studies have shown encouraging coherence in field maps as SH truncation degree is increased (Holme *et al.* 2011; Aubert 2018) care is needed when interpreting the resulting fields. Furthermore, it has been argued that the temporal spectra of the core field is such that higher order time derivatives of the field, in particular the SA, may be formally undefined as the time window used to estimate them goes towards zero (Gillet *et al.* 2013; Bouligand *et al.* 2016; Lesur *et al.* 2017). Pushing towards signal recovery on smaller length scales and shorter timescales, careful appraisal, comprising of resolution analysis and variance estimation, is required in order to assess limitations of the data and to establish the validity of features of interest in field reconstruction.

Here we propose another approach to the above problems. We adopt a formalism for estimating the CMB radial field which is not founded on spherical harmonics, thus is free of signal truncation in the spectral domain, relying instead on spatial averaging of the field. We investigate the inverse problem using the Backus–Gilbert philosophy of appraisal (Backus and Gilbert, 1968; Backus and Gilbert, 1970; Parker, 1977; Oldenburg, 1984), which provides the only unique information directly obtainable from the data, thereby enabling us to explore whether all constructed models contain certain spatial field features of interest. In the case of accurate data, any linear data combination will give a uniquely specified value of the magnetic field; this is equivalent to an unique spatial average value, determined by the inner product of an averaging kernel with the true model around some location of interest (Oldenburg 1984; Pujol 2013). In the case of inaccurate data, a variance is assigned to the estimated average and a trade-off arises between spatial resolution and variance. It should be stressed that the obtained average will in general not fit the original data, nor is it directly supposed to. Any model obtained (e.g. in the least-squares sense) which reproduces the data must attain this estimated average. It is relevant to note here that regularized least-square solutions are biased towards a background model that is often assumed to be zero. A result of this is that rows of the model resolution matrix can sum to less than 1 (see e.g. Nolet 2008, pp. 277–281). Another undesirable effect of regularization is to produce model covariance estimates that can be unrealistically small. In contrast Backus–Gilbert estimates are unbiased (the averaging kernels integrate to 1) and the variances of the estimated averages are meaningful. The Backus–Gilbert philosophy is thus fundamentally different from that of the conventional regularized inversion construction approach, and it has been applied to a wide range of geophysical topics (e.g. Tanimoto 1985; Masters & Gubbins

2003; Pujol 2013). In geomagnetism, Whaler & Gubbins (1981) used the Backus–Gilbert formalism to invert for an average vertical field component at the CMB, taking Gauss coefficients derived from 80 ground observatories as data. Later Whaler (1984) used Backus–Gilbert theory to estimate null-flux patch integrals of the radial SV component. Modifications to the original Backus–Gilbert method (referred to as quelling by its authors and mollifying in mathematical literature), resembling the so-called Dirichlet deltaness criterion, have been developed independently by Louis & Maass (1990) and Pijpers & Thompson (1992) in helioseismology, and termed Subtractive Optimally Localized Averages (SOLA) by the latter. The SOLA approach estimates the coefficients of linear data combinations by minimizing a norm measuring the squared distance between the averaging kernel and some chosen target kernel.

Here, we implement the SOLA technique such that at specified locations on the CMB, local spatial averages of the radial field are calculated, that then allow for appraisal to be carried out. To do this we represent the magnetic potential, which satisfies the Neumann boundary value problem for the Laplace equation, using the Green's function method so that the CMB field is related to the observations via appropriate Green's functions (e.g. Gubbins & Roberts 1983). A general formalism is presented where the potential is described by both internal and external source contributions. Section 2 provides a description of the selection criteria and processing procedures for the data used in our chosen applications. Section 3.1 describes the potential field formulation relating the radial magnetic field at the source regions to the satellite magnetic data. In Section 3.2, aspects of the SOLA approach to the inverse problem are described, allowing for estimates of the field to be determined as localized spatial averages. Section 3.3 considers our numerical implementation of the theory and Section 3.4 describes in detail how appraisal of the results can be carried out. Section 4 contains results from applications based on (i) using *Swarm* data to estimate the field at the CMB and (ii) using *Swarm* and CHAMP data to estimate the secular variation, and the accumulated secular acceleration over chosen time windows, also at the CMB. Discussions and conclusions are given in Section 5.

2 DATA

We take CHAMP vector magnetometer measurements from 2000 July 19 to 2010 September 1 and *Swarm* vector magnetometer measurements, from all three satellites (*Alpha*, *Bravo*, *Charlie*), from 2013 December 1 up to the end of August 2018. We extract samples every 15 s from low rate (5 Hz for CHAMP and 1 Hz for *Swarm*) calibrated magnetic field data in the Vector Field Magnetometer (VFM) frame (in units of nT) provided by the CHAMP MAG-L3 and *Swarm* Level 1b MAG-L version 0505 data products. The VFM data are then transformed into an Earth-Centred Earth-Fixed (ECEF) local Cartesian North-East-Centre (NEC) coordinate frame. This is done by data alignment in which the VFM data are rotated into the Common Reference Frame (CRF) of the star tracker using the Euler rotation angles as determined by the CHAOS-6-x7 model (an extension of the CHAOS-6 model using *Swarm* data and ground observation data up until the end of August 2018, http://www.spacecenter.dk/files /magnetic-models/CHAOS-6/). We reject measurements for known disturbed days where satellite manoeuvres took place and remove gross data outliers for which the vector field components deviate more than 500 nT from CHAOS-6-x7 field predictions. Based on previous experience (e.g. Olsen *et al.* 2015; Finlay *et al.* 2016) we adopt the following selection criteria: (1) only dark region data requiring the sun to be at least 10° below horizon in order to reduced ionospheric field contamination; (2) for quiet time conditions we require the geomagnetic planetary activity index $K_p < 2^o$; (3) for the magnethospheric ring current and its Earth induced contribution the *RC* disturbance index is required to have $|d\mathrm{RC}/dt| < 2$ nT hr^{-1} (Olsen *et al.* 2014) and (4) restricting the merging electric field at the magnetopause such that $E_m \leq 0.8$ mV m^{-1} with $E_m = 0.33 v^{4/3} B_t^{2/3} \sin(|\Theta|/2)$ where v is the solar wind speed, $\Theta = \arctan(B_y/B_z)$ and $B_t = \sqrt{B_y^2 + B_z^2}$ is the magnitude of the interplanetary magnetic field (IMF) having components in the geocentric solar magnetospheric (GSM) coordinate y–z plane, calculated using 2 hourly means based on 1-min values of the IMF and solar wind extracted form the OMNI database (http://omniweb.gsfc.nasa.gov); (5) requiring that IMF $B_Z > 0$nT and IMF $|B_Y| < 6$nT in order to reduce substorm auroral electrojet contamination originating from field-aligned currents (Ritter *et al.* 2004). Finally, CHAOS-6-x7 model estimates of the crustal field for SH degrees 14–120 and the external magnetospheric (plus induced) field together with the CM4 (Sabaka *et al.* 2004) estimates of the ionospheric field and its induced counterpart scaled by the F10.7 solar flux index are subtracted.

We work with magnetic vector field data as well as with sums and differences of the magnetic field components $B_k = \hat{\mathbf{k}} \cdot \mathbf{B}(\mathbf{r})$ in geographic spherical polar coordinates where $(k = r, \theta, \phi)$, such that Δd_k and Σd_k are data differences and sums, respectively. We construct along-track (AT) and east–west (EW) differences $\Delta d_k = (\Delta d_k^{\mathrm{AT}}, \Delta d_k^{\mathrm{EW}})$, and data sums $\Sigma d_k = (\Sigma d_k^{\mathrm{AT}}, \Sigma d_k^{\mathrm{EW}})$. Note that it is necessary to consider data sums as well as differences to ensure sufficient information on longer wavelengths. The along-track differences are calculated using 15 s differences $\Delta d_k^{\mathrm{AT}} = [B_k(\mathbf{r}, t) - B_k(\mathbf{r} + \delta\mathbf{r}, t + 15s)]$. With a satellite speed of ≈7.7 km s^{-1} this corresponds to an along-track distance of 115 km (Olsen *et al.* 2015). The along-track summations are calculated as $\Sigma d_k^{AT} = [B_k(\mathbf{r}, t) + B_k(\mathbf{r} + \delta\mathbf{r}, t + 15s)]/2$. The EW differences are calculated as $\Delta d_k^{\mathrm{EW}} = [B_k^{\mathrm{SWA}}(\mathbf{r}_1, t_1) - B_k^{\mathrm{SWC}}(\mathbf{r}_2, t_2)]$ having an EW orbit separation between the *Swarm Alpha* (SWA) and *Charlie* (SWC) satellites of ≈1.4° (corresponding to 155 km) at the equator (Olsen *et al.* 2015). The EW summation is calculated as $\Sigma d_k^{\mathrm{EW}} = [B_k^{\mathrm{SWA}}(\mathbf{r}_1, t_1) + B_k^{\mathrm{SWC}}(\mathbf{r}_2, t_2)]/2$. For a particular orbit of *Alpha* we select the corresponding *Charlie* data to be the one closest in colatitude such that $|\Delta t| = |t_1 - t_2| < 50$ s.

We adopt error estimates that depend on quasi-dipole (QD) latitude (Richmond 1995) and make use of robust (Huber) weights appropriate for a long tailed error distribution (Constable 1988). First, using all available data d_i within bins of 2° QD latitude, we determine separately

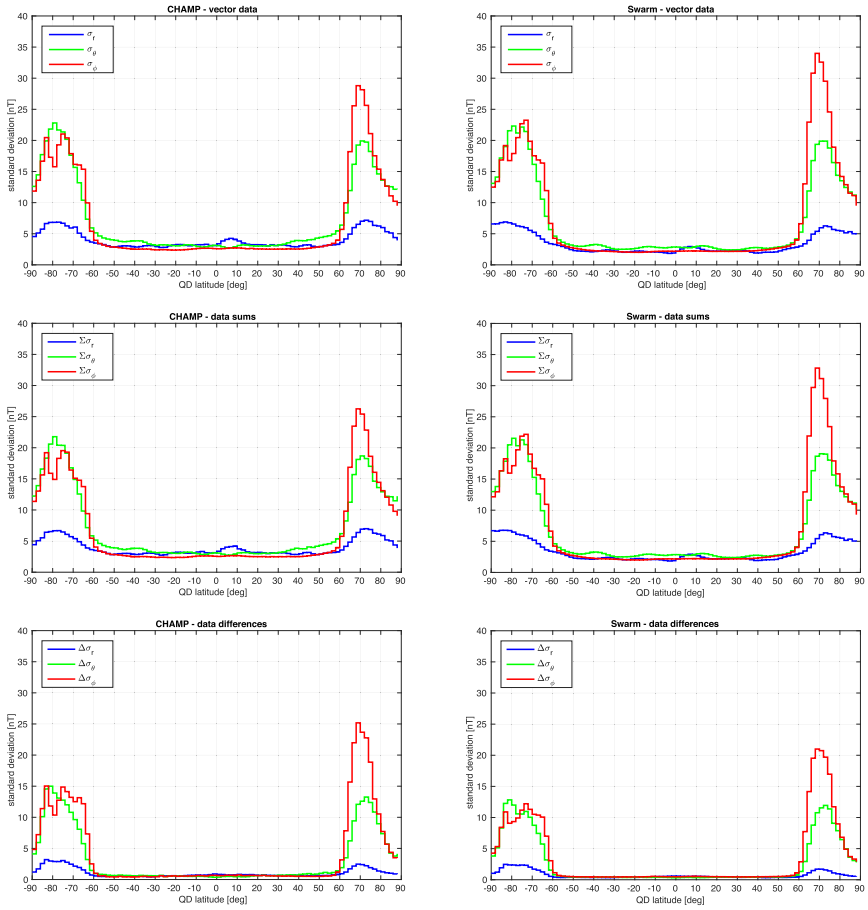

Figure 1. Latitude-dependent Huber weighted standard deviations in 2° bands (Northern hemisphere having positive QD) for CHAMP data (left-hand figures) and *Swarm* data (right-hand figures). Top panels: using vector data, centre using data sums and bottom panels using data differences.

for each field component and their sums and differences for each satellite standard deviations, $\sigma(\theta_{QD})$ according to

$$\sigma(\theta_{QD}) = \sqrt{\frac{\sum_i w_i(\epsilon_i - \mu)^2}{\sum w_i}}, \tag{1}$$

where ($i = 1, ..., D$) denotes the data elements within the bin, ε_i are the residuals to the CHAOS-6-x7 field predictions for SH degrees 1–13, μ is the weighted mean residual and w_i are the weights $w_i = \min(c_w/\varepsilon_i, 1)$ with a selected breakpoint $c_w = 1.5$ (e.g. Constable 1988). Considering separately each field component and their sums and differences for each satellite, weighted data error variances for data element n, where ($n = 1, ..., N$), were specified as $\sigma^2_{w,n}(\theta_{QD}) = \sigma^2(\theta_{QD})/w_n$, where $\sigma(\Theta_{QD})$ is the standard deviation for the QD latitude, data element and satellite in question from (1), and w_n is the Huber weight for data element n. Fig. 1 presents these latitude-dependent, Huber weighted, error estimates as a function of QD latitude for CHAMP and *Swarm* vector data as well as data differences and sums. Large data error estimates are confined to polar region latitudes (i.e. QD latitudes 60° to 90° and −60° to −90° for the northern and southern polar regions, respectively). Data error estimates are larger for the horizontal components exhibiting a noticeable asymmetry between the northern and southern polar regions, a feature also observed in previous studies (Kotsiaros *et al.* 2015).

3 METHODOLOGY

3.1 Potential field formulation

Measurements of the magnetic field are made at geocentric radius r in the volume V of a spherical shell bounded as $r_c \leq r \leq r_m$, that is assumed to contain no magnetization and no electric nor displacement currents. That is, V is bounded by a surface S having the disconnected parts S_C and S_M; S_C is closed and finite at radius r_c and S_M is closed and finite at radius r_m. In the ECEF frame the magnetic vector field $\mathbf{B}$ of this volume can be then represented by the gradient of a scalar potential function, $\mathbf{B} = -\nabla\psi$, which fulfils the Laplace equation $\nabla^2\psi = 0$ (e.g. Backus *et al.* 1996). The Laplace equation subject to prescribed values of the outward normal derivative on S_C/S_M is known, respectively, as the exterior/interior Neumann boundary value problem. Care is needed for geomagnetists with the notation here; the 'exterior' problem involves fields produced by internal sources while the 'interior' problem involves fields produced by external sources. Because Maxwell's equations are linear with respect to the sources, the total field is a superposition of fields produced by the two sources, that is $\mathbf{B} = \mathbf{B}_C + \mathbf{B}_M = -\nabla\psi_C - \nabla\psi_M$, where ψ_C here describes the internal (core) sources and ψ_M describes the external (large-scale magnetospheric) sources. From the Laplace equation, Green's identities can be derived from which Green's second identity allows a solution for the potential to be formulated. The uniqueness theorem then assures that the solution found is unique up to an additive constant (e.g. Barton 1989).

In the ECEF geographic spherical polar coordinate system the magnetic field components ($k = r, \theta, \phi$) at some observation location, $\mathbf{r}$, are linked to the radial field at surfaces S_C and S_M having position vector, $\mathbf{r}'$, which we take to be at the CMB ($r' = r_c = 3480$ km) and at the magnetosphere ($r' = r_m = 4r_a$) (where $r_a = 6371.2$ km is the mean Earth reference radius), respectively, by the gradient of the potential

$$\begin{aligned} B_k(\mathbf{r}, t) &= -\oint_{S_C} \nabla_k N_C(\mathbf{r}|\mathbf{r}') B_r(\mathbf{r}', t) r_c^2 \mathrm{d}S'_C - \oint_{S_M} \nabla_k N_M(\mathbf{r}|\mathbf{r}') B_r(\mathbf{r}', t) r_m^2 \mathrm{d}S'_M \\ &= \oint_{S_C} G_{C,k}(\mathbf{r}|\mathbf{r}') B_r(\mathbf{r}', t) \mathrm{d}S'_C + \oint_{S_M} G_{M,k}(\mathbf{r}|\mathbf{r}') B_r(\mathbf{r}', t) \mathrm{d}S'_M, \end{aligned} \tag{2}$$

where $\mathrm{d}S'_C$, $\mathrm{d}S'_M = \sin\theta' \mathrm{d}\theta' \mathrm{d}\phi'$. Eq. (2) is a linear system which consists of a sum of two homogeneous Fredholm integral equations of the first kind, for the unknown radial fields at the CMB and the magnetosphere. $N_C(\mathbf{r}|\mathbf{r}')$, having absorbed the term r_c^2, is the exterior Neumann Green's function and $N_M(\mathbf{r}|\mathbf{r}')$, having absorbed the term r_m^2, is the interior Neumann Green's function (Barton 1989, p. 412). The directional derivatives of the Green's functions (with respect to $\mathbf{r}$), $G_{C,k}(\mathbf{r}|\mathbf{r}')$ and $G_{M,k}(\mathbf{r}|\mathbf{r}')$, are known as the data kernels and can be derived using the chain rule (Gubbins & Roberts 1983). The exterior data kernels (associated with internal sources) are given by

$$G_{C,r} = -\frac{\partial N_C}{\partial r} = \frac{1}{4\pi} \frac{h^2(1-h^2)}{f^3} \tag{3}$$

$$G_{C,\theta} = -\frac{1}{r}\frac{\partial N_C}{\partial \theta} = -\frac{1}{r}\frac{\partial N_C}{\partial \mu}\frac{\partial \mu}{\partial \theta} = -\frac{1}{r}\frac{\partial N_C}{\partial \mu}[\cos\theta \sin\theta' \cos(\phi - \phi') - \sin\theta \cos\theta'] \tag{4}$$

$$G_{C,\phi} = -\frac{1}{r\sin\theta}\frac{\partial N_C}{\partial \phi} = -\frac{1}{r\sin\theta}\frac{\partial N_C}{\partial \mu}\frac{\partial \mu}{\partial \phi} = \frac{1}{r}\frac{\partial N_C}{\partial \mu}[\sin\theta' \sin(\phi - \phi')], \tag{5}$$

where the derivative with respect to μ is

$$\frac{1}{r}\frac{\partial N_C}{\partial \mu} = \frac{h}{4\pi}\left[\frac{1 - 2h\mu + 3h^2}{f^3} + \frac{\mu}{f(f + h - \mu)} - \frac{1}{1-\mu}\right]. \tag{6}$$

The corresponding interior data kernels (associated with external sources) are given by

$$G_{M,r} = -\frac{\partial N_M}{\partial r} = \frac{1}{4\pi}\left[h + \frac{h^2(1-h)}{f^3}\right] \tag{7}$$

$$G_{M,\theta} = -\frac{1}{r}\frac{\partial N_M}{\partial \theta} = -\frac{1}{r}\frac{\partial N_M}{\partial \mu}\frac{\partial \mu}{\partial \theta} = -\frac{1}{r}\frac{\partial N_M}{\partial \mu}[\cos\theta \sin\theta' \cos(\phi - \phi') - \sin\theta \cos\theta'] \tag{8}$$

$$G_{M,\phi} = -\frac{1}{r\sin\theta}\frac{\partial N_M}{\partial \phi} = -\frac{1}{r\sin\theta}\frac{\partial N_M}{\partial \mu}\frac{\partial \mu}{\partial \phi} = \frac{1}{r}\frac{\partial N_M}{\partial \mu}[\sin\theta' \sin(\phi - \phi')], \tag{9}$$

where the derivative with respect to μ is

$$\frac{1}{r}\frac{\partial N_M}{\partial \mu} = -\frac{h}{4\pi}\left[\frac{2h^2}{f^3} + \frac{r'/f}{r' - \mu r + rf)}\right]. \tag{10}$$

In the above expressions we have used $h = r'/r$, $f = R/r$, $R = \sqrt{r^2 + r'^2 - 2rr'\mu}$ and $\mu = \cos\gamma = \cos\theta\cos\theta' + \sin\theta\sin\theta'\cos(\phi - \phi')$, γ being the angular distance. Note that in Gubbins & Roberts (1983) these expressions include the monopole term that was removed by Constable *et al.* (1993) but we retain this terms as it proves useful when constructing localised Backus–Gilbert averaging kernels (see Section 3.2).

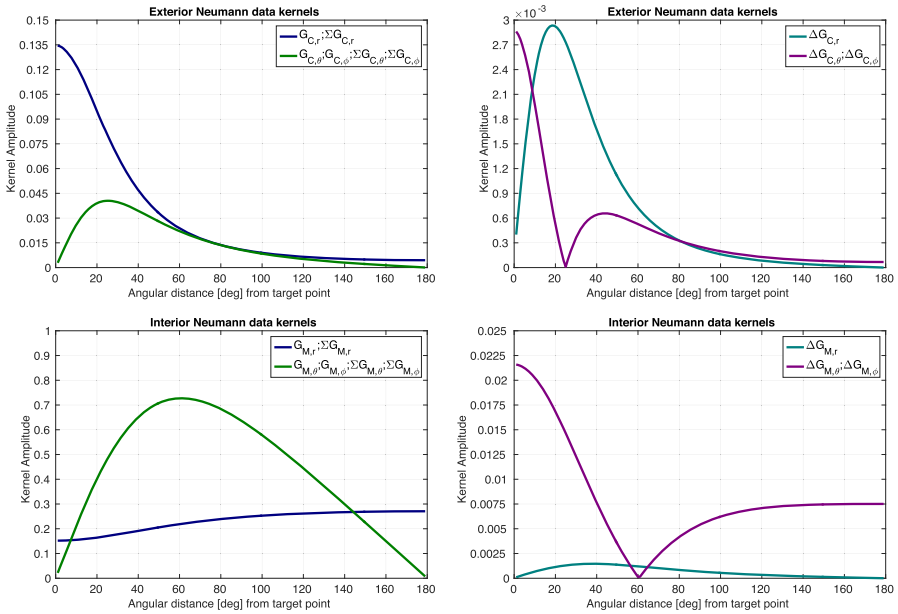

Figure 2. Sensitivity of satellite measurements to the CMB field versus angular distance from target point as determined by data kernels using an observation altitude of $r_{obs} = r_a + 400$ km. Top panel: exterior data kernels plotted using a source radius $r' = r_c$. Bottom panel: interior data kernels plotted using a source radius $r' = 4r_a$.

3.2 Modified Backus–Gilbert method

Applying the Backus–Gilbert formalism to the linear system (2), we determine an estimate, $\widehat{B}_r$, of the radial field as a spatial average that is optimally localized around a particular location and time of interest $(\mathbf{r}_0, t_0) = (r_c, \theta_0, \phi_0, t_0)$. The estimate is an inner product of the field of interest and some averaging kernel, and can be written as a linear combination of the data (Backus & Gilbert 1968, Backus & Gilbert 1970)

$$\widehat{B}_r(\mathbf{r}_0, t_0|\mathbf{r}_n, t_n) = \sum_n^N q_n(\mathbf{r}_0, t_0) d_n(\mathbf{r}, t), \tag{11}$$

where $(n = 1, ..., N)$ is the total number of data used over the specified time span. Data d_n for a particular position $\mathbf{r}_n$ at times t_n and field component k, are related to the radial field $B_r(\mathbf{r}', t)$ at the CMB and the magnetosphere as in (2), but we also allow the field at the core surface to be time-dependent by adopting a first order Taylor expansion assumed valid close to a reference time t_0

$$\begin{aligned} d_k(\mathbf{r}_n, t_n) &= \oint_{S_C} G^*_{C,k}(\mathbf{r}_n|\mathbf{r}') B_r(\mathbf{r}', t_n) \mathrm{d}S'_C + \oint_{S_M} G^*_{M,k}(\mathbf{r}_n|\mathbf{r}') B_r(\mathbf{r}', t_n) \mathrm{d}S'_M \\ &\approx \oint_{S_C} G^*_{C,k}(\mathbf{r}_n|\mathbf{r}') \left[B_r(\mathbf{r}', t_0) + \dot{B}_r(\mathbf{r}', t_0) \Delta t_n \right] \mathrm{d}S'_C + \oint_{S_M} G^*_{M,k}(\mathbf{r}_n|\mathbf{r}') B_r(\mathbf{r}', t_n) \mathrm{d}S'_M, \end{aligned} \tag{12}$$

where $G^*_k(\mathbf{r}_n|\mathbf{r}')$ are the appropriate data kernels for the vector field components or their sums and differences. The time difference to some given reference time t_{ref} is $\Delta t_n = t_n - t_{ref}$. Here we select the reference time to be the target time, that is $t_{ref} = t_0$. The first order Taylor expansion adopted is sufficient given the short time windows considered here, more complex time parametrizations are also in principle possible. Fig. 2 presents examples of the exterior and interior data kernels for vector data denoted $\{G_{C,k}; G_{M,k}\}$, data sums denoted $\{\sum G_{C,k}; \sum G_{M,k}\}$ and data differences denoted $\{\Delta G_{C,k}; \Delta G_{M,k}\}$, using an observation altitude above ground of 400 km. The plots illustrate how a given measurement samples the CMB and the magnetosphere ; for instance the radial data d_r samples the radial core field, via $G_{C,r}$, most strongly directly below the observation site while the radial difference Δd_r samples the radial core field, via $\Delta G_{C,r} = [G_{C,r}(\mathbf{r}_1|\mathbf{r}') - G_{C,r}(\mathbf{r}_2|\mathbf{r}')]$, most strongly at an angular distance of approximately 20° having no sensitivity directly beneath the observation site.

Inserting (12), via the chosen data, into (11), the estimate at target time t_0 can be written as

$$\widehat{B}_r(\mathbf{r}_0, t_0|\mathbf{r}_n, t_n) = \oint_{S_C} \sum_n^N q_n G^*_{C,k}(\mathbf{r}_n|\mathbf{r}') B_r(\mathbf{r}', t_0) \mathrm{d}S'_C + \oint_{S_C} \sum_n^N q_n G^*_{C,k}(\mathbf{r}_n|\mathbf{r}') \dot{B}_r(\mathbf{r}', t_0) \Delta t_n \mathrm{d}S'_C + \oint_{S_M} \sum_n^N q_n G^*_{M,k}(\mathbf{r}_n|\mathbf{r}') B_r(\mathbf{r}', t_n) \mathrm{d}S'_M. \quad (13)$$

The weighting coefficients, q_n, define spatial averaging kernels that are linear combinations of the data kernels

$$\mathcal{K}_C(\mathbf{r}_0, t_0|\mathbf{r}', t) = \sum_n^N q_n(\mathbf{r}_0, t_0) G^*_C(\mathbf{r}_n|\mathbf{r}') \quad (14)$$

$$\mathcal{K}_{\dot{C}}(\mathbf{r}_0, t_0|\mathbf{r}', t) = \sum_n^N q_n(\mathbf{r}_0, t_0) G^*_C(\mathbf{r}_n|\mathbf{r}') \Delta t_n \quad (15)$$

$$\mathcal{K}_M(\mathbf{r}_0, t_0|\mathbf{r}', t) = \sum_n^N q_n(\mathbf{r}_0, t_0) G^*_M(\mathbf{r}_n|\mathbf{r}'), \quad (16)$$

where the notation $\mathcal{K}_{\dot{C}}$ highlights the inclusion of the time difference Δt_n from the Taylor expansion to the data kernel defining $G^*_{\dot{C}} = G^*_C \Delta t_n$. Thus the estimated radial field consists of spatial integrals over the source spheres of the true field convolved with averaging kernels

$$\widehat{B}_r(\mathbf{r}_0, t_0|\mathbf{r}_n, t_n) = \oint_{S_C} \mathcal{K}_C(\mathbf{r}_0, t_0|\mathbf{r}', t) B_r(\mathbf{r}', t_0) \mathrm{d}S'_C + \oint_{S_C} \mathcal{K}_{\dot{C}}(\mathbf{r}_0, t_0|\mathbf{r}', t) \dot{B}_r(\mathbf{r}', t_0) \mathrm{d}S'_C + \oint_{S_M} \mathcal{K}_M(\mathbf{r}_0, t_0|\mathbf{r}', t) B_r(\mathbf{r}', t) \mathrm{d}S'_M. \quad (17)$$

Varying the coefficients, q_n, changes the shape of the averaging kernels. Incorporating the time differences in the averaging kernel may be thought of as assigning temporal weights to that kernel. These weights may act in such a way as to produce SV field estimates; for instance, selecting data from a time window of 2 yr centred on the reference time will assign equal weights having opposite signs relative to t_0 such that field differences are computed. In order for the estimate to represent a meaningful physical average and to avoid a biased result, a normalization of the averaging kernels is implemented requiring a unimodular constraint to be fulfilled

$$\oint_{S_C} \mathcal{K}_C(\mathbf{r}_0, t_0|\mathbf{r}', t) \mathrm{d}S'_C + \oint_{S_C} \mathcal{K}_{\dot{C}}(\mathbf{r}_0, t_0|\mathbf{r}', t) \mathrm{d}S'_C + \oint_{S_M} \mathcal{K}_M(\mathbf{r}_0, t_0|\mathbf{r}', t) \mathrm{d}S'_M = 1. \quad (18)$$

In practice, we want the term of interest to integrate to one and the other terms to be zero. Seeking the radial main field, data from narrow time windows are used such that the second term is neglected and the third term should integrate to zeros. Seeking an estimate of the temporal radial field change during a selected time window, the first and last terms should integrate to zero while the second term should integrate to one. It should be noted that the monopole term was retained in (3–10). This is necessary in order to prevent the averaging kernel from integrating to zero in violation of the unimodular constraint (Whaler 1984).

A generalized formulation of the Backus–Gilbert method, known as Optimally Localized Averages (OLA) involves minimizing some suitable measure of the averaging kernel (Pijpers & Thompson 1992; Pujol 2013)

$$\oint_S \mathcal{J}(\mathbf{r}_0)[\mathcal{K}(\mathbf{r}_0|\mathbf{r}') - \mathcal{T}(\mathbf{r}_0|\mathbf{r}')]^2 \mathrm{d}S', \quad (19)$$

where $\mathcal{J}$ is a weight function and $\mathcal{T}$ is a target function. Selecting ($\mathcal{J} = 12(\mathbf{r} - \mathbf{r}_0)^2; \mathcal{T} = 0$) corresponds to the original Backus–Gilbert approach of minimizing a product of the weight function and averaging kernel, also known as Multiplicative OLA (MOLA). The Subtractive OLA (SOLA) approach, pioneered and publicized in a series of papers by Pijpers & Thompson (1992, 1994), instead uses a norm measuring the squared distance between the averaging kernel, $\mathcal{K}$, and some chosen target function, $\mathcal{T} \neq 0$, taking $\mathcal{J} = 1$. The advantage of using SOLA over the MOLA, is that significant computational time can be saved when performing calculation of multiple estimates, see Section 3.3 for more details. For the target kernel, $\mathcal{T}$, we choose a Fisher function on a sphere using the angular distance $\Psi(\mathbf{r}_0|\mathbf{r}')$

$$\mathcal{T}(\Psi) = \frac{\kappa}{4\pi \sinh\kappa} e^{\kappa \cos\Psi}, \quad (20)$$

where κ is the width of the distribution (Fisher 1953). Here $\cos\Psi = \cos\theta_0 \cos\theta' + \sin_0\theta \sin\theta' \cos(\phi_0 - \phi')$, Ψ being the angular distance between points $\mathbf{r}_0$ and $\mathbf{r}'$ on the sphere. We enforce that $\mathcal{T}(\Psi)$ integrates to one for the term of interest in (18) and zero for the remaining terms. Following the SOLA approach, we define an objective function to be minimized, which comprises terms involved in the determination

of the estimate

$$\Theta = \oint_{S_C} [\mathcal{K}_C(\mathbf{r}_0|\mathbf{r}') - \mathcal{T}_C(\mathbf{r}_0|\mathbf{r}')]^2 \mathrm{d}S'_C + \oint_{S_C} [\mathcal{K}_{\hat{C}}(\mathbf{r}_0|\mathbf{r}') - \mathcal{T}_{\hat{C}}(\mathbf{r}_0|\mathbf{r}')]^2 \mathrm{d}S'_C + \oint_{S_M} [\mathcal{K}_M(\mathbf{r}_0|\mathbf{r}') - \mathcal{T}_M(\mathbf{r}_0|\mathbf{r}')]^2 \mathrm{d}S'_M + \lambda^2 \mathbf{q}^T \underline{\underline{\mathbf{E}}} \mathbf{q}, \quad (21)$$

where λ (units of [nT^{-1}]) is a trade-off parameter and $\underline{\underline{\mathbf{E}}}$ is the data error covariance matrix that is necessary because the real geophysical problem involves noisy data. Which terms to include in the objective function depends on what we seek to estimate; for instance estimating the radial field over a time window short enough that field time-dependence can be ignored, means that the second term is not included. On the other hand estimation of the SV involves retaining the second term as well while setting the target kernels $\mathcal{T}_C$, $\mathcal{T}_M$ to zero. The diagonal elements of the data error covariance matrix are constructed from a combination of the QD latitude-dependent data error estimates, and Huber weights, w_n appropriate for a long-tailed error distribution (see Section 2)

$$\sigma^2_{w,n}(\theta_{QD}) = \frac{\sigma^2(\theta_{QD})}{w_n} \quad (22)$$

$$E_{ln} = \sigma^2_{w,n} e^{\frac{-\Delta t_{ln}}{\tau}}, \quad (23)$$

where the indices (l, $n = 1, ..., N$), $\Delta t_{ln} = t_l - t_n$ are data time differences and τ is the serial error correlation time set to 600 s based on the findings of Lowes and Olsen (2004). We note that the covariance matrix is symmetric (i.e. $E_{ln} = E_{nl}$) and positive definite. When deriving main field estimates using data taking along the satellite tracks at a sampling rate of 15 s, see Section 4.1, we multiply variances by a factor $\sin\theta$, where θ is geographic co-latitude, to account for there being more data close to the poles and in order to simulate an equal-area distribution (Olsen *et al.* 2014). For estimates of the SV, see Section 4.2, data are selected such that a good global coverage is obtained overthe chosen time window; in this case the differences in the data time are much longer than the correlation time and we are able to neglect the temporal correlation.

3.3 Numerical implementation

The minimization of the objective function (21) is performed by taking the derivative with respect to q_n,and requiring that $\partial\Theta/\partial q_n = 0$. Discretizing the integrals using a quadrature rule, the resulting set of equations subject to the constraint (17) may be written in the following form (Larsen & Hansen 1997)

$$\left[\underline{\underline{\mathbf{K}}}_C \underline{\underline{\mathbf{W}}} \underline{\underline{\mathbf{K}}}_C^T + \underline{\underline{\mathbf{K}}}_{\hat{C}} \underline{\underline{\mathbf{W}}} \underline{\underline{\mathbf{K}}}_{\hat{C}}^T + \underline{\underline{\mathbf{K}}}_M \underline{\underline{\mathbf{W}}} \underline{\underline{\mathbf{K}}}_M^T + \lambda^2 \underline{\underline{\mathbf{E}}}\right] \mathbf{q}(\mathbf{r}_0) = \underline{\underline{\mathbf{K}}}_C \underline{\underline{\mathbf{W}}} \mathbf{t}_C(\mathbf{r}_0) + \underline{\underline{\mathbf{K}}}_C \underline{\underline{\mathbf{W}}} \mathbf{t}_{\hat{C}}(\mathbf{r}_0) + \underline{\underline{\mathbf{K}}}_M \underline{\underline{\mathbf{W}}} \mathbf{t}_M(\mathbf{r}_0) \quad (24)$$

$$\textit{subject to} \quad \left[\mathbf{e}_p^T \underline{\underline{\mathbf{W}}} \underline{\underline{\mathbf{K}}}_C^T + \mathbf{e}_p^T \underline{\underline{\mathbf{W}}} \underline{\underline{\mathbf{K}}}_{\hat{C}}^T + \mathbf{e}_p^T \underline{\underline{\mathbf{W}}} \underline{\underline{\mathbf{K}}}_M^T\right] \mathbf{q}(\mathbf{r}_0) = 1. \quad (25)$$

Here we define $\mathbf{K}$ matrices of size $N \times M$, where M is the size of the quadrature grid, such that

$$(\mathbf{K})_{np} = \left[G^*_{C,n}(\mathbf{r}_p), G^*_{\hat{C},n}(\mathbf{r}_p), G^*_{M,n}(\mathbf{r}_p)\right], \quad n = 1, ..., N \quad p = 1, ..., M \quad (26)$$

and $\mathbf{W}$ is a diagonal matrix of the integration points of size $M \times M$

$$(\mathbf{W})_{pp} = l_p, \quad p = 1, ..., M \quad (27)$$

and we have introduced the three vectors: $\mathbf{e}_p = (1, ..., 1)^T$, $\mathbf{t}(\mathbf{r}_0)$ having elements $(\mathbf{t}(\mathbf{r}_0))_p = \mathcal{T}(\mathbf{r}_0|\mathbf{r}_p)$ and $\mathbf{k}(\mathbf{r}_0)$ having elements $(\mathbf{k}(\mathbf{r}_0))_p = \mathcal{K}(\mathbf{r}_0|\mathbf{r}_p)$ for $p = 1, ..., M$. The discretized averaging kernel is calculated as $\mathbf{k}(\mathbf{r}_0) = \underline{\underline{\mathbf{K}}}^T \mathbf{q}(\mathbf{r}_0)$. The required angular integrations over the CMB and magnetosphere are performed numerically using Lebedev angular quadrature weights l_p on a grid $\mathbf{r}_p = (r_c, \theta_p, \phi_p)$ (Lebedev & Laikov 1999; Parrish 2010) that allow efficient calculation of integrals on a sphere

$$\int_S F(\mathbf{r}')\mathrm{d}S' \approx \sum_{p=1}^{M} l_p F(\mathbf{r}_p). \quad (28)$$

We found that using $M = 1730$ Lebedev points, corresponding to SH degree and order 71, were sufficient to perform the integrations to the required accuracy. We solve the normal equations for the coefficients, $\mathbf{q} = (q_1, ..., q_N)$, using a Lagrange multiplier ν as proposed by Pijpers & Thompson (1994)

$$\begin{pmatrix} \underline{\underline{\mathbf{K}}}_C \underline{\underline{\mathbf{W}}} \underline{\underline{\mathbf{K}}}_C^T + \underline{\underline{\mathbf{K}}}_{\hat{C}} \underline{\underline{\mathbf{W}}} \underline{\underline{\mathbf{K}}}_{\hat{C}}^T + \underline{\underline{\mathbf{K}}}_M \underline{\underline{\mathbf{W}}} \underline{\underline{\mathbf{K}}}_M^T + \lambda^2 \underline{\underline{\mathbf{E}}} & \underline{\underline{\mathbf{K}}}_C \underline{\underline{\mathbf{W}}} \mathbf{e}_p + \underline{\underline{\mathbf{K}}}_{\hat{C}} \underline{\underline{\mathbf{W}}} \mathbf{e}_p + \underline{\underline{\mathbf{K}}}_M \underline{\underline{\mathbf{W}}} \mathbf{e}_p \\ \mathbf{e}_p^T \underline{\underline{\mathbf{W}}} \underline{\underline{\mathbf{K}}}_C^T + \mathbf{e}_p^T \underline{\underline{\mathbf{W}}} \underline{\underline{\mathbf{K}}}_{\hat{C}}^T + \mathbf{e}_p^T \underline{\underline{\mathbf{W}}} \underline{\underline{\mathbf{K}}}_M^T & 0 \end{pmatrix} \begin{pmatrix} \mathbf{q}(\mathbf{r}_0) \\ \nu \end{pmatrix} = \begin{pmatrix} \underline{\underline{\mathbf{K}}}_C \underline{\underline{\mathbf{W}}} \mathbf{t}_C(\mathbf{r}_0) + \underline{\underline{\mathbf{K}}}_{\hat{C}} \underline{\underline{\mathbf{W}}} \mathbf{t}_{\hat{C}}(\mathbf{r}_0) + \underline{\underline{\mathbf{K}}}_M \underline{\underline{\mathbf{W}}} \mathbf{t}_M(\mathbf{r}_0) \\ 1 \end{pmatrix}.$$

The first matrix term on the left-hand side is independent of estimate position $\mathbf{r}_0$. It therefore only needs to be computed once, significantly reducing the amount of computation required for producing a number of estimates at different locations. The linear system is solved for the vector containing $(q_1, ..., q_N, \nu)$, then the averages, the averaging kernels and the uncertainty estimates (variances) are computed. We note that alternative LSQR solution schemes could also be used to solve such systems (Larsen & Hansen 1997; Zaroli 2016). When estimating the radial MF at a given location, data from within a month is used, such that the term involving $\underline{\underline{\mathbf{K}}}_C$ is neglected and the target kernel terms $\mathbf{t}_C(\mathbf{r}_0)$, $\mathbf{t}_M(\mathbf{r}_0)$ are set to zero. When estimating the radial SV the target kernel terms $\mathbf{t}_C(\mathbf{r}_0)$, $\mathbf{t}_M(\mathbf{r}_0)$ are set to zero.

3.4 Appraisal of the constructed averages

A primary concern of the Backus–Gilbert method is the appraisal of solutions, that is to attain information regarding the resolvability offered by the magnetic field observations. A crucial insight is that the estimated average field is the only unique information offered by the data; that is, the estimated average along with the averaging kernel constitutes our knowledge of the field in the vicinity of the target location (Oldenburg 1984; Parker 1994). Appraisal typically consists of obtaining the averaging kernel, often described in terms of its width, together with the uncertainty of the average. Here, we define the kernel width to be the angular distance between points at which the averaging kernel reaches zero amplitude moving away from its maximum value (note that in contrast the original Backus–Gilbert method used the width as the full width at half maximum). We calculate the variance, $\widehat{\sigma}^2(\mathbf{r}_0, t_0)$, of the estimate of the radial field at location $(\mathbf{r}_0, t_0)$ propagated from the data error covariance matrix by

$$\widehat{\sigma}^2(\mathbf{r}_0, t_0) = \sum_{l,n}^{N} q_l E_{ln} q_n = \mathbf{q}^T \underline{\underline{E}} \mathbf{q}. \tag{29}$$

A family of solutions with different levels of trade-off between fitting the target function and obtaining an estimate with low variance is obtained; a small λ corresponds to fitting only the target function which decreases the width of the averaging kernel increasing the spatial resolution but at the expense of the statistical reliability (i.e. yielding a large variance and error magnification), while increasing λ broadens the averaging kernel lowering the spatial resolution, but produces a more reliable estimate (smaller variance). Note that contamination from averaging kernel side lobs and from leakage of co-estimated fields have not been included in the variance estimates described here.

4 RESULTS

Here we demonstrate our geomagnetic SOLA method in two applications: estimation of the radial component of the core field (Section 4.1) and estimation of the radial component of the secular variation (Section 4.2) at the CMB. Furthermore, we present computations of the change in the radial secular variation (i.e. the accumulated SA) from differences in SV estimates.

4.1 Application to the main field

We begin by illustrating the SOLA method by determining estimates of the radial core field at a sequence of target locations at the CMB using sums and differences of *Swarm* field measurements taken from March 2017 using data with a 15 sec sampling rate. Working with sums and differences of the vector field, the data vector is $\mathbf{d} = \{\Delta\mathbf{d}_r, \Sigma\mathbf{d}_r, \Delta\mathbf{d}_\theta, \Sigma\mathbf{d}_\theta, \Delta\mathbf{d}_\phi, \Sigma\mathbf{d}_\phi\}$. The data kernels are then constructed as

$$G^* = \left\{\Delta G_{C,r}, \Sigma G_{C,r}, \Delta G_{C,\theta}, \Sigma G_{C,\theta}, \Delta G_{C,\phi}, \Sigma G_{C,\phi}\right\},$$

where $\Delta G_{C,k} = [G_{C,k}(\mathbf{r}_1|\mathbf{r}') - G_{C,k}(\mathbf{r}_2|\mathbf{r}')]$ and $\Sigma G_{C,k} = [G_{C,k}(\mathbf{r}_1|\mathbf{r}') + G_{C,k}(\mathbf{r}_2|\mathbf{r}')]/2$ are data kernels for the differences and sums, respectively with $(k = r, \theta, \phi)$. Focusing solely on estimating the radial component of the core field and ignoring time-dependency, the second term is omitted from the objective function (21) and the constraint (18). Note that in this application, using magnetic data sampled every 15 sec, we have included an exponential serial data error covariance model and the equal area weighting factor as described in Section 3.2. In Fig. 3 we investigate the behaviour of the averaging kernel, $\mathcal{K}_C$, as a function of the target kernel width parameter κ and the trade-off parameter λ by considering a series of example averaging kernels at QD latitude 0° and longitude −168°. The plots provide the error estimate $\widehat{\sigma}$ for the field average and the kernel width in degrees. Increasing κ (i.e. going from left to right in the plot columns) causes the kernel to become narrower while increasing its amplitude and the variance. However, increasing κ induces more oscillations in the kernel structure around the target location. Increasing λ (i.e. going from top to bottom in the plot rows) decreases the kernel amplitude and increases its width, reducing the side lobe oscillations. In order to obtain a good resolution it is desirable to select a narrow, high amplitude, kernel, while at the same time trying to keep the side lobe oscillations to a minimum. The kernels are all well behaved showing only minor side lobes compared to the kernel amplitudes, hence we are motivated to push towards a high κ value. In general, we found that increasing the amount of data tends to decrease the width of the averaging kernel and lower the variance.

Next we consider how the SOLA method performs at four different QD latitudes: (0°, 35°, 70°, 85°). The reason for choosing these QD latitudes is to investigate the performance of the SOLA method in regions of external field disturbance with different amplitudes and different data coverage; in the Arctic region QD latitudes 70° and 85° are located approximately within and poleward of the auroral oval, respectively, while QD 35° represents mid-latitudes and QD 0° represents low-latitudes. The left-hand plot in Fig. 4 presents the local error

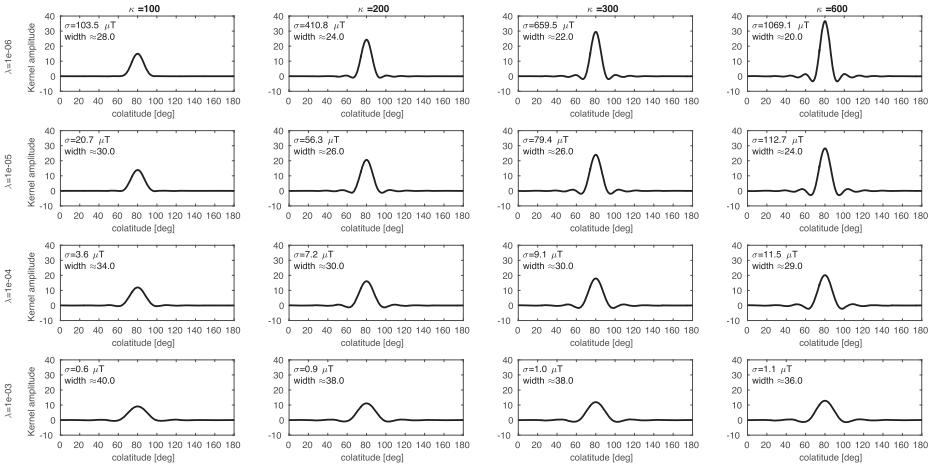

Figure 3. Main field application using data from March 2017 shown at target location with QD latitude 0°: behaviour of the averaging kernel as a function of Fisher function width κ and trade-off parameter λ. The value of κ increases from the left column having $\kappa = 100$ to the right column having $\kappa = 600$. The value of λ increases from the top row of $\lambda = 10^{-6}$ nT^{-1} to the bottom row having $\lambda = 10^{-3}$ nT^{-1}. In each plot the estimated uncertainty on the average, $\hat{\sigma}$,and kernel width in degrees are stated.

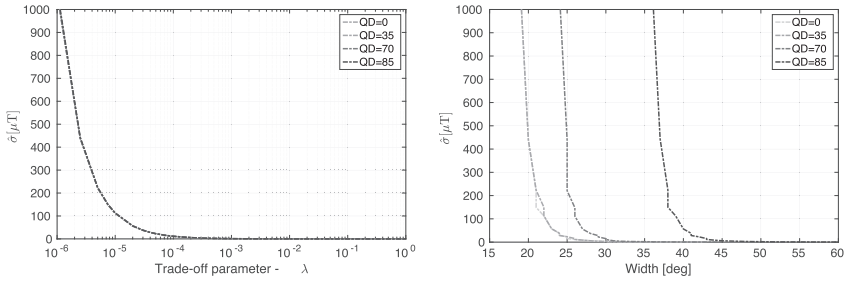

Figure 4. Main field application to the minimization problem eq. (21) using data from March 2017 for various target locations at QD latitudes 0°, 35°, 70° and 85°. Left-hand panel: local average error estimate $\hat{\sigma}(\mathbf{r}_0)$ versus trade-off parameter λ. Right-hand panel: local average error estimate $\hat{\sigma}(\mathbf{r}_0)$ versus main field averaging kernel width in degrees.

estimate versus the trade-off parameter λ.We find the size of the error estimates are of similar independent of the QD latitude for the various trade-off parameters. Hence, we may use the left-hand plot in Fig. 4 to pinpoint a suitable λ that yields more or less uniform error estimates for regional or global collections of point estimates. The right-hand plot in Fig. 4 presents the local error estimate versus the averaging kernel width in degrees, and shows a characteristic L-curve shape (the curves for latitudes 0° and 35° are coinciding). Here we note a right-shift of the L-curves as the QD latitude increases; for each curve the plot clearly illustrates how a low error estimate is associated with a large averaging kernel width and vice versa. The low and mid-latitude kernel widths are seen to be significantly smaller than in the auroral regions. This behaviour is expected since the data error estimates are larger in the auroral regions; hence to obtain the same variance the averaging kernel needs to become broader. Based on the information contained in Figs 3 and 4 we have chosen to use a Fisher's parameter $\kappa = 600$ and trade-off parameter $\lambda = 1 \times 10^{-4}$ nT^{-1} in the following calculations of the main field.

The top left plot in Fig. 5 presents a global collection of such radial field estimates at the CMB with a 1° spacing. Associated plots present the related error estimates (top right), the kernel widths (bottom left) and the data distribution under consideration (bottom right). We observe that the radial field patches and their amplitudes are very similar to those seen in the CHAOS-6-x7 field model predictions for SH degrees 1–13. Error estimates remain homogeneous as expected from Fig. 4. Kernel widths are seen to be more or less uniform at non-polar latitudes showing coherence with the data distribution, while distinct behaviour of the kernels is found in the polar regions; in particular, a striking region of increased kernel width coinciding with the auroral oval is observed as expected given the data error estimates shown in

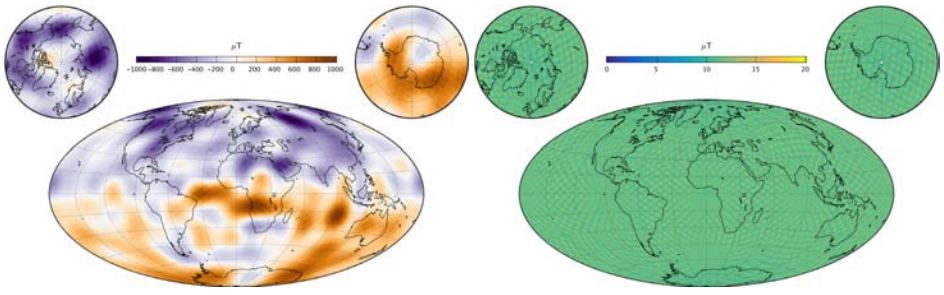

(a) Map collecting local estimates of CMB radial field $\widehat{B_r}(\mathbf{r}_0, t_0)$ in [μT].

(b) Map collecting local error estimates $\widehat{\sigma}(\mathbf{r}_0, t_0)$ in [μT].

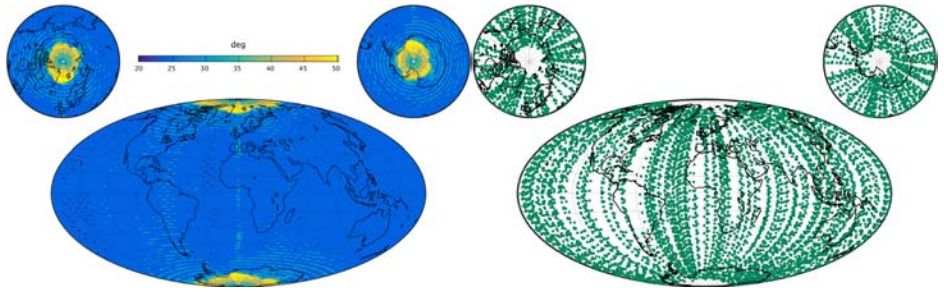

(c) Width of averaging kernel $\mathcal{K}_C(\mathbf{r}_0|\mathbf{r}')$ for local estimates in [deg].

(d) Location of observations used in March 2017 example.

Figure 5. Main field application using March 2017 *Swarm* data sums and differences using $\kappa = 600$ and $\lambda = 10^{-4}$ nT^{-1} showing: (a) radial MF estimates at the CMB for a global 1° spaced collection of target locations, (b) uncertainty estimates for each target point, (c) averaging kernel widths for each target point and (d) *Swarm* data distribution.

Fig. 1. On the CMB, at radius r_c, the wavelength λ_n associated with a particular SH degree n is $\lambda_n = (2\pi r_c)/n$ (1° ≈ 61 km). Averaging kernels having widths of ≈30° correspond approximately to SH degree 12. Hence, the resolution we obtain for the core field is comparable to that provided by conventional core field models, but note that each local estimate is the result of an individual inversion.

4.2 Application to the secular variation and accumulated secular acceleration

Next we illustrate an application of the SOLA method to the radial field secular variation at the CMB using a time window of 2 yr of *Swarm* vector field data from 2015.0 to 2017.0. Here we use only the radial field component of the satellite data in order to reduce external field contamination at high latitudes and in an effort to maximize the data coverage for a given number of data, such that the data vector is here $\mathbf{d} = \{\mathbf{d}_r\}$, and the data kernels are $G^* = \{G_{C,r}\}$. For 2 month time windows starting from 2015.0, we constructed a regularly spaced global distribution by randomly selecting data in time (within the 2 month window) on an equal area grid. A data set covering the period 2015.0 to 2017.0 was then generated by accumulating these 2 month data sets from the entire 2 yr, resulting in a total of 43 540 radial field data points. Here, serial error correlation in the data was not accounted for as data were selected randomly from within the 2 months. We start by considering the L-curve behaviour for the same QD positions investigated in the MF case. Fig. 6 presents the local error estimate versus the trade-off parameter λ (left-hand plot) and versus the averaging kernel width in degrees (right-hand plot). As in the MF case the error estimates are seen to be independent of location for a given λ value; for a given value of λ a corresponding $\widehat{\sigma}(\mathbf{r}_0)$ is fixed and we may read off the value of the kernel width at a given QD latitude. Furthermore, in both plots we mark blue, red and green dots for selected λ values studied in more detail in Figs 7 and 8. Here, we consider in detail three different λ values in order to investigate the resolvability of the SV with different choices of the average kernel. Fig. 7 shows examples of the averaging kernels obtained using $\lambda = 2.5 \times 10^{-4}$ nT^{-1} (the blue dot in Fig. 6) top left-hand plot, $\lambda = 5 \times 10^{-4}$ nT^{-1} (the red dot in Fig. 6) top right-hand plot and $\lambda = 5 \times 10^{-3}$ nT^{-1} (the green dot in Fig. 6) bottom plot, having widths of ≈30°, 33° and 42°; comparing the three kernels it is clear that using $\lambda = 2.5 \times 10^{-4}$ nT^{-1} results in higher amplitudes and a narrower averaging kernel. Fig. 8 presents a global collection of radial field SV estimates at the CMB having a 1° spacing on the left and associated kernel widths on the right, here shown for $\lambda = 2.5 \times 10^{-4}$ nT^{-1} in the top plots, $\lambda = 5 \times 10^{-4}$ nT^{-1} in the centre plots and $\lambda = 5$

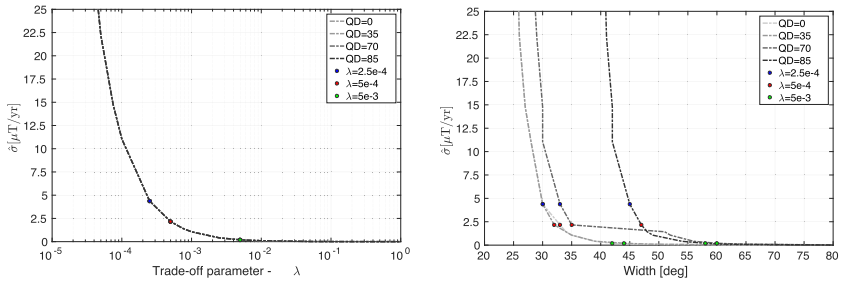

Figure 6. SV radial field application to the minimization problem eq. (21) using 2 yr of *Swarm* data between 2015.0 and 2017.0 having $\kappa = 600$. Plots showing $\widehat{\sigma}(\mathbf{r}_0)$ trade-off curves at various target locations for QD latitudes 0°, 35°, 70° and 85° as a function of λ (left-hand panel) and kernel width (right-hand panel).

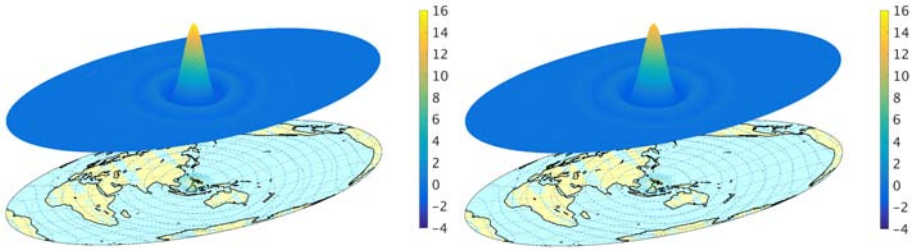

(a) SV averaging kernel for $\lambda = 2.5 \times 10^{-4}\mathrm{nT}^{-1}$. Kernel width ≈ 30°. (b) SV averaging kernel using $\lambda = 5 \times 10^{-4}\mathrm{nT}^{-1}$. Kernel width ≈ 33°.

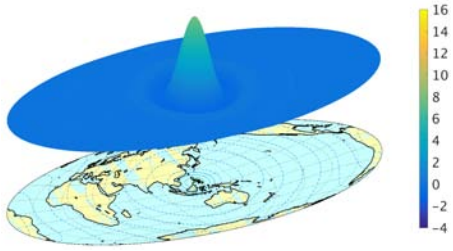

(c) SV averaging kernel using $\lambda = 5 \times 10^{-3}\mathrm{nT}^{-1}$. Kernel width ≈ 42°.

Figure 7. SV radial field application using 2 yr of *Swarm* data between 2015.0 and 2017.0 having $\kappa = 600$. Plots show example kernels at target location QD latitude 0° for : (a) $\lambda = 2.5 \times 10^{-4}$ nT^{-1}, (b) $\lambda = 5 \times 10^{-4}$ nT^{-1} and (c) $\lambda = 5 \times 10^{-3}$ nT^{-1} marked with blue, green and red dots in Fig. 6, respectively. The green dot in the map locates the kernel centre. Contour interval is 2.0. Negative contours are dashed.

$\times 10^{-4}$ nT^{-1} in the bottom plots. The effect of changing λ, and thus the averaging kernel, is clearly seen in the these plots: the field structures become smeared out as the kernel width is increased (i.e. going from top plots to bottom plots), decreasing the amplitude while a decrease in the associated error estimates is also observed. The kernel width increases towards the polar regions resembling the results in the MF case study, peaking at areas matching those of the auroral oval.

Remembering that our method involves no explicit spectral regularization of higher spatial frequencies of the signal, it is interesting to compare our global SV estimates to SV field predictions of the CHAOS-6-x7 model. Though the method, as well as the data and the data selection criteria, are not the same in the two approaches, similar SV structures can clearly be identified; in particular high amplitude features appearing at low latitudes stretching over a longitudinal band of ±90°, lower activity in the pacific region (at least for the broader averaging kernels) and a sequence of high latitude patches encircling the north pole. Though decreasing kernel width may cause noise to become more influential in the average estimate, in particular at mid-latitudes and polar regions, a clear change in the eastern pacific region is evident for λ

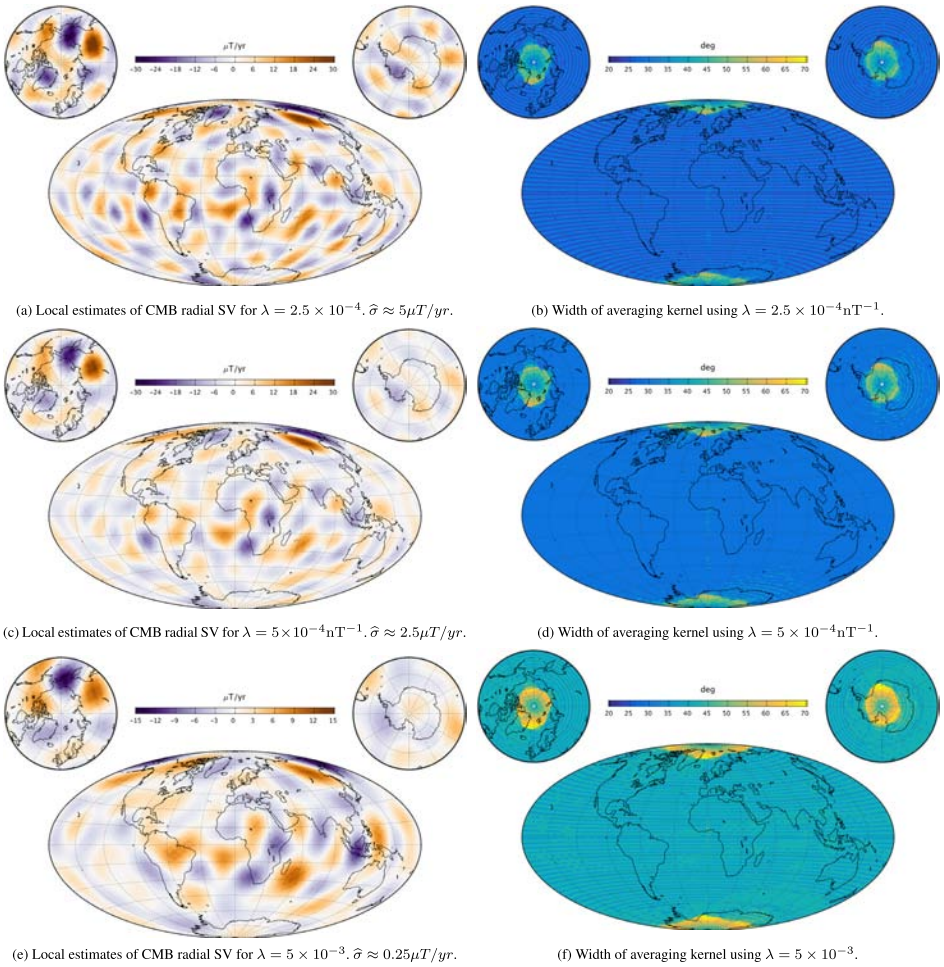

(a) Local estimates of CMB radial SV for $\lambda = 2.5 \times 10^{-4}$. $\widehat{\sigma} \approx 5\mu T/yr$.

(b) Width of averaging kernel using $\lambda = 2.5 \times 10^{-4}\mathrm{nT}^{-1}$.

(c) Local estimates of CMB radial SV for $\lambda = 5\times10^{-4}\mathrm{nT}^{-1}$. $\widehat{\sigma} \approx 2.5\mu T/yr$.

(d) Width of averaging kernel using $\lambda = 5 \times 10^{-4}\mathrm{nT}^{-1}$.

(e) Local estimates of CMB radial SV for $\lambda = 5 \times 10^{-3}$. $\widehat{\sigma} \approx 0.25\mu T/yr$.

(f) Width of averaging kernel using $\lambda = 5 \times 10^{-3}$.

Figure 8. SV radial field application using 2 yr of *Swarm* data between 2015.0 and 2017.0 showing a global collection of target points (1° spacing) having $\kappa = 600$. Results shown are: (a and b) using $\lambda = 2.5 \times 10^{-4}$ nT^{-1}, (c and d) using $\lambda = 5 \times 10^{-4}$ nT^{-1} and (e and f) using $\lambda = 5 \times 10^{-3}$ nT^{-1}.

$= 2.5 \times 10^{-4}$ nT^{-1}, which is interesting as recent SH based field models find distinct SA features in this region (Chulliat *et al.* 2015; Finlay *et al.* 2016).

Fig. 9 reports the radial SA computed as the accumulated change in the radial SV between years 2015 to 2017, 2007 to 2009 and 2005 to 2007. To determine this, the SV in 2017.0 was computed from 2 yr of data (as above) using $\lambda = 5 \times 10^{-3}$ nT^{-1}; that is, seeking SV maps having detail levels as given in Fig. 8(e). In a second step, the averaging kernels determined using this value of λ, were used as the target kernels for the SV in 2005, 2007 and 2015.0 in order to ensure the quantities to be differenced have been averaged in the same fashion. Finally the accumulated SA was computed as the difference in SV between 2005 and 2007, respectively 2015 and 2017. Comparing such maps of the accumlated SA with the SA predictions of the CHAOS-6-x7 model up to SH degree 10, the SOLA maps agree well with the CHAOS-6 model predictions. Even small scale field features can be found in both models, though the high latitude SA signal is perhaps not as prominent in the SOLA maps. Thus the SA predictions of regularized SH based models up to SH degree 10 are essentially reproduced by our approach.

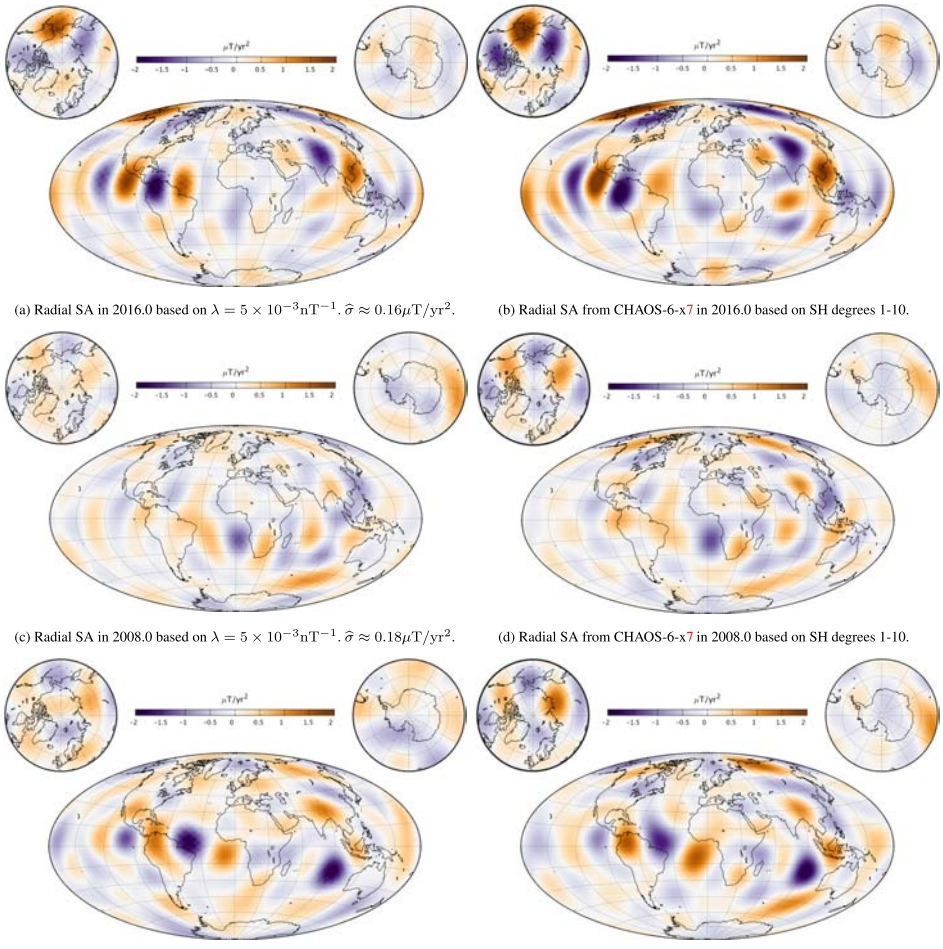

(a) Radial SA in 2016.0 based on $\lambda = 5 \times 10^{-3}\mathrm{nT}^{-1}$. $\widehat{\sigma} \approx 0.16\mu\mathrm{T/yr}^2$.

(b) Radial SA from CHAOS-6-x7 in 2016.0 based on SH degrees 1-10.

(c) Radial SA in 2008.0 based on $\lambda = 5 \times 10^{-3}\mathrm{nT}^{-1}$. $\widehat{\sigma} \approx 0.18\mu\mathrm{T/yr}^2$.

(d) Radial SA from CHAOS-6-x7 in 2008.0 based on SH degrees 1-10.

(e) Radial SA in 2006.0 based on $\lambda = 5 \times 10^{-3}\mathrm{nT}^{-1}$. $\widehat{\sigma} \approx 0.25\mu\mathrm{T/yr}^2$.

(f) Radial SA from CHAOS-6-x7 in 2006.0 based on SH degrees 1-10.

Figure 9. SA computed as accumulated change in radial SV at the CMB from: (a) years 2015−2017, (c) years 2007–2009 and years 2005–2007 using $\lambda = 5 \times 10^{-3}$ nT^{-1}. Plots (b), (d) and (f) show the CHAOS-6-x7 model SA predictions truncated at SH degree 10 for years 2016, 2008 and 2006 at the CMB, respectively.

The evolution of the radial SA at the CMB is shown in Fig. 10, presenting time-longitude plots along the geographic equator as determined using our approach. Here we have experimented by looking at 1 and 2 yr SV differences derived from data windows sliding in steps of 1 and 2 month s, respectively. The reason for not showing results prior to 2004 in plots (c) and (d) is that using a 1 month sliding time window causes a severe lack of data during this time with our data selection criteria. The left-hand plots show the SA evolution at the equator while the right-hand plots show corresponding error estimates. From plots (a) and (c) coherent evolving structures are observed. This is important as it illustrates the ability of our method to track temporal changes. As can be seen, much higher temporal resolution is gained in (c) using 1 yr SV differences. Associated uncertainty estimates show an increase in amplitude between 2004 and 2005, which is likely related to there being less data at this time. Striped looking patterns in the error estimates can be seen, which are probably related to the regular spatial grid of the selected data . This behaviour may be reduced by seeking a different data grid setup. The SA patterns observed in

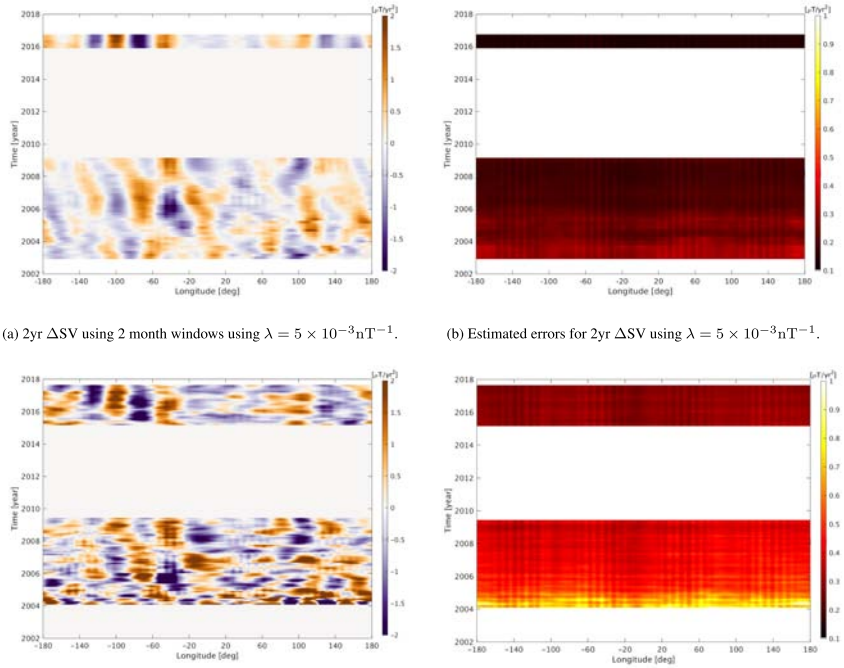

(a) 2yr ΔSV using 2 month windows using $\lambda = 5 \times 10^{-3}\mathrm{nT}^{-1}$.

(b) Estimated errors for 2yr ΔSV using $\lambda = 5 \times 10^{-3}\mathrm{nT}^{-1}$.

(c) 1yr ΔSV using 1 month windows using $\lambda = 5 \times 10^{-3}\mathrm{nT}^{-1}$.

(d) Estimated errors for 1yr ΔSV using $\lambda = 5 \times 10^{-3}\mathrm{nT}^{-1}$.

Figure 10. Time-longitude plot of the accumulated SA along the geographical equator at the CMB. Showing (a) Difference of SV estimates 2 yr apart, each derived over a 2 yr window, windows moving in 2 month steps, and derived using $\lambda = 5 \times 10^{-3}$ nT^{-1}, (b) uncertainty estimates for plot (a), (c) Difference of SV estimates 1 yr apart, each derived over a 1 yr window, windows moving in 1 month steps, again using $\lambda = 5 \times 10^{-3}$ nT^{-1}, (d) uncertainty estimates for plot (c).

plots (a) and (c), correspond qualitatively to those found in the CHAOS-6 model and in previous studies (Chulliat *et al.* 2015); in particular the prominent features appearing between 2005 and 2009 in the longitude band from -100° to 20°.

5 DISCUSSION AND CONCLUSION

We have presented an application of the modified Backus-Gilbert formalism called SOLA, originally developed in helioseismology, to determine local average estimates of the core-generated magnetic field and its time derivatives. These estimates are in good agreement with maps of the CMB radial MF, SV and SA derived using conventional spherical harmonic modelling techniques.

The Backus–Gilbert formalism offers a useful alternative approach to retrieving information on the geomagnetic field in comparison to conventional field modelling; instead of relying on a truncated and regularized spherical harmonic representation being downward continued to the CMB, we average over the field directly at the CMB and thus obtain unbiased estimates. An important advantage of our method is that it automatically provides the spatial averaging kernels and variances associated with the estimates thus allowing for a detailed appraisal of the field averages; a range of well-characterized solutions can be realized by varying the target kernel width via the trade-off parameter λ; it is desirable to have a low target width while at the same time having a sufficiently low uncertainty estimate for the field averages. In contrast it is not straight-forward to provide variances for point estimates at the CMB field derived from truncated and regularized SH models, and workers rarely compute the associated spatial averaging kernels. An advantage of SOLA compared to regularized least-squares inversion is that the variance estimates are not artificially suppressed. The Backus–Gilbert estimate can in some circumstances be closer to the true value than the least-squares solution, provided the quantity being estimated (in our case the radial field at the CMB, $B_r(\mathbf{r}', t)$) is sufficiently smooth (Parker 1977; Pujol 2013). Although the Backus–Gilbert approach was not originally intended for global model construction, the union of a

collection of point estimates has been considered by some authors to constitute a sensible approach (e.g. Parker 1994; Nolet 2008). In principle a trade-off curve could be calculated for each location under consideration. We have instead selected one value for the trade-off parameter for all locations, so the variances of the estimates and the kernel widths can vary with position reflecting for example uneven data distribution or enhanced data errors in regions such as the auroral zone. Although the kernel width provides only a very crude summary of the actual averaging scale (Parker 1994), for the satellite data considered here with their good global coverage, it is found to be a useful diagnostic. Our averaging kernels are generally well behaved when using the same trade-off parameter for all locations, having averaging kernels without significant side lobes (amplitudes are less than 10 per cent of the kernel peak amplitude). The possibility also exists of pre-specifying other target kernels in order to estimate a particular form of spatial average; here we have chosen for simplicity to focus on a Fisher distribution but other possibilities including for example a disc boxcar averaging function are possible depending on the desired application.

We obtained stable and spatially coherent local estimates of both the MF and SV at the CMB. Using 2 yr of data it is possible to make stable SV maps at the CMB with averaging widths as small as 30°, a wavelength similar to a SH representation up to degree 12. The SV is thus known at this wavelength without regularization. Motivated by this we went a step further and determined the accumulated SA between two epochs by differencing the SV estimates for the epochs. The resulting maps of radial SA at the CMB were found to be in good agreement with the CHAOS-6-x7 field model truncated at degree 10. By varying the width of the spatial averaging kernel, and observing the change in the resulting maps and their variance estimates, we can directly appraise how well the accumulated SA is known, something that has up to now been difficult to assess in regularized field models. We carry out our SA estimates locally, so we are able to find the optimal spatial averaging width for a specific location and time window of interest, without worrying that the inversion might be unstable due to high amplitude noise in some other region. This enables us to study in detail rapid field changes in particular locations. Looking at time-longitude plots of the accumulated SA at the equator, we have explored the coherence of the accumulated SA as the width of the averaging kernel is decreased, and the time window is shortened. We find encouraging coherence at the equator down to an averaging width of 30°, and for accumulated SA within 1 yr based on 1 yr time windows for the SV. This may be a sign that we are unveiling a coherent underlying signal, albeit one that has more power on shorter wavelengths (see also Holme *et al.* 2011; Aubert 2018). Note that since no spectral truncation is carried out, higher spatial frequencies in our estimates may have a different appearance than that found in SH based models such as CHAOS-6 where temporal regularization is known to heavily influence the SA above SH degree 9so the SA is often analysed by truncating or filtering above this degree (e.g. Chulliat *et al.* 2015; Finlay *et al.* 2016). As an example, considering the accumulated SA at the equator derived from 1 yr differences in the SV estimates, we find a distinctive 'cross-over' feature in mid 2007 at 25° West. This involves two adjacent and oppositely directed radial SA features that change sign within a year. Estimates of the accumulated SV made using longer time windows show a more gradual evolution, and perhaps westward motions, as a result of smearing between patches on either side of the cross over. The SA cross-over is more clearly seen for shorter time windows, confirming hints at its presence in models such as CHAOS-6 (Chulliat *et al.* 2015). The origin of such features, that may involve a rapid change in sign of the azimuthal core flow acceleration (Gillet *et al.* 2015) may reveal new aspects of core dynamics, so it is important that their characteristics are robustly determined. The method presented here is well suited to such investigations.

One shortcoming of the SOLA method at present is that it requires the solution of a linear system of size (number of data x number of data). For large numbers of data locations, as are available from satellite missions, this can becomes prohibitive, especially if one wishes to consider single satellite and inter-satellite sums and differences for each vector field component at each location. As the results presented here show, the problem is not insurmountable, particularly if one is only interested in field estimates within a short time window, or is willing to perform data decimation in order to obtain a data set with good spatial and temporal coverage. If we wish to push towards higher local resolution in space and time, it is clear that using data sets that are as large as possible can be an advantage. Despite this, the major source of error in the present determination of the core field is probably the incomplete separation of crustal and ionospheric signals. Since our method is based on a potential field formulation, it is unable to perform such a separation with data from satellite altitude alone; bias from incompletely separated non-core field sources cannot be excluded in the maps we have presented and is difficult to quantify. Including data from several altitudes will help, as will experiments carried out for different external field selection criteria.

Having established here the utility of the SOLA approach in geomagnetism, there are now a number of interesting possibilities for future applications. First, as the time-series collected by the *Swarm* mission lengthens, there will be more and more rapid field evolution events that can be studied in detail. The ability to appraise inferred core field features will be especially important as we seek to study the temporal evolution of small scale SA signals on shorter and shorter timescales, in an effort to understand the underlying geophysical processes. Moving further back in time, the method could be applied to data from other satellite missions such as DMSP (Alken *et al.* 2014) or Cryosat to try to fill the gap between the CHAMP and *Swarm* era. The method could be also be applied to ground observatory magnetic data; this would be of particular interest in regions such as Europe, North America and Australia where there is excellent coverage with ground-based observatories. This would provide an opportunity to study the local field evolution at high resolution and provide an important means of validating results obtained with satellite data. The method could also be applied to produce local estimates at locations other than the CMB, for example on a grid at mean satellite altitudes, as an alternative method of producing so-called virtual observatories (Mandea & Olsen 2006). Field estimates on regular grids with suitable averaging and variance information would certainly be well suited for data assimilation applications. Looking further afield, it may also be possible to apply the method in archeomagnetism and palaeomagnetism where the data coverage is even more sparse, and appraisal information would again be valuable. As an example, perhaps the SOLA method could be used to study what is happening at the CMB during archeomagnetic intensity spike events (Ben-Yosef *et al.* 2009; Shaar *et al.* 2016; Korte & Constable 2018), although this would require linearization approaches in order to deal with non-linear intensity and directional data (e.g. Snieder 1991). The

ability to study core field features directly from observations, independent of regularized spherical harmonic field models or other *a priori* constraints, seems to be attractive for a broad range of applications.

ACKNOWLEDGEMENTS

The authors would like to thank Nils Olsen for providing various Matlab tools including those to determine the CM4 ionospheric model predictions and the internal/external CHAOS-6-x7 model predictions. We wish to thank Kathy Whaler for helpful discussions on the Backus–Gilbert method. We would also like to thank Aslak Stubsgaard for helpful discussions regarding computational considerations. We thank the GFZ German Research Centre for Geoscience for providing access to the CHAMP MAG-L3 data and ESA for providing access to the *Swarm* L1b MAG-L data. High resolution 1-min OMNI data was provided by the Space Physics Data Facility (SPDF), NASA Goddard Space Flight Centre. The Lebedev integration was performed using a Matlab function by Parrish (2010). The exponential correlation model was build using the Matlab tool Synthetic_Variogram by T. Mejer-Hansen. This project was supported by the The Danish Council for Independent Research, Natural Sciences (grant DFF 4002-00366). The financial support is gratefully acknowledged.

REFERENCES

Alken, P., Maus, S., Lühr, H., Redmon, R., Rich, F., Bowman, B. & O'Malley, S., 2014. Geomagnetic main field modeling with DMSP, *J. geophys. Res.: Space Phys.,* **119**(5), 4010–4025.

Aubert, J., 2018. Geomagnetic acceleration and rapid hydromagnetic wave dynamics in advanced numerical simulations of the geodynamo, *Geophys. J. Int.,* **214**(1), 531–547.

Backus, G. & Gilbert, F., 1968. The resolving power of gross Earth data, *Geophys. J. Int.,* **16**(2), 169–205.

Backus, G. & Gilbert, F., 1970. Uniqueness in the inversion of inaccurate gross Earth data, *Phil. Trans. R. Soc. Lond., A: Math. Phys. Eng. Sci.,* **266**(1173), 123–192.

Backus, G., Parker, R. & Constable, C., 1996. *Foundations of Geomagnetism,* Cambridge Univ. Press.

Barton, G., 1989. *Elements of Green's Functions and Propagation: Potentials, Diffusion, and Waves,* Oxford Univ. Press.

Ben-Yosef, E., Tauxe, L., Levy, T.E., Shaar, R., Ron, H. & Najjar, M., 2009. Geomagnetic intensity spike recorded in high resolution slag deposit in Southern Jordan, *Earth planet. Sci. Lett.,* **287**(3), 529–539.

Bloxham, J., Gubbins, D. & Jackson, A., 1989. Geomagnetic secular variation, *Phil. Trans. R. Soc. Lond., A,* **329**(1606), 415–502.

Bouligand, C., Gillet, N., Jault, D., Schaeffer, N., Fournier, A. & Aubert, J., 2016. Frequency spectrum of the geomagnetic field harmonic coefficients from dynamo simulations, *Geophys. Suppl. Mon. Not. R. Astron. Soc.,* **207**(2), 1142–1157.

Chulliat, A. & Maus, S., 2014. Geomagnetic secular acceleration, jerks, and a localized standing wave at the core surface from 2000 to 2010, *J. geophys. Res.: Solid Earth,* **119**(3), 1531–1543.

Chulliat, A., Alken, P. & Maus, S., 2015. Fast equatorial waves propagating at the top of the Earth's core, *Geophys. Res. Lett.,* **42**(9), 3321–3329.

Constable, C. & Parker, R., 1988. Smoothing, splines and smoothing splines; their application in geomagnetism, *J. Comput. Phys.,* **78**(2), 493–508.

Constable, C.G., Parker, R.L. & Stark, P.B., 1993. Geomagnetic field models incorporating frozen-flux constraints, *Geophys. J. Int.,* **113**(2), 419–433.

Constable, C., 1988. Parameter estimation in non-Gaussian noise, *Geophys. J. Int.,* **94**(1), 131–142.

Finlay, C.C., Olsen, N., Kotsiaros, S., Gillet, N. & Tøffner-Clausen, L., 2016. Recent geomagnetic secular variation from Swarm and ground observatories as estimated in the CHAOS-6 geomagnetic field model, *Earth, Planets Space,* **68**(1), 1–18.

Fisher, R., 1953. Dispersion on a sphere, *Proc. R. Soc. Lond., A: Math., Phys. Eng. Sci.,* in , Vol. **217,** pp. 295–305, .

Gillet, N., Jault, D., Finlay, C. & Olsen, N., 2013. Stochastic modeling of the Earth's magnetic field: inversion for covariances over the observatory era, *Geochem., Geophys., Geosyst.,* **14**(4), 766–786.

Gillet, N., Jault, D. & Finlay, C., 2015. Planetary gyre, time-dependent eddies, torsional waves, and equatorial jets at the Earth's core surface, *J. geophysi. Res.: Solid Earth,* **120**(6), 3991–4013.

Gubbins, D. & Roberts, N., 1983. Use of the frozen flux approximation in the interpretation of archaeomagnetic and palaeomagnetic data, *Geophys. J. Int.,* **73**(3), 675–687.

Holme, R., Olsen, N. & Bairstow, F., 2011. Mapping geomagnetic secular variation at the core–mantle boundary, *Geophys. J. Int.,* **186**(2), 521–528.

Holschneider, M., Chambodut, A. & Mandea, M., 2003. From global to regional analysis of the magnetic field on the sphere using wavelet frames, *Phys. Earth planet. Inter.,* **135**(2-3), 107–124.

Holschneider, M., Lesur, V., Mauerberger, S. & Baerenzung, J., 2016. Correlation-based modeling and separation of geomagnetic field components, *J. geophys. Res.: Solid Earth,* **121**(5), 3142–3160.

Jackson, A., Constable, C., Walker, M. & Parker, R., 2007. Models of Earth's main magnetic field incorporating flux and radial vorticity constraints, *Geophys. J. Int.,* **171**(1), 133–144.

Korte, M. & Constable, C.G., 2018. Archeomagnetic intensity spikes: global or regional geomagnetic field features? *Front. Earth Sci.,* **6,** 17.

Kotsiaros, S., Finlay, C. & Olsen, N., 2015. Use of along-track magnetic field differences in lithospheric field modelling, *Geophys. J. Int.,* **200**(2), 878–887.

Langel, R.A., 1987. The main field, in *Geomagnetism,* Vol. **1,** pp. 249–512, ed. Jacobs, J.A., Academic Press.

Larsen, R.M. & Hansen, P.C., 1997. Efficient implementations of the SOLA mollifier method, *Astron. Astrophys. Suppl. Ser.,* **121**(3), 587–598.

Lebedev, V.I. & Laikov, D., 1999. A quadrature formula for the sphere of the 131st algebraic order of accuracy, in *Doklady. Mathematics,* Vol. **59,** pp. 477–481, MAIK Nauka/Interperiodica.

Lesur, V., Wardinski, I., Rother, M. & Mandea, M., 2008. Grimm: the GFZ Reference Internal Magnetic Model based on vector satellite and observatory data, *Geophys. J. Int.,* **173**(2), 382–394.

Lesur, V., Wardinski, I., Baerenzung, J. & Holschneider, M., 2017. On the frequency spectra of the core magnetic field Gauss coefficients, *Phys. Earth planet. Inter.*

Louis, A.K. & Maass, P., 1990. A mollifier method for linear operator equations of the first kind, *Inverse Problems,* **6**(3), 427.

Lowes, F. & Olsen, N., 2004. A more realistic estimate of the variances and systematic errors in spherical harmonic geomagnetic field models, *Geophys. J. Int.,* **157**(3), 1027–1044.

Mandea, M. & Olsen, N., 2006. A new approach to directly determine the secular variation from magnetic satellite observations, *Geophys. Res. Lett.,* **33**(15) .

Masters, G. & Gubbins, D., 2003. On the resolution of density within the Earth, *Phys. Earth planet. Inter.,* **140**(1), 159–167.

Nolet, G., 2008. *A Breviary of Seismic Tomography: Imaging the Interior of the Earth and Sun,* Cambridge Univ. Press.

Oldenburg, D.W., 1984. An introduction to linear inverse theory, *IEEE Trans. Geosci. Rem. Sens.,* **GE-22**(6), 665–674.

Olsen, N. *et al.*, 2015. The Swarm initial field model for the 2014 geomagnetic field, *Geophys. Res. Lett.,* **42**(4), 1092–1098.

Olsen, N. & Mandea, M., 2008. Rapidly changing flows in the Earth's core, *Nat. Geosci.,* **1**(6), 390.

Olsen, N., Mandea, M., Sabaka, T.J. & Tøffner-Clausen, L., 2009. CHAOS-2—a geomagnetic field model derived from one decade of continuous satellite data, *Geophys. J. Int.*

Olsen, N., Lühr, H., Finlay, C.C., Sabaka, T.J., Michaelis, I., Rauberg, J. & Tøffner-Clausen, L., 2014. The CHAOS-4 geomagnetic field model, *Geophys. J. Int.,* **197**(2), 815–827.

Olsen, N., Finlay, C.C., Kotsiaros, S. & Tøffner-Clausen, L., 2016. A model of Earth's magnetic field derived from 2 years of Swarm satellite constellation data, *Earth, Planets Space,* **68**(1), 124.

Parker, R.L. & Shure, L., 1982. Efficient modelling of the Earth's magnetic field with harmonic splines, *Geophys. Res. Lett.,* **9,** 812–815.

Parker, R.L., 1977. Understanding inverse theory, *Ann. Rev. Earth planet. Sci.,* **5**(1), 35–64.

Parker, R.L., 1994. *Geophysical Inverse Theory,* Princeton Univ. Press.

Parrish, R., 2010. Matlab code: getlebedevsphere.

Pijpers, F. & Thompson, M., 1992. Faster formulations of the optimally localized averages method for helioseismic inversions, *Astron. Astrophys.,* **262,** L33–L36.

Pijpers, F. & Thompson, M., 1994. The SOLA method for helioseismic inversion, *Astron. Astrophys.,* **281,** 231–240.

Plattner, A. & Simons, F.J., 2017. Internal and external potential-field estimation from regional vector data at varying satellite altitude, *Geophys. J. Int.,* **211**(1), 207–238.

Pujol, J.M., 2013. The Backus-Gilbert method and their minimum-norm solution, *Geophysics,* **78**(3), W9–W30.

Richmond, A., 1995. Ionospheric electrodynamics using magnetic apex coordinates., *J. Geomagnet. Geoelectr.,* **47**(2), 191–212.

Ritter, P., Lühr, H., Maus, S. & Viljanen, A., 2004. High-latitude ionospheric currents during very quiet times: their characteristics and predictability, *Ann. Geophys.*, **22,** 2001–2014.

Sabaka, T.J., Olsen, N. & Purucker, M.E., 2004. Extending comprehensive models of the Earth's magnetic field with Ørsted and CHAMP data, *Geophys. J. Int.,* **159**(2), 521–547.

Shaar, R., Tauxe, L., Ron, H., Ebert, Y., Zuckerman, S., Finkelstein, I. & Agnon, A., 2016. Large geomagnetic field anomalies revealed in Bronze to Iron Age archeomagnetic data from Tel Megiddo and Tel Hazor, Israel, *Earth planet. Sci. Lett.,* **442,** 173–185.

Shure, L., Parker, R.L. & Backus, G.E., 1982. Harmonic splines for geomagnetic modelling, *Phys. Earth planet. Inter.,* **28,** 215–229.

Snieder, R., 1991. An extension of Backus-Gilbert theory to nonlinear inverse problems, *Inverse Problems,* **7**(3), 409.

Tanimoto, T., 1985. The Backus-Gilbert approach to the three-dimensional structure in the upper mantle-I. Lateral variation of surface wave phase velocity with its error and resolution, *Geophys. J. Int.,* **82**(1), 105–123.

Whaler, K. & Gubbins, D., 1981. Spherical harmonic analysis of the geomagnetic field: an example of a linear inverse problem, *Geophys. J. Int.,* **65**(3), 645–693.

Whaler, K.A., 1984. Fluid upwelling at the core-mantle boundary—resolvability from surface geomagnetic data, *Geophys. J. Int.,* **78**(2), 453–473.

Zaroli, C., 2016. Global seismic tomography using Backus–Gilbert inversion, *Geophys. Suppl. Mon. Not. R. Astron. Soc.,* **207**(2), 876–888.

Geophysical Journal International

Geophys. J. Int. (2018) **215,** 695–712 doi: 10.1093/gji/ggy297
Advance Access publication 2018 July 23
GJI Geomagnetism, rock magnetism and paleomagnetism

Assimilation of ground and satellite magnetic measurements: inference of core surface magnetic and velocity field changes

O. Barrois,[1] M.D. Hammer,[2] C.C. Finlay,[2] Y. Martin[1] and N. Gillet[1]

[1]*Univ. Grenoble Alpes, CNRS, ISTerre, CS* 40700, F-38058 *Grenoble cedex* 9, *France. E-mail: oli.barrois@gmail.com*
[2]*Division of Geomagnetism, DTU Space, Technical University of Denmark, DK-2800 Lyngby, Denmark*

Accepted 2018 July 19. Received 2018 July 16; in original form 2018 March 13

SUMMARY

We jointly invert for magnetic and velocity fields at the core surface over the period 1997–2017, directly using ground-based observatory time-series and measurements from the CHAMP and *Swarm* satellites. Satellite data are reduced to the form of virtual observatory time-series distributed on a regular grid in space. Such a sequential storage helps incorporate voluminous modern magnetic data into a stochastic Kalman filter, whereby spatial constraints are incorporated based on a norm derived from statistics of a numerical geodynamo model. Our algorithm produces consistent solutions both in terms of the misfit to the data and the estimated posterior model uncertainties. We retrieve core flow features previously documented from the analysis of spherical harmonic field models, such as the eccentric anticyclonic gyre. We find enhanced diffusion patterns under both Indonesia and Africa. In contrast to a steady flow that is strong under the Atlantic hemisphere but very weak below the Pacific, interannual motions appear evenly distributed over the two hemispheres. Recovered interannual to decadal flow changes are predominantly symmetrical with respect to the equator outside the tangent cylinder. In contrast, under the Northern Pacific we find an intensification of a high latitude jet, but see no evidence for a corresponding feature in the Southern hemisphere. The largest flow accelerations that we isolate over the studied era are associated with meanders, attached to the equatorward meridional branch of the planetary gyre in the Eastern hemisphere, that are linked to the appearance of an eastward equatorial jet below the Western Pacific.

Key words: Core; Magnetic field variations through time; Inverse theory; Probabilistic forecasting.

1 INTRODUCTION

Inferring information on the motions of the liquid outer core of the Earth requires properly separating the numerous sources of observed magnetic fields (geodynamo, crustal magnetization, ionospheric and magnetospheric currents and their Earth induced counterparts). To circumvent some of the leakage issues, magnetic field models are often built using regularizations, to ensure spectral convergence of the core field and its time variations. This prevents a proper assessment of *a posteriori* errors on model coefficients. When these are used as data in reconstructions of the core dynamics, it can lead to biased estimates. Furthermore, by proceeding in successive steps (to a field model and then on to the core flow), one loses information.

From the early 1990s alternative avenues of research arose, through which field models were built under topological constraints derived from physical insights. Constable *et al.* (1993) and O'Brien *et al.* (1997) proposed algorithms to apply, on single epoch pairs of models, magnetic flux conservation conditions at the core–mantle boundary (CMB) that are appropriate assuming that magnetic diffusion is negligible. Along the same lines, Jackson *et al.* (2007) added a constraint on the radial vorticity. They showed that it was possible for a magnetic model to satisfy both these topological conditions, and the constraint from magnetic observations, from the late 19th century onwards.

Conversely, Chulliat & Olsen (2010) tested the validity of the frozen flux hypothesis using data from Magsat, Oersted and CHAMP satellite missions. They found an increase of the data misfit in some areas, potentially suggesting local failures of the constraint. Such studies motivated the coestimation, from magnetic observations, of both the field and the flow, imposing with a weak formalism the frozen flux radial induction equation at the CMB (Lesur *et al.* 2010; Wardinski & Lesur 2012). They concluded that the frozen flux constraint remained compatible with ground-based and satellite magnetic records. Pursuing an alternative approach, Beggan & Whaler (2009) and Whaler & Beggan (2015) obtained piecewise constant or linear flow models directly from magnetic data (see also Whaler *et al.* 2016).

One limitation though of such approaches is related to the uncertainties associated with the large-scale induction equation itself (and associated null-flux curves), assuming models truncated at spherical harmonic degree $n \simeq 13$ (Gillet *et al.* 2009). Subgrid-scale effects arising due to the nonlinear induction process (e.g. Eymin & Hulot 2005; Pais & Jault 2008; Gillet *et al.* 2009; Baerenzung *et al.* 2016) turn out to be the main source of uncertainty in the recovery of core surface flows from modern geomagnetic records. Barrois *et al.* (2017)—hereafter referred as BGA17—illustrate how ignoring their impact leads to severely biased flow models (see also Baerenzung *et al.* 2017, on the reliability of core flow reconstructions).

BGA17 furthermore show from the analysis of geodynamo simulations that magnetic diffusion at the core surface, enslaved to poloidal flow below the CMB, affects the recorded field changes at all timescales including rapid changes. This may seem at odds with the often used assumption of negligible magnetic diffusion that follows the argument of a high magnetic Reynolds number for large-scale motions in the core (see Holme 2015).

In the present work we invert, from magnetic field observations collected at and above the Earth's surface, for both the magnetic and velocity fields at the core surface, taking into account both magnetic diffusion and subgrid induction. We merge spatial information provided by numerical simulations, specifically from the Coupled Earth dynamo (CED) model (Aubert *et al.* 2013) and temporal constraints coming from a restriction of the field evolution to a chosen class of stochastic process. The sequential algorithm of BGA17, which considers as input data time-series of spherical harmonic coefficients of the main field, is extended to account for both virtual observatory (Mandea & Olsen 2006) and ground observatory time-series that cover the period 1997–2017. Our approach has similarities with the previous works of Gillet *et al.* (2015a) and Baerenzung *et al.* (2016), which favoured flat flow spatial spectra at the CMB, since the spatial dynamo norm employed here departs from the norms often employed to ensure spectral convergence. In addition, our stochastic framework allows us to discuss posterior model errors for both the flow and the magnetic field.

The paper is organized as follows. In Section2 we describe the ground-based observatory data and satellite-based virtual observatory data, and the methodology we follow to recover magnetic and velocity fields at the CMB. In Section3.1, we present our resulting geomagnetic model and its associated uncertainties, before we analyse in Section 3.2 our core flow solutions. Finally, implications for our understanding of the core dynamics and possible further improvements for the algorithm are given in Section4.

2 METHODOLOGY

2.1 Ground-based and virtual observatory data

2.1.1 Ground observatory data

We use magnetic measurements made at 186 ground observatories (GOs) covering the period 1997–2017. Hourly mean values are taken from the BGS database[1], version 0111, using Intermagnet and WDC Edinburgh data as available in May 2017. The data have been checked and corrected for known baseline jumps (Macmillan & Olsen 2013). 'Revised monthly means' were then derived from these hourly means, following the procedure described by Olsen *et al.* (2014). Briefly, predictions of the large-scale magnetospheric field (and the associated induced field) from the CHAOS-6 field model, as well as predictions for the ionospheric Sq field (and the associated induced field) from the CM4 model (Sabaka *et al.* 2004) are subtracted from the hourly mean values, and then robust (Huber-weighted) monthly mean values are computed using an iterative-reweighting procedure. Annual differences of such revised monthly means are routinely used in deriving the CHAOS series of field models and in order to study high resolution secular variation since, compared with simple monthly means, they are less contaminated by external field effects. Here, since we also wish to use the field itself for model construction, the median difference between each series and CHAOS-6 predictions was removed, in order to account in a simple way for the bias due to unmodelled crustal fields. In order to obtain the same sampling rate as that adopted for the virtual observatory series described below, the revised monthly mean series were finally averaged over 4 months windows to obtain the GO series used in our data assimilation scheme.

2.1.2 Virtual observatory data

In addition to GO data, we make use of satellite measurements from the CHAMP and *Swarm* missions covering respectively 2000–2010 and 2014–2017, through so-called virtual observatory (VO) data (Mandea & Olsen 2006; Olsen & Mandea 2007). These provide a regular spatial and temporal sampling of the global field, convenient for our Kalman filter algorithm (detailed in Section 2.2) and involve estimates from an easily manageable number of locations, which has computational advantages.

VO data were computed using measurements collected by the CHAMP vector field magnetometer between July 2000 and September 2010 and from the *Swarm* vector field magnetometers, onboard all three satellites (*Alpha*, *Bravo*, *Charlie*), between January 2014 and April 2017. Starting from the CHAMP MAG-L3 and *Swarm* Level 1b MAG-L, version 0501, data products, we subsampled at 15 s intervals the data in the vector field magnetometer (VFM) frame. Using the Euler rotation angles as given by the CHAOS-6-x3 model (which was based on *Swarm* and ground observation data up until April 2017[2]), we rotated the VFM data into an Earth-Centered Earth-Fixed (ECEF) coordinate frame.

Measurements from known problematic days were removed, for instance where satellite manoeuvres happened. Furthermore, gross data outliers with deviations more than 500 nT from CHAOS-6-x3 field model predictions were rejected. Based on previous studies of VO estimates (e.g. Beggan *et al.* 2009), we then employed data selection criteria retaining only data for which:

(1) the sun was at maximum 10° above horizon;
(2) geomagnetic activity index $K_p < 3°$;
(3) the RC disturbance index (Olsen *et al.* 2014) had $|\mathrm{dRC/dt}| < 3$ nT hr^{-1};
(4) merging electric field at the magnetopause $E_m \leq 0.8$ mV m^{-1}, with $E_m = 0.33 v^{4/3} B_t^{2/3} \sin(|\Theta|/2)$. v is the solar wind speed, $\Theta = \arctan(B_y/B_z)$ and $B_t = \sqrt{B_y^2 + B_z^2}$. B_y and B_z are components of the interplanetary magnetic field (IMF) in the geocentric solar magnetospheric (GSM) coordinate system, calculated using 2

[1] ftp://ftp.nerc-murchison.ac.uk/geomag/Swarm/AUX_OBS

[2] http://www.spacecenter.dk/files/magnetic-models/CHAOS-6/

hourly means of 1 min values of the IMF and solar wind extracted from the OMNI database[3];

(5) IMF $B_z > 0$ nT and IMF $|B_y| < 10$ nT, again based on 2 hourly mean of 1 min values.

Following this data selection, estimates of the fields due to various unmodelled sources were next removed from the data:

(1) the magnetospheric and its induced fields as given by the CHAOS-6-x3 model;

(2) the ionospheric and its induced fields as given by the CM4 model (Sabaka *et al.* 2004);

(3) the static internal field for spherical harmonic degrees $n > 20$ given by the CHAOS-6-x3 model.

Although imperfect, in our opinion it is more consistent to remove such estimates rather to ignore known field sources.

Based on this data we then carried robust inversions for time-averaged point estimates (i.e. VOs) using data windows of 4 months width (60 d each side of an epoch t_j). In order to aid the robust inversion procedure in identifying and downweighting outliers, following Olsen & Mandea (2007) as a pre-processing step, we also removed a time-dependent internal field, here taken from the CHAOS-6-x3 model (Finlay *et al.* 2016b), for spherical harmonic degrees 1 to 20, within each four month window. The CHAOS-6x-3 prediction at the target point and time was then added back at the end of the analysis. Note that this does not prevent our 4-monthly VO series, and the derived SV series from departing from CHAOS-6x-3; information about the time-dependence within each 4 month window is however lost.

We assume that the residual field $\tilde{\mathbf{B}}$, after the removal of the time-dependent internal field from the CHAOS-6-x3, can be represented as the gradient of a scalar potential V, that is,

$$\tilde{\mathbf{B}} = -\nabla V. \tag{1}$$

The residual field and associated positions are transformed into a local Cartesian coordinate system with origin at the VO points of interest, with x pointing towards geographic south, y pointing towards east and z pointing upwards. We use an expansion of the local potential up to cubic terms. Because the geomagnetic field is irrotational ($\nabla \times \tilde{\mathbf{B}} = 0$) and solenoidal ($\nabla \cdot \tilde{\mathbf{B}} = 0$), this local potential is entirely determined by 15 independent parameters:

$$\begin{aligned} V(x,y,z) = {} & v_x x + v_y y + v_z z + v_{xx}x^2 + v_{yy}y^2 - (v_{xx}+v_{yy})z^2 \\ & + 2v_{xy}xy + 2v_{xz}xz + 2v_{yz}yz - (v_{xyy}+v_{xzz})x^3 \\ & + 3v_{xxy}x^2y + 3v_{xxz}x^2z + 3v_{xyy}xy^2 + 3v_{xzz}xz^2 \\ & + 6v_{xyz}xyz - (v_{xxy}-v_{yzz})y^3 + 3v_{yyz}y^2z \\ & + 3v_{yzz}yz^2 - (v_{xxz}+v_{yyz})z^3. \end{aligned} \tag{2}$$

For each VO position vector $\mathbf{r}_k = (\theta_k, \phi_k, r_k)$ and at epoch t_j, all data positioned within a cylinder of radius 850km ($\approx 7.5^\circ$) of the VO target $\mathbf{r}_k$, and within 60 days either side of t_j were used to build a local data vector $\mathbf{d}^{k,j}$. These data are then related to the 15 parameters defining the VO potential model $\mathbf{m}_{vo}^{k,j}$ at that site and epoch via $\mathbf{d}^{k,j} = \underline{\underline{\mathbf{g}}}^{k,j}\mathbf{m}_{vo}^{k,j}$, where the elements of the matrix $\underline{\underline{\mathbf{g}}}^{k,j}$ are determined from eqs (1) and (2).

Rather than working directly with $\mathbf{d}^{k,j}$ in deriving $\mathbf{m}_{vo}^{k,j}$ we make use of along-track (AT) and east–west (using *Swarm Alpha* and *Charlie* only) sums and differences of the magnetic field components. An advantage of using field differences is that these have a reduced sensitivity to large-scale external signals, although data sums also need to be included in order to ensure sufficient information on the longer wavelengths core field. Using sums and differences has been found advantageous in a number of other field modelling efforts (Olsen *et al.* 2015; Sabaka *et al.* 2015). We calculate AT sums (Σ) and differences (Δ) as

$$\begin{cases} \Sigma d_i^{\mathrm{AT}} = [\tilde{B}_i(\mathbf{r},t) + \tilde{B}_i(\mathbf{r}+\delta\mathbf{r}, t+15\,\mathrm{s})]/2 \\ \Delta d_i^{\mathrm{AT}} = [\tilde{B}_i(\mathbf{r},t) - \tilde{B}_i(\mathbf{r}+\delta\mathbf{r}, t+15\,\mathrm{s})] \end{cases}. \tag{3}$$

$\tilde{B}_i = \mathbf{1}_i \cdot \tilde{\mathbf{B}}(\mathbf{r})$ are the residual magnetic field components in spherical polar coordinates (where $i = r, \theta$ or ϕ, and $\mathbf{1}_\mathbf{i}$ are unit vectors). The east–west cross-track (CT) sums and differences between are calculated as

$$\begin{cases} \Sigma d_i^{\mathrm{CT}} = [\tilde{B}_i^{\mathrm{Alpha}}(\mathbf{r}_1,t_1) + \tilde{B}_i^{\mathrm{Charlie}}(\mathbf{r}_2,t_2)]/2 \\ \Delta d_i^{\mathrm{CT}} = [\tilde{B}_i^{\mathrm{Alpha}}(\mathbf{r}_1,t_1) - \tilde{B}_i^{\mathrm{Charlie}}(\mathbf{r}_2,t_2)] \end{cases}. \tag{4}$$

Here, for a given orbit of *Alpha* we select the corresponding *Charlie* data to be the one closest in colatitude such that $|\delta t| = |t_1 - t_2| < 50$ s. Crucially, in order to relate these sums and differences to the VO model parameters, we also take sums and differences of the elements of the design matrices $\underline{\underline{\mathbf{g}}}^{k,j}$ associated with the predictions of the VO model for the field components at the individual data locations. This results in a design matrix

$$\underline{\underline{\mathbf{G}}}^{k,j} = \begin{bmatrix} \underline{\underline{\Sigma\mathbf{g}}}^{k,j} \\ \underline{\underline{\Delta\mathbf{g}}}^{k,j} \end{bmatrix} \tag{5}$$

associated with the data vector $\mathbf{D}^{k,j} = \left[\Sigma\mathbf{d}^{k,j} \;\; \Delta\mathbf{d}^{k,j}\right]^T$. In this way we fully account for the change in the unit vectors associated with the two locations contributing to the sums and differences when deriving the parameters $\mathbf{m}_{vo}^{k,j}$. The inversion for each $\mathbf{m}_{vo}^{k,j}$ is carried out via a robust Huber weighted least-squares fit

$$\mathbf{m}_{vo}^{k,j} = \left[(\underline{\underline{\mathbf{G}}}^{k,j})^T\mathbf{W}\underline{\underline{\mathbf{G}}}^{k,j}\right]^{-1}(\underline{\underline{\mathbf{G}}}^{k,j})^T\mathbf{D}^{k,j} \tag{6}$$

where $\mathbf{W}$ is a diagonal vector of Huber weights that ensure a robust solution (Olsen 2002; Sabaka *et al.* 2004) and are iteratively updated until convergence. Once $\mathbf{m}_{vo}^{k,j}$ is determined, the three field components at the site and epoch of interest, $\tilde{\mathbf{B}}_k(\mathbf{r}_k, t_j) = -\nabla V_k(\mathbf{r}_k, t_j)$, are computed and added back on to the CHAOS-6-x3 prediction for the internal field (for degrees 1–14 only, to avoid as far as possible the lithospheric field) at the target location.

We constructed VO estimates at $P_{\mathrm{VO}} = 200$ locations, with a spacing of about 1600 km ($\approx 14^\circ$, see dots in Fig. 1), located in an approximately equal area grid based on the spherical surface partition algorithm of Leopardi (2006). The altitude of the VOs are 300 and 500 km during the CHAMP and *Swarm* periods, respectively. Using predictions of the three components (B_r, B_θ, B_ϕ) of the magnetic field at P_{VO} locations, we finally obtain $3P_{\mathrm{VO}}$ time-series (i.e. one point every 4 months during CHAMP and Swarm times, 48 epochs in all), stored in a vector $\mathbf{y}_{\mathrm{VO}}(t)$. The SV was computed as annual differences of the 4 month time-series.

2.1.3 *Uncertainty estimates for the GO and VO series*

In order to obtain as much information as possible from the GO and VO data, while at the same time seeking to avoid overfitting them, it is important that appropriate uncertainty estimates are specified for each time-series. We define $\mathbf{C}_{\mathrm{GO}}$ and $\mathbf{C}_{\mathrm{VO}}$ to be the measurement error cross-covariance matrices for GO and VO data at each epoch,

[3] http://omniweb.gsfc.nasa.gov

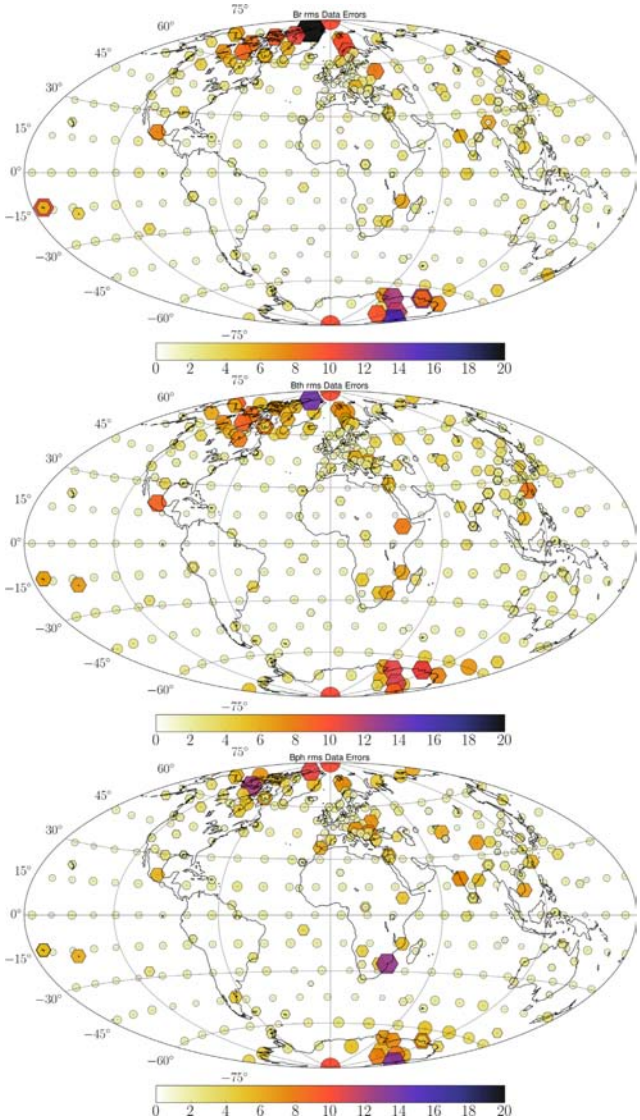

Figure 1. SV observation error estimates (colour scale in nT yr^{-1}) at all location where GOs (hexagons) and VOs (circles) are used in this study, for the three components $\dot{B}_r$, $\dot{B}_\theta$ and $\dot{B}_\phi$ (from top to bottom). The size of the markers is proportional to the magnitude of the *a priori* error estimates.

of sizes respectively $3P_{GO} \times 3P_{GO}$ and $3P_{VO} \times 3P_{VO}$. Data errors are supposed to be independent of time. Different data uncertainties are assigned for the VO's derived from CHAMP and *Swarm* respectively.

Regarding the GO time-series described above, we follow a similar approach to that used in CHAOS field model series (Olsen *et al.* 2014; Finlay *et al.* 2016b) and derive uncertainty estimates as follows. A 3×3 covariance matrix was computed for each observatory location from the time-series of the three components, after removing the predictions of the CHAOS-6 field model and detrending. The square roots of the diagonal elements of these covariance matrices were taken to be the uncertainty estimates for each component at each observatory. The same procedure was applied to both the MF and SV series.

For consistency, a very similar procedure was also applied to the VO series in order to obtain their uncertainty estimates. For each VO location, covariances were calculated between the time-series of the three components (after removing from each series the predictions of the CHAOS-6 model and de-trending), in order to obtain a 3×3 covariance matrix. A robust procedure for calculating the covariances (using the Minimum Covariance Determinant estimator, Verboven & Hubert 2005) was employed. However, only the square roots of the diagonal elements of the covariance matrices were taken to be the uncertainty estimates for each series, with similar procedures applied to both MF and SV series. To illustrate the range of the adopted uncertainty estimates, we show in Fig.1 the r.m.s. SV uncertainty estimates for all locations where data (GO or VO) are used in this study.

Note that by using only the diagonal elements of $\mathbf{C}_{GO}$ and $\mathbf{C}_{VO}$ we effectively consider the errors on each GO and VO series to be uncorrelated with the errors on other series. In reality errors between components and between series will be correlated. This can be taken into account using full (i.e. dense) covariance matrices. It is however challenging to estimate cross-covariances for matrices of size larger than the length of the contributing times series (consisting of one sample every 4 months). We therefore postpone this step to future studies. Instead, by restricting to only 200 VO locations and ensuring that there was little overlap between the VO search radii we reduce as far as possible the correlations between distinct VO series.

Finally, we concatenate the above GO and VO main field data vectors for each epoch into $\mathbf{y}^o(t) = [\mathbf{y}_{VO}^T \, \mathbf{y}_{GO}^T]^T$. The associated observation errors covariance matrix $\mathbf{R}_{y^o}$, of rank $P = 3P_{VO} + 3P_{GO}$, is thus derived from the diagonals of $\mathbf{C}_{VO}$ and $\mathbf{C}_{GO}$. In the next section we will consider both main field and secular variation data. SV data $\dot{\mathbf{y}}^o(t)$ are computed as annual differences of the four monthly (GO or VO) series. We follow the same approach as above to estimate the SV data errors variances (shown in Fig. 1) that are stored in a diagonal matrix $\mathbf{R}_{\dot{y}^o}$ of rank P.

2.2 Reanalysis of GO and VO data ground and satellite magnetic observations

The assimilation algorithm used in this study is essentially the one derived by BGA17 (see their table 2 for a summary). It is a sequential tool, consisting of a succession of forecast and analysis steps. The main modifications concern the direct integration of observations at and above the Earth's surface, while BGA17 considered data in the form of MF and SV spherical harmonic coefficients. We begin by recalling the main points of our stochastic forecast model, before we go on to describe the changes implemented in the present study regarding the analysis step. These essentially concern the observation operator linking the state variables to the observations.

2.2.1 Stochastic forecast model

We forecast the evolution of the radial magnetic field, B_r, at the CMB using the radial component of the induction equation, written as

$$\frac{\partial \overline{B}_r}{\partial t} = -\overline{\nabla_h \cdot \left(\boldsymbol{u}_H \overline{B}_r\right)} + e_r + d_r(\boldsymbol{u}_H, \overline{B}_r)\,, \tag{7}$$

where overlines mean the projection onto large length-scales. e_r stands for the subgrid induction processes arising due to the unresolved magnetic field at small length-scales, $\boldsymbol{u}_H$ is the horizontal flow, and d_r, enslaved to $\overline{B}_r$ and $\boldsymbol{u}_H$, approximates the radial component of the diffusion operator (see below). The evolutions of e_r and $\boldsymbol{u}_H$ are governed by order one autoregressive stochastic processes,

$$\frac{\mathrm{d}e_r}{\mathrm{d}t} + \frac{e_r}{\tau_e} = \zeta_e\,, \tag{8}$$

$$\frac{\mathrm{d}\boldsymbol{u}_H}{\mathrm{d}t} + \frac{(\boldsymbol{u}_H - \hat{\boldsymbol{u}}_H)}{\tau_u} = \zeta_u\,, \tag{9}$$

with ζ_e and ζ_u white noise processes, and $\hat{\boldsymbol{u}}_H$ the background flow model (obtained as the time-averaged flow from the CED model). These processes come from the same family of process as employed by Baerenzung *et al.* (2017). For each process, an effective restoring force is implemented via single time scales that we respectively fix as $\tau_e = 10$ yr and $\tau_u = 30$ yr. Spatial cross-covariances of the two above fields are derived from statistics of a free run of the CED (Aubert *et al.* 2013).

The advected fields e_r, $\boldsymbol{u}_H$, $\overline{B}_r$ and d_r are represented through spherical harmonics, whose coefficients are stored in vectors $\mathbf{e}(t)$, $\mathbf{u}(t)$, $\mathbf{b}(t)$ and $\mathbf{d}(t)$, respectively. Diffusion in eq. (7), and its dependence on e_r and $\mathbf{u}_H$, is also an expression of cross-covariances extracted from the CED (involving the radial magnetic field below the CMB). The projection onto large length-scales is processed in the spectral domain, restricting the induction equation (and thus the expansion of the fields e_r, $\overline{B}_r$ and d_r) to spherical harmonic degrees $n \leq n_b = 14$, while the velocity field is truncated at $n_u = 18$. We write as $\dot{\mathbf{b}}(t)$ the vector of SV spherical harmonic coefficients.

2.2.2 Integrating ground and satellite data in the assimilation tool

We write as $\mathbf{M}$ the operator that links the vector $\mathbf{b}(t)$ to the three components main field observations $\mathbf{y}(t)$ in the spatial domain (e.g. Olsen *et al.* 2010):

$$\mathbf{y}(t) = \mathbf{M}\mathbf{b}(t). \tag{10}$$

At each epoch it is of size $n_o \times n_b(n_b + 2)$, with $n_o = 3(P_{VO} + P_{GO})$ the size of the observation vector. The matrix $\mathbf{M}$ is composed of submatrices $\mathbf{M}_r$, $\mathbf{M}_\theta$ and $\mathbf{M}_\phi$, depending on the considered component of the magnetic field. In practice, elements of the matrix are, for a column j corresponding to a coefficient $g_{n_j}^{m_j}$, and a line i to an observation at a coordinate $\mathbf{r}_i = (r_i, \theta_i, \phi_i)$,

$$\mathbf{M}_{ri,j} = (n_j + 1)\left(\frac{a^\oplus}{r_i}\right)^{n_j+2} \mathscr{P}_n^m(\theta_i)\cos(m_j\phi_i)\,, \tag{11}$$

$$\mathbf{M}_{\theta i,j} = \left(\frac{a^\oplus}{r_i}\right)^{n_j+2} \frac{\mathrm{d}\mathscr{P}_n^m(\theta_i)}{\mathrm{d}\theta}\cos(m_j\phi_i)\,, \tag{12}$$

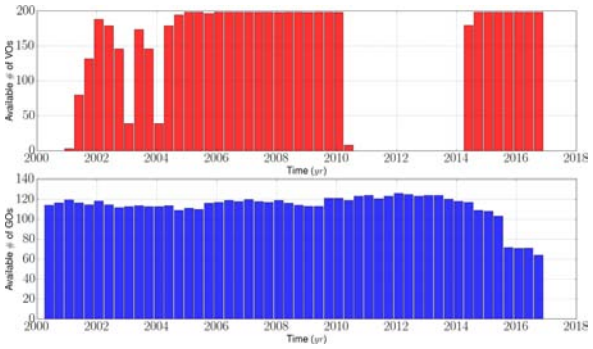

Figure 2. Time evolution of the number of SV data points (VOs in red, GOs in blue).

$$\mathbf{M}_{\phi i,j} = \left(\frac{a^{\oplus}}{r_i}\right)^{n_j+2} \frac{m_j \mathscr{P}_n^m(\theta_i)}{\sin(\theta_i)} (-1)\sin(m_j\phi_i). \tag{13}$$

For a line j corresponding to a coefficient $h_{n_j}^{m_j}$, the function sin replaces cos in eqs (11) and (12), and cos replaces (-1)sin in (13). $a^{\oplus} = 6371.2$ km is the Earth's spherical reference radius and $\mathscr{P}_n^m$ are the Legendre polynomials.

The analysis in the Kalman filter algorithm employed by BGA17 consists of two steps: first an analysis of the vector **b** containing MF spherical harmonic coefficients from MF spherical harmonic coefficients data, and second an analysis of the vector **z** (that concatenates **u** and **e**) from SV spherical harmonic coefficients data. Writing as $\mathbf{P}_{bb}^f$ the forecast model covariance matrix for **b**, the first analysis (eq. 19 of BGA17) is replaced here by

$$\forall k \in [1, N_m],\ \mathbf{b}^{ka}(t_a) = \mathbf{b}^{kf}(t_a) + \mathbf{P}_{bb}^f \mathbf{M}^T \left[\mathbf{M}\mathbf{P}_{bb}^f \mathbf{M}^T + \mathbf{R}_{yy}\right]^{-1} \left(\mathbf{y}^{ko}(t_a) - \mathbf{M}\mathbf{b}^{kf}(t_a)\right), \tag{14}$$

with t_a the analysis epoch and the superscript k referring to the kth realization within an ensemble chosen to be of size $N_m = 50$. Writing as $\mathbf{P}_{zz}^f$ the forecast model covariance matrix for **z**, the second analysis (eq. 20 of BGA17) is replaced here by

$$\forall k \in [1, N_m],\ \mathbf{z}^{ka}(t_a) = \mathbf{z}^{kf}(t_a) + \mathbf{P}_{zz}^f \mathbf{G}^{kT} \left[\mathbf{G}^k \mathbf{P}_{zz}^f \mathbf{G}^{kT} + \mathbf{R}_{\dot{y}\dot{y}}\right]^{-1} \left(\delta\dot{\mathbf{y}}^{ko}(t_a) - \mathbf{G}^k \mathbf{z}^{kf}(t_a)\right), \tag{15}$$

where the new observation operator is $\mathbf{G}^k = \mathbf{M}\mathbf{H}(\mathbf{b}^{ka})$, with **H** as defined in BGA17. Here $\delta\dot{\mathbf{y}}^{ko}(t_a) = \dot{\mathbf{y}}^{ko}(t_a) - \mathbf{M}\mathbf{d}^{kf}(t_a)$ are the direct SV observations corrected by the forecast contribution from diffusion to the radial induction equation. This latter is sought iteratively at each analysis step, as in BGA17. Note that we consider an ensemble of observations $\mathbf{y}^o$ and $\dot{\mathbf{y}}^o$, which are perturbed by random noise according to respectively $\mathbf{R}_{yy}$ and $\mathbf{R}_{\dot{y}\dot{y}}$. We recall that we consider in eqs (14) and (15) forecast covariance matrices $\mathbf{P}_{zz}$ and $\mathbf{P}_{bb}^f$ that are frozen throughout the reanalysis period. These are derived directly from the CED cross-covariances on **b**, **u** and **e** spherical harmonic coefficients, involving scaling pre-factors obtained analytically from the stochastic model presented in Section2.2.1 (see BGA17 for details). For comparison, Baerenzung *et al.* (2017) employ a full implementation of the Ensemble Kalman filter (Evensen 2003), that is, they update the cross-covariances at each analysis step, requiring many more realizations to obtain well-conditioned matrices.

Finally, an extra complexity arises because the number of observation sites changes over time. Indeed, because of the selection criteria, the number of satellite data available may not always be sufficient to make a reliable VO estimate. Under these conditions the VO data point is considered to be absent: the associated elements of the data vector $\mathbf{y}^o(t)$ at a given time t are removed, together with the corresponding lines and columns of $\mathbf{R}_{yy}$, and the corresponding lines of the matrix **M** (and thus **G**). This procedure is performed during each analysis. Thus, the size P of the data vector changes through time, reflecting the changing number of available satellite observations through time (see Fig. 2).

To summarize, in this study we work with predictions made by spherical harmonic coefficients that are projected in physical space, where they are adjusted during the analysis step according to the observations and the covariance matrices. As such, our algorithm is still based almost entirely on the spectral domain; only the analysis steps are performed in physical space, in order to match the observed magnetic field data. Note that we corrected for two mistakes in the implementation of the algorithm by BGA17: a sign error in the background flow $\hat{\mathbf{u}}$, and off-diagonal elements of the covariance matrix for **e** were non-intentionally ignored. Performing comparisons between reanalyses before and after correction, we found two consequences: a reduction of the dispersion within the ensemble of realizations, and a (almost stationary) shift in the analysed diffusion for some coefficients (including the axial dipole, see Section3.1.2). This latter is almost entirely compensated by a shift in the analysed e_r, with minor impact on the recovered flow. Otherwise, the qualitative conclusions of BGA17 remain unaltered.

2.3 Posterior diagnostics

We now define several diagnostics used to evaluate the quality and the consistency of our results. We shall compare a quantity $\boldsymbol{x}$ (MF, SV, subgrid error, diffusion... in the spatial or spectral domain) with observations $\boldsymbol{x}^o$ (when available), or with the same quantities $\boldsymbol{x}^c$ from the CHAOS-6 geomagnetic model (Finlay *et al.* 2016b). We define its time average

$$\hat{\boldsymbol{x}} = \frac{1}{t_f - t_i} \int_{t_i}^{t_f} \boldsymbol{x}(t)\mathrm{d}t\,, \tag{16}$$

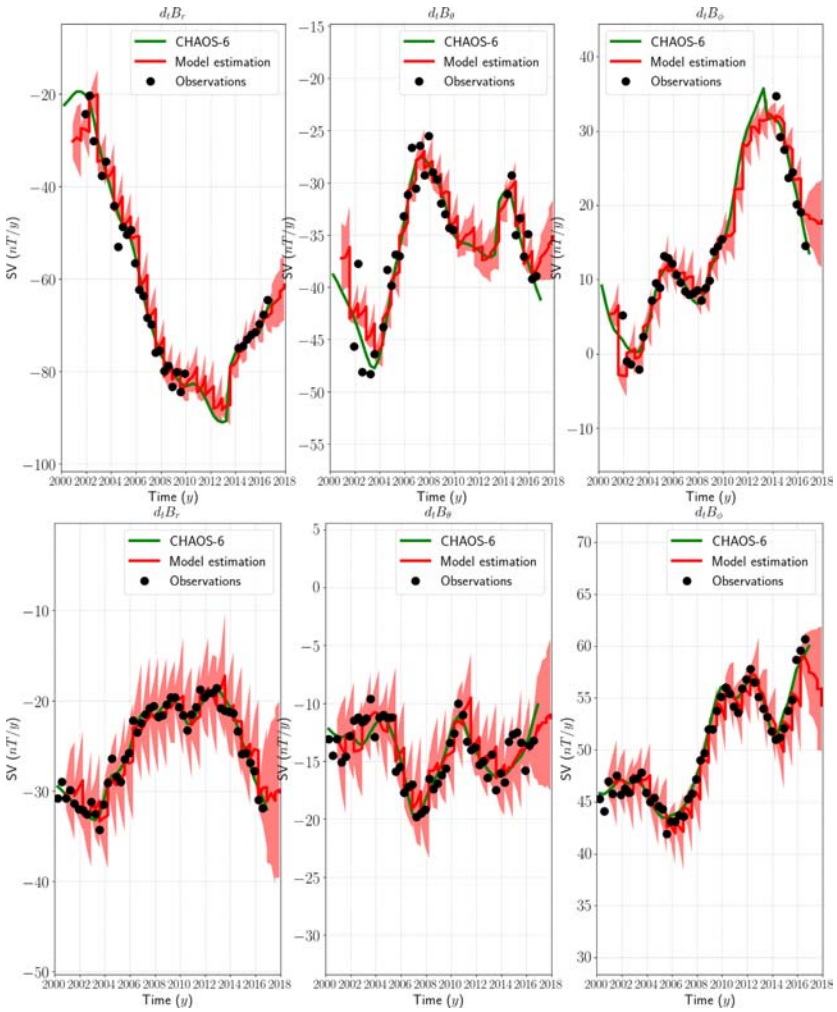

Figure 3. SV time-series for the three components ($\mathrm{d}B_r/\mathrm{d}t$, $\mathrm{d}B_\theta/\mathrm{d}t$, $\mathrm{d}B_\phi/\mathrm{d}t$), at one VO location $\{r = 6671\,\mathrm{km},\ \theta = 90^\circ,\ \phi = 88,\ 8^\circ\}$ (top), and at Chambon-la-forêt $\{r = 6366\,\mathrm{km},\ \theta = 42^\circ,\ \phi = 2^\circ\}$ (bottom). SV observations are shown in black, CHAOS-6 predictions in green and predictions from our analysis in red. The shaded area correspond to $\pm\sigma_b$, see eq. (18).

with t_i and t_f the initial and final epochs, its ensemble mean

$$\langle \boldsymbol{x}(t) \rangle = \frac{1}{N_m} \sum_{k=1}^{N_m} \boldsymbol{x}^k(t)\,, \tag{17}$$

the dispersion within the ensemble

$$\boldsymbol{\sigma}_x(t) = \sqrt{\frac{1}{N_m - 1} \sum_{k=1}^{N_m} \left(\boldsymbol{x}^k(t) - \langle \boldsymbol{x}(t) \rangle\right)^2}\,, \tag{18}$$

and finally the bias between our ensemble mean model and the reference $\boldsymbol{x}^c$,

$$\boldsymbol{\delta}_x(t) = \boldsymbol{x}^c - \langle \boldsymbol{x}(t) \rangle\,. \tag{19}$$

We also define spatial power spectra of any magnetic trajectory $\mathbf{b}(t)$ as

$$\mathcal{R}_b(n, t) = (n+1) \left(\frac{a^\oplus}{c}\right)^{2n+4} \sum_{m=0}^{n} \left[g_n^m(t)^2 + h_n^m(t)^2\right]\,, \tag{20}$$

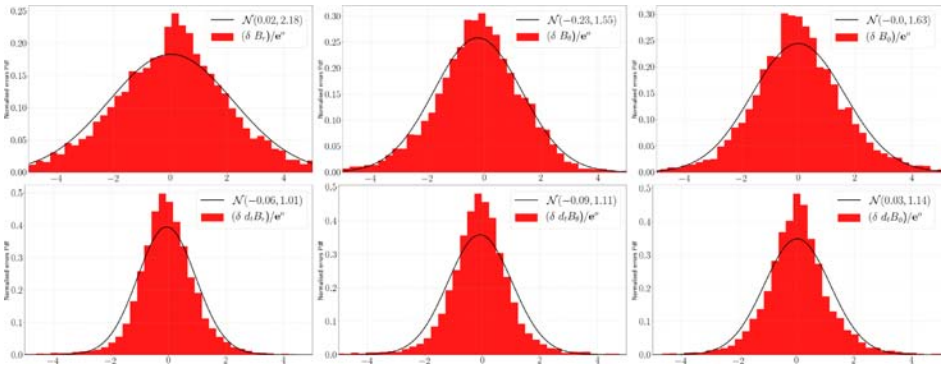

Figure 4. Top: histograms of MF prediction errors δ_{MF} (eq. 19), accumulated over all analysis epochs, normalized to the observation errors, for the components B_r (left), B_θ (middle) and B_ϕ (right). Superimposed in black are the Gaussian distribution fits obtained with the mean μ and the variance σ^2 for each of the three distributions. Bottom: same histograms for the SV prediction errors δ_{SV}.

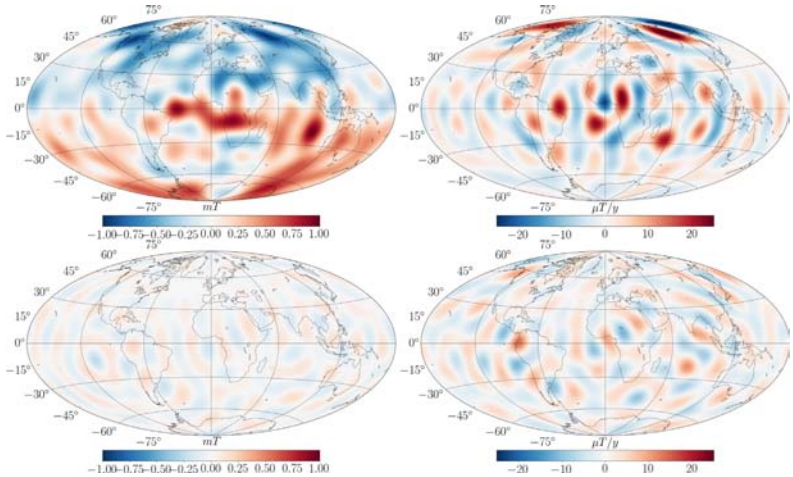

Figure 5. Top: CMB maps of the ensemble average radial magnetic field $\langle \mathbf{b} \rangle$ (eq. 17) in 2017 (left: MF in mT; right: SV in μT yr^{-1}), as estimated with our algorithm. Bottom: MF (left) and SV (right) maps of the difference of our ensemble average field with CHAOS-6 (truncated at degree 14) at the CMB (with the same colour scales).

with similar notations for $\dot{\mathbf{b}}(t)$, $\mathbf{d}(t)$ and $\mathbf{e}(t)$. $c = 3485$ km is the Earth's core radius, and g_n^m and h_n^m are Schmidt semi-normalized spherical harmonic coefficients for the magnetic field at the Earth's surface. Finally, the spatial power spectrum for core flow trajectories $\mathbf{u}$ writes

$$\mathcal{S}(n,t) = \frac{n(n+1)}{2n+1} \sum_{m=0}^{n} \left[{t_{c_n}^m}(t)^2 + {t_{s_n}^m}(t)^2 + {s_{c_n}^m}(t)^2 + {s_{s_n}^m}(t)^2 \right], \tag{21}$$

with ${t_{c,s_n}^m}$ and ${s_{c,s_n}^m}$ Schmidt semi-normalized spherical harmonic coefficients for the toroidal and poloidal components of the flow.

We also define the flow norm

$$\mathcal{N} = \sum_{n=1}^{n_u} \frac{n(n+1)}{2n+1} \sum_{m=0}^{n} \left[{t_{c_n}^m}^2 + {t_{s_n}^m}^2 + {s_{c_n}^m}^2 + {s_{s_n}^m}^2 \right]. \tag{22}$$

The above power spectra can be considered for the ensemble mean or the dispersion within the ensemble, in which case they are respectively noted $\mathcal{R}_{<x>}(n,t)$ and $\mathcal{R}_{\delta x}(n,t)$. Additionally, all those quantities may be averaged in time and/or computed only at analysis periods. For example, the time-averaged spatial power spectrum of the dispersion of magnetic field solutions at analysis epochs is $\hat{\mathcal{R}}_{\delta b}^a(n)$. The same convention as above holds for core flow spectra.

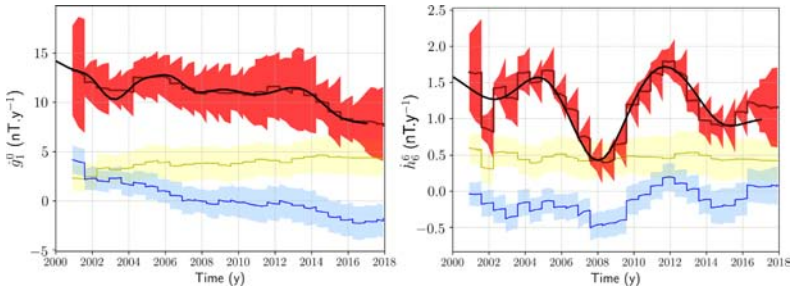

Figure 6. SV spherical harmonic coefficient time-series for $\dot{g}_1^0$ (left) and $\dot{h}_6^6$ (right). Predictions from our ensemble average model are shown in dark red ($\pm 2\sigma_b$ in red) and CHAOS-6 in black. Contributions from subgrid errors and diffusion extracted from our ensemble of realizations are superimposed in respectively blue and yellow (with dispersions $\pm 1\sigma_{\text{diff}}$ and $\pm 1\sigma_{\text{er}}$ in the corresponding colours).

3 RESULTS

We apply our algorithm to VO and GO magnetic field observations over a period spanning from $t_i = 1996.92$ to $t_f = 2016.92$. We recall that since we use satellite measurements from CHAMP and *Swarm* missions, VOs are available only over the periods 2000–2010 and 2014–2017, whereas GOs are available over the whole time span. Analysis are performed every $\Delta t^a = 4$ months. The sequences of analyses and forecasts between 1997 and 2001 are used to warm up the filter (see fig. 7 in BGA17), avoiding an increase in the ensemble spread over the first years of the targeted satellite era. This warm-up period is not considered below when interpreting the ensemble of inverted magnetic field and flow. We first describe predictions from our reanalysis for observations in the physical domain (Section3.1.1), before we present the resulting magnetic model (Section 3.1.2), and insights on core flows over various timescales (Section3.2).

3.1 Geomagnetic field models

3.1.1 Predictions for GO and VO series

We compare in Fig. 3 our series of SV forecasts and analysis with two examples of observation series (one VO and one GO), and with the predictions from CHAOS-6. The large spread of the SV forecasts is to be expected given the large uncertainties associated with subgrid errors and the large-scale flow (see BGA17). At both sites, the dispersion within the ensemble of SV trajectories encompasses most of the time the observations. Moreover the predictions from CHAOS-6 and from our ensemble of SV models are generally consistent. Our algorithm thus seems able to provide a coherent estimate of the SV probability density function (PDF) at the Earth's surface and at satellite altitude. In addition, we highlight that even during the period 2010-2014 where no VO data are available, the trajectory of SV model, controlled by the stochastic prior and GO data only, remains reasonable, with a slight increase in the ensemble spread that always contains CHAOS-6. Note that our algorithm tends to drive the system toward low SV values (see the saw-tooth patterns in Fig. 3). This feature is to be expected given our choice of the stochastic models for $\boldsymbol{u}_H$ and e_r, which control the evolution of the SV. In the absence of data constraints, the process will drift back the ensemble average trajectories for $\boldsymbol{u}_H$ and e_r towards the average dynamo state, which by construction is responsible for a weak SV. This is not a major drawback as soon as we analyse frequently enough, though it does limit the prediction capabilities of our tool (as discussed in BGA17).

We check in Fig. 4 the accuracy with which our model fits MF and SV observations, with the histograms of the prediction errors (over all analyses) normalized to the observation errors, for the three components of the magnetic field. Concerning the MF, prediction errors are only weakly biased, excepted for B_θ (normalized biases on the three components are $\mu_r = -0.02$, $\mu_\theta = -0.23$ and $\mu_\phi = 0.0$). The histograms of prediction errors are reasonably close to Gaussian for the three components with observation errors that appear to be under-estimated on average, in particular on B_r (normalized r.m.s. errors on the three components are $\sigma_r = 2.18$, $\sigma_\theta = 1.55$ and $\sigma_\phi = 1.63$). The SV predictions errors are remarkably consistent with the a priori errors with small biases and standard deviation close to unity for the three components ($\mu_r = -0.06$, $\sigma_r = 1.01$; $\mu_\theta = -0.09$, $\sigma_\theta = 1.11$ and $\mu_\phi = 0.03$, $\sigma_\phi = 1.14$), even though the distributions appears more peaked than a Gaussian. The Kalman filter employed here implicitly assumes Gaussian distributed data errors. However, the above remark suggests that alternative treatments of data residuals may be worth considering in future studies (e.g. L1 or Huber norms, see Constable 1988; Farquharson & Oldenburg 1998).

3.1.2 Field models, and contributions to the SV

We now describe in more detail our MF and SV models. We present in Fig. 5 MF and SV maps for our ensemble average model at the CMB truncated at spherical harmonic degree $n = 14$. Comparing it to a more traditional field model CHAOS-6, which is temporally regularized, the overall agreement is very good, indicating that our tool is indeed capable of producing reasonable field models. MF discrepancies to CHAOS-6 are relatively small, with peak to peak values less than 10% of the total amplitude for a field truncated at degree 14. They are dominated by isotropically distributed, small length-scale patterns. As well as being dominated by small length-scales, the disagreements are larger for the SV, with peak to peak differences about 30% of the total amplitude, which is to be expected given the blue SV spectrum at the CMB, meaning that small length scales dominate. Interestingly, the largest differences are localized under South America and the Indian Ocean, where the planetary gyre respectively detaches from and joins the equatorial belt (Pais

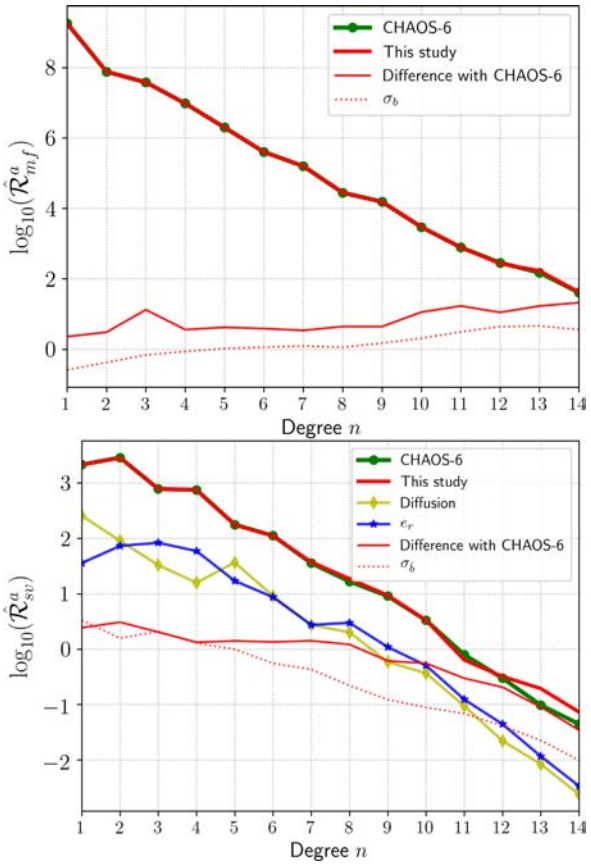

Figure 7. Top: time averaged spatial power spectra at the Earth surface of the magnetic field of CHAOS-6 ($\hat{\mathcal{R}}^a_{b^c}$, eq. 20, in green), our estimate ($\hat{\mathcal{R}}^a_{\langle b \rangle}$, in red), the difference between the two ($\hat{\mathcal{R}}^a_{\delta b}$, red thin line) and the dispersion within our ensemble of analyses ($\hat{\mathcal{R}}^a_{\sigma_b}$, dotted line). Bottom: *idem* for the SV, superimposed with the spectra of the contributions from subgrid errors (blue) and from diffusion (yellow).

& Jault 2008) and where rapid time-dependence is observed (Finlay *et al.* 2016a).

In Fig. 6 we show the various contributions in our model to two SV spherical harmonic coefficient series. The dispersion within the ensemble of models is large enough to include time changes as estimated by CHAOS-6, with some exceptions during the high solar activity era, for example, in 2002 for h^6_6, and at the very end of the CHAOS-6 era (this latter possibly in link with the damping of SA towards end-points in the regularized field model). We note a larger spread of the analysis for the axial dipole than for non-zonal coefficients of intermediate length-scale such as h^6_6. This may be a consequence of the weaker constraint on zonal coefficients from surface observations (e.g. Kotsiaros & Olsen 2012), although we only note such behaviour for g^0_1. An enhancement of the dispersion is notable between 2010 and 2014, displaying in the spectral domain the impact of the decreasing number of data during this era when no vector satellite data were available. Over 2001–2006, the ensemble average h^6_6 trajectory shows distinctive square shaped variations, probably partly related to variations in the number of data satisfying selection criteria during this interval of enhanced solar activity when only CHAMP data were available.

Spatial spectra shown in Fig. 7 summarize the characteristics of our model in the spectral domain. We find excellent agreement with CHAOS-6 for the main field and its secular variation, except at the small length scales of the SV ($n > 10$), which are more likely to be affected by the different data set chosen and by the different temporal kernel used (short time windows in our case against whole time span for CHAOS-6). The ensemble spread gives a good approximation of the characteristic distance between our model and CHAOS-6. Diffusion and subgrid errors in the SV have

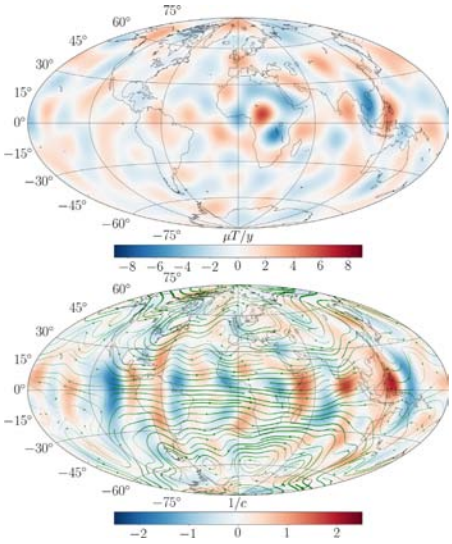

Figure 8. Magnetic diffusion at the CMB (top, colour scale in μT y^{-1}), and horizontal divergence $\nabla_h \cdot \mathbf{u}_h$ (bottom, colour scale in 10^{-3} yr^{-1}) superimposed with passive tracers trajectories (black, tracer size scale in km yr^{-1}), for the ensemble average model in 2017. Core flow visualizations are performed using the tools provided at `https://geodyn.univ-grenoble-alpes.fr/`. The size of the tracers is proportional to the velocity field (see the legend). The initial positions of the tracers is random; each trajectory is advected by the velocity field for a fixed time; along each trajectory, the late (early) positions are darker (lighter).

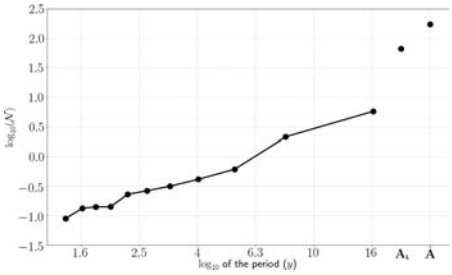

Figure 9. Core flow norm $\mathcal{N}$ for all flow constituents that enter eq. (23). The norm $\mathcal{N}$ for the linear flow acceleration is obtained by integrating the linear trend over the 16 yr.

approximately the same amplitude except for the dipole. The power stored in these two SV sources represents about 10 to 20% of the total SV energy at all scales.

Even though the dispersion within the model predictions is large enough to encompass most of the MF and SV observations, the dispersion within the ensemble of realizations is lower, by a factor about 2.5, than the distance between the ensemble average model and CHAOS-6 for both the MF (at all length-scales) and the SV (towards small length-scales only). A complete account of SV errors from all subgrid interactions (see Baerenzung *et al.* 2017) may help reduce the above under-estimation. Our current estimate is nevertheless larger than that obtained for the COV-OBS.x1 model Gillet *et al.* (see fig. 4 in 2015a, the error spectrum in 2010). We suspect that the accumulation of data (assumed independent) during the construction of this latter field model involved too strong a decrease of the posterior error within the COV-OBS framework. The more consistent approach to error propagation developed here and presented in Fig. 7 favours larger uncertainties on spherical harmonic coefficients during the satellite era.

Overall, we are generally able to retrieve earlier well-established results. For instance the contribution from advection dominates (over diffusion) the axial dipole decay (Finlay *et al.* 2016b; Barrois *et al.* 2017) and its fluctuations—even though our estimate for the contribution from diffusion to dg_1^0/dt, shifted upward by a couple of nT yr^{-1} in comparison with the results of BGA17 (see Section 2.2.2), amounts to a relatively larger fraction over the latest years where the dipole decay tends to be weaker. The ensemble average SV originating from diffusion is presented in Fig. 8 for 2017: the most significant contributions appear below Africa and Indonesia. The strongest diffusion appears linked to intense patches of up-/downwellings in the equatorial belt at the CMB (see Fig.8) and/or where strong gradient of $\mathbf{B}$ occur. This is a direct consequence of our estimation of diffusion through cross-covariances involving core surface velocity and magnetic fields (see BGA17 and Amit & Christensen 2008). In the framework of our modelling, such diffusion patterns seem to be required by magnetic observations rather by the imposed prior cross-covariances (or if it is the case, it does not show up in the background state).

3.2 Core flow solutions

Next, we study with more details the temporal information contained in our core flow solutions. The idea is to extract an average signal and a linear acceleration, together with the flow at different periods, to check if we witness any preferential frequency, or if the characteristics of the flow change with the period. To do so, we apply a least-squares regression to our core flow solution with a function of the form

$$\mathbf{u}(t) = \hat{\mathbf{A}} + \mathbf{A}_L(t - t_0) + \sum_{k=1}^{11} \left[\mathbf{A}_k^s \sin\left(2\pi(t - t_0)\frac{k}{T}\right) + \mathbf{A}_k^c \cos\left(2\pi(t - t_0)\frac{k}{T}\right) \right], \quad (23)$$

with $t_0 = (t_i + t_f)/2 = 2008.92$ and $T = t_f - t_i = 16$ yr. Vectors $\hat{\mathbf{A}}$, $\mathbf{A}_L$, $\mathbf{A}_k^c$ and $\mathbf{A}_k^s$ store respectively the spherical harmonic coefficients of the time average velocity, time average flow acceleration, and cosines and sines from periods 16 yr (for $k = 1$) to 1.45 yr (for $k = 11$) – of course the longer periods are not well constrained given the short time span considered here.

We show in Fig. 9 the norm (22) of all flow constituents for the ensemble average solution. The flow is dominated by long periods, translating onto core surface motions the red SV temporal spectrum (see Gillet *et al.* 2015a; Lesur *et al.* 2017). In comparison with a r.m.s. time average flow of 11.1 km yr^{-1}, the linear acceleration $\mathbf{A}_L$ corresponds, integrated over 16 yr, to a r.m.s. flow increment of 6.6 km yr^{-1}.

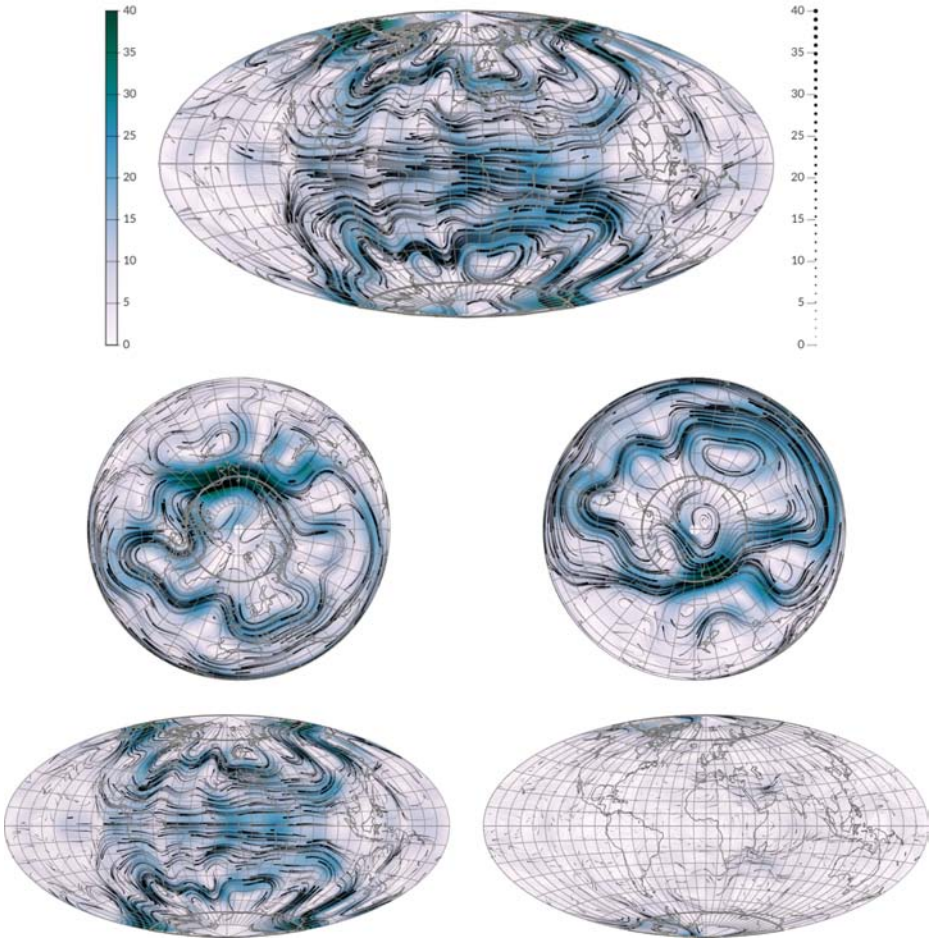

Figure 10. Intensity maps at the CMB of the flow constituents $\hat{\mathbf{A}}$ (in km yr^{-1}) for the ensemble average flow solution, superimposed with passive tracers trajectories (black). Top: Aitoff projection. Middle: north (right) and south (left) polar projections. Bottom: Aitoff projection for equatorially symmetric (left) and antisymmetric (right) components. The colour scale and tracer size scale are the same for all subfigures.

3.2.1 Stationary motions, and flow model uncertainties

We show in Fig. 10 core surface maps of the flow intensity and tracers trajectories for the ensemble average flow constituents $\hat{\mathbf{A}}$. We retrieve on the map for the time average flow classical features, such as the westward gyre offset towards the Atlantic Ocean found in many studies (e.g. Pais & Jault 2008; Aubert 2014;; Gillet *et al.* 2015b Baerenzung *et al.* 2017), with a Pacific hemisphere that is on average much less energetic. The most energetic flow features are associated with (i) azimuthal motions in the equatorial belt below Africa, (ii) high latitudes azimuthal jets in the Pacific hemisphere and (iii) meridional circulations, poleward (resp. equatorward) around 90°W (resp. 90°E).

Our solution is dominated by equatorially symmetric features (see Fig. 10, bottom), as expected outside the tangent cylinder (or TC, the cylinder tangent to the inner core, whose axis coincides with the rotation axis) when rotation forces dominates the momentum balance (e.g. Pais & Jault 2008). Nevertheless, the symmetry may be locally broken. The most striking examples of this are anticyclonic circulations within the TC, retrieved in both the Northern and Southern hemispheres (Fig.10, middle). In contrast with polar

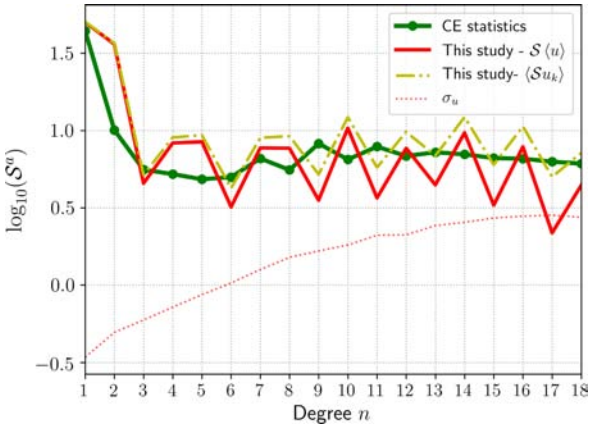

Figure 11. Time averaged spatial power spectra for ensemble average core flows ($\hat{\mathcal{S}}^a_{\langle u\rangle}$, red thick line) and the spectra for the ensemble average of each realization ($\left\langle \hat{\mathcal{S}}^a_{uk} \right\rangle$, yellow thick dotted line, eq.21), obtained from the reanalysis of VO and GO data. Spectra for the corresponding dispersion within the ensembles of models are displayed in dotted lines. In green is shown the averaged spectrum for the prior CED.

vortices previously inferred from geomagnetic observations (Olson & Aurnou 1999; Amit & Olson 2006), features we isolate here are offset to one side of the polar caps (i.e. they contain an important $m = 1$ contribution). This is a common configuration for polar vortices found in the most up to date numerical simulations (Schaeffer *et al.* 2017), which show much variability through epochs.

We show in Fig. 11 the time-average spatial power spectra for the ensemble average solution and for the dispersion within the ensemble of models. The former is comparable with the spectrum of the prior CED. The latter indicates that uncertainties, as measured by the ensemble spread, constitute a large fraction of the flow magnitude for degrees $n \geq 10$. The oscillation in the power seen between odd and even degrees might be magnified by possibly too low subgrid error budget (see Section 3.1.2).

3.2.2 *On transient core surface motions*

We now explore transient flow motions. We particularly focus on the amount of equatorial symmetry of our solutions inside and outside the TC, in order to detect if our model is sensitive to the specific geometry of the Earth's core (does it hold a signature of the TC?). As for the time-average flow, the linear acceleration over the past 16 yr is primarily symmetric with respect to the equator (see Fig.12). The largest contributions consist of accelerating circulations around the meridional, Eastern branch of the gyre. Associated with these time-changing eddies around the equatorward branch of the planetary gyre, an Eastward equatorial jet intensifies under the Western Pacific. This suggests an underlying dynamics more complex than a simple longitudinal shift of the planetary gyre.

Interestingly, our average solution does not show a major intensification of equatorially symmetric azimuthal jets at high latitudes in the Pacific hemisphere, as inferred by Livermore *et al.* (2017). Indeed, we see an increase of the Northern jet only, by about 67% in average (the one σ dispersion within the ensemble of flow realizations allowing for an increase up to 100%). Although still an appreciable acceleration, it is significantly less than the factor of 3 found by Livermore *et al*. The disagreement is likely due to our global inversion (in opposition to their local model). The difference seems to be related with antisymmetric circulations within the TC. One should keep in mind that in these high and low latitude areas, gradients of B_r are much larger in the Northern Hemisphere, meaning that the signature of any motions near the TC below the Southern Pacific are significantly weaker. As for the stationary constituent, the equatorial symmetry is not perfectly respected, and we retrieve the largest antisymmetrical features within the TC, associated with polar jets.

We give in Fig. 13 an example of one interannual flow constituent at the CMB for a period of 5.3 yr. In this case, the most energetic flows are concentrated into non-axisymmetric azimuthal jets near the equator (already highlighted by Gillet *et al.* 2015b; Finlay *et al.* 2016b), and into localized circulations at mid and high latitudes. These are not confined to the Atlantic hemisphere: despite being less energetic on average, the Pacific hemisphere shows interesting interannual flow variations. At these sub-decadal periods, we have not detected any obvious propagation of non-zonal flow patterns, which might be interpreted as the signature of azimuthally propagating waves (as advocated for by Chulliat & Maus 2014; Chulliat *et al.* 2015). The other periods display globally the same kind of features and no particular behaviour is found at any period. At these timescales also show up less intense antisymmetric features; the most significant shows up in the equatorial area (for instance under the Atlantic ocean and the Western Pacific), and towards high latitudes on the edge of the TC.

Fig. 14 summarizes the amount of equatorial symmetry found in regions inside and outside the TC, for our core flow solutions at all periods. It appears almost independent of the considered period: outside the TC, it is within 90 to 95% of the surface energy

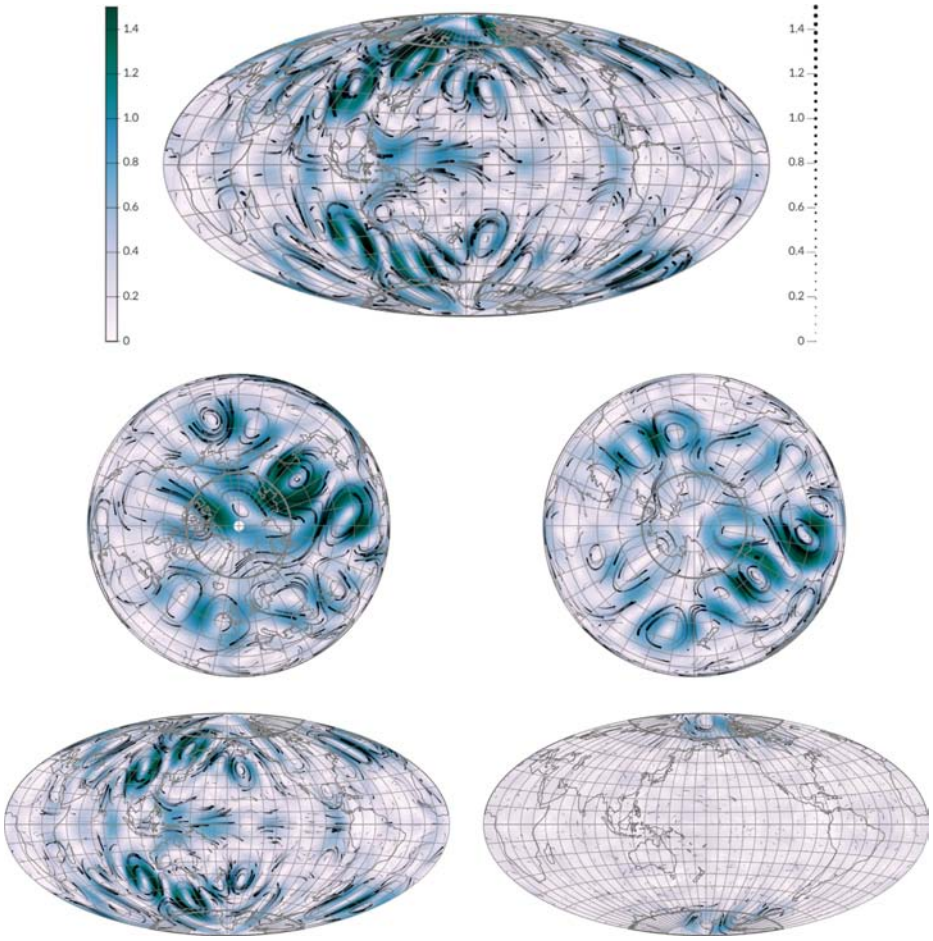

Figure 12. Same as Fig. 10 for the flow constituent $\mathbf{A}_L$ (in km yr^{-2}).

for all flow constituents of eq. (23). The partition of energy between symmetric and antisymmetric flow components is more balanced inside the TC where, depending on the considered timescale, $\approx$55 $\pm$ 15% of the energy is contained in equatorially symmetric flows. This latter observation could be expected because the presence of the inner core is intended to partially break the equatorial symmetry However, it is remarkable that the algorithm appears accurate enough to detect a specific behaviour within the tiny areas covered by polar caps. Moreover, although our ensemble average model and the CED show very similar amounts of equatorial symmetry outside the TC (the value for the CED model is 95% of symmetrical flows inside and outside TC), they differ significantly inside the TC (it is much less in the inverted flows). As a consequence, the larger proportion of equatorial antisymmetry inside the TC is driven by observations (against the prior information).

4 SUMMARY AND DISCUSSION

Following earlier strategies for geomagnetic field model reconstruction (e.g. Jackson *et al.* 2007; Lesur *et al.* 2010), and moving towards geomagnetic data assimilation (Aubert 2015; Gillet *et al.* 2015a; Baerenzung *et al.* 2017), we continue the work initiated in BGA17. We retain their idea of combining spatial information from

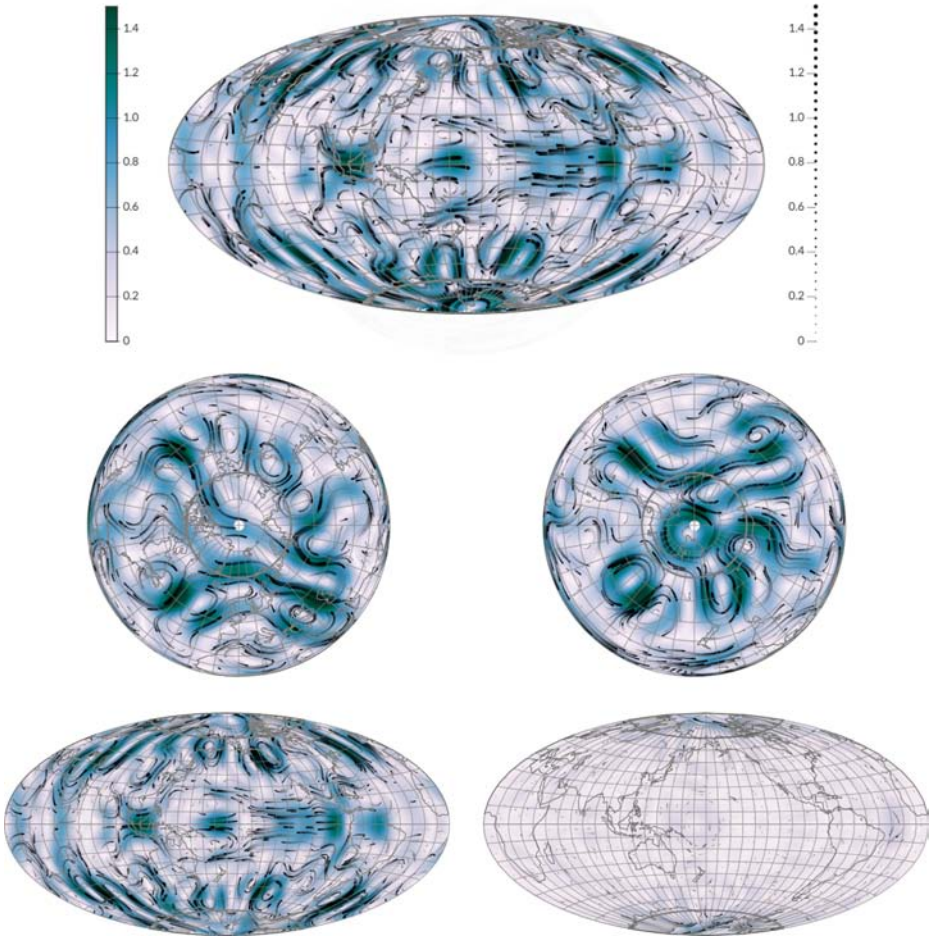

Figure 13. Same as Fig. 10 for the flow constituent $\mathbf{A}_3^c$ (in km yr^{-1}).

numerical simulations of the geodynamo with temporal information implemented through stochastic equations, chosen to replicate the frequency spectrum of ground-based geomagnetic series. However, instead of considering spherical harmonic coefficients of the main field as data, here we have inverted observations (GOs and VOs) directly, at and above the Earth's surface. In this respect we follow the studies by Beggan & Whaler (2009) and Whaler & Beggan (2015), although we account for subgrid processes (of great importance, as shown by BGA17 or Baerenzung *et al.* 2016) and for surface magnetic diffusion. This avenue allows us to propose PDFs for the main field and its secular variation, as well as for the recovered core motions.

4.1 Geophysical insights

The MF models presented here are consistent both with observations and with the imposed dynamical prior. The model uncertainties, as suggested by the ensemble spread, are slightly less than the distance of the average model to CHAOS-6. We recover in our core flow solutions a westward gyre that circulates around the TC at high latitudes in the Pacific hemisphere, and flows closer to the equator in the Atlantic hemisphere. The largest contributions from magnetic diffusion are associated with up-/downwellings where the gyre meets the equatorial region (under Indonesia) and in the equatorial region below Africa. At all timescales, the flow is predominantly symmetric with respect to the equator, except inside the TC where the

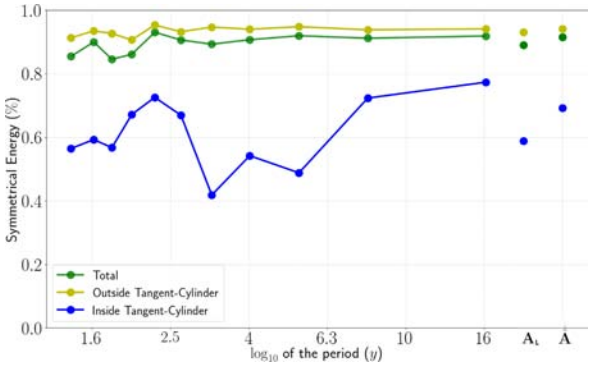

Figure 14. Fraction of energy contained into the equatorial symmetric part of the flow, inside (blue line) and outside (yellow line) of the tangent cylinder (TC), for each of the flow constituent that enters eq. (23). The total symmetric part of the flow is also displayed in green. The value for the CED dynamo used as a prior is 0.95 both inside and outside the TC.

situation is more balanced (contrary to our dynamo prior that is mostly symmetric everywhere).

The most intense time-average flow acceleration over the past 16 yr is linked with evolving meanders around the equatorward branch of the gyre in the Eastern hemisphere, also associated with the appearance of an Eastward equatorial jet under the Western Pacific. We do find a decadal intensification of jets near the TC, although the magnitude of the acceleration we infer is lower than that estimated by Livermore *et al.* (2017) with their reduced model. In our study, it is furthermore confined to the Northern Hemisphere. This equatorial asymmetry may be interpreted as the signature of an ageostrophic acceleration, keeping in mind that main field gradients are weak in the Southern Pacific, implying a weaker constraint on flow motions there (see fig. 7 in Baerenzung *et al.* 2016). However, because our prior does not show any particular bias in those areas, it is likely that those features are mostly driven by the data. On interannual periods, we find relatively energetic flow changes in both the Atlantic and the Pacific hemispheres, with both non-zonal equatorial jets and time-dependent mid-to-high latitudes eddies evident.

4.2 Future work

We currently lack a physical understanding for the features described above, whether it be through quasi-geostrophic flows (e.g. Labbé *et al.* 2015), motions within a stratified layer (e.g. Buffett & Knezek 2017), or any other interpretation through a reduced model. We also lack suitable long coverage by high quality satellite records to perform spectral analyses with a refined sampling in the frequency domain, which would allow us to isolate possible waves at interannual periods. Development of such reduced models, and their coupling with stochastic processes for modelling unresolved processes, will be an important next step in our ability to understand and predict geomagnetic field changes.

Meanwhile, our stochastic model itself could be improved; in particular it is desirable to avoid driving back the average trajectory towards an average dynamo simulation. This is indeed an unlikely state for the current era (say over decadal to centennial timescales), which might be better represented by a reanalysis of for instance centennial motions from historical records (Jonkers *et al.* 2003). Furthermore, because of the short time span covered today by satellite data, we found it challenging to derive well-conditioned matrices for VO uncertainties. This is a key-point for such data assimilation studies, which calls for further developments, for example, through projections onto reduced basis in the data space. Alternatively, we may wish to coestimate, together with the core state, time-dependent external fields. Although possible, this calls for a severe re-encoding of both the forecast and analysis steps, in order to integrate satellite measurements along the tracks.

The general philosophy of our work is to retrieve information on the state of the Earth's core, and to provide realistic uncertainties on all state variables in a simple way. The encouraging magnetic models obtained with this approach render our algorithm suitable for deriving candidates to the International Geomagnetic Reference Field (Thébault *et al.* 2015). Remaining in a stochastic framework, modifications of the forward model parametrization—such as accounting for a background state closer to the flow responsible for the magnetic field over the past decades—may extend the prediction capability of our algorithm. However, targeting accurate field predictions one will have to resort to deterministic (i.e. dynamically based) equations for the core state.

ACKNOWLEDGEMENTS

We thank Julien Aubert for providing the Coupled-Earth dynamo series used to build the core state statistics, and Loic Huder for spotting two errors in the code at the origin of the results of BGA17. We also thank Julien Baerenzung and an anonymous referee for their useful comments that helped improve the quality of our manuscript. We would like to thank as well GFZ German Research Centre for Geoscience for providing access to the CHAMP MAG-L3 data and to ESA for providing access to the Swarm L1b MAG-L data. We also like to thank the staff of the geomagnetic observatories and INTERMAGNET for supplying high-quality observatory data. NG and OB were partially supported by the French Centre National d'Etudes Spatiales (CNES) for the study of Earth's core dynamics in the context of the *Swarm* mission of ESA. ISTerre is part of Labex OSUG@2020 (ANR10 LABX56), which with the

CNES also finance the PhD grant of OB. Numerical computations were performed at the Froggy platform of the CIMENT infrastructure (https://ciment.ujf-grenoble.fr) supported by the Rhône-Alpes region (GRANT CPER07 13 CIRA), the OSUG@2020 Labex (reference ANR10 LABX56) and the Equip@Meso project (referenceANR-10-EQPX-29-01). MH and CF were supported by the Danish Council for Independent Research - Natural Sciences, Grant DFF-4002-00366.

REFERENCES

Amit, H. & Christensen, U.R., 2008. Accounting for magnetic diffusion in core flow inversions from geomagnetic secular variation, *Geophys. J. Int.,* **175**(3), 913–924.

Amit, H. & Olson, P., 2006. Time-average and time-dependent parts of core flow, *Phys. Earth planet. Inter.,* **155,** 120–139.

Aubert, J., 2014. Earth's core internal dynamics 1840–2010 imaged by inverse geodynamo modelling, *Geophys. J. Int.,* **197,** 1321–1334.

Aubert, J., 2015. Geomagnetic forecasts driven by thermal wind dynamics in the Earth's core, *Geophys. J. Int.,* **203**(3), 1738–1751.

Aubert, J., Finlay, C.C. & Fournier, A., 2013. Bottom-up control of geomagnetic secular variation by the Earth's inner core, *Nature,* **502**(7470), 219–223.

Baerenzung, J., Holschneider, M. & Lesur, V., 2016. The flow at the Earth's core-mantle boundary under weak prior constraints, *J. geophys. Res.,* **121**(3), 1343–1364.

Baerenzung, J., Holschneider, M., Wicht, J., Sanchez, S. & Lesur, V., 2017. Modeling and predicting the short term evolution of the Geomagnetic field, *J. geophys. Res.,* **123,** 4539–4560.

Barrois, O., Gillet, N. & Aubert, J., 2017. Contributions to the geomagnetic secular variation from a reanalysis of core surface dynamics, *Geophys. J. Int.,* **211**(1), 50–68.

Beggan, C. & Whaler, K., 2009. Forecasting change of the magnetic field using core surface flows and ensemble Kalman filtering, *Geophys. Res. Lett.,* **36**(18), 1–5.

Beggan, C., Whaler, K. & Macmillan, S., 2009. Biased residuals of core flow models from satellite-derived virtual observatories, *J. geophys. Int.,* **177**(2), 463–475.

Buffett, B.A. & Knezek, N., 2017. Stochastic generation of MAC waves and implications for convection in Earth's core, *Geophys. J. Int.,* **212,** 1523–1535.

Chulliat, A. & Maus, S., 2014. Geomagnetic secular acceleration, jerks, and a localized standing wave at the core surface from 2000 to 2010, *J. geophys. Res.,* **119**(3), 1531–1543.

Chulliat, A. & Olsen, N., 2010. Observation of magnetic diffusion in the Earth's outer core from Magsat, Ørsted, and CHAMP data, *J. geophys. Res.,* **115**(B5), 1–13.

Chulliat, A., Alken, P. & Maus, S., 2015. Fast equatorial waves propagating at the top of the Earth's core, *Geophys. Res. Lett.,* **42**(9), 3321–3329.

Constable, C., 1988. Parameter estimation in non-Gaussian noise, *Geophys. J. Int.,* **94**(1), 131–142.

Constable, C.G., Parker, R.L. & Stark, P.B., 1993. Geomagnetic field models incorporating frozen-flux constraints, *Geophys. J. Int.,* **113**(2), 419–433.

Evensen, G., 2003. The ensemble Kalman filter: Theoretical formulation and practical implementation, *Ocean Dyn.,* **53**(4), 343–367.

Eymin, C. & Hulot, G., 2005. On core surface flows inferred from satellite magnetic data, *Phys. Earth planet. Inter.,* **152**(3), 200–220.

Farquharson, C.G. & Oldenburg, D.W., 1998. Non-linear inversion using general measures of data misfit and model structure, *Geophys. J. Int.,* **134**(1), 213–227.

Finlay, C.C., Aubert, J. & Gillet, N., 2016a. Gyre-driven decay of the Earth's magnetic dipole, *Nat. Communi.,* **7,** 1–8.

Finlay, C.C., Olsen, N., Kotsiaros, S., Gillet, N. & Tøffner-Clausen, L., 2016b. Recent geomagnetic secular variation from Swarm, *Earth Planets Space,* **68**(1), 1–18.

Gillet, N., Pais, M. & Jault, D., 2009. Ensemble inversion of time-dependent core flow models, *Geochem. Geophys. Geosyst.,* **10**(6), 1–20.

Gillet, N., Barrois, O. & Finlay, C.C., 2015a. Stochastic forecasting of the geomagnetic field from the COV-OBS. x1 geomagnetic field model, and candidate models for IGRF-12, *Earth Planets Space,* **67**(1), 1–14.

Gillet, N., Jault, D. & Finlay, C., 2015b. Planetary gyre, time-dependent eddies, torsional waves, and equatorial jets at the Earth's core surface, *J. geophys. Res.,* **120**(6), 3991–4013.

Holme, R., 2015. Large scale flow in the core, in *Treatise in Geophysics, Core Dynamics,* Vol. **8,** chap. 4, pp. 91–113, eds Olson, P. & Schubert, G., Elsevier.

Jackson, A., Constable, C., Walker, M. & Parker, R., 2007. Models of Earth's main magnetic field incorporating flux and radial vorticity constraints, *Geophys. J. Int.,* **171**(1), 133–144.

Jonkers, A.R., Jackson, A. & Murray, A., 2003. Four centuries of geomagnetic data from historical records, *Rev. Geophys.,* **41**(2), 1–37.

Kotsiaros, S. & Olsen, N., 2012. The geomagnetic field gradient tensor, properties and parametrization in terms of spherical harmonics, *Int. J. Geomath.,* **3,** 297–314.

Labbé, F., Jault, D. & Gillet, N., 2015. On magnetostrophic inertia-less waves in quasi-geostrophic models of planetary cores, *Geophys. Astrophys. Fluid Dyn.,* **109**(6), 587–610.

Leopardi, P., 2006. A partition of the unit sphere into regions of equal area and small diameter, *Electron. Trans. Numer. Anal.,* **25**(12), 309–327.

Lesur, V., Wardinski, I., Asari, S., Minchev, B. & Mandea, M., 2010. Modelling the Earth's core magnetic field under flow constraints, *Earth Planets Space,* **62**(6), 503–516.

Lesur, V., Wardinski, I., Baerenzung, J. & Holschneider, M., 2017. On the frequency spectra of the core magnetic field Gauss coefficients, *Phys. Earth planet. Inter.,* **276,** 145–158.

Livermore, P.W., Hollerbach, R. & Finlay, C.C., 2017. An accelerating high-latitude jet in Earth's core, *Nat. Geosci.,* **10**(1), 62–68.

Macmillan, S. & Olsen, N., 2013. Observatory data and the Swarm mission, *Earth Planets Space,* **65**(11), 1189–1200.

Mandea, M. & Olsen, N., 2006. A new approach to directly determine the secular variation from magnetic satellite observations, *Geophys. Res. Lett.,* **33**(15), 1–5.

O'Brien, M.S., Constable, C.G. & Parker, R.L., 1997. Frozen-flux modelling for epochs 1915 and 1980, *Geophys. J. Int.,* **128**(2), 434–450.

Olsen, N., 2002. A model of the geomagnetic field and its secular variation for epoch 2000 estimated from ørsted data, *Geophys. J. Int.,* **149**(2), 454–462.

Olsen, N. & Mandea, M., 2007. Investigation of a secular variation impulse using satellite data: The 2003 geomagnetic jerk, *Earth planet. Sci. Lett.,* **255**(1), 94–105.

Olsen, N., Glassmeier, K.-H. & Jia, X., 2010. Separation of the magnetic field into external and internal parts, *Space Sci. Rev.,* **152**(1–4), 135–157.

Olsen, N., Lühr, H., Finlay, C.C., Sabaka, T.J., Michaelis, I., Rauberg, J. & Tøffner-Clausen, L., 2014. The CHAOS-4 geomagnetic field model, *Geophys. J. Int.,* **197**(2), 815–827.

Olsen, N. *et al.*, 2015. The swarm initial field model for the 2014 geomagnetic field, *Geophys. Res. Lett.,* **42**(4), 1092–1098.

Olson, P. & Aurnou, J., 1999. A polar vortex in the Earth's core, *Nature,* **402**(6758), 170–173.

Pais, M. & Jault, D., 2008. Quasi-geostrophic flows responsible for the secular variation of the Earth's magnetic field, *Geophys. J. Int.,* **173**(2), 421–443.

Sabaka, T.J., Olsen, N. & Purucker, M.E., 2004. Extending comprehensive models of the Earth's magnetic field with Ørsted and CHAMP data, *Geophys. J. Int.,* **159**(2), 521–547.

Sabaka, T.J., Olsen, N., Tyler, R.H. & Kuvshinov, A., 2015. CM5, a pre-Swarm comprehensive geomagnetic field model derived from over 12 yr of CHAMP, Ørsted, SAC-C and observatory data, *Geophys. J. Int.,* **200**(3), 1596–1626.

Schaeffer, N., Jault, D., Nataf, H.-C. & Fournier, A., 2017. Turbulent geodynamo simulations: a leap towards Earth's core, *Geophys. J. Int.,* **211**(1), 1–29.

Thébault, E. *et al.*, 2015. International geomagnetic reference field: the 12th generation, *Earth Planets Space,* **67**(1), 1–19.

Verboven, S. & Hubert, M., 2005. LIBRA: a MATLAB library for robust analysis, *Chemometr. Intell. Lab. Syst.,* **75**(2), 127–136.

Wardinski, I. & Lesur, V., 2012. An extended version of the C3FM geomagnetic field model: application of a continuous frozen-flux constraint, *Geophys. J. Int.,* **189**(3), 1409–1429.

Whaler, K. & Beggan, C., 2015. Derivation and use of core surface flows for forecasting secular variation, *J. geophys. Res.,* **120**(3), 1400–1414.

Whaler, K., Olsen, N. & Finlay, C., 2016. Decadal variability in core surface flows deduced from geomagnetic observatory monthly means, *J. geophys. Int.,* **207**(1), 228–243.

Appendix B

Virtual Observatory Model - Synthetic Data

This appendix is concerned with the validation and documentation of the implemented VO modelling approach described in Chapter 4. A series of synthetic data test have been performed in order to validate the VO model using both regular vector and gradient data. Herein a few of these investigations are presented. Synthetic data was generated at satellite observation locations from Data Set 1, using the CHAOS-6-x5 model predictions to SH degrees $n \in [1, 20]$ multiplied by a factor of 1.01 on the Gauss coefficients. The CHAOS-6-x5 field model predictions for SH degree $n \in [1, 20]$ was subtracted at each location and then added back for the target point location. The figures shown here are for one example case study being a VO above the Niemegk ground observatory.

Figure B.1 presents comparisons between quadratic and cubic potential descriptions for search radii $d_0 = 500$km (fig. a and c) and $d_0 = 1000$km (fig. b and d). The figure shows the difference in the main field components at the VO target point, between the VO model approach and the CHAOS-6-x5 predictions using regular vector data binned in 4 month time windows. Red and blue dots are for CHAMP and *Swarm* periods, respectively. Note here, that because the synthetic data are build using Data Set 1, having geomagnetic quiet dark time selection criteria, the number of data points are small especially for $d_0 = 500$km, emphasising the possible advantage of increasing the search radius when using those type of data selection criteria. Visual inspection reveals that the quadratic fit is not performing well for a large search radius of $d_0 = 1000$km as indicated by the size of the difference and their scatter (notice here the scale in this particular plot). The cubic description using both a 500km and a 1000km search radius provides an acceptable fit.

Figure B.2 presents comparisons using a cubic description for $N_{VO} = 30$ for various search radii of 500, 700 800 and 1000km using using data sums and differences. During the synthetic runs it was realized that using data differences alone was not enough to constrain the first three coefficients of the potential description, thus requiring the data sums to be added. Increasing the search radius from 500km to 700km increases the number of VOs in the times series dramatically. Furthermore, having a large search radius the cubic description is suitable obtaining differences < 0.2nT. Notice here the apparent slope in the radial field component during the CHAMP period in the radial component for the large search range $d_0 = 1000$km; this may be ascribed to the steady decrease of the CHAMP

satellite during its lift time not being properly captured due to a fixed VO altitude during the entire time series. Figure B.3 presents the number of available data for the various search radii. From this it is evident that choosing a large search radius is highly beneficial, especially during CHAMP time. Due to the poor performance of the quadratic description using search ranges >500km, no further results using the quadratic potential are provided. Figure B.4 presents the retrieved main field and SV obtained from a VO model in red dots using a search range of $d_0 = 700$km. This is also the preferred VO setup used in the subsequent computations for the field and field gradient time series presented in Sections 4.5 and 4.6, respectively.

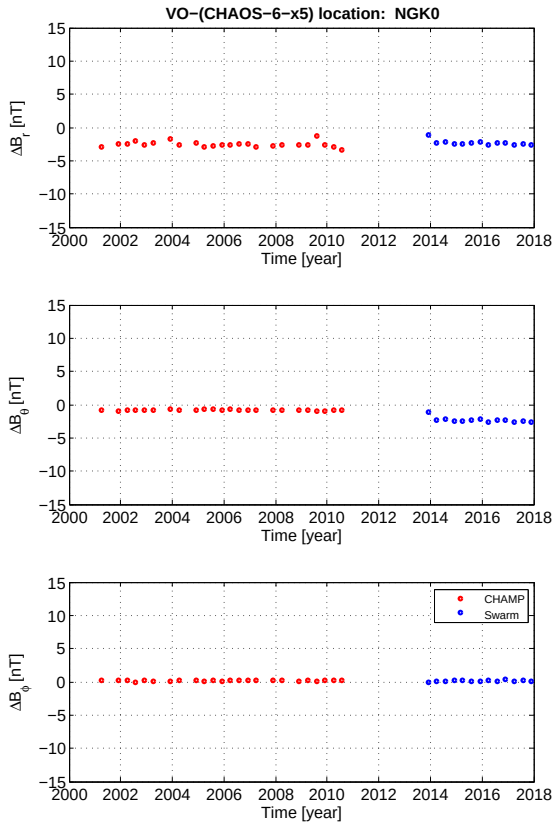

(a) Quadratic - $\{d_0, N_{VO}\} = \{500\text{km}, 30\}$.

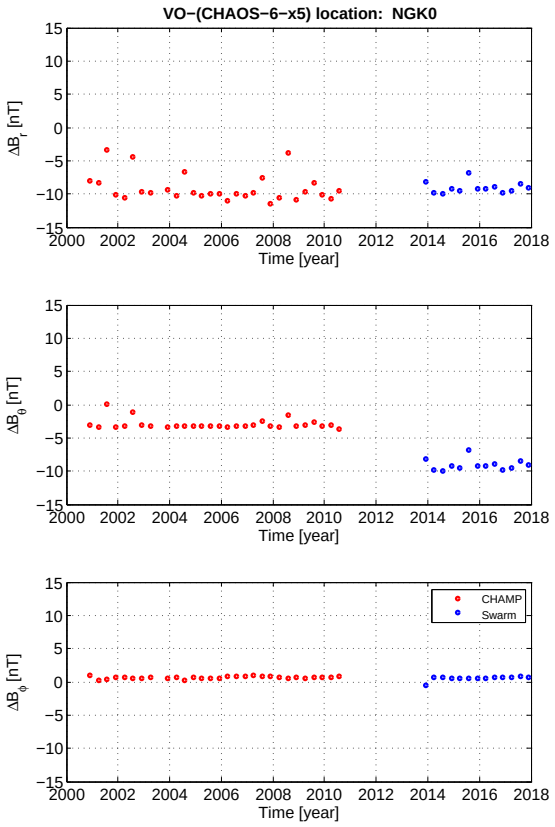

(b) Quadratic - $\{d_0, N_{VO}\} = \{1000\text{km}, 30\}$.

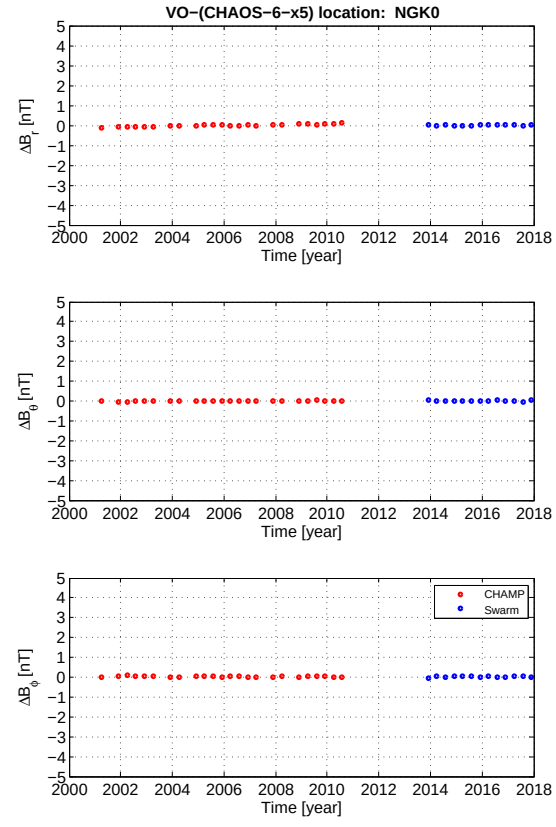

(c) Cubic - $\{d_0, N_{VO}\} = \{500\text{km}, 30\}$.

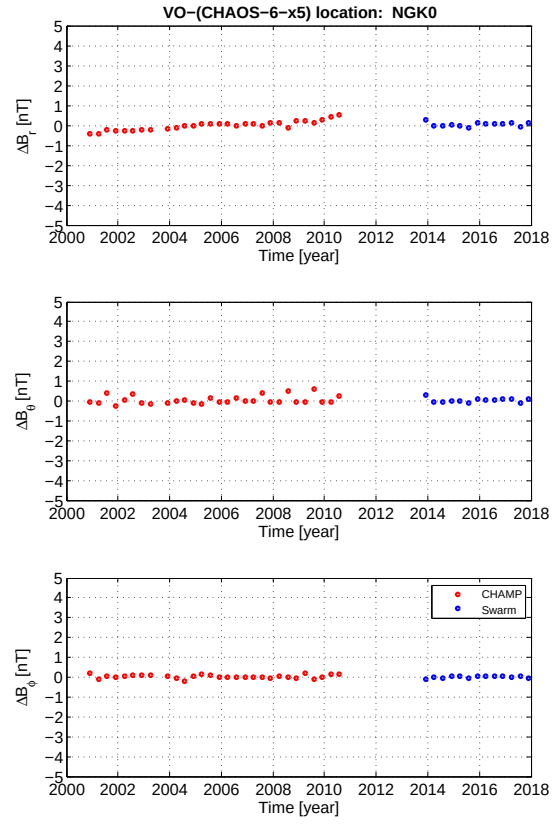

(d) Cubic - $\{d_0, N_{VO}\} = \{1000\text{km}, 30\}$.

Figure B.1: Synthetic vector data: quadratic (top) and cubic (bottom) descriptions.

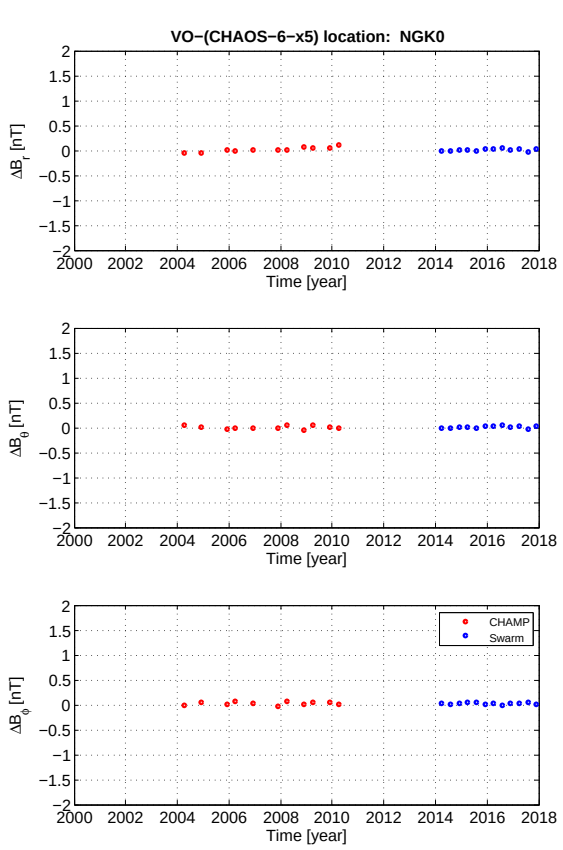

(a) Cubic - $\{d_0, N_{VO}\} = \{500\text{km}, 30\}$.

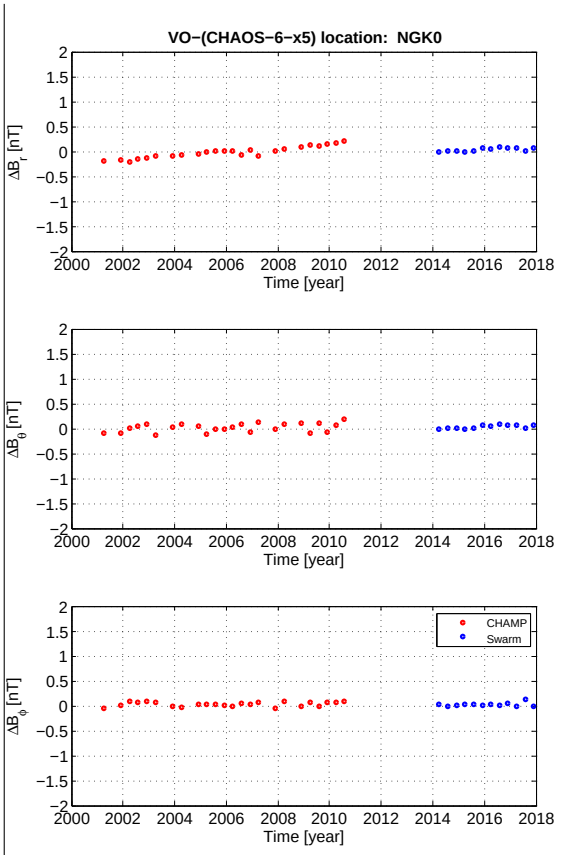

(b) Cubic - $\{d_0, N_{VO}\} = \{700\text{km}, 30\}$.

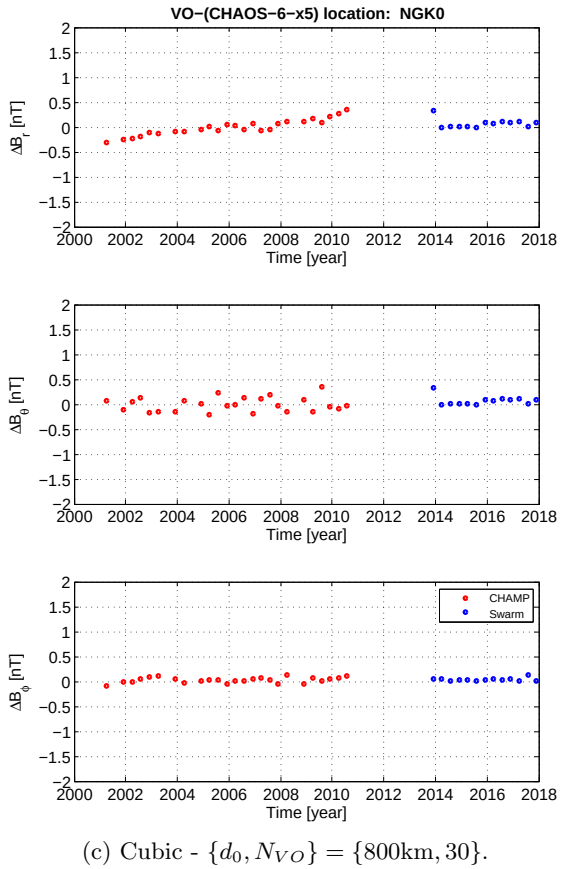

(c) Cubic - $\{d_0, N_{VO}\} = \{800\text{km}, 30\}$.

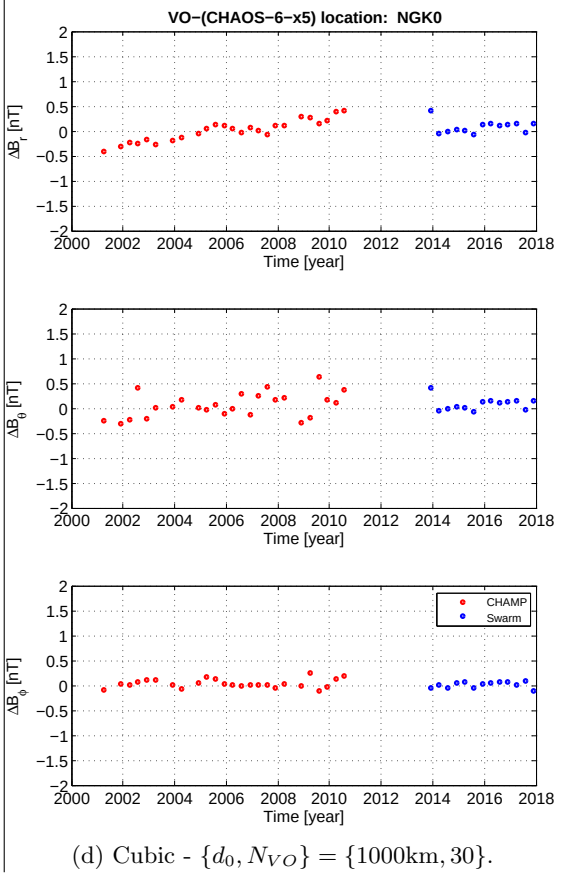

(d) Cubic - $\{d_0, N_{VO}\} = \{1000\text{km}, 30\}$.

Figure B.2: Synthetic data sums and differences: search range.

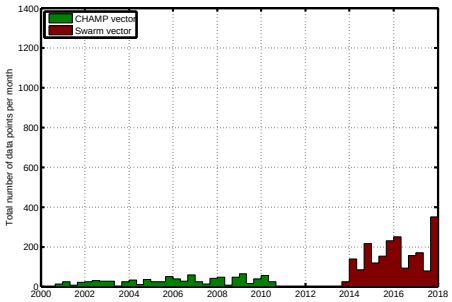

(a) Cubic - $\{d_0, N_{VO}\} = \{500\text{km}, 30\}$.

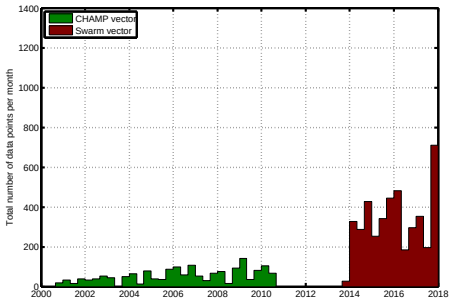

(b) Cubic - $\{d_0, N_{VO}\} = \{700\text{km}, 30\}$.

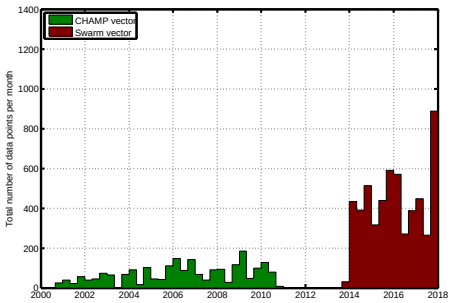

(c) Cubic - $\{d_0, N_{VO}\} = \{800\text{km}, 30\}$.

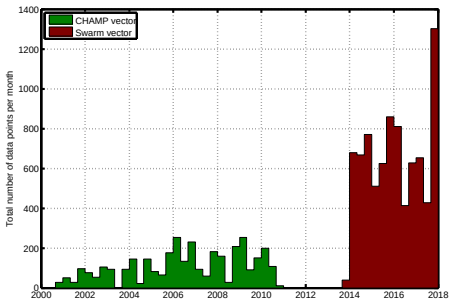

(d) Cubic - $\{d_0, N_{VO}\} = \{1000\text{km}, 30\}$.

Figure B.3: Synthetic data sums and differences: number of available data.

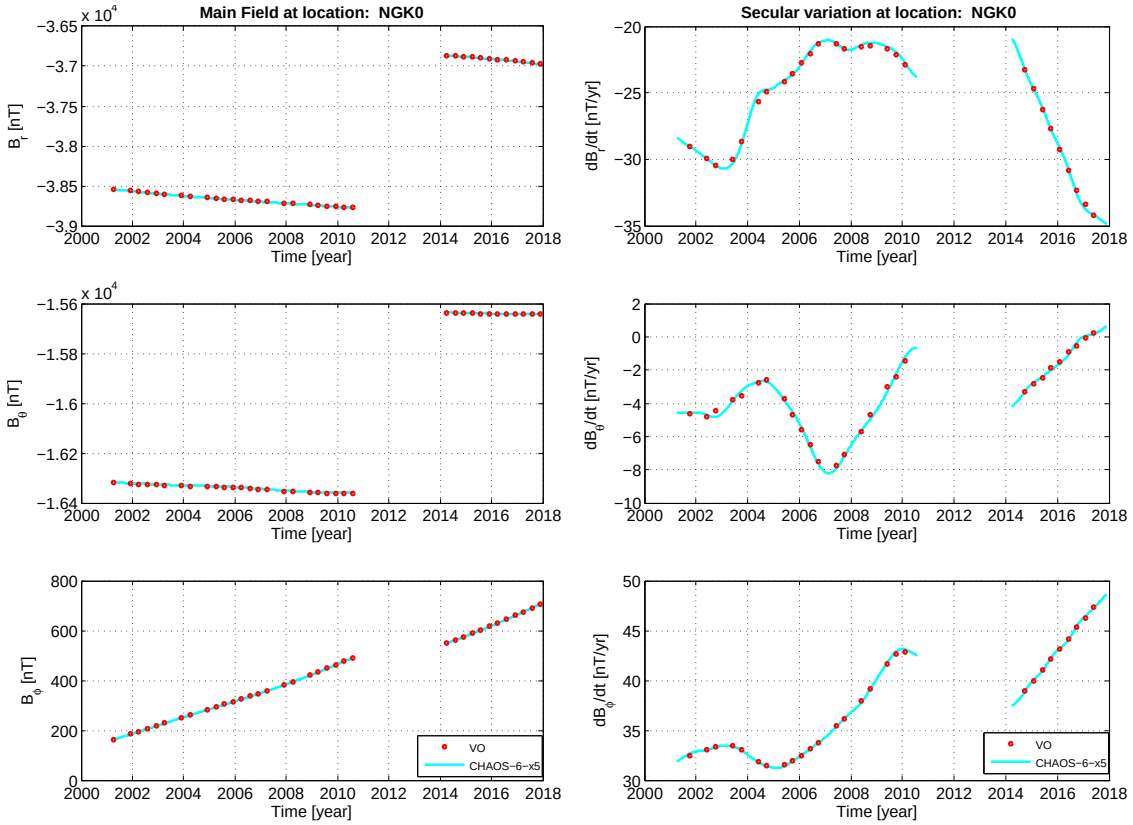

(a) Main field - $\{d_0, N_{VO}\} = \{700\text{km}, 30\}$.

(b) Secular variation - $\{d_0, N_{VO}\} = \{700\text{km}, 30\}$.

Figure B.4: Synthetic data sums and differences: MF (left column) and SV (right column).

Appendix C

Virtual Observatory Model - Field Computations

This appendix contains VO time series of annual differences of the main field (i.e. the SV) and of the secular variation (i.e. the SA) at the selected ground observatories listed in Table 4.2. The figures are listed in alphabetic ordering of the observatories; shown with black dots are the revised monthly mean of the GO's, in red dots the VO estimates and with the green curves the CHAOS-6-x5 model predictions at the VO altitudes during CHAMP and *Swarm* periods for SH degrees $n \in [1, 16]$. For each station the left (top or bottom) plots show the SV estimates while the right (top or bottom) plots show the SA estimates of the three field components. The VO's are plotted at altitudes 370km and 490km during CHAMP and *Swarm* times, respectively.

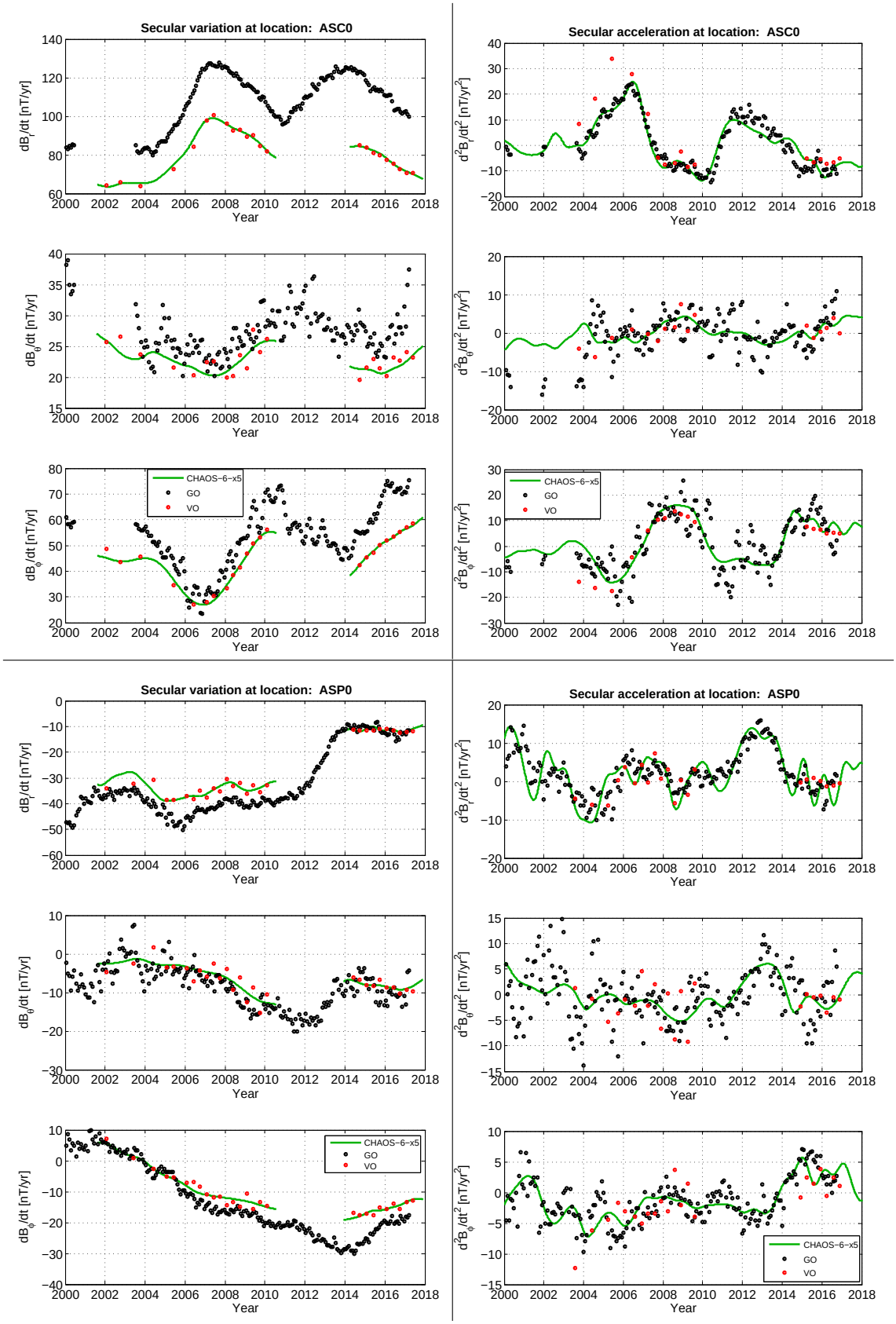

Figure C.1: Time series of SV (left) and SA (right) showing VO's (red dots) using 4 month data windows, GO's (black dots) and CHAOS-6-x5 model predictions (green) using SH degrees up to $n = 16$. For SV and SA fields the CHAOS-6-x5 estimates are plotted at VO altitudes (i.e. 370km and 490km) and at Earth's surface, respectively.

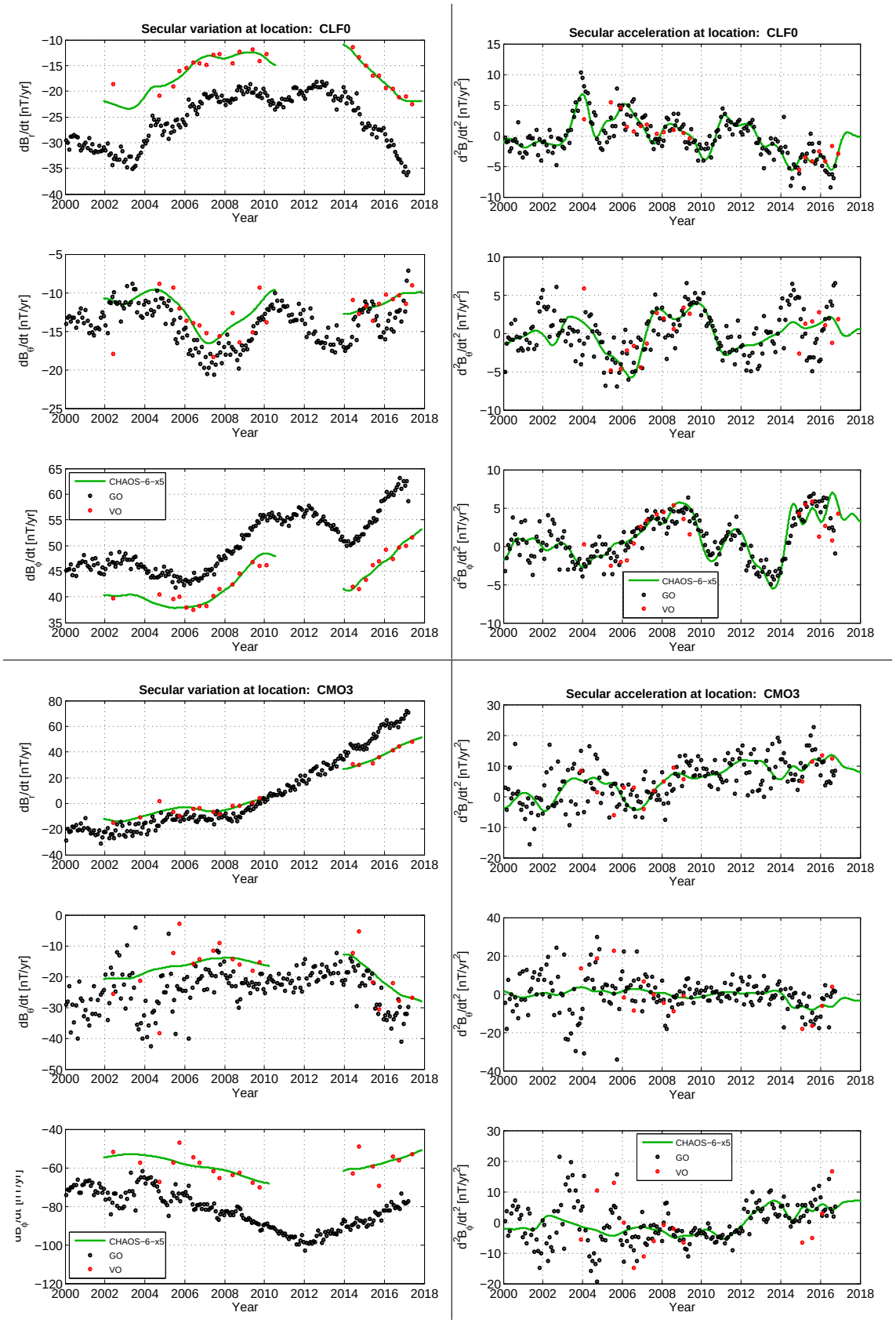

Figure C.2: Time series of SV (left) and SA (right) showing VO's (red dots) using 4 month data windows, GO's (black dots) and CHAOS-6-x5 model predictions (green) using SH degrees up to $n = 16$. For SV and SA fields the CHAOS-6-x5 estimates are plotted at VO altitudes (i.e. 370km and 490km) and at Earth's surface, respectively.

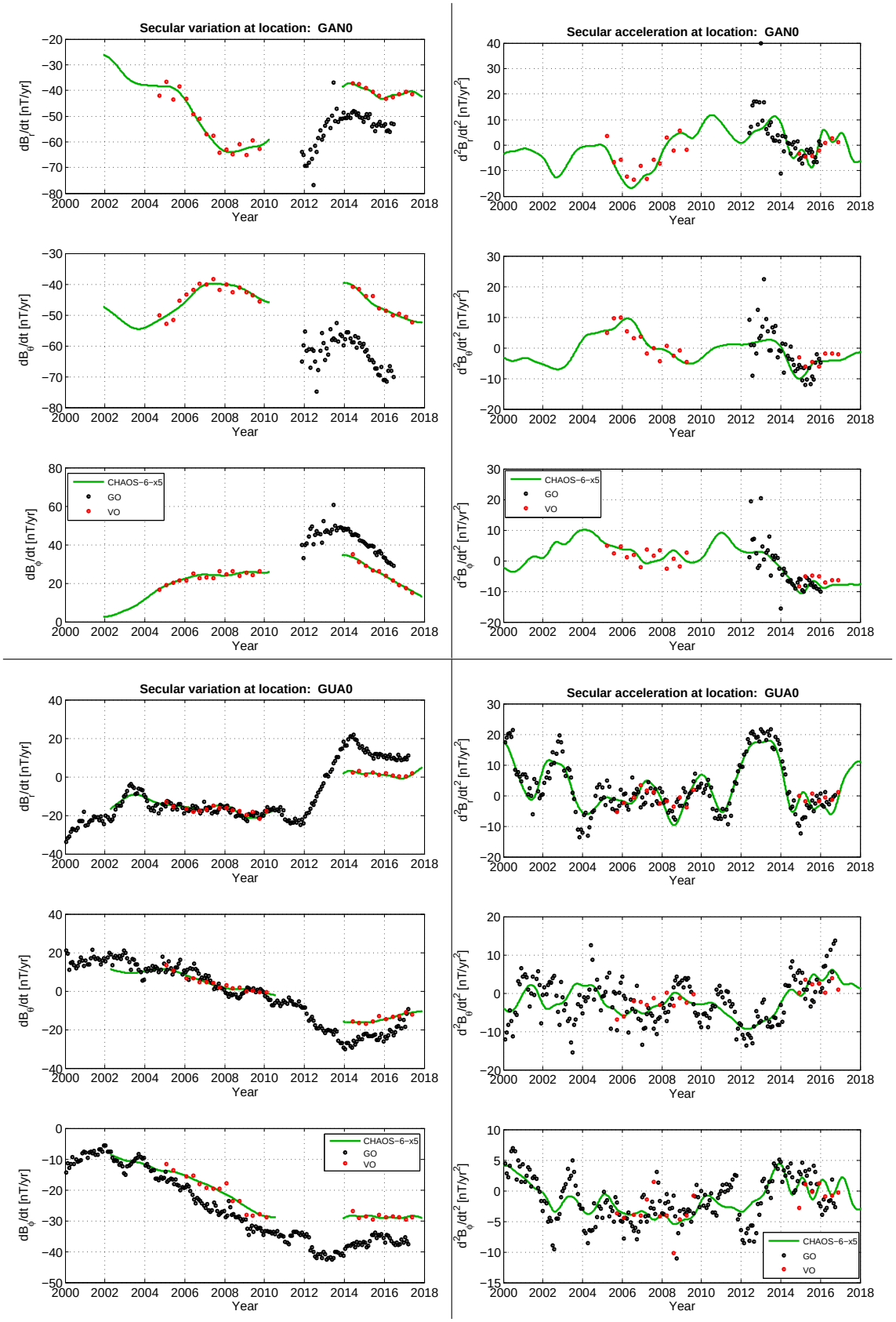

Figure C.3: Time series of SV (left) and SA (right) showing VO's (red dots) using 4 month data windows, GO's (black dots) and CHAOS-6-x5 model predictions (green) using SH degrees up to $n = 16$. For SV and SA fields the CHAOS-6-x5 estimates are plotted at VO altitudes (i.e. 370km and 490km) and at Earth's surface, respectively.

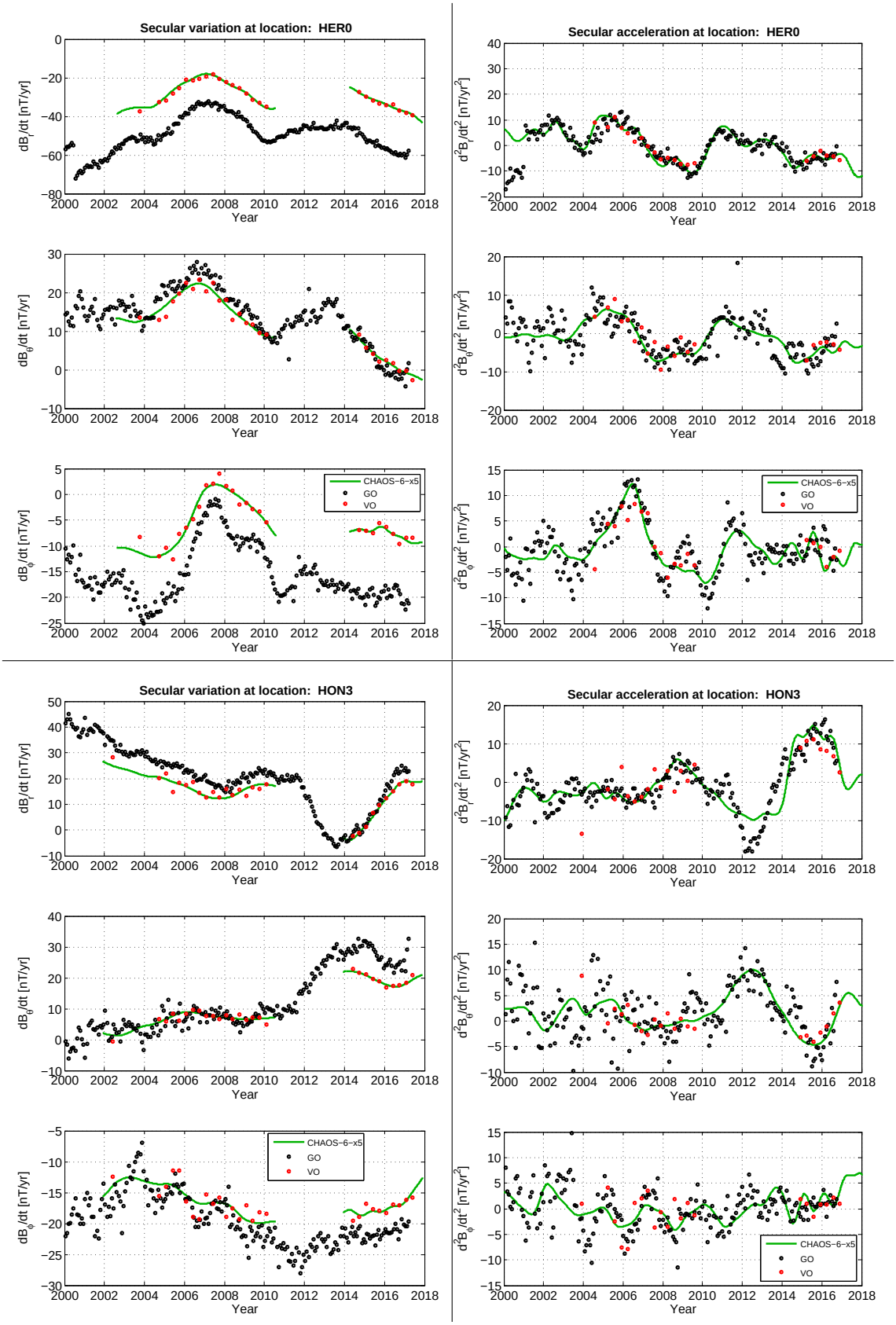

Figure C.4: Time series of SV (left) and SA (right) showing VO's (red dots) using 4 month data windows, GO's (black dots) and CHAOS-6-x5 model predictions (green) using SH degrees up to $n = 16$. For SV and SA fields the CHAOS-6-x5 estimates are plotted at VO altitudes (i.e. 370km and 490km) and at Earth's surface, respectively.

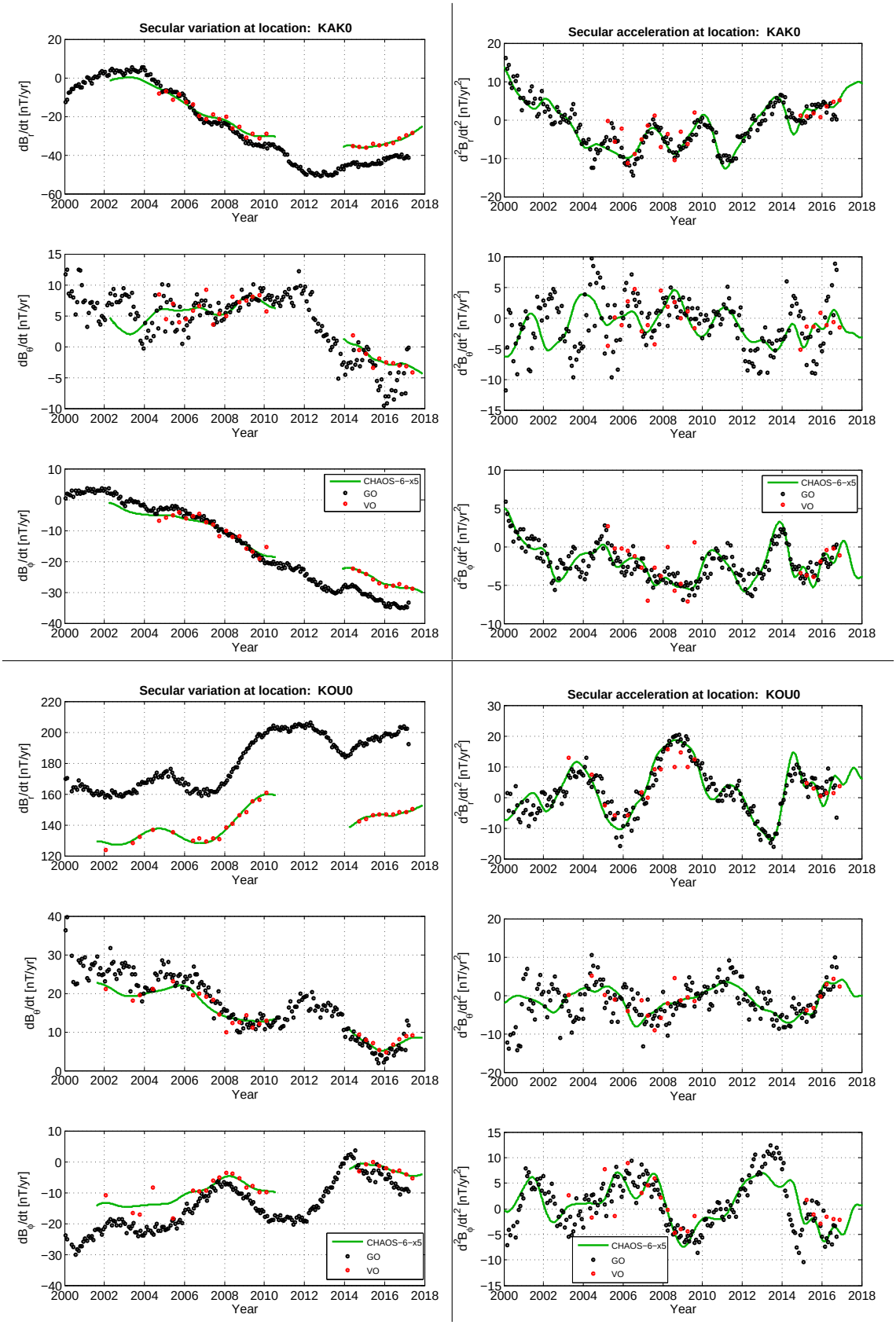

Figure C.5: Time series of SV (left) and SA (right) showing VO's (red dots) using 4 month data windows, GO's (black dots) and CHAOS-6-x5 model predictions (green) using SH degrees up to $n = 16$. For SV and SA fields the CHAOS-6-x5 estimates are plotted at VO altitudes (i.e. 370km and 490km) and at Earth's surface, respectively.

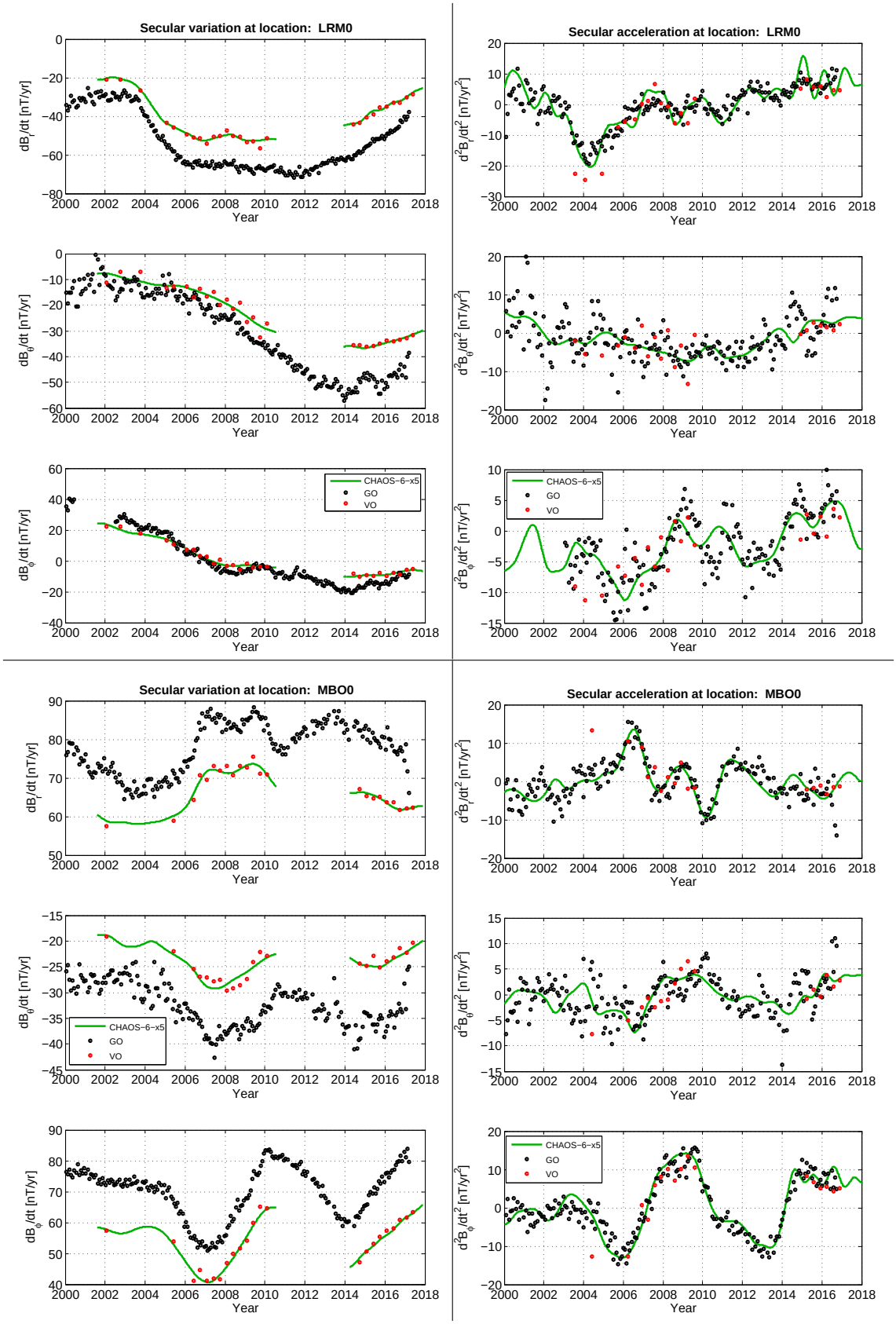

Figure C.6: Time series of SV (left) and SA (right) showing VO's (red dots) using 4 month data windows, GO's (black dots) and CHAOS-6-x5 model predictions (green) using SH degrees up to $n = 16$. For SV and SA fields the CHAOS-6-x5 estimates are plotted at VO altitudes (i.e. 370km and 490km) and at Earth's surface, respectively.

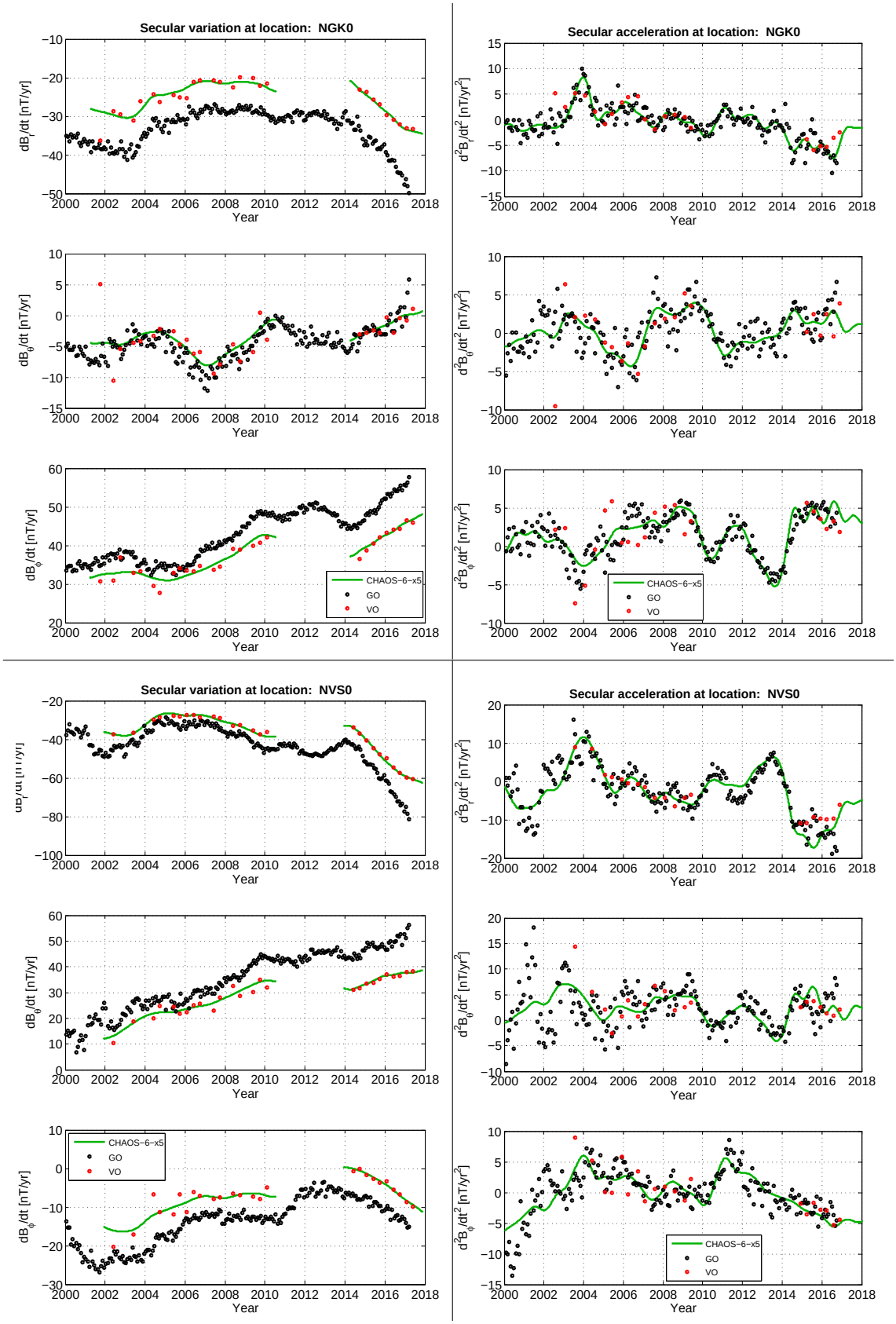

Figure C.7: Time series of SV (left) and SA (right) showing VO's (red dots) using 4 month data windows, GO's (black dots) and CHAOS-6-x5 model predictions (green) using SH degrees up to $n = 16$. For SV and SA fields the CHAOS-6-x5 estimates are plotted at VO altitudes (i.e. 370km and 490km) and at Earth's surface, respectively.

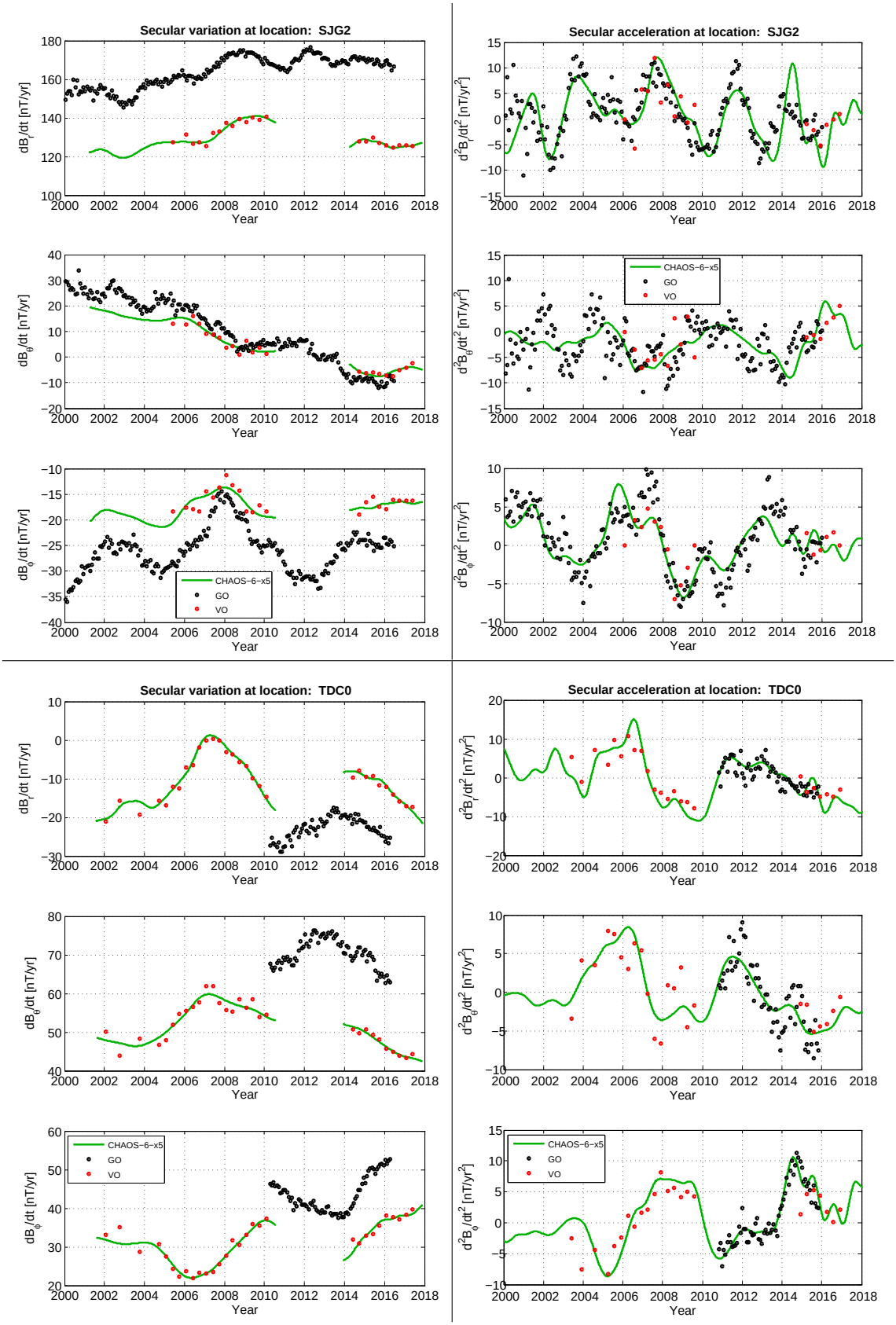

Figure C.8: Time series of SV (left) and SA (right) showing VO's (red dots) using 4 month data windows, GO's (black dots) and CHAOS-6-x5 model predictions (green) using SH degrees up to $n = 16$. For SV and SA fields the CHAOS-6-x5 estimates are plotted at VO altitudes (i.e. 370km and 490km) and at Earth's surface, respectively.